Πρόγραμμα Διδακτορικών Σπουδών της Σχολής Ηλεκτρολόγων Μηχανικών και Μηχανικών Υπολογιστών
Εθνικό Μετσόβιο Πολυτεχνείο

Πολυκλιμακωτή Προσομοίωση της Ασθένειας του Καρκίνου και *In Silico* Ιατρική (Μάθημα 705)

ΔΙΑΦΑΝΕΙΕΣ ΟΛΩΝ ΤΩΝ ΠΑΡΑΔΟΣΕΩΝ

(ΤΕΤΑΡΤΗ ΒΕΛΤΙΩΜΕΝΗ ΕΚΔΟΣΗ, 6 Νοεμβρίου 2020)

Γεώργιος Σ. Σταματάκος

Διευθυντής Ερευνών - Research Professor – Καθηγητής Ερευνας
Ερευνητικό Πανεπιστημιακό Ινστιτούτο Συστημάτων Επικοινωνιών και Υπολογιστών (ΕΠΙΣΕΥ)
Σχολή Ηλεκτρολόγων Μηχανικών και Μηχανικών Υπολογιστών (ΣΗΜΜΥ)
Εθνικό Μετσόβιο Πολυτεχνείο (ΕΜΠ)
Διευθυντής της Ερευνητικής Ομάδας για την In Silico Ογκολογία και την In Silico Ιατρική, ΕΠΙΣΕΥ-ΣΗΜΜΥ-ΕΜΠ
Επισκέπτης Καθηγητής της Ιατρικής Σχολής του Πανεπιστημίου του Saarland, Γερμανία (1/7/2019-15/9/2019)
Επισκέπτης Καθηγητής της ΣΗΜΜΥ, ΕΜΠ (2016-2019)
gestam@central.ntua.gr, http://in-silico-oncology.iccs.ntua.gr/

Πρόγραμμα Διδακτορικών Σπουδών της Σχολής Ηλεκτρολόγων Μηχανικών και Μηχανικών Υπολογιστών ΕΜΠ

Πολυκλιμακωτή Προσομοίωση της Ασθένειας του Καρκίνου και *In Silico* Ιατρική (705)

Μάθημα 1ο

Εισαγωγή στην Πολυκλιμακωτή Προσομοίωση Ασθενειών (ΠΚΠΑ) και την *In Silico* Ιατρική. Τα Παραδείγματα της Πολυκλιμακωτής Προσομοίωσης του Καρκίνου (ΠΚΠΚ) και της *In Silico* Ογκολογίας

Γεώργιος Σ. Σταματάκος

Διευθυντής Ερευνών - Research Professor– Καθηγητής Ερευνας
Ερευνητικό Πανεπιστημιακό Ινστιτούτο Συστημάτων Επικοινωνιών και Υπολογιστών (ΕΠΙΣΕΥ)
Σχολή Ηλεκτρολόγων Μηχανικών και Μηχανικών Υπολογιστών (ΣΗΜΜΥ)
Εθνικό Μετσόβιο Πολυτεχνείο (ΕΜΠ)
Διευθυντής της Ερευνητικής Ομάδας για την In Silico Ογκολογία και την In Silico Ιατρική, ΕΠΙΣΕΥ-ΣΗΜΜΥ-ΕΜΠ
Επισκέπτης Καθηγητής της Ιατρικής Σχολής του Πανεπιστημίου του Saarland, Γερμανία (1/7/2019-15/9/2019)
Επισκέπτης Καθηγητής της ΣΗΜΜΥ, ΕΜΠ (2016-2019)
gestam@central.ntua.gr, http://in-silico-oncology.iccs.ntua.gr/


New postgraduate subject
www.vph-institute.org/news/new-postgraduate-subject-on-multiscale-cancer-modelling-and-in-silico-medicine-mscm-ism.html
VPH Institute
Building the Virtual Physiological Human
ABOUT
MEMBERSHIP
GOVERNANCE
COLLABORATIONS
VIDEOS
DOCUMENTS
NATIONAL NETWORKS
NEWSLETTER
Subscribe to the VPH
Home » News list » New postgraduate subject on Multiscale Cancer Modelling and In Silico Medicine (MSCM & ISM)
NEW POSTGRADUATE SUBJECT ON MULTISCALE CANCER MODELLING AND IN SILICO MEDICINE (MSCM & ISM)
The School of Electrical and Computer Engineering (SECE) of the National Technical University of Athens (NTUA) will be opening this new post-graduate course in October 2014.
MSCM & ISM will be the first postgraduate subject specifically dedicated to in silico medicine. This is a really positive sign for the VPH community that reinforces the increasing importance of computer simulation in medical research.
The subject has been proposed by Research Professor Georgios Stamatakos, ICCS-NTUA, a very active VPH member and coordinator of the running VPH project CHIC "Computational Horizons In Cancer" (http://chic-vph.eu/)
The basic textbook that will be used in the course is "Multiscale Cancer Modeling", edited by Tomas Deisboeck and Georgios S . Stamatakos, together with additional material including the Proceedings of the Virtual Physiological Human Conference held in London in 2012: "VPH2012 – Integrative Approaches to Computational Biomedicine"
The postgraduate course will focus on the following 8 topics:

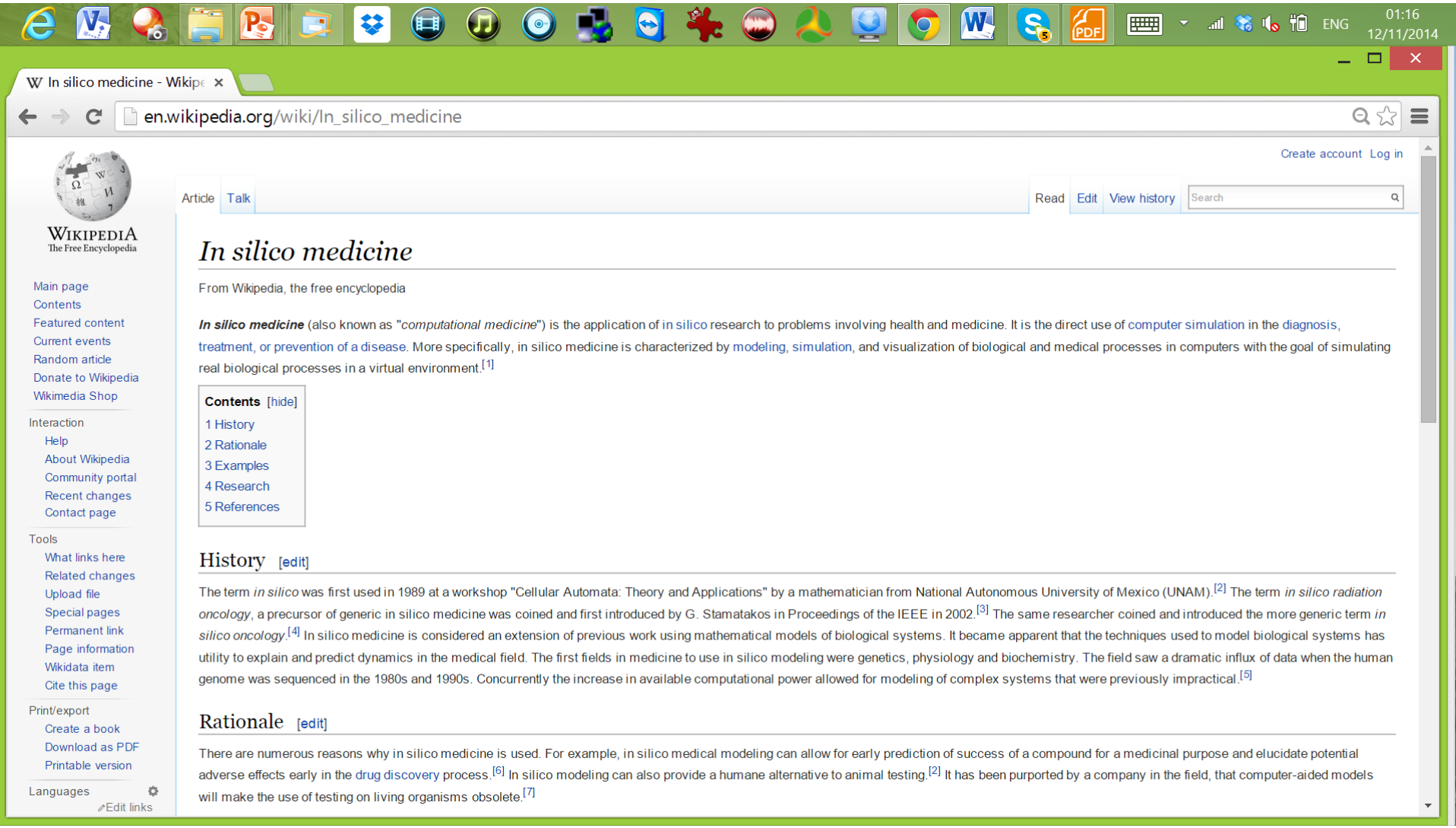

VISITED ON 12 NOV. 2014

PHILOSOPHIÆ
NATURALIS
PRINCIPIA
MATHEMATICA

PARS SECUNDA
DE MATERIA VIVENTI

DE PHENOMENIS IN MULTIS PLANIS

Sectio : De Cancro

A "book" to be written by ***thousands*** of interdisciplinary researchers WORLDWIDE

ΤΙΤΛΟΣ, ΑΝΤΙΚΕΙΜΕΝΟ, ΣΚΟΠΟΣ, ΒΑΣΙΚΟ ΔΙΔΑΚΤΙΚΟ ΕΓΧΕΙΡΙΔΙΟ ΚΑΙ ΠΕΡΙΕΧΟΜΕΝΑ ΤΟΥ ΠΡΟΤΕΙΝΟΜΕΝΟΥ ΑΠΟ ΤΟ Γ. ΣΤΑΜΑΤΑΚΟ ΝΕΟΥ ΜΕΤΑΠΤΥΧΙΑΚΟΥ ΜΑΘΗΜΑΤΟΣ ΤΗΣ ΣΗΜΜΥ

i. ΤΙΤΛΟΣ ΤΟΥ ΜΑΘΗΜΑΤΟΣ

Πολυκλιμακωτή Προσομοίωση της Ασθένειας του Καρκίνου και *In Silico* Ιατρική

ii. ΑΝΤΙΚΕΙΜΕΝΟ ΤΟΥ ΜΑΘΗΜΑΤΟΣ

Αντικείμενο του μαθήματος είναι οι μαθηματικές και υπολογιστικές μέθοδοι, οι τεχνολογίες, τα ολοκληρωμένα τεχνολογικά συστήματα και οι μέθοδοι κλινικής επιβεβαίωσης της αξιοπιστίας των συστημάτων που έχουν αναπτυχθεί ή αναπτύσσονται με σκοπό την πολυκλιμακωτή (multiscale) προσομοίωση γενικά των ασθενειών, και ειδικά του υπερπολύπλοκου *φυσικού φαινομένου* του καρκίνου, και της απόκρισής τους σε ποικίλες θεραπευτικές στρατηγικές και σχήματα εντός του *πραγματικού* κλινικού περιβάλλοντος.

Ο όρος «πολυκλιμακωτή προσομοίωση» (multiscale modelling) υποδηλώνει την προσομοιωτική θεώρηση πολλών χωροχρονικών κλιμάκων της βιοπολυπλοκότητας *συγχρόνως*. Αυτό το χαρακτηριστικό διαφοροποιεί θεμελιωδώς την πολυκλιμακωτή προσομοίωση βιολογικών συστημάτων από τις κλασσικές προσομοιώσεις βιολογικών ή φυσιολογικών συστημάτων, δεδομένου ότι στην πολυκλιμακωτή προσομοίωση απαιτείται η διατύπωση και ο έλεγχος εφαρμοσιμότητας νέων αρχών (principles/principia) διαρκούς μεταφοράς πληροφορίας μεταξύ των κλιμάκων της βιοπολυπλοκότητας (π.χ. από την μοριακή προς την κυτταρική προς την ιστική προς την οργανική προς τη συστημική κλίμακα κλίμακα κτλ. και αντιστρόφως). Μία τέτοια αρχή είναι η αρχή της «σύνοψης και μεταπήδησης» ("summarize and jump") που έχει προταθεί από τον προτείνοντα το μάθημα.

Ο συνδυασμός τέτοιων αρχών με τη λεπτομερή μοντελοποίηση των κρίσιμων βιολογικών μηχανισμών σε πολλές χωροχρονικές κλίμακες *συγχρόνως* έχει οδηγήσει στην ανάπτυξη πολυκλιμακωτών *μηχανιστικών μοντέλων* και προσομοιωτικών συστημάτων όπως των Ογκοπροσομοιωτών (Oncosimulators) στην περίπτωση της Ογκολογίας. Τα εν λόγω μοντέλα, σε αντίθεση με τα ευρύτατα διαδεδομένα μέχρι σήμερα μοντέλα που βασίζονται σε γενικές στοχαστικές/στατιστικές μεθόδους και/ή σε μεθόδους μηχανικής μάθησης (όπως π.χ. νευρωνικά δίκτυα), που είναι γνωστές και σαν «μέθοδοι μαύρου κουτιού» ή "black box methods", μπορούν να προσφέρουν σε βάθος ποιοτική και ποσοτική κατανόηση των σύνθετων πολυκλιμακωτών βιολογικών φαινομένων, δηλαδή των *φυσικών φαινομένων της ζώσας ύλης*. Μια τέτοια "Νευτώνια" προσέγγιση, σε συνέχεια της ολοκλήρωσης της κλινικής της επιβεβαίωσης μέσω αυστηρών κλινικών ελέγχων, προσφέρει μεγάλες δυνατότητες στον επιστημονικά θεμελιωμένο (rational) εξατομικευμένο σχεδιασμό της θεραπείας με την αξιοποίηση των ατομικών πολυκλιμακωτών δεδομένων του ασθενούς (μοριακών, ιστολογικών, απεικονιστικών κτλ. *συγχρόνως*). Επίσης προσφέρει μεγάλες δυνατότητες στο σχεδιασμό νέων κλινικών ελέγχων καθώς και στην επιστημονική κατανόηση των αποτελεσμάτων τους, στο σχεδιασμό νέων φαρμάκων, στην ανάπτυξη νέων θεραπευτικών στρατηγικών, στη διαμόρφωση νέων και πρωτότυπων συνδυασμών θεραπευτικών στρατηγικών που είναι ήδη σε χρήση κτλ. Σημειώνεται ότι η μη περίληψη της διδασκαλίας μέθοδων "black box" στο προτεινόμενο μάθημα δε σημαίνει ότι αυτές δεν χρησιμοποιούνται επικουρικά κατά την πρακτική εφαρμογή των μηχανιστικών πολυκλιμακωτών μοντέλων. Το τελευταίο γίνεται για τη βελτιστοποίηση της τελικής φάσης της κλινικής προσαρμογής των μηχανιστικών πολυκλιμακωτών μοντέλων. Η διδασκαλία "black box" μεθόδων καλύπτεται ήδη ικανοποιητικά από άλλα μαθήματα.

Η εξατομίκευση της θεραπείας επιτυγχάνεται μέσω της διεξαγωγής πειραμάτων στον υπολογιστή ή σε μεγάλα υπολογιστικά συστήματα (*in silico*). Ο όρος *in silico* χρησιμοποιείται ήδη εκτεταμένα ακριβώς για να υποδηλώσει την εισαγωγή μιας νέας μεθόδου πειραματισμού στην κλινική πράξη η οποία επεκτείνει δραστικά τις δυνατότητες των κλασικών πειραματισμών *in vitro* και *in vivo*. Ετσι ανοίγονται νέοι ορίζοντες στην έρευνα και στην κλινική εφαρμογή.

Το παρόν μάθημα, άν και παρουσιάζει κατά πλάτος βασικές αρχές της πολυκλιμακωτής προσομοίωσης που εφαρμόζονται σε πολλές διαφορετικές ασθένειες, χρησιμοποιεί το πλέον χαρακτηριστικό παράδειγμα δηλαδή αυτό του καρκίνου και της *In Silico* Ογκολογίας για να παρουσιάσει κατά βάθος και αρκετά ολοκληρωμένα τον τρόπο προσέγγισης, σκέψης και υλοποίησης του μηχανικού στον εν λόγω αναδυόμενο χώρο. Ο καρκίνος αποτελεί ένα εξαιρετικό διδακτικό παράδειγμα (paradigm) για τον ευρύτερο χώρο των ιατρικών επιστημών, κλινικών πρακτικών και τεχνολογιών, αφού η γενική φιλοσοφία προσέγγισης που υιοθετείται είναι ως ένα βαθμό εφαρμόσιμη και σε πολλούς άλλους ιατρικούς χώρους και ειδικότητες. Αυτό συμβαίνει κυρίως λόγω του ότι ο καρκίνος μπορεί να εμπλέξει δυνητικά κάθε ιστό, όργανο και σύστημα του ανθρώπινου οργανισμού. Σημειώνεται ότι η κατ'αυτό τον τρόπο αναδυόμενη επιστημονική, τεχνολογική και μελλοντικά κλινική περιοχή της *In Silico* Ογκολογίας αποτελεί ένα άριστο παράδειγμα θεμελίωσης, διαμόρφωσης και εξέλιξης της ευρύτερης περιοχής της *In Silico* Ιατρικής. Αλλωστε ο όρος *In Silico* Ιατρική ιστορικά αποτέλεσε επέκταση της έννοιας της *In Silico* Ογκολογίας. (http://cordis.europa.eu/result/brief/rcn/6061_en.html). Αυτό εξηγείται εύκολα και απο το γεγονός ότι ο καρκίνος είναι *η κατ' εξοχήν πολυκλιμακωτή ασθένεια*, η οποία εκφράζεται πολύ έντονα σε όλες τις χωροχρονικές κλίμακες βιοπολυπλοκότητας με τη δημιουργία νέων ιστών παθολογικής σύστασης (νεοπλασίες).

Διευκρινίζεται ότι η έννοια της *In Silico* Ογκολογίας (και κατ' επέκταση της *In Silico* Ιατρικής), ως επιστημονικής και τεχνολογικής περιοχής που οδηγείται από συγκεκριμένα πρακτικά κλινικά ερωτήματα - τα οποία διατυπώνονται στα πλαίσια κλινικών ελέγχων (clinical trials) - ακολουθεί *πρωτίστως* την «εκ των άνω προς τα κάτω» («top-down») προσομοιωτική προσέγγιση, όπως αυτή έχει προταθεί από τον προτείνοντα το μάθημα και έχει γίνει αποδεκτή από την επιστημονική κοινότητα που δραστηριοποιείται στο χώρο. Αυτή η ρεαλιστική προσέγγιση αποβλέπει στην απάντηση πρακτικών κλινικών προβλημάτων ξεκινώντας από τη συνήθη κλινική μακροσκοπική κλίμακα και τα αντίστοιχα δεδομένα του ασθενούς. Ακολουθεί ο εμπλουτισμός τους με πρόσθετη πληροφορία καθώς προχωρεί προς τις μικροσκοπικές κλίμακες και αξιοποιεί τα αντίστοιχα δεδομένα. Διευκρινίζεται επίσης ότι στην κλασσική προσομοίωση βιολογικών συστημάτων ή ασθενειών οι αντίστοιχες μοντελοποιήσεις κατά κανόνα αναπτύσσονται στα πλαίσια της γενικής Βιολογίας και Φυσιολογίας με την προφανή προσέγγιση «εκ των κάτω προς τα άνω» («bottom-up»), δηλαδή ξεκινούν από τη μικροσκοπική θεώρηση και προχωρούν προς μακροσκοπικές κλίμακες. Αποσκοπούν δε αυτές στην απόκτηση καλύτερης (αν και μερικές φορές απλώς διαισθητικής) κατανόησης των βιολογικών φαινομένων υπό ιδεατές συνθήκες παρά στην ανάπτυξη συγκεκριμένων και κλινικά εφαρμόσιμων εργαλείων και συστημάτων για την *εξατομικευμένη* βελτιστοποίηση της θεραπείας ασθενιών στο *πραγματικό* και πολύ συγκεκριμένο κλινικό περιβάλλον.

iii. ΣΚΟΠΟΣ ΤΟΥ ΜΑΘΗΜΑΤΟΣ

Ο σκοπός του μαθήματος συνίσταται στα εξής:

1. Να διδάξει στους ενδιαφερόμενους μεταπτυχιακούς σπουδαστές τις βασικές αρχές, μεθόδους και αντιπροσωπευτικά παραδείγματα δυνητικών εφαρμογών της Πολυκλιμακωτής Προσομοίωσης Ασθενειών και της *In Silico* Ιατρικής με ιδιαίτερη έμφαση στον καρκίνο και την *In Silico* Ογκολογία.

2. Να διδάξει στο σπουδαστή ο οποίος *δεν* ενδιαφέρεται κατ' ανάγκη να δραστηριοποιηθεί στους παραπάνω χώρους προχωρημένες μαθηματικές και υπολογιστικές μεθόδους και τεχνικές οι οποίες άν και παρουσιάζονται μέσω του χώρου της Βιοϊατρικής/Βιοτεχνολογίας έχουν πολύ γενικότερες εφαρμογές σε εντελώς διαφορετικούς χώρους. Παραδείγματα τέτοιων μεθόδων και τεχνικών αποτελούν τα ακόλουθα κεφάλαια/υποκεφάλαια:

   a) Η αριθμητική επίλυση με τη μέθοδο των πεπερασμένων διαφορών στο πεδίο τοιυ χρόνου του προβλήματος της τρισδιάτατης αντίδρασης-διάχυσης με σύνορο τυχαίας γεωμετρίας και οριακές συνθήκες Neumann. Εφαρμογή της μεθόδου Crank Nicolson και της μεθόδου των συζυγών κλίσεων (conjugate gradient).
   b) Οι βασικές αρχές της γενικής προσομοίωσης Monte Carlo. Παρδείγματα εφαρμογών και περιορισμοί της εφαρμόσιμότητάς της.
   c) Η γενική μέθοδος Προσομοίωσης Διακριτών Γεγονότων (Discrete Event Simulation (DES)) και επεκτάσεις της.

3. Να εξοικειώσει τον ενδιαφερόμενο μεταπτυχιακό σπουδαστή με τον τρόπο σκέψης του μηχανικού όταν αυτός καλείται να επινοήσει λύσεις και να αναπτύξει εφαρμογές σε χώρους υψηλής προτεραιότητας, όπου όμως το υλικό υπόστρωμα στο οποίο καλείται να εργασθεί δεν περιλαμβάνεται στα κλασσικά υλικά υποστρώματα δραστηριοποίησησης του ηλεκτρολόγου μηχανικού και μηχανικού υπολογιστών όπως π.χ. μέταλλα, διηλεκτρικά, κενό κτλ.

4. Να διευρύνει τις γνώσεις του μεταπτυχιακού σπουδαστή στο χώρο της Βιολογίας και της Ιατρικής, ο οποίος φαίνεται να εξελίσσεται σε μείζονα ερευνητικό χώρο για όλες τις περιοχές της επιστήμης και της τεχνολογίας. Αξίζει να σημειωθεί ότι στη λίστα των δέκα σημαντικότερων επιτευγμάτων του 2013 σύμφωνα με την επιθεώρηση Science (http://www.tovima.gr/science/article/?aid=551084) οκτώ από τα δέκα επιτεύγματα αφορούν στη Βιολογία και στην Ιατρική και δύο μόνο σε όλους τους άλλους χώρους. Ειδικά η ανοσοθεραπεία κατά του καρκίνου, δηλαδή η στρατολόγηση του ανοσοποιητικού συστήματος για την εξουδετέρωση των καρκινικών όγκων, ανακηρύχθηκε *το σημαντικότερο επίτευγμα του 2013.* Σημειώνεται ότι η μαθηματική και υπολογιστική προσομοίωση της ανοσοθεραπείας του καρκίνου και η ανάπτυξη αντιστοίχου Ογκοπροσομοιωτή εντός ενός κορυφαίου κλινικού περιβάλλοντος αποτελεί ένα από τα κεντρικά αντικείμενα του ευρωαμερικανικού ολοκληρωμένου ερευνητικού προγράμματος μεγάλης κλίμακας CHIC (Computational Horizons in Cancer: Developing Meta- and Hyper-multiscale Models and Repositories for *In Silico* Oncology) http://chic-vph.eu/ , του οποίου επιστημονικός συντονιστής είναι ο προτείνων το μάθημα. Το θέμα αυτό περιλαμβάνεται και στην ύλη του προτεινόμενου μαθήματος. Σημειώνεται επίσης ότι στο ερευνητικό πρόγραμμα CHIC συμμετέχουν 17 ακαδημαϊκοί, ερευνητικοί και βιομηχανικοί οργανισμοί και η χρηματοδότηση από την Ευρωπαϊκή Επιτροπή ανέρχεται στο ποσό των 10,582,000.00 €. Το παραπάνω γεγονός σε συνδυασμό με πλήθος

Επιτροπή ανέρχεται στο ποσό των 10,582,000.00 €. Το παραπάνω γεγονός σε συνδυασμό με πλήθος άλλων στοιχείων καταδεικνύει την ιδιαίτερη σημασία και την υψηλή προτεραιότητα που δίνει η Ευρωπαϊκή Επιτροπή στην ανάπτυξη της παραδειγματικής επιστημονικής, τεχνολογικής και μελλοντικά κλινικής περιοχής του μαθήματος, δηλαδή της **Πολυεπίπεδης Προσομοίωσης του Καρκίνου και της *In Silico* Ογκολογίας.** Επιπρόσθετα η εκ των κεντρικών θέσεων την οποία κατέχουν τόσο η Πολυκλιμακωτή Προσομοίωση Ασθενειών στο Κλινικό Περιβάλλον όσο και η *In Silico* Ιατρική στο νέο πλαίσιο έρευνας της Ευρωπαικής Επιτροπής HORIZON 2020 οδηγεί αβίαστα στο συμπέρασμα ότι η ενεργή παρακολούθηση του εν λόγω μαθήματος αναμένεται να διευρύνει τις δυνατότητες ερευνητικής επαγγελματικής απασχόλησης μεταπτυχιακών σπουδαστών στον εν λόγω χώρο. Αξίζει ακόμη να σημειωθεί ότι από τα 11 μέλη της Ομάδας για την *In Silico* Ογκολογία του ΕΠΙΣΕΥ-ΕΜΠ, και κατά συνεκδοχή της οικείας Σχολής Ηλεκτρολόγων Μηχανικών και Μηχανικών Υπολογιστών (ΣΗΜΜΥ) του ΕΜΠ, τα 6 μέλη (δηλαδή η πλειοψηφία) είναι απόφοιτοί της. Σε αυτά περιλαμβάνεται και ο Επιστημονικός Υπεύθυνος της Ομάδας και προτείνων το παρόν μάθημα. Οι εξαιρετικές προπτυχιακές σπουδές που παρέχει η ΣΗΜΜΥ σε συνδυασμό με τα ήδη διδασκόμενα μαθήματα στο χώρο της Βιοϊατρικής/Βιοτεχνολογίας αλλά και σε συνδυασμό με το προτεινόμενο μάθημα μπορούν να προσφέρουν συνεργατικά στο μεταπτυχιακό σπουδαστή της ΣΗΜΜΥ ένα στέρεο υπόβαθρο που θα του επιτρέψει χωρίς ιδιαίτερη δυσκολία να δραστηριοποιηθεί επαγγελματικά-ερευνητικά, εφόσον το επιθυμεί, με πρωτότυπο, ευρηματικό και αποτελεσματικό χώρο *και* σε αυτόν τον ταχύτατα εξελισσόμενο χώρο αιχμής και υψηλής κοινωνικής προτεραιότητας. Αξίζει επίσης να τονιστεί ότι η ΣΗΜΜΥ δια της

χώρο αιχμής και υψηλής κοινωνικής προτεραιότητας. Αξίζει επίσης να τονιστεί ότι η ΣΗΜΜΥ δια της Ομάδας για την *In Silico* Ογκολογία του ΕΠΙΣΕΥ-ΕΜΠ είναι **διηπειρωτική ηγέτιδα** στη θεμελίωση, διαμόρφωση και προαγωγή της εν λόγω αναδυόμενης επιστημονικής και τεχνολογικής περιοχής και συνεπώς έχει ένα συγκριτικό επαγγελματικό πλεονέκτημα στο διεθνή ερευνητικό χώρο. Επιβάλλεται λοιπόν η στήριξη της περιοχής με κάθε μέσο, περιλαμβανομένης και της μεταπτυχιακής διδασκαλίας του αντικειμένου της σε δυνητικά νέους ερευνητές του χώρου. Περιττεύει να σχολιασθεί η προφανής σημασία που έχει για την εθνική οικονομία, απασχόληση, ανάπτυξη και μείωση της διαφυγής «μυαλών» (brain drain) μια τέτοια επιβεβλημένη στρατηγική. Αρκεί μόνο να αναφερθεί ότι από το 2006 και μέχρι το 2017 θα έχουν εισρεύσει στο ΕΠΙΣΕΥ-ΕΜΠ και προφανώς στην Ελλάδα από *άκρως ανταγωνιστικά* ευρωπαϊκά και διηπειρωτικά ερευνητικά προγράμματα με αντικείμενο την *In Silico* Ογκολογία αρκετά περισσότερα από 3.5 εκαττομμύρια ευρώ και θα απασχολούνται αμοιβόμενοι ικανοποιητικά τουλάχιστο 11 ερευνητές απόφοιτοι της ΣΗΜΜΥ-ΕΜΠ ή άλλων Πανεπιστημιακών Σχολών.

iv. ΣΥΛΛΟΓΗ ΕΠΙΣΤΗΜΟΝΙΚΩΝ ΕΡΓΑΣΙΩΝ (PROCEEDINGS) ΓΙΑ ΤΗΝ ΠΟΛΥΚΛΙΜΑΚΩΤΗ ΠΡΟΣΟΜΟΙΩΣΗ ΠΟΙΚΙΛΩΝ ΑΣΘΕΝΕΙΩΝ

VPH2012 – Integrative Approaches to Computational Biomedicine
(Proceedings of the Virtual Physiological Human Conference, London 2012) – "**PROCEEDINGS"**

v. ΒΑΣΙΚΟ ΔΙΔΑΚΤΙΚΟ ΕΓΧΕΙΡΙΔΙΟ (TEXTBOOK) ΓΙΑ ΤΗΝ ΠΟΛΥΚΛΙΜΑΚΩΤΗ ΠΡΟΣΟΜΟΙΩΣΗ ΤΟΥ ΚΑΡΚΙΝΟΥ

Multiscale Cancer Modeling, T. Deisboeck and G. Stamatakos Eds, CRC Press, Boca Raton, FL , USA, 2011.
http://www.crcnetbase.com/isbn/9781439814420 - "**TEXTBOOK**"

Σημειώνεται ότι όλοι οι μεταπτυχιακοί σπουδαστές οι οποίοι θα παρακολουθήσουν το εν λόγω μάθημα θα παραλάβουν ηλεκτρονικά αντίγραφα της Συλλογής Εργασιών (PROCEEDINGS) και του Βασικού Διδακτικού Εγχειριδίου (TEXTBOOK) δωρεάν. Πρόσθετο υλικό, όπως διεθνείς δημοσιεύσεις και παρουσιάσεις σε ηλεκτρονική μορφή, θα είναι επίσης διαθέσιμο.

vi. ΠΕΡΙΕΧΟΜΕΝΑ ΤΟΥ ΜΑΘΗΜΑΤΟΣ

Πολυκλιμακωτή Προσομοίωση της Ασθένειας του Καρκίνου και *In Silico* Ιατρική			
ΥΛΗ ΤΟΥ ΜΑΘΗΜΑΤΟΣ			
ΑΥΞΩΝ ΑΡΙΘΜΟΣ ΚΕΦΑΛΑΙΟΥ	**ΤΙΤΛΟΣ ΚΕΦΑΛΑΙΟΥ**	**ΠΕΡΙΕΧΟΜΕΝΑ**	**ΠΑΡΑΠΟΜΠΕΣ ΣΤΟ ΒΑΣΙΚΟ ΕΓΧΕΙΡΙΔΙΟ (TEXTBOOK) ΚΑΙ ΣΕ *ΕΝΔΕΙΚΤΙΚΕΣ* ΑΛΛΕΣ ΠΗΓΕΣ**
1.	Εισαγωγή στην Πολυκλιμακωτή Προσομοίωση Ασθενειών (ΠΚΠΑ) και την *In Silico* Ιατρική. Τα παραδείγματα της Πολυκλιμακωτής Προσομοίωσης του Καρκίνου (ΠΚΠΚ) και *της In Silico* Ογκολογίας.	Ορισμοί. Κλινικό, επιστημονικό και τεχνολογικό πλαίσιο. Αναγκαιότητα και προοπτικές της ΠΚΠΑ και ΠΚΠΚ και της *In Silico* Ιατρικής / *In Silico* Ογκολογίας. Σύντομη ιστορική αναδρομή. Σημασία του μαθήματος και προοπτικές για τον Ηλεκτρολόγο Μηχανικό και Μηχανικό Υπολογιστών. Γενική επισκόπηση της ύλης.	PROCEEDINGS TEXTBOOK - Preface PAPER_A [G. Stamatakos, D. Dionysiou, A. Lunzer, R. Belleman, E. Kolokotroni, E. Georgiadi, M. Erdt, J. Pukacki, S. Rueping, S.Giatili, A. d' Onofrio, S. Sfakianakis, K. Marias, Ch. Desmedt, M. Tsiknakis, N. Graf, "The Technologically Integrated Oncosimulator: Combining multiscale cancer modeling with information technology in the *in silico* oncology context," IEEE J. Biomedical and Health Informatics (πρώην IEEE Transactions on Information Technology in Biomedicine) DOI: 10.1109/JBHI.2013.2284276 (in press, 2013-2014)]

2.	*In Silico* Ιατρική / *In Silico* Ογκολογία: Θέματα Βασικής Επιστήμης.	Βασικές αρχές πολυκλιμακωτής υπολογιστικής προσομοίωσης ασθενειών. Το παράδειγμα του καρκίνου. Παραδείγματα από ασθένειες του καρδιαγγειακού, του μυοσκελετικού, του ανοσοποιητικού και άλλων συστημάτων. Η θεμελιώδης αρχή "Summarize and Jump". Είδη μοντέλων ασθενειών. Κλάσεις μαθηματικών μεθόδων (διακριτές - συνεχείς, νετερμινιστικές - στατιστικές, μηχανιστικές -	TEXTBOOK - Chapter 18 PAPER_B [G. Stamatakos, E. Kolokotroni, D. Dionysiou, E. Georgiadi, C. Desmedt, "An advanced discrete state–discrete event multiscale simulation model of the response of a solid tumor to chemotherapy: Mimicking a clinical study," Journal of Theoretical Biology 266 (2010) 124–13] PROCEEDINGS

		μηχανικής μάθησης κτλ.) . Παραδείγματα κατηγοριών/ τύπων όγκων που θα προσεγγιστούν προσομοιωτικά στο μάθημα (μη-μικροκυτταρικό καρκίνωμα του πνεύμονος, καρκίνος του μαστού, πολύμορφο γλοιοβλάστωμα, νεφροβλάστωμα, καρκίνος του τραχήλου της μήτρας, οξεία λεμφοκυτταρική λευχαιμία). Εξατομίκευση της θεραπείας με πειραματισμό *in silico* (στον υπολογιστή). Ο Ογκοπροσομοιωτής. Πολυδιάστατοι χώροι. Ο υπερπίνακας της ανατομικής περιοχής ενδιαφέροντος. Τελεστές στοιχειωδών βιολογικών μηχανισμών. Χρήση Διακριτών Μαθηματικών (μηχανές	

		Τελεστες στοιχειωδων βιολογικών μηχανισμών. Χρήση Διακριτών Μαθηματικών (μηχανές πεπερασμένων καταστάσεων, κυτταρικά αυτομάτα, τεχνική Monte Carlo, ομαδοποίηση κυττάρων σε κλάσεις ισοδυναμίας, εξειδικευμένοι αλγόριθμοι κτλ). Προσομοίωση Διακριτών Καταστάσεων – Διακριτών Γεγονότων (Discrete Entity – Discrete Event Simulation).Τετραδιάστατη πολυκλιμακωτή προσομοίωση της ανάπτυξης καρκινικών όγκων *in vivo*. Τετραδιάστατη πολυκλιμακωτή προσομοίωση της απόκρισης καρκινικών όγκων *in vivo* σε κλασσικά θεραπευτικά σχήματα (χημειοθεραπεία, ακτινοθεραπεία με εξωτερική ακτινοβόληση,	

		βραχυθεραπεία). Υπολογιστική προσομοίωση της ανάπτυξης και απόκρισης μη στερεών όγκων (π.χ. λευχαιμίας) σε θεραπευτικά σχήματα. Υπολογιστική προσομοίωση της απόκρισης καρκινικών όγκων σε νέες θεραπευτικές μεθόδους (ανοσοθεραπευτικά σχήματα, αντιαγγειογενετικά σχήματα κτλ.). Υπολογιστική προσομοίωση της απόκρισης φυσιολογικών ιστών σε θεραπευτικά σχήματα. Ανάπτυξη σημασιολογικών μεταμοντέλων και υπερμοντέλων για τον καρκίνο και την Ογκολογία. **Αντιστοιχίες με / επεκτάσεις σε άλλες ασθένειες και τη γενική *In Silico* Ιατρική**.	

		***Silico* Ιατρική.**	
3.	*In Silico* Ιατρική / *In Silico* Ογκολογία: Θέματα Τεχνολογίας	Αρχιτεκτονική του Τεχνολογικά Ολοκληρωμένου Ογκοπροσομοιωτή. Συστήματα σχεδιασμού και προγραμματισμού ροής εργασιών (workflow). Υπολογιστικές υποδομές μεγάλης κλίμακας και αυτοματοποιημένα σενάρια εκτέλεσης προσομοιώσεων σε αυτές. Προεπεξεργασία πολυκλιμακωτών κλινικών δεδομένων (απεικονιστικών, ιστοπαθολογικών, μοριακών, θεραπευτικών σχημάτων κτλ.). Ανωνυμοποίηση και ψευδο-ανωνυμοποίηση κλινικών δεδομένων. Ηθικά και νομικά ζητήματα και τεχνολογίες υποστήριξης. Αποθετήρια (repositories)	TEXTBOOK - Chapter 18 PAPER_A PROCEEDINGS

		πολυκλιμακωτών κλινικών δεδομένων, μοντέλων και προβλέψεων. Μέθοδοι οπτικοποίησης των πολυδιάστατων προβλέψεων του Ογκοπροσομοιωτή. Συστήματα παρουσίασης και ανάλυσης των αποτελεσμάτων, της συμπεριφοράς και της αξιοπιστίας του ογκοπροσομοιωτή. Τεχνολογίες ολοκλήρωσης των στοιχείων του ογκοπροσομοιωτή. Διεπαφές. **Αντιστοιχίες με / επεκτάσεις σε άλλες ασθένειες και τη γενική *In Silico* Ιατρική.**	
			ΤΕΧΤΒΟΟΚ Chapter 10

		***Silico* Ιατρική.**	
4.	*In Silico* Ιατρική / *In Silico* Ογκολογία: Θέματα Κλινικών Απαιτήσεων και Εφαρμογών	Θεμελιώδεις αρχές και διαδικασίες κλινικής επιβεβαίωσης της αξιοπιστίας ογκοπροσομοιωτών. Κλινικοί έλεγχοι (clinical trials) ως αξιόπιστες πηγές παροχής πολυκλιμακωτών κλινικών δεδομένων για την κλινική προσαρμογή και επιβεβαίωση της αξιοπιστίας του Ογκοπροσομοιωτή. Τράπεζες βιοπτικού υλικού (υλικού από βιοψίες). Τεχνολογίες διαχείρισης τραπεζών βιοπτικού υλικού. Προϋποθέσεις για την αποδοχή μαθηματικών και υπολογιστκών μοντέλων στην κλινική πράξη. Βασικά κλινικά ερωτήματα – «οδηγοί» για το σχεδιασμό και την ανάπτυξη ογκοπροσομοιωτών. **Αντιστοιχίες με / επεκτάσεις σε άλλες ασθένειες και στη γενική *In Silico* Ιατρική.**	TEXTBOOK - Chapter 19 PROCEEDINGS

5.	Προσομοίωση της διήθησης κλινικών καρκινικών όγκων με τη χρήση της μερικής διαφορικής εξίσωσης (ΜΔΕ) της αντίδρασης – διάχυσης και κατάλληλων οριακών συνθηκών. Αντίστοιχα μαθηματικά και υπολογιστικά προβλήματα στη γενική *In Silico* Ιατρική.	Η περίπτωση του γλοιώματος. Μη επεμβατική εκτίμηση κινητικών παραμέτρων του γλοιώματος *in vivo*. Μαθηματική περιγραφή της εκτίμησης παραμέτρων. Ανισοτροπική κυτταρική κινητικότητα σε ανομοιογενή εγκεφαλικό ιστό. Εκτίμηση της νέκρωσης και του επαναποικισμού του όγκου με μαθηματικές παραμέτρους. Εκτίμηση της επίδρασης του μικροπεριβάλλοντος του όγκου στην αύξηση του γλοιώματος με την παράλληλη σύγκριση τομογραφιών MRI και PET. **Αντιστοιχίες με / επεκτάσεις σε άλλες ασθένειες και τη γενική *In Silico* Ιατρική.**	TEXTBOOK - Chapter 16 TEXTBOOK - Chapter 17 PROCEEDINGS

6.	Αριθμητικές Μέθοδοι για την επίλυση του χωρο-χρονικού προβλήματος της διήθησης καρκινικών όγκων σε υγιείς ιστούς με οριακές συνθήκες. Αντίστοιχα μαθηματικά και υπολογιστικά προβλήματα στη γενική *In Silico* Ιατρική.	Μέθοδοι πεπερασμένων διαφορών στο πεδίο του χρόνου (Finite Difference Time Domain methods). Εφαρμογή της Μεθόδου Crank-Nicolson σε συνδυασμό με τη μεθοδο των συζυγών κλίσεων (conjugate gradient) για την αριθμητική επίλυση της ΜΔΕ της αντίδρασης-διάχυσης κατά την αύξηση του γλοιοβλαστώματος και τη διήθησή του στον εγκέφαλο. Αριθμητική εφαρμογή των οριακών συνθηκών Neumann μεταξύ κρανίου και ενδοκρανιακών ιστών. Χρήση των αποτελεσμάτων για τον εξατομικευμένο σχεδιασμό της ακτινοθεραπείας. Εμβιομηχανική του	PAPER_C [S. Giatili and G. Stamatakos, "A detailed numerical treatment of the boundary conditions imposed by the skull on a diffusion–reaction model of glioma tumor growth. Clinical validation aspects," Applied Mathematics and Computation 218(2012) pp. 8779-8799] PROCEEDINGS

		γλοιώματος και προσομοίωσή της με αριθμητικές μεθόδους όπως πεπερασμένα στοιχεία. **Αντιστοιχίες με / επεκτάσεις σε άλλες ασθένειες και τη γενική *In Silico* Ιατρική.**	
7.	Προσομοίωση της αγγειογένεσης κατά την αύξηση καρκινικών όγκων. Αντίστοιχα μαθηματικά και υπολογιστικά προβλήματα στη γενική *In Silico* Ιατρική.	Αλληλεπίδραση όγκου - μικροπεριβάλλοντος. Μερική διαφορική εξίσωση της αγγειογένεσης. Προσομοίωση της αιματικής ροής και της ανάπτυξης δικτύου τριχοειδών αγγείων. Προσαρμογή του δικτύου τριχοειδών αγγείων και αναδιάταξή του. Αριθμητικές μέθοδοι επίλυσης. Υπολογιστική διερεύνηση του φαινομένου και των βασικών παραγόντων που επιδρούν στην εξέλιξή του. **Αντιστοιχίες με / επεκτάσεις σε άλλες ασθένειες και τη γενική *In Silico* Ιατρική.**	TEXTBOOK - Chapter 13 PROCEEDINGS

		***Silico* Ιατρική.**	
8.	Προσομοίωση μοριακών μονοπατιών, μοριακών δικτύων, διαβίβασης μοριακών σημάτων και της προκύπτουσας συμπεριφοράς του καρκινικού κυττάρου. Αντίστοιχα μαθηματικά και υπολογιστικά προβλήματα στη γενική *In Silico* Ιατρική.	Μοριακές προσομοιώσεις με βάση τις εξισώσεις του Νεύτωνα, το νόμο του Coulomb και τις αρχές της Κβαντομηχανικής. Μοντέλα μοριακής πρόσδεσης. Παραδείγματα προσομοίωσης της αλληλεπίδρασης μορίων φαρμάκων και πρωτεϊνών στην Ογκολογία. Μέθοδοι μοριακής δυναμικής για το χαρακτηρισμό των δομικών ιδιοτήτων μεταλλαγμένων γονιδιακών προϊόντων. Χρήση συνήθων διαφορικών εξισώσεων για την περιγραφή ογκογενετικών και γενικών δικτύων και μονοπατιών μοριακής	TEXTBOOK - Chapter 2 PROCEEDINGS

		σηματοδότησης και αλληλεπίδρασης. Προκύπτουσα συμπεριφορά του καρκινικού κυττάρου. **Αντιστοιχίες με / επεκτάσεις σε άλλες ασθένειες και τη γενική *In Silico* Ιατρική.**	

Outline

- *In Silico* Oncology: An Introduction
- The CHIC Project
- A. A Preliminary Study Exploiting Clinical Trial Data for the Clinical Adaptation of the Core ALL Model
- B. Supporting the prediction of the ALL Oncosimulator parameter values by using machine learning methods on gene expression data
- Conclusions

- ***In Silico* Oncology** is a complex and multiscale combination of sciences and technologies intending to simulate malignant tumour growth and tumour and normal tissue response to therapeutic modalities *at all levels of biocomplexity (multiscale cancer modelling)*
- The **long term goal** is to quantitatively understand cancer and related phenomena and optimize therapeutic interventions by performing in silico (on the computer) experiments based on the individual patient's clinical, imaging, histopathological, molecular and pharmacogenomic data.
- In order to achieve such an ambitious goal translation of cancer models into **the clinical trials** arena is a sine qua non condition

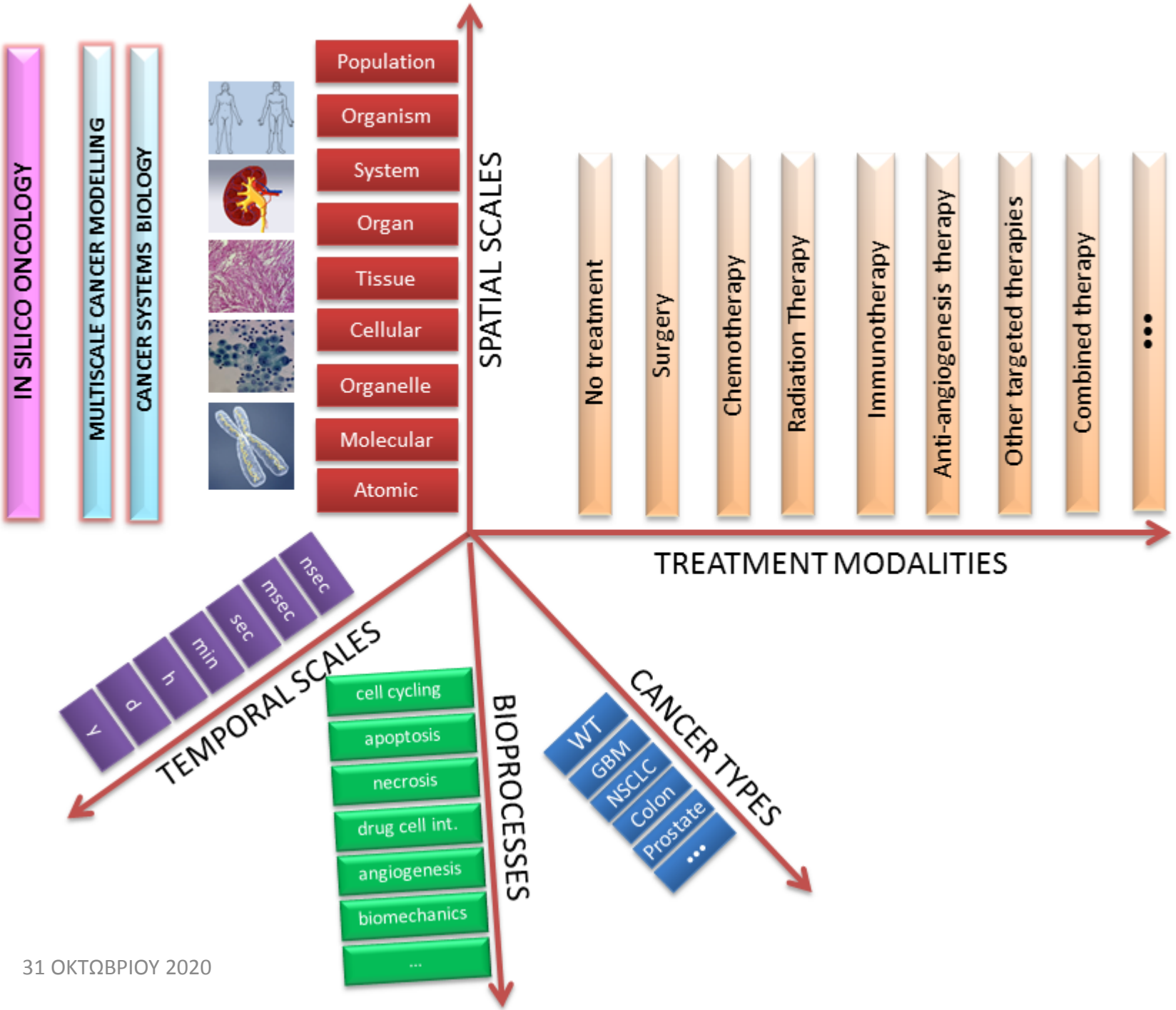
IN SILICO ONCOLOGY
MULTISCALE CANCER MODELLING
CANCER SYSTEMS BIOLOGY
Population
Organism
System
Organ
Tissue
Cellular
Organelle
Molecular
Atomic
SPATIAL SCALES
No treatment
Surgery
Chemotherapy
Radiation Therapy
Immunotherapy
Anti-angiogenesis therapy
Other targeted therapies
Combined therapy
...
TREATMENT MODALITIES
y
d
h
min
sec
msec
nsec
TEMPORAL SCALES
cell cycling
apoptosis
necrosis
drug cell int.
angiogenesis
biomechanics
...
BIOPROCESSES
WT
GBM
NSCLC
Colon
Prostate
...
CANCER TYPES

Cancer Hypermodeling

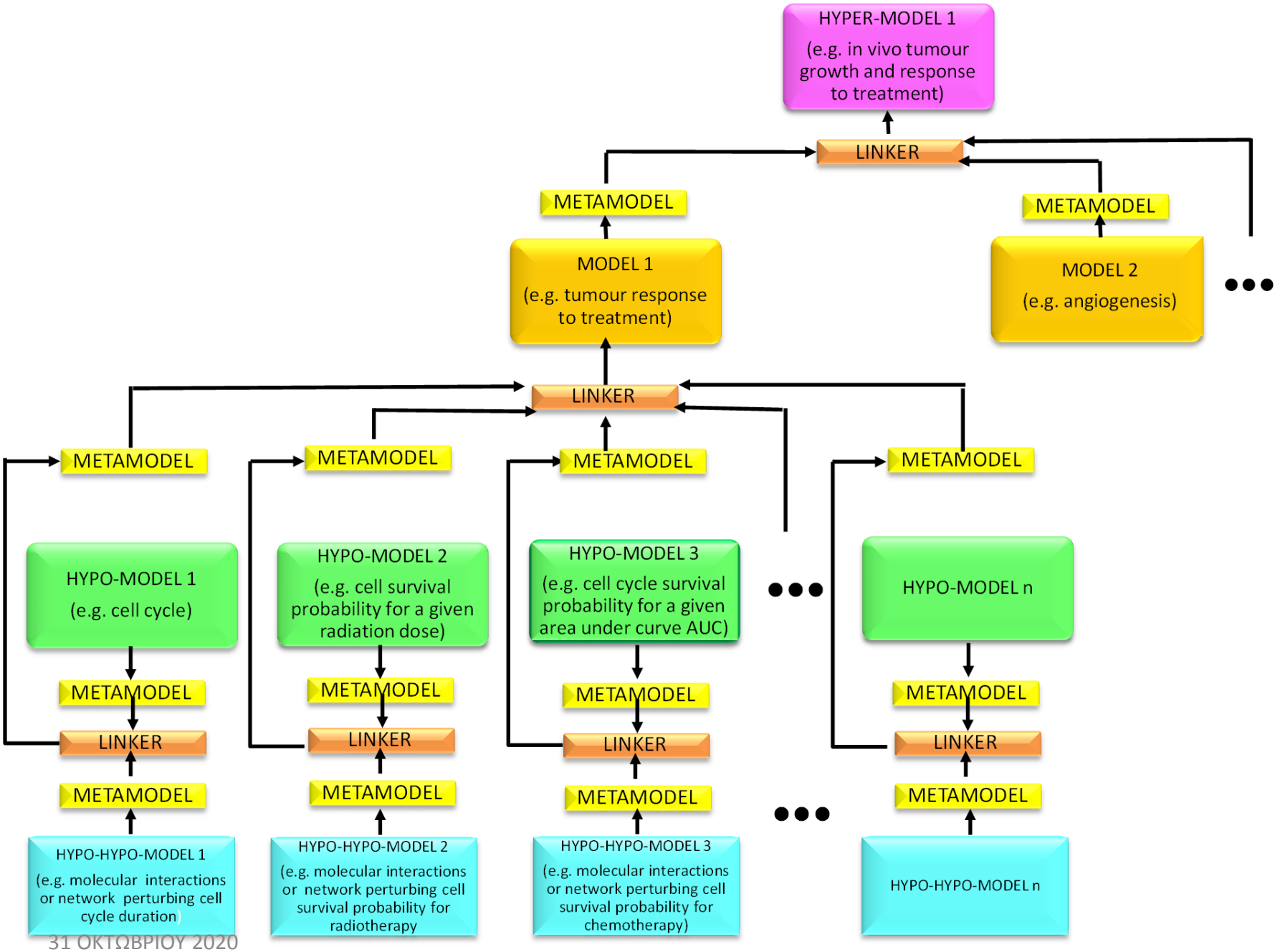
HYPER-MODEL 1
(e.g. in vivo tumour growth and response to treatment)
LINKER
METAMODEL
METAMODEL
MODEL 1
(e.g. tumour response to treatment)
MODEL 2
(e.g. angiogenesis)
LINKER
METAMODEL
METAMODEL
METAMODEL
METAMODEL
HYPO-MODEL 1
(e.g. cell cycle)
HYPO-MODEL 2
(e.g. cell survival probability for a given radiation dose)
HYPO-MODEL 3
(e.g. cell cycle survival probability for a given area under curve AUC)
HYPO-MODEL n
METAMODEL
METAMODEL
METAMODEL
METAMODEL
LINKER
LINKER
LINKER
LINKER
METAMODEL
METAMODEL
METAMODEL
METAMODEL
HYPO-HYPO-MODEL 1
(e.g. molecular interactions or network perturbing cell cycle duration)
HYPO-HYPO-MODEL 2
(e.g. molecular interactions or network perturbing cell survival probability for radiotherapy
HYPO-HYPO-MODEL 3
(e.g. molecular interactions or network perturbing cell survival probability for chemotherapy)
HYPO-HYPO-MODEL n

The Hypermodel Based Oncosimulator

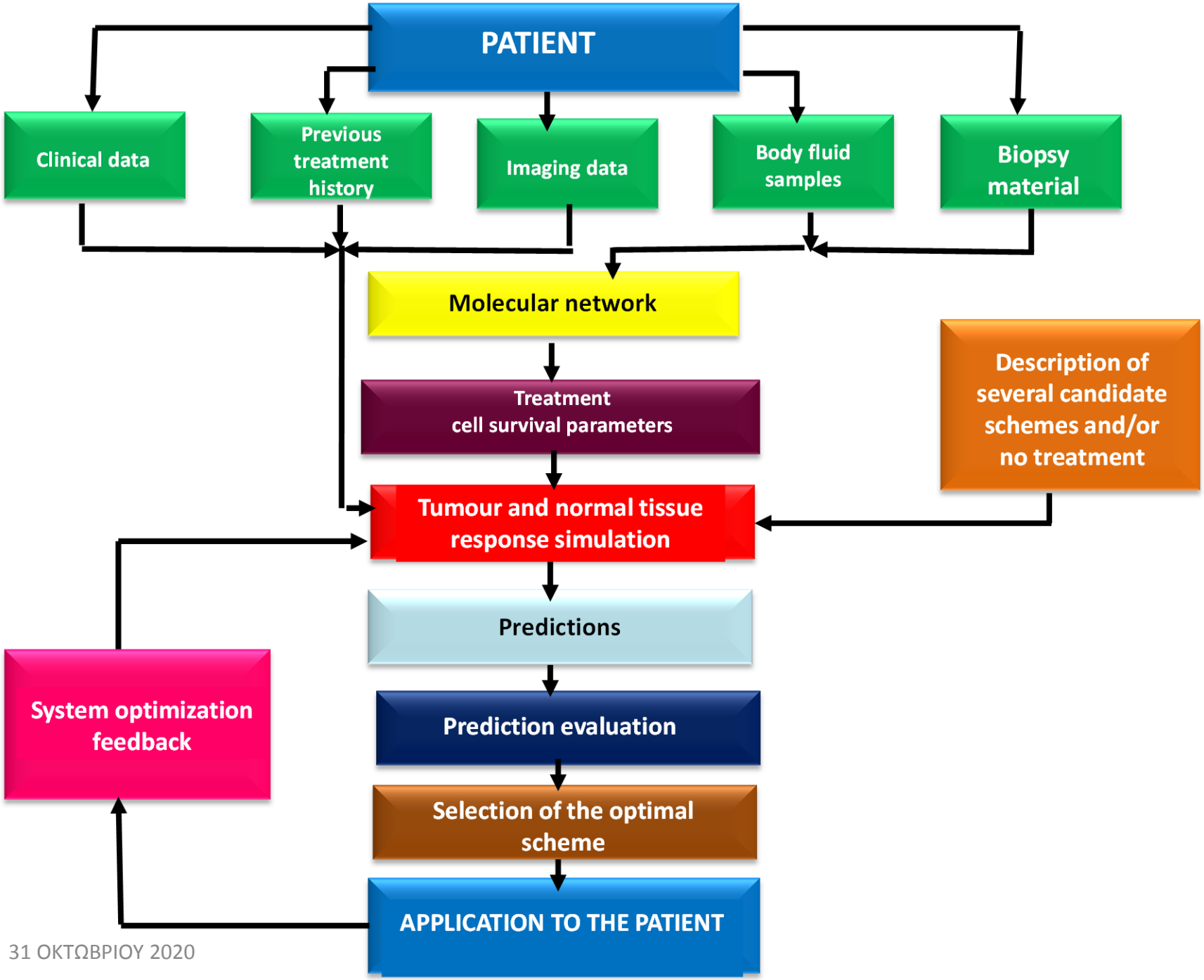
PATIENT
Clinical data
Previous treatment history
Imaging data
Body fluid samples
Biopsy material
Molecular network
Treatment cell survival parameters
Description of several candidate schemes and/or no treatment
Tumour and normal tissue response simulation
Predictions
System optimization feedback
Prediction evaluation
Selection of the optimal scheme
APPLICATION TO THE PATIENT

Multimodeler Hypermodels

The transatlantic (EU-US) CHIC project approach

“Computational Horizons In Cancer (**CHIC**): Developing Meta- and Hyper-Multiscale Models and Repositories for In Silico Oncology”



CHIC PROJECT DATA

- FP7-ICT-2011-9-600841
- 17 partners
- 16 from EU + UPENN from US
- Duration: 48 months (start date: April 2013)
- Project Funding: 10,582,000.00 €
- Coordinating Institution: ICCS-NTUA
- Coordinator (Scientific and Overall): Research Professor Georgios Stamatakos

chic-vph.eu

No	Name	Short name	Country
1	INSTITUTE OF COMMUNICATION AND COMPUTER SYSTEMS	ICCS	Greece
2	EUROPEAN RESEARCH AND PROJECT OFFICE GMBH	EURICE	Germany
3	UNIVERSITAET DES SAARLANDES	USAAR	Germany
4	KATHOLIEKE UNIVERSITEIT LEUVEN	KU Leuven	Belgium
5	UNIVERSITY OF BEDFORDSHIRE	BED	United Kingdom
6	THE UNIVERSITY OF SHEFFIELD	USFD	United Kingdom
7	FOUNDATION FOR RESEARCH AND TECHNOLOGY HELLAS	FORTH	Greece
8	GOTTFRIED WILHELM LEIBNIZ UNIVERSITAET HANNOVER	LUH	Germany
9	THE TRUSTEES OF THE UNIVERSITY OF PENNSYLVANIA	UPENN	United States
10	THE CHANCELLOR, MASTERS AND SCHOLARS OF THE UNIVERSITY OF OXFORD	UOXF	United Kingdom
11	UNIVERSITA DEGLI STUDI DI TORINO	UNITO	Italy
12	UNIVERSITAET BERN	UBERN	Switzerland
13	CUSTODIX NV	CUSTODIX	Belgium
14	PHILIPS ELECTRONICS NEDERLAND B.V.	PHILIPS	Netherlands
15	UNIVERSITY COLLEGE LONDON	UCL	United Kingdom
16	CONSORZIO INTERUNIVERSITARIO CINECA	CINECA	Italy
17	TECHNOLOGICAL EDUCATIONAL INSTITUTE OF CRETE	TEI-C	Greece

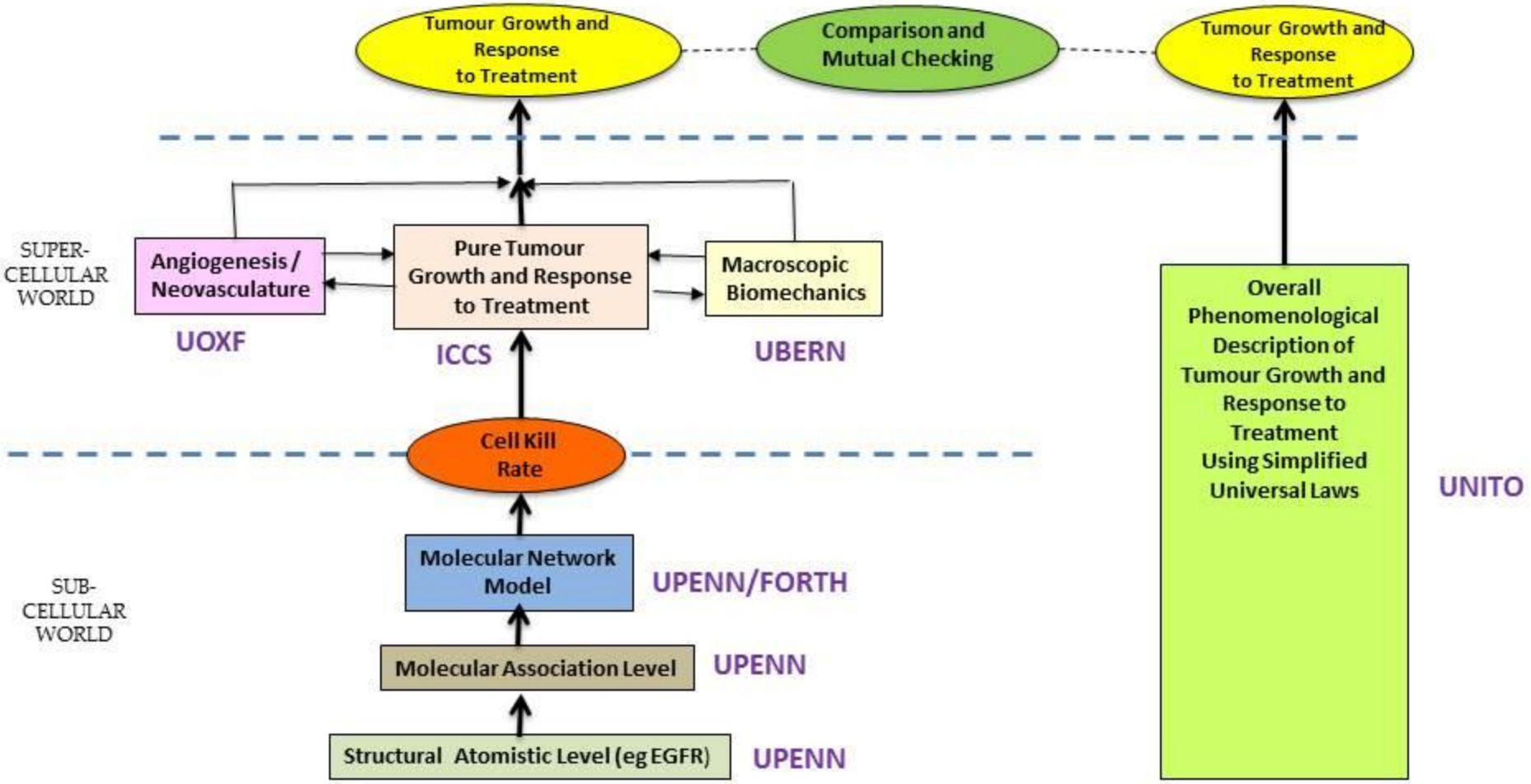

CHIC WP6 ARCHITECTURE OF THE LUNG CANCER MULTI-MODELLER HYPERMODEL

High Level CHIC Platform Architecture

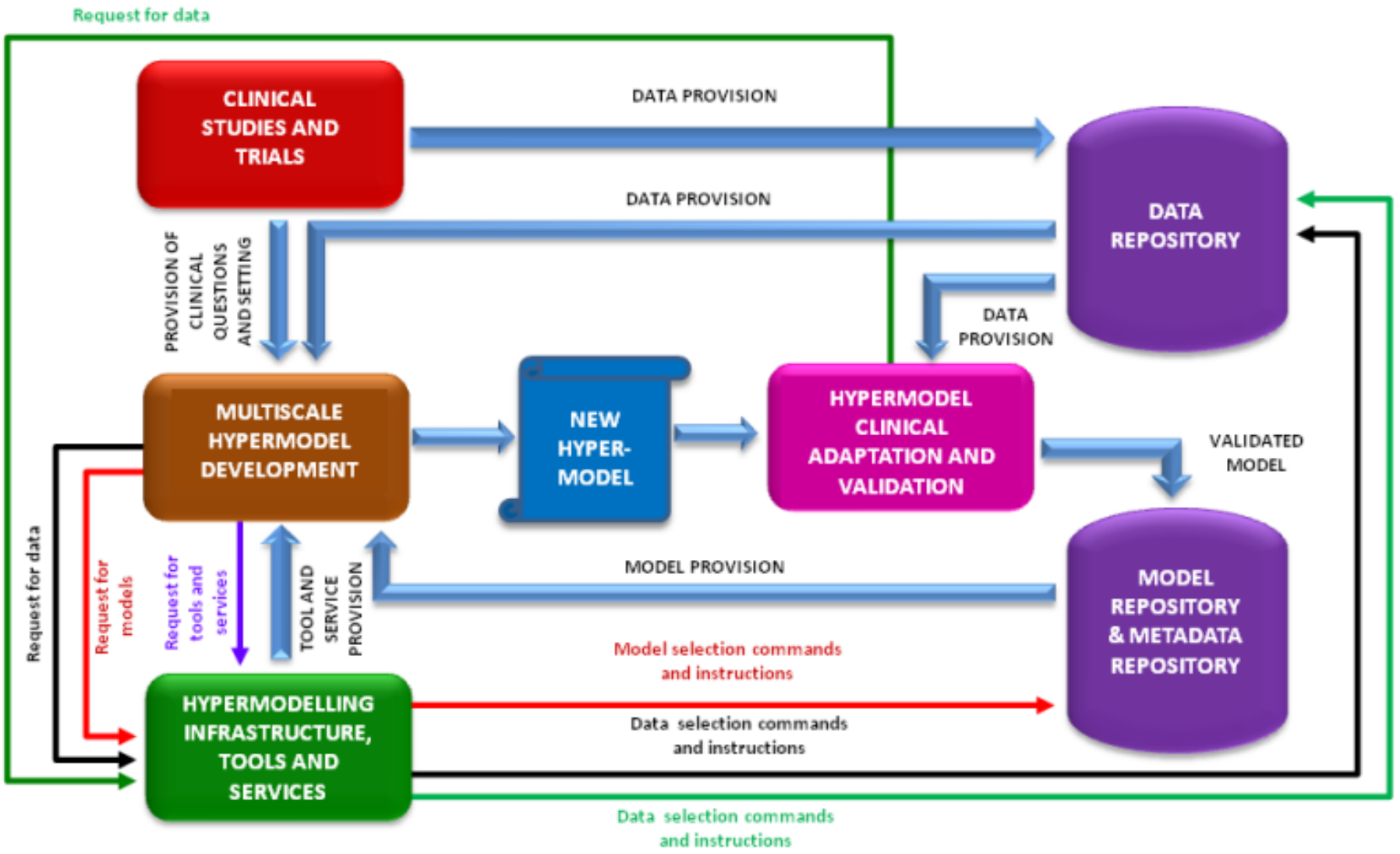

ΒΙΚΙΠΑΙΔΕΙΑ

Ανάδελτα

Από τη Βικιπαίδεια, την ελεύθερη εγκυκλοπαίδεια

Ανάδελτα είναι διανυσματικός διαφορικός τελεστής των μερικών παραγώγων μιας συνάρτησης πολλών ανεξαρτήτων μεταβλητών (συνήθως των 3 διαστάσεων του χώρου). Γενικά, δείχνει τον τρόπο με τον οποίο μεταβάλλεται ένα μέγεθος στο $\mathbf{R}^n$ (συνήθως στο χώρο $\mathbf{R}^3$). Συμβολίζεται με ∇, το οποίο σύμβολο μοιάζει με αναποδογυρισμένο κεφαλαίο Δ. Η χρήση του ανάδελτα εμφανίζεται σε 3 διαφορετικούς τελεστές: Της κλίσης (∇), της απόκλισης ($\nabla\cdot$) και του στροβιλισμού ($\nabla\times$).

Πίνακας περιεχομένων

Κλίση
Ιδιότητες

Απόκλιση
Ιδιότητες

Στροβιλισμός
Ιδιότητες

Τελεστής Laplace (Λαπλάς)

Δείτε επίσης

Παραπομπές

Κλίση

Αν έχουμε μια βαθμωτή συνάρτηση με ανεξάρτητες μεταβλητές τις διαστάσεις του χώρου $f(x, y, z)$ τότε η κλίση της βαθμωτής συνάρτησης είναι το διάνυσμα $\nabla f = gradf = \begin{bmatrix} \frac{\partial f}{\partial x} \\ \frac{\partial f}{\partial y} \\ \frac{\partial f}{\partial z} \end{bmatrix}$. Το διάνυσμα της κλίσης, έχει διάσταση όσες οι ανεξάρτητες μεταβλητές της συνάρτησης.

Αν έχουμε μια διανυσματική συνάρτηση $F(x_1, x_2, x_3) = \begin{bmatrix} f_1(x_1, x_2, x_3) \\ f_2(x_1, x_2, x_3) \\ f_3(x_1, x_2, x_3) \end{bmatrix}$ τότε η κλίση της διανυσματικής συνάρτησης είναι ο πίνακας $\nabla F = gradF = \begin{bmatrix} \nabla f_1 \\ \nabla f_2 \\ \nabla f_3 \end{bmatrix} = \begin{bmatrix} \frac{\partial f_1}{\partial x_1} & \frac{\partial f_1}{\partial x_2} & \frac{\partial f_1}{\partial x_3} \\ \frac{\partial f_2}{\partial x_1} & \frac{\partial f_2}{\partial x_2} & \frac{\partial f_2}{\partial x_3} \\ \frac{\partial f_3}{\partial x_1} & \frac{\partial f_3}{\partial x_2} & \frac{\partial f_3}{\partial x_3} \end{bmatrix}$. Οι στήλες του πίνακα είναι όσες οι ανεξάρτητες μεταβλητές της συνάρτησης. Ο πίνακας που προκύπτει, αποτελεί και τον Ιακωβιανό πίνακα της συνάρτησης F.

Γενικά μιλώντας, η κλίση τανυστή n βαθμού δίνει έναν τανυστή $n+1$ βαθμού (π.χ. η βαθμωτή συνάρτηση βαθμού 0, έδωσε διάνυσμα βαθμού 1). Η επιπλέον διάσταση του τανυστή, είναι ίση με τον αριθμό ανεξάρτητων μεταβλητών της συνάρτησης.

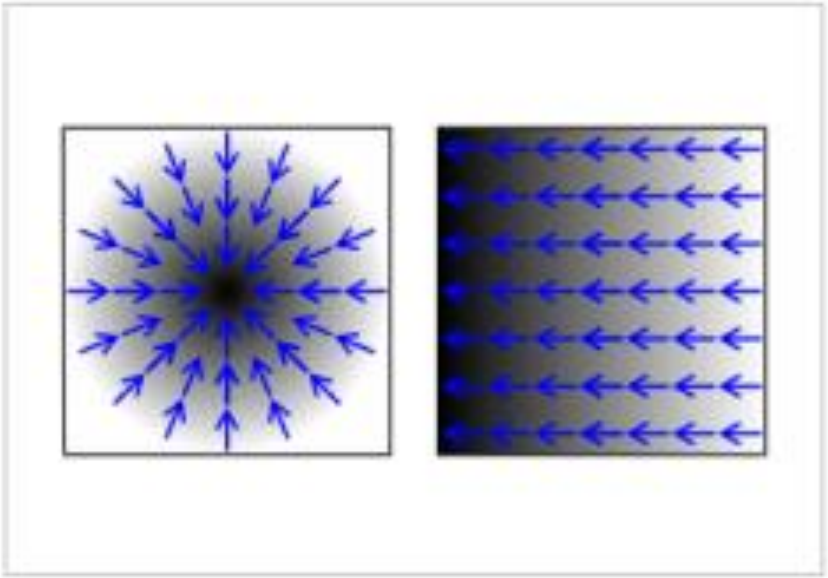

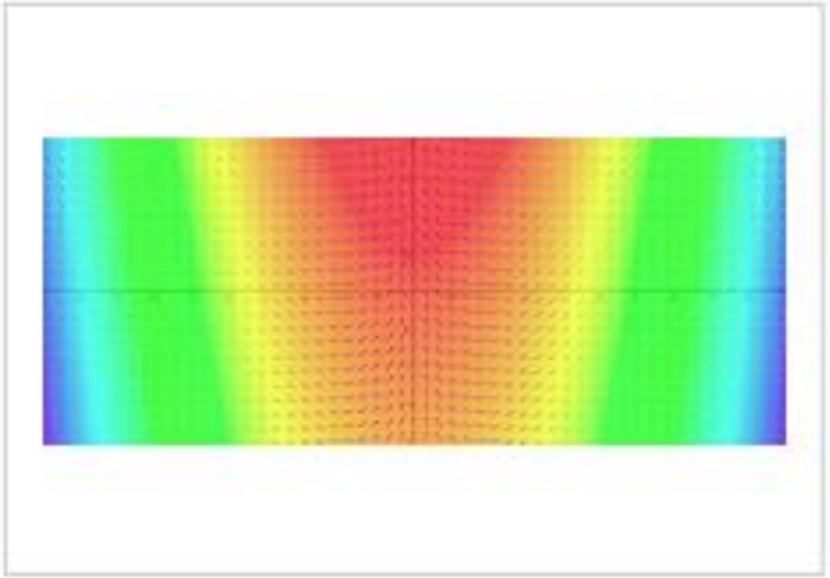

Γραφική απεικόνιση πραγματικής συνάρτησης f και της κλίσης της ∇f η οποία είναι διανυσματική. Η συνάρτηση αναπαρίσταται χρωματικά, όσο πιο μαύρο είναι ένα σημείο, τόσο μεγαλύτερη είναι η τιμή της συνάρτησης. Παρατηρήστε ότι η κλίση δείχνει προς την κατεύθυνση αύξησης των τιμών.

Παρομοίως με προηγουμένως, αλλά αντί για κλίμακα του γκρίζου χρησιμοποιείται χρωματική κλίμακα με μπλε τις μικρότερες τιμές και κόκκινο τις μεγαλύτερες.

Ιδιότητες

- $\nabla(f+g) = \nabla f + \nabla g$
- $\nabla(cf) = c\nabla f$ όταν c μια σταθερά.
- $\nabla(fg) = g\nabla f + f\nabla g$
- Η ∇f δείχνει την κατεύθυνση μέγιστης ανηφόρας για τη συνάρτηση f, και το μέτρο της είναι η παράγωγος κατά κατεύθυνση σε αυτή τη διεύθυνση.
- Αν $\vec{s}$ κανονικό διάνυσμα ($|\vec{s}| = 1$), τότε η $\nabla f \cdot \vec{s}$ είναι η παράγωγος της f στην κατεύθυνση $\vec{s}$.
- Στην εξίσωση $F(x,y,z) = 0$ η οποία αναπαριστά μια επιφάνεια στο χώρο, η κλίση ∇F αναπαριστά το κάθετο (όχι απαραίτητα κανονικό) διάνυσμα σε αυτή την επιφάνεια (άρα το διάνυσμα του εφαπτόμενου επιπέδου στην επιφάνεια). Το κάθετο διάνυσμα στην επιφάνεια $z = f(x,y)$ είναι $\nabla(z - f(x,y))$.
- Το στοιχειώδες εμβαδό της επιφάνειας $F(x,y,z) = 0$ είναι $\left|\frac{\nabla F}{\frac{\partial F}{\partial z}}\right| dxdy = \left|\frac{\nabla F}{\frac{\partial F}{\partial y}}\right| dxdz = \left|\frac{\nabla F}{\frac{\partial F}{\partial x}}\right| dydz$. Το στοιχειώδες εμβαδό της επιφάνειας $z = f(x,y)$ προκύπτει $\sqrt{1 + \left(\frac{\partial F}{\partial x}\right)^2 + \left(\frac{\partial F}{\partial y}\right)^2}\, dxdy$.

Απόκλιση

Αν έχουμε μια διανυσματική συνάρτηση $\boldsymbol{F}(x_1, x_2, x_3) = \begin{bmatrix} f_1(x_1, x_2, x_3) \\ f_2(x_1, x_2, x_3) \\ f_3(x_1, x_2, x_3) \end{bmatrix}$ τότε η απόκλιση της, είναι ο βαθμωτός $\nabla \cdot \boldsymbol{F} = div\boldsymbol{F} = \frac{\partial f_1}{\partial x_1} + \frac{\partial f_2}{\partial x_2} + \frac{\partial f_3}{\partial x_3}$.

Γενικά μιλώντας, η απόκλιση τανυστή $n+1$ βαθμού δίνει έναν τανυστή n βαθμού (π.χ. η διανυσματική συνάρτηση βαθμού 1, έδωσε βαθμωτό βαθμού 0).

Η απόκλιση αν είναι θετική, σημαίνει ότι σε ένα στοιχειώδη όγκο, έχουμε παραγωγή του μεγέθους, δηλαδή πηγή. Αν είναι αρνητική σημαίνει ότι στο στοιχειώδη όγκο έχουμε κατανάλωση του μεγέθους δηλαδή καταβόθρα.

Στον τανυστή των τροπών (τον πίνακα των παραμορφώσεων ενός στερεού συνεχούς σώματος) η απόκλιση δείχνει τη διόγκωση του υλικού σε κάθε υλικό σημείο.

Ιδιότητες

- $\nabla \cdot (\boldsymbol{F} + \boldsymbol{G}) = \nabla \cdot \boldsymbol{F} + \nabla \cdot \boldsymbol{G}$
- $\nabla \cdot (c\boldsymbol{F}) = c\nabla \cdot \boldsymbol{F}$ όταν c μια σταθερά.
- $\nabla \cdot (f\boldsymbol{F}) = \nabla f \cdot \boldsymbol{F} + f\nabla \cdot \boldsymbol{F}$ όπου η συνάρτηση f είναι τανυστής ενός βαθμού μικρότερου από την $\boldsymbol{F}$.
- Αν $\nabla \cdot \boldsymbol{F} = 0$, τότε η $\boldsymbol{F}$ είναι ένα σωληνοειδές διανυσματικό πεδίο.
- Αν $\boldsymbol{F} = \nabla f$, τότε η βαθμωτή συνάρτηση f καλείται δυναμικό.

Στροβιλισμός

Στο στροβιλισμό, σε αντίθεση με την κλίση και την απόκλιση, είναι υποχρεωτικό οι ανεξάρτητες μεταβλητές να είναι ακριβώς 3. Αυτό συμβαίνει γιατί ο τελεστής έχει μορφή που μοιάζει με το εξωτερικό γινόμενο.

Αν έχουμε μια διανυσματική συνάρτηση $\boldsymbol{F(x,y,z)} = \begin{bmatrix} f_x(x,y,z) \\ f_y(x,y,z) \\ f_z(x,y,z) \end{bmatrix}$ τότε ο στροβιλισμός της, είναι η επίσης διανυσματική συνάρτηση $\nabla \times \boldsymbol{F} = \boldsymbol{rotF} = \boldsymbol{curlF} = \begin{vmatrix} \vec{i} & \vec{j} & \vec{k} \\ \frac{\partial}{\partial x} & \frac{\partial}{\partial y} & \frac{\partial}{\partial z} \\ f_x & f_y & f_z \end{vmatrix} = \begin{bmatrix} \frac{\partial f_z}{\partial y} - \frac{\partial f_y}{\partial z} \\ -\frac{\partial f_z}{\partial x} + \frac{\partial f_x}{\partial z} \\ \frac{\partial f_y}{\partial x} - \frac{\partial f_x}{\partial y} \end{bmatrix}$. Η ορίζουσα με το εξωτερικό γινόμενο, παραβιάζει τους κανόνες της τυπικής γλώσσας καθώς οι τελεστές δεν εφαρμόζονται άμεσα σε συναρτήσεις, αλλά χρησιμεύει ως μνημονικός κανόνας.

Αν υποθέσουμε ότι βρισκόμαστε σε ένα κανάλι όπου τρέχει νερό, σε ένα πολύ συγκεκριμένο σημείο, τότε αν πολύ κοντά σε αυτό το σημείο, όλα τα μόρια νερού τρέχουν με ταχύτητα ιδίου μέτρου και κατεύθυνσης, δεν έχουμε στροβιλισμό. Αν π.χ. τα μόρια που έρχονται κάπως δεξιότερα είναι κατά τι πιο γρήγορα από αυτά που μας έρχονται από κάπως αριστερότερα, τότε έχουμε στροβιλισμό. Π.χ. μέσα σε ένα κανάλι με στρωτή ροή, τα μόρια νερού κοντά στα τοιχώματα κινούνται πιο αργά από ότι στο κέντρο του καναλιού, λόγω τριβής. Αυτό σημαίνει ότι παρότι έχουμε στρωτή ροή, έχουμε επίσης και στροβιλισμό. Κλασικό φαινόμενο στροβιλισμού είναι το να βγάλουμε το πώμα ενός νιπτήρα γεμάτου νερό.

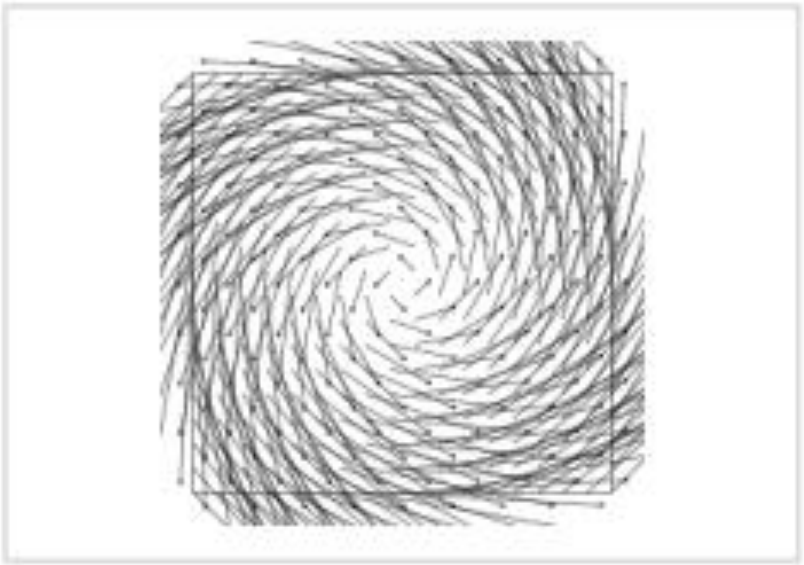

Η διανυσματική συνάρτηση f(x,y)=(-y,x). Εμφανίζει σαφώς στροβιλισμό. Ο στροβιλισμός της ισούται με $\nabla \times \boldsymbol{f} = 2\hat{\boldsymbol{z}}$, το οποίο είναι ένα διάνυσμα κάθετο στο επίπεδο της εικόνας προς τον αναγνώστη με μέτρο δύο.

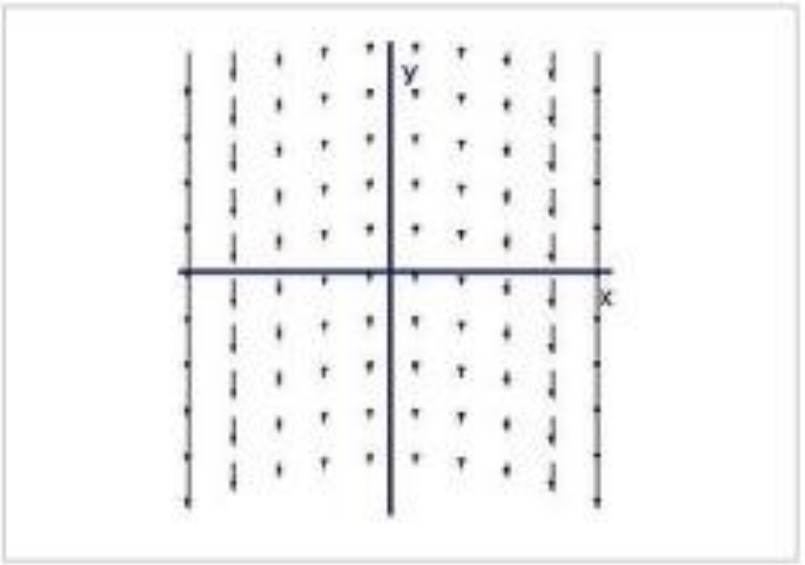

Αναπαράσταση της διανυσματικής συνάρτησης $\vec{\boldsymbol{f}}(\boldsymbol{x},\boldsymbol{y},\boldsymbol{z}) = -\boldsymbol{x}^2\hat{\boldsymbol{y}}$. Είναι $\nabla \times \vec{\boldsymbol{f}}(\boldsymbol{x},\boldsymbol{y},\boldsymbol{z}) = \vec{\boldsymbol{0}}$,λογικό αφού η συνάρτηση δεν παρουσιάζει δίνες.

Ιδιότητες

- $\nabla \times (F + G) = \nabla \times F + \nabla \times G$
- $\nabla \times (cF) = c\nabla \times F$ όταν c μια σταθερά.
- $\nabla \times (fF) = \nabla f \times F + f\nabla \times F$ όπου η συνάρτηση f είναι βαθμωτή συνάρτηση και F διανυσματική διάστασης 3.
- $\nabla \times \nabla \times F = \nabla(\nabla \cdot F) - \nabla^2 F = \nabla(\nabla \cdot F) - \Delta F$
- $\nabla \times (\nabla f) = \vec{0}$, δηλαδή ο στροβιλισμός της κλίσης ενός δυναμικού είναι μηδέν.
- $\nabla \cdot (F \times G) = (\nabla \times F) \cdot G - F \cdot (\nabla \times G)$.
- Αν $\nabla \times F = \vec{0}$, τότε η F είναι ένα αστρόβιλο πεδίο.

Τελεστής Laplace (Λαπλάς)

Ο τελεστής Λαπλάς[1] συμβολίζεται με Δ και ισούται με $\Delta f = \nabla \cdot \nabla f = \nabla^2 f$, δηλαδή είναι η απόκλιση της κλίσης μιας συνάρτησης.

Δείτε επίσης

- διαφορική γεωμετρία

Παραπομπές

1. «Τελεστής ανάδελτα» (http://www.hellenica.de/Math/Telestis/TelestisAnadelta.html) (html). www.hellenica.de. Ανακτήθηκε στις 24 Ιουνίου 2010.

Ανακτήθηκε από "https://el.wikipedia.org/w/index.php?title=Ανάδελτα&oldid=8319239"

Τελευταία τροποποίηση 07:41, 27 Ιουνίου 2020.

Όλα τα κείμενα είναι διαθέσιμα υπό την Creative Commons Attribution-ShareAlike License· μπορεί να ισχύουν και πρόσθετοι όροι. Χρησιμοποιώντας αυτό τον ιστότοπο, συμφωνείτε στους Όρους Χρήσης και την Πολιτική Ιδιωτικότητας. Το Wikipedia® είναι καταχωρημένο σήμα του Wikimedia Foundation, Inc., ενός μη κερδοσκοπικού οργανισμού.

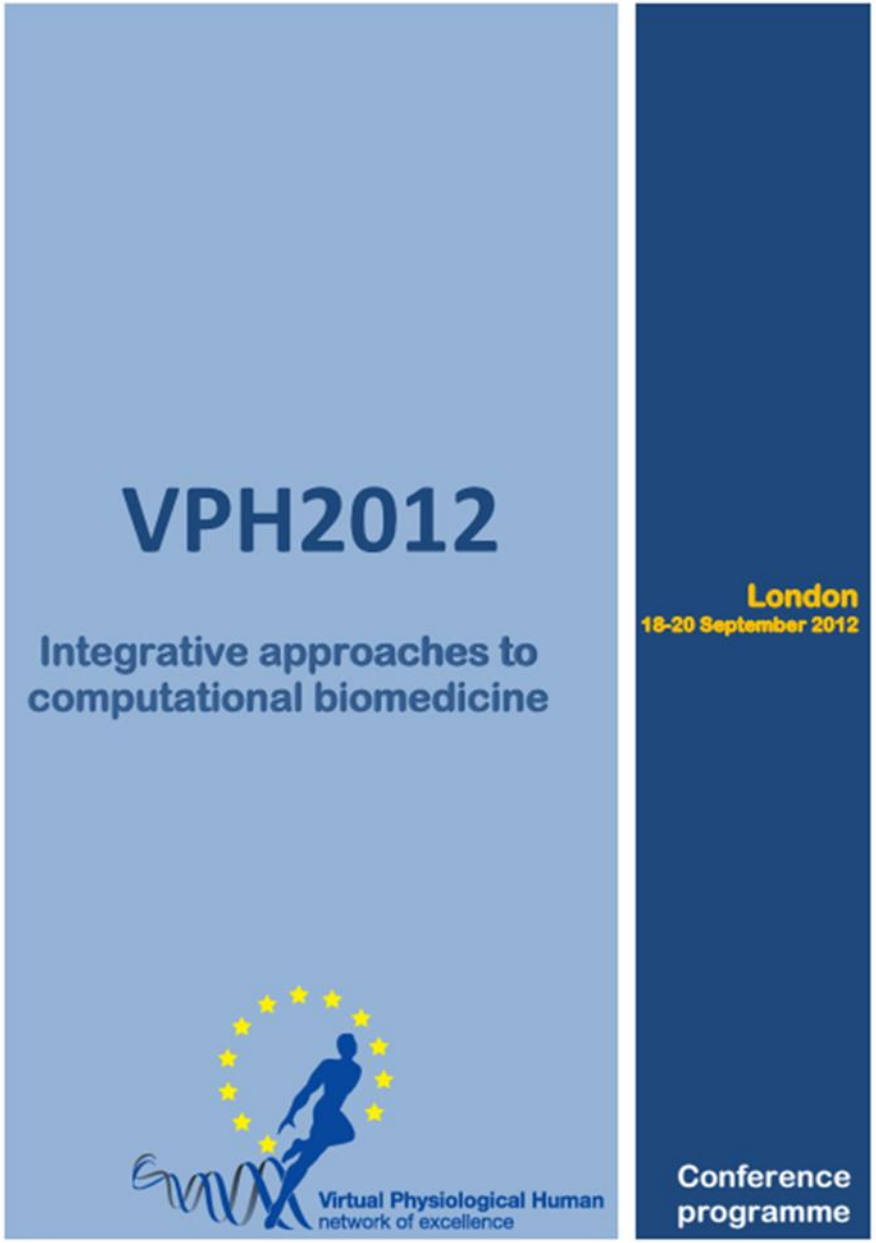
VPH2012
Integrative approaches to computational biomedicine
Virtual Physiological Human
network of excellence
London
18-20 September 2012
Conference programme

PROCEEDINGS-VPH2012_INTEGRATIVE_APPROACHES_TO_COMPUTATIONAL_BIOMEDICINE-LONDON_CONF_2012.pdf PAGE **98**/488 (PLEASE USE THE PDF PAGE COUNTER)

In Silico Oncology: a Novel and Explicit Numerical Treatment of the Neumann Boundary Conditions Imposed by the Skull on a Multiscale Diffusion-Reaction Model of Glioblastoma Growth. Clinical Validation Aspects.

Georgios S. Stamatakos[1,*] and Stavroula Giatili[2]

[1,2] *In Silico* Oncology Group, Laboratory of Microwave and Fibre Optics, Institute of Communication and Computer Systems, National Technical University of Athens. 9, Iroon Polytechniou, Zografos, GR-157 80, Greece.

* Corresponding Author (gestam@central.ntua.gr)

In Silico Oncology: a Novel and Explicit Numerical Treatment of the Neumann Boundary Conditions Imposed by the Skull on a Multiscale Diffusion-Reaction Model of Glioblastoma Growth. Clinical Validation Aspects.

Georgios S. Stamatakos[1,*] and Stavroula Giatili[2]

[1,2] *In Silico* Oncology Group, Laboratory of Microwave and Fibre Optics, Institute of Communication and Computer Systems, National Technical University of Athens. 9, Iroon Polytechniou, Zografos, GR-157 80, Greece.

* Corresponding Author (gestam@central.ntua.gr)

Abstract- Modelling of the diffusive-invasive behaviour of glioma tumour growth is an active field of Virtual Physiological Human (VPH) research with considerable therapeutic implications. A crucial component of the corresponding computational problem is the numerical handling of the adiabatic Neumann boundary conditions imposed by the skull on the diffusive growth of gliomas and in particular glioblastoma multiforme (GBM). In order to become clinically acceptable such a numerical handling should ensure that no potentially life-threatening glioma cells disappear artificially due to oversimplifying assumptions applied to the simulated region boundaries. However, to the best of the authors' knowledge no explicit numerical treatment of the 3D boundary conditions under consideration has appeared in the literature. Therefore, this paper aims at providing an outline of a novel, explicit and thorough numerical solution to this problem. Additionally, a brief exposition of the numerical solution process for a homogeneous approximation of glioma diffusion-invasion using the Crank – Nicolson technique in conjunction with the Conjugate Gradient system solver is outlined. The entire mathematical and numerical treatment is also in principle applicable to mathematically similar physical, chemical and biological phenomena. A comparison of the numerical solution for the special case of pure diffusion in the absence of boundary conditions with its analytical counterpart has been made. *In silico* experimentation with various adiabatic boundary geometries and non zero net tumour growth rate support the validity of the corresponding mathematical treatment. Through numerical experimentation on a set of real brain imaging data, a simulated tumour has shown to satisfy the expected macroscopic behaviour of glioblastoma multiforme including the adiabatic behaviour of the skull. The expected GBM macroscopic behaviour has been based on concrete published clinical imaging data. The paper concludes with a number of remarks pertaining to the potential and the limitations of the diffusion-reaction approach to modelling multiscale malignant tumour dynamics.

I. INTRODUCTION

Glioblastoma multiforme (GBM) is a very aggressive glioma and a classical example of a highly invasive and diffusive tumour. GBM cell diffusion in the brain is a reasonable first approximation of the migration of glioma cells along structures such as the basement membranes of blood vessels or the glial limitans externa that contain extracellular matrix (ECM) proteins. Frequentlty, invasive glioma cells are also found to migrate along myelinated fiber tracts of white matter. Due to its markedly diffusive character, a significant component of the tumour cannot be delineated based on standard tomographic imaging techniques such as CT, MRI and PET. This constitutes an important limitation to the optimal design of both surgical excision and therapeutic irradiation of the tumour. In order to partly alleviate the problem, mathematical modelling of diffusive tumour growth has been proposed. To this end a number of diffusion-reaction based models dealing primarily with the morphology of tumour growth have been developed [1 – 3].

According to the diffusion-reaction based approach, the tumour is considered a spatiotemporal distribution of continuous cell density which follows the general diffusion-reaction law. The macroscopic formulation of diffusion, leads to a partial parabolic differential equation. A single tumour cell may constitute the initial tumour within a three-dimensional medium. Tumour growth can be expressed by the following statement [1,2]:

Rate of change of tumour cell population= diffusion (motility) of tumour cells + net proliferation of tumour cells - loss of tumour cells due to treatment

Getting an idea of the discretization mesh applied to the anatomical region of interest .

The values of the quantities of interest are assigned and/or calculated only on the nodes of the mesh

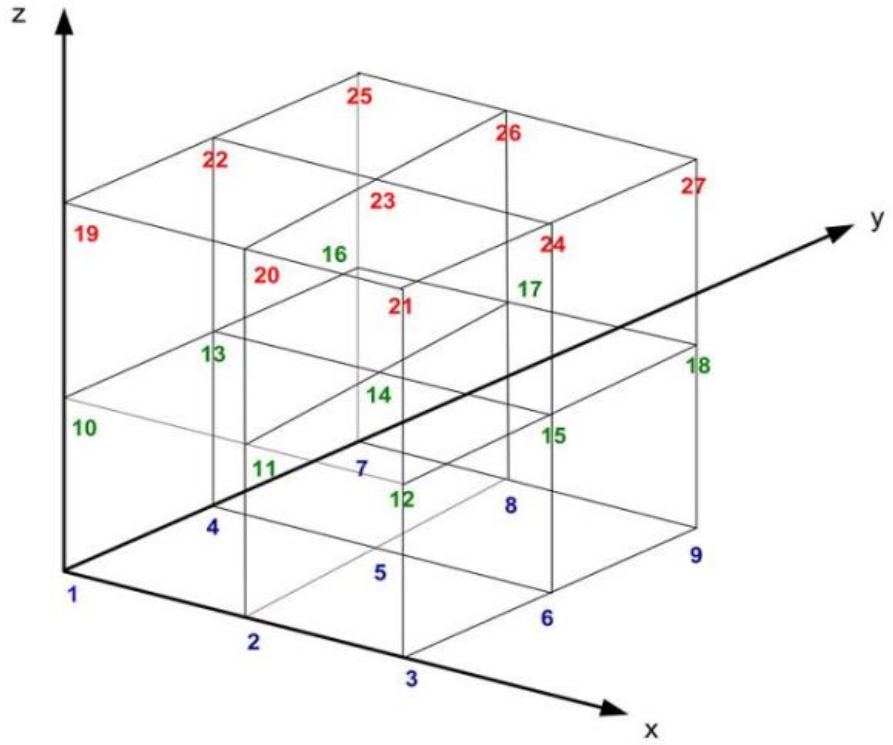

Fig. 2. Lexicographic order. To find the structure of the coefficient matrix $\overleftrightarrow{A}$, a common numbering scheme has been used namely the lexicographic ordering. Starting at the bottom left corner of the computational grid, the unknowns are numbered consecutively from left to right and from bottom to top. The number written next to the location of each unknown is the lexicographic number associated with the unknown.

of tumour cells due to treatment

In the case of glioma, the simulated region of interest may include part of the skull. The latter acts as an adiabatic boundary for the diffusion of the brain tumour, precluding migration beyond it. As a result, the mathematical treatment of the biophysical processes taking place in the vicinity of anatomic boundaries must satisfy specific constraints. Zero flux boundary conditions have to be applied on the anatomic boundaries of the skull surface. Thus if Ω is the brain domain on which the diffusion equation is to be solved the previous statement can be symbolically formulated through the following differential equation [1]:

$$\left\{\begin{array}{l} \frac{\partial c}{\partial t} = \nabla \cdot (D\nabla c) + \rho c - G(t)c \quad in\ \Omega \\ c(\vec{x}, 0) = f(\vec{x}), \qquad initial\ condition \\ \hat{n} \cdot D\nabla c(\vec{x}, t) = 0 \ \ on\ \ \partial\Omega, \ \ Neumann\ boundary\ condition \end{array}\right\} \tag{1}$$

The variable c denotes the cell concentration at any spatial point defined by the position vector $\vec{x}$ and time t. The parameter D denotes the diffusion coefficient and represents the active motility of tumour cells. The term ρ represents the net rate of tumour growth including proliferation, loss and death, $\hat{n}$ is the unit vector normal to the boundary $\partial\Omega$ of the domain Ω and $f(\vec{x})$ is a known function that defines the initial spatial distribution of malignant cells. The term $G(t)$ accounts for the temporal profile of treatment and as a first facilitating approximation $G(t) = k$ may be assumed constant. The latter may crudely model a continuous administration of radiation e.g. through special radioisotope based

implants. A more realistic assumption is to assign $G(t)$ different values for different time intervals reflecting various chemotherapeutic and/or radiotherapeutic schedules. The simulation domain R of which Ω is a subdomain is defined as:

$$R = \{(x, y, z) | a < x < b, s < y < d, e < z < f\} \quad (2)$$

WIKIPEDIA

Numerical differentiation

In numerical analysis, **numerical differentiation** describes algorithms for estimating the derivative of a mathematical function or function subroutine using values of the function and perhaps other knowledge about the function.

Contents

- Finite differences
- Step size
- Other methods
  - Higher-order methods
  - Higher derivatives
- Complex-variable methods
- Differential quadrature
- See also
- References
- External links

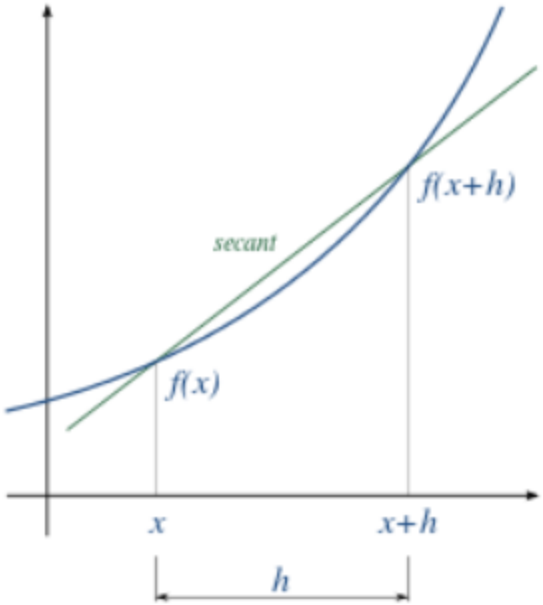

Finite differences

The simplest method is to use finite difference approximations.

A simple two-point estimation is to compute the slope of a nearby secant line through the points $(x, f(x))$ and $(x + h, f(x + h))$.[1] Choosing a small number h, h represents a small change in x, and it can be either positive or negative. The slope of this line is

$$\frac{f(x+h) - f(x)}{h}.$$

This expression is Newton's difference quotient (also known as a first-order divided difference).

The slope of this secant line differs from the slope of the tangent line by an amount that is approximately proportional to h. As h approaches zero, the slope of the secant line approaches the slope of the tangent line. Therefore, the true **derivative of f at x** is the limit of the value of the difference quotient as the secant lines get closer and closer to being a tangent line:

$$f'(x) = \lim_{h \to 0} \frac{f(x+h) - f(x)}{h}.$$

Since immediately substituting 0 for h results in $\frac{0}{0}$ indeterminate form , calculating the derivative directly can be unintuitive.

Equivalently, the slope could be estimated by employing positions $(x - h)$ and x.

Another two-point formula is to compute the slope of a nearby secant line through the points $(x - h, f(x - h))$ and $(x + h, f(x + h))$. The slope of this line is

$$\frac{f(x+h) - f(x-h)}{2h}.$$

This formula is known as the symmetric difference quotient. In this case the first-order errors cancel, so the slope of these secant lines differ from the slope of the tangent line by an amount that is approximately proportional to h^2. Hence for small values of h this is a more accurate approximation to the tangent line than the one-sided estimation. However, although the slope is being computed at x, the value of the function at x is not involved.

ΓΙΑ ΤΗ ΔΙΑΣΘΗΤΙΚΗ ΚΑΤΑΝΟΗΣΗ ΤΟΥ ΦΑΙΝΟΜΕΝΟΥ ΤΗΣ ΔΙΑΧΥΣΗΣ ΣΕ ΑΝΤΙΔΙΑΣΤΟΛΗ ΜΕ ΤΟ ΦΑΙΝΟΜΕΝΟ ΤΗΣ ΡΟΗΣ

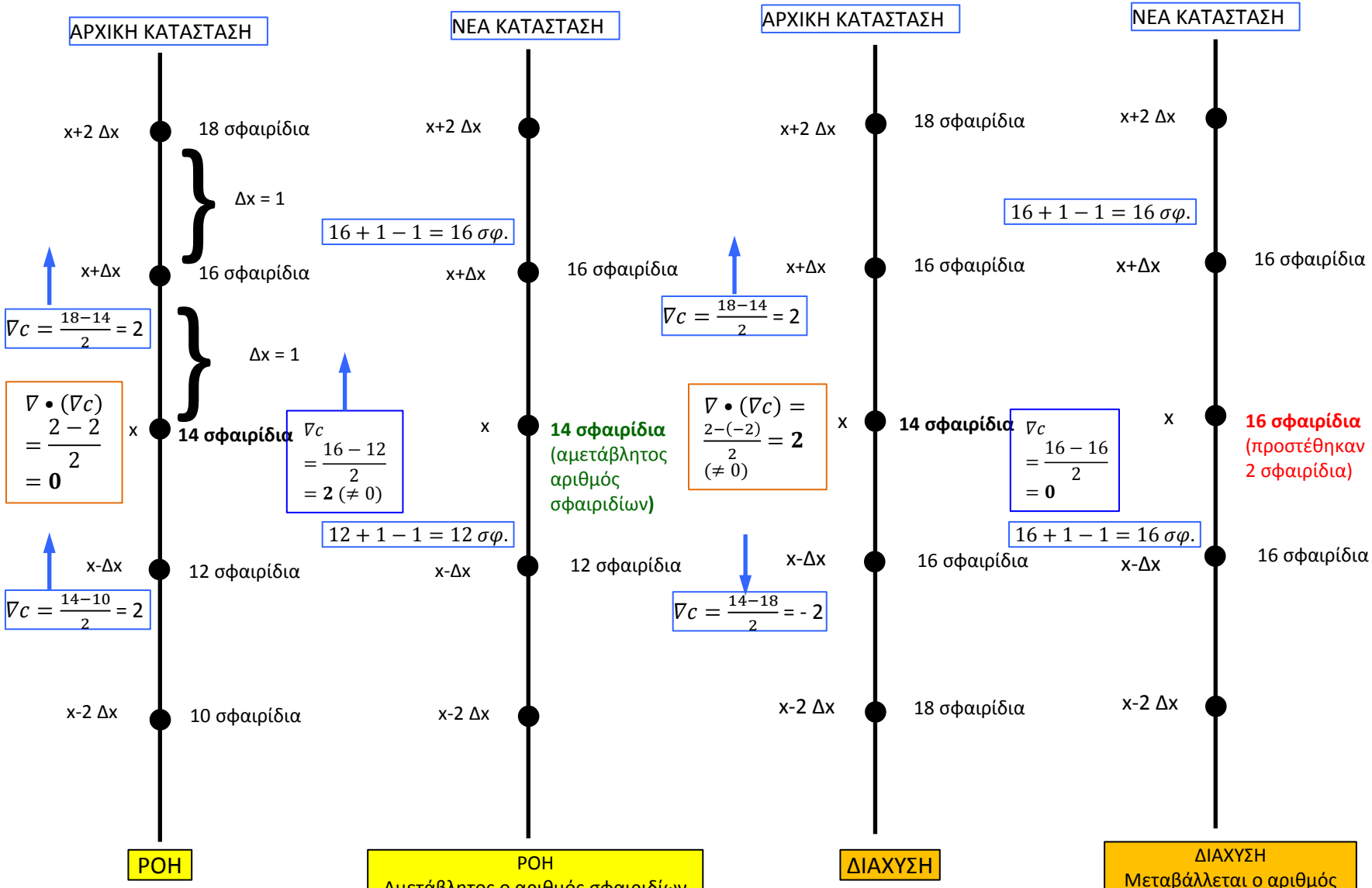

Αναφερόμαστε πάντα στο σημείο x (και στη γειτονιά του)

ΓΙΑ ΤΗΝ ΚΑΤΑΝΟΗΣΗ ΤΩΝ ΑΡΙΘΜΗΤΙΚΩΝ ΧΕΙΡΙΣΜΩΝ ΓΙΑ ΤΗΝ ΕΦΑΡΜΟΓΗ ΤΗΣ ΟΡΙΑΚΗΣ ΣΥΝΘΗΚΗΣ DIRICHLET (ΛΑΘΟΣ) ΚΑΙ ΤΗΣ ΟΡΙΑΚΗΣ ΣΥΝΘΗΚΗΣ NEUMANN (ΣΩΣΤΟ) ΚΑΤΑ ΤΗΝ ΕΠΙΛΥΣΗ ΤΗΣ ΜΕΡΙΚΗΣ ΔΙΑΦΟΡΙΚΗΣ ΕΞΙΣΩΣΗΣ ΑΝΤΙΔΡΑΣΗΣ-ΔΙΑΧΥΣΗΣ ΣΤΗΝ ΠΡΟΣΟΜΟΙΩΣΗ ΤΗΣ ΔΙΗΘΗΣΗΣ ΓΛΟΙΟΒΛΑΣΤΩΜΑΤΟΣ ΣΤΟ ΦΥΣΙΟΛΟΓΙΚΟ ΙΣΤΟ ΤΟΥ ΕΓΚΕΦΑΛΟΥ

(c = συγκέντρωση καρκινικών κυττάρων γλοιοβλαστώματος)

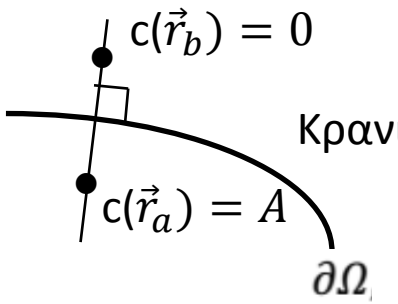

Εγκέφαλος

ΑΡΙΘΜΗΤΙΚΗ ΕΦΑΡΜΟΓΗ ΤΗΣ ΟΡΙΑΚΗΣ ΣΥΝΘΗΚΗΣ **DIRICHLET**

Υποθετικός (fictitious) κόμβος μέσα στο κρανίο με διάνυσμα θέσης $\vec{r}_b$

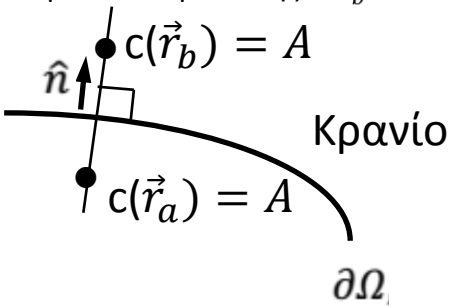

Εγκέφαλος

ΑΡΙΘΜΗΤΙΚΗ ΕΦΑΡΜΟΓΗ ΤΗΣ ΟΡΙΑΚΗΣ ΣΥΝΘΗΚΗΣ **NEUMANN:**

$$\hat{n} \cdot D\nabla c(\vec{x}, t) = 0 \ \ on \ \ \partial\Omega, \ \ Neumann\ boundary\ condition$$

II. EXPLICIT NUMERICAL FORMULATION OF THE BOUNDARY CONDITIONS

The diffusion component of the problem is numerically solved using the Crank Nicolson numerical method in conjunction with the conjugate gradient method. The glioma invasion problem involves an irregularly shaped domain. Therefore, a biologically meaningful solution has to allow for the investigation of a wide range of elementary local domain geometries. Several specific cases have been examined in order to address the geometry of the irregularly shaped skull boundary. For each boundary mesh node (lying at the center of the multi-grey level structure of Fig.1 (and therefore not visible) all its 6 adjacent nodes (lying towards all the $x+, x-, y+, y-, z+, z-$ directions) are considered in order to numerically apply the boundary condition on it i.e. on (x_i, y_j, z_k) [4]

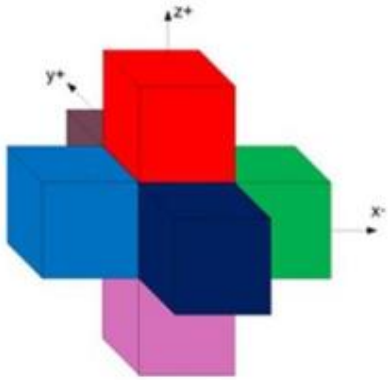

Fi.1 A boundary mesh node with its 6 adjacent nodes. For each boundary mesh node (lying at the center of the multi-coloured structure and therefore not visible) all its 6 adjacent nodes (lying towards the $x+, x-, y+, y-, z+, z-$ directions) are considered in order to numerically apply the boundary conditions on the node under consideration.

The boundary condition according to Eq.1 is:

$$\hat{n} \cdot D\nabla c = 0 \quad on \quad \partial\Omega \qquad (2)$$

In order to evaluate the boundary condition for each grid point (x_i, y_j, z_k) and maintain the block tridiagonal structure of the coefficient matrix $\vec{A}$ of the resulting linear system of algebraic equations $\vec{A}\vec{x} = \vec{b}$ and the second-order accuracy of the approximation we introduce a "fictitious node" into the computational grid. The "fictitious node" produces an extra row of unknowns in the computational grid. Evaluating the boundary condition at each boundary grid point (x_i, y_j, z_k) yields six equations mathematically similar (but not identical) to the equation corresponding to the following case:

At the boundary grid point (x_i, y_j, z_k) in the negative x direction $x-$:

$$-\left.\frac{\partial c}{\partial x}\right|_{(x_i, y_j, z_k)} = 0 \Rightarrow c_{i+1,j,k} = c_{F_{i-1,j,k}} \quad (3)$$

where $F_{i,j,k}$ denotes a fictitious node.

The total number of the different cases of nodes having boundary node(s) as their neighbour(s) that have been considered is 26. This has led to the formulation of 26 algebraic equations mathematically similar (but not identical) to Eq. (4). An appropriate equation out of the set of these 26 equations is used for any index triplet (i, j, k) belonging to the boundary. By fixing indices i, j, k to specific values, the 26 equations can produce all elementary boundary arrangements encountered in the case of an arbitrarily shaped boundary. An indicative case and equation is the following:

At the boundary grid point (x_i, y_j, z_k) where the skull lies only in the positive x direction:

$$[1 + 6\lambda - \frac{\Delta t}{2}(\rho - G)]c_{i,j,k}^{t+1} - \lambda(2c_{i-1,j,k}^{t+1} + c_{i,j+1,k}^{t+1} + c_{i,j-1,k}^{t+1} + c_{i,j,k+1}^{t+1} + c_{i,j,k-1}^{t+1}) =$$

$$[1 - 6\lambda + \frac{\Delta t}{2}(\rho - G)]c_{i,j,k}^{t} + \lambda(2c_{i-1,j,k}^{t} + c_{i,j+1,k}^{t} + c_{i,j-1,k}^{t} + c_{i,j,k+1}^{t} + c_{i,j,k-1}^{t}) \quad (4)$$

where $\lambda = D\Delta t \,/\, [2(h)^2]$, $h = \Delta x = \Delta y = \Delta z$, $t_n = n\,\Delta t$, for $n = 0,1,2\ldots.$ (5)

III. NUMERICAL EXPERIMENTS

In order to test the numerical schemes implemented for solving Eq. (1) and support the correctness of the overall mathematical treatment presented, a number of pertinent computational scenarios have been executed. They have included inter alia: numerical checks regarding convergence and stability of the algorithm and the code, checks regarding mass conservation and linearity for the theoretical case of pure diffusion, comparison of the model with the analytical solution to the special case of an initial Gaussian cell concentration profile, spatial symmetry studies for simple symmetric geometries and numerical validation of the adiabatic behaviour of the boundary implementation.

IV CLINICAL VALIDATION ASPECTS

Several snapshots of a growing virtual glioblastoma tumour corresponding to various time points are depicted in Fig. 2. It is noted that although the internal anatomy of brain is visible in the panels of this figure, homogeneous diffusion of tumour cells has been assumed within the skull cavity as a first approximation. The concentration of tumour cells within the initial simulated tumour has been arbitrarily assumed uniform and equal to 10^6 cells/ mm^3. The following parameter values have been used: diffusion coefficient $D = 0.0065\ cm^2/d$, [1], $h = 0.2$ cm, $\Delta t = 0.5$ d , and net tumour growth rate $\rho = 0.012\ d^{-1}$. [1] It should be noted that the gross spatial pattern of glioblastoma growth, especially in the vicinity of the skull boundary, is in very good agreement with actual published clinical observations [5-6]. The diameter of a sphere with volume equal to a glioblastoma tumour of fatal imageable dimensions is about 6 cm. [1] The latter corresponds to a volume V_{fatal} of $113.04\ cm^3$. In order for the tumour to increase in imageable volume from $V_{fatal}/2$ to V_{fatal}, 26 days are needed according to the simulations. This approximation to doubling time is in good agreement with the clinically reported glioblastoma doubling time in [7]. It is noted that in order to avoid a somewhat artificial diffusion behaviour during the first simulated days which would be dictated by the deliberately assumed abrupt boundaries of the initial tumour, the first 14 simulated days have not been taken into account in the

theoretical estimation of doubling time. A typical execution instance of the code for 6 simulated months, $\Delta t = 0.5d$ and for descritized mesh 130x130x130, on a 32-bit Windows Vista Platform, 4 GB RAM and processor Intel® Core™2 Duo CPU P8600 @ 2.4GHz, takes 214 sec. Further acceleration of the code execution could be achieved by using high performance computing resources.

V. CONCLUSIONS

A novel explicit numerical treatment of the boundary conditions to be used in conjunction with a homogeneous diffusion - reaction based glioma growth model has been presented.

Systematic checking of the corresponding computer code based on numerical simulations for various adiabatic boundary geometries, zero and non zero net tumour growth rate and zero and

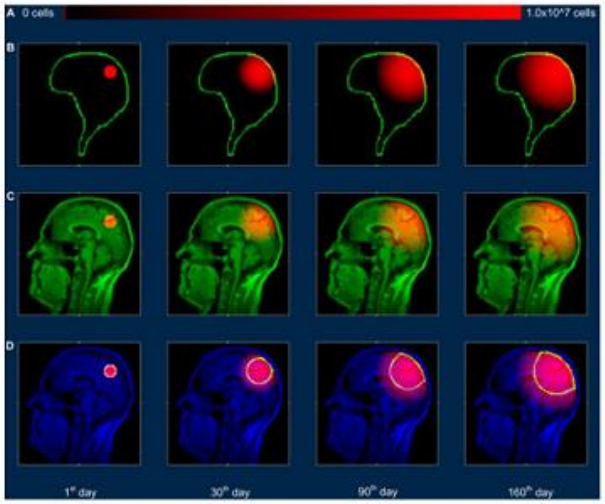

Fig.2 Schematic representation of the growth of a virtual glioblastoma tumour *in vivo* in sagittal planes at various time points (panel columns from left to right correspond to days 1, 30, 90 and 160 respectively). (A) The red colour intensity level I depends on cell concentration according to the function $I = k \log_{10} c$, where c denotes tumour cell concentration, the constant $k = 255/\log_{10} c_{max}$, c_{max} is the maximum value of tumour cell concentration *over the entire space and time range* considered during all simulations that have been included in this figure. Maximum and zero cell concentration corresponds to RGB(255,0,0) and RGB(0,0,0) respectively. The numerical values appearing on the intensity scale of panel A are per 8 mm^3. It is noted that the voxel in the present simulation had dimensions 2mm x 2mm x 2mm (B), (C) As time increases, the tumour diffuses theoretically over the interior space of the skull cavity of the human head. (D) The yellow/bright contour defines the boundary of the tumour component in 2D that is tomographically detectable and has a cell density higher than the assumed threshold of 8000 cells/mm^3.

non zero loss rate due to treatment have supported the validity of the corresponding mathematical treatment. Numerical experimentation on a set of real brain imaging data has demonstrated that a simulated glioblastoma tumour can satisfy the expected macroscopic behaviour of its real counterpart, including the adiabatic behaviour of the skull. The detailed treatment of the boundary conditions presented could considerably contribute to the accuracy of the solution to the diffusion-reaction equation in particular for glioblastoma tumours having their main bulk close to the skull. The composite model proposed appears to have the potential to correctly predict clinically meaningful and measurable quantities of critical importance related to the course of the disease, such as the imaging based doubling time. Obviously a strict clinical adaptation and validation procedure is a *sine qua non* requirement before clinical translation is envisaged. Additionally, translation or extension of the analysis presented to mathematically similar physical systems is a possibility. Extension to both inhomogeneous and anisotropic glioma diffusion is pretty straightforward. It should be noted, however, that although the continuous - finitized approach partly delineated in this paper appears to be a good choice for pure tumour growth-invasion-diffusion modelling, it seems not to be ideal for the integration of the massive multiscale biological complexity that is necessary in order to study in depth tumour response to treatment. Discrete entity – discrete event based approaches [8-11] on the contrary have demonstrated considerable integrative potential in the context of cancer response o treatment due to the discrete character of many biological entities and features involved in this domain (e.g. discrete cell categories based on their mitotic potential such as stem cells, progenitor cells, differentiated cells; discrete cell cycle phases generally characterized by differing treatment sensitivities; discrete character of cell state transitions etc.). Nevertheless, both continuous/finitized and discrete approaches are important for the development [10] and the clinical translation [12] of the emerging oncosimulators [10].

ACKNOWLEDGEMENTS

This work has been supported in part by the European Commission under the projects ContraCancrum: (FP7-ICT-2007-2- 223979), TUMOR: Transatlantic Tumor Model Repositories (FP7-ICT-2009.5.4-247754) and p-Medicine: Personalized Medicine (FP7-ICT-2009.5.3-270089). Fruitful discussions with N. Graf, University Hospital of Saarland, Germany, and D. Dionysiou, E. Georgiadi and N. Uzunoglu, ICCS, National Technical University of Athens, Greece are duly acknowledged.

REFERENCES

[1] J.D. Murray,Mathematical Biology II, 3rd Ed., Springer-Verlag Inc.,New York, ,2003, pp. 536-613.

[2] K. R. Swanson, Quantifying glioma cell growth and invasion in vitro, Math. and Comp. Modelling. 47 (2008) 638–648.

[3] O. Clatz, P.Y Bondiau, H. Delingette, M Sermesant, S.K. Warfield, G. Malandain, N. Ayache, Brain Tumor Growth Simulation. Institute National de Recherché en Informatique et en Automatique, Rapport de recherche. 5187 (2004).

[4] S.G. Giatili and G.S. Stamatakos, A detailed numerical treatment of the boundary conditions imposed by the skull on a diffusion–reaction model of glioma tumor growth. Clinical validation aspects, Appl. Math. Comput. (2012) doi:10.1016/j.amc.2012.02.036 *in press*

[5] A.D. Waldman, A. Jackson, S. J. Price, C.A. Clark, T.C. Booth, D.P. Auer, P.S. Tofts, D.J. Collins, M.O. Leach, J.H. Rees, Quantitative imaging biomarkers in neuro-oncology, Nature Reviews Clinical Oncology. 6 (2009) 445-454.

[6] Glioblastoma multiforme. http://en.wikipedia.org/wiki/Glioblastoma_multiforme (2011). Accessed 26 November 2011.

[7] N.G. Burnet, R. Jena, S. J. Jefferies, S. P. Stenning, N.F. Kirkby, Mathematical Modelling of Survival of Glioblastoma Patients Suggests a Role for Radiotherapy Dose Escalation and Predicts Poorer Outcome After Delay to Start Treatment, Clinical Oncology 19 (2006) 93-103.

[8] G.S. Stamatakos ,D.D. Dionysiou, E.I. Zacharaki, N.A. Mouravliansky, K.S. Nikita, N.K. Uzunoglu, In silico radiation oncology: combining novel simulation algorithms with current visualization techniques, Proc IEEE, Special Issue on Bioinformatics: Advances and Chalenges. 90 (11) (2002) 1764-1777.

[9] D.D. Dionysiou, G.S. Stamatakos, N.K. Uzunoglu, K.S. Nikita, A. Marioli, A Four Dimensional In Vivo Model of Tumor Response to Radiotherapy: Parametric Validation Considering Radiosensitivity, Genetic Profile and Fractionation , J. Theor. Biol. 230 (2004) 1-20.

[10] G. Stamatakos, *In Silico Oncology*: PART I Clinically oriented cancer multilevel modeling based on discrete event simulation in: T. S. Deisboeck and G. S. Stamatakos (Eds.) Multiscale Cancer Modeling. CRC Press 2010/2011 pp 407–436, Print ISBN: 978-1-4398-1440-6, eBook ISBN: 978-1-4398-1442-0, DOI: 10.1201/b10407-19.

[11] G.S.Stamatakos, E.Ch.Georgiadi, N.Graf, E.A.Kolokotroni, D.D.Dionysiou, Exploiting Clinical Trial Data Drastically Narrows the Window of Possible Solutions to the Problem of Clinical Adaptation of a Multiscale Cancer Model, PLoS One. 2011;6(3):e17594.

[12] N. Graf, *In Silico* Oncology Part II: Clinical Requirements Regarding *In Silico* Oncology, in T. Deisboeck and G. S . Stamatakos (Eds), Multiscale Cancer Modeling, CRC Press 2010/2011, pp. 437–446, Print ISBN: 978-1-4398-1440-6, eBook ISBN: 978-1-4398-1442-0, DOI: 10.1201/b10407-20

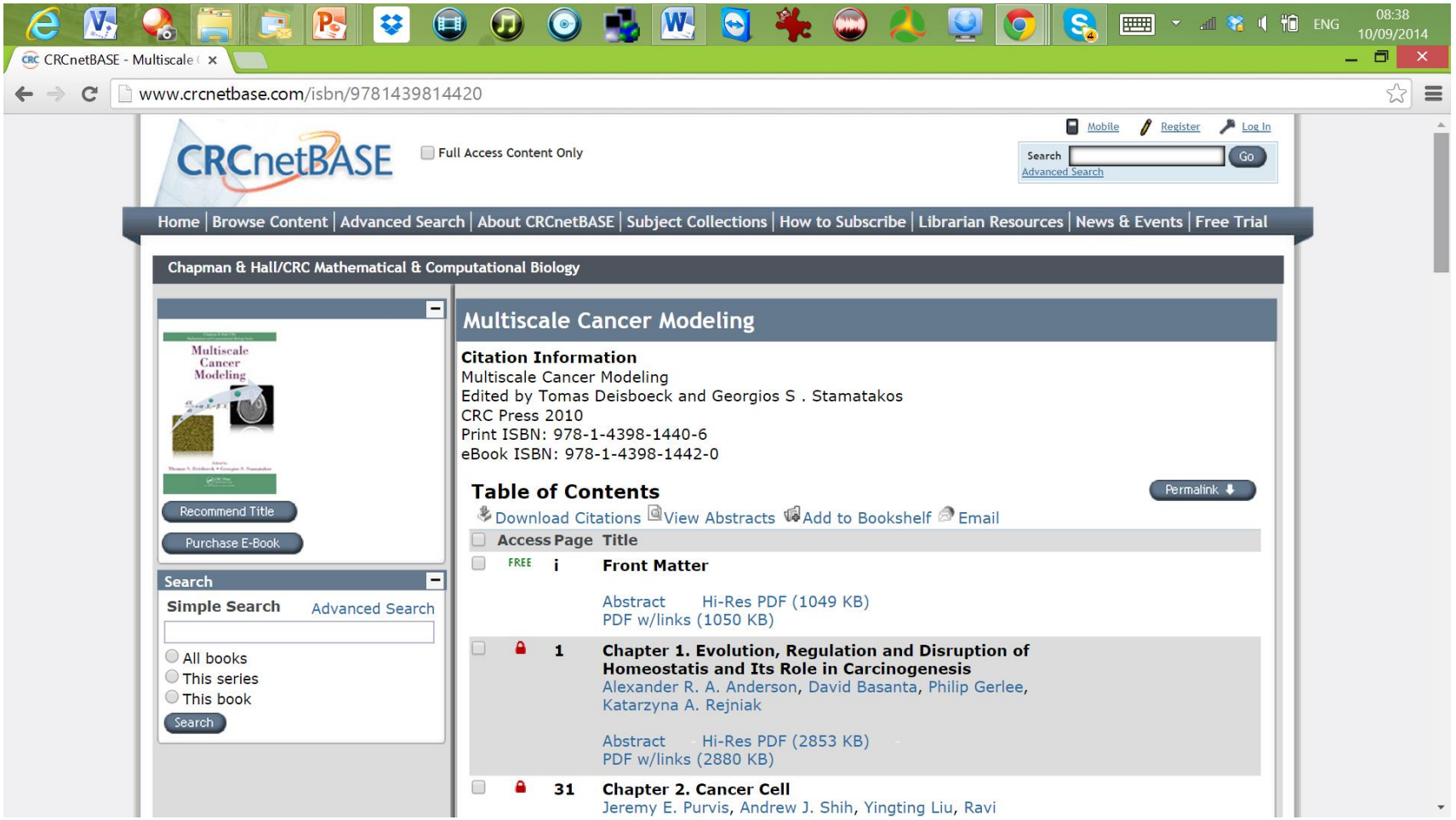

Editor Bio(s)

Thomas S. Deisboeck, M.D., is an associate professor of radiology at Massachusetts General Hospital, where he directs the Complex Biosystems Modeling Laboratory. He is also an affiliated faculty member of the Harvard-MIT Health Sciences and Technology Division and a member of the Dana Farber/Harvard Cancer Center.

Georgios S. Stamatakos, Ph.D., is a research professor of biological systems analysis and simulation in the Institute of Communication and Computer Systems as well as founder and leader of the *In Silico* Oncology Group, Laboratory of Microwaves and Fiber Optics at the National Technical University of Athens.

Home - 6th-iarwisoci

6th-iarwisoci.iccs.ntua.gr/index.php/

6th International Advanced Research Workshop on In Silico Oncology and Cancer Investigation - The CHIC Project Workshop

Home | In Silico Oncology | The CHIC Workshop | Call For Papers | Committees | Sponsors | Contact

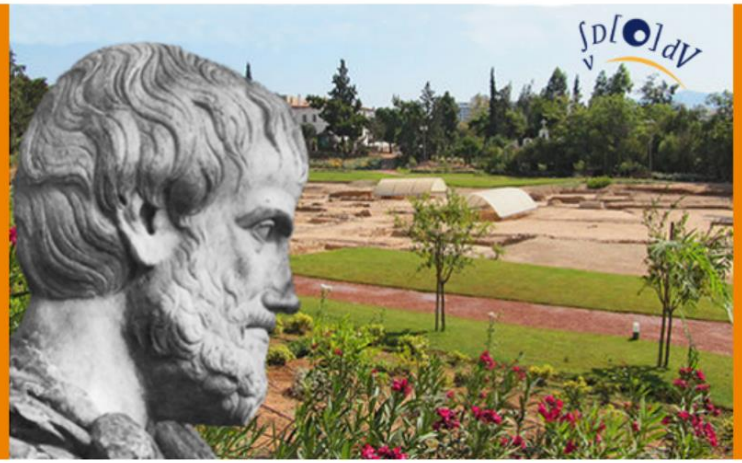

3-4 November 2014

Athens, Greece

Paper submissions due: **20 September 2014**

Notification of acceptance: **10 October 2014**

Camera ready papers due: **20 October 2014**

Home

In silico medicine, an emergent scientific and technological domain based on clinically driven and

Ευχαριστώ

Πρόγραμμα Διδακτορικών Σπουδών της Σχολής Ηλεκτρολόγων Μηχανικών και Μηχανικών Υπολογιστών ΕΜΠ

Πολυκλιμακωτή Προσομοίωση της Ασθένειας του Καρκίνου και *In Silico* Ιατρική (705)

Μάθημα 2ο

In Silico Ιατρική / *In Silico* Ογκολογία: Θέματα Βασικής Επιστήμης.

Γεώργιος Σ. Σταματάκος

Διευθυντής Ερευνών - Research Professor– Καθηγητής Ερευνας
Ερευνητικό Πανεπιστημιακό Ινστιτούτο Συστημάτων Επικοινωνιών και Υπολογιστών (ΕΠΙΣΕΥ)
Σχολή Ηλεκτρολόγων Μηχανικών και Μηχανικών Υπολογιστών (ΣΗΜΜΥ)
Εθνικό Μετσόβιο Πολυτεχνείο (ΕΜΠ)
Διευθυντής της Ερευνητικής Ομάδας για την In Silico Ογκολογία και την In Silico Ιατρική, ΕΠΙΣΕΥ-ΣΗΜΜΥ-ΕΜΠ
Επισκέπτης Καθηγητής της Ιατρικής Σχολής του Πανεπιστημίου του Saarland, Γερμανία (1/7/2019-15/9/2019)
Επισκέπτης Καθηγητής της ΣΗΜΜΥ, ΕΜΠ (2016-2019)
gestam@central.ntua.gr, http://in-silico-oncology.iccs.ntua.gr/

ΠΡΟΤΕΙΝΟΜΕΝΑ ΒΙΒΛΙΑ ΥΠΟΒΑΘΡΟΥ ΓΙΑ ΤΗΝ *IN SILICO* ΙΑΤΡΙΚΗ

- G. J. Tortora and B. Derrickson, **Principles of Anatomy and Physiology**, 13th Edition, John Wiley and Sons, Inc. (2012)
- M. Longmore, I. B.Wilkinson, A.Baldwin, E. Wallin, **Oxford Handbook of Clinical Medicine**, 9th Edition, Oxford University Press (2014)
- A.Kremling, **Systems Biology** (Mathematical Modeling and Model Analysis), Chapman and Hall/ CRC (2014)
- Ενα Αγγλο-Ελληνικό και Ελληνο-Αγγλικό **Λεξικό** (Βιο-)Ιατρικής Ορολογίας

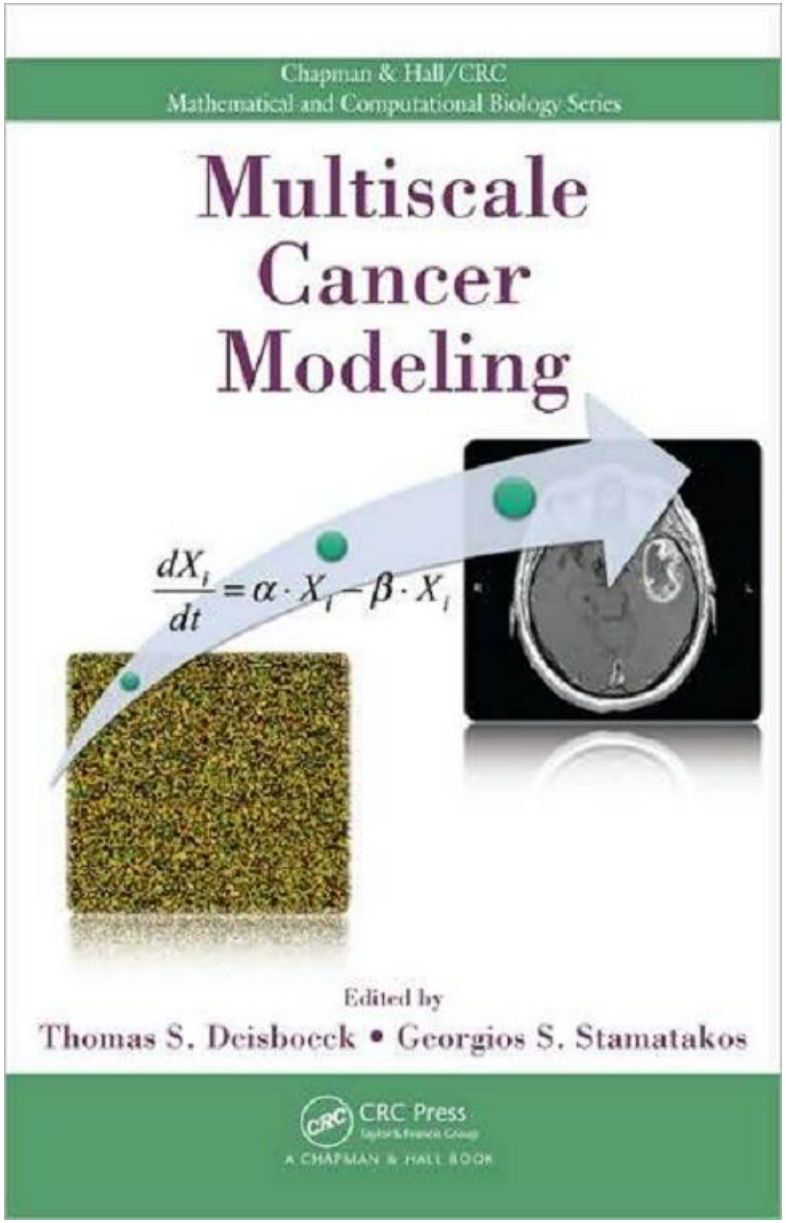

CRC Press
Taylor & Francis Group
6000 Broken Sound Parkway NW, Suite 300
Boca Raton, FL 33487-2742

© 2011 by Taylor and Francis Group, LLC
CRC Press is an imprint of Taylor & Francis Group, an Informa business

CHAPTER 18

In Silico Oncology

Part I—Clinically Oriented Cancer Multilevel Modeling Based on Discrete Event Simulation

Georgios S. Stamatakos

CHAPTER 18

In Silico Oncology

Part I—Clinically Oriented Cancer Multilevel Modeling Based on Discrete Event Simulation

Georgios S. Stamatakos

CONTENTS

Introduction	407
The Oncosimulator	411
Model—A Symbolic Mathematical Formulation of DEBCaST	414
Hypermatrix of the Anatomical Region of Interest	414
Practical Considerations Regarding the Construction of the Discretization Mesh	415
Hypermatrix and Operator Formulation of DEBCaST	415
Results	420
Model A: Tumor Response to Chemotherapeutic Schemes	420
Model B: Tumor Response to Radiotherapeutic Schemes	422
Discussion and Future Perspectives	426
Acknowledgments	431
References	431

ABSTRACT

In this chapter the Discrete Event Based Cancer Simulation Technique (DEBCaST), developed in order to simulate primarily multiscale tumor growth and response to treatment in the *clinical* context, is briefly outlined. DEBCaST has been designed and is continuously refined so as to *pragmatically* respond to real clinical questions concerning the optimization of treatment strategies in the patient individualized context. It is basically a *top-down* biomodeling approach in the sense that macroscopic data, including i.a. anatomic and metabolic tomographic images of the tumor, provide the framework for the integration of *realistically obtainable data* and *clinically relevant mechanisms* pertaining to lower and lower biocomplexity levels such as *clinically approved* cellular and molecular biomarkers. Nevertheless, DEBCaST *does* also provide a powerful framework for the investigation of multilevel (multiscale) tumor biology in the *generic investigational* context. The *Oncosimulator*, a biomedical engineering concept and construct tightly associated with DEBCaST and currently being under clinical adaptation, optimization and validation, is also sketched. A concise symbolic mathematical formulation of DEBCaST in terms of a hypermatrix and discrete operators is provided. Two specific models of tumor response to chemotherapeutic and radiotherapeutic schemes are briefly outlined and indicative results are presented so as to exemplify DEBCaST's application potential. The chapter concludes with a discussion of several critical aspects of the method including i.a. convergence, sensitivity, massive parallel code execution, asscociated technologies, model extensions and validation within the framework of actual running clinico-genomic trials. Future perspectives and challenges are also discussed.

1. INTRODUCTION

Most cancer modeling techniques developed up to now adopt the straightforward *bottom-up* approach focusing on the better understanding and quantification of rather microscopic tumor dynamics mechanisms and the investigation of crucial biological entity interdependences including i.a. tumor response to treatment in the *generic investigational* context. To this end several combinations of mathematical concepts, entities and techniques have been developed and/or recruited and appropriately adapted. They include i.a. population dynamics models (Guiot et al 2006), diffusion related continuous and finite mathematics treatments (Murray 2003; Swanson et al 2002; Breward et al 2003; Cristini et al 2005; 1992; Frieboes et al 2006; Enderling et al 2007; Ramis-Conde et al 2008), cellular automata and hybrid techniques (Duechting and Vogelsaenger 1981; Duechting et al 1992; Ginsberg et al 1993; Kansal et al 2000; Stamatakos et al 2001a, 2001b; Zacharaki et al 2004), agent based techniques (Deisboeck et al 2001) etc. Additionally, a number of large clinical tumor models focusing mainly on invasion and tumor growth morphology rather than on tumor response to concrete therapeutic schemes as administered in the clinical setting have appeared. Finite difference and finite element based solutions of the diffusion and classical mechanics equations constitute the core working tools of the corresponding techniques (Murray 2003; Swanson et al 2002; Clatz et al 2005).

However, a number of concrete and pragmatic clinical questions of importance cannot be dealt with neither by the *bottom-up* approach nor by the morphologically oriented large tumor growth models in a direct and efficient way. Two examples of such questions are the following (Graf and Hoppe 2006): *Can the response of the local tumor and the metastases to a given treatment be predicted in size and shape over time?, What is the best treatment schedule for a patient regarding drugs, surgery, irradiation and their combination, dosage, time schedule and duration?* A promising modeling method designed with the primary aim of answering such questions is the Discrete Event Based Cancer Simulation Technique (DEBCaST) (Stamatakos et al 2001c, 2002, 2006b, 2006c, 2006d, 2006e, 2007a, 2007b, 2009a; Dionysiou et al 2004, 2006a, 2006b, 2006c; 2007; 2008; Antipas et al 2004, 2007; Stamatakos and Uzunoglu 2006b; Stamatakos and Dionysiou 2009) . DEBCaST is basically a *top-down*

biomodeling approach in the sense that macroscopic data, including i.a. anatomic and metabolic tomographic images of the tumor, provide the framework for the integration of *available* and *clinically trusted* biological information pertaining to lower and lower biocomplexity levels such as *clinically approved* histological and molecular markers. However, DEBCaST *does* also provide a powerful framework for the investigation of multiscale tumor biology in the *generic investigational* context.

From the mathematical standpoint DEBCaST is primarily a *discrete* mathematics method, although *continuous* mathematics (continuous functions, differerential equations) are used in order to tackle specific aspects of the models such as pharmacokinetics and cell survival probabilities based on pharmacodynamical and radiobiological models. Adoption of the discrete approach as the core mathematical strategy of DEBCaST has been dictated by the obvious fact that from the cancer treatment perspective it is the *discrete* i.e. the integer number of the usually few biological cells surviving treatment and their discrete mitotic potential categorization (stem cells, progenitor cells of various mitotic potential levels and differentiated cells) that really matter. These *discrete* entities and quantities in conjunction with their complex interdependences may give rise to tumor relapse or to ensure tumor control over a given time interval following completion of the treatment course. Cell cycle phases have a clearly discrete character too. Moreover, the properties of the different cell phases may vary immensely from the clinical significance perspective. A classical example is the lack of effect of cell cycle specific drugs on living tumor cells residing in the quiescent G0 phase.

It is noted that complex interdependencies of microscopic factors in the surrounding milieu of the cells such as oxygenation, nutrient supply and molecular signals emitted by other cells play a critical role in the mitotic fate of tumor cells. Their effect is taken into account in DEBCaST through the local mean values of the corresponding model parameters. To this end imaging, histological and molecular data is exploited as will be described further down.

Due to the numerical character of the method a careful and realistically thorough numerical analysis concerning consistency, convergence and sensitivity/stability issues is absolutely necessary before any application is envisaged. A discussion of this critical issue is included in Section 5.

Tumor neovascularisation is taken into account in an indirect yet pragmatic way by exploiting grey level and/or color information contained within slices of tomographic imaging modalities sensitive to blood perfusion and/or the metabolic status of the tumor. (Stamatakos et al 2001a,2002, 2006c; Dionysiou et al 2004, 2007; Marias et al 2007). The reason for adopting the above mentioned strategy rather than developing or integrating detailed tumor angiogenesis models is that no microscopic information regarding the exact mesh of the neovascularization *capillaries* throughout the tumor can be currently extracted from clinically utilized imaging modalities. Nevertheless, the microscopic functional capillary *density distribution* over the tumor can be grossly estimated based on various imaging modalities such as T1 gadolinium enhanced MRI in the case of glioblastoma multiforme (GBM) and arterial spin labelling (ASL) MRI.

Precursors of DEBCaST can be traced in the well established and clinically applicable disciplines of pharmacology and radiobiology. Integration of molecular biology in DEBCaST may be viewed as the introduction of a perturbator or adaptor of the cellular and higher biocomplexity level parameters. In such a way *in vivo measurable* clinical manifestation of tumor dynamics is placed the foreground. This is one of the reasons why DEBCaST is gaining wider and wider acceptance within the clinical and the industrial environment including the emergent domain of *in silico* oncology (Stamatakos et al 2002, 2006a, 2007b, 2008, 2009a; Graf and Hoppe 2006; Graf et al 2007, 2009). Both the large scale European Commission (EC) and Japan funded ACGT research and development (R&D) project

(ACGT) and the EC funded ContraCancrum R&D project (ContraCancrum) have adopted DEBCaST as their core cancer simulation method. It is worth noting that in both projects the role of clinicians is prominent. A biomedical engineering concept and construct tightly associated with DEBCaST, the *Oncosimulator*, which is currently under clinical adaptation, optimization and validation is also sketched.

In order to convey the core philosophy of the method to the reader in a concise way a symbolic mathematical formulation of DEBCaST in terms of a hypermatrix and discrete operators is introduced. Two specific models of tumor response to chemotherapeutic and radiotherapeutic schemes are briefly outlined so as to exemplify DEBCaST's application potential. The chapter concludes with a discussion of several critical aspects including numerical analysis, massive parallel code execution, associated technologies, extensions and validation within the framework of clinico-genomic trials and future challenges and perspectives.

An encouraging fact as far as industrial and eventually clinical translation of the method is concerned is that both DEBCaST and the *Oncosimulator* have been selected and endorsed by a worldwide leading medical technology company and now constitute modules of their research and development line (ContraCancrum). One of the envisaged final products of this endeavor is a radiotherapy treatment planning system based on both physical and multiscale biological optimization of the spatiotemporal dose administration scheme. A clinical trial based validation process for the system is currently at the final stage of its detailed formulation.

2 THE ONCOSIMULATOR

The *Oncosimulator* is at the same time a concept of multilevel integrative cancer biology, a complex algorithmic construct, a biomedical engineering system and eventually in the future a clinical tool which primarily aims at supporting the clinician in the process of optimizing cancer treatment in the patient individualized context through conducting experiments *in silico* i.e. on the computer. Additionally it is a platform for simulating, investigating, better understanding and exploring the *natural phenomenon* of cancer, supporting the design and interpretation of clinicogenomic trials and finally training doctors, researchers and interested patients alike (Stamatakos et Uzunoglu 2006b; Stamatakos et al 2007a; Graf et al 2009).

A synoptic outline of the clinical utilization of a specific version of the *Oncosimulator*, as envisaged to take place following an eventually successful completion of its clinical adaptation, optimization and validation process, is provided in the form of the following seven steps (Figure 1). *First step: Obtain patient's individual multiscale and inhomogeneous data.* Data sets to be collected for each patient include: clinical data (age, sex, weight etc.), eventual previous anti-tumor treatment history, imaging data (e.g. MRI, CT, PET etc images), histopathological data (e.g. detailed identification of the tumor type, grade and stage, histopathology slide images whenever biopsy is allowed and feasible etc.), molecular data (DNA array data, selected molecular marker values or statuses, serum markers etc.). It is noted that the last two data categories are extracted from biopsy material and/or body fluids. *Second step: Preprocess patient's data.* The data collected are preprocessed in order to take an adequate form allowing its introduction into the "Tumor and Normal Tissue Response Simulation" module of the *Oncosimulator*. For example the imaging data are segmented, interpolated, eventually fused and subsequently the anatomic entity/-ies of interest is/are three dimensionally reconstructed. This reconstruction will provide the framework for the integration of the rest of data and the execution of the simulation. In parallel the molecular data is processed via molecular interaction networks so as to perturb and individualize the average pharmacodynamic or radiobiological cell survival parameters.

Third step: Describe one or more candidate therapeutic scheme(s) and/or schedule(s). The clinician describes a number of candidate therapeutic schemes and/or schedules and/or no treatment, obviously leading to free tumor growth, to be simulated *in silico* i.e. on the computer. *Fourth step: Run the simulation.* The computer code of tumor growth and treatment response is massively executed on distributed grid or cluster computing resources so that several candidate treatment schemes and/or schedules are simulated for numerous combinations of possible tumor parameter values *in parallel* (see Section 5 for detailed justification). Predictions concerning the toxicological compatibility of each candidate treatment scheme are also produced. *Fifth step: Visualize the predictions.* The expected reaction of the tumor as well as toxicologically relevant side effect estimates for all scenarios simulated are visualized using several techniques ranging from simple graph plotting to four dimensional virtual reality rendering. *Sixth step: Evaluate the predictions and decide on the optimal scheme or schedule to be administered to the patient.* The Oncosimulator's predictions are carefully evaluated by the clinician by making use of their logic, medical education and even qualitative experience. If no serious discrepancies are detected, the predictions support the clinician in taking their final and expectedly optimal decision regarding the actual treatment to be administered to the patient. *Seventh step: Apply the theoretically optimal therapeutic scheme or schedule and further optimize the Oncosimulator*. The expectedly optimal therapeutic scheme or schedule is administered to the patient. Subsequently, the predictions regarding the finally adopted and applied scheme or schedule are compared with the actual tumor course and a *negative feedback signal* is generated and used in order to optimize the *Oncosimulator*.

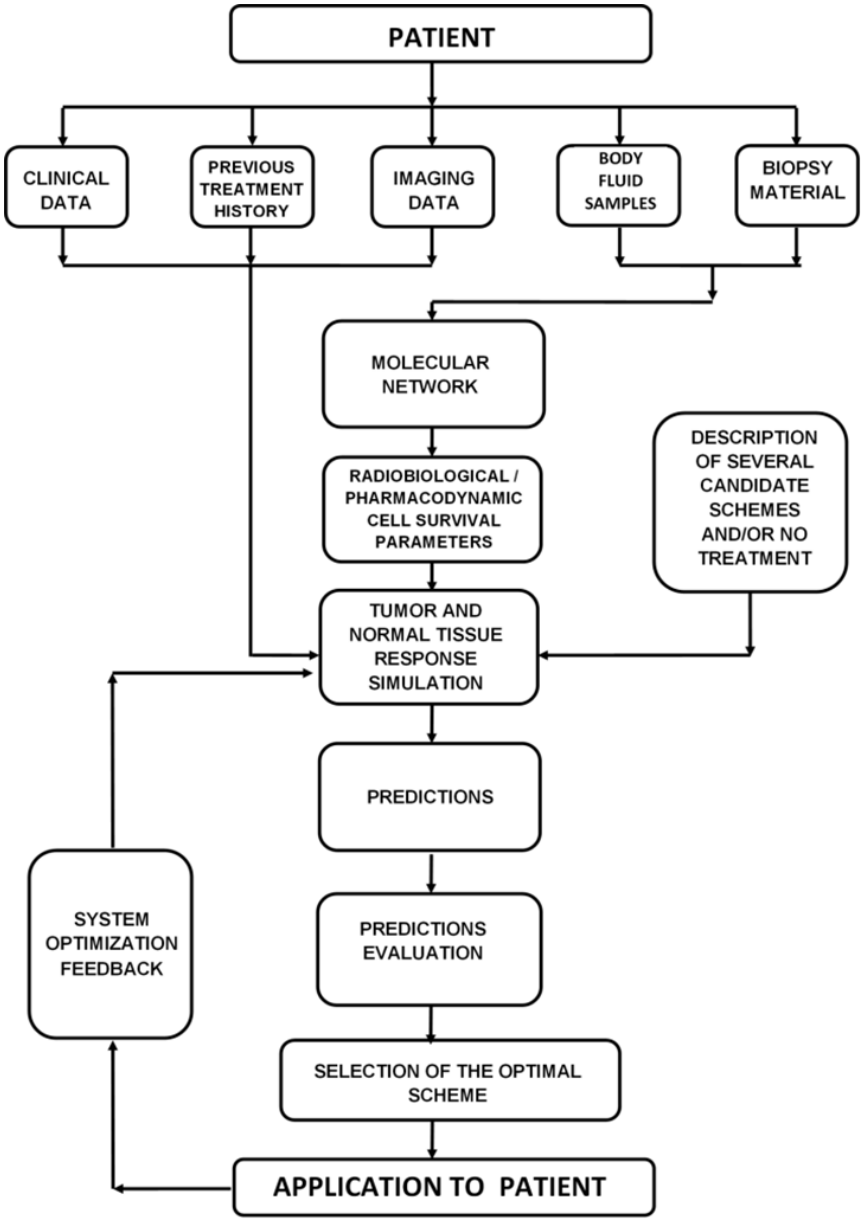

Figure 1: Oncosimulator: a synoptic workflow diagram of one of the system versions

3. A SYMBOLIC MATHEMATICAL FORMULATION OF DEBCaST

3.1 The Hypermatrix of the Anatomical Region of Interest

A special operator notation is introduced in order to concisely describe DEBCaST as applied to the modeling of malignant tumor response to therapeutic schemes in the *clinically oriented setting*. In order to convey the basic philosophy of the method in the simplest possible way a deliberately simplified version of DEBCaST is considered throughout the chapter. The anatomical region of interest, primarily including the tumor and possibly adjacent normal tissues and edema, in conjunction with its biological, physical and chemical dynamics is represented by hypermatrix $\bar{\bar{\mathbf{a}}}$. A *hypermatrix* is a

Matrix of (Matrices of (Matrices…of (Scalars or Vectors or Matrices)…)).

The hypermatrix $\bar{\bar{\mathbf{a}}}$ is created by a cubic discretization mesh which is virtually superimposed upon the anatomical region of interest. Biological cells residing within each geometrical cell of the mesh are conceptually clustered into mathematical *equivalence classes*. Equivalence classes primarily correspond to the various phases within or out of the cell cycle that a biological cell of the tumor can be found. Since a tumor cell at any given instant also belongs to a mitotic potential category (stem, progenitor, terminally_differentiated) the latter acts as a further partitioner of the biological cells into equivalence classes. One of the reasons, though *not* the single most important, for clustering biological cells into equivalence classes within each geometrical cell of the discretization mesh is computing resource limitations. Complex computational treatment of each single cell of a large clinical tumor undergoing therapeutic treatment as a *separate entity* is still not achievable within acceptable resource and time limits.

Discrete time represents a further dimension of the hypermatrix. An important discretization aspect of the method is the mean time spent in the phase of an equivalence class by the biological cells belonging to the equivalence class (Stamatakos et al 2001c, 2002, 2006c, 2006e; Dionysiou et al 2004, 2006; Stamatakos and Dionysiou 2009b). In order to allow for spatiotemporal perturbations of critical

parameter values throughout the tumor and also avoid artificial cell synchronizations due to quantization, use of pseudo-random numbers is extensively made (Monte Carlo technique).

3.2. Practical Considerations Regarding the Construction of the Discretization Mesh

Collection of the appropriate mono-modality or far better multi-modality tomographic data of the patient such as slices of T1 weighted contrast enhanced MRI, T2 weighted MRI, CT, PET or other modalities, image segmentation, slice interpolation, three dimensional reconstruction of the anatomical entities of interest centered at the tumor, and eventually fusion of more than one modality images constitute the initial steps for the creation of the discretization mesh covering and discretizing the anatomical region of interest. Processed microscopic data (histological, molecular) are then utilized in order to enhance the patient individualization of the hypermatrix.

3.3 Hypermatrix and Operator Formulation of DEBCaST

The following mathematical entities are introduced:

$\bar{\bar{\mathbf{a}}}$ denotes the hypermatrix corresponding to the anatomical region of interest that includes the tumor and possibly parts of the surrounding normal tissue and edema. $\bar{\bar{\mathbf{a}}}$ describes explicitly or implicitly the biological, physical and chemical dynamics of the anatomical region of interest. For a given geometrical cell of the discretization mesh each vector element of the hypermatrix $\bar{\bar{\mathbf{a}}}$ can be written as follows:

$$\bar{\bar{\mathbf{a}}}\left(x_i, y_j, z_k, t_l, c_m, p_n\right) = \left(g^{ijklmn}, N^{ijklmn}, X^{ijklmn}, h^{ijklmn}, \tilde{h}^{ijklmn}\right) \quad (1)$$

$$\bar{\bar{\mathbf{a}}}(t_0) = \bar{\bar{\mathbf{a}}}_0 \quad (2)$$

The following symbols are used. x_i, y_j, z_k denote the spatial coordinates of the discrete points of the discretization mesh with spatial indices i, j, k respectively. Each discrete spatial point lies at the center of a geometrical cell of the mesh. t_l denotes the temporal coordinate of the discrete time point with temporal index l. c_m represents the mitotic potential category (i.e. stem or progenitor or terminally differentiated) of the biological cells with mitotic potential category index m. p_n denotes the cell phase (within or out of the cell cycle) of the biological cells with cell phase index n.

For the biological cells belonging to the mitotic potential category c_m *AND* residing in cell phase p_n *AND* being accommodated within the geometrical cell whose center lies at the spatial point (x_i, y_j, z_k) *AND* being considered at the time point t_l - in other words for the biological cells clustered in the same equivalence classs denoted by ijklmn - the following state parameters are provided by the corresponding hypermatrix element $\bar{\bar{\mathbf{a}}}(x_i, y_j, z_k, t_l, c_m, p_n)$**:** g^{ijklmn} : local oxygen and nutrient provision level; N^{ijklmn} : number of biological cells; X^{ijklmn} : average time spent by the biological cells in phase n; h^{ijklmn} : number of biological cells hit by treatment; $\tilde{h}^{ijklmn}$: number of biological cells *not* hit by treatment. The symbol $\bar{\bar{\mathbf{a}}}_0$ represents the initial biological, physical and chemical state of the entire anatomical region of interest or equivalently of the hypermatrix under consideration. This state corresponds to the instant just before the start of the treatment course to be simulated.

The previously mentioned discrete variables can take values from proper or improper subintervals of the discrete intervals appearing below or from proper or improper subsets of the discrete sets appearing also below.

$$x_i \in [x_{min}, x_{max}] \quad (3)$$

where x_{min} and x_{max} denote the minimum and the maximum value respectively of the parameter x_i within the discretization mesh,

$$y_j \in [y_{min}, y_{max}]$$

where y_{min} and y_{max} denote the minimum and the maximum value respectively of the parameter y_j within the discretization mesh,

$z_k \in [z_{min}, z_{max}]$

(5)

where z_{min} and z_{max} denote the minimum and the maximum value respectively of the parameter z_k within the discretization mesh,

$t_n \in [t_{min}, t_{max}]$

(6)

where t_{min} and t_{max} denote the initial and the final simulation timepoint respectively

$c_m \in \{stem,\ progenitor,\ terminally_differentiated\}$

(7)

$p_n \in \{G_1, S, G_2, M, G_0, A, N, D\}$

(8) where G_1 denotes the G_1 cell cycle phase; S denotes the DNA synthesis phase; G_2 denotes the G_2 cell cycle phase; M denotes mitosis; G_0 denotes the quiescent (dormant) G0 phase; A denotes the apoptotic phase; N denotes the necrotic phase and D denotes the remnants of dead cells.

$g^{ijklmn} \in \{s, \tilde{s}\}$
(9)
where s stands for "oxygen and nutrient provision level *sufficient* for tumor cell proliferation"; $\tilde{s}$ stands for "oxygen and nutrient provision level *insufficient* for tumor cell proliferation". Obviously the binary character of the oxygen and nutrient provision level is to be considered only a first simplifying approximation. More elaborate descriptions have been proposed and applied (Stamatakos et al 2002, 2006c, 2006d; Dionysiou et al 2004, 2006a; Antipas et al 2004).
$N^{ijklmn} \in \{0, \ldots, N_{max}\}$
(10)
where N_{max} denotes the maximum number of biological cells irrespectively of mitotic potential category or cell phase that can be accommodated in any geometrical cell under either normal or temporary conditions.
$X^{ijklmn} \in [0, X_{max}]$
(11)
where X_{max} denotes the maximum average time that can be spent by biological cells in phase n
$h^{ijklmn} \in \{0, N_{max}\}$
(12)
$\tilde{h}^{ijklmn} \in \{0, N_{max}\}$
(13)
In the six dimensional *discrete abstract space* of tumor dynamics delineated above, three discrete dimensions represent space, one discrete dimension represents time, another one represents mitotic potential and the last one represents cell phase. Combinations of all possible values from these 6 discrete dimensions produce all the biological cell *equivalence classes* that have been introduced so far.

TYPO CORRECTION:

Equation (12) : CORRECT FORM: $h^{ijklmn} \in \{0,1,2,\ldots N_{max}\}$

Equation (13) : CORRECT FORM: $\tilde{h}^{ijklmn} \in \{0,1,2,\ldots N_{max}\}$

The entire simulation can be viewed as the periodic and sequential application of a number of discrete algorithmic operators on the hypermatrix $\bar{\bar{\mathbf{a}}}$ of the anatomic region of interest. The *operator application period* is equal to the time separating two consecutive *complete scans* of the discretization mesh. A complete scan includes mesh scans performed by all operators for any given time point. The operator application period is usually taken 1 h since this is approximately the duration of mitosis, the shortest of the cell cycle phases. It should be noted that although the parameter values *exported* by the simulation execution at any desired instant for visualization and analysis purposes have a discrete character, certain parameters are handled by the computer *internally* and *temporarily* as real numbers (even with enhanced precision) in order to minimize quantization error propagation, in particular when dealing with small numbers of discrete entities in the stochastic context. By no means, however, does this technicality can affect the fundamentally discrete character of DEBCaST.

The various processes or modules of the complex (*not* in the sense of complex numbers) algorithmic manipulations applied on the hypermatrix can be thought of as corresponding to discrete operators acting on the discrete hypermatrix of the anatomical region of interest in analogy to the action of

continuous operators on a continuous wave function in quantum mechanics (Schiff 1981). The great importance of introducing abstract (vector) spaces and operators has been established in virtually all fields of the essentially *non living matter* physics (Morse and Feshbach 1953). Compactness, clarity, amenability to in depth mathematical analysis and propensity to provide stimulating and eventually highly creative analogies with other scientific fields are but a few of the advantages of the particular formalism. Therefore, extending such a strategy to multiscale *living matter* physics i.e. biology seems to be a straightforward step forward.

In order to proceed to the operator application on the hypermatrix the following symbols are introduced.
f stands for the composite discrete operator i.e. the operator formed by the synthesis of all partial operators that are sequentially applied on the hypermatrix at each discrete time step. Therefore, the updated hypermatrix at the time point t_{n+1} is given by

$$f\left(\bar{\bar{\mathbf{a}}}(t_n)\right) = \bar{\bar{\mathbf{a}}}(t_{n+1})$$

(14)

The composite operator can be written as

$$f = f^U\, f^E\, f^C\, f^H\, f^O\, f^T$$

(15)

where

$f^J,\ J \in \{U, E, C, H, O, T\}$ stands for a *partial operator*

(16)

T stands for time updating i.e. increasing time by a time unit (e.g. 1h). Action of operator f^T on the hypermatrix should not be confused with the updated state of the entire hypermatrix $\bar{\bar{\mathbf{a}}}$ at time t_l . O stands for estimating the local oxygen and nutrient provision level. H stands for the effect of treatment (therapy) referring mainly to cell hitting by treatment, cell killing and cell survival. C stands for cell cycling, possibly perturbed by treatment. Transition between mitotic potential cell categories such as transition of the offspring of a terminally divided progenitor cell into the terminally differentiated cell category is also tackled by this operator. E stands for differential expansion or shrinkage or more generally for geometry and mechanics handling. U stands for the updating of the local oxygen and nutrient provision level following application of the rest of operators at each time step.

It is noted parenthetically that the outcome of appropriate processing of the molecular and/or histopathological data via e.g. molecular networks and signaling pathways is used as a perturbator of the cell survival probabilities included in operator f^H so as to considerably enhance patient individualization of the simulation. A realistic estimate of the extent of such perturbations for a given tumor type subclass in the framework of a clinico-genomic trial is achieved in a stepwise way. Initial rough modifications of the cell survival probabilities based on the baseline-pretreatment data, pertinent literature information and logic are subsequently corrected through utilization of the corresponding post treatment data via a process of parameter fitting.

Therefore, equation 14 becomes:

$$f^{U}\left(f^{E}\left(f^{C}\left(f^{H}\left(f^{O}\left(f^{T}\,\bar{\bar{\mathbf{a}}}(t_n)\right)\right)\right)\right)\right) = \bar{\bar{\mathbf{a}}}(t_{n+1}), \quad n = 0,1,2,\ldots$$

(17)

or in a more compact form:

$$f^{U}\,f^{E}\,f^{C}\,f^{H}\,f^{O}\,f^{T}\,\bar{\bar{\mathbf{a}}}(t_n) = \bar{\bar{\mathbf{a}}}(t_{n+1}), \quad n = 0,1,2,\ldots$$

(18)

where the application of operators takes place from the right to the left.

It is pretty obvious that the above mentioned concepts and symbols cannot convey all the details needed for the simulation to run. Their role is rather to identify and decompose the major conceptual mathematical and computational steps than to list all modeling details. The interested reader is referred to the website of the *In Silico* Oncology Group where they may find lists of pertinent publications providing detailed descriptions of several DEBCaST models including i.a. assumptions, mathematical

treatment, numerical aspects such as convergence and quantization error minimization, sensitivity analysis, validation, applications and suggested extensions.

It is worth noting that discrete simulation under certain constraints can efficiently replace analytical solutions to a wide range of mathematical problems which, although being formulated in terms of *continuous* mathematics - usually including symbolically formulated differential equations - refer in fact to *discrete* physical quantities such as biological cells and cell state transition rates. Moreover, in many cases the *continuous* symbolic formulation of mathematical operators, such as the well known differential operator, when acting on discrete physical quantities can be readily replaced by a conceptually more straightforward *algorithmic* formulation. Several techniques leading to the minimization of error propagation for those cases where small numbers of discrete entities are dealt with by stochastic processes are available. The above generic policy has been extensively adopted in DEBCaST models. For extensions of DEBCaST currently under implementation see Section 5.

4. EXAMPLES OF DEBCaST APPLICATIONS - RESULTS

In this section two indicative models denoted by Model A and Model B are briefly outlined so as to exemplify the application potential of DEBCaST in the clinical context.

4.1 Model A: Tumor Response to Chemotherapeutic Schemes

Model A is a four dimensional, patient specific DEBCaST simulation model of solid tumor response to chemotherapeutic treatment *in vivo*. The special case of imageable glioblastoma multiforme (GBM) treated by temozolomide (TMZ) has been addressed as a simulation paradigm. Nevertheless, a considerable number of the involved algorithms are quite generic. The model is based on the patient's imaging, histopathologic and genetic data. For a given drug administration schedule lying within acceptable toxicity boundaries, the concentration of the prodrug and its metabolites within the tumor is calculated as a function of time based on the drug pharamacokinetics and is conceptually included in [operator H]. A discretization mesh is superimposed upon the anatomical region of interest and within each geometrical cell of the mesh the basic biological, physical and chemical *"laws"* such as the rules concerning oxygen and nutrient provision [operators O and U], cell cycling [operator C] (Salmon and Sartorelli 2001), mechanical deformation [operator E] etc. are applied at each discrete time point [operator T]. The biological cell fates are predicted based on the drug pharmacodynamics, constituting part of [operator H] (Perry 2001; Katzung 2001; FDA; Newlands et al 1992; Bobola et al 1996; Chinot et al 2001; Stupp et al 2001). The outcome of the simulation is a prediction of the spatiotemporal activity of the entire tumor and is i.a. virtual reality visualized. A good qualitative agreement of the model's predictions with clinical experience (Stamatakos et al 2006d, 2006e) supports the applicability of the approach. Model A has provided a basic platform for performing patient individualized *in silico* experiments as a means of chemotherapeutic treatment optimization in the *theoretical* context. A few indicative aspects of the model are sketched below. Since the complexity of the analysis is high the interested reader is referred to (Stamatakos et al 2006d, 2006e) for a detailed description of the model. The work has also provided the basis for the development of the ACGT (ACGT) and ContraCancrum (ContraCancrum) chemotherapy treatment response models.

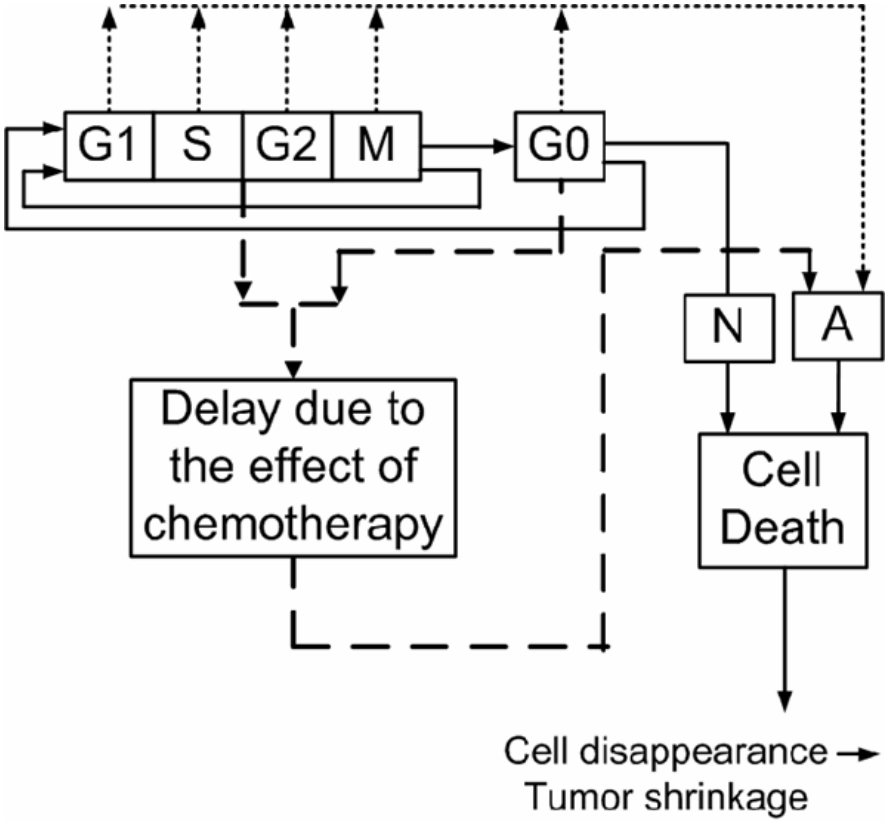

Figure 2: Simplified cytokinetic model of a tumor cell proposed and adopted in model A. Symbols: G1: G1 phase; S: DNA synthesis phase; G2: G2 phase; G0: G0 phase; N: necrosis; A: apoptosis. The cytotoxicity produced by TMZ is primarily modeled by a delay in the S phase compartment (TDS) ("Delay due to the effect of chemotherapy" in the diagram) and subsequent apoptosis. The delay box simply represents the time corresponding to at most two cell divisions being required before the emergence of temozolomide cytotoxicity. It is not a time interval additional to the times represented by the cell cycle phase boxes. (From Stamatakos G. S., Antipas V. P. and N.K.Uzunoglu. 2006. A spatiotemporal, patient individualized simulation model of solid tumor response to chemotherapy *in vivo*: the paradigm of glioblastoma multiforme treated by temozolomide. IEEE Trans Biomed Eng 53(8): 1467- 1477. Reprinted with permission from the Institute of Electrical and Electronics Engineers (IEEE), © 2006 IEEE)

Figure 2 depicts the simplified cytokinetic model of a tumor cell that has been proposed and adopted in Model A. The cytotoxicity produced by TMZ is primarily modeled by a delay in the S phase compartment (TDS) which is denoted by “Delay due to the effect of chemotherapy” in the diagram of Figure 2 and by subsequent apoptosis. Further details are provided in the caption of Figure 2.

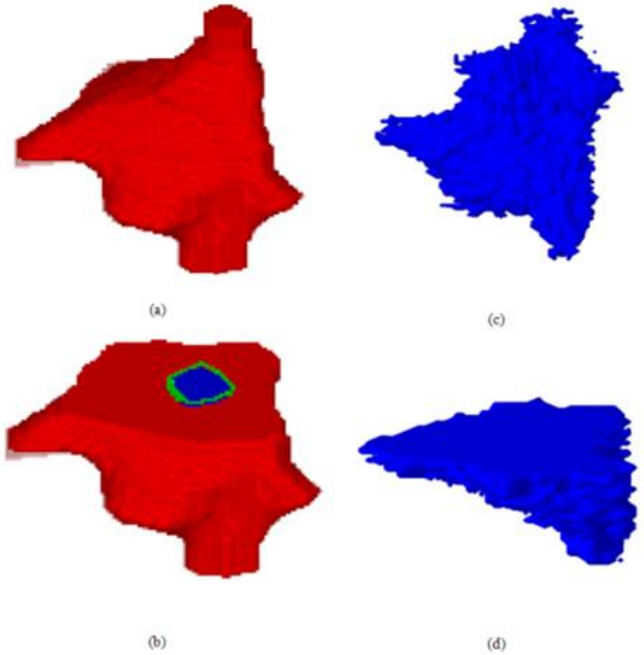

Figure 3: A three dimensional visualization of the simulated response of a clinical GBM tumor to one cycle of the TMZ chemotherapeutic scheme: 150 mg/m^2 orally once daily for 5 consecutive days per 28-day treatment cycle. (a) external surface of the tumor before the beginning of chemotherapy, (b) internal structure of the tumor before the beginning of chemotherapy, (c) predicted external surface of the tumor 20 days after the beginning of chemotherapy (d) predicted internal structure of the tumor 20 days after the beginning of chemotherapy. The following pseudocolor code has been applied: *red*: proliferating cell layer; *green*: dormant cell layer (G0); *blue*: dead cell layer. The "99.8%" pseudo-coloring criterion has been devised and applied as follows. "For a geometrical cell of the discretizing mesh, if the percentage of dead cells within it is lower than 99.8% then {if percentage of proliferating cells > percentage of G0 cells, then paint the geometrical cell red (proliferating cell layer), else paint the geometrical cell green (G0 cell layer)} else paint the geometrical cell blue (dead cell layer)." (From Stamatakos G. S., Antipas V. P. and N.K.Uzunoglu. 2006. A spatiotemporal, patient individualized simulation model of solid tumor response to chemotherapy *in vivo*: the paradigm of glioblastoma multiforme treated by temozolomide. IEEE Trans Biomed Eng 53(8): 1467- 1477. Reprinted with permission from the Institute of Electrical and Electronics Engineers (IEEE), © 2006 IEEE)

Figure 3 provides a three dimensional visualization of the simulated response of a clinical GBM tumor to one cycle of the TMZ chemotherapeutic scheme: 150 mg/m^2 orally once daily for 5 consecutive days per 28-day treatment cycle (Stamatakos et al 200d). Panel (a) shows the external surface of the tumor before the beginning of chemotherapy. Panel (b) shows the internal structure of the tumor before the beginning of chemotherapy. Panel (c) shows the predicted external surface of the tumor 20 days after the beginning of chemotherapy. Panel (d) shows the predicted internal structure of the tumor 20 days after the beginning of chemotherapy. The pseudo-coloring criterion proposed and utilized is described in the caption of Figure 3.

4.2 Model B: Tumor Response to Radiotherapeutic Schemes

Model B is a spatiotemporal simulation model of *in vivo* tumor growth and response to radiotherapy exemplified by the special case of imageable GBM treated by the treatment modality under consideration. The main constitutive processes of the model can be summarized as follows. A discretizing cubic mesh is superimposed upon a three dimensional virtual reconstruction of the tumor including its necrotic region and the surrounding anatomical features based on imaging data. In a way analogous to Model A, within each geometrical cell of the mesh a number of biological cell equivalence classes are defined based i.a. on the biological cell distribution over the various phases within or out of the cell cycle for the various mitotic potential categories. Sufficient registers are used in order to store the current state of each equivalence class such as the average time spent by clustered biological cells in phase G1 etc. The mesh is scanned every one hour [operator T]. The basic *biological, physical* and *chemical "laws"* including the metabolic activity dynamics [operators O and U], cell cycling [operator C], mechanical and geometrical aspects [operator E], cell survival probability following irradiation with dose D [operator H] (Perez and Brady 1998; Steel 2002) are applied on each geometrical cell at each complete scan. A spatial and functional restructuring of the tumor takes place during each discrete time point since new biological cells are eventually produced, leading to differential tumor growth, or

existing cells eventually die and subsequently disappear through specific molecular and cellular event cascades, thus leading to differential tumor shrinkage. Simulation predictions can be two or three dimensionally visualized at any simulated instant of interest. In the particular model special attention has been paid to the influence of oxygenation on radiosensitivity in conjunction with the introduction of a refined imaging based description of the neovasculature density distribution. In order to validate the model two identical - except for the p53 gene status - virtual GMB tumors of large size, complex shape and complex internal necrotic region geometry were considered. The first one possessed a wild type p53 gene whereas the second one was characterized by a mutated p53 (Stamatakos et al 2006c; Dionysiou et al 2004). The values of the α and β parameters of the standard linear quadratic radiobiological model for cell survival (Steel 2002, Perez and Brady 1998) have been determined experimentally for the two cell lines considered (Haas-Kogan et al 1995). Simulation predictions agree at least semi-quantitatively with clinical experience and in particular with the outcome of the Radiation Therapy Oncology Group RTOG Study 83 02 (Werner-Wasik et al 1996). The model allows for a quantitative study of the inter-relationship between the competing influences in a complex, dynamic tumor environment. Therefore, the model is already useful as an educational tool with which to theoretically study, understand and demonstrate the role of various parameters on tumor growth and response to irradiation. A long term quantitative clinical adaptation and validation of a considerably extended version of the model is in progress within the framework of the ContraCancrum project (ContraCancrum). The long term goal is obviously integration into the clinical treatment planning procedure.

Figure 4 provides the simulation outcomes corresponding to several branches of the clinical study RTOG Study 83 02. Panel (a) shows the total predicted number of proliferating and dormant tumor cells as a function of time for the hyperfractionated (1.2 Gy twice daily to the dose of 81.6 Gy, "HF-81.6") and accelerated hyperfractionated (1.6 Gy twice daily to the dose of 54.4 Gy, "AHF-54.4") radiotherapy schedules. All schemes start on the first day of the radiotherapy course. HF-81.6 is completed on day 46 after initiation of treatment whereas AHF-54.4 is completed on day 23. Figure 4 (b) depicts the total number of proliferating and dormant tumor cells as a function of time for the hyperfractionated (1.2 Gy twice daily to the dose of 76.8 Gy, "HF-76.8") and accelerated hyperfractionated (1.6 Gy twice daily to the dose of 48 Gy, "AHF-48") radiotherapy schedules. Both irradiation schedules start on the first day of the first week of treatment. HF-76.8 is completed on day 44 after initiation of treatment whereas AHF-48 is completed on day 19. According to the graphs, before completion of the AHF course cell kill due to AHF irradiation is more pronounced than cell kill induced by the HF scheme. This can be explained by the fact that a higher total dose has been administered to the tumor by the AHF scheme whereas for the period under consideration both schemes are characterized by the same time intervals between consecutive sessions. In case that not all living cells have been killed by AHF irradiation, tumor repopulation is considerable so that by the time the HF scheme is completed living tumor cells and their progeny which have escaped AHF irradiation outnumber tumor cells which have escaped HF irradiation. Improved tumor control following HF irradiation in comparison with the AHF scheme is in agreement with the conclusions of the clinical trial RTOG-83-02.

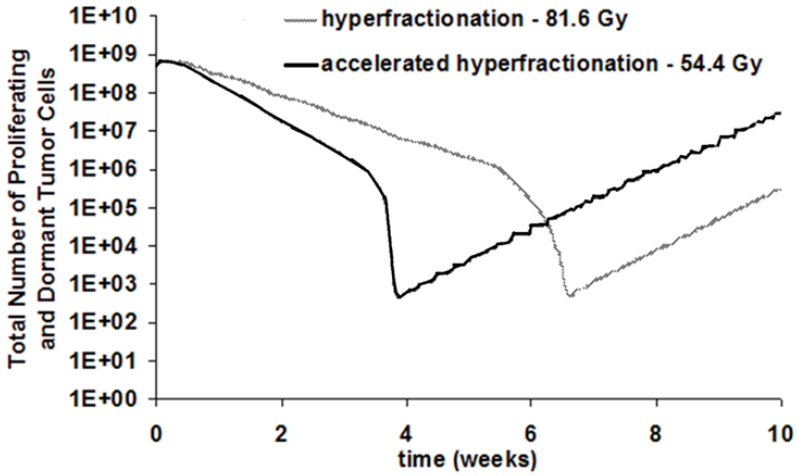

(a)

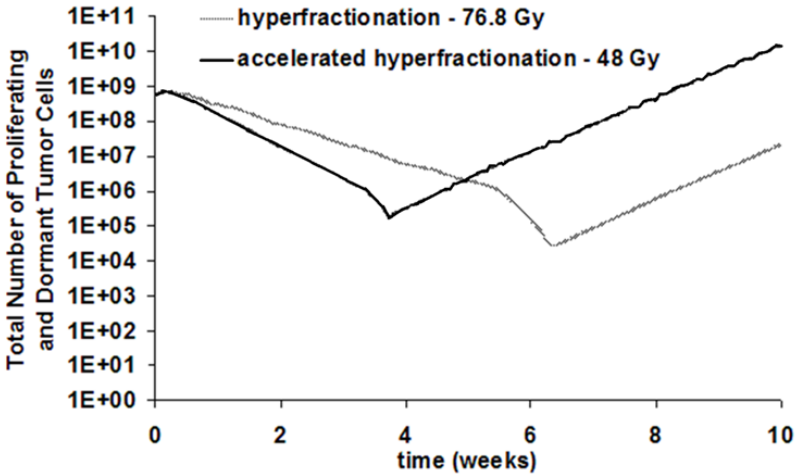

(b)

Figure 4: Simulation predictions corresponding to several branches of the RTOG Study 83 02. (a) total predicted number of proliferating and dormant tumor cells as a function of time for the hyperfractionated (1.2 Gy twice daily to the dose of 81.6 Gy, "HF-81.6") and accelerated hyperfractionated (1.6 Gy twice daily to the dose of 54.4 Gy, "AHF-54.4") radiotherapy schedules. All schemes start on the first day of the radiotherapy course. HF-81.6 is completed on day 46 after initiation of treatment whereas AHF-54.4 is completed on day 23. (b) total number of proliferating and dormant tumor cells as a function of time for the hyperfractionated (1.2 Gy twice daily to the dose of 76.8 Gy, "HF-76.8") and accelerated hyperfractionated (1.6 Gy twice daily to the dose of 48 Gy, "AHF-48") radiotherapy schedules. Both irradiation schedules start on the first day of the first week of treatment. HF-76.8 is completed on day 44 after initiation of treatment whereas AHF-48 is completed on day 19. (From Stamatakos G.S., V.P. Antipas, N.K. Uzunoglu, and R.G. Dale. 2006. A four dimensional computer simulation model of the *in vivo* response to radiotherapy of glioblastoma multiforme: studies on the effect of clonogenic cell density. Br J Radiol 79: 389-400. Reprinted with permission from the British Institute of Radiology, © 2006 BIR)

5. DISCUSSION AND FUTURE PERSPECTIVES

Since DEBCaST is a numerical method, a thorough convergence and sensitivity/stability analysis that includes the study of multiple parameter interdependences is imperative before any application is envisaged. Numerical analysis should satisfactorily cover at least those regions of the abstract parameter space that correspond to the envisaged applications. It is noted that of particular importance is the creation of the baseline tumor constitution by exploiting the relevant multiscale data available. Convergence of the tumor initialization has to be ensured. All of the above issues have been successfully addressed for specific tumor treatment cases such as breast cancer treated with epirubicin and nephroblastoma treated with vincristine and dactinomycin. The numerical behavior of the corresponding models has been checked through massive numerical experimentation. Concrete applicability intervals, restrictions and limitations have been identified (Internal ACGT project reports and deliverables; Kolokotroni et al 2008; Georgiadi 2008). Since the entire parameter space of DEBCaST models is rather large, numerical studies covering regions that correspond to further applications are in progress. Special attention is paid to the inherent relative biological instability of the cancer system itself when the model's stability is investigated.

It is well known that the values of critical parameters determining treatment outcome can vary considerably around what is assumed to be their population based average values. *Even after* incorporation of patient specific multiscale data into the simulation model no *accurate* evaluation of several critical model parameters is expected to be achieved. Moreover, as already mentioned, a tumor may behave as a relatively unstable system. Therefore, in order to compare candidate treatment schemes and/or schedules *in silico*, several possible combinations of parameter values lying around their apparently most probable estimates have to be constructed so as to cover the abstract parameter space as best as possible. Code executions have to be performed for all these selected parameter combinations. If for example the clinical question addressed is “Which out of the two candidate treatment schedules dented by I and II is the most promising for a given patient?”, simulations have to run for both

schedules I and II and for all parameter value combinations selected in the way briefly delineated above. If based on the simulation predictions schedule I outperforms schedule II for a sufficiently large percentage of the total parameter combinations considered, say 90%, then there is ground to suggest adoption of schedule I. Candidate scheme/schedule selection criteria are currently under formulation in tight collaboration with specialist clinicians within the framework of the ACGT (ACGT) and ContraCancrum (ContraCancrum) R&D projects. Obviously the above sketched treatment optimization strategy dictates the need for a large number of parallel code executions on either cluster of grid platforms. This necessity has been addressed by specific actions of the previosly mentioned projects.

Critical constraints imposed by toxicological limits of the treatment affected normal tissues should also be taken into account in order to judge whether or not a candidate scheme could be toxicologically acceptable. This issue may be addressed by exploiting the outcome of eventually relevant clinical trials and in particular of their phase I results. Ideally, direct multiscale spatiotemporal simulation of the effects of a given candidate scheme on specific normal tissues would provide quantitatively refined predictions. However, due to the extremely high complexity of the homeostatic mechanisms governing normal tissue dynamics, the large number of normal tissue functional aspects and the potential induction of serious late effects by treatment such as radiotherapy, clinical translation of the second scenario seems to be a long term enterprise (Antipas et al 2007).

Since many solid tumors are microscopically inhomogeneous in space, the applications presented so far essentially make use of the *mean values* of certain biological parameters over each *imaging based segmented* sub-region of the tumor (Stamatakos et al 2002, 2006b, 2006c, 2006d, 2006e, 2007b, Dionysiou et al 2004, 2006a, 2006c; 2007; 2008; Antipas et al 2004, 2007). Small perturbations around these values are nevertheless implemented across each region through Monte Carlo simulation by DEBCaST. In the paradigmal case of MRI T1 gadolinium enhanced imaging modality, strong grey level fluctuations over a tomographic slice can lead to an approximate delineation of the internal necrotic and the well neovascularized region of the tumor. Despite the fact that different values of certain parameters may be assigned to these two regions, sub-imaging scale inhomogeneties may still create spatial fluctuations of certain parameter values. In order to theoretically investigate the role of such biological inhomogeneities, pertaining for example to the genotypic and/or phenotypic tumor constitution, as well as the role of biochemical inhomogeneities of the extra tumoral environment such as acidity, necrosis exudate concentration etc the BEBCaST basic platform can be still used provided that specific adaptations have taken place. Furthermore, tumor cell - tumor cell, tumor cell - host cell and tumor cell - local environment interactions in the microscopic setting can in principle be studied. In order to implement the above scenarios, the density of the discretization mesh should considerably increase, deeper level partitioning into more equivalence (sub-)classes has to be introduced into the hypermatrix of the anatomical region of interest and the operators should be extended accordingly. However, such an approach dictates a sharp increase in computing memory and time demands and therefore tumor size must be kept small if restrictions in these resources apply, as is usually the case.

Following appropriate adaptation of specific modeling modules or equivalently operators such as [operator H], DEBCaST is in principle able to simulate tumors of any shape, size, geometry, macroscopic distribution of the metabolic or neovascularisation field, differentiation grade, spatial inhomogeneities, molecular profile and treatment scheme/schedule such as radiotherapeutic, chemotherapeutic, combined, new treatment modality etc. However, great care should be taken so that the model parameter values are estimated as best as possible based on real multiscale data. If such data is not available use of at least population based average parameter value estimates or qualitative experience based plausible values may be utilized only for *generic exploratory* reasons.

Hybridization of DEBCaST with continuous and finite mathematics approaches such as diffusion based tumor growth modeling and detailed biomechanics is currently under implementation (ContraCancrum). The aim of the task is to integrate into a DEBCaST GBM model the microscopic tumor invasion process that conceptually constitutes part of [operator E]. The detailed biomechanics of the system calculated via a finite element module and constituting also part of [operator E] is also being integrated. Such a hybrid model is expected to be able to reproduce in relative detail both *physical and biological* aspects of tumor dynamics within the *generic investigational* framework. It should be noted that the non imageable diffusive component of GBM does play an important role in the development of the disease and therefore merits an in depth theoretical investigation. However, since the non imageable boundaries of GBM cannot be defined and monitored in a sufficiently objective way i.e. based on observational data such as clinically obtainable tomograhic images, direct handling of the non imageable component by treatment planning systems in the patient individualized treatment context seems not to be a fully mature scenario as yet. Furthermore, by focusing on the imageable component within the treatment optimization context, one may argue that if for the imageable component a candidate treatment scheme denoted by scheme I outperforms another candidate scheme denoted by scheme II *in silico*, the same would be true for the non imageable component of the tumor as well. From the *treatment perspective* again the main advantage of focusing on the imageable component, although this may represent even less than half of the total number of all viable tumor cells, is that this very component is amenable to relatively objective measurement *in vivo* and not only *post mortem*. Therefore, glioma dynamics models based on the imageable component are amenable to validation, at least in part, *in vivo*. Besides, incorporation of the immune system response to tumor (D'Onofrio 2005) and simulation of the effects of antiangiogenetic drugs on the tumor are two further scenarios, currently under investigation in the ACGT Oncosimulator extension context (ACGT).

Referring to the molecular level from the *generic investigational* standpoint, a large number of mechanisms, such as pathways leading to apoptosis or survival, that can be informed by available molecular data can be readily integrated into DEBCaST models by applying the *summarize and jump strategy* of bio-data and bio-knowledge integration across bio-complexity scales (Stamatakos et al 2009a). This is in fact one of the actions currently taking place within the framework of the ContraCancrum project (ContraCancrum). However, if the same biocomplexity level is viewed from the *clinical* perspective, care has to be taken so that only those characteristics and /or mechanisms whose predictive potential has been proved and established in the *clinical* setting - normally though clinical trials – may be incorporated into the models.

Regarding the envisaged clinical translation of DEBCaST based models and systems, including the *Oncosimulator*, a *sine qua non* prerequisite is a systematic, formal and strict clinical validation. Designing the models so as to mimick actual clinical or far better *clinico-genomic* trials seems to be the optimal way to achieve this goal (Stamatakos et al. 2006c, 2007a; Graf and Hoppe 2006; Graf 2007, 2008, 2009). Therefore, involvement of clinicians in the model and system design and validation process should start at the *very beginning* of the endeavor (Graf 2007, 2008, 2009). Real clinicogenomic trials can provide invaluable multiscale data (imaging, histological, molecular, clinical, treatment) before, during and after a treatment course so as to best adapt and optimize the models and subsequently validate them. This is one of the core tasks of both the ACGT (ACGT) and the ContraCancrum R&D (ContraCancrum) projects. Nephroblastoma and breast cancer are the tumor types addressed by ACGT whereas gliomas and lung cancer are the ones addressed by ContraCancrum.

A further important challenge is to develop reliable, efficient, highly versatile and user friendly technological platforms which, following clinical adaptation, optimization and validation of the models would facilitate translation of *oncosimulators* into the clinical practice so as to efficiently support,

enhance and accelerate patient individualized treatment optimization. Advanced image processing, visualization and parallel code execution modules are but a few of the components necessary to achieve this goal. Both the ACGT and ContraCancrum R&D projects constitute exemplary initiatives towards this direction.

In summary having taken into account the hyper-complex and heavily multiscale character of the *natural phenomenon* of cancer as well as the constantly expanding accumulation of experimental and clinical knowledge pertaining to the *disease*, both DEBCaST and the *Oncosimulator* have been designed so as to be readily optimizable, extensible and adaptable to varying clinical, biological, and research contexts. In other words both entities, being primarily *biomedical engineering* geared, have a clearly *pragmatic* and *evolutionary* character. This has been largely achieved through the extensive application of the principles of *discrete event simulation* and *system modularity*.

ACKNOWLEDGEMENTS

This work has been supported in part by the European Commission under the projects “ACGT: Advancing Clinicogenomic Trials on Cancer” (FP6-2005-IST-026996) and ContraCancrum: Clinically Oriented Translational Cancer Multilevel Modelling” (FP7-ICT-2007-2- 223979).

REFERENCES

ACGT: Advancing Clinicogenomic Trials on Cancer: Open Grid Services for Improving Medical Knowledge Discovery. EC and Japan funded R&D project. (FP6-2005-IST-026996) [http://eu-acgt.org/acgt-for-you/researchers/in-silico-oncology/oncosimulator.html and http://www.eu-acgt.org/]

Antipas, V., G. S. Stamatakos, N. Uzunoglu, D. Dionysiou and R. Dale. 2004. A spatiotemporal simulation model of the response of solid tumors to radiotherapy *in vivo*: parametric validation concerning oxygen enhancement ratio and cell cycle duration. Phys Med Biol 49: 1-20.

Antipas, V.P., G.S.Stamatakos and N.K.Uzunoglu. 2007. A patient-specific *in vivo* tumor and normal tissue model for prediction of the response to radiotherapy: a computer simulation approach. Meth Inf Med 46: 367-375.

Bobola, M. S., S. H. Tseng, A. Blank, M. S. Berger and J. R. Silber. 1996. Role of O6-methylguanine-DNA methyltransferase in resistance of human brain tumor cell lines to the clinically relevant methylating agents temozolomide and streptozotocin. Clin Cancer Res 2: 735-741.

Breward, C.J., Byrne H.M. and C.E. Lewis. 2003. A multiphase model describing vascular tumour growth. Bull Math Biol 65(4): 609-40.

Clatz, O., Sermesant M., Bondiau P.Y., Delingette H., Warfield S.K., Malandain G. and Ayache N. 2005. Realistic simulation of the 3-D growth of brain tumors in MR images coupling diffusion with biomechanical deformation. IEEE Trans Med Imaging 24(10):1334-46.

ContraCancrum: Clinically Oriented Translational Cancer Multilevel Modelling. EC funded R&D project. (FP7-ICT-2007-2- 223979) [www.contracancrum.eu]

Cristini, V., H.B. Frieboes, R. Gatenby, S. Caserta, M.Ferrari and J.P. Sinek. 2005. Morphological instability and cancer invasion. Clin Cancer Res 11: 6772–6779.

Deisboeck, T.S., M.E. Berens, A.R. Kansal, S. Torquato, A.O. Stemmer-Rachamimov and E.A. Chiocca. 2001. Pattern of self-organization in tumour systems: Complex growth dynamics in a novel brain tumour spheroid model. Cell Prolif 34: 115-34.

Dionysiou, D. D., G. S. Stamatakos, N.K. Uzunoglu, K. S. Nikita and A. Marioli, 2004. A four-dimensional simulation model of tumour response to radiotherapy *in vivo*: parametric validation considering radiosensitivity, genetic profile and fractionation. J Theor Biol 230:1–20.

Dionysiou, D. D., G. S. Stamatakos, N.K., Uzunoglu and K. S. Nikita. 2006a. A computer simulation of in vivo tumour growth and response to radiotherapy: New algorithms and parametric results. Comput Biol Med 36:448–464.

Dionysiou, D.D., and G.S.Stamatakos. 2006b. Applying a 4D multiscale in vivo tumor growth model to the exploration of radiotherapy scheduling: the effects of weekend treatment gaps and p53 gene status on the response of fast growing solid tumors. Cancer Informatics 2:113-121.

Dionysiou, D.D., G.S. Stamatakos, N.K.Uzunoglu and K.S.Nikita. 2006c. A computer simulation of *in vivo* tumour growth and response to radiotherapy: new algorithms and parametric results. Comp Biol Med 36:448-464.

Dionysiou D.D., G.S.Stamatakos and K.Marias. 2007. Simulating cancer radiotherapy on a multi-level basis: biology, oncology and image processing. Lect Notes Comp Sci 4561: 569-575.

Dionysiou, D.D., G.S. Stamatakos, D. Gintides, N. Uzunoglu and K. Kyriaki. 2008. Critical parameters determining standard radiotherapy treatment outcome for glioblastoma multiforme: a computer simulation. Open Biomed Eng J 2: 43-51.

D'Onofrio, A. 2005. A general framework for modeling tumor-immune system competition and immunotherapy: analysis and medical inferences. Physica D 208: 220-235.

Duechting, W. and T.Vogelsaenger. 1981. Three-dimensional pattern generation applied to spheroidal tumor growth in a nutrient medium. Int. J. Biomed. Comput., 12 (5), 377–392.

Duechting, W., W. Ulmer, R. Lehrig, T. Ginsberg, and E. Dedeleit. 1992. Computer simulation and modeling of tumor spheroid growth and their relevance for optimization of fractionated radiotherapy. Strahlenther Onkol 168(6): 354–360.

Enderling, H., M. A.J. Chaplain, A.R.A Anderson and J.S. Vaidya. 2007. A mathematical model of breast cancer development, local treatment and recurrence. J Theor Biol. 246:245–259.

Frieboes, H.B., X. Zheng, C.H. Sun, B. Tromberg, R. Gatenby and V. Cristini. 2006. An integrated computational/experimental model of tumor invasion. Cancer Res 66(3):1597-604.

FDA, Center for Drug Evaluation and Research. 1999 a. Application Number:21029, Drug Name: Temozolomide (Temodal), New Drug Application, Clinical Pharmacology and Biopharmaceutics Reviews, (Revision date: 2/2/1999), pp. 19-20.

Georgiadi, E. Ch., G. S. Stamatakos, N. M. Graf, E. A. Kolokotroni, D. D. Dionysiou, A. Hoppe and N. K. Uzunoglu. 2008. Multilevel Cancer Modeling in the Clinical Environment: Simulating the Behavior of Wilms Tumor in the Context of the SIOP 2001/GPOH Clinical Trial and the ACGT Project. Proc. 8th IEEE International Conference on Bioinformatics and Bioengineering (BIBE 2008), Athens, Greece, 8-10 Oct. 2008. IEEE Catalog Number: CFP08266, ISBN: 978-1-4244-2845-8, Library of Congress: 2008907441, Paper No. BE-2.1.2.

Ginsberg T., W. Ulmer, W. Duechting. 1993. Computer simulation of fractionated radiotherapy: further results and their relevance to percutaneous irradiation and brachytherapy. Strahlenther Onkol 169: 304-310.

Graf N. and Hoppe A. 2006. What are the expectations of a clinician from *in silico* oncology ? Proc. 2nd International Advanced Research Workshop on *In Silico* Oncology, Kolympari, Chania, Greece, Sept. 25-26, 2006. Edited by K.Marias and G. Stamatakos. pp. 36-38. [www.ics.forth.gr/bmi/2nd-iarwiso/pdf/conf_proceedings_final.pdf]

Graf, N., C.Desmedt, A. Hoppe, M.Tsiknakis, D.Dionysiou and G. Stamatakos. 2007. Clinical requirements of "*in silico* oncology" as part of the integrated project ACGT (Advancing Clinico-Genomic Trials on Cancer). Eur J Cancer Suppl 5(4): 83.

Graf, N., C.Desmedt, F.Buffa, D.Kafetzopoulos, N.Forgo, R.Kollek, A.Hoppe, G.Stamatakos and M.Tsiknakis. 2008. Post-genomic clinical trials - the perspective of ACGT. Ecancermedicalscience 2.

Graf, N., A. Hoppe , E. Georgiadi, R. Belleman, C. Desmedt, D. Dionysiou, M. Erdt , J. Jacques, E. Kolokotroni, A. Lunzer, M. Tsiknakis and G. Stamatakos. 2009. "*In silico* oncology" for clinical decision making in the context of nephroblastoma. Klin Paediatr 221: 141-149.

Guiot, C, P.P. Delsanto, A. Carpinteri, N. Pugno, Y. Mansury and T.S. Deisboeck. 2006. The dynamic evolution of the power exponent in a universal growth model of tumors. J Theor Biol 240(3): 459-63.

Haas-Kogan D.A., G.Yount, M. Haas, D. Levi, S.S. Kogan, L. Hu et al. 1995. p53-dependent G1 arrest and p53 independent apoptosis influence the radiobiologic response of glioblastoma. Int J Radiat Oncol Biol Phys 36: 95–103.

In Silico Oncology Group, Institute of Communications and Computer Systems, National Technical University of Athens [www.in-silico-oncology.iccs.ntua.gr].

Kansal, A.R, S. Torquato, G.R. Harsh, E.A. Chiocca and T.S. Deisboeck. 2000. Simulated brain tumour growth dynamics using a three-dimensional cellular automaton. J Theor Biol 203:367-82.

Katzung, B. G. Ed. 2001. Basic and Clinical Pharmacology, 8th Ed. Lange Medical Books, McGraw-Hill, New York.

Kolokotroni, E. A., G. S. Stamatakos, D. D. Dionysiou, E. Ch. Georgiadi, Ch. Desmedt and N. M. Graf. 2008. Translating Multiscale Cancer Models into Clinical Trials: Simulating Breast Cancer Tumor Dynamics within the Framework of the “Trial of Principle” Clinical Trial and the ACGT Project.,” Proc. 8th IEEE International Conference on Bioinformatics and Bioengineering (BIBE 2008), Athens, Greece, 8-10 Oct. 2008. IEEE Catalog Number: CFP08266, ISBN: 978-1-4244-2845-8, Library of Congress: 2008907441, Paper No. BE-2.1.1.

Marias K., D.Dionysiou, G.S. Stamatakos, F.Zacharopoulou, E.Georgiadi, T.G.Maris and I.Tollis. 2007. Multi-level analysis and information extraction considerations for validating 4D models of human function. Lect Notes Comput Sci 4561: 703-709.

Morse, P.M. and H. Feshbach. 1953. Methods of Theoretical Physics. Part I, Mc Graw-Hill, New York. pp.76-92.

Murray, J.D., 2003. Mathematical Biology II. Spatial Models and Biomedical Applications. Third Edition. Springer-Verlag, Heidelberg, pp.543-546.

Newlands, E. S., G. R. P. Blackledge, J. A. Slack, et al. 1992. Phase I trial of temozolomide (CCRG 81045: M&B 39831:NSC 362856)", Br. J. Cancer 65:287-291.

Perez C. and L. Brady Eds, 1998. Principles and Practice of Radiation Oncology 3rd Ed.. Lippincott-Raven, Philadelphia.

Perry, M. C. Ed. 2001. The Chemotherapy Source Book", 3rd Ed. Lippincott Williams and Wilkins, Philadelphia.

Ramis-Conde I., M.A.J. Chaplain, A.R.A. Anderson. 2008. Mathematical modelling of cancer cell invasion of tissue. Math Comput Model 47: 533-545.

Salmon S.E. and A.C. Sartorelli. 2001. Cancer chemotherapy. In Basic & Clinical Pharmacology. B.G.Katzung Ed. Lange Medical Books/McGraw-Hill, International Edition, pp.923-1044.

Schiff, L. I. 1981. Quantum Mechanics 3rd Ed. McGraw Hill Kogakusha, Tokyo.pp. 148-186.

Stamatakos, G., E.Zacharaki, M.Makropoulou, N.Mouravliansky, A.Marsh, K.Nikita, and N.Uzunoglu. 2001a. Modeling tumor growth and irradiation response in vitro- a combination of high-performance computing and web based technologies including VRML visualization. IEEE Trans Inform Technol Biomed 5(4): 279-289.

Stamatakos, G.S, E.I. Zacharaki, N.K. Uzunoglu and K.S. Nikita. 2001b. Tumor growth and response to irradiation in vitro: a technologically advanced simulation model , Int. J. Radiat Oncol Biol Phys 51(3) Sup.1: 240-241.

Stamatakos, G.S., D.Dionysiou, K.Nikita, N.Zamboglou, D.Baltas, G.Pissakas and N.Uzunoglu. 2001c. *In vivo* tumour growth and response to radiation therapy: a novel algorithmic description , Int. J. Radiat. Oncol. Biol. Phys 51(3) Sup.1: 240.

Stamatakos G.S., D.D. Dionysiou, E.I. Zacharaki, N.A. Mouravliansky, K.S. Nikita, and N.K. Uzunoglu 2002. *In silico* radiation oncology: combining novel simulation algorithms with current visualization techniques. Proc IEEE. Special Issue on Bioinformatics: Advances and Chalenges 90(11):1764-1777.

Stamatakos, G. 2006a. Spotlight on Cancer Informatics. Cancer Informatics 2: 83-86.

Stamatakos, G. S. and Uzunoglu, N. 2006b. Computer simulation of tumour response to therapy. In S. Nagl Ed. Cancer Bioinformatics: from therapy design to treatment. John Wiley & Sons Ltd, Chichester,UK. pp.109-125.

Stamatakos G.S., V.P. Antipas, N.K. Uzunoglu, and R.G. Dale. 2006c. A four dimensional computer simulation model of the in vivo response to radiotherapy of glioblastoma multiforme: studies on the effect of clonogenic cell density. Br J Radiol 79: 389-400.

Stamatakos G. S., Antipas V. P. and N.K.Uzunoglu. 2006d. A spatiotemporal, patient individualized simulation model of solid tumor response to chemotherapy *in vivo*: the paradigm of glioblastoma multiforme treated by temozolomide. IEEE Trans Biomed Eng 53: 1467- 1477.

Stamatakos G.S., V.P. Antipas, N.K. Uzunoglu. 2006e. Simulating chemotherapeutic schemes in the individualized treatment context: the paradigm of glioblastoma multiforme treated by temozolomide *in vivo*. Comput Biol Med. 36(11): 1216-34.

Stamatakos G.S., D.D. Dionysiou, N.M. Graf, N.A. Sofra, C. Desmedt, A. Hoppe, N. Uzunoglu and M. Tsiknakis. 2007a. The Oncosimulator: a multilevel, clinically oriented simulation system of tumor growth and organism response to therapeutic schemes. Towards the clinical evaluation of *in silico* oncology. Proc 29th Annual Intern Conf IEEE EMBS. Cite Internationale, Lyon, France Aug 23-26. SuB07.1: 6628-6631

Stamatakos, G.S., D.D.Dionysiou and N.K.Uzunoglu. 2007b. *In silico* radiation oncology: a platform for understanding cancer behavior and optimizing radiation therapy treatment. In M.Akay Ed. Genomics and Proteomics Engineering in Medicine and Biology. Wiley-IEEE Press, Hoboken NJ. pp.131-156.

Stamatakos, G.S., 2008. *In silico* oncology: a paradigm for clinically oriented living matter engineering. Proc. 3rd International Advanced Research Workshop on *In Silico* Oncology, Istanbul, Turkey, Sept. 23-24, 2008. Edited by G. Stamatakos and D. Dionysiou. pp.7-9. [www.3rd-iarwiso.iccs.ntua.gr/procs.pdf]

Stamatakos, G.S., E.Kolokotroni, D.Dionysiou, E.Georgiadi, S.Giatili. 2009a. *In silico* oncology: a top-down multiscale simulator of cancer dynamics. Studying the effect of symmetric stem cell division on the cellular constitution of a tumour. Proc. 11th Int Congress of the IUPESM, Medical Physics and Biomedical Engineering World Congress 2009, Sept. 7-12, Munich, Germany. In press.

Stamatakos G. and D. Dionysiou. 2009b. Introduction of hypermatrix and operator notation into a discrete mathematics simulation model of malignant tumour response to therapeutic schemes *in vivo*. Some operator properties. Cancer Informatics. *Accepted* for publication

Steel G. Ed. Basic Clinical Radiobiology 3rd Ed.,2002. Oxford University Press, Oxford.

Stupp, R., M. Gander, S. Leyvraz and E. Newlands. 2001. Current and future developments in the use of temozolomide for the treatment of brain tumours. Lancet Oncol Rev 2(9): 552-560.

Swanson K.R., E.C. Alvord, J.D. Murray. 2002. Virtual brain tumours (gliomas) enhance the reality of medical imaging and highlight inadequacies of current therapy. Br J Cancer 86:14-18.

Werner-Wasik M., C.B. Scott, D.F. Nelson, L.E. Gaspar, K.J. Murray, J.A. Fischbach, J.S. Nelson, A.S.Weinstein and WJ Jr. Curran. 1996. Final report of a phase I/II trial of hyperfractionated and accelerated hyperfractionated radiation therapy with carmustine for adults with supratentorial malignant gliomas. Radiation Oncology Therapy Group Study 83-02. Cancer 77(8): 1535-43.

Zacharaki, E. I., G. S.Stamatakos, K.S. Nikita and N. K.Uzunoglu. 2004. Simulating growth dynamics and radiation response of avascular tumour spheroid model validation in the case of an EMT6/Ro multicellular spheroid. Comput Methods Programs Biomed 76:193-206.

EXCERPTS FROM A PRESENTATION GIVEN AT DIMACS, Rutgers University, USA Aug. 2006

Towards a collaborative formulation of the "*Mathematical Principles of Natural Philosophy: Living Matter*." The paradigm of *In Silico* Oncology

Georgios S. Stamatakos

In Silico Oncology Group
Institute of Communication and Computer Systems
School of Electrical and Computer Engineering
National Technical University of Athens
(gestam@central.ntua.gr)

EXCERPTS FROM A PRESENTATION GIVEN AT DIMACS, Rutgers University, USA, Aug. 2006

- The tremendous rate of accumulation of both **experimental** and **observational** (clinical) knowledge pertaining to **living matter** dictates the formulation of a parsimonious system of **“laws”** in analogy to Newton’s *Mathematical Principles of Natural Philosophy*.

- This seems to be a necessary step if a **rational**, **coherent** and **transparent understanding** of the **biological phenomena** is to be sought.
- Such a system would consist of a finite, yet **considerable number of *principles*** and refer to ***all* levels of biocomplexity**, as according to D. Noble *there is no privileged level of causality*.

- The experimental, observational and theoretical study of **cancer**, a markedly **mutiscale biological *phenomenon*** of obvious clinical importance, may be viewed as excellent ground for the establishment of a number of such **multilevel *laws.***
- Their formulation might well be achieved primarily in ***algorithmic - discrete mathematics*** **terms**

- Within this frame the emerging field of ***in silico (computational) oncology*** has already provided some quite reliable descriptions of several biological mechanisms characterizing cancer, of both **continuous** and **discrete nature**.
- Obviously cancer is **far from being a purely deterministic phenomenon**.

- Cancer seems to behave like a **mixture** of **deterministic** (e.g. sequence of cell cycle phases) and **stochastic** (e.g. radiation cell kill probability) **processes**.
- Subsequently, **stochasticity aspects** should always be taken into account.
- Nevertheless, **the more critical knowledge** becomes available, **the more deterministic** the *cancer phenomenon* appears to become.

- An **illustrative observation** supporting this hypothesis is that more detailed knowledge of the **genetic status** of a tumor may lead to a **better prediction** of its response to therapeutic interventions, thus to an apparently **more deterministic** tumor behavior.

- Based on the previous thoughts, the ***In Silico Oncology Group***, **National Technical University of Athens**, has developed a number of **mixed** (continuous and discrete) **yet predominantly discrete** Monte Carlo simulation models of tumor growth and response to therapeutic modalities ranging from **tumor growth** and **radiotherapy response *in vitro*** to the **clinical tumor response to radiotherapeutic and chemotrherapeutic schemes *in vivo***, based i.a. on *actual imaging data*, *histopathologic* and *genetic* data.

INDICATIVE ISOG SIMULATION MODELING ELEMENTS

- Processed **molecular data** is used in order **to *perturb*** the **radiobiological** or **pharmacodynamic** cell kill parameters about their **population based mean values**.
- A prototype system of **quantizing cell clusters** included within each **geometrical cell** of a **discretizing mesh** covering the **anatomic area of interest** lies at the heart of the proposed simulation approach.

- **Cell cycle phase durations** and **imaging based metabolism distribution** define i.a. the quantization **equivalence classes** considered.
- Several **algorithms** have been developed so as to simulate i.a. various macroscopic mechanisms such as **tumor expansion/shrinkage** and mechanical **boundary conditions** as well as the **effects of particular drugs** (e.g. temozolomide) and **radiation** on the tumor under consideration.

- A number of the models developed, mainly referring to **imageable glioblastomas**, have already been **clinically validated to a substantial degree**.
- Long term clinical testing and adaptation procedures are in progress.
- The response of treatment affected **normal tissues** by radiotherapeutic schemes has also been addressed for certain cases.

- Currently, a substantial extension of the simulation models to the **nephroblastoma (Wilm's tumor)** and **breast cancer** cases is being performed within the frame of the four year duration **European Commission** funded project **ACGT (Advancing Clinico-Genomic Trials on Cancer**), in collaboration with several clinical and technological institutions across Europe.

- The whole effort profits considerably from the **US NIH-NCI supported Center for the Development of a Virtual Tumor (CViT).**
- It is worth noting the remarkably ***collaborative*** **character** of this and other complementary research efforts on a global scale.

- The expected **practical usefulness** of the type of models mentioned would be the possibility of virtually **experimenting *in silico* (on the computer)** with the intention of **optimizing cancer treatment strategy** based on the specific molecular, histopathologic, imaging and historical data of **each individual patient**.

- Deeper **understanding of the cancer disease** and at the same time of the related ***natural phenomenon*** is a further intermediate goal of considerable importance.

ISOG MODELING APPOACH EXAMPLES

In Vitro Tumor Growth and Response to Radiotherapeutic Schemes

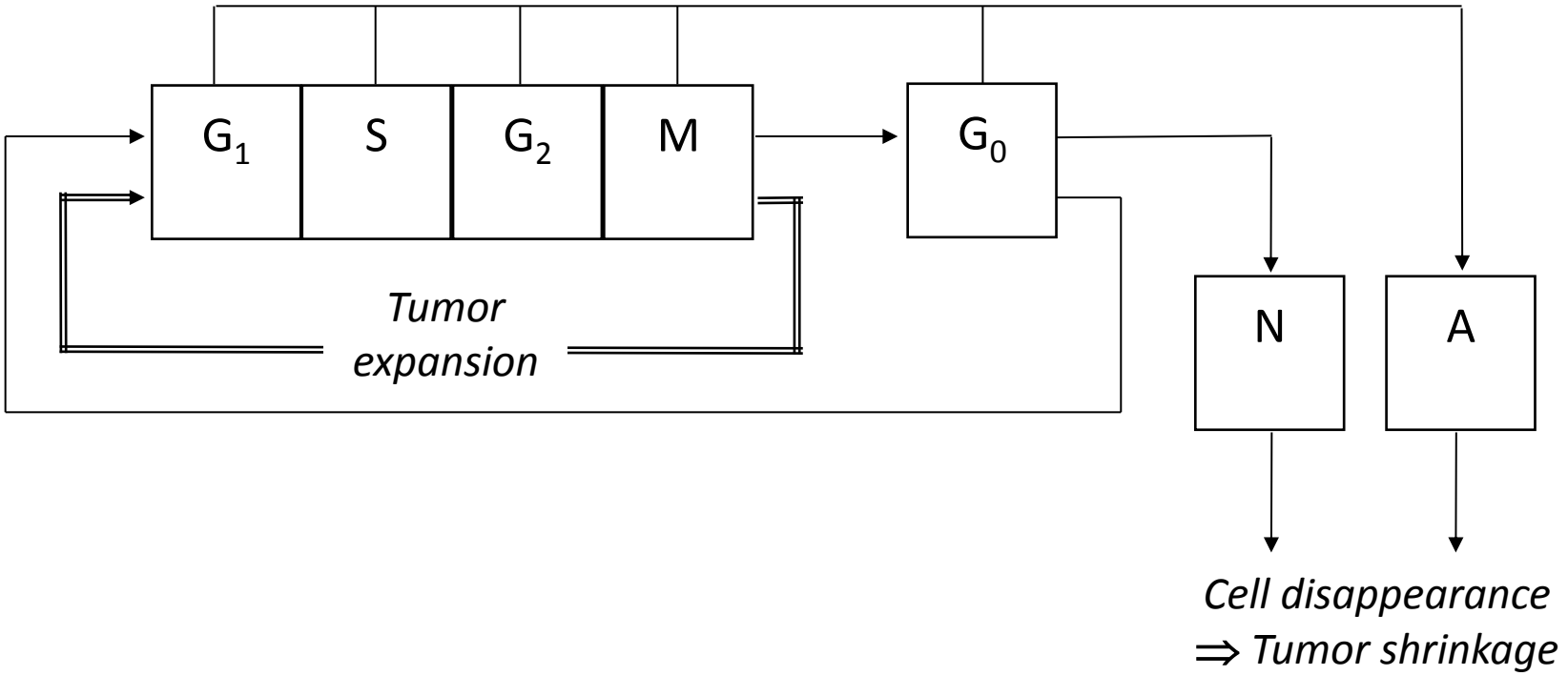

Cytokinetic model of a tumor cell.

Symbol explanation: G1: G1 phase, S: DNA synthesis phase, G2: G2 phase, G0: G0 phase, N: necrosis, A: apoptosis.

[see G.Stamatakos, D.Dionysiou, E.Zacharaki, N.Mouravliansky, K.Nikita, and N.Uzunoglu, "*In Silico* Radiation Oncology: Combining Novel Simulation Algorithms with Current Visualization Techniques," Proc. IEEE, Special Issue on "Bioinformatics: Advances and Challenges" Vol.90, No.11, November 2002, pp.1764-1777]

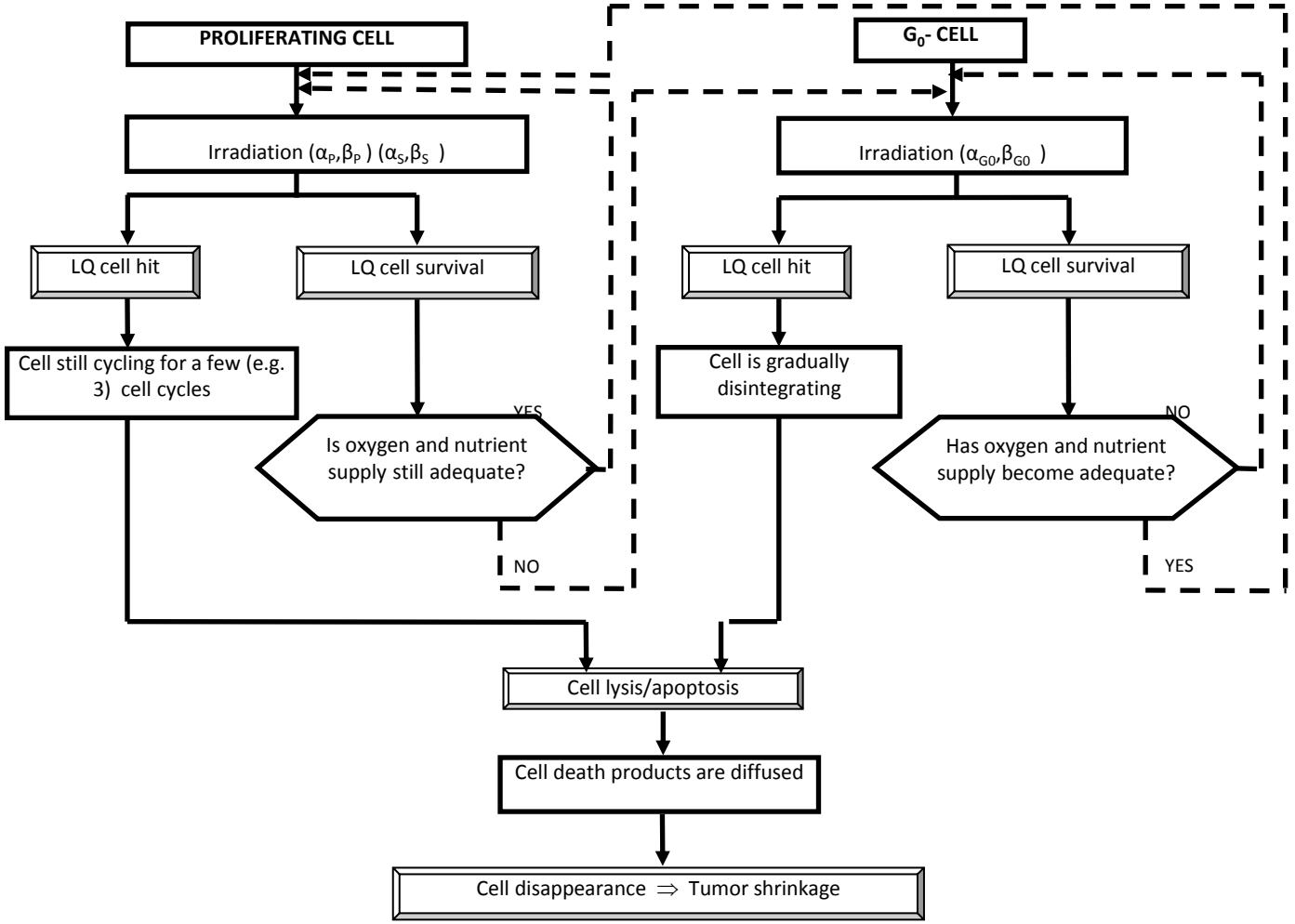

Simplified flow chart for the response of a single tumor cell to irradiation. Symbol explanation: α_P and β_P stand for the α and β parameters of the linear quadratic model for the tumor proliferating cells excluding those in phase S. The subscript S denotes cells in the DNA synthesis phase, whereas the subscript G0 denotes cells in the resting (dormant) phase G0.

[see G.Stamatakos, D.Dionysiou, E.Zacharaki, N.Mouravliansky, K.Nikita, and N.Uzunoglu, "*In Silico* Radiation Oncology: Combining Novel Simulation Algorithms with Current Visualization Techniques," Proc. IEEE, Special Issue on "Bioinformatics: Advances and Challenges" Vol.90, No.11, November 2002, pp.1764-1777]

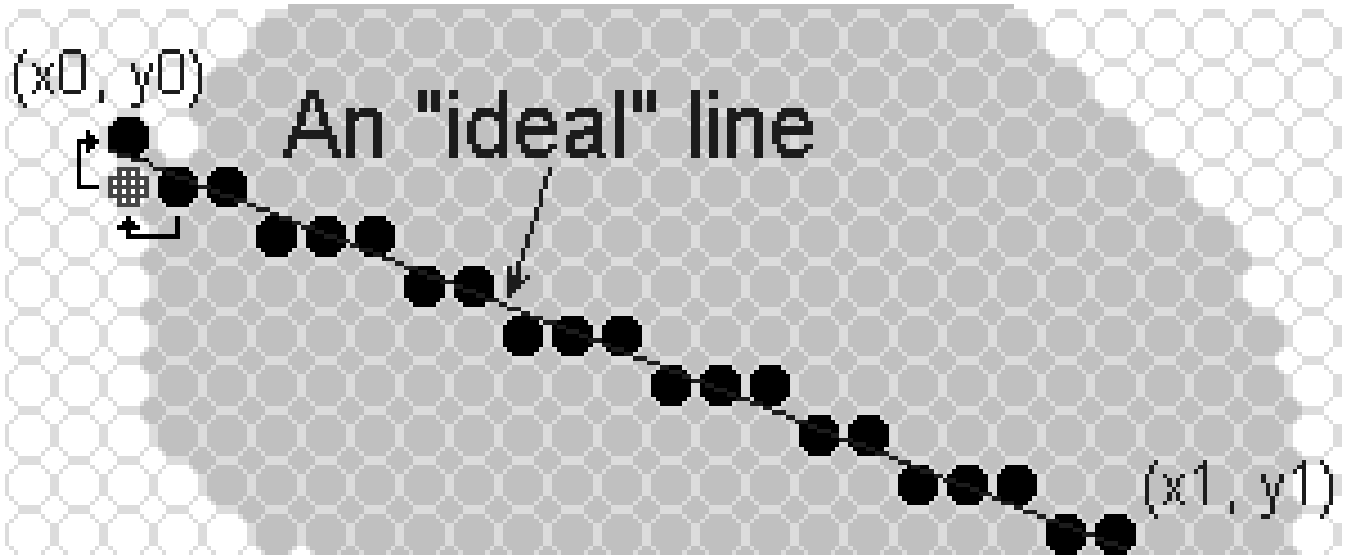

A line drawing algorithm (shown for simplicity in two dimensions) is applied to construct the best possible approximation of an ideal "cell sliding" line given a discretizing mesh. The white geometrical cells are occupied by nutrient medium while the gray ones stand for tumor cells.

[see G.Stamatakos, D.Dionysiou, E.Zacharaki, N.Mouravliansky, K.Nikita, and N.Uzunoglu, "*In Silico* Radiation Oncology: Combining Novel Simulation Algorithms with Current Visualization Techniques," Proc. IEEE, Special Issue on "Bioinformatics: Advances and Challenges" Vol.90, No.11, November 2002, pp.1764-1777]

Mean Values and Standard Deviations of the Cell Cycle Phase Durations for Brain Tumor Cells

(based on available literature data: use with caution!)

Cell phase	Necrosis (N)	G_0	G_1	DNA Synthesis (S)	G2	Mitosis (M)
Mean Duration	T_{NM}=40h	T_{G0M}=25h	T_{G1M}=11h	T_{SM}=13h	T_{G2M}=4h	T_{MM}=2h
Standard Deviation	T_{ND}=2h	T_{G0D}=5h	T_{G1D}=1h	T_{SD}=2h	T_{G2D}=1h	T_{MD}=0h

[see G.Stamatakos, D.Dionysiou, E.Zacharaki, N.Mouravliansky, K.Nikita, and N.Uzunoglu, "*In Silico* Radiation Oncology: Combining Novel Simulation Algorithms with Current Visualization Techniques," Proc. IEEE, Special Issue on "Bioinformatics: Advances and Challenges" Vol.90, No.11, November 2002, pp.1764-1777]

Mean Values of The LQ Model Parameters for Brain Tumor Cells

(based on available literature data: use with caution!)

$\alpha_P = 0.6\ Gy^{-1}$	$\alpha_S = 0.4\ Gy^{-1}$	$\alpha_{G0} = 0.2\ Gy^{-1}$
$\beta_P = 0.06\ Gy^{-2}$	$\beta_S = 0.04\ Gy^{-2}$	$\beta_{G0} = 0.02\ Gy^{-2}$

[see G.Stamatakos, D.Dionysiou, E.Zacharaki, N.Mouravliansky, K.Nikita, and N.Uzunoglu, "*In Silico* Radiation Oncology: Combining Novel Simulation Algorithms with Current Visualization Techniques," Proc. IEEE, Special Issue on "Bioinformatics: Advances and Challenges" Vol.90, No.11, November 2002, pp.1764-1777]

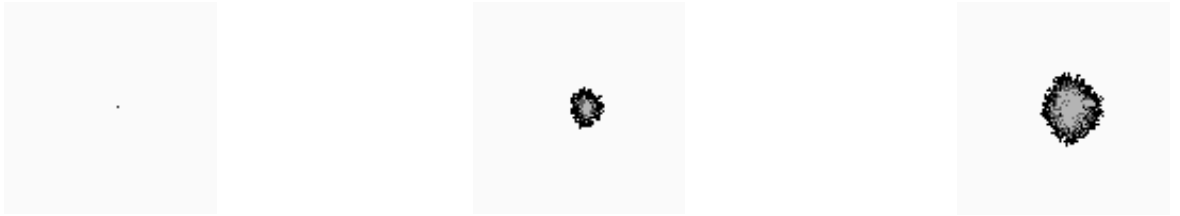

Time = 1h Time = 400h Time = 600h

Simulated evolution of a brain tumor spheroid *in vitro* (equatorial cross section). *Gray scale code*: white: nutrient medium, light gray: dead cells, dark gray: cells in G0, black: cells in proliferating phases.

[see G.Stamatakos, D.Dionysiou, E.Zacharaki, N.Mouravliansky, K.Nikita, and N.Uzunoglu, "*In Silico* Radiation Oncology: Combining Novel Simulation Algorithms with Current Visualization Techniques," Proc. IEEE, Special Issue on "Bioinformatics: Advances and Challenges" Vol.90, No.11, November 2002, pp.1764-1777]

Time	Standard Fractionation	Hyperfractionation
800 h	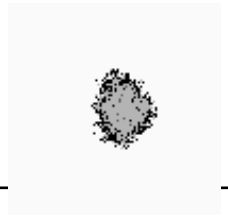	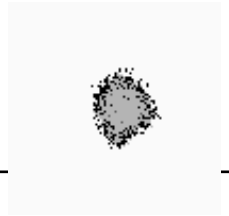
1000 h	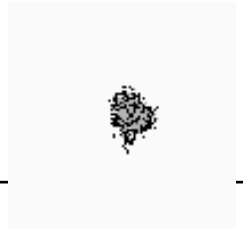	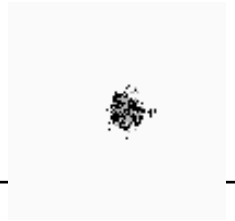
1200 h		

Simulated response of the tumor **of the previous figure** to the (left) **standard fractionation scheme** (2 Gy once a day, 5 days per week, 60 Gy in total) and (right) **hyperfractionation scheme** (1.2 Gy twice a day, 5 days per week, 72 Gy in total).
The gray scale code and the time reference of the previous figure are used. Irradiation begins 672 h after the placement of a single tumor cell in the phase of mitosis at the center of the discretizing mesh.

[see G.Stamatakos, D.Dionysiou, E.Zacharaki, N.Mouravliansky, K.Nikita, and N.Uzunoglu, "*In Silico* Radiation Oncology: Combining Novel Simulation Algorithms with Current Visualization Techniques," Proc. IEEE, Special Issue on "Bioinformatics: Advances and Challenges" Vol.90, No.11, November 2002, pp.1764-1777]

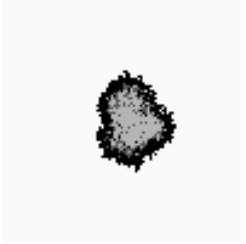

Regrowth of the brain tumor after completion of the standard fractionation scheme.

[see G.Stamatakos, D.Dionysiou, E.Zacharaki, N.Mouravliansky, K.Nikita, and N.Uzunoglu, "*In Silico* Radiation Oncology: Combining Novel Simulation Algorithms with Current Visualization Techniques," Proc. IEEE, Special Issue on "Bioinformatics: Advances and Challenges" Vol.90, No.11, November 2002, pp.1764-1777]

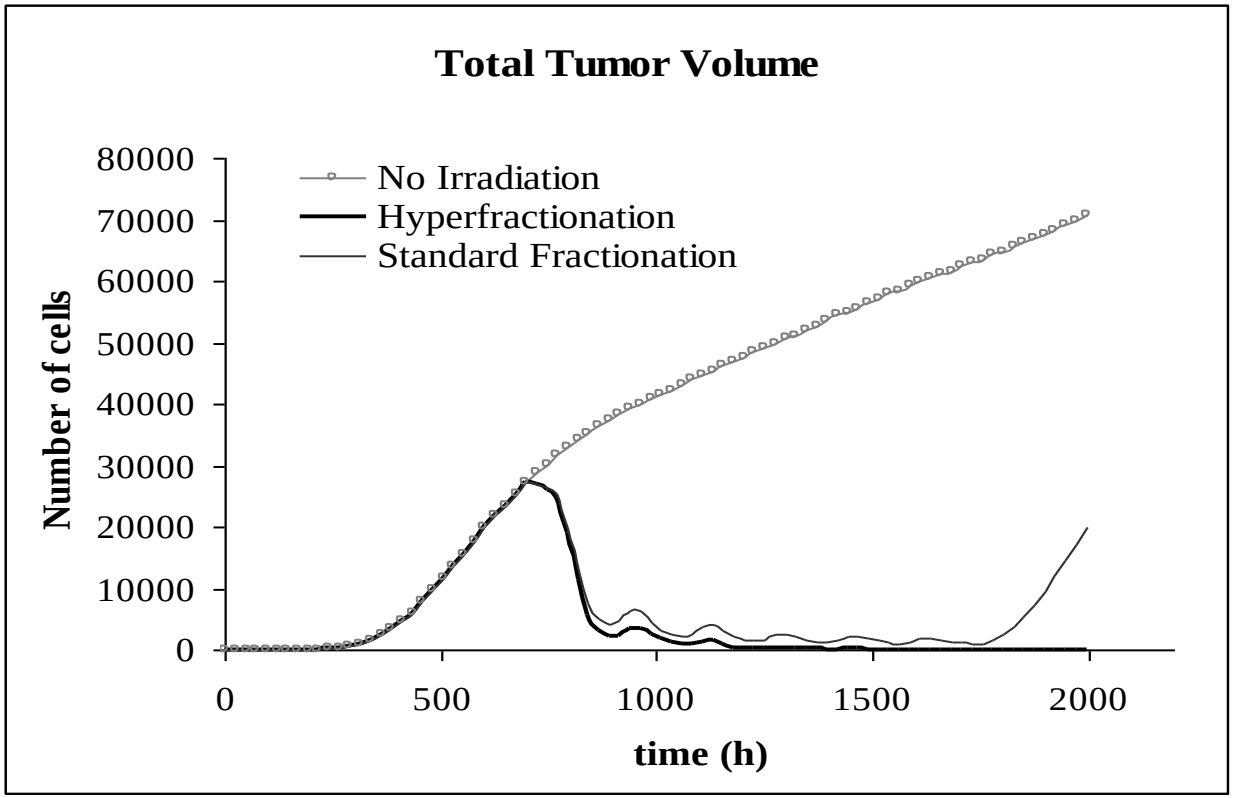

The total volume (number of living and dead cells) of a brain tumor spheroid as a function of time without external interventions and by applying the **standard fractionation** (2 Gy once a day, 5 days per week, 60 Gy in total) and the **hyperfractionation** scheme (1.2 Gy twice a day, 5 days per week, 72 Gy in total) respectively. Irradiation begins 672 h after the placement of a single tumor cell in the phase of mitosis at the center of the discretizing mesh.

[see G.Stamatakos, D.Dionysiou, E.Zacharaki, N.Mouravliansky, K.Nikita, and N.Uzunoglu, "*In Silico* Radiation Oncology: Combining Novel Simulation Algorithms with Current Visualization Techniques," Proc. IEEE, Special Issue on "Bioinformatics: Advances and Challenges" Vol.90, No.11, November 2002, pp.1764-1777]

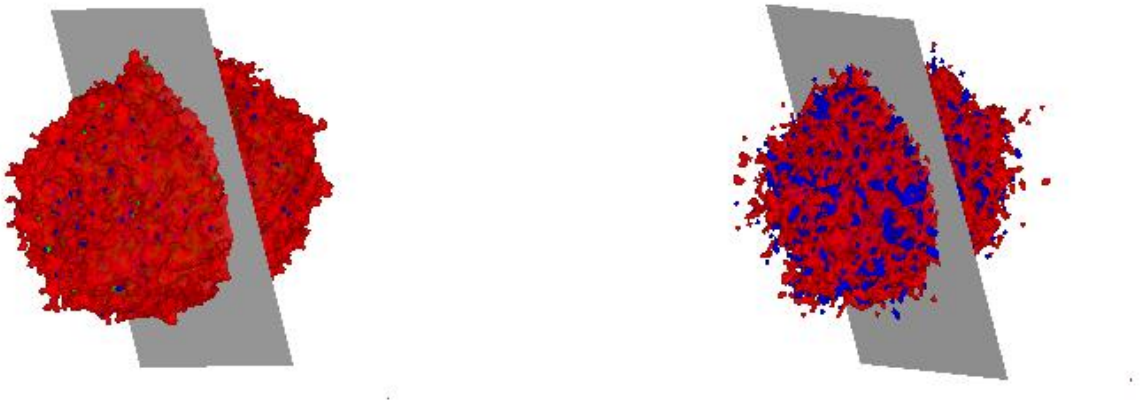

(a) (b)

Time = 800 h

A 3-D representation of the external surface of a brain tumor spheroid using AVS/Express 4.2. The snapshots correspond to the instant t=800 h. Left: **no external interventions** take place. Right: the **hyperfractionation** scheme (1.2 Gy twice a day, 5 days per week, 72 Gy total) is applied starting at t=672 h. ***Color code***: white: nutrient medium, blue: products of cell necrosis/apoptosis, green: cells in G0, red: cells in proliferating phases

[see G.Stamatakos, D.Dionysiou, E.Zacharaki, N.Mouravliansky, K.Nikita, and N.Uzunoglu, "*In Silico* Radiation Oncology: Combining Novel Simulation Algorithms with Current Visualization Techniques," Proc. IEEE, Special Issue on "Bioinformatics: Advances and Challenges" Vol.90, No.11, November 2002, pp.1764-1777]

In Vivo Tumor Growth and Response to Radiotherapeutic Schemes

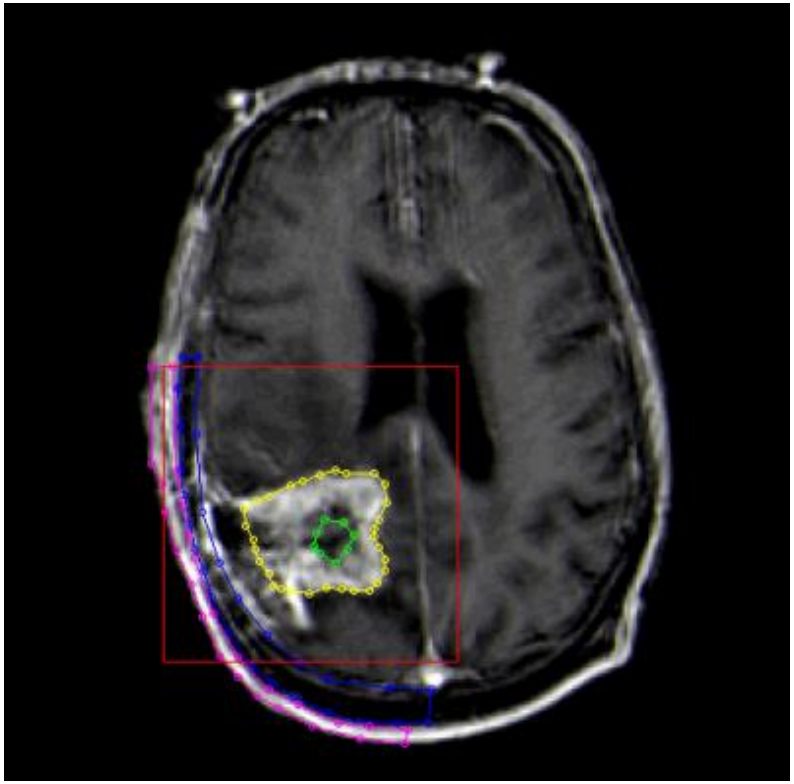

An MRI slice depicting a glioblastoma mutiforme. Both the clinical volume of the tumour and its central necrotic area have been delineated. The present case has been considered for the preliminary checks of the simulation model.

[see G.Stamatakos, D.Dionysiou, E.Zacharaki, N.Mouravliansky, K.Nikita, and N.Uzunoglu, "*In Silico* Radiation Oncology: Combining Novel Simulation Algorithms with Current Visualization Techniques," Proc. IEEE, Special Issue on "Bioinformatics: Advances and Challenges" Vol.90, No.11, November 2002, pp.1764-1777]

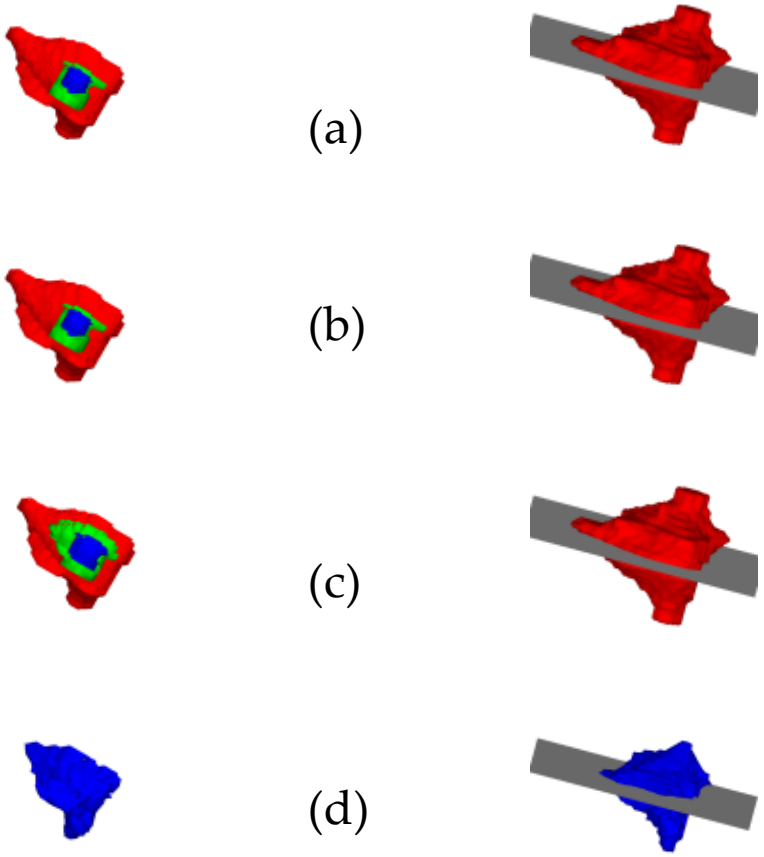

Irradiation according to the standard fractionation scheme

(2 Gy once a day, 5 days per week, 60 Gy in total). Left panel: three dimensional sections of the tumor shown in the right panel: (a) **before the beginning of irradiation**, (b) **1 *fictitious* day after the beginning of irradiation**, (c) **2 *fictitious* days** after the beginning of irradiation and (d) **3 *fictitious* days** after the beginning of irradiation. ***Color code* red:** proliferating cell layer, **green**: dormant cell layer (G0), **blue**: dead cell layer. The **coloring criterion "99.8%"** used to visualize the predictions has been defined as follows.

"For a geometrical cell of the discretizing mesh, if the percentage of dead cells is lower than 99.8% then
{ if percentage of proliferating cells > percentage of G0 cells, then paint the geometrical cell red (proliferating cell layer),
else paint the geometrical cell green (G0 cell layer) } else paint the geometrical cell blue (dead cell layer)"

The values of certain parameters (e.g. cell loss) have been **deliberately exaggerated** in order to facilitate the demonstration of the ability of the model to simulate the **shrinkage effect**. [see G.Stamatakos, D.Dionysiou, E.Zacharaki, N.Mouravliansky, K.Nikita, and N.Uzunoglu, "*In Silico* Radiation Oncology: Combining Novel Simulation Algorithms with Current Visualization Techniques," Proc. IEEE Special Issue on "Bioinformatics: Advances and Challenges" Vol.90, No.11, November 2002, pp.1764-1777]

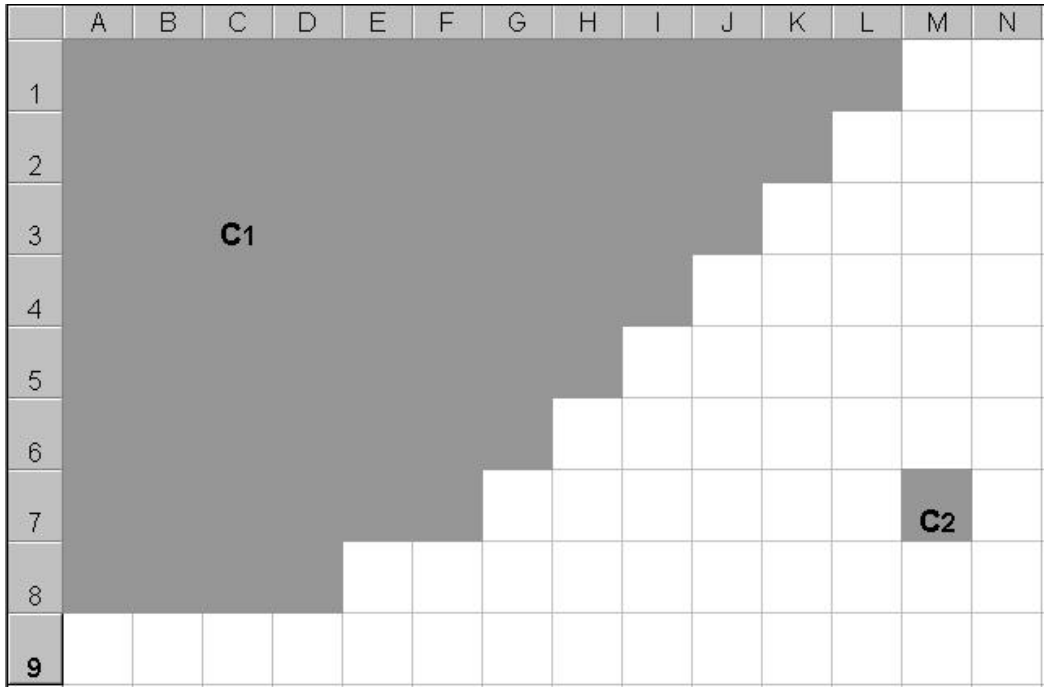

A schematic illustration of the Center of Mass Algorithm (CMA) in two dimensions (for simplification reasons). C1 represents the **center of mass of the main cohesive tumor component**. C2 represents a **geometrical cell occupied by the tumor** and lying **outside the main cohesive tumor component**. C2 can move to either L7 or M6, so that its distance from C1 decreases. The **same process** takes place **when C2 belongs to the main cohesive tumor component**. It is noted that only shifting along the principal axes (x-, x+, y-, y+, z-, z+) is allowed in this algorithm version.

[see V. P Antipas, G. S Stamatakos, N. K Uzunoglu, D. D Dionysiou, R. G Dale, " A spatio-temporal simulation model of the response of solid tumours to radiotherapy *in vivo*: parametric validation concerning oxygen enhancement ratio and cell cycle duration," *Phys. Med. Biol.* 49 (2004) 1485–1504 [Pubmed Link: http://www.ncbi.nlm.nih.gov/entrez /query.fcgi?cmd=Retrieve&db=pubmed&dopt=Abstract&list_uids=15152687&query_hl=14]]

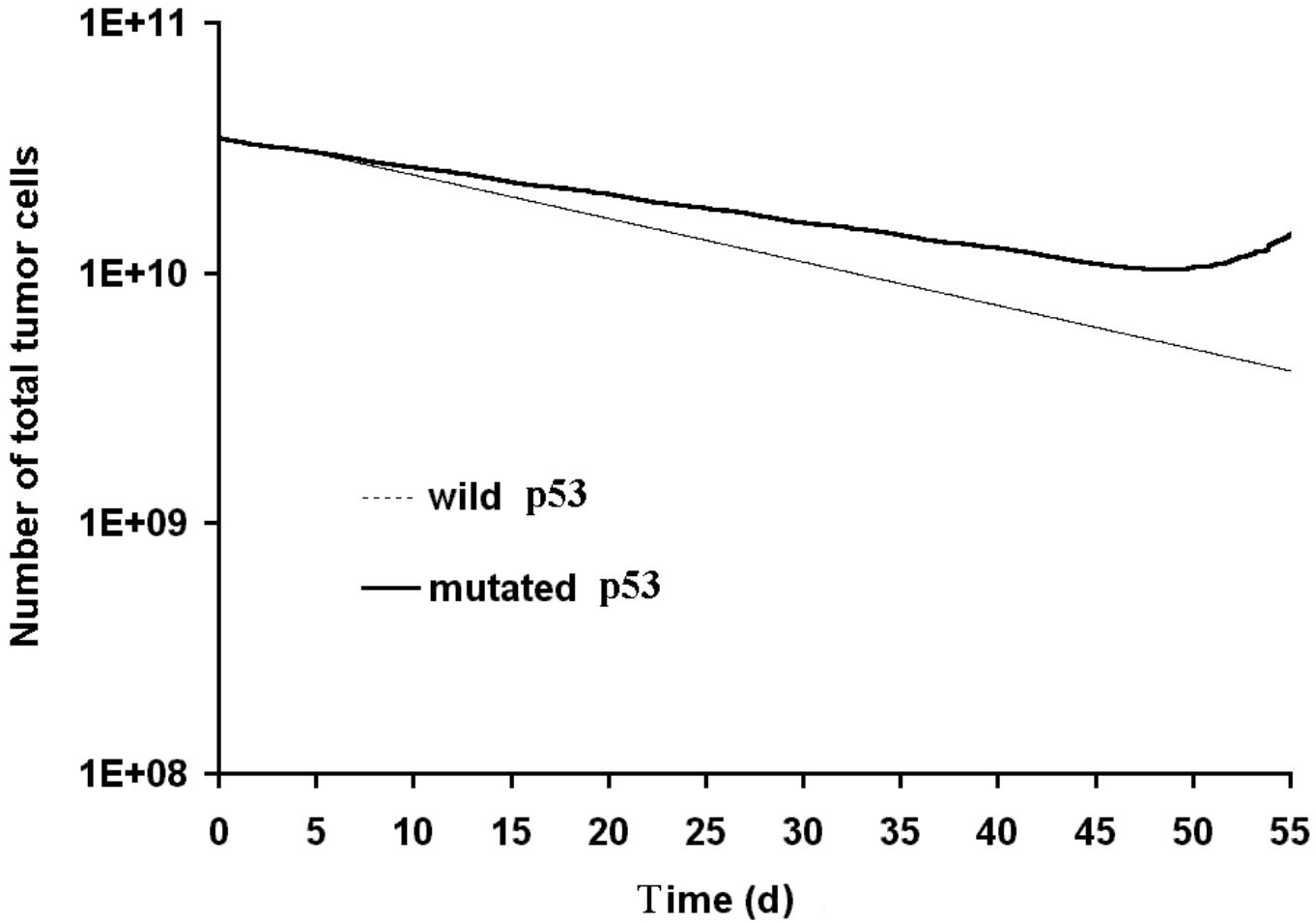

Simulation predictions of the number of total tumor cells (mt p53 and wild type p53) for the standard fractionation scheme. An OER=3.0 has been assumed.

[see V. P Antipas, G. S Stamatakos, N. K Uzunoglu, D. D Dionysiou, R. G Dale, " A spatio-temporal simulation model of the response of solid tumours to radiotherapy *in vivo*: parametric validation concerning oxygen enhancement ratio and cell cycle duration," *Phys. Med. Biol.* 49 (2004) 1485–1504 [Pubmed Link: http://www.ncbi.nlm.nih.gov/entrez /query.fcgi?cmd=Retrieve&db=pubmed&dopt=Abstract&list_uids=15152687&query_hl=14]]

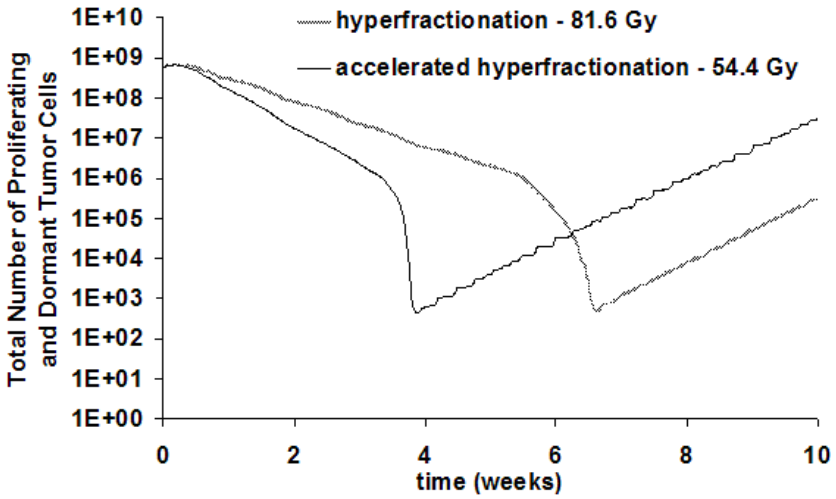

(a)

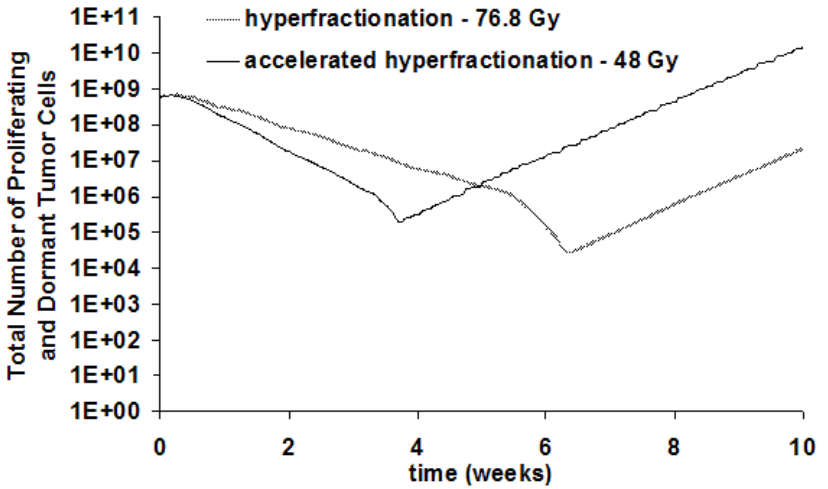

(b)

(a) **Total number of proliferating and dormant tumor cells as a function of time for the hyperfractionated** (1.2 Gy twice daily, 5 days per week to the dose of 81.6 Gy, "HF-81.6") and **accelerated hyperfractionated** (1.6 Gy twice daily, 5 days per week to the dose of 54.4 Gy, "AHF-54.4") **radiotherapy schedules.** HF-81.6 is completed on day 46 after initiation of treatment whereas AHF-54.4 is completed on day 23. In all fractionation schedules considered in this paper no radiation is administered on Saturdays and Sundays. **(b) Total number of proliferating and dormant tumour cells as a function of time for the hyperfractionated** (1.2 Gy twice daily, 5 days per week to the dose of 76.8 Gy, "HF-76.8") and **accelerated hyperfractionated** (1.6 Gy twice daily, 5 days per week to the dose of 48 Gy, "AHF-48") **radiotherapy schedules.** Both irradiation schedules start on the first day of the first week of treatment. HF-76.8 is completed on day 44 after initiation of treatment whereas AHF-48 is completed on day 19.

[see G. S. Stamatakos, V.P. Antipas, N. K. Uzunoglu, R. G. Dale, "A four dimensional computer simulation model of the *in vivo* response to radiotherapy of glioblastoma multiforme: studies on the effect of clonogenic cell density." *British Journal of Radiology*, 2006, vol. 79, 389-400 [http://bjr.birjournals.org/cgi/content/abstract/79/941/389].]

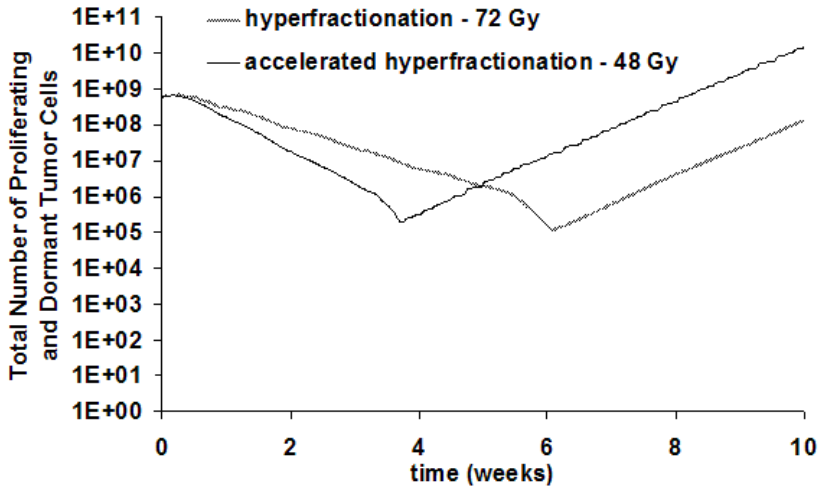

(a)

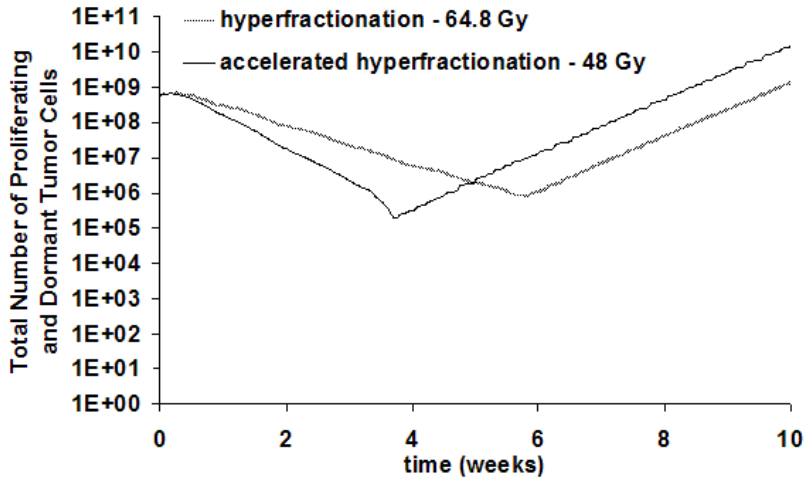

(b)

(a) **Total number of proliferating and dormant tumour cells as a function of time for the hyperfractionated** (1.2 Gy twice daily, 5 days per week to the dose of 72 Gy, "HF-72") and **accelerated hyperfractionated** (1.6 Gy twice daily, 5 days per week to the dose of 48 Gy, "AHF-48") **radiotherapy schedules.** HF-72 is completed on day 40 after initiation of treatment whereas AHF-48 is completed on day 19. **(b) Total number of proliferating and dormant tumour cells as a function of time for the hyperfractionated** (1.2 Gy twice daily, 5 days per week to the dose of 64.8 Gy, "HF-64.8") and **accelerated hyperfractionated** (1.6 Gy twice daily, 5 days per week to the dose of 48 Gy, "AHF-48") **radiotherapy schedules.** HF-64.8 is completed on day 37 after initiation of treatment whereas AHF-48 is completed on day 19. Both irradiation schedules start on the first day of the first week of treatment.

[see G. S. Stamatakos, V.P. Antipas, N. K. Uzunoglu, R. G. Dale, "A four dimensional computer simulation model of the *in vivo* response to radiotherapy of glioblastoma multiforme: studies on the effect of clonogenic cell density." *British Journal of Radiology*, 2006, vol. 79, 389-400 [http://bjr.birjournals.org/cgi/content/abstract/79/941/389].]

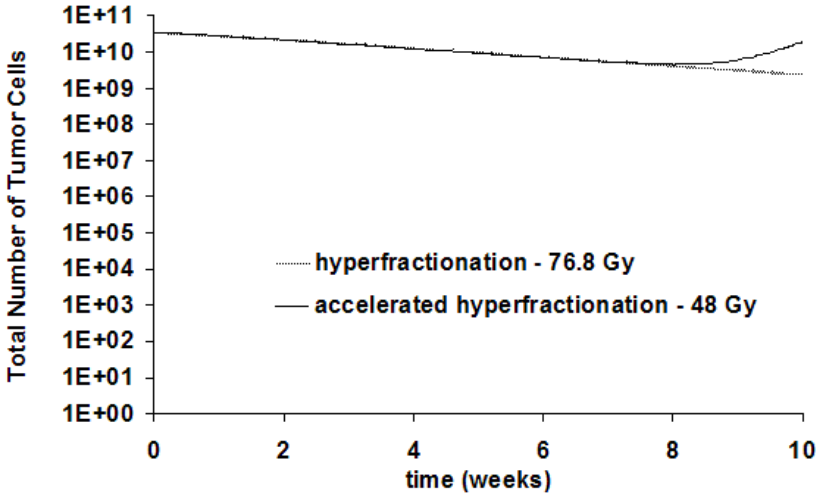

Total number of tumour cells (proliferating, dormant and dead cells) as a function of time for the hyperfractionated (1.2 Gy twice daily, 5 days per week to the dose of 76.8 Gy, "HF-76.8") and **accelerated hyperfractionated** (1.6 Gy twice daily, 5 days per week to the dose of 48 Gy, "AHF-48") **radiotherapy schedules.** Irradiation starts on the first day of the first week. HF-76.8 is completed on day 44 after initiation of treatment whereas AHF-48 is completed on day 19. Both irradiation schedules start on the first day of the first week of treatment.

[see G. S. Stamatakos, V.P. Antipas, N. K. Uzunoglu, R. G. Dale, "A four dimensional computer simulation model of the *in vivo* response to radiotherapy of glioblastoma multiforme: studies on the effect of clonogenic cell density." *British Journal of Radiology*, 2006, vol. 79, 389-400 [http://bjr.birjournals.org/cgi/content/abstract/79/941/389].]

Simulation predictions agree with the outcome of the Radiation Therapy Oncology Group **(RTOG) Study 83-02**.

[see G. S. Stamatakos, V.P. Antipas, N. K. Uzunoglu, R. G. Dale, "A four dimensional computer simulation model of the *in vivo* response to radiotherapy of glioblastoma multiforme: studies on the effect of clonogenic cell density." *British Journal of Radiology*, 2006, vol. 79, 389-400 [http://bjr.birjournals.org/cgi/content/abstract/79/941/389].]

In Vivo Tumor Growth and Response to Chemotherapeutic Schemes (Temozolomide)

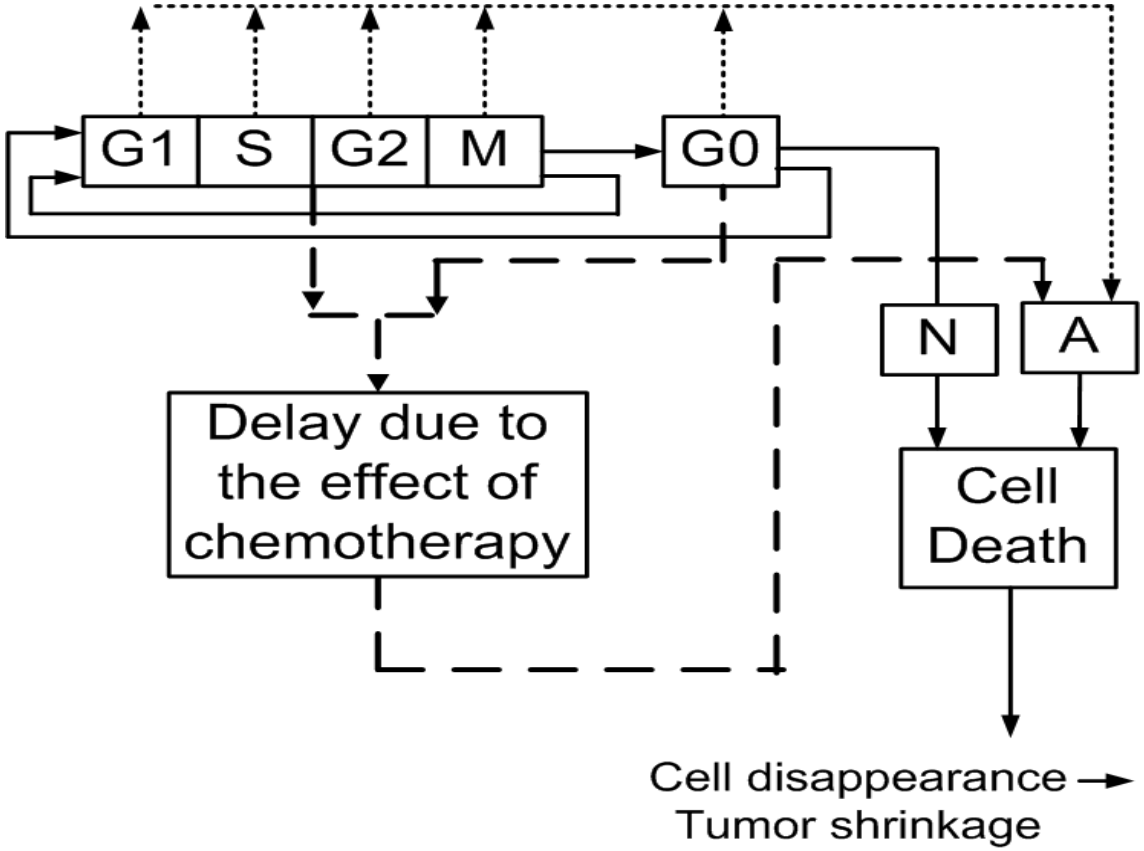

A simplified cytokinetic model of a tumor cell. *Symbol explanation*: G1: G1 phase; S: DNA synthesis phase; G2: G2 phase; G0: G0 phase; N: necrosis; A: apoptosis. The cytotoxicity produced by **TMZ** is primarily modeled by a delay in the S phase compartment (TDS) ("Delay due to the effect of chemotherapy" in the diagram) and subsequent apoptosis. The *delay box* simply represents the time corresponding to at most two cell divisions being required before the emergence of temozolomide cytotoxicity. It is not a time interval additional to the times represented by the cell cycle phase boxes.

[see G. S. Stamatakos, V. P.Antipas, and N. K. Uzunoglu, "A spatiotemporal, patient individualized simulation model of solid tumor response to chemotherapy *in vivo*: the paradigm of glioblastoma multiforme treated by temozolomide" *IEEE Transactions on Biomedical Engineering*, Vol. 53, No 8, August 2006 (in press)]

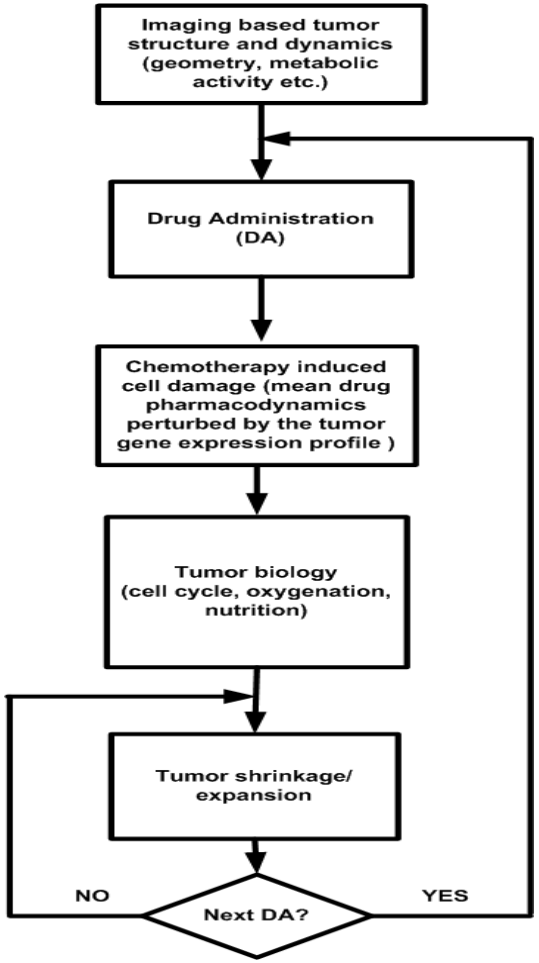

A simplified flowchart of the proposed chemotherapy simulation algorithm. Following introduction of the baseline **tumor structure** and **metabolic activity** data and the **drug administration schedule**, simulation of the various response stages takes place as shown in the flowchart.

[see G. S. Stamatakos, V. P.Antipas, and N. K. Uzunoglu, "A spatiotemporal, patient individualized simulation model of solid tumor response to chemotherapy *in vivo*: the paradigm of glioblastoma multiforme treated by temozolomide" *IEEE Transactions on Biomedical Engineering*, Vol. 53, No 8, August 2006 (in press)]

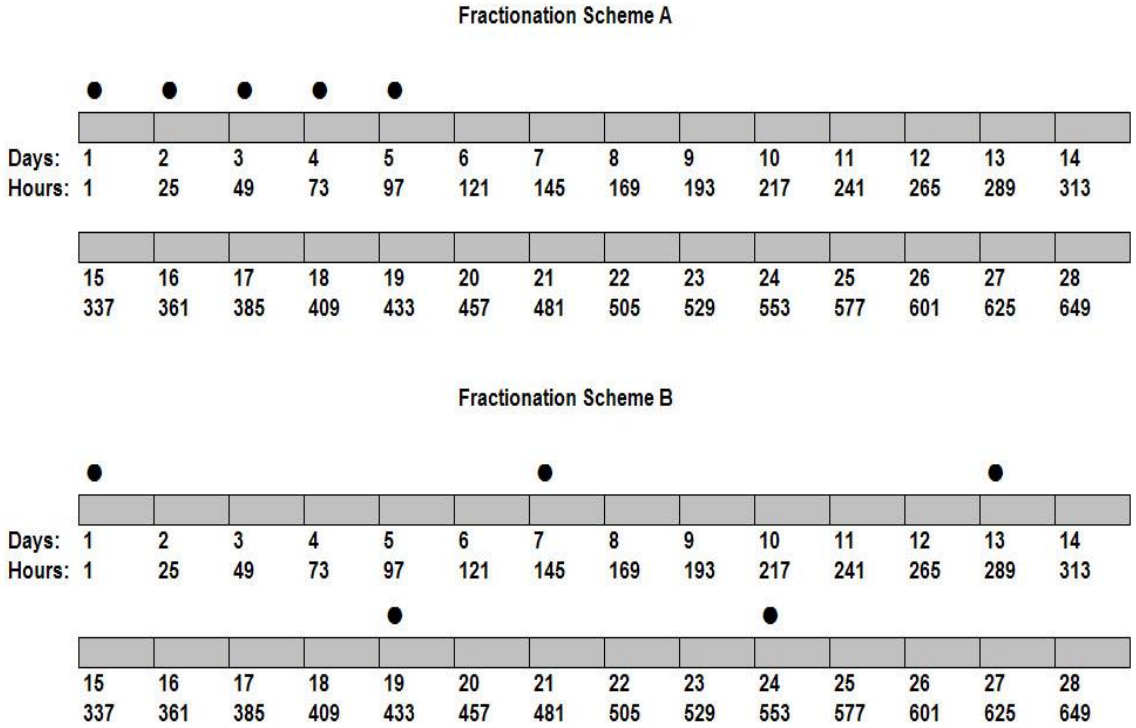

Two chemotherapy fractionations simulated .

Fractionation A corresponds to the standard TMZ administration scheme (once daily for 5 consecutive days per 28-day treatment cycle) whereas **Fractionation B** corresponds to a hypothetical drug administration almost uniformly distributed throughout the chemotherapy cycle. Each drug administration session is denoted by a small black disk (pill).

[see G. S. Stamatakos, V. P.Antipas, and N. K. Uzunoglu, *"*A spatiotemporal, patient individualized simulation model of solid tumor response to chemotherapy *in vivo*: the paradigm of glioblastoma multiforme treated by temozolomide" *IEEE Transactions on Biomedical Engineering*, Vol. 53, No 8, August 2006 (in press)]

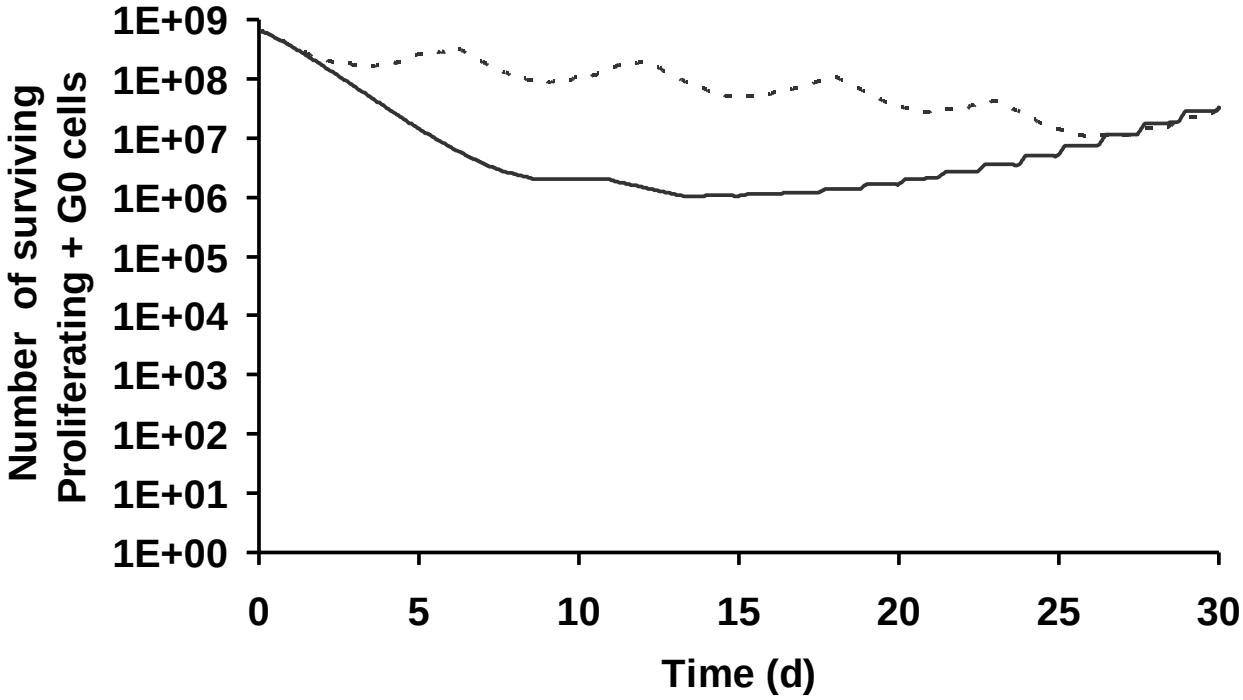

Number of surviving (metabolically living) proliferating and dormant (G0) tumor cells corresponding to the particular GBM tumor considered as a function of time. TMZ is administered according to fractionation **scheme A** (solid line) or **B** (dashed line) (see previous figure). Each chemotherapy fraction corresponds to **150mg/m^2**. The cell cycle has been assumed equal to Tc=30h and the mean clonogenic cell density equal to CCD = 10^4 cells/mm^3 (clonogenic cell density in the *proliferating cell layer* = 2×10^4 cells/mm^3). Only one chemotherapy cycle per scheme has been simulated.

[see G. S. Stamatakos, V. P.Antipas, and N. K. Uzunoglu, "A spatiotemporal, patient individualized simulation model of solid tumor response to chemotherapy *in vivo*: the paradigm of glioblastoma multiforme treated by temozolomide" *IEEE Transactions on Biomedical Engineering*, Vol. 53, No 8, August 2006 (in press)]

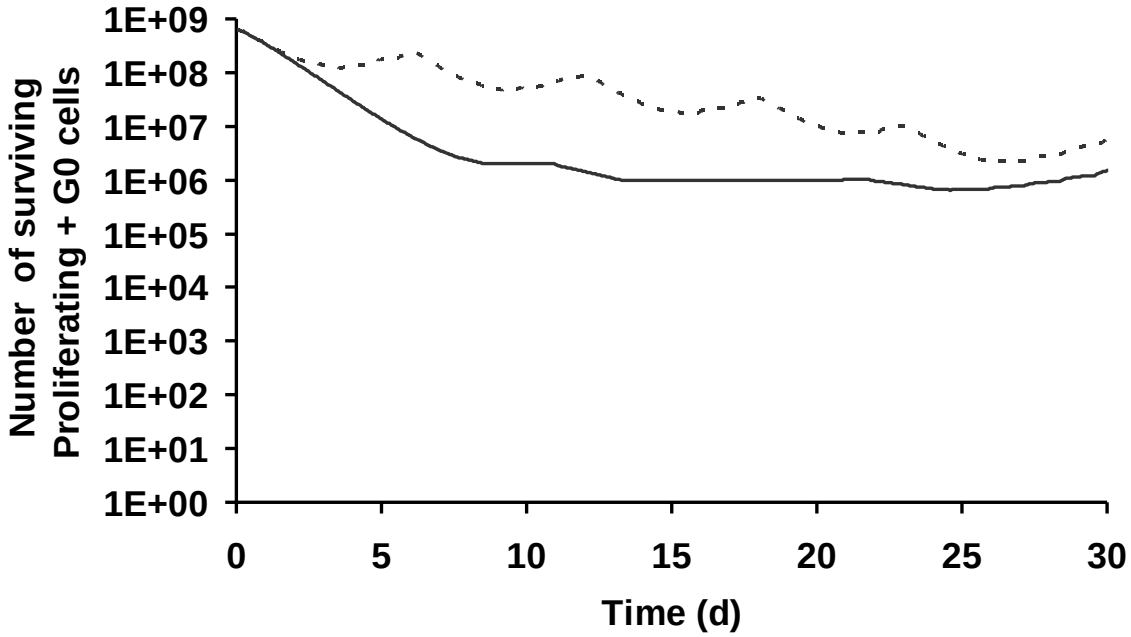

Number of surviving (metabolically living) proliferating and dormant (G0) tumor cells corresponding to the particular GBM tumor considered as a function of the time. TMZ is administered according to fractionation **scheme A** (solid line) or **B** (dashed line) (see drug administration schemes figure). Each chemotherapy fraction corresponds to 200mg/m^2. The cell cycle has been assumed equal to Tc=30h and the mean clonogenic cell density equal to CCD = 10^4 cells/mm^3 (clonogenic cell density in the *proliferating cell layer* = 2×10^4 cells/mm3). Only one chemotherapy cycle per scheme has been simulated.

[see G. S. Stamatakos, V. P.Antipas, and N. K. Uzunoglu, "A spatiotemporal, patient individualized simulation model of solid tumor response to chemotherapy *in vivo*: the paradigm of glioblastoma multiforme treated by temozolomide" *IEEE Transactions on Biomedical Engineering*, Vol. 53, No 8, August 2006 (in press)]

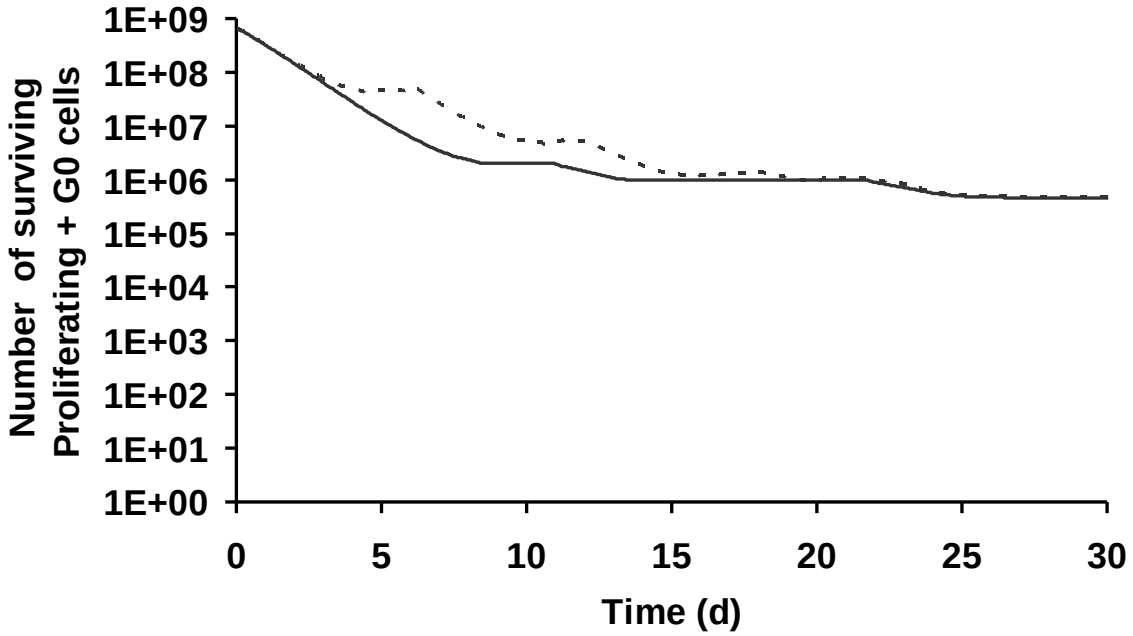

Number of surviving (metabolically alive) proliferating and dormant (G0) tumor cells corresponding to the particular GBM tumor considered as a function of the time. TMZ is administered according to fractionation **scheme A** (solid line) or **B** (dashed line) (see drug administration schemes figure). Each chemotherapy fraction corresponds to 250mg/m^2. The cell cycle has been assumed equal to Tc=30h and the mean clonogenic cell density equal to CCD = 10^4 cells/mm^3 (clonogenic cell density in the *proliferating cell layer* = 2×10^4 cells/mm^3). Only one chemotherapy cycle per scheme has been simulated.

[see G. S. Stamatakos, V. P.Antipas, and N. K. Uzunoglu, *"*A spatiotemporal, patient individualized simulation model of solid tumor response to chemotherapy *in vivo*: the paradigm of glioblastoma multiforme treated by temozolomide" *IEEE Transactions on Biomedical Engineering*, Vol. 53, No 8, August 2006 (in press)]

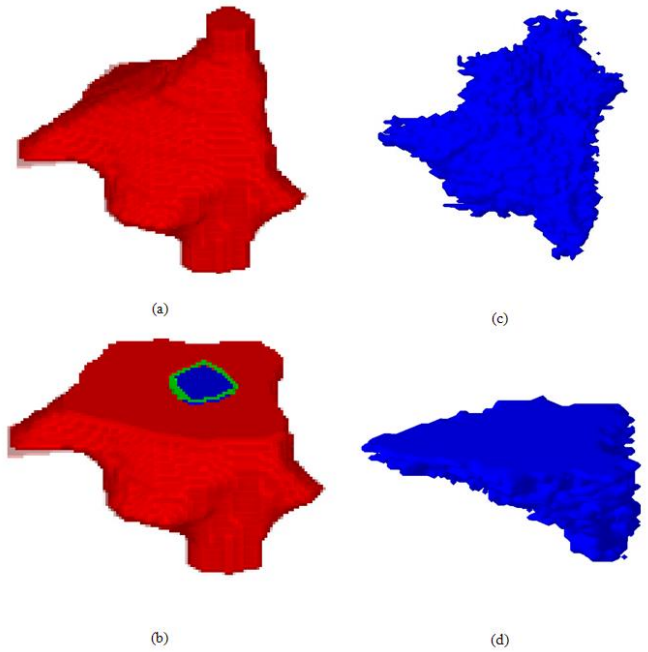

Three dimensional visualization of the simulated response of a clinical glioblastoma multiforme tumor to 1 cycle of chemotherapeutic scheme (**150 mg/m²** orally once daily for 5 consecutive days per 28-day treatment cycle, (fractionation scheme A)). (a) External surface of the tumor before the beginning of chemotherapy, (b) internal structure of the tumor before the beginning of chemotherapy, (c) external surface of the tumor 20 days after the beginning of chemotherapy (d) internal structure of the tumor 20 days after the beginning of chemotherapy. Pseudocolor Code: red: proliferating cell layer, green: dormant cell layer (G0), blue: dead cell layer. The following "99.8%"criterion has been devised and applied: "For a geometrical cell of the discretizing mesh, if the percentage of dead cells within it is lower than 99.8% then {if percentage of proliferating cells > percentage of G0 cells, then paint the geometrical cell red (proliferating cell layer), else paint the geometrical cell green (G0 cell layer) } else paint the geometrical cell blue (dead cell layer)"

[see G. S. Stamatakos, V. P.Antipas, and N. K. Uzunoglu, *"*A spatiotemporal, patient individualized simulation model of solid tumor response to chemotherapy *in vivo*: the paradigm of glioblastoma multiforme treated by temozolomide" *IEEE Transactions on Biomedical Engineering*, Vol. 53, No 8, August 2006 (in press)]

ACGT

Advancing Clinicogenomic Trials on Cancer

a European Commission funded 4 year integrated project (FP6-2005-IST-026996)

Start date: 1 February 2006

WORKPACKAGE 8

Technologies and Tools for In Silico Oncology

(Leader: Institute of Communication and Computer Systems – National Technical University of Athens)

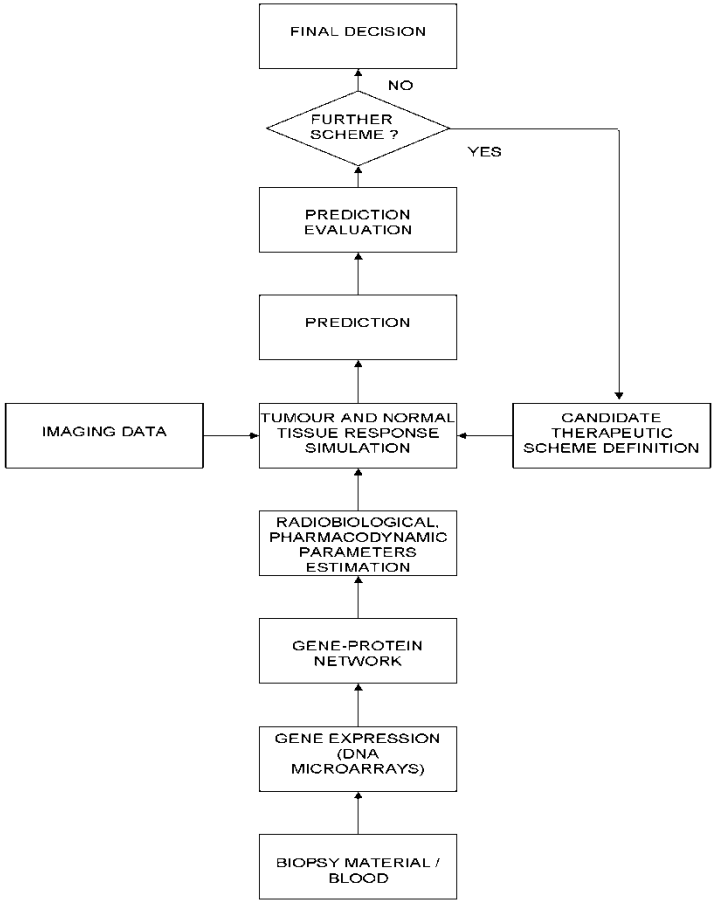

The "**Oncosimulator**"

An early oversimplified diagram of the "Oncosimulator" to be ***clinically*** validated, adapted and optimized within the frame of the ACGT project (Workpackage 8 etc.)

REPRESENTATIVE PUBLICATIONS

•G.S.Stamatakos, D.D.Dionysiou, E.I.Zacharaki, N.A.Mouravliansky, K.Nikita, N.Uzunoglu, "***In silico* radiation oncology**: combining novel simulation algorithms with current visualization techniques", *Proceedings of the IEEE*, vol. 90, No 11, pp.1764-1777, Nov. 2002. http://ieeexplore.ieee.org/search/wrapper.jsp?arnumber=1046955

(http://dx.doi.org/doi:10.1109/JPROC.2002.804685)

•D. D. Dionysiou, G. S. Stamatakos, N.K. Uzunoglu, K. S. Nikita, A. Marioli, "A four-dimensional simulation model of tumour response to **radiotherapy** in vivo: parametric validation considering radiosensitivity, genetic profile and fractionation," *Journal of Theoretical Biology* 230 (2004) 1–20 [Pubmed Link: http://www.ncbi.nlm.nih.gov/entrez/query.fcgi?cmd=Retrieve&db=pubmed&dopt=Abstract&list_uids=15275995&query_hl=2](http://dx.doi.org/10.1016/j.jtbi.2004.03.024)

•E. I.Zacharaki, G. S.Stamatakos, K.S. Nikita, N. K.Uzunoglu, "Simulating **growth dynamics** and **radiation response** of avascular tumour spheroid model validation in the case of an EMT6/Ro multicellular spheroid," *Computer Methods and Programs in Biomedicine* (2004) 76, 193—206. [Pubmed link: http://www.ncbi.nlm.nih.gov/entrez/query.fcgi?cmd=Retrieve&db=pubmed&dopt=Abstract&list_uids=15501506&query_hl=3]

•V. P Antipas, G. S Stamatakos, N. K Uzunoglu, D. D Dionysiou, R. G Dale, " A spatio-temporal simulation model of the response of solid tumours to **radiotherapy** *in vivo*: parametric validation concerning oxygen enhancement ratio and cell cycle duration," *Phys. Med. Biol.* 49 (2004) 1485–1504 [Pubmed Link: http://www.ncbi.nlm.nih.gov/entrez/query.fcgi?cmd=Retrieve&db=pubmed&dopt=Abstract&list_uids=15152687&query_hl=1](http://stacks.iop.org/PMB/49/1485)

REPRESENTATIVE PUBLICATIONS (cont.)

•G.S.Stamatakos GS, V.P. Antipas VP, N.K. Uzunoglu, "Simulating **chemotherapeutic** schemes in the individualized treatment context: The paradigm of glioblastoma multiforme treated by temozolomide in vivo." *Comput Biol Med.* 2005 Oct 2; [Epub ahead of print, Pubmed Link: http://www.ncbi.nlm.nih.gov/entrez/query.fcgi?cmd=Retrieve&db=pubmed&dopt=Abstract&list_uids=16207487&query_hl=14]

•G. S. Stamatakos, V.P. Antipas, N. K. Uzunoglu, R. G. Dale, "A four dimensional computer simulation model of the *in vivo* response to radiotherapy of glioblastoma multiforme: studies on the effect of clonogenic cell density." *British Journal of Radiology***,** 2006, vol. 79, 389-400 [http://bjr.birjournals.org/cgi/content/abstract/79/941/389].

•D.D.Dionysiou, G.S. Stamatakos, N.K.Uzunoglu, K.S.Nikita "A Computer Simulation Of **In Vivo Tumour Growth** And Response To **Radiotherapy:** New Algorithms And Parametric Results", *Computers In Biology And Medicine*, In Press, Corrected Proof, Available Online 23 May 2005. (http://dx.doi.org/10.1016/j.compbiomed.2005.02.003)

•G. S. Stamatakos, V. P.Antipas, and N. K. Uzunoglu, *"*A spatiotemporal, patient individualized simulation model of solid tumor response to chemotherapy *in vivo*: the paradigm of glioblastoma multiforme treated by temozolomide" *IEEE Transactions on Biomedical Engineering*, Vol. 53, No 8, August 2006 (in press)

•G. S. Stamatakos and N.Uzunoglu *"Computer Simulation of Tumour Response to Therapy"*in Cancer Bioinformatics: from therapy design to treatment Edited by Sylvia Nagl © 2006 John Wiley & Sons, Ltd (http://eu.wiley.com/Wi l e y C D A / Wi l e y T i t l e / p r o d u c t C d -0470863048,descCd-tableOfContents.html)

Thank you
(2006)

PAPER_B-Stamatakos_et-al_JTB_2010.pdf

Journal of Theoretical Biology 266 (2010) 124–139

Contents lists available at ScienceDirect

Journal of Theoretical Biology

journal homepage: www.elsevier.com/locate/yjtbi

An advanced discrete state–discrete event multiscale simulation model of the response of a solid tumor to chemotherapy: Mimicking a clinical study

G.S. Stamatakos [a,*], E.A. Kolokotroni [a], D.D. Dionysiou [a], E.Ch. Georgiadi [a], C. Desmedt [b]

[a] In Silico Oncology Group, Laboratory of Microwaves and Fiber Optics, Institute of Communication and Computer Systems, School of Electrical and Computer Engineering, National Technical University of Athens, Iroon Polytechniou 9, Zografos GR 157 80, Greece

[b] Institut Jules Bordet - Centre des Tumeurs, rue Héger Bordet 1, 1000 Bruxelles, Belgium

ARTICLE INFO

Article history:
Received 1 December 2009
Received in revised form
29 March 2010
Accepted 14 May 2010
Available online 31 May 2010

Keywords:
Breast cancer
Simulation
Cancer modeling
Chemotherapy
In silico oncology

ABSTRACT

In this paper an advanced, clinically oriented multiscale cancer model of breast tumor response to chemotherapy is presented. The paradigm of early breast cancer treated by epirubicin according to a branch of an actual clinical trial (the Trial of Principle, TOP trial) has been addressed. The model, stemming from previous work of the In Silico Oncology Group, National Technical University of Athens, is characterized by several crucial new features, such as the explicit distinction of proliferating cells into stem cells of infinite mitotic potential and cells of limited proliferative capacity, an advanced generic cytokinetic model and an improved tumor constitution initialization technique. A sensitivity analysis regarding critical parameters of the model has revealed their effect on the behavior of the biological system. The favorable outcome of an initial step towards the clinical adaptation and validation of the simulation model, based on the use of anonymized data from the TOP clinical trial, is presented and discussed. Two real clinical cases from the TOP trial with variable molecular profile have been simulated. A realistic time course of the tumor diameter and a reduction in tumor size in agreement with the clinical data has been achieved for both cases by selection of reasonable model parameter values, thus demonstrating a possible adaptation process of the model to real clinical trial data. Available imaging, histological, molecular and treatment data are exploited by the model in order to strengthen patient individualization modeling. The expected use of the model following thorough clinical adaptation, optimization and validation is to simulate either several candidate treatment schemes for a particular patient and support the selection of the optimal one or to simulate the expected extent of tumor shrinkage for a given time instant and decide on the adequacy or not of the simulated scheme.

© 2010 Elsevier Ltd. All rights reserved.

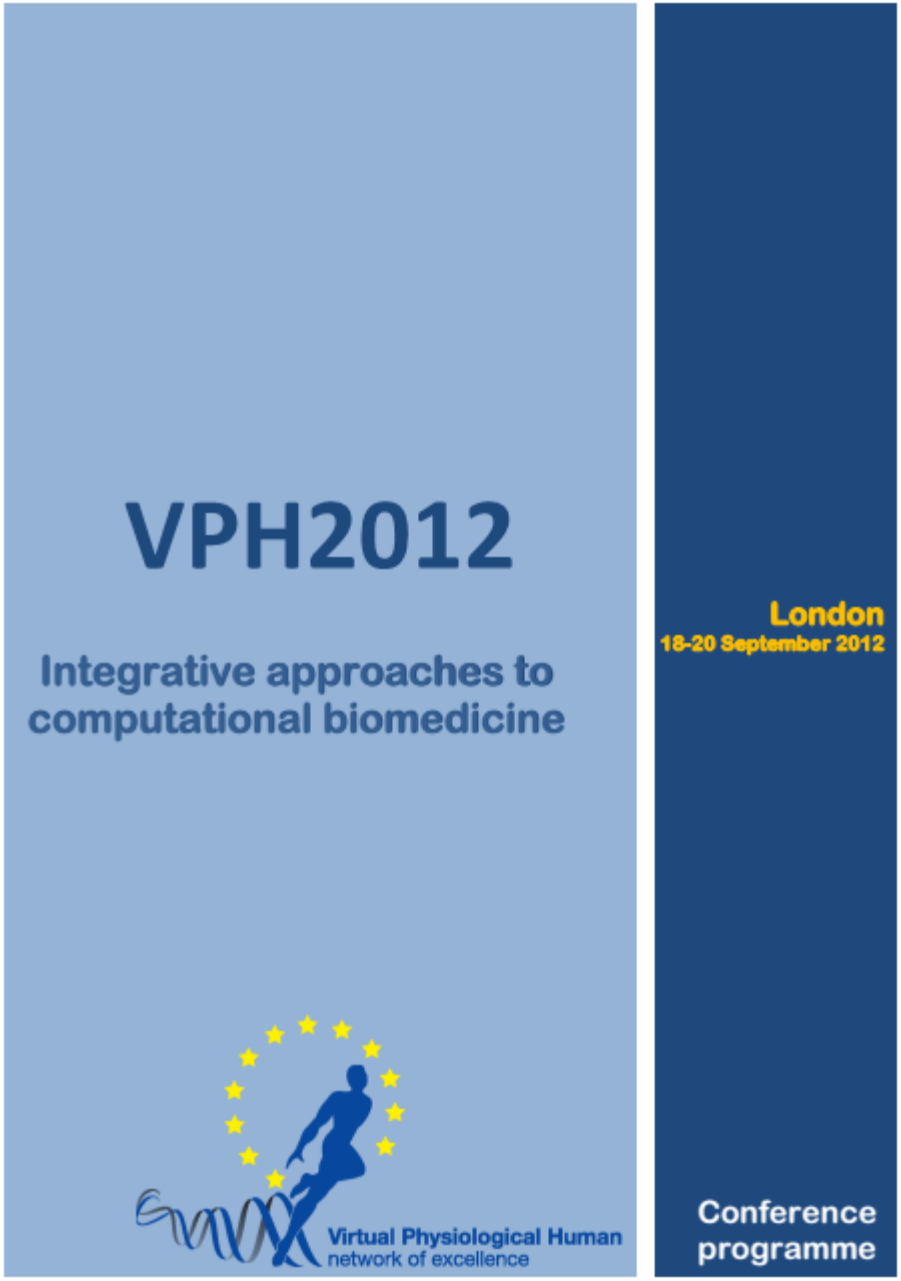
VPH2012
Integrative approaches to computational biomedicine
Virtual Physiological Human
network of excellence
London
18-20 September 2012
Conference programme

EXAMPLES OF MULTISCALE BIO-MODELLING BEYOND THE DOMAIN OF CANCER

PROCEEDINGS-VPH2012_INTEGRATIVE_APPROACHES_TO_COMPUTATIONAL_BIOMEDICINE-LONDON_CONF_2012.pdf PAGE **130**/488 (PLEASE USE THE PDF PAGE COUNTER)

Improving the Pulsatility in a CF-LVAD Supported Cardiovascular System Applying a Model Control to CF-LVAD Flow Rate

Selim Bozkurt, Frans N van de Vosse, and Marcel CM Rutten

Eindhoven University of Technology, The Netherlands

Correspondence: s.bozkurt@tue.nl; 0031(0)40 247 2245; Eindhoven University of Technology, Biomedical Engineering, Materials Technology, PO Box 513, GEM-Z 4.18, 5600 MB, Eindhoven, The Netherlands

Introduction

Continuous Flow Left Ventricular Assist Devices (CF-LVADs) reduce the pulsatility in the cardiovascular system while supporting the failing heart. It has been reported that enhanced pulsatility has significant benefits on vital organ function in the patients [1]. In this study, the operating speed of a CF-LVAD was regulated to control the flow rate through the CF-LVAD, to improve the pulsatility and the shape of the systemic arterial pressure signal over a cardiac cycle.

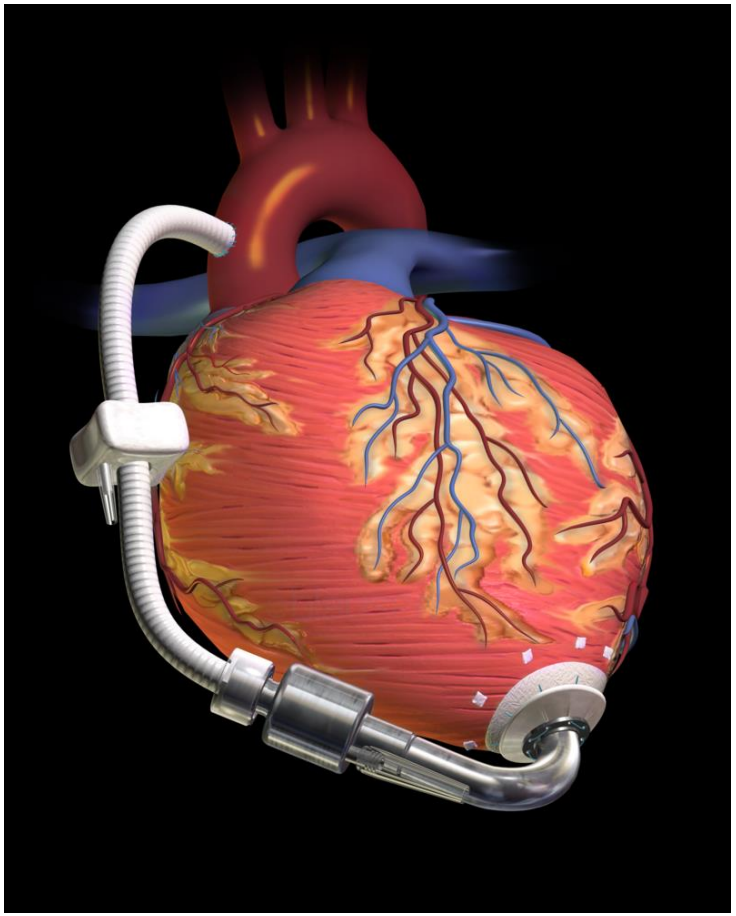

Close-up illustration of typical left ventricular assist device (LVAD)

https://en.wikipedia.org/wiki/Ventricular_assist_device

Blausen Medical Communications, Inc. - Donated via OTRS

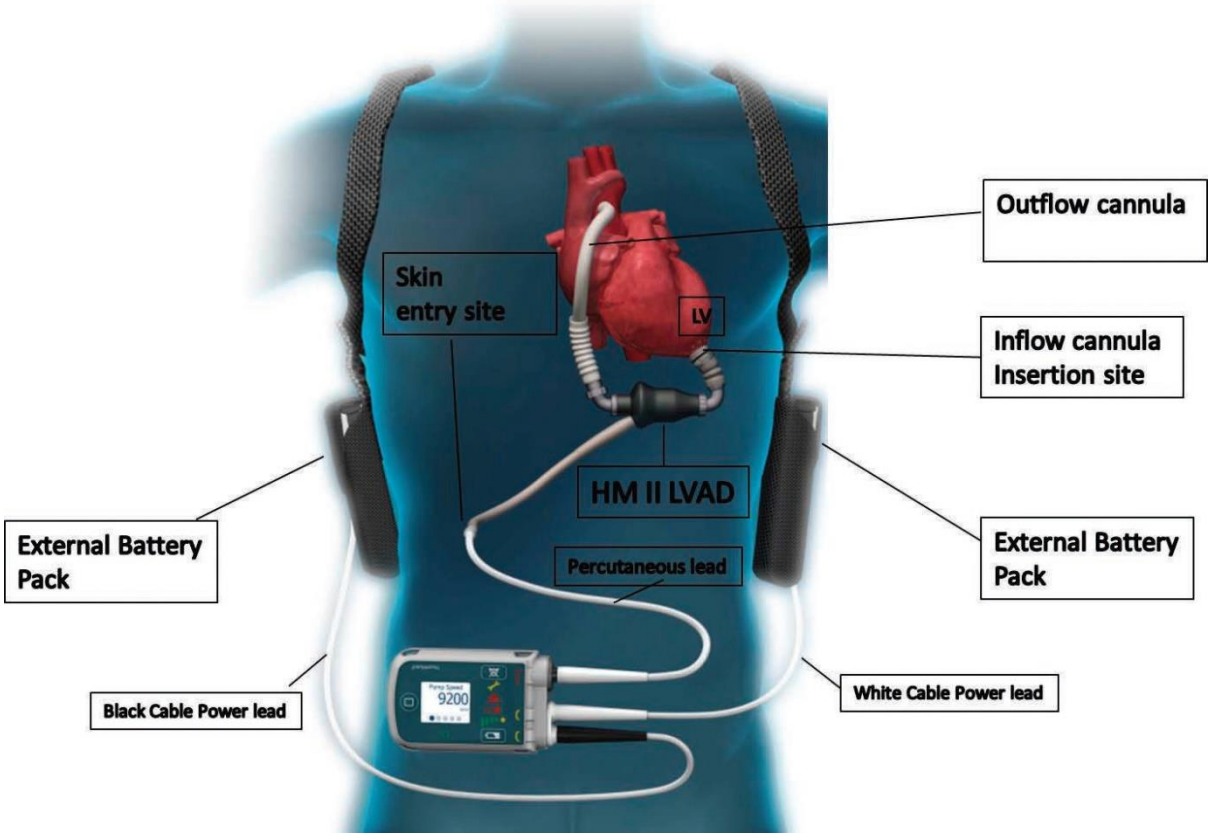

HeartMate II device and equipment illustration. HM: HeartMate II; LVAD: left ventricular assist device; LV: left ventricle

Jerry D. Estep, Barry H. Trachtenberg, Laurie P. Loza, Brian A. Bruckner, "Continuous flow left ventricular assist devices: shared care goals of monitoring and treating patients," houstonmethodist.org/debakey-journal, MDCVJ | XI (1) 2015 pp. 33-44

https://www.ncbi.nlm.nih.gov/pmc/articles/PMC4362063/pdf/i1947-6094-11-1-33.pdf

MicroMed Debakey Heart Assist 5

An excellent video on YouTube explaining the use of a continuous flow left ventricular assist device (CF-LVAD), available at

https://www.youtube.com/watch?v=mO53uCKo3k8

Materials and Methods

To simulate the healthy and dilated cardiomyopathic (DCM) heart in a combination with the circulatory system a model was developed considering the analogy between electrical and hemodynamical systems [2]. The complete cardiovascular system model consists of the heart chambers and heart valves, systemic arteries and veins and pulmonary arteries and veins. The model of the ventricles describes the ventricular wall mechanics, myocardial constitutive properties and intramyocardial pressure [3,4]. The heart rate in the CVS model was modulated using a baroreflex model [5]. To simulate LVAD support, a model which estimates the pressure difference across the Micromed DeBakey CF-LVAD considering the operating speed of the pump, flow rate and change of the flow rate through the pump [6] was integrated into the cardiovascular system model. In the simulations of the assisted cardiovascular system, the operating speed of the CF-LVAD was regulated applying proportional-integral control to flow rate through the CF-LVAD. The reference flow rate was obtained from a model which describes the dynamics of a healthy left ventricle and systemic arteries. This model is given below (Eq. 1-3). The electric-analogue of the assisted cardiovascular system model and block diagram of the control application are given in Figure1.

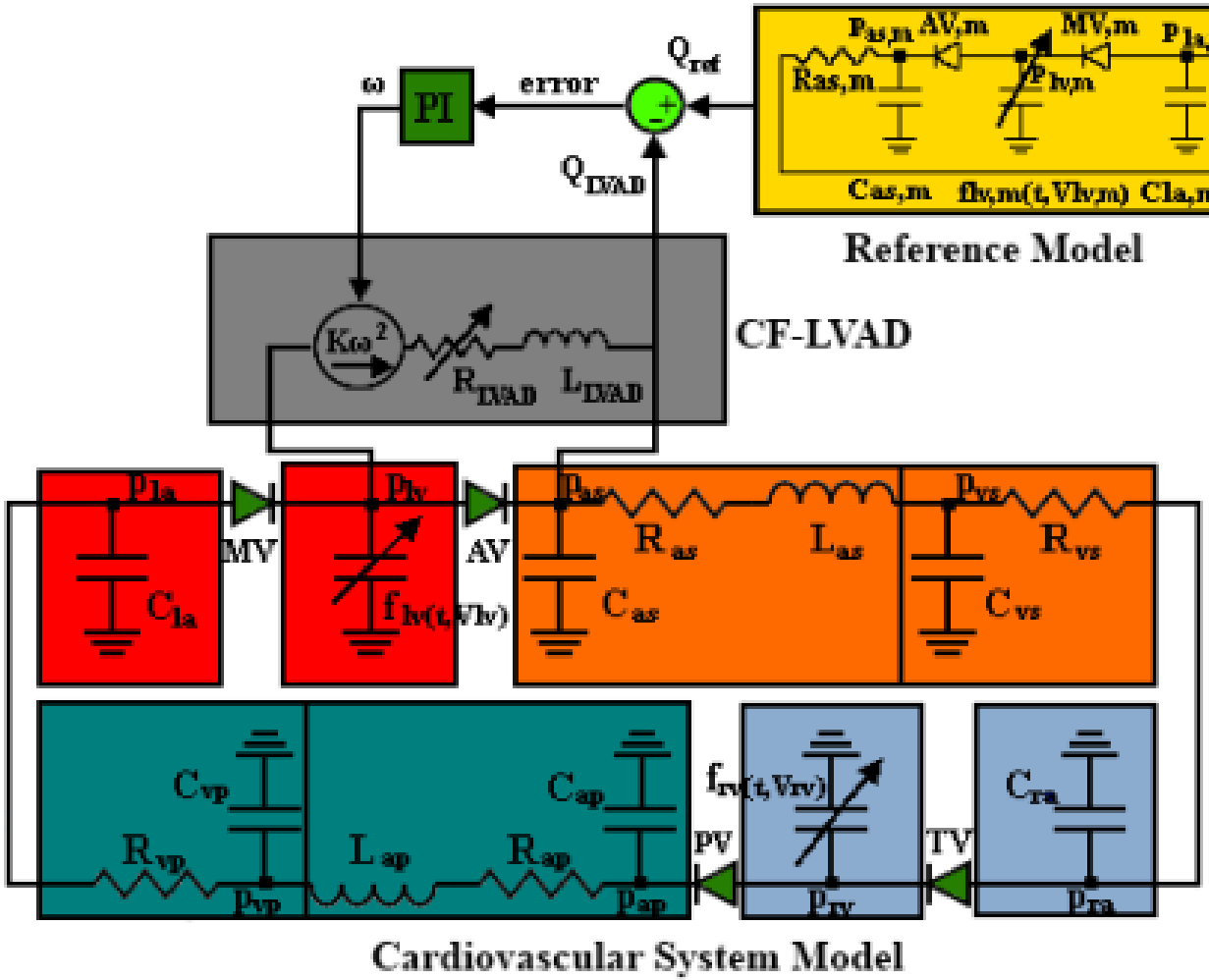

Figure 1. Electric-analogue of CF-LVAD integrated cardiovascular system model and block diagram of control application

$$dp_{as,m}/dt = ((p_{lv,m} - p_{as,m})/R_{av,m} - (p_{as,m} - (V_{tot,m} - V_{u,m} - V_{lv,m} - p_{as,m}C_{as,m}) /C_{la,m})/R_{as,m})/C_{as,m} \quad (1)$$

$$Q_{as,m} = (p_{as,m} - (V_{tot,m} - V_{u,m} - V_{lv,m} - p_{as,m}C_{as,m}) /C_{la,m})/R_{as,m} \quad (2)$$

$$Q_{ref} = K_1 dP_{as,m}/dt + K_2 Q_{as,m} \quad (3)$$

dp/dt is the change of pressure with respect to time, *p* is pressure, *V* is volume *Q* is flow rate, *R* is resistance and *C* is compliance in the equations above. The subscripts *as, lv, av, la, tot,* refer to systemic arteries, left ventricle, aortic valve, left atrium, total respectively. u denotes unstressed blood volume. Subscripts ref and m denote reference and model parameters. K_1 and K_2 are the coefficients in the equation describing the reference CF-LVAD flow. *AV, MV, TV* and *PV* denote aortic, mitral tricuspid and pulmonary valves respectively. L denotes inertance and f denotes ventricle models. The subscripts *vs, ra, rv, ap* and *vp* denote systemic veins, right atrium,

right ventricle, pulmonary arteries and veins respectively. Finally, *t* denotes instantaneous time in Figure 1.

In the varying speed CF-LVAD operating application the highest and lowest speeds were set to 16000 rpm and 4000 rpm respectively. To make an accurate comparison between pulsatility of the vascular haemodynamics in the varying speed regulated CF-LVAD assistance and constant speed CF-LVAD assistance mean pump output (MPO) of the regulated CF-LVAD was calculated. The same MPO was obtained approximately at 11160 rpm speed in constant speed CF-LVAD assistance. Body surface area of the patient was assumed to be 1.9 m^2 to enable the calculation of cardiac index (CI). Simulations were performed using Matlab Simulink with the ode15s solver. Maximum step size was 0.0005 s.

Results and Discussion

Simulations were performed for healthy and DCM cardiovascular system models without assistance first. LV, RV, systemic and pulmonary arterial pressures, LV and RV volumes, cardiac outputs and heart rates for healthy and DCM cardiovascular systems are in summarized in Table 2.

Table 1. Hemodynamic variables for healthy and DCM models

	p_{lv}[mmHg]	p_{as}[mmHg]	p_{rv}[mmHg]	p_{ap}[mmHg]	V_{lv}[mL]	V_{rv}[mL]	CO[mL/min]	HR[bpm]
Healthy	5-123	84-122	1-29	16-29	49-125	37-113	5548	73
DCM	33-82	60-80	1-49	40-48	227-269	42-84	3906	93

As indicated in Table 1, systolic pressure in the left ventricle and systemic arteries decreased significantly. In DCM diastolic pressure in left ventricle increased. Systolic pressure in right ventricle and pulmonary arteries increased. Left ventricular volume increased over a cardiac cycle, however, stroke volume in both ventricles decreased. Cardiac output decreased and heart rate increased in DCM condition. So the model is capable of describing the circulatory dynamics of an LVAD implantation candidate.

The model results with CF-LVAD incorporated for mean arterial pressure, pulse pressure in systemic arteries, cardiac output and mean pump output, end systolic and end diastolic volumes heart rates and cardiac index for the healthy model, DCM model, varying CF-LVAD operating speed application and constant CF-LVAD operating speed application are given in Figure 2.

As shown in Figure 2, varying speed CF-LVAD support and constant speed CF-LVAD support increases the mean arterial pressure in healthy state. However, pulse pressure in varying speed CF-LVAD support was almost two times higher than in constant speed CF-LVAD support. The LV volume in DCM model decreased in both varying and constant speed CF-LVAD support. Both varying and constant speed CF-LVAD support provided more than 5L/min mean output. So, the cardiac

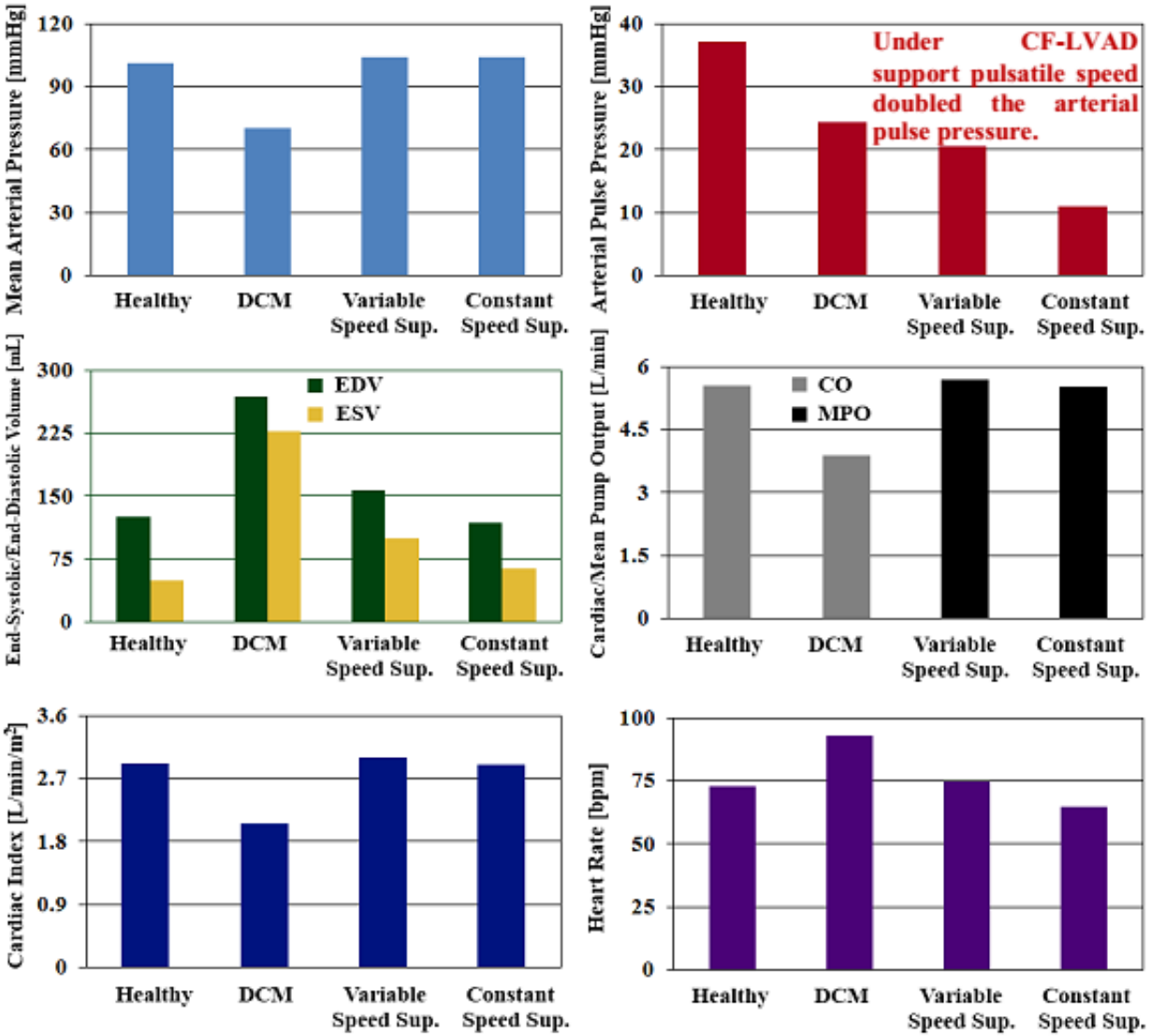

Figure 2. Comparison of the hemodynamic variables in healthy and DCM models, varying and constant speed CF-LVAD support

index was at the healthy level for both operating modes. Decreased arterial pressure caused the increase in heart rate in the DCM model. In both operating modes heart rate decreased to a healthy level again. As mentioned before arterial pulse pressure doubled under the pulsatile speed CF-LVAD support.
In future studies, the method will be validated experimentally.

Conclusion

Simulation results showed that applying a pulsatile pump speed to the CF-LVAD, provides sufficient support to a DCM cardiovascular system model. Also varying speed over a cardiac cycle increases the pulse pressure and may reduce the long term complications associated with CF-LVAD support.

Acknowledgements

This study is part of the MeDDiCA project and funded under FP7, People Programme, Marie Curie Actions. Grant agreement PITN-GA-2009-238113.

References

1. Ündar A. 2004 Myths and Truths of Pulsatile and Nonpulsatile Perfusion During Acute and Chronic Cardiac Support. *Artificial Organs* 28, 439-443 (doi: 10.1111/j. 1525-1594.2004.00086.x)

2. De Pater L. & van den Berg J.W. 1964 An Electrical Analogue of Entire Human Circulatory System. *Med Electron Biol Eng* 2, 161-166.

3. Bovendeerd, P.H.M., Borsje P., Arts, T. & De Vosse, F.N. 2006 Dependence of Intramyocardial Pressure and Coronary Flow on Ventricular Loading and Contractility: A Model Study. *Ann Biomed Eng* 34, 1833-1845. (doi:10.1007/s10439-006-9189-2)

4. Cox L.G.E., Loerakker S., Rutten M.C.M., de Mol B.A.J.M. & van de Vosse F. N. 2009 A Mathematical Model to Evaluate Control Strategies for Mechanical Support. *Artificial Organs* 33, 593-603. (doi:10.1111/j.1525-1591.2009.00755.x)

5. Ursino M. 1998 Interaction Between Carotid Baroregulation and Pulsating Heart: A Mathematical Model *Am J Physiol* 275, 1733-1747.

6. Moscato F., Danieli G.A. & Schima H. 2009 Dynamic Modeling and Identification of an Axial Flow Ventricular Assist Device. *Int J Artif Organs* 32, 336-343.

Ευχαριστώ

Πρόγραμμα Διδακτορικών Σπουδών της Σχολής Ηλεκτρολόγων Μηχανικών και Μηχανικών Υπολογιστών ΕΜΠ

Πολυκλιμακωτή Προσομοίωση της Ασθένειας του Καρκίνου και *In Silico* Ιατρική (705)

Μάθημα 3ο

In Silico Ιατρική / *In Silico* Ογκολογία: Θέματα Τεχνολογίας.

Γεώργιος Σ. Σταματάκος

Διευθυντής Ερευνών -Research Professor– Καθηγητής Ερευνας
Ερευνητικό Πανεπιστημιακό Ινστιτούτο Συστημάτων Επικοινωνιών και Υπολογιστών (ΕΠΙΣΕΥ)
Σχολή Ηλεκτρολόγων Μηχανικών και Μηχανικών Υπολογιστών (ΣΗΜΜΥ)
Εθνικό Μετσόβιο Πολυτεχνείο (ΕΜΠ)
Διευθυντής της Ερευνητικής Ομάδας για την In Silico Ογκολογία και την In Silico Ιατρική, ΕΠΙΣΕΥ-ΣΗΜΜΥ-ΕΜΠ
Επισκέπτης Καθηγητής της Ιατρικής Σχολής του Πανεπιστημίου του Saarland, Γερμανία (1/7/2019-15/9/2019)
Επισκέπτης Καθηγητής της ΣΗΜΜΥ, ΕΜΠ (2016-2019)
gestam@central.ntua.gr, http://in-silico-oncology.iccs.ntua.gr/

The Technologically Integrated Oncosimulator: Combining Multiscale Cancer Modeling With Information Technology in the *In Silico* Oncology Context

Georgios Stamatakos, *Member, IEEE*, Dimitra Dionysiou, Aran Lunzer, Robert Belleman, Eleni Kolokotroni, Eleni Georgiadi, Marius Erdt, Juliusz Pukacki, Stefan Rüeping, Stavroula Giatili, Alberto d' Onofrio, Stelios Sfakianakis, Kostas Marias, *Member, IEEE*, Christine Desmedt, Manolis Tsiknakis, *Member, IEEE*, and Norbert Graf, *Member, IEEE*

***Abstract*—This paper outlines the major components and function of the technologically integrated oncosimulator developed primarily within the Advancing Clinico Genomic Trials on Cancer (ACGT) project. The Oncosimulator is defined as an information technology system simulating *in vivo* tumor response to therapeutic modalities within the clinical trial context. Chemotherapy in the neoadjuvant setting, according to two real clinical trials concerning nephroblastoma and breast cancer, has been considered. The spatiotemporal simulation module embedded in the Oncosimulator is based on the multiscale, predominantly top-down, discrete entity—discrete event cancer simulation technique developed by the *In Silico* Oncology Group, National Technical University of Athens. The technology modules include multiscale data handling, image processing, invocation of code execution via a spreadsheet-inspired environment portal, execution of the code on the grid, and the visualization of the predictions. A refining scenario for the eventual coupling of the oncosimulator with immunological models is also presented. Parameter values have been adapted to multiscale clinical trial data in a consistent way, thus supporting the predictive potential of the oncosimulator. Indicative results demonstrating various aspects of the clinical adaptation and validation process are presented. Completion of these processes is expected to pave the way for the clinical translation of the system.**

***Index Terms*—Advancing Clinico Genomic Trials on Cancer (ACGT) project, breast cancer, *in silico* medicine, *in silico* oncology, multiscale cancer modeling, nephroblastoma, oncosimulator, Virtual Physiological Human (VPH).**

I. Introduction

IN silico medicine, an emergent scientific and technological domain based on clinically driven and oriented multiscale biomodeling, appears to be the latest trend regarding the translation of mathematical and computational biological science to clinical practice through massive exploitation of information technology. The term *multiscale* refers to several scales or levels of the manifestation of life such as the molecular, the cellular, the tissue, the organ, and the body system scales addressed concurrently. The idea is to view disease as a hypercomplex and multiscale *natural phenomenon* amenable to modeling and simulation [1]–[10]. *In silico* (i.e., on the computer) experimentation for each individual patient using their own multiscale biomedical data is expected to significantly improve the effectiveness of treatment in the future, since reliable computer predictions could suggest the optimal treatment scheme(s) and schedules(s) for each separate case.

It is noted that generic treatment schemes and schedules are based on the average response of a population of patients. Despite the fact that those patients share certain characteristics

of the disease, other critical disease characteristics may differ tremendously across the population. This may lead to remarkably differing actual responses to the same treatment among patients.Therefore, a thorough exploitation of all the critical disease characteristics of a given patient and their dynamic interdependences at several spatiotemporal scales is expected to lead to an optimal treatment tailored to the patient's biological constitution. Such an approach may dictate the prescription of more effective drugs and dosages for any given patient and the minimization of side effects. This may obviously have considerable clinical, societal, and financial implications.

In order to address this vision, a number of combined multiscale modeling and information technology approaches have appeared over the last few years [1]. In the area of *in silico oncology* the technologically integrated oncosimulator (IOS) developed primarily within the framework of the European Commission (EC) funded integrated project ACGT (Advancing ClinicoGenomic Trials on Cancer, FP6–2005-IST-026996) appears to be the first worldwide effort of its kind. [11].

The ACGT project proposed the design and implementation of a dedicated cancer information technology (IT) environment able to seamlessly integrate clinico-genomic data and support the development of complex models. Within this context, simulating disease evolution and/or disease outcome was a milestone for the technological advancement of predictive medicine-based decision support. The major expected outcome is twofold: first, we hope to alleviate the patient from unnecessary treatment. Excess treatment may be administered in cases where lack of knowledge regarding critical aspects of the molecular constitution and the multiscale dynamics of the tumor prevents the prediction of an eventually good and fast response to a given therapeutic scheme from being formulated. *In silico* oncology is expected to substantially alleviate the potentially serious side effects of excess treatment in such cases. Second, we hope to eventually optimize treatment via *in silico* simulation of candidate therapeutic schemes.

The IOS embedded within the ACGT architecture is a software system simulating *in vivo* tumor response to therapeutic modalities within the clinical trial context. The four dimensional (4-D) (spatiotemporal) simulation module that has been embedded in the oncosimulator is primarily based on the multiscale, predominantly top-down, discrete entity—discrete event cancer simulation technique developed by the *In Silico* Oncology Group (ISOG) of the Institute of Communication and Computer Systems, National Technical University of Athens (www.in-silico-oncology.iccs.ntua.gr) [2]–[10]. The top-down method starts from the macroscopic imaging data and proceeds toward lower biocomplexity levels. When there is a need for an upward movement in the biocomplexity scales, a summary of the available information pertaining to the previous lower level is used.

Within the ACGT project, we have addressed two preoperative chemotherapy scenarios using real clinical trial data: nephroblastoma and breast cancer. The technology modules include multiscale data handling, image processing, invocation of code execution via a spreadsheet-inspired environment portal (RecipeSheet), execution of the computer code on the grid, and

visualization of the predictions of the simulations. Adaptation of parameter values to multiscale clinical trial data has been achieved in a consistent way as described in Section IX. The latter endorses the predictive potential of the oncosimulator. Both clinical adaptation and validation procedures are in progress. In addition to already published predictive results [8], [10] demonstrating various aspects of the clinical adaptation and validation procedures, new illustrative simulation examples are presented in this paper. Clinical adaptation and validation, when completed, are expected to pave the way for the clinical translation of the system. A scenario for the eventual coupling of the oncosimulator with immunological models so as to refine the original simulation tumor dynamics models is also presented.

A. *Nephroblastoma Case*

Nephroblastoma is the most common malignant renal tumor in children. Treatments are based on prospective multicenter trials and studies conducted by the International Society of Pediatric Oncology (SIOP) in Europe and the Children's Oncology Group, North America (COG) in North America [12]. Information from these nephroblastoma studies on both sides of the Atlantic have allowed the identification of prognostic indicators independent of whether patients are treated by immediate surgery (COG) or surgery after preoperative chemotherapy (SIOP).

The identification of histological subtypes of Wilms' tumor in addition to stage classification and response to treatment is of prognostic value. In this way, the SIOP trials and studies largely focus on the issue of preoperative therapy [13], [14]. Response to treatment can be measured individually by tumor volume reduction and percentage of therapy-induced necrosis or remaining vital blastema at the time of surgery in the histological specimen. In nephroblastoma, the blastemal subtype after preoperative chemotherapy is recognized as an unfavorable entity. This gives an early individual prognostic parameter and is used for further stratification and more individualization of the postoperative treatment [12], [13].

The nephroblastoma case is ideal for the development and validation of *in silico* models since the highly successful treatment rate in SIOP provides an excellent, reliable reference for both developing and validating such models. The main goal in this context is to quantitatively predict the response to preoperative chemotherapy in every case. The model aims at avoiding unnecessary treatment in nonresponding tumors and applying chemotherapy only to those patients that would benefit most. At the same time, the provision of a clinical decision support tool for the less experienced clinicians treating this disease is of particular importance.

B. Breast Cancer Case

The breast cancer branch of the oncosimulator addresses breast cancer treatment with epirubicin, an anthracycline drug used for chemotherapy. Although anthracycline drugs are among the most effective chemotherapies in breast cancer, their efficacy is restricted to a subset of the breast cancer patient population, and a small proportion of women suffer severe side

effects, including congestive heart failure. By identifying those women who are most likely to benefit from treatment, it might be possible to reduce the unnecessary exposure of some women to such a risk and to take an important step toward the individualization of breast cancer treatment. The traditional approach to tackle this problem has been the identification of novel predictive biomarkers. Topoisomerase IIA (TOP2 A) is arguably the most promising marker for predicting the efficacy of anthracycline-based chemotherapy for breast cancer patients. However, several groups have reported conflicting results with regard to its predictive value. The primary aim of the TOP trial [15] was to prospectively evaluate the predictive value of TOP2 A and the secondary aim to identify biomarkers of response/resistance to anthracyclines.

This trial has demonstrated a significant correlation of TOP2 A amplification—but not protein overexpression—with the response to anthracyclines [15]. Additionally, an anthracycline-based score (A-Score) using gene expression data has been proposed. By including the A-Score into the IOS, a multiscale model has been developed to simulate treatment outcome based on the characteristics of individual patients for optimizing breast cancer treatment.

II. Brief Outline of the Multiscale Model of Cancer Dynamics and Response to Treatment Units

In this section, a brief description of the basics of the IOS multiscale models is provided. The models start from the macroscopic high biocomplexity level (imaging data) and proceeds toward lower biocomplexity levels. The macroscopic anatomic region of interest is either manually or semi-automatically annotated by the clinicians on MRI imaging sets acquired at time of diagnosis (see Section III.) A virtual cubic mesh is used for the discretization of the area of interest (tumor) of which the elementary cube is termed geometrical cell [2]–[9]. A hypermatrix, i.e., a mathematical matrix of [matrices of (matrices. . .of (matrices or vectors or scalars))] corresponding to the anatomic region of interest is subsequently defined [9]. The latter describes explicitly or implicitly the local biological, physical, and chemical dynamics of the region [2]–[10]. The following (sets of) parameters are used to identify a cluster of biological cells belonging to a given equivalence class within a geometrical cell of the mesh at a given time point.

mesh at a given time point:

1) The spatial coordinates of the discrete points of the discretization mesh with spatial indices i, j, k, respectively. It is noted that each discrete spatial point lies at the center of a geometrical cell of the discretization mesh.
2) The temporal coordinate of the discrete time point with temporal index l.
3) The mitotic potential category (i.e., stem or progenitor or terminally differentiated) of the biological cells with mitotic potential category index m.
4) The cell phase (within or out of the cell cycle) of the biological cells with cell phase index n. The following phases are considered: {G1, S, G2, M, G0, A, N, D}, where G1 denotes the G1 cell cycle phase, S denotes the DNA synthesis phase, G2 denotes the G2 cell cycle phase,

M denotes mitosis, G0 denotes the quiescent (dormant) G0 phase, A denotes the apoptotic phase, N denotes the necrotic phase and D denotes the remnants of dead cells.

For the biological cells belonging to a given mitotic potential category AND residing in a given cell phase AND being accommodated within the geometrical cell whose center lies at a given spatial point AND being considered at a given time point; in other words for the biological cells clustered in the same equivalence class denoted by the index combination ijklmn, the following state parameters are provided:

1) local oxygen and nutrient provision level;
2) number of biological cells;
3) average time spent by the biological cells in the given phase;
4) number of biological cells hit by treatment;
5) number of biological cells not hit by treatment.

The *initial* constitution of the tumor has to be estimated based on the available medical data through the application of pertinent algorithms [8]. This state corresponds to the instant just before the start of the treatment course to be simulated. The entire simulation can be viewed as the periodic and sequential application of a number of algorithms (operators) on the hypermatrix of the anatomic region of interest which takes place in the following order. 1) time updating, i.e., increasing time by a time unit (e.g., 1 h); 2) estimation of the local oxygen and nutrient provision level; 3) estimation of the effect of treatment referring mainly to cell hit by the treatment, cell killing, and cell survival. Available molecular and/or histological information is integrated primarily at this point. 4) Application of cell cycling, possibly perturbed by treatment. Transition between mitotic potential cell categories such as transition of the offspring of a terminally divided progenitor cell into the terminally differentiated cell category is also tackled by this algorithm set. 5) Handling of differential tumor expansion/ shrinkage or more generally spatial geometry and tumor mechanical dynamics. 6) Updating the local oxygen and nutrient provision level at each time step. It is worth noting that stochastic perturbations about the mean values of several model parameters are considered (hybridization with the Monte Carlo technique). A generic tumor cell cytokinetic model is depicted in Fig. 1. For further details see [8] and [10].

III. Image Processing of the Medical Data

For patients with nephroblastoma, imaging studies (MRI $T1$, $T1$ with contrast enhancement, $T2$ and $T2$ flair) are available at the time of diagnosis and after 4 weeks of preoperative chemotherapy. The imaging studies at the time of diagnosis are used for the prediction of tumor shrinkage during and after 4 weeks of vincristine and actinomycin-D chemotherapy.

One of the main inputs into the IOS is the volumetric data of nephroblastoma. This data consists of isotropic voxel dimensions in order to facilitate the computation of tumor dynamics simulation. Since MRI slices are usually reconstructed containing highly nonisotropic voxels, interpolation of the binary segmentation volumes is performed [16].

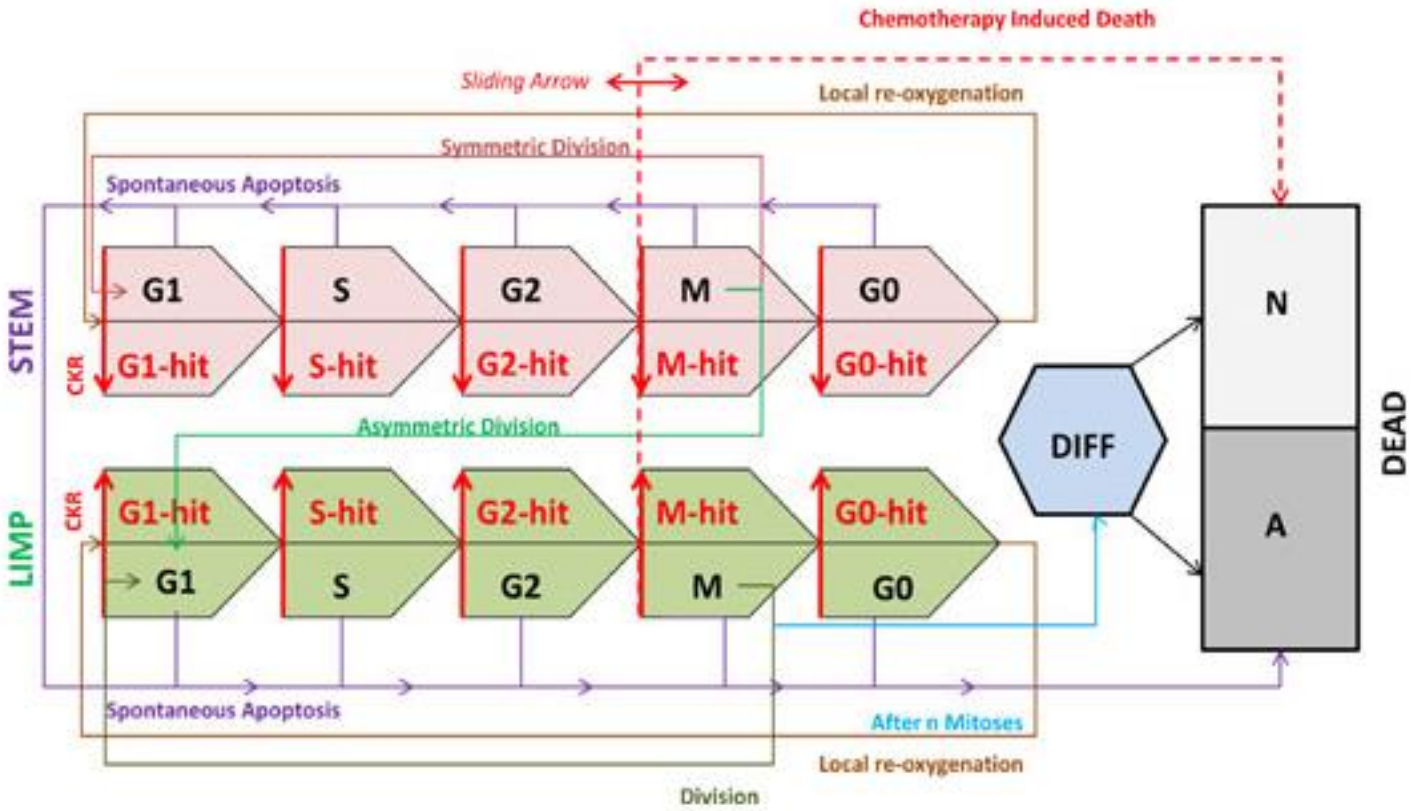

Fig. 1. Generic cytokinetic model used. LIMP: Limited Mitotic Potential cells. DIFF: terminally differentiated cells. G1: Gap 1 phase. S: DNA synthesis phase. G2: Gap 2 phase. M: Mitosis. G0: dormant phase. N: necrosis. A: apoptosis. Hit: cells lethally hit by chemotherapy. CKR: Cell Kill Rate. The arrow indicating chemotherapy-induced death is a sliding arrow, with position dependent on drug pharmacodynamics.

Segmentation of the tumor is important in order to provide information on the shape and location of the tumor. This process is also important for model validation since it allows quantitative comparison of the simulation predictions with the actual development of the tumor *in vivo*. Within the ACGT project, a novel semiautomatic snake-based method for cancer segmentation was developed, where a spatially adaptive behavior of the snake is accomplished with minimal user interaction. The method achieved has improved results over traditional snakes, due to local snake bending. This spatially adaptive active contour technique introduced a local snake bending to improve traditional snake's performance for segmenting tumors. The key point is the use of adaptable parameters, instead of constant ones, in order to adjust the bending of the curve locally according to image characteristics such as gradient magnitude and corner strength. The result is a more flexible/accurate delineation of tumor regions reported in more than 150 real MRI cases. Validation has been performed using the clinical expert's annotations as ground truth [17]. Fig. 2, shows an example where this improved method better delineates the tumor without getting stuck in local maxima.

IV. Subjunctive Interface System for the Exploration of the Oncosimulator

In this section, the front-end facilities that were created to support the IOS developers in its technical validation are briefly described. Validation, in the sense used here, means confirming that the simulator delivers credible results when applied to tumors of differing sizes and shapes, and that adjustment to each of its parameters, singly or in combination, has the expected impact on the results.

The validation is therefore a form of exploration within the space of possible simulation results, with the following characteristics. 1) The exploration must be overseen by a human user. For each simulation, the developers must confirm not just that the final predicted outcome (percentage growth or shrinkage of the tumor) is reasonable, but that the simulation followed a le-

gitimate and credible course to that outcome. 2) The parameter space is very large. The versions of the simulator being validated have between 35 and 40 independently variable parameters. An interface offering simultaneous access to all these parameters would be unwieldy, so the users must be able to choose which parameters to vary. They must also be assisted in keeping track of which parameter–value combinations have been explored so far. 3) Validation calls heavily on comparison. The developers must initially confirm that for each step in the value of a single parameter, the results change by a reasonable increment in the predicted direction. They must also check the effects of changing settings on multiple parameters. 4) Some result visualizations require interaction. The results from the oncosimulator include representations of the tumor shape in three dimensions; these can be rendered in 2-D for on-screen display, but in order to understand the entire solid shape a user typically needs to interact with the view, for example by rotating it or taking slices.

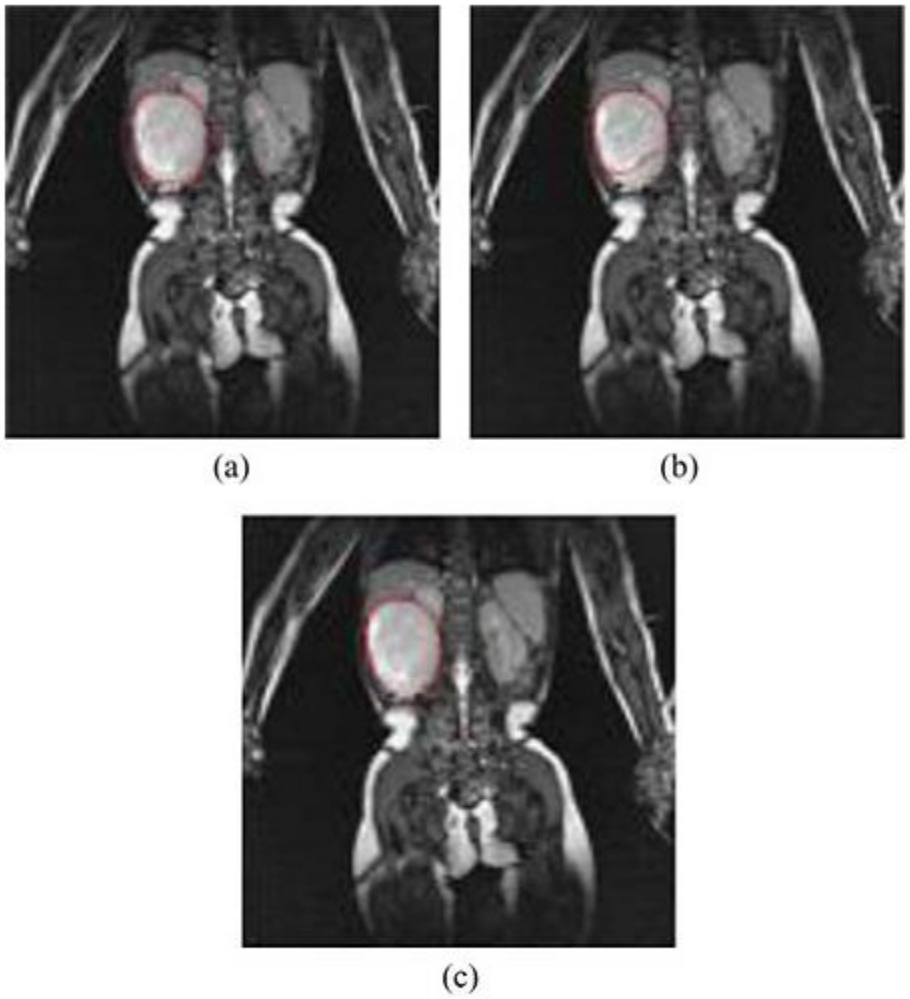

Fig. 2. Renal tumor segmentation on MR abdominal images: (a) clinician's annotation, (b) result using traditional snakes due to tumor inhomogeneity, and (c) result using spatially adaptive active contours.

Data presentations and visualizations for the validation are obtained through RESTful web services. These provide both alphanumeric ("raw") representations of IOS results as well as graphical, such as graph plots, 2-D views (isocontours, scatterplots, cutting planes), 3-D views (isosurfaces, volume rendering), and animated views that show the evolution of a tumor over time. Multimodal visualizations are also supported that simultaneously represent IOS results with medical images (e.g., CT, MRI) and manual annotations of pre/post-therapy tumor regions. Given the importance of comparison between alternative cases, as noted above, linked views are supported to provide a consistent view on multiple cases at the same time.

The validation interface is based on the RecipeSheet [18], an end-user programming environment that explicitly includes subjunctive interface facilities [19], [20] to help users request, compare, and interact with multiple alternative results simultaneously. On the "OncoRecipeSheet" (ORS) created for this project, a user can specify up to 12 independent scenarios at a time, each scenario defining a combination of simulation–parameter values. If a simulation has already been run for a specified parameter combination, visualizations of its results are retrieved from an online server and displayed on the sheet; if the simulation has not yet been run, the ORS includes a simple tool for submitting it immediately as a grid job.

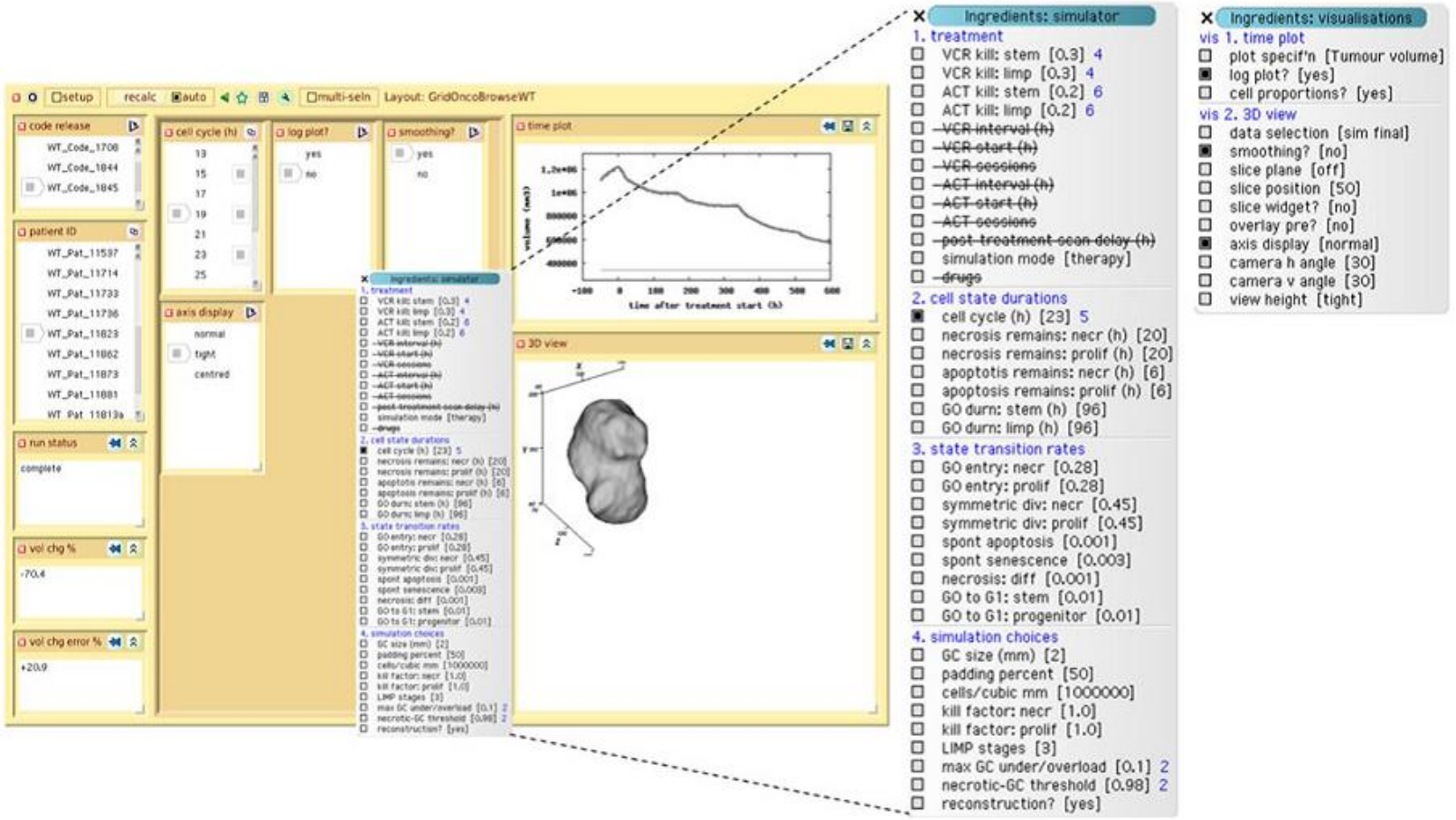

Fig. 3. Main OncoRecipeSheet (ORS) showing the menus for selecting simulation and visualization parameters.

Fig. 3 presents the main ORS interface with a single scenario showing the results. The patient identifier and the version of simulator code are chosen using the sheet cells at top left. The large pop-up menu (shown expanded on the right) offers the 38 parameters that can be varied in the chosen code version; here, the user has requested a control to vary the "cell cycle" parameter, which the menu shows would otherwise default to 23 h. The displayed result is from a simulation run with default values for all other parameters. On the far right is an expanded version of a second menu that offers parameters for tailoring the result display. Here, the user has asked to control three of those parameters, so they too appear as cells on the sheet. Fig. 4 shows three examples of how a sheet can be set up with multiple scenarios, defined by choosing alternative values for simulation or visualization parameters, and how the scenarios' results are displayed to assist comparison.

By the end of the ACGT project some 7000 simulations had been run using the ORS; early results of this work were published in [21] and [22], [23]. In general, the simulator was shown to be robust and predictable across a broad range of parameter settings, but the ability to make comparisons did help to discover various unexpected behaviors that the simulator developers were then able to resolve.

V. Executing the Oncosimulator on the Grid Via the OncoRecipeSheet (ORS) and Via the Workflow Environment

The oncosimulator application can take an advantage of the Grid environment designed within the ACGT project [24]. The most important components of the grid [25] infrastructure that take part in the grid execution of the IOS are the following: grid resource management service (GRMS), responsible for resource management, and data management system (DMS), a grid storage system (see Fig. 5). GRMS is an open source metascheduling system which allows developers to build and deploy resource management systems for large scale distributed computing infrastructures. GRMS is based on dynamic resource selection, mapping and an advanced scheduling methodology, and deals with dynamic grid environment and resource management challenges, e.g., load-balancing among clusters, remote job control, or file staging support.

Therefore, the main goal of the GRMS is to manage the whole process of remote job submission to various batch queuing systems, clusters, or resources. It has been designed as an independent core component for resource management processes, which can take advantage of various low-level core services and existing technologies. The main features of GRMS are job submission, job control (suspending, resuming, canceling), the ability to choose "the best" resource for the job execution using multicriteria matching algorithms, support for job checkpointing and migration, support for file staging, storing information about the job execution, user notifications support, workflow jobs support, etc.

The data management system (DMS) is composed of several specialized components and allows building a distributed system of services capable of delivering mechanisms for seamless management of large amounts of data. It is based on the pattern

of autonomic agents using the accessible network infrastructure for mutual communication. From the external applications point of view DMS is a virtual file system keeping the data organized in a tree-like structure. The main units of this structure are metadirectories, that enable the creation of hierarchies which encompass other data objects and metafiles. Metafiles represent a logical view of data regardless of their physical storage location. The DMS consists of three logical layers: the data broker, which serves as the access interface to the DMS system and implements the brokering of storage resources, the metadata repository that keeps the information about the data managed by the system, and the data container, which is responsible for the physical storage of data. In addition, DMS contains modules which extend its functionality to fulfill the enterprise requirements. These include the fully functional web-based administrator interface and a proxy to external scientific databases. The proxy provides a simple object access protocol, interface to the external databases, such as those provided by sequence retrieval system.

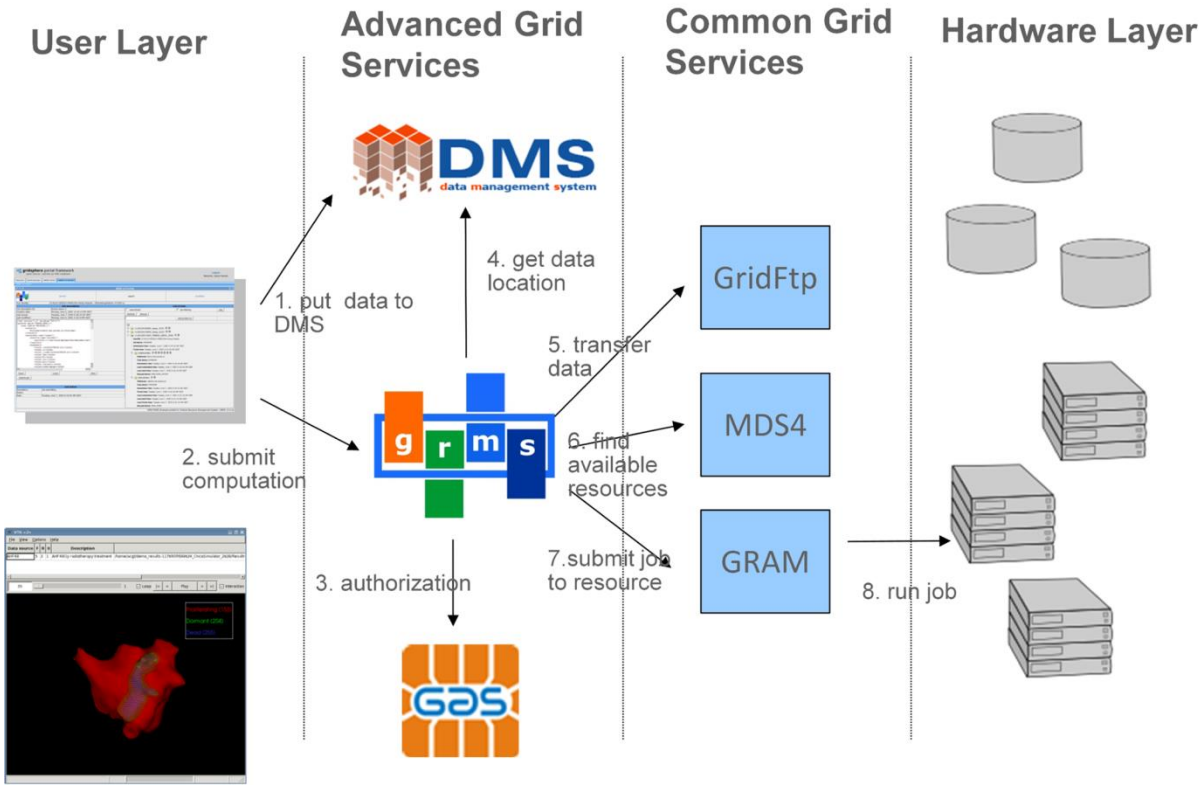

Fig.5. Components of the grid environment: DMS: Data Management System, GRMS: Grid Resource Management System, GAS – Grid Authorization Service, GridFTP – Grid Fie Transfer Service, GRAM – Globus Resource Allocation Manager, MDS4 - Monitoring and Discovery System ver. 4

The scenario for running the oncosimulator in the grid environment is mostly based on the aforementioned services. The first step is devoted to the preparation of input data for the computation. The clinician needs to prepare, e.g., MRI sets of slices of a nephroblastoma tumor corresponding to the tumor before chemotherapeutic treatment with vincristine and dactinomycin. Using specialized tools they also need to delineate the tumor boundaries on the provided slices as well as to prepare the rest of the multiscale input data. The user uploads all required files from their machine to the DMS using a web client. The files are then managed by DMS and can be accessed by the user or the other services acting on behalf of the user.

To execute the IOS in the grid, an appropriate job description XML (Extensible Markup Language) document is produced. It defines the job as a set of tasks with dependences among them. Each task is described as resource requirements and description

of the executable: environment variables, parameters of the execution, input and output files (or directories), executable file etc.

Users are supported in the production of the Job Description XML document through the use of the OncoRecipeSheet (ORS) [18]–[23], [26], which is responsible for creating a proper XML document based on the forms that are presented to the user, showing parameters of the application in a convenient way for the user. Subsequently ORS submits the description to the GRMS and monitors job execution. Based on the provided information GRMS finds available resources on the grid, transfers the input data from DMS to the grid node, and starts the computation. On successful completion of the job it moves the output data to DMS thus making it available for ORS for downloading. Using the ORS interface users can browse the results, compare the values, and submit new simulations if necessary. An overview of the scenario and the infrastructure components that are taking part in it is depicted in Fig. 5.

An alternative way of integrating the IOS into the ACGT architectural framework is a service implementation. In this approach, grid execution of the application is wrapped with the web service implementation such that the IOS can be used within the workflow environment of ACGT. The workflow infrastructure is a set of services and tools that allows the users to create scientific experiments by joining different service invocations into a single flow of actions. There are many services that are incorporated into the environment, some of them are focused on accessing different databases while others are able to process the data using statistical packages (e.g., R).

The workflow environment lies on the top of the grid infrastructure of ACGT. The oncosimulator service has been designed and developed in order to take advantage of the workflow environment of ACGT and to provide a means to integrate it with the rest of ACGT software (see Fig. 6).

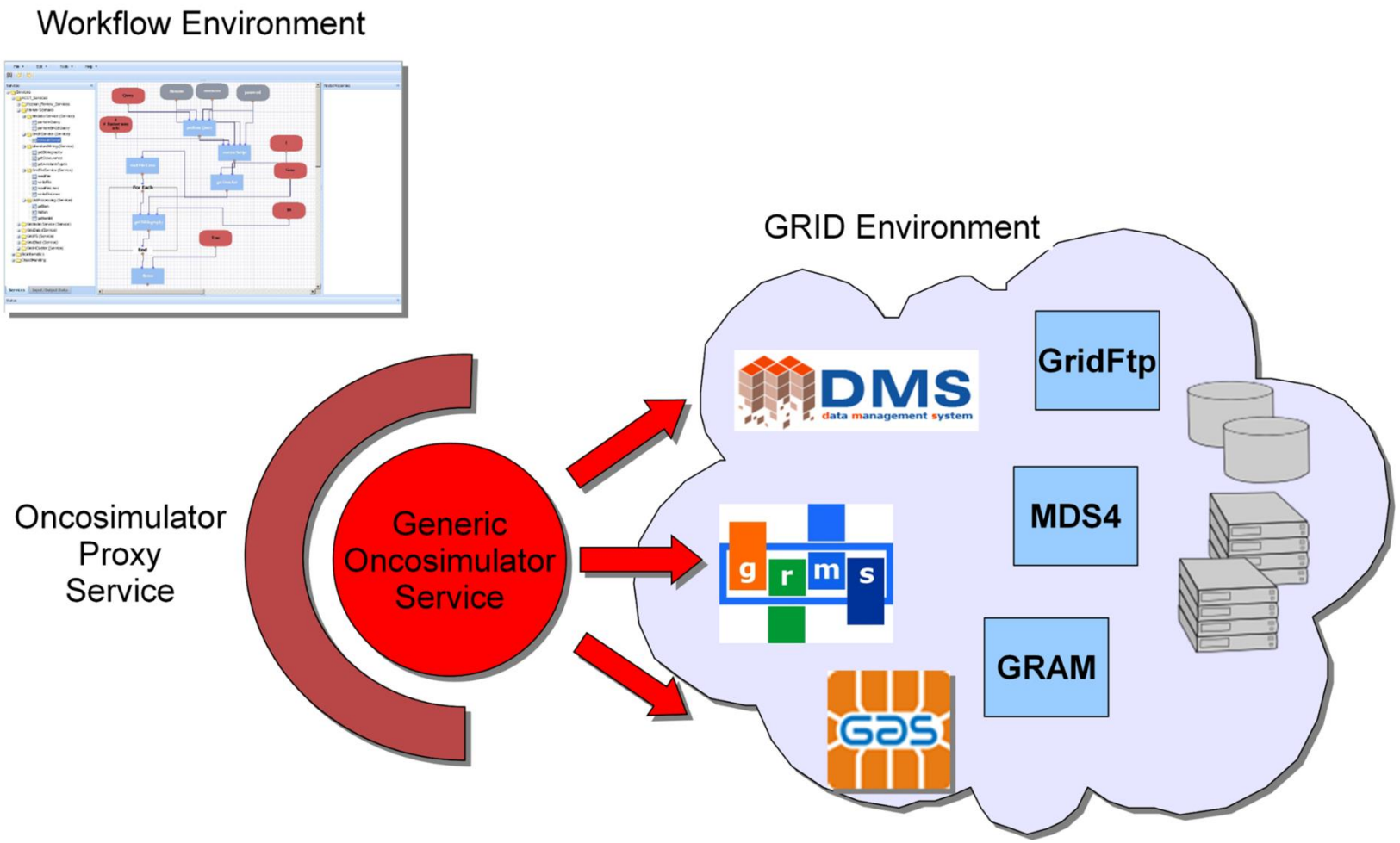

Fig. 6. Oncosimulator service.

VI. Executing the Oncosimulator Through Workflows

The ACGT Workflow Editor [27], [28] is the end user application for designing and executing high-level scientific workflows (see Fig. 7). In this web-based application, the user is encouraged to graphically combine the data retrieval and discover services and the knowledge extraction and data analysis tools. The

definition of the syntactic representation of the data and most importantly the annotation of the services with semantic metadata descriptions gives great flexibility in the workflow editor for supporting user friendliness and intelligence. If properly annotated, incompatible services cannot be directly connected because the data types of their inputs and outputs do not conform to each other, either in the syntactic or the semantic level, while service recommendation and intelligent workflow composition can also be supported.

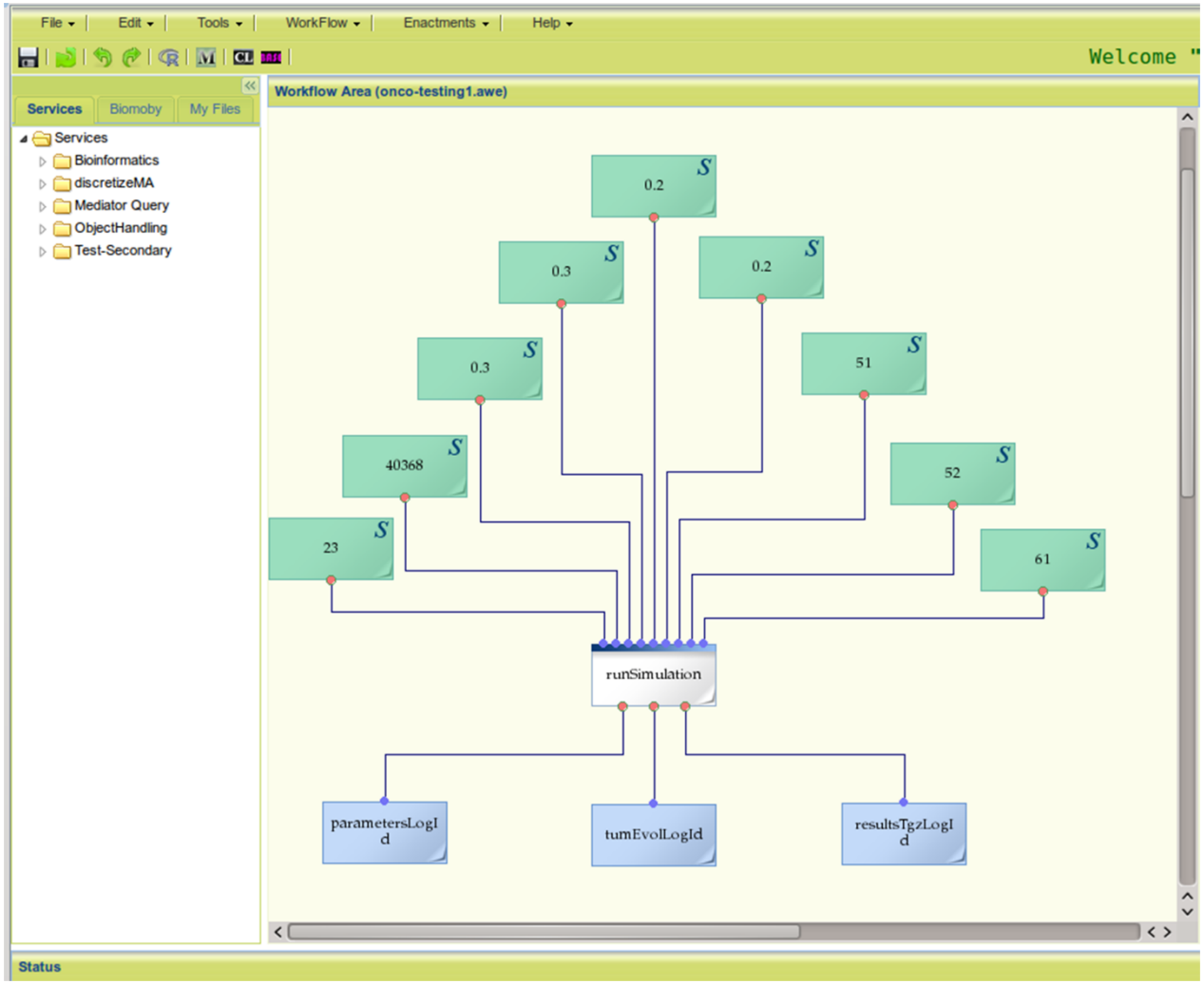

Fig. 7. Example of workflow created in the ACGT workflow environment.

Furthermore, the ACGT Workflow Editor features the following functionality: 1) provides a graphical environment for the end users to build their scientific experiments by combining the ACGT tools and facilitate their execution on the Grid; 2) supports access to all the ACGT tools and services, including the gridified version of the R package; 3) supports separate storage area per user, gives access to grid file system, and supports publication of a workflow to the ACGT community, execution monitoring and logging of a workflow; 4) supports user provided metadata (tagging) for custom search and retrieval of workflows; and 5) supports the storage and management of the provenance information gathered during the execution of the user workflows.

The oncosimulator when wrapped as another Grid Service, as described in Section V, can be integrated into more complex scientific workflows. This integration is achieved in a transparent way. The user creates their own workflow by creating a distinct functional entity which accepts its own parameter set and delivers its output. This seamless integration is further enhanced by the ability to include multiple instances of the onsosimulator in the same workflow but with different input parameters. Under the hood, all the different executions of the oncosimulator can be performed in parallel enabled by the scheduling and the run time support of the grid infrastructure. In this way, scientific experimentation and discovery becomes less time consuming, more efficient, and more productive.

VII. Clinical Adaptation and Validation Aspects

In order to adapt and validate the oncosimulator, clinical data including preoperative and postoperative imaging studies is bei

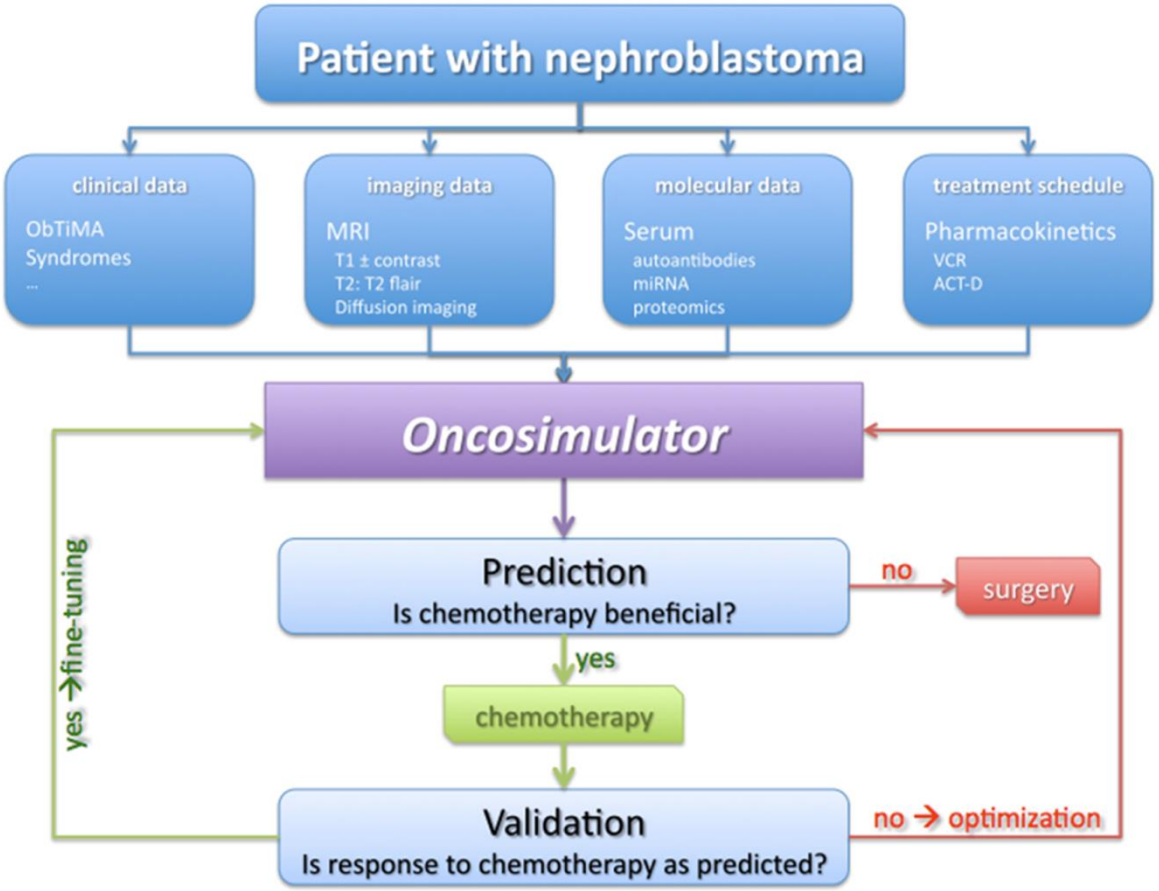

Fig. 8. Workflow of the Oncosimulator for nephroblastoma.

learning loop included in the biomedical usage workflow of the oncosimulator and shown in Fig. 8 for the special case of nephroblastoma is utilized to finely tune the models.

Up to now 16 cases of nephroblastoma and 20 cases of breast cancer have been collected and their multiscale data are under exploitation. Initial clinical adaptation results using this data have already been published [8], [10], whereas a number of new relevant articles are currently in the publication process. Additional results demonstrating aspects of the clinical adaptation and validation process are presented in Section IX (A and B.)

VIII. Coupling the Oncosimulator With Immunological Models in the Future: A Plausible Scenario

Tumor cells (TCs) are characterized by a vast number of genetic and epigenetic events leading to the appearance of specific antigens triggering reactions by the immune system (IS) [29]. Thus, the competition between TCs and the IS is complex and also involves many spatial phenomena [30]. Currently a number of immunotherapies are being developed, although the results of their clinical trials are often puzzling. Theoretical immunology [31] suggests that the latter mirror the dynamic complexity of this interplay. This demands an approach that is based on detailed multiscale models that are amenable to clinical validation.

Thus, the Oncosimulator might be an ideal frame for the patient-specific simulation of immunotherapies. Moreover, the integration of an "Immune System Module" (ISM) might also allow the oncosimulator to perform finer predictions of the postchemotherapeutic time course of immunogenic tumors. In such tumors, the role of the IS in the elimination of the residual disease could be highly important.

An ISM has been designed at the information flow level by adopting a hybrid, i.e., partly stochastic and partly deterministic modeling approaches. A stochastic detailed model (the Oncosimulator) describing the dynamics of tumor growth and treatment response is coupled to a stochastic mean-field model for the description of the IS effectors. In this case, this approach has some advantageous features. There is no need to modify the core component of the oncosimulator, whereas only simple

changes in accessory components accounting for the exchange of information between the main component and the ISM are required.

Due to the polymorphic interplay of TCs-IS, ISM does not implement a single specific model, but it is rather a tool for the definition and validation of models. Users may choose a specific model from a database of models, or they may choose from some more general families of models. Here, "parameters" are user-defined functions, whose "adherence" to the chosen family is checked by the system.

The implementation of ISM adopts the following design challenges: 1) the user is in charge: support of human guided exploration; 2) the "plug-and-play" principle: no essential changes in the Oncosimulator are required; 3) a large model space: ISM must support the implementation of large families of models; 4) model comparison is key: validation requires that the user is able to compare results between multiple possible models; 5) supporting "multi-mathematics": models of TCs-IS interplay are symbolically challenging and heterogeneous.

f
f

IX. Results

In the following two sections, we demonstrate how the oncosimulator can be adapted to various scenarios. This is achieved through the processing of multiscale data and the adjustment of simulation codes.

The paradigms of breast cancer treated with epirubicin and nephroblastoma (Wilms tumor) treated according to the SIOP 2001/GPOH clinical trial protocol are addressed. For both the clinical adaptation and the clinical validation of each one of the models the same kind of data—although not the same data itself—and the same simulation code are to be used. Therefore, the following examples also convey important aspects of the clinical validation process. The presented proof of concept adaptation studies focus on one breast cancer and two nephroblastoma clinical cases. Simulation results involving the full set of clinical cases provided within ACGT project and related clinical adaptation/validation methods will be the subject of dedicated journal papers under preparation.

A. *Breast Cancer*

In this section, a clinical adaptation paradigm of the breast cancer branch of the *oncosimulator* is provided. A plausible value range of the apparent *cell kill rate* (CKR) of epirubicin is suggested following the exploitation of the actual clinical data originating from one real clinical breast cancer case and the simulation itself. CKR can be thought of as summarizing important genetic determinants influencing the tumor response to epirubicin monotherapy.

The available patient specific data utilized by the model are the following (see Fig. 9): 1) the maximum dimension of the tumor before and after completion of treatment as measured by ultrasound; 2) the dates of the corresponding examinations; 3) the detailed chemotherapeutic scheme including the dates and the dose of each epirubicin administration session; 4) the histological grade of the tumor determining the degree of differentiation; and 5) the available proliferation markers and more

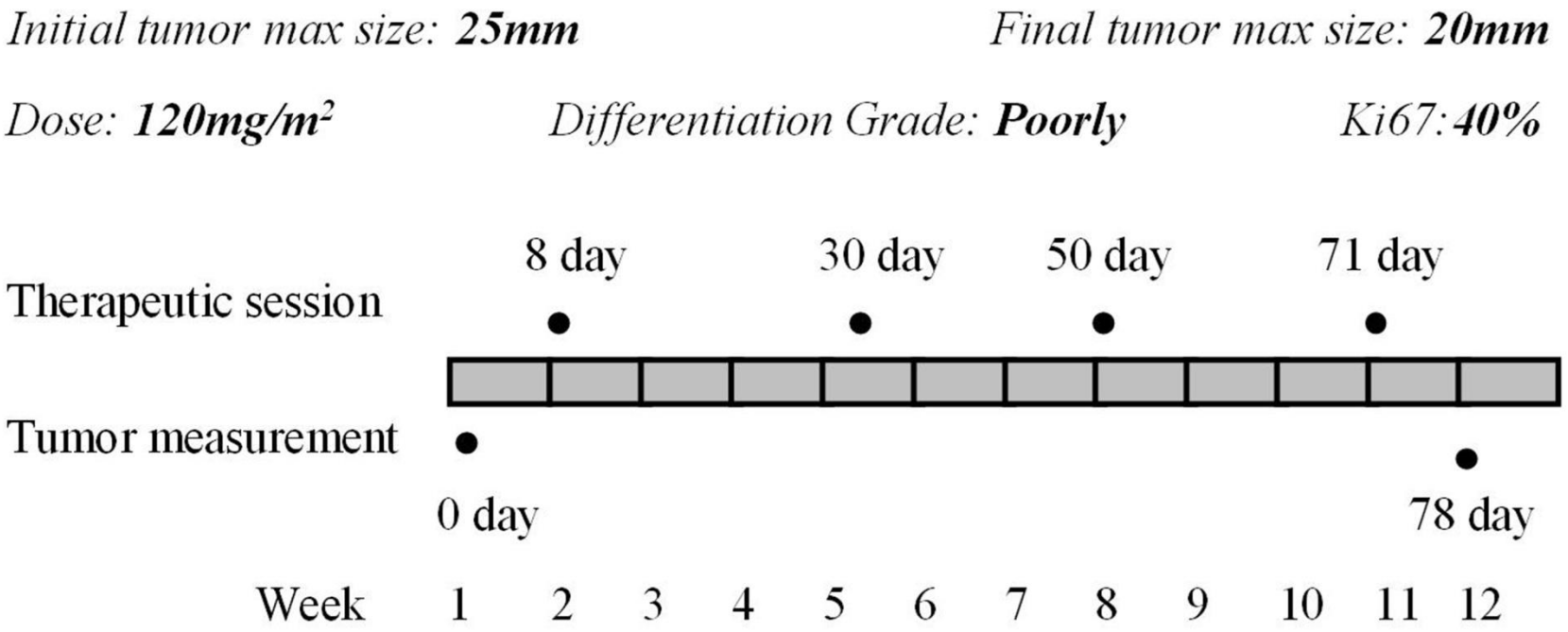

Fig. 9. Treatment schedule and tumor measurement time points for the set of multiscale data considered.

specifically the Ki67 index serving as a quantitative measure of the tumor growth fraction.

A macroscopically spatially homogeneous tumor of spherical shape has been assumed, with a diameter equal to the given maximum size. This approximation is dictated by 1) the provision of only a single tumor dimension at each measurement time point and 2) the nonavailability of MRI or CT data that could enable both the 3-D reconstruction of the tumor shape and the consideration of internal regions of variable metabolic activity (proliferating, quiescent, necrotic).

A two-step adaptation process is followed. The first step refers to the adaptation of the model parameters regulating tumor-free growth kinetics. In general a large number of virtual tumor implementations (virtual instances) corresponding to certain given or known parameter values exist. Narrowing this large window of possible solutions, ideally to one solution for a specific clinical case, is a critical first step in the adaptation procedure. In the present paradigm, the following assumptions/constrains were imposed, based on the literature and patient specific kinetics data.

1) *Cell cycle duration:* Breast cancer cell cycle duration estimated based on cell line studies or *in vivo* methods (such as percent labeled mitosis curves) may vary from approximately 20 to 96 h [32]–[34]. A mean value of 60 h is considered here [32]–[34].
2) *Growth fraction:* $\pm 10\%$ of patient Ki67 index (=40%).
3) *Volume doubling time (T_d):* Studies aiming at determining breast cancer growth rate based on volumetric methods have revealed a great interindividual variability with volume doubling times ranging from a few weeks to years [35], [36]. In the present analysis, we assume a lower limit of Td $>$ 30 days.
4) *Fraction of stem cells:* Based on [37], breast tumor stem cells are a minority population with a frequency of 5% at best. Here, we assume that the frequency of cancer stem cells among living tumor cell population does not exceed the above value ($< 5\%$).

The free growth adaptation outcome is presented in Table I

In the second step, CKR is adapted to the observed tumor size reduction yielding the apparent CKR of the specific virtual tumor implementation. Since no data on the tumor growth rate of the patient are available, the procedure is repeated for other virtual tumor implementations with growth rates that cover the value range reported in the literature. This is achieved by varying a model parameter that primarily influences growth rate

while ensuring consistency with the aforementioned imposed constraints. The chosen parameter is the fraction of stem cells that perform symmetric divisions (P_{sym}). According to Figs. 10 and 11 even though the variation of P_{sym} for the range of values considered has a negligible effect on the tumor cell composition, it does nevertheless induce a dramatic change in the volume

doubling time. In the present paradigm, T_d varies from 43 days up to 2562 days ($\sim$ 7 years). In Fig. 12, we observe that virtual tumor implementations with shorter T_d (higher P_{sym}) require a higher CKR in order to achieve the same tumor shrinkage. Based on those results, the apparent CKR for the clinical case considered lies approximately in the range 0.17–0.41.

TABLE I MODEL (CODE) INPUT PARAMETERS
RELATED TO BREST CANCER FREE TUMOR GROWTH
AND THEIR VALUES FOLLOWING CLINICAL ADAPTATION

Description	Value
Cell cycle duration	60 h
Duration of the dormant phase	170 h
Time interval needed for the necrosis products to disappear	120 h
Time interval needed for the apoptosis products to disappear	6 h
Number of mitoses performed by progenitor cells before they become differentiated	10
Apoptosis rate of stem and progenitor cells	0.001 h^{-1}
Apoptosis rate of differentiated cells	0.005 h^{-1}
Necrosis rate of differentiated cells	0.01 h^{-1}
Fraction of dormant cells that have just left the dormant compartment and re-enter the cell cycle	0.01
Fraction of cells that enter G0 phase following mitosis	0.27
Fraction of stem cells that perform symmetric division	0.451-0.51

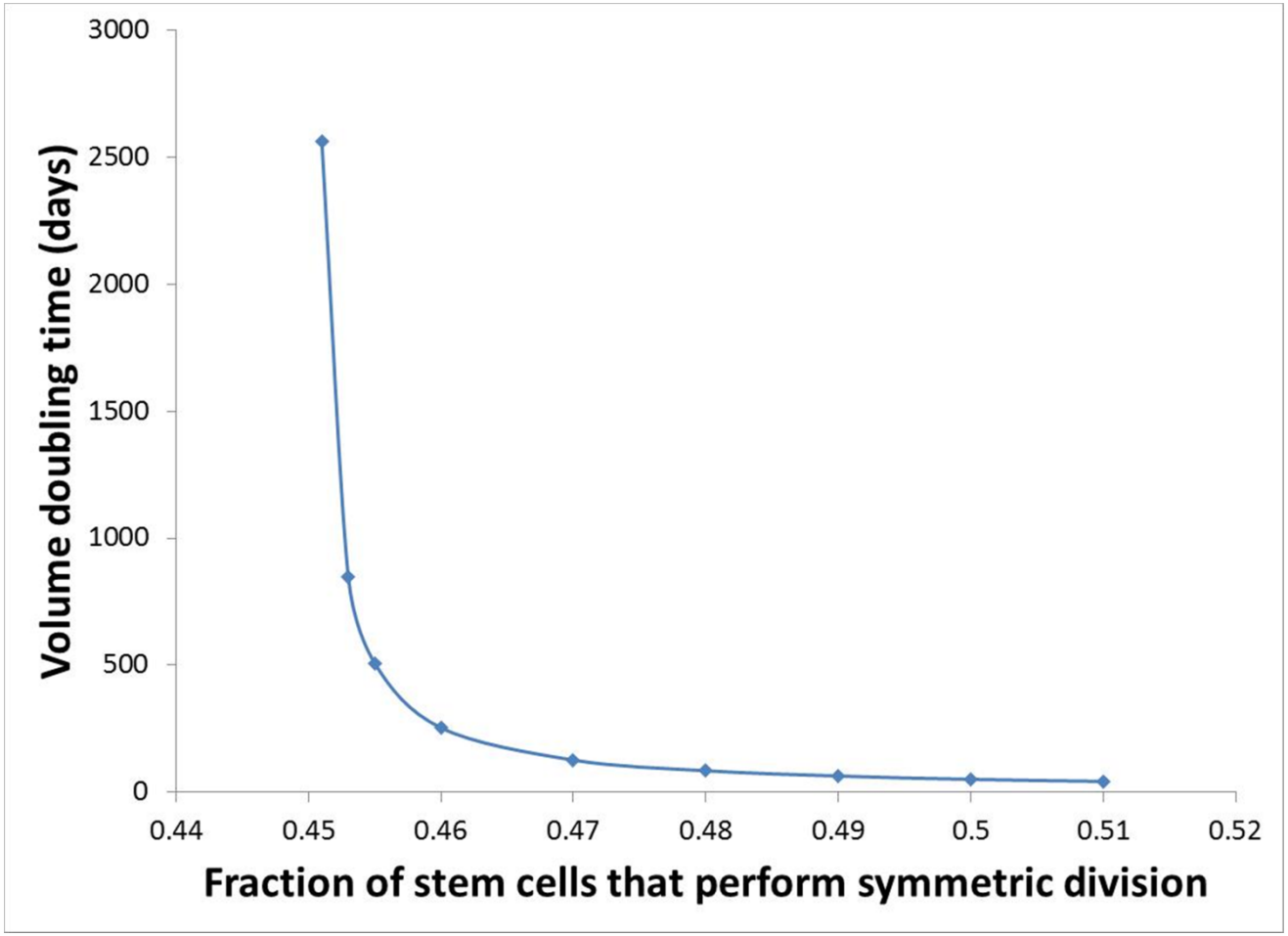

Fig. 10. Predicted volume doubling time as a function of the fraction of stem cells that perform symmetric division.

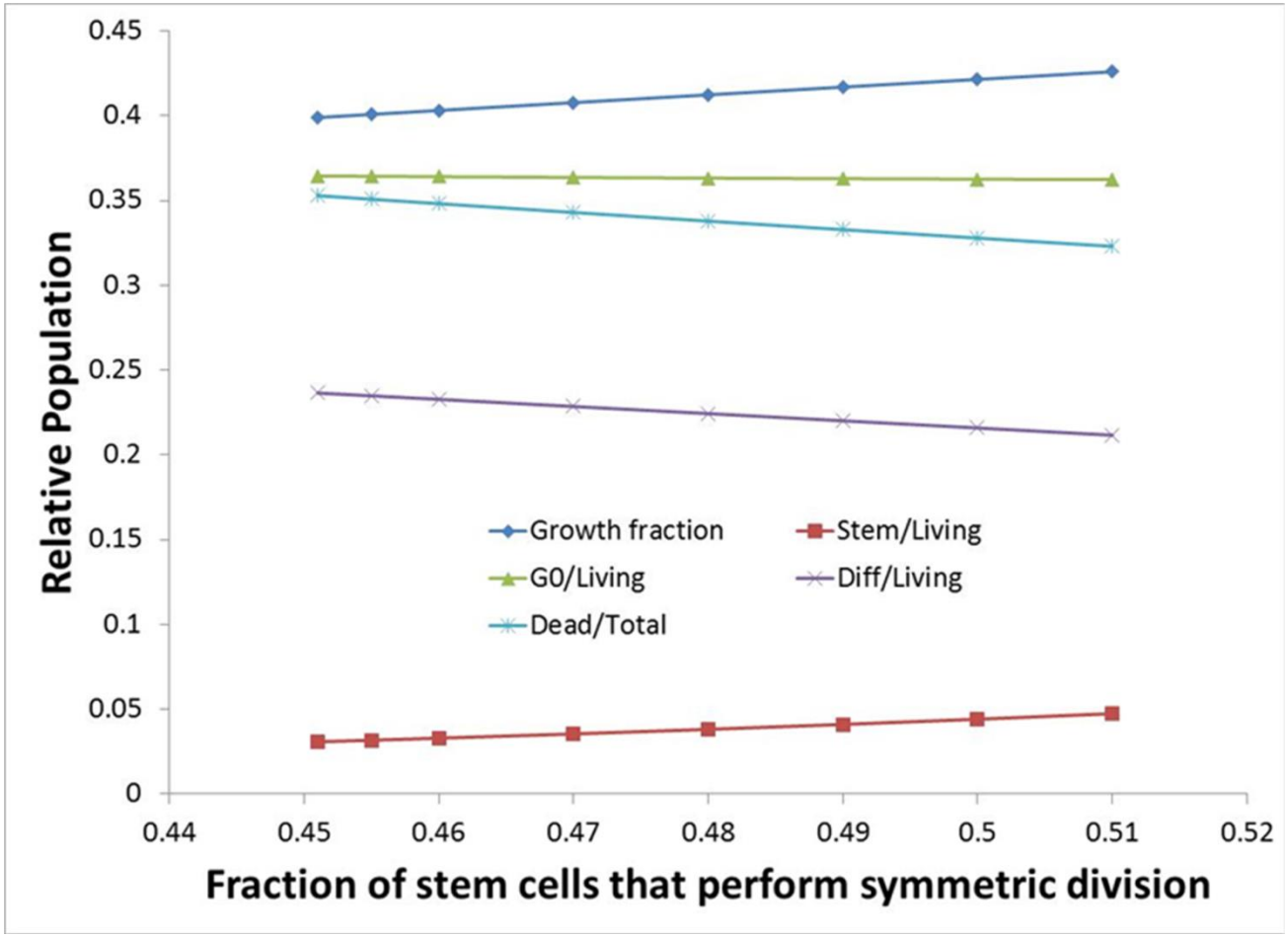

Fig. 11. Predicted relative population of various tumor cell categories as a function of the fraction of stem cells that perform symmetric division.

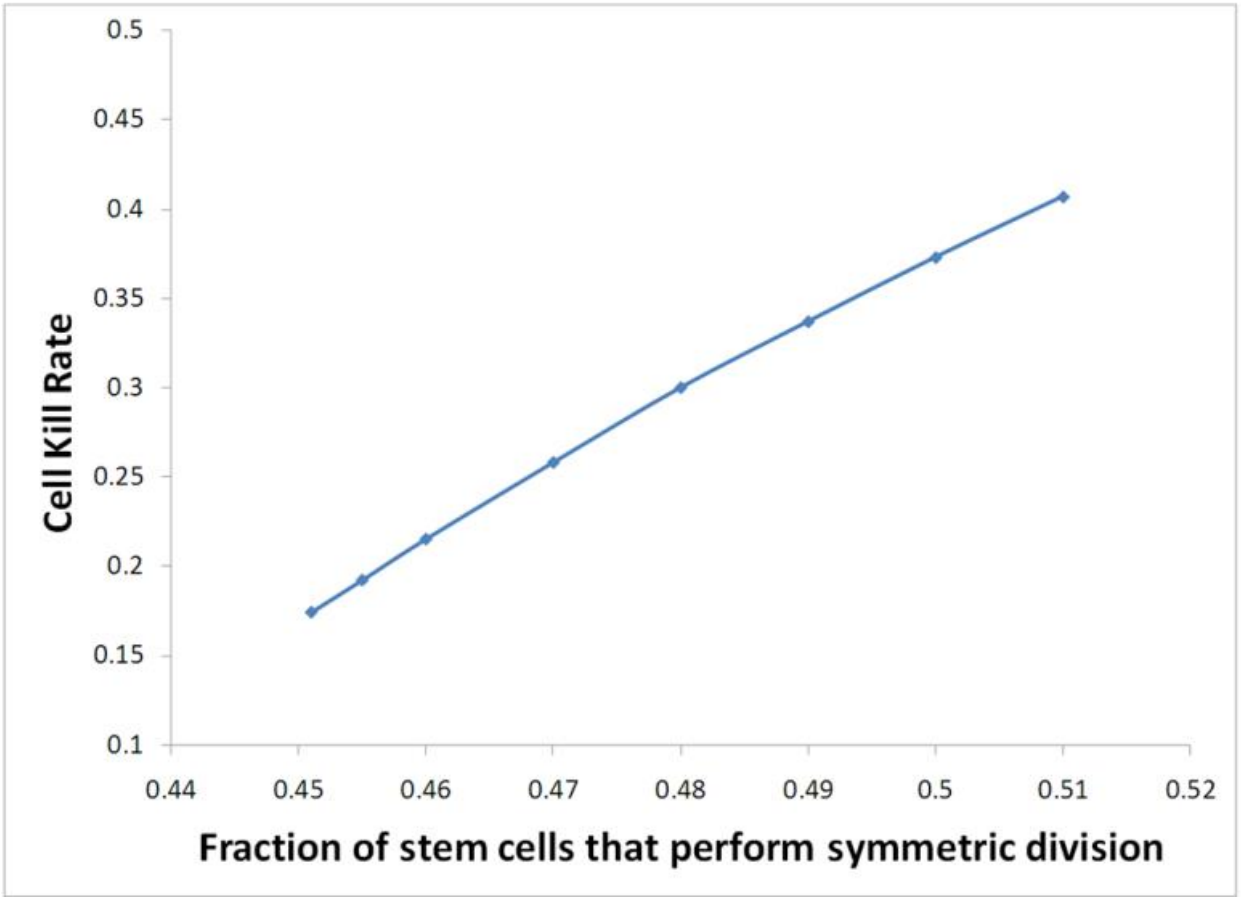

Fig. 12. Predicted cell kill rate as a function of the fraction of tumor stem cells that perform symmetric division.

Concluding, the realism of the model behavior has been demonstrated in previous publications [8]. More specifically tumor shrinkage after each chemotherapeutic session and the consequent tumor repopulation has been successfully demonstrated in accordance to clinical experience. In the present analysis, the model has been applied for the *in vivo* estimation of the apparent CKR, a measure of drug toxicity on tumor cells, taking into consideration the repopulation of tumor cells after each therapeutic session. The validity of our results is ensured by 1) the compliance of the virtual tumors kinetic characteristics with the ones reported in the literature and 2) the negligible deviation between the simulation results and the patient volumetric data (less than 0.2%) for all virtual tumor implementations with different P_{sym} (data not shown).

B. Nephroblastoma

Several nephroblastoma tumor cases of which sets of multi-scale data were collected in the context of SIOP 2001/GPOH trial have been modeled with IOS so far. As an indicative example, the *in silico* response of two nephroblastoma cases (cases I and II) of stromal type to preoperative combined chemotherapy with actinomycin-D and vincristine in the context of SIOP 2001/GPOH trial is presented in this section.

Anonymized imaging and clinical data have been provided. The initial and final virtual tumors have been spatiotemporally initialized based on the MRI tomograms of their real clinical counterparts collected at two time instants before the start of chemotherapy (2 days for case I and 6 days for case II) and after the completion (4 days for case I and 0 days for case II). The chemotherapeutic scheme administered is according to the SIOP 2001/GPOH clinical trial protocol for unilateral stages I–III nephroblastoma tumors (see Fig. 13). In [38]–[54] the authors provide pertinent literature that has been utilized throughout the following analysis.

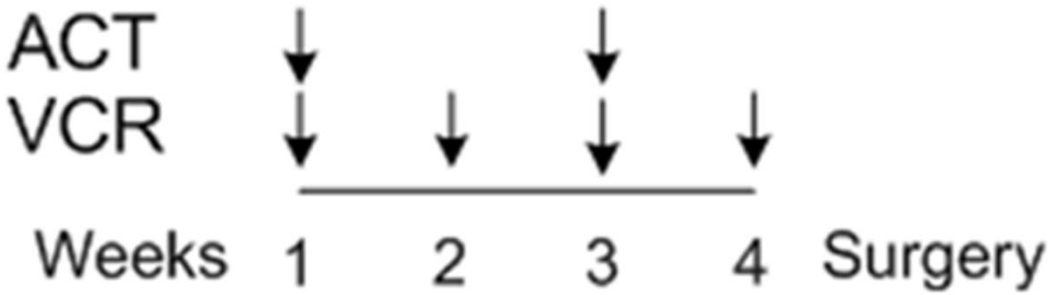

ACT: Actinomycin-D. 45μg/kg i.v. bolus injection (max 2000μg)
VCR: Vincristine. 1.5mg/m^2 i.v. bolus injection (max 2.0mg)

If body weight < 12kg: dose reduction to 2/3 for each drug
Major intolerance: doses on the next course should be reduced to 2/3

Fig. 13. Simulated Wilms tumor preoperative chemotherapy treatment protocol of the SIOP/GPOH clinical trial.

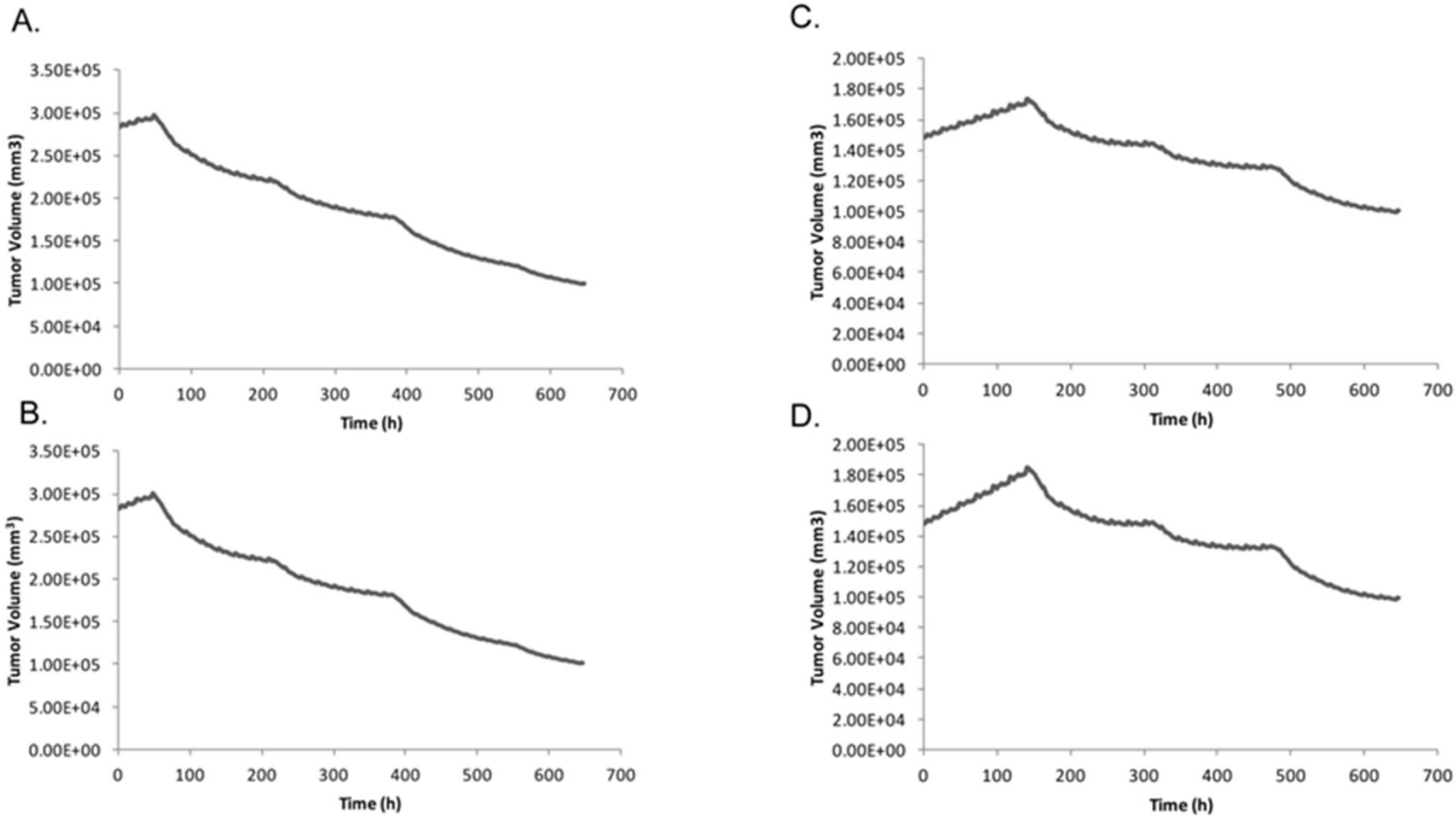

Fig. 14. Time evolution of tumor volume for the four virtual scenarios of Table II: (a). T1 (Case I-Scenario A), (b). T2 (Case I-Scenario B), (c). T3 (Case II-Scenario A), and (d). T4 (Case II-Scenario B).

following analysis.

Two adaptation scenarios are considered. The following assumptions have been made based on both literature and imaging clinical information.

1) Doubling time in the range of 11–40 days [49]–[53].
2) Growth fraction 1.5–20% for stromal type nephroblastomas [54].
3) The imaging data-specified volume reduction of case I is 65% and of case II is 32%.

According to the first adaptation scenario (A), both nephroblastoma tumors are considered to have common growth kinetics as they are of the same histological type (stromal). The CKR of the chemotherapeutic drugs is adapted in order to simulate the volume reduction induced by chemotherapy.

According to the second adaptation scenario (B), the effect of the chemotherapeutic drugs is considered common in both cases and the growth rate of the tumors is adapted within the range defined by the reported literature. This is achieved by perturbing the values of important growth kinetic parameters according to model sensitivity analyses [10].

The aforementioned assumptions, in conjunction with accumulated basic science and clinical experience based plausible values, lead to the selection of the entries for the run-time parameters of the tumor model (see Table II) for cases I, II, and under scenarios A and B. The time course of the four virtual tumors is presented in Fig. 14.The resultant virtual tumor characteristics and volume reduction are given in Table III. All four virtual scenarios are in good agreement with the clinical data in terms of volume reduction (see Table III). In addition, a good agreement is also accomplished in terms of the tumor growth characteristics presented in Table III when compared with values reported in the literature.

TABLE II: DEFINITION OF THE TUMOR MODEL PARAMETERS. REFERENCE VALUES AND CORRESPONDING LITERATURE REFERENCES. VALUES ASSIGNED TO THE MODEL PARAMETERS FOR THE IMPLEMENTATION OF FOUR VIRTUAL TUMORS. (CKR_{TOTAL} IS NOT AN INDEPENDENT PARAMETER OF THE MODEL)

Symbol (Unit)	Definition	Reference Value	References	T1 (Case A-Scenario A)	T2 (Case A-Scenario B)	T3 (Case B-Scenario A)	T4 (Case B-Scenario B)
Model Parameters Studied in the Sensitivity Analyses							
T_c (h)	Cell cycle duration	23.0	[44]	23.0	40	23.0	55
T_{G0} (h)	G0 (dormant phase) duration, i.e. time interval before a dormant cell dies through necrosis	96	[45]	96	96	96	40
T_N (h)	Time needed for necrosis to be completed and its lysis products to be eliminated from the tumor	20	[38,39, 46]	20	20	20	120
T_A (h)	Time needed for apoptosis to be completed and its products to be eliminated from the tumor	6	[47,48]	6	6	6	6
R_A (h^{-1})	Apoptosis rate of living stem and LIMP tumor cells (fraction of non-differentiated cells dying through apoptosis per hour)	0.001	Derived from T_A, based on [47,48]	0.001	0.0008	0.001	0.001
R_{ADiff} (h^{-1})	Apoptosis rate of differentiated tumor cells per hour	0.003		0.003	0.003	0.003	0.05
R_{NDiff} (h^{-1})	Necrosis rate of differentiated tumor cells per hour	0.001	Derived from T_N, based on [38,46]	0.001	0.001	0.001	0.05
P_{G0toG1}	The fraction of stem or LIMP cells having just left the G0 compartment that re-enter the cell cycle	0.01		0.01	0.01	0.01	0.01
N_{LIMP}	The maximum number of mitoses that a LIMP cell can perform before becoming terminally differentiated	3		3	3	3	3
P_{sym}	Fraction of stem cells that perform symmetric division.	0.45		0.71	**0.44**	0.45	**0.465**
P_{sleep}	Fraction of cells that enter G0 phase following mitosis	0.28		0.40	0.28	0.28	0.36
CKR_{VCR}	Cell kill rate for the specific vincristine dose	0.3	Derived based on [40,41]	**0.32**	0.3	**0.252**	0.33
CKR_{ACT}	Cell kill rate for the specific actinomycin-D dose	0.2	Derived based on [42,43]	**0.213**	0.2	**0.168**	0.22
CKR_{TOTAL}*	Combined cell kill rate of the two drugs (dependent parameter)	0.5	Additive drug effect considered	**0.533**	0.5	**0.42**	0.55

TABLE III: TUMOR CHARACTERISTICS AND VOLUME REDUCTION PERCENTAGES FOR THE FOUR VIRTUAL TUMOR SCENARIOS DEFINED BY THE PARAMETER VALUES GIVEN IN TABLE II.

RESULTANT INITIAL TUMOR CHARACTERISTICS	**T1 (Case A-Scenario A)**	**T2 (Case A-Scenario B)**	**T3 (Case B-Scenario A)**	**T4 (Case B-Scenario B)**
Volume Doubling Time, $T_d = \ln 2/k$ (days)	28.5	40.37	28.5	19.8
Initial percentage of proliferating cells (Growth Fraction) (%)	13.38	12.62	13.38	14.52
Tumor volume reduction percentage (%)	64.24	65.02	32.17	32.58

X. Discussion and Conclusion

A synoptic delineation of the IOS, primarily developed *within the framework* of the EC funded ACGT project but also extended within the framework of other EC funded projects, has been presented. Both the modeling principles and the technological components of the system have been briefly, yet comprehensively addressed. Successful demonstrations of the system during the implementation of the ACGT project have ensured its

technological reliability as well as its potential to be translated into the clinic following completion of the ongoing lengthy and demanding clinical validation process.

Clinical adaptation and validation of the multiscale modeling component of the system continues among other environments within the framework of the currently running EC funded projects p-medicine (FP7-ICT-2009–6–270089) and CHIC (FP7-ICT-2011–9–600841.) A number of clinical adaptation scenarios addressed in this paper have demonstrated the basics of several aspects of the clinical adaptation and validation process. Following the completion of the latter, the IOS is expected to be translated into clinical practice and serve as a platform for optimizing both patient individualized treatment and the design of new clinical trials.

ACKNOWLEDGMENT

The authors would like to thank the highly constructive feedback provided by the following ACGT external reviewers appointed by the European Commission (EC): Prof. D. Ingram, University College London, Prof. O. Björk, Karolinska University, Stockholm, Dr L.Toldo, and Dr E.Tsiporkova. They would also like to thank the EC appointed ACGT project officer Dr R. Bergström for strong encouragement and Prof. N. Uzunoglu from National Technical University of Athens for his support. Last but not least they acknowledge the valuable, detailed feedback provided by the anonymous reviewers of the manuscript.

REFERENCES

[1] *Multiscale Cancer Modeling*, T. S. Deisboeck and G. Stamatakos Eds., Boca Raton, FL, USA: CRC Press, 2011.

[2] G. S. Stamatakos, D. D. Dionysiou, E. I. Zacharaki, N. A. Mouravliansky, K. S. Nikita, and N. K. Uzunoglu, "*In silico* radiation oncology: Combining novel simulation algorithms with current visualization techniques," *Proc. IEEE*, vol. 90, no. 11, pp. 1764–1777, Nov. 2002.

[3] D. D. Dionysiou, G. S. Stamatakos, N. K. Uzunoglu, K. S. Nikita, and A. Marioli, "A four dimensional *in vivo* model of tumour response to radiotherapy: Parametric validation considering radiosensitivity, genetic profile and fractionation," *J. Theor. Biol.*, vol. 230, pp. 1–20, 2004.

[4] G. S. Stamatakos, V. P. Antipas, and N. K. Uzunoglu, "A spatiotemporal, patient individualized simulation model of solid tumor response to chemotherapy in vivo: The paradigm of glioblastoma multiforme treated by temozolomide," *IEEE Trans. Biomed. Eng.*, vol. 53, no. 8, pp. 1467–1477, Aug. 2006.

[5] G. S. Stamatakos, D. D. Dionysiou, N. M. Graf, N. A. Sofra, C. Desmedt, A. Hoppe, N. Uzunoglu, and M. Tsiknakis, "The oncosimulator: A multilevel, clinically oriented simulation system of tumor growth and organism response to therapeutic schemes. Towards the clinical evaluation of *in silico* oncology," in *Proc. 29th Annu. Int. Conf. IEEE Eng. Med. Biol. Society*, Lyon, France, 2007, pp. 6628–6631.

[6] D. D. Dionysiou, G. S. Stamatakos, D. Gintides, N. Uzunoglu, and K. Kyriaki, "Critical parameters determining standard radiotherapy treatment outcome for glioblastoma multiforme: A computer simulation," *The Open Biomed. Eng. J.*, vol. 2, pp. 43–51, 2008.

[7] E. A. Kolokotroni, D. D. Dionysiou, N. K. Uzunoglu, and G. S. Stamatakos, "Studying the growth kinetics of untreated clinical tumors by using an advanced discrete simulation model," *Math. Comput. Modelling*, vol. 54, pp. 1989–2006, 2011.

[8] G. S. Stamatakos, E. A. Kolokotroni, D. D. Dionysiou, E. C. Georgiadi, and C. Desmedt, "An advanced discrete state – discrete event multiscale simulation model of the response of a solid tumor to chemotherapy: Mimicking a clinical study," *J. Theor. Biol.*, vol. 266, pp. 124–139, 2010.

[9] G. Stamatakos, "Cancer Multiscale Modeling," in *In Silico Oncology Part I: Clinically Oriented Cancer Multilevel Modeling Based on Discrete Event Simulation*, T. Deisboeck and G. Stamatakos, Eds. Boca Raton, Florida, USA: CRC Press, 2010, pp. 407–436.

[10] G. S. Stamatakos, E. C. Georgiadi, N. Graf, E. A. Kolokotroni, and D. D. Dionysiou, "Exploiting clinical trial data drastically narrows the window of possible solutions to the problem of clinical adaptation of a multiscale cancer model," *PLoS ONE*, vol. 6, no. 3, p. e17594, 2011.
[11] (2013, 30 Jan.). [Online]. Available: http://cordis.europa.eu/result/brief/rcn/6061_en.html
[12] J. De Kraker, N. Graf, H. van Tinteren, F. Pein, B. Sandstedt, J. Godzinski, and M. F. Tournade, *SIOP*, "Reduction of postoperative chemotherapy in children with stage I intermediate-risk and anaplastic Wilms' tumour (SIOP 93–01 trial): A randomised controlled trial," *Lancet*, vol. 364, pp. 1229–1235, 2004.
[13] N. Graf, M. F. Tournade, and J. de Kraker, "The role of preoperative chemotherapy in the management of Wilms' Tumor — The siop studies," *Urol. Clin. North Amer.*, vol. 27, pp. 443–454, 2000.
[14] M. F. Tournade, C. Com-Nougué, P. A. Voûte, J. Lemerle, J. de Kraker, J. F. Delemarre, M. Burgers, J. L Habrand, C. G. Moorman, and D. Bürger, "Results of the sixth international society of pediatric oncology wilms' tumor trial and study: A risk-adapted therapeutic approach in wilms' tumor," *J. Clin. Oncol.*, vol. 11, pp. 1014–1023, 1993.
[15] Ch. Desmedt, A. Di Leo, E. de Azambuja, D. Larsimont, B. Haibe-Kains, J. Selleslags, S. Delaloge, C. Duhem, J.-P. Kains, B. Carly, M. Maerevoet, A. Vindevoghel, G. Rouas, F. Lallemand, V. Durbecq, F. Cardoso, R. Salgado, R. Rovere, G. Bontempi, S. Michiels, M. Buyse, J.-M. Nogaret, Y. Qi, F. Symmans, L. Pusztai, V. D'Hondt, M. Piccart-Gebhart, and C. Sotiriou, "Multifactorial approach to predicting resistance to anthracyclines," *J. Clin. Oncol.*, vol. 29, no. 12, pp. 1578–1586, 2011.
[16] R. Whitaker, "Reducing aliasing artifacts in iso-surfaces of binary volumes," in *Proc. IEEE Volume Vis. Graphics Symp.*, Oct. 2000, pp. 23–32.
[17] C. Farmaki, K. Marias, V. Sakkalis, and N. Graf, "Spatially adaptive active contours: A semi-automatic tumor segmentation technique," *Inter. J Comput.-Assisted Radiol. Surg.*, vol. 5, no. 4, pp. 369–84, 2010.
[18] A. Lunzer and K. Hornbæk, "RecipeSheet: Creating, combining and controlling information processors," in *Proc. 19th Annu. ACM Symp. User Interface Softw. Technol.*, Montreux, Switzerland, Oct. 2006, pp. 145–153.
[19] A. Lunzer, "Choice and comparison where the user wants them: Subjunctive interfaces for computer-supported exploration," in *Proc. IFIP TC 13 Int. Conf. Human–Comput. Interaction*, 1999, pp. 474–482.
[20] A. Lunzer and K. Hornbæk, "Subjunctive interfaces: Extending applications to support parallel setup, viewing and control of alternative scenarios," *ACM Trans. Comput.–Human Interaction*, vol. 14, no. 4, Jan. 2008.
[21] N. Graf, A. Hoppe, E. Georgiadi, R. Belleman, C. Desmedt, D. Dionysiou, M. Erdt, J. Jacques, E. Kolokotroni, A. Lunzer, M. Tsiknakis, and G. Stamatakos, "*In silico* oncology for clinical decision making in the context of nephroblastoma," *Klinische Pädiatrie*, vol. 221, pp. 141–149, 2009.

[22] A. Lunzer, R. Belleman, P. Melis, J. Pukacki, P. Spychała, and G. Stamatakos, "Validating the ACGT Oncosimulator with a grid-supported visualisation environment," in *Proc. 4th Int. Adv. Res. Workshop on In Silico Oncology Cancer Investigation*, Athens, Greece, 2010, pp. 93–96, [Online]. Available: http://www.4th-iarwisoci.iccs.ntua.gr/

[23] A. Lunzer, R. Belleman, P. Melis, and G. Stamatakos, "Preparing, exploring and comparing cancer simulation results within a large parameter space," in *Proc. 3rd Int. Symp. Inf. Vis. in Biomed. Inf.*, London, U.K., 2010, pp. 258–264.

[24] M. Tsiknakis, M. Brochhausen, J. Nabrzyski, J. Pucacki, S. Sfakianakis, G. Potamias, C. Desmedt, and D. Kafetzopoulos, "A semantic grid infrastructure enabling integrated access and analysis of multilevel biomedical data in support of postgenomic clinical trials on cancer," *IEEE Trans. Inf. Technol. Biomed*, vol. 12, no. 2, pp. 205–217, Mar. 2008.

[25] I. Foster, "The grid: Computing without bounds," *Sci. Amer.*, vol. 288, no. 4, pp. 60–67, 2003.

[26] R. G. Belleman, M. Scarpa, and B. Stolk, "Interactive simulation and visualization for cancer treatment planning with grid-based technology," *ERCIM News*, vol. 69, pp. 22–23, 2007.

[27] S. Ruping, S. Sfakianakis, and M. Tsiknakis, "Extending work flow management for knowledge discovery in clinico-genomic data," in *Proc. Healthgrid 2007: From Genes to Personalized Health Care: Grid Solutions Life Sci.*, 2007, pp. 183–193.

[28] D. Wegener, T. Sengstag, S. Sfakianakis, S. Ruping, and A. Assi, "GridR: An r-based grid-enabled tool for data analysis in acgt clinico-genomics trials," in *Proc. 3rd IEEE Int. Conf. e-Sci. Grid Comput.*, 2007, pp. 228–235.

[29] T. J. Kindt, B. A. Osborne, and R. A. Goldsby, Kuby Immunology. San Francisco, CA: Freeman, 2006.

[30] A. Matzavinos, M. Chaplain, and V. A. Kuznetsov, "Mathematical modelling of the spatio-temporal response of cytotoxic T-lymphocytes to a solid tumour," *Math. Med.Biol.*, vol. 21, pp. 1–34, 2004.
[31] A. d'Onofrio, "A general framework for modeling tumor-immune system competition and immunotherapy: Analysis and medical inferences," *Phys. D*, vol. 208, pp. 220–235, 2005.
[32] S. Cos, J. Recio, and E. J. Sanchez-Barcelo, "Modulation of the lenght of cell cycle time of MCF-7 human breast cancer cells by melatonin," *Life Sci.*, vol. 58, pp. 811–816, 1996.
[33] S. Descamps, X. Lebourhis, M. Delehedde, B. Boilly, and H. Hondermarck, "Nerve growth factor is mitogenic for cancerous but not normal human breast epithelial cells," *J. Biol. Chem.*, vol. 273, no. 27, pp. 16659–16662, 1998.
[34] J. S. Meyer, R. McDivitt, K. Stone, M. Prey, and W. Bauer, "Practical breast carcinoma cell kinetics: Review and update," *Breast Cancer Res. Treat.*, vol. 4, pp. 79–88, 1984.
[35] D. Von Fournier, E. Weber, W. Hoeffken, M. Bauer, F. Kubli, and V. Barth, "Growth rate of 147 mammary carcinomas," *Cancer*, vol. 45, no. 8, pp. 2198–2207, Apr. 15, 1980.
[36] P. Peer, J. van Dijck, J. Hendriks, R. Holland, and A. Verbeek, "Age-dependent growth rate of primary breast cancer," *Cancer*, vol. 71, no. 11, pp. 3547–51, Jun. 1, 1993.
[37] J. Stingl and C. Caldas, "Molecular heterogeneity of breast carcinomas and the cancer stem cell hypothesis," *Nat. Rev. Cancer*, vol. 7, no. 10, pp. 791–9, Oct. 2007.
[38] W. Duechting, W. Ulmer, R. Lehrig, T. Ginsberg, and E. Dedeleit, "Computer simulation and modeling of tumor spheroids growth and their relevance to optimization of fractionated radiotherapy," *Strahlenther Onkol*, vol. 168, no. 6, pp. 354–360, 1992.
[39] B. Titz and R. Jeraj, "An imaging-based tumour growth and treatment response model: investigating the effect of tumour oxygenation on radiation therapy response," *Phys. Med. Biol.*, vol. 53, pp. 4471–4488, 2008.
[40] E. Groninger, T. Meeuwsen-de Boer, P. Koopmans, D. Uges, W. Sluiter, A. Veerman, W. Kamps, and S. de Graaf, "Pharmacokinetics of vincristine monotherapy in childhood acute lymphoblastic leukemia," *Pediatric Res.*, vol. 52, pp. 113–118, 2002.
[41] W. Dahl, R. Oftebro, E. Pettersen, and T. Brustad, "Inhibitory and cytotoxic effects of Oncovin (Vincristine Sulfate) on cells of human line NHIK 3025," *Cancer Res*, vol. 36, pp. 3101–3105, 1976.
[42] K. Sawada, K. Noda, H. Nakajima, N. Shimbara, Y. Furuichi, and M. Sugimoto, "Differential cytotoxicity of anticancer agents in pre- and post-immortal lymphoblastoid cell lines," *Biol. Pharm. Bull.*, vol. 28, pp. 1202–1207, 2005.

[43] G. Veal, M. Cole, J. Errington, A. Parry, J. Hale, A. D. Pearson, K. Howe, J. C. Chisholm, C. Beane, B. Brennan, F. Waters, A. Glaser, S. Hemsworth, H. Mc Dowell, Y. Wright, K. Pritchard-Jones, R. Pinkerton, G. Jenner, J. Nicholson, A. M. Elsworth, A. V. Boddy; Kingdom Children's Cancer Study Group Pharmacology Working Group, "Pharmacokinetics of Dactinomycin in a pediatric patient population: a United Kingdom Children's Cancer Study group study," *Clin. Cancer Res.*, vol. 11, no. 16, pp. 5893–5899, 2005.

[44] E. Revazova and A. Petrova, "Cell cycle and proliferative pool of human tumor strains transplanted into athymic mice," *Biull Eksp Biol Med*, vol. 92, pp. 335–337, 1981. (in Russian).

[45] K. Maseide and E. Rofstad, "Mathematical modeling of chronical hypoxia in tumors considering potential doubling time and hypoxic cell lifetime," *Radiother. Oncol.*, vol. 54, pp. 171–177, 2000.

[46] L. Wein, J. Cohen, and J. Wu, "Dynamic optimization of a linear-quadratic model with incomplete repair and volume-dependent sensitivity and repopulation," *Int. J. Radiat. Oncol. Biol. Phys.*, vol. 47, no. 4, pp. 1073–1083, 2000.

[47] B. Ribba, T. Colin, and S. Schnell, "A multiscale mathematical model of cancer, and its use in analyzing irradiation therapies," *Theor. Biol. Med. Model*, vol. 3, p. 7 (Feb. 10, 2006). [Online].

[48] W. Dewey, C. Ling, and R. Meyn, "Radiation-induced apoptosis: Relevance to radiotherapy," *Int. J. Radiat. Oncol. Biol. Phys.*, vol. 33, no. 4, pp. 781–796, 1995.

[49] T. Tan and D. Amor, "Tumour surveillance in Beckwith–Wiedermann syndrome and hemihyperplasia: A critical review of the evidence and suggested guidelines for local practice," *J. Paedeatrics Child Health*, vol. 42, pp. 486–490, 2006.

[50] S. Shackney, G. McCormack, and G. Cuchural, "Growth rate patterns of solid tumours and their relation to responsiveness to therapy," *Ann. Intern. Med.*, vol. 89, pp. 107–121, 1978.

[51] A. Craft, "Growth rate of Wilms' tumour," *Lancet*, vol. 354, no. 9184, p. 1127, 1999.
[52] A. Zoubek, I. Slavc, G. Mann, G. Trittenwein, and H. Gadner, "Natural course of a Wilms' tumour," *Lancet*, vol. 354, p. 344, 1999.
[53] A. Carré, C. Frantz, R. Weksberg, L. Nicholson, L. Ciarlo *et al.*, "Wilms tumor in an 11-year old with hemihyperplasia," *Amer. J. Med. Genetics*, vol. 139 A, pp. 165–166, 2005.
[54] D. Berrebi, J. Leclerc, G. Schleiermacher, I. Zaccaria, L. Boccon-Gibod, M. Fabre, F. Jaubert, A. El Ghoneimi, C. Jeanpierre, and M. Peuchmaur, "High cyclin-E staining index in blastemal, stromal or epithelial cells is correlated with tumor aggressiveness in patients with nephroblastoma," *PLoS ONE*, vol. 3, no. 5, e2216, 2008.

Παραδείγματα Τεχνολογικών Θεμάτων Γενικής *In Silico* Ιατρικής

PROCEEDINGS-VPH2012_INTEGRATIVE_APPROACHES_TO_COMPUTATIONAL_BIOMEDICINE-LONDON_CONF_2012.pdf PAGES **266-268** (PLEASE USE THE PDF PAGE COUNTER)

A Virtual Imaging Platform for the Virtual Physiological Human

Tristan Glatard[1], William A. Romero R.[1], Stefan J. Zasada[2], Peter V. Coveney[2], and Denis Friboulet[1]

[1] Université de Lyon, CREATIS; CNRS UMR5220; Inserm U1044; INSA-Lyon; UCBL, France
[2]Centre for Computational Science, University College London, UK

Correspondence: Tristan.Glatard@creatis.insa-lyon.fr

1 Introduction

Healthcare is being metamorphosed by pervasive digital worlds exploiting human models and medical simulations enabled by large computing infrastructures. Medical images, in particular, can be simulated from numerical models of the human body for a variety of applications including fast prototyping of new imaging devices and the evaluation of image analysis algorithms such as computer-aided detection, or segmentation. Image simulation is also used in the modeling of virtual humans by identifying model parameters leading to the most realistic images. Several image modalities, among which Magnetic Resonance Imaging (MRI), ultrasound imaging (US), Positron Emission Tomography (PET), and Computed Tomography (CT) are complementary to simulate and study the various aspects of biology, i.e., anatomy, physiology, metabolism, and function.

Currently, image simulation remains mastered only by a few due to the complexity and heaviness of most pipelines. Both the simulation code and the physical model of the imaged object can be very elaborated, and they are usually not designed by the same person or group: sharing them is thus required. In addition, computing times and the volume of produced data are potential showstoppers if no appropriate infrastructure is available. This abstract describes the Virtual Imaging Platform (VIP), an openly-accessible online platform used to share models and simulators, and to support the execution of heavy simulations. Its integration with the VPH ToolKit is also described.

2 The Virtual Imaging Platform

2.1 Support for heavy simulations

Simulators are integrated in VIP based on their workflow description. Marion et al[2] proposed a workflow template to facilitate integration. Simulation parallelization relies on data parallelism to avoid refactoring simulator codes. Simulators are iterated on subsets of the simulation scene or of input parameter sets, and the resulting partial results are eventually merged by another process. Simulations are launched on the *biomed* virtual organization (VO) of the European Grid Infrastructure (EGI).[3] This VO has access to 100+ computing clusters world-wide. The MOTEUR engine is used to enact the workflows.

VIP uses the EGI data management system to store files. Files are distributed on different storage sites supporting the *biomed* virtual organization. Resources expose a homogeneous interface to access files. A central logical file catalog provides a common indexing space for these files. 3.5 PB are available for storage, among which 2 PB are currently used.

2.2 Interface with the VPH ToolKit

Grid computing resources on EGI are abundant and easily accessed. However, they are shared among different user groups, which hampers efficiency and reliability. In particular, parallel jobs executed with the message-passing interface (MPI) are notably not well supported. Conversely, supercomputing resources available on PRACE[4] can only be accessed by a few (as a result of a specific application procedure), but resource efficiency is then guaranteed and reliability is high.

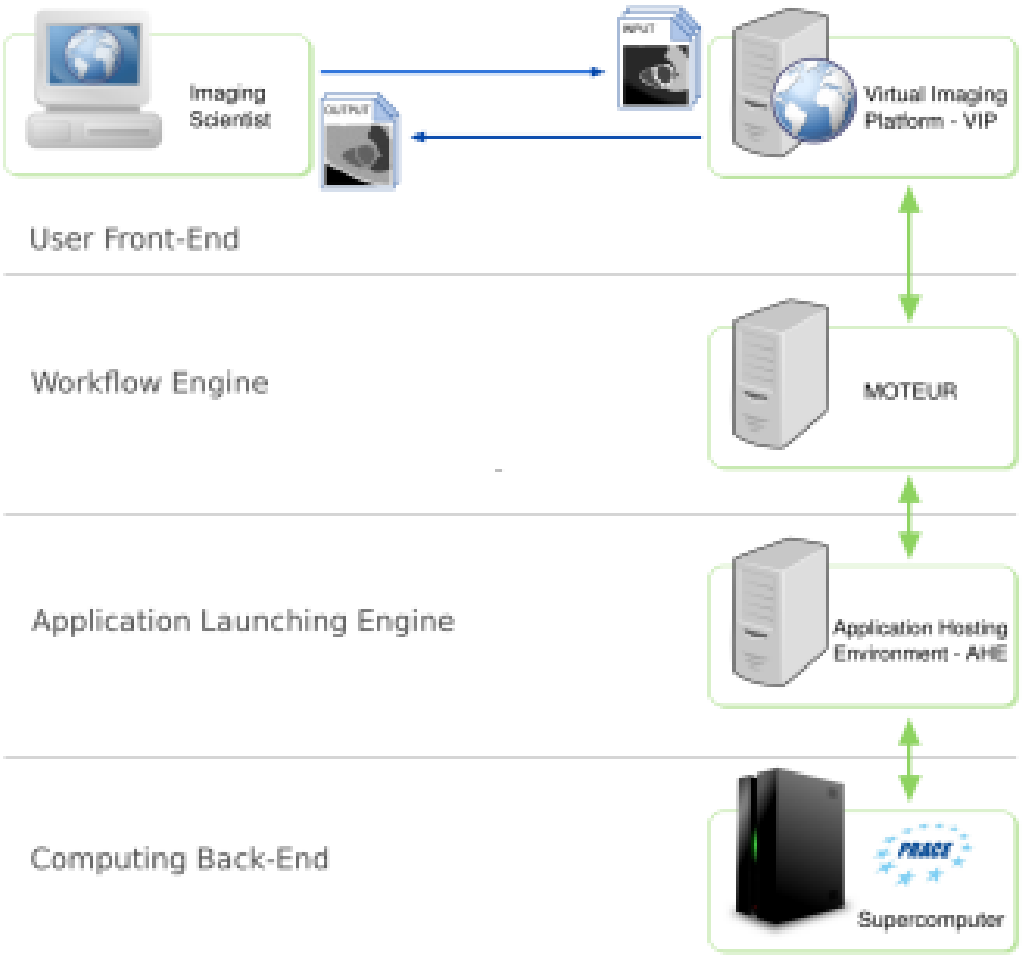

Figure 1: System architecture

We are in the process of interfacing the VIP portal with PRACE. Combining both infrastructures will provide high reliability and efficiency to support simulation challenges while keeping grid resources accessible for daily simulation activity. These developments consist of an interface between the MOTEUR workflow engine and the Application Hosting Environment.[5] AHE is an application launching engine that interfaces to a number of back end middlewares, including Globus 2/4 and Unicore 6. It manages the submission and monitoring of jobs, as well as data transfer, on behalf of a user. Here, AHE will be used as an interface between MOTEUR and the Unicore middleware running on PRACE systems. In the past, AHE has been successfully employed within DEISA DECI and Virtual Community projects to submit and manage jobs on the PRACE Tier 1 re-

sources at SARA and EPCC.

The required steps are (i) porting of simulation codes to PRACE architectures, (ii) enabling data transfers between EGI and PRACE, and (iii) enabling AHE job submission and monitoring in MOTEUR. The figure 1 outlines the system architecture. More details are available online.[6]

2.3 Results

VIP is publicly available as a web portal[7] where users can access the model repository (browsing and importing), define a simulation scene through the 3D interface, launch new simulations, monitor performance, and transfer input/output files. Example of images simulated with VIP for various imaging modalities are shown on Figure 2.

3 Conclusion

VIP is an online platform for image simulation. It currently relies on the European Grid Infrastructure to support the computation and storage. Four medical image modalities are supported. The VPH ToolKit is being used to interface it to PRACE computing resources. VIP also offers functionality for the sharing of digital object models as presented by Forestier *et al.*[11]

References

1. G. Forestier, A. Marion, H. Benoit-Cattin, P. Clarysse, D. Friboulet, w T. Glatard, P. Hugonnard, C. Lartizien, H. Liebgott, J. Tabary, and B. Gibaud, "Sharing object models for multi-modality medical image simulation: a semantic approach," in *IEEE CBMS*, Bristol, UK, 2011, pp. 1–6.

2. Marion A., Forestier G., Benoit-Cattin H., Camarasu-Pop S., Clarysse P., Ferreira da Silva R., Gibaud B., Glatard T., Hugonnard P., Lartizien C., Liebgott H., Tabary J. Valette S., and Friboulet D.. Multi-modality medical image simulation of biological models with the Virtual Imaging Platform (VIP). In: Proceedings of the 24th International Symposium on Computer-Based Medical Systems; 2011 June 27-30; Bristol, UK. Bristol: IEEE 2011.

3. European Grid Infrastructure - EGI [Internet]. 2012 [cited 2012 June 18]. Available from: http://www.egi.eu.

4. Partnership for Advanced Computing in Europo - PRACE [Internet] 2012 [cited 2012 June 18]. Available from: http://www.prace-ri.eu.

5. Zasada S.J. and Coveney P.V.. Virtualizing access to scientific applications with the application hosting environment. Computer Physics Communications, 2009, December; Volume 180, Issue 12: Pages 2513-2525.

6. VPH NoE Exemplar Projects and the VPH ToolKit - 9. VIP for VPH : Execution of medical image simulation workflows on DEISA through workflow interoperability between the Virtual Imaging Platform and the VPH toolkit [Internet] 2012 [cited 2012 June 18]. Available from: http://www.vph-noe.eu/exemplarprojects?start=9

7. Virtual Imaging Platform - VIP [Internet] 2012 [cited 2012 June 18]. Available from: htpp://vip.creatis.insa-lyon.fr

Figure 2: Simulation examples computed on VIP.

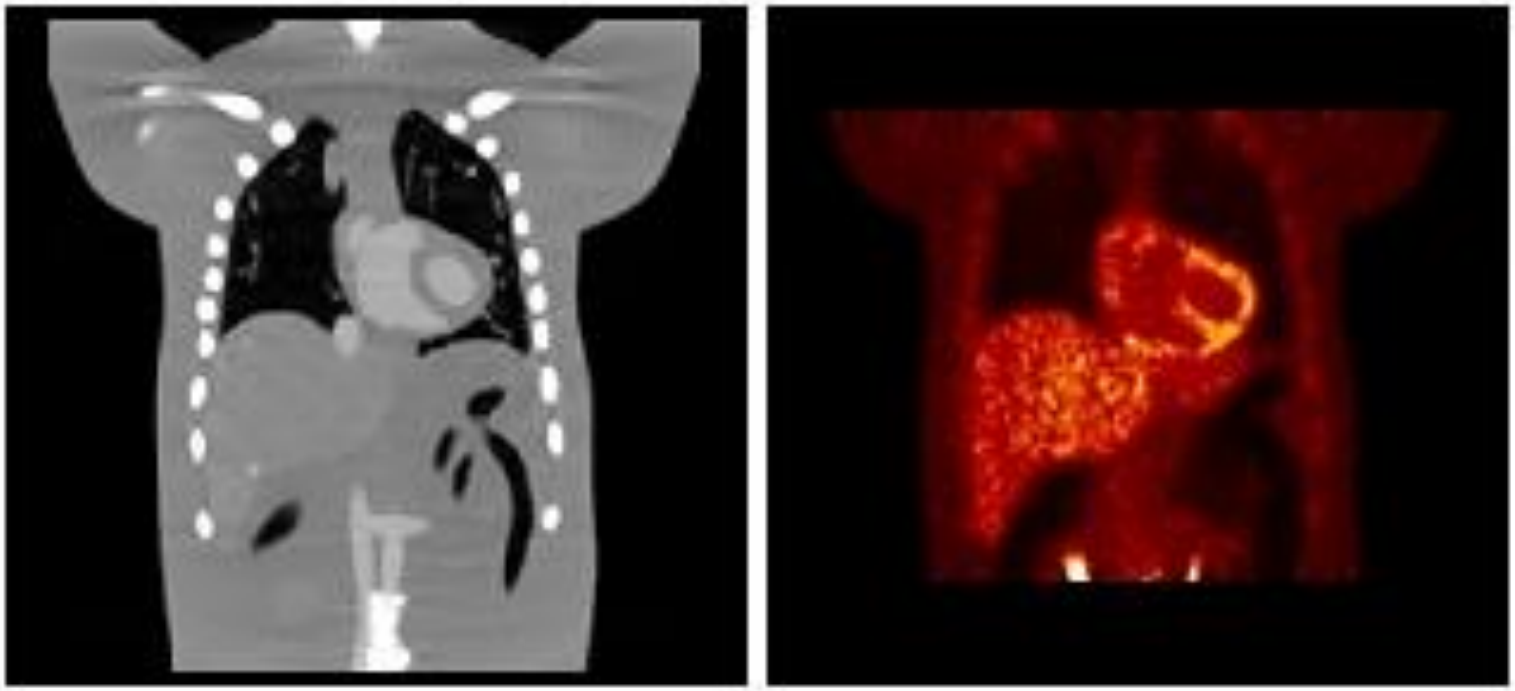

(a) Left: simulated whole-body 0.5s CT acquisition. Simulation courtesy of Carole Lartizien, and Joachim Tabary. Right: simulated whole-body static 224s FDG-PET acquisition. Simulation courtesy of Carole Lartizien and Simon Marache.

Figure 2: Simulation examples computed on VIP.

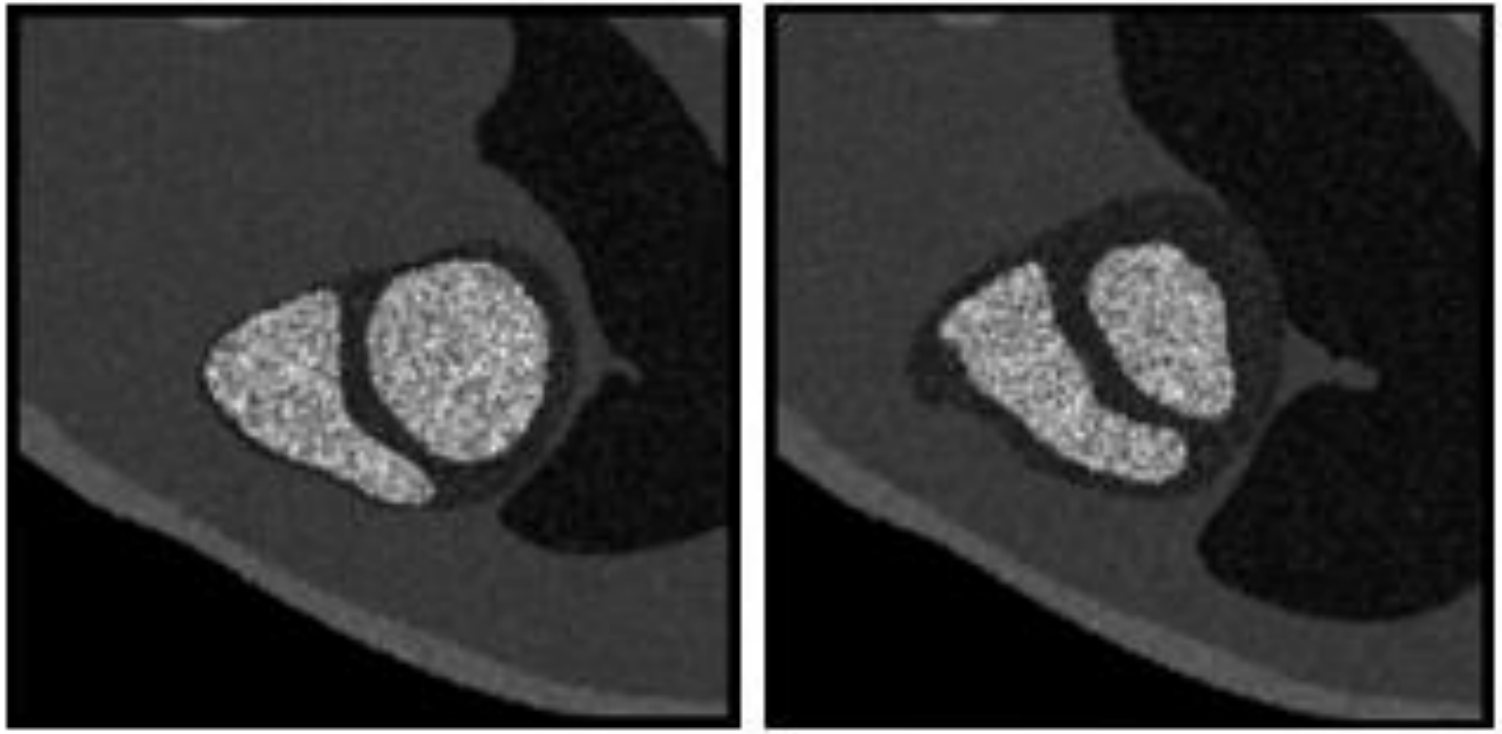

(b) Simulated cardiac short-axis MRI. Left: end diastole; right: end systole. Simulations courtesy of Patrick Clarysse, Sorina Camarasu-Pop, and Hugues Benoit-Cattin.

Figure 2: Simulation examples computed on VIP.

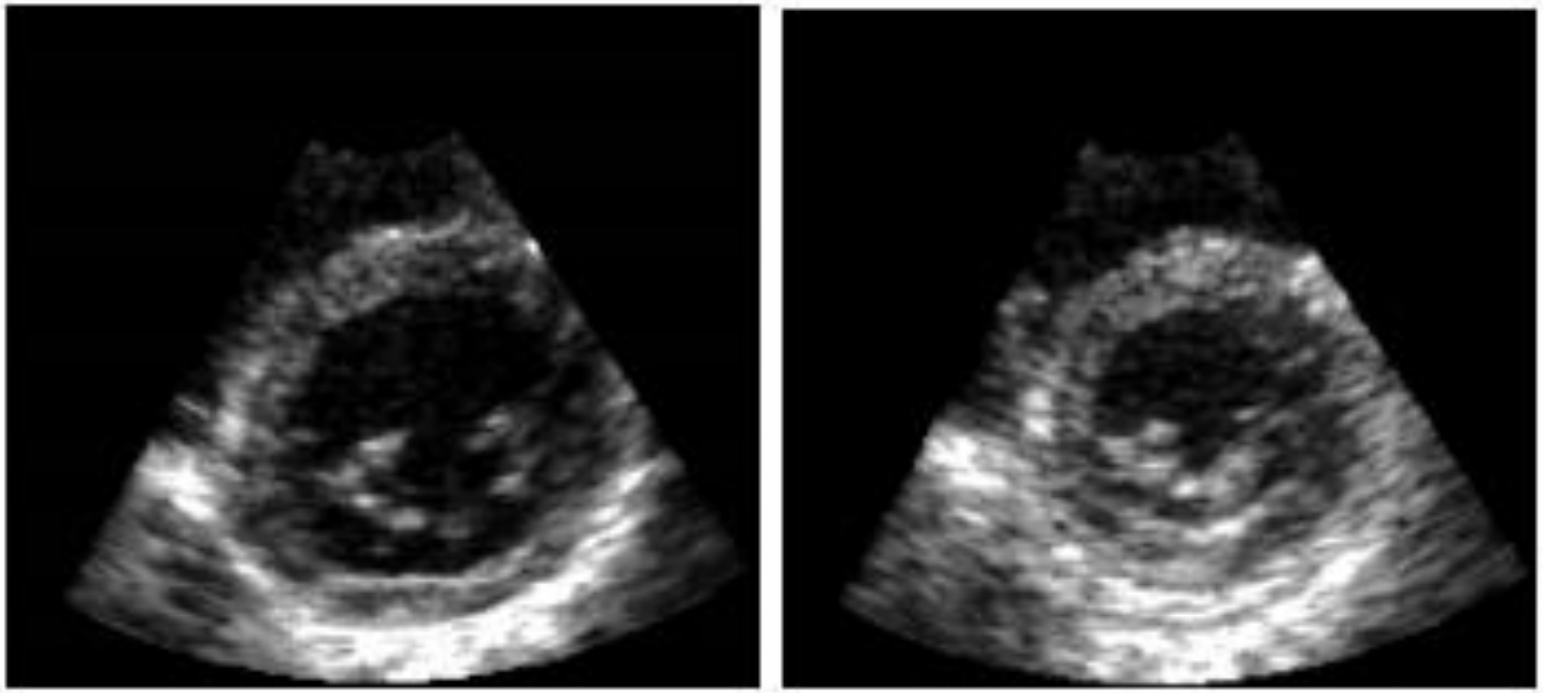

(c) End diastolic (left) and end systolic (right) instants of a simulated 2D+t echocardiography with scatterer distributions extracted from a real image. Simulation courtesy of Olivier Bernard and Martino Alessandrini.

Figure 2: Simulation examples computed on VIP.

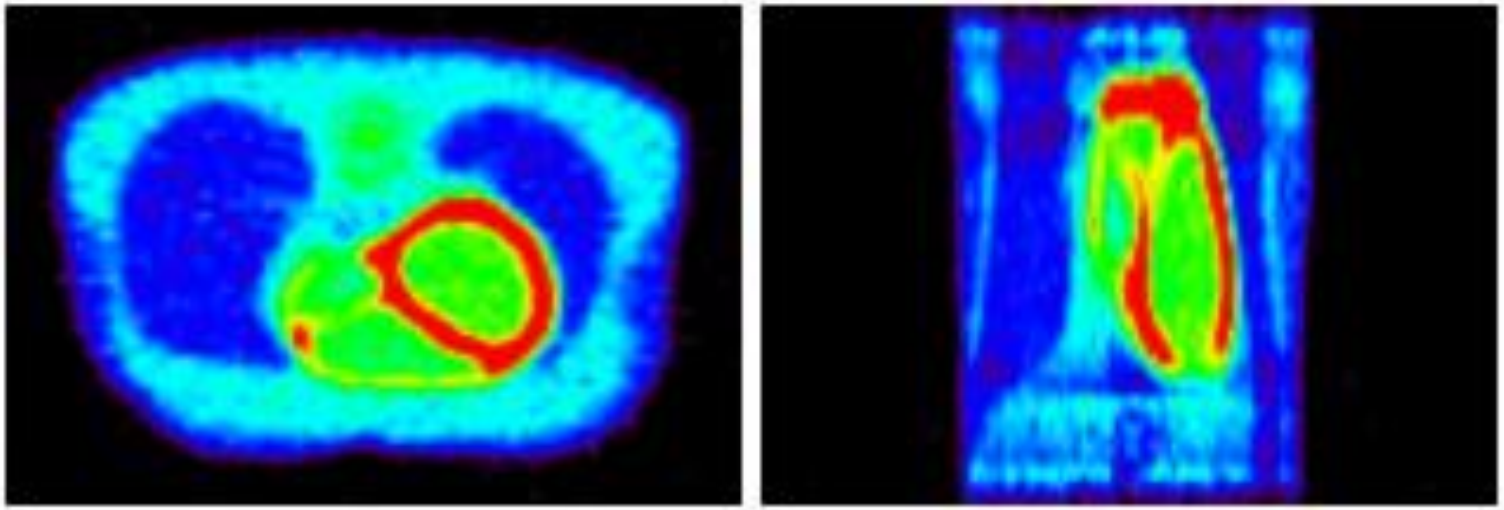

(d) Simulated cardiac FDG-PET. Left: transverse; right: coronal. Simulations courtesy of Patrick Clarysse and Frédéric Cervenansky.

Ευχαριστώ

Πρόγραμμα Διδακτορικών Σπουδών της Σχολής Ηλεκτρολόγων Μηχανικών και Μηχανικών Υπολογιστών ΕΜΠ

Πολυκλιμακωτή Προσομοίωση της Ασθένειας του Καρκίνου και *In Silico* Ιατρική (705)

Μάθημα 4ο

In Silico Ιατρική */ In Silico* Ογκολογία: Θέματα Κλινικών Απαιτήσεων και Εφαρμογών

Γεώργιος Σ. Σταματάκος

Διευθυντής Ερευνών - Research Professor– Καθηγητής Ερευνας
Ερευνητικό Πανεπιστημιακό Ινστιτούτο Συστημάτων Επικοινωνιών και Υπολογιστών (ΕΠΙΣΕΥ)
Σχολή Ηλεκτρολόγων Μηχανικών και Μηχανικών Υπολογιστών (ΣΗΜΜΥ)
Εθνικό Μετσόβιο Πολυτεχνείο (ΕΜΠ)
Διευθυντής της Ερευνητικής Ομάδας για την In Silico Ογκολογία και την In Silico Ιατρική, ΕΠΙΣΕΥ-ΣΗΜΜΥ-ΕΜΠ
Επισκέπτης Καθηγητής της Ιατρικής Σχολής του Πανεπιστημίου του Saarland, Γερμανία (1/7/2019-15/9/2019)
Επισκέπτης Καθηγητής της ΣΗΜΜΥ, ΕΜΠ (2016-2019)
gestam@central.ntua.gr, http://in-silico-oncology.iccs.ntua.gr/

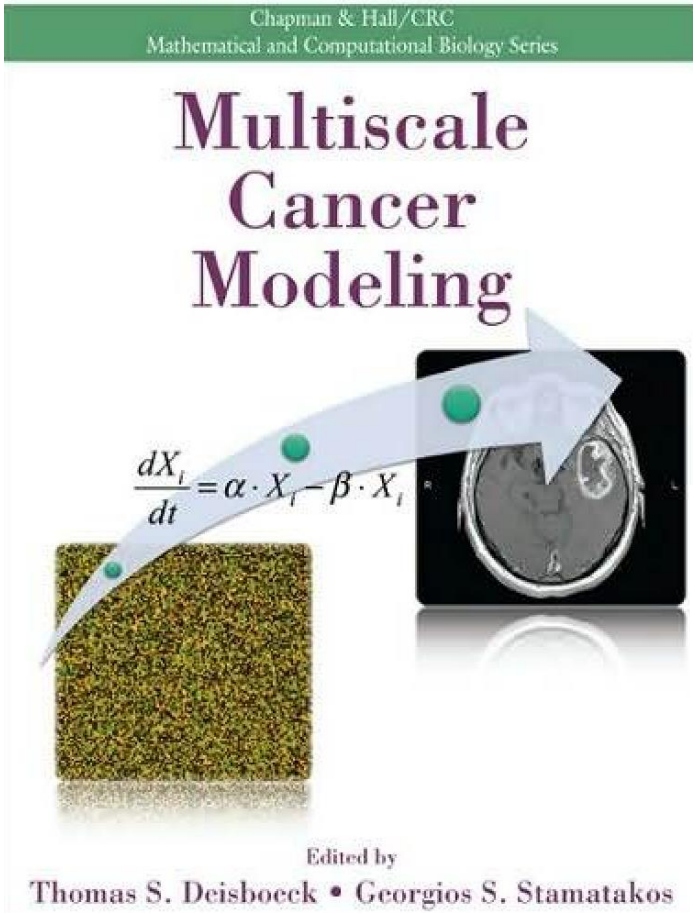

CRC Press
Taylor & Francis Group
6000 Broken Sound Parkway NW, Suite 300
Boca Raton, FL 33487-2742

© 2011 by Taylor and Francis Group, LLC
CRC Press is an imprint of Taylor & Francis Group, an Informa business

No claim to original U.S. Government works

Printed in the United States of America on acid-free paper
10 9 8 7 6 5 4 3 2 1

International Standard Book Number-13: 978-1-4398-1442-0 (Ebook-PDF)

CHAPTER 19

In Silico Oncology

Part II—Clinical Requirements Regarding In Silico *Oncology*

Norbert Graf

CHAPTER 19

In Silico Oncology

Part II—Clinical Requirements Regarding In Silico *Oncology*

Norbert Graf

CONTENTS

Introduction	437
Enrollment in Clinical Trials	438
Need of Bio-Banks	439
Seamless Integration of Heterogeneous Data	441
In Silico Oncology	442
Clinical Preconditions of In Vivo Cancer Modeling	443
Clinical Questions to Be Addressed	444
Conclusions	444
References	445

INTRODUCTION

This chapter deals with the clinical potential and some clinical translation prerequisites of multiscale cancer modeling as perceived from the standpoint of the clinician engaged in clinical trial research. Therefore, the aim is to propose clinical translation guidelines for clinically oriented cancer modeling, rather than to provide the description of any particular mathematical model.

Cancer as a leading cause of death accounted for 7.9 million or 13% of all deaths worldwide in 2007 [1]. The main types of cancer leading to overall mortality are lung, stomach, liver, colon, and breast cancer in adults. To reduce the burden of cancer, evidence-based strategies are needed for

its prevention, early detection, treatment, and care. In 2007 the WHO initiated an action plan against cancer with the following four goals:

- Prevent what is preventable.
- Cure what is curable.
- Provide palliative care for all cancer patients.
- Manage and monitor results.

In clinical oncology, today's treatment is still based on surgery, radiotherapy, chemotherapy, and supportive care, including psychosocial support, pain relievers, and palliation. Individualization of treatment is just starting by introducing small molecules as targeted therapies for specific diseases. But there is a significant amount of further knowledge needed, and to be translated to the clinics, before personalized medicine becomes reality. This knowledge is mainly coming from molecular biology (genomics, proteomics, metabolomics, etc.) and clinico-genomic trials. A third source for the individualization of treatment is based on system-biology-driven concepts in biomedicine, which are based on mathematical cancer models, and that belong to *in silico* oncology. Such mathematical models are just at the beginning. But it can be anticipated that they will play an important role as clinical decision makers in the near future. The demand for better treatments based on individual risk factors is obvious as most patients do respond to treatment but fewer will be cured.

ENROLLMENT IN CLINICAL TRIALS

An increase in the number of patients that are enrolled in clinical trials is needed. This can be achieved by simplifying and supporting the clinical trial process—from obtaining the idea, writing of the protocol, and setting up the trial, to collecting and analyzing the data. Today, only 5–10% of adult cancer patients are enrolled in prospective and randomized clinical trials [2] (see Figure 19.1). The fact that a patient is enrolled in a clinical trial increases his chance to be cured per se [3]. In pediatric oncology, more than 90% of patients are enrolled in prospective clinical trials [4]. This is one of the reasons, why survival rates in childhood cancer have risen to 80% today. The need for clinical trials is also based on the fact that for translational research, as well as for mathematical modeling of

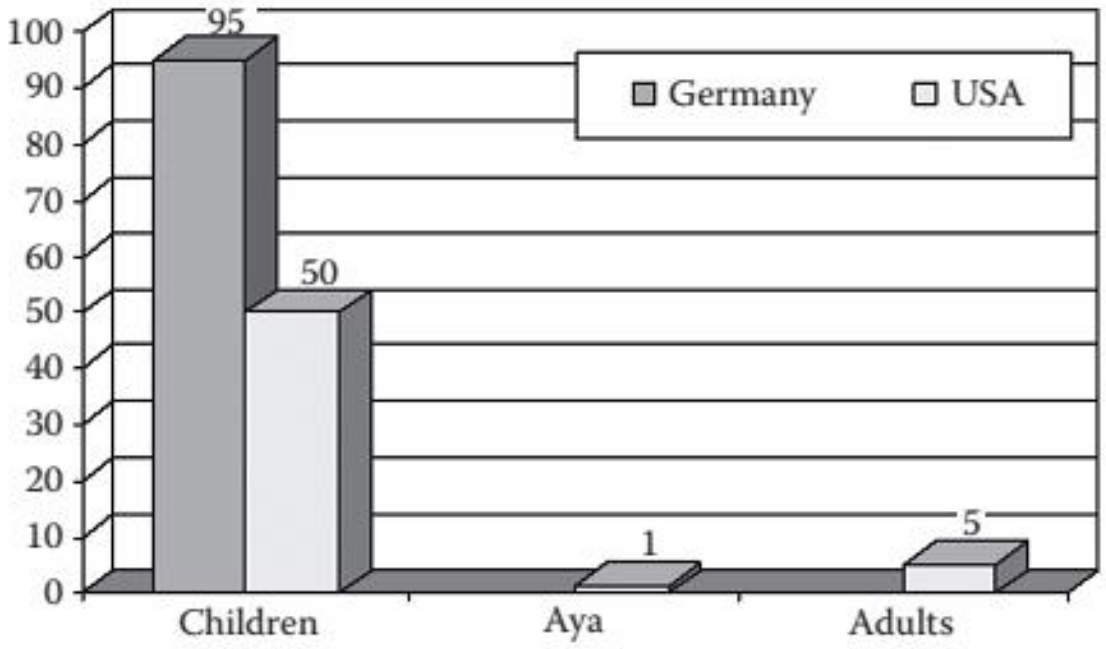

FIGURE 19.1 Enrollment of patients in clinical trials in percentage of patients. (AYA: adolescents and young adults). (From Couzin, J. *Science* 317:1160–1162, 2007.)

cancer, reliable clinical data are needed. These data can only be generated in prospective clinico-genomic trials. Only with such trials can new risk factors for outcome be found, which will allow a better stratification of patients according to their individual risk factors. This will help to spare toxic chemotherapy (CT) in patients who do not need them and increase dose intensity of CT or change of treatment options for those patients with a poor prognosis. Such a treatment plan is given in Figure 19.2 for the prospective randomized trial SIOP 2001/GPOH for the treatment of nephroblastoma in children, adolescents, and young adults in Europe.

NEED OF BIO-BANKS

In every clinical trial there is a demand for bio-banking and analyzing tumor samples in molecular genetic laboratories to gain more insights into the biology of cancer. An example of such a bio-bank is given in Figure 19.3 for the SIOP nephroblastoma trials. A variety of different analytical techniques and methods are available today. This will increase our knowledge with regard to the molecular biology of cancer. As a result, new therapeutics can be awaited that will lead to higher cure rates. Such therapeutics will be small molecules and used as targeted therapies. Drivers for such molecular therapeutics are the following subjects:

- Human Genome Project
- Bioinformatics

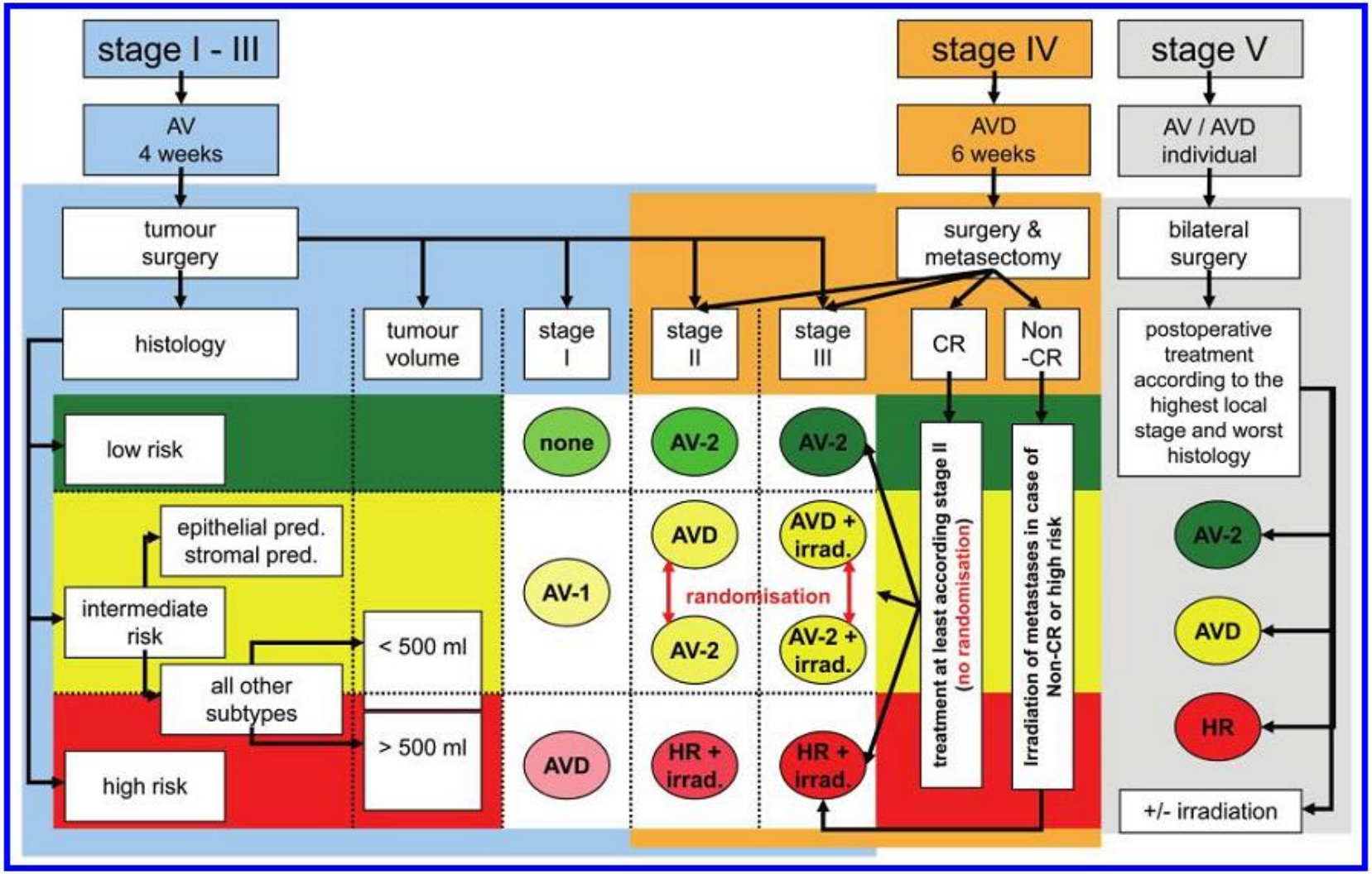

FIGURE 19.2 **(See color insert following page 40)** Treatment schema for nephroblastoma. SIOP 2001/GPOH trial for children, adolescents, and young adults.

ABBREVIATIONS

CR= Complete Remission (πλήρης ύφεση)
COG= Children's Oncology Group
AV= Actinomycin D and Vincristine
AVD= Actinomycin D, Vincristine and Doxorubicin
AV-1, AV-2: two different treatment schemes (see SIOP Protocol 2001)
HR= High Risk

GLOSSARY

Metastatectomy: the surgical removal of metastases

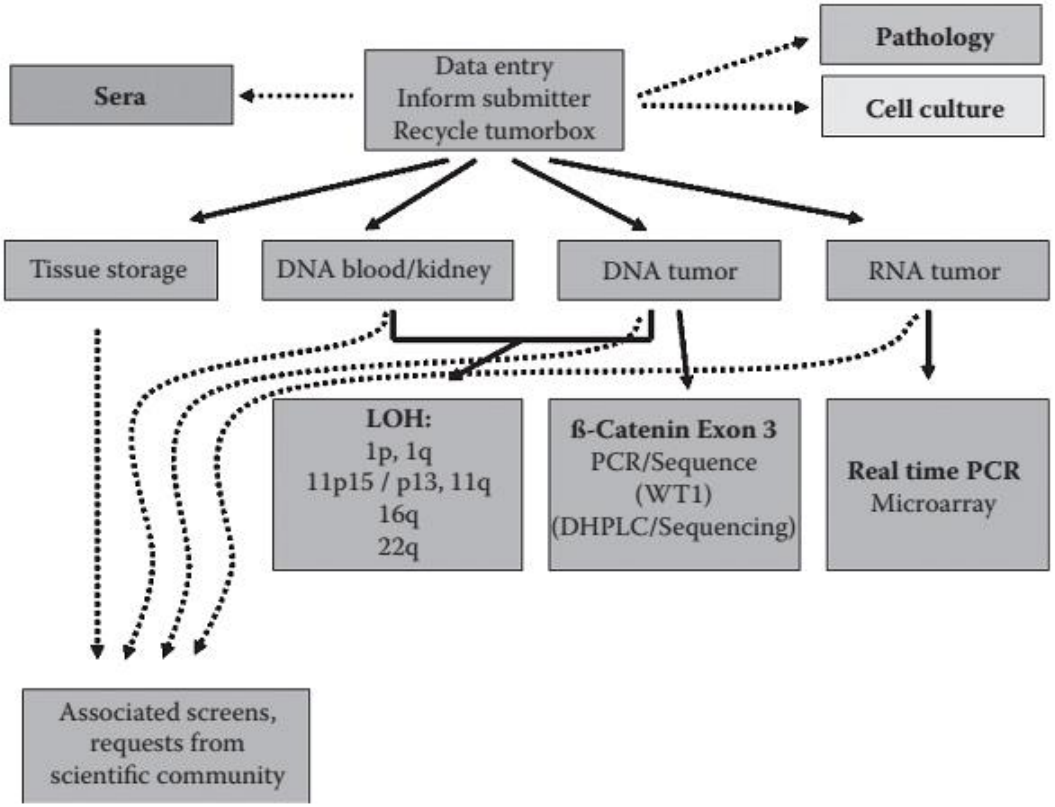

FIGURE 19.3 Schema for a bio-bank as used in the SIOP nephroblastoma trials.

- Robotic high-throughput screening
- Computer-aided drug design
- Expression vectors for novel protein target production

ABBREVIATIONS

LOH= Loss of heterozygocity
PCR= polymerase chain reaction
DHPLC= Denaturing high performance liquid chromatography

SEAMLESS INTEGRATION OF HETEROGENEOUS DATA

Besides clinical data and molecular biological data, imaging data, pathological data, and other data will be collected in prospective clinical trials. Such heterogeneous data need to be seamlessly integrated in the individual patient's clinical record. An integrated IT platform as it is developed in ACGT (Advancing Clinico Genomic Trials, a European Integrated Project of Framework Package 6) is very helpful for this purpose. Pseudonymized or anonymized data can then be used for translational research in accordance to legal, ethical, and regulatory requirements. Risk-adapted treatment in the future is only possible by fostering translational research [5,6]. Statisticians and bioinformatics can then analyze these data to gain new knowledge in an effort to get closer to personalized medicine.

IN SILICO ONCOLOGY

The aim of *in silico* oncology is to develop patient-specific computer simulation models of malignant tumors and normal tissues in order to optimize the planning of various therapeutic schemes. Ultimately, the goal is to aid in the process of effectively treating cancer and to contribute to the understanding of the disease at the molecular, cellular, organ, and body level.

Only with the help of powerful integrative platforms for the seamless integration of molecular biological, clinical, imaging, and other data, as well as public databases mathematical models of cancer can be generated. To run *in silico* experiments successfully, the characterization of the underlying disease, its biology, and treatment is needed, as well as computational mathematical methods and techniques. From system biology, physiological and pharmacokinetic models have to be developed for usage in such experiments.

From a clinical point of view it is expected that cancer growth and response to different treatments can be simulated. In simulating response to treatment in a given cancer, this knowledge is significant for assessing better methods for treatment efficacy as the RECIST criteria [7,8] provide. It might be time to improve traditional measures of clinical response as trial end points and to evaluate the activity on rare and resistant cancer cells. If *in silico* experiments are to be of more help for a clinician than providing a prediction of changes in tumor volume and shape, the response of treatment of the small fraction of resistant cancer cells will be of utmost importance in the future [9].

There are two possibilities for *in silico* experiments, the top-down and the bottom-up approach. The top-down approach uses clinical observations and the knowledge about the behavior of a cancer as a whole [10]. This approach tries to identify subsystems based on physiological and biological findings that are required to build a reproducible model of a specific cancer [11]. An iterative process continues to find the highest granularity of the system in making the *in silico* model as accurate as possible in reflecting reality. In doing so, the model is kept under surveillance by the overall behavior of the entire system [12,13]. In contrast, a bottom-up approach assembles all known parts of a system, starting with genes and proteins, and brings them into a formal structure until a model of the system is attained [12,14]. The disadvantage of the bottom-up approach is the fact that the discovery of each new component requires a reconfiguration

of the whole model [12]. For further information, available biosimulation software is summarized by Ho and Bartsell 2004 [15] and Deisboeck et al., 2009 [16], who gives an excellent overview of *in silico* cancer modeling by reviewing selected studies on modeling the progression and therapy of highly malignant brain tumors.

CLINICAL PRECONDITIONS OF IN VIVO CANCER MODELING

Such *in silico* experiments might help clinicians in the future to find the best way of treating an individual patient by simulating different treatments in the computer before starting the treatment in reality. Two preconditions are of utmost importance before one can rely on *in silico* oncology models [17]:

1. Every *in silico* method should be part of a clinico-genomic trial.
2. Every prediction of an *in silico* method has to be compared with the reality.

After establishing the *in silico* model it is necessary to define the needed data in a first step, including data from the tumor (molecular biology, pathology, imaging), from the patient (clinical data), and from the possible treatment (pharmacokinetics of drugs that will be used, the treatment schema), as well as from the literature and open-source databases. To make the simulation predictions precise and realistic, it is crucial to get as much information as possible from each of the different categories. The amount of data will be restricted by the availability of tumor material, imaging data, and clinical data. Therefore, *in silico* oncology should always be integrated into or be part of a clinico-genomic trial, where data management including data security and anonymization or pseudonymization of data, along with tumor banking, are well established. In addition, the trial is always reviewed by an ethical committee and fulfills all other GCP criteria to get approval by regulatory authorities [18].

The simulation prediction of each *in silico* model must always be compared with the reality, in other words, the actual treatment outcome. The actual outcome provides feedback for tuning the *in silico* model to get better predictions. Such a control loop, executed automatically, must be a component in any *in silico* model whose predictions are to be used for treatment. In that way *in silico* experiments should be considered and established as

learning systems. Only if there are no or minimal deviations between the prediction and the reality can the *in silico* method be allowed to be used in a clinical setting. The clinician has to define what can be accepted as a maximal deviation between prediction and reality in a trial. This definition should always be included in the biometrics part of a clinico-genomic trial protocol. For the safety of patients, a stopping rule has to be defined if clinical decisions are based on *in silico* experiments.

CLINICAL QUESTIONS TO BE ADDRESSED

For a clinician it is important that the *in silico* experiments can address and answer precisely for each patient the following questions [10,17]:

1. What is the natural course of the tumor growth over time, in size and shape?
2. When and to which site(s) is the tumor metastasizing?
3. Can the response of the local tumor and the metastases to a given treatment be predicted over time, in size and shape?
4. What is the best treatment schedule regarding medication, surgery, irradiation, and their combination, dosage, time schedule, and duration to achieve a cure?
5. Is it possible to predict severe adverse events (SAE) of a treatment and to propose alternatives to avoid them without deteriorating the outcome?
6. Is it possible to predict a cancer before it becomes clinically manifest, and to recommend treatment options to prevent the occurrence or a recurrence?

Which question will be addressed is decided by the clinician and will influence the model. It has to be accentuated as stated before, that every *in silico* experiment should be part of a prospective clinical trial.

CONCLUSIONS

The question "What is the best treatment for a given tumor in an individual patient?" leads to a high level of individualization. To attain this goal it is of utmost importance that the result of the *in silico* experiment is available in a short timeframe after diagnosis. This implies that all data that are necessary for running the *in silico* experiment have to be available

in a timely manner. This is especially important for molecular biologists, radiologists, and clinicians, who have to produce reliable data very fast [10]. Besides this, a high acceptance rate of *in silico* oncology experiments by clinicians is needed in the future. For this purpose, curricula of medical schools need to be changed and physicians need to be trained to use *in silico* experiments as a support system for clinical decision making in the daily clinical care of patients.

REFERENCES

1. WHO: http://www.who.int/mediacentre/factsheets/fs297/en/index.html (last accessed 07/19/2009).
2. Couzin, J. 2007. Survival in young adults with Cancer. *Science* 317:1160–1162.
3. Pritchard-Jones, K. et al. 2008. Improving recruitment to clinical trials for cancer in childhood. *The Lancet Oncol* 9:392–399.
4. Graf, N. and Göbel, U. 2004. Therapieoptimierungsstudien der Gesellschaft für Pädiatrische Onkologie und Hämatologie (GPOH) und 12. Novelle des Arzneimittelgesetzes zur Umsetzung der EU-Richtlinie. *Klin Pädiatr* 216:129–131.
5. Göbel, U. and Jürgens, H. 2003. Translation der kliniknahen Grundlagen-forschung in der pädiatrischen Onkologie. *Klin Pädiatr* 215:289–290.
6. Graf, N. et al. 2008. Post-genomic clinical trials: The perspective of ACGT. *eCancerMedicalScience J*, (online journal) 1, Article Num. 66, DOI:10.3332/eCMS.2007.66.

7. Bogaerts, J. et al. 2009. Individual patient data analysis to assess modifications to the RECIST criteria. *EJC* 45:248–260.
8. Therasse, P. et al. 2000. New guidelines to evaluate the response to treatment in solid tumors. *J Natl Cancer Inst* 92:205–216.
9. Huff, C.A. et al. 2006. The paradox of response and survival in cancer therapeutics. *Blood* 107:431–434.
10. Tsiknakis, M. et al. 2008. A semantic grid infrastructure enabling integrated access and analysis of multilevel biomedical data in support of post-genomic clinical trials on Cancer. *IEEE Trans Information Technology in Biomedicine, Special issue on Bio-Grids* 12:191–204.
11. Stamatakos, G. et al. 2002. In silico radiation oncology: combining novel simulation algorithms with current visualization techniques, *Proc. IEEE, Special Issue on Bioinformatics: Advances and Challenges* 90:1764–1777.
12. Friedrich, C.M. and Paterson, T.S. 2004. In silico predictions of target clinical efficacy. *Drug Disc Today* 3:216–222.
13. Michelson, S. 2006. In silico prediction of clinical efficacy. *Curr Opin Biotechnol* 17:666–670.
14. Noble, D. 2002. Modeling the heart—from genes to cells to the whole organ. *Science* 295:1678–1682.
15. Ho, R.L. and Bartsell, L.T. 2004. Biosimulation software is changing research. *Biotechnol Annu Rev* 10:297–302.

16. Deisboeck, T.S. et al. 2009. In silico cancer modeling: is it ready for prime time? *Nat Clin Pract Oncol* 6:34–42.
17. Graf, N. and Hoppe, A. 2006. What are the expectations of a clinician from in silico oncology? In Marias K, Stamatakos G (Hrsg). *Proc. 2nd Int Adv Res Workshop on In Silico Oncology*, Kolympari, Chania, Greece, September 25–26, 2006, pp. 36–38 (http://www.ics.forth.gr/bmi/2nd-iarwiso/; last accessed 07/19/2009).
18. Graf, N. et al. 2009. "In Silico" oncology for clinical decision-making in the context of nephroblastoma. *Klin Pädiatr* 221:141–149.

ΓΕΝΙΚΗ ΠΟΛΥΚΛΙΜΑΚΩΤΗ ΠΡΟΣΟΜΟΙΩΣΗ ΑΣΘΕΝΕΙΩΝ ΚΑΙ *IN SILICO* ΙΑΤΡΙΚΗ

Integration of knowledge for personalized medicine: a pharmacogenomics case-study

Robert Hoehndorf[1], Michel Dumontier[2] and Georgios V. Gkoutos[1,3]

[1]*University of Cambridge,* [2]*Carleton University,* [3]*University of Aberystwyth*

Correspondence: rh497@cam.ac.uk, Department of Genetics, University of Cambridge, Downing Street, Cambridge CB2 3EH, UK

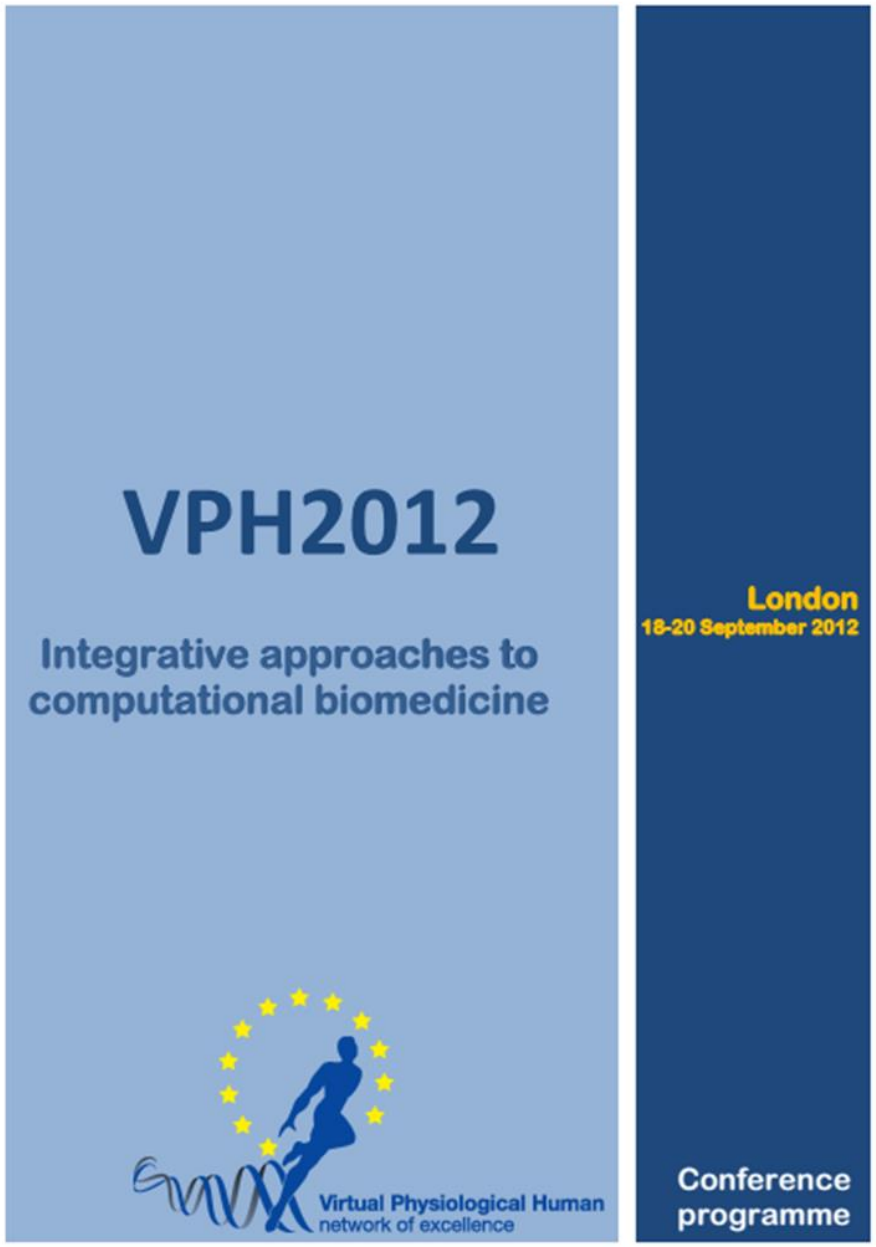
VPH2012
Integrative approaches to computational biomedicine
Virtual Physiological Human
network of excellence
London
18-20 September 2012
Conference programme

PROCEEDINGS-VPH2012_INTEGRATIVE_APPROACHES_TO_COMPUTATIONAL_BIOMEDICINE-LONDON_CONF_2012.pdf PAGE **121**/488 (PLEASE USE THE PDF PAGE COUNTER)

Integration of knowledge for personalized medicine: a pharmacogenomics case-study

Robert Hoehndorf[1], Michel Dumontier[2] and Georgios V. Gkoutos[1,3]

[1]*University of Cambridge,* [2]*Carleton University,* [3]*University of Aberystwyth*

Correspondence: rh497@cam.ac.uk, Department of Genetics, University of Cambridge, Downing Street, Cambridge CB2 3EH, UK

Abstract

The semantic integration of pharmacogenomic knowledge that is currently distributed in several resources extends the access to information that is crucial for new scientific analyses that bridge multiple resources and domains. We demonstrate how to combine formal ontological analysis and Semantic Web technology to integrate three major pharmacogenomics databases and link the combined resource to chemical and disease ontologies. We show how the additional background knowledge in these ontologies can be used to perform expressive queries in the domain of pharmacogenomics that specifically leverage the collection of formalized ontologies and enable access to knowledge that is not available in either database alone.

Introduction

The rapid increase of data generated from genetic analyses and functional genomics has necessitated the development of a number of pharmacogenomics related databases that provide invaluable resources for discovering information related to the impact of gene variations to drug responses and toxicity [1]. Such resources increasingly annotate their data with ontologies to integrate and share data across domains and resources. Ontologies provide a rich taxonomic structure and axioms that make some aspects of background domain knowledge explicit.

Different pharmacogenomics resources provide different aspects about drugs, genes, diseases, pathways and their relations. Integrating these aspects into a single framework has the potential to extend and improve the databases' utility for scientific analyses and allow them to play a crucial role in the personalization of disease intervention strategies. Here, we demonstrate how to integrate the pharmacogenomics knowledge base *PharmGKB*, DrugBank and the Comparative Toxicogenomics Database (CTD) using the Web Ontology Language (OWL) [2] such that it becomes possible to perform queries through automated reasoning over the combination of these three databases. The resulting integrated resource can be used to answer powerful queries spanning multiple databases and ontologies. In particular, we demonstrate how the integration of knowledge in pharmacogenomics with information about diseases provides a means to associate drugs with anatomical structures and systems in which they become active, and how the integration with chemical ontologies allows the reuse of chemical background knowledge to group drugs based on their chemical properties and to access their biological functions.

Methods

We have created formalized knowledge bases using OWL for several resources in pharmacogenomics, listed in Table 1. We then utilized property chains in order to infer additional information based on participation in pathways. Using the ELK OWL reasoner [3], we can classify the resulting integrated pharmacogenomics knowledge base in less than one minute and answer queries in under one second. To enable the use of these resources and the software in clinical information systems and the support of personalized treatment of disease, we make the resulting OWL knowledge bases and associated software freely available on `http://pharmgkb-owl.googlecode.com`.

Resource	Description
Anatomical Therapeutic Chemical Classification System (ATC)	Classification of drugs based on organ or system of action, therapeutic characteristics and chemical properties.
Medical Subject Headings (MESH) vocabulary	Controlled vocabulary used for indexing, cataloging, and searching for biomedical and health-related information and documents.
Comparative Toxicogenomics Database (CTD)	CTD contains manually curated data about chemical–gene/protein, gene/protein–disease and chemical–disease associations, as well as predictions based on a complex interaction network.
DrugBank	DrugBank contains detailed information about drugs and drug targets.
PharmGKB	PharmGKB contains information about the effects of human variation on drug responses.

Table 1: List of resources and software tools provided.

Results

Based on the formal representation we generate for the DrugBank, CTD and PharmGKB, we can perform an integration with other ontologies. First, we utilize mappings to ontologies of *diseases* and other *abnormalities* to perform an integration with ontologies of these domains. Such an integration allows us to use background knowledge contained in these ontologies for queries, to increase the expressivity of the representation and establish new connections between classes in PharmGKB. For example, we can use automated reasoning over the Human Disease Ontology to query for things that are associated with *Parasitic infectious disease* (`DOID:1398`) and will retrieve, among others, drugs associated with *Malaria*, *Scabies* or *Schistosomiasis* in either the CTD, PharmGKB or DrugBank. We retrieve 129 classes as result to this query, including the anti-malarial drugs *Chloroquine* and *Artemether*.

The second dimension of integrating pharmacogenomics knowledge is in respect to ontologies of chemicals and drugs. The PharmGKB, CTD and DrugBank provide references for the drugs they contain based on the ATC, the ChEBI ontology and MeSH. For this work, we generated OWL versions of the ATC and MeSH. Integration with the ATC, MeSH and ChEBI ontologies of chemicals enables expressive queries using the background knowledge contained in all three ontologies. For example, using the ChEBI ontology, we are able to query for diseases associated with some alcohol (`ChEBI:30879`) and obtain, amongst others, *Alcoholism* (`PA443309`) and *Bubonic plague* (`PA445338`) as a result. The disease *Alcoholism* is directly associated with *Ethanol* (*CHEBI:16236*), a subclass of *Alcohol* in ChEBI. *Bubonic plague*, on the other hand, is directly associated with the drug *Phenylephrine* in PharmGKB which is, in turn, a subclass of *Alcohol* in ChEBI.

PharmGKB data can list druggene and drugdisease associations which are obtained by applying the following rule: if a drug D is a component of a pathway, and that pathway has another drug, gene or disease X as component, then the drug is associated (through a pathway) with X. This kind of reasoning can be captured in OWL with *property chains*. A property chain allows to construct complex properties from simple properties by chaining two or more properties together. We have created a number of such property chains to close the knowledge in the integrated pharmacogenomics ontology against information in pathways. As a consequence, we are able to infer from the assertions that a drug participates in a pathway and this pathway has a gene as participant that there is a novel pathway-based association relation between the drug and the gene. Such property chains allows to extend our queries over the integrated resources.

Our approach of integrating resources within a domain through integration of the ontologies that provide meta-data for them is not limited to the domain of pharmacogenomics alone, but can serve as a model for other areas, including model organism databases, databases of protein functions, disease and phenotype databases. In each case, it is crucial to identify relevant biomedical ontologies based on which the content of the databases can be aligned and formalize the content of the databases in such a way that it becomes possible to answer the relevant queries. Such a model of knowledge integration can enable novel analyses that connect different domains, based on methods such as semantic similarity measures [4] or ontology enrichment analyses [5].

Acknowledgements

Funding for RH was provided by the European Commission's 7th Framework Programme, RICORDO project, grant number 248502. Funding for MD was provided by a NSERC Discovery Grant. Funding for GVG was provided by the NIH (grant number R01 HG004838-02).

References

[1] Sim SC, Altman RB, Ingelman-Sundberg M. Databases in the area of pharmacogenetics. Hum Mutat. 2011;Available from: http://www.biomedsearch.com/nih/Databases-in-area-pharmacogenetics/21309040.html.

[2] Grau B, Horrocks I, Motik B, Parsia B, Patelschneider P, Sattler U. OWL 2: The next step for OWL. Web Semantics: Science, Services and Agents on the World Wide Web. 2008 November;6(4):309–322. Available from: http://dx.doi.org/10.1016/j.websem.2008.05.001.

[3] Kazakov Y, Krötzsch M, Simančík F. Unchain My $\mathscr{E}\mathscr{L}$ Reasoner. In: Proceedings of the 23rd International Workshop on Description Logics (DL'10). CEUR Workshop Proceedings. CEUR-WS.org; 2011. .

[4] Hoehndorf R, Schofield PN, Gkoutos GV. PhenomeNET: a whole-phenome approach to disease gene discovery. Nucleic Acids Research. 2011;39(18):e119. Available from: http://nar.oxfordjournals.org/content/39/18/e119.

[5] LePendu P, Musen M, Shah N. Enabling Enrichment Analysis with the Human Disease Ontology. Journal of Biomedical Informatics. 2011;In press.

Ευχαριστώ

Πρόγραμμα Διδακτορικών Σπουδών της Σχολής Ηλεκτρολόγων Μηχανικών και Μηχανικών Υπολογιστών ΕΜΠ

Πολυκλιμακωτή Προσομοίωση της Ασθένειας του Καρκίνου και *In Silico* Ιατρική (705)

Μάθημα 5ο

Προσομοίωση της διήθησης κλινικών καρκινικών όγκων με τη χρήση της μερικής διαφορικής εξίσωσης (ΜΔΕ) της αντίδρασης – διάχυσης και κατάλληλων οριακών συνθηκών. Αντίστοιχα μαθηματικά και υπολογιστικά προβλήματα στη Γενική *In Silico* Ιατρική.

Γεώργιος Σ. Σταματάκος

Διευθυντής Ερευνών - Research Professor– Καθηγητής Ερευνας
Ερευνητικό Πανεπιστημιακό Ινστιτούτο Συστημάτων Επικοινωνιών και Υπολογιστών (ΕΠΙΣΕΥ)
Σχολή Ηλεκτρολόγων Μηχανικών και Μηχανικών Υπολογιστών (ΣΗΜΜΥ)
Εθνικό Μετσόβιο Πολυτεχνείο (ΕΜΠ)
Διευθυντής της Ερευνητικής Ομάδας για την In Silico Ογκολογία και την In Silico Ιατρική, ΕΠΙΣΕΥ-ΣΗΜΜΥ-ΕΜΠ
Επισκέπτης Καθηγητής της Ιατρικής Σχολής του Πανεπιστημίου του Saarland, Γερμανία (1/7/2019-15/9/2019)
Επισκέπτης Καθηγητής της ΣΗΜΜΥ, ΕΜΠ (2016-2019)
gestam@central.ntua.gr, http://in-silico-oncology.iccs.ntua.gr/

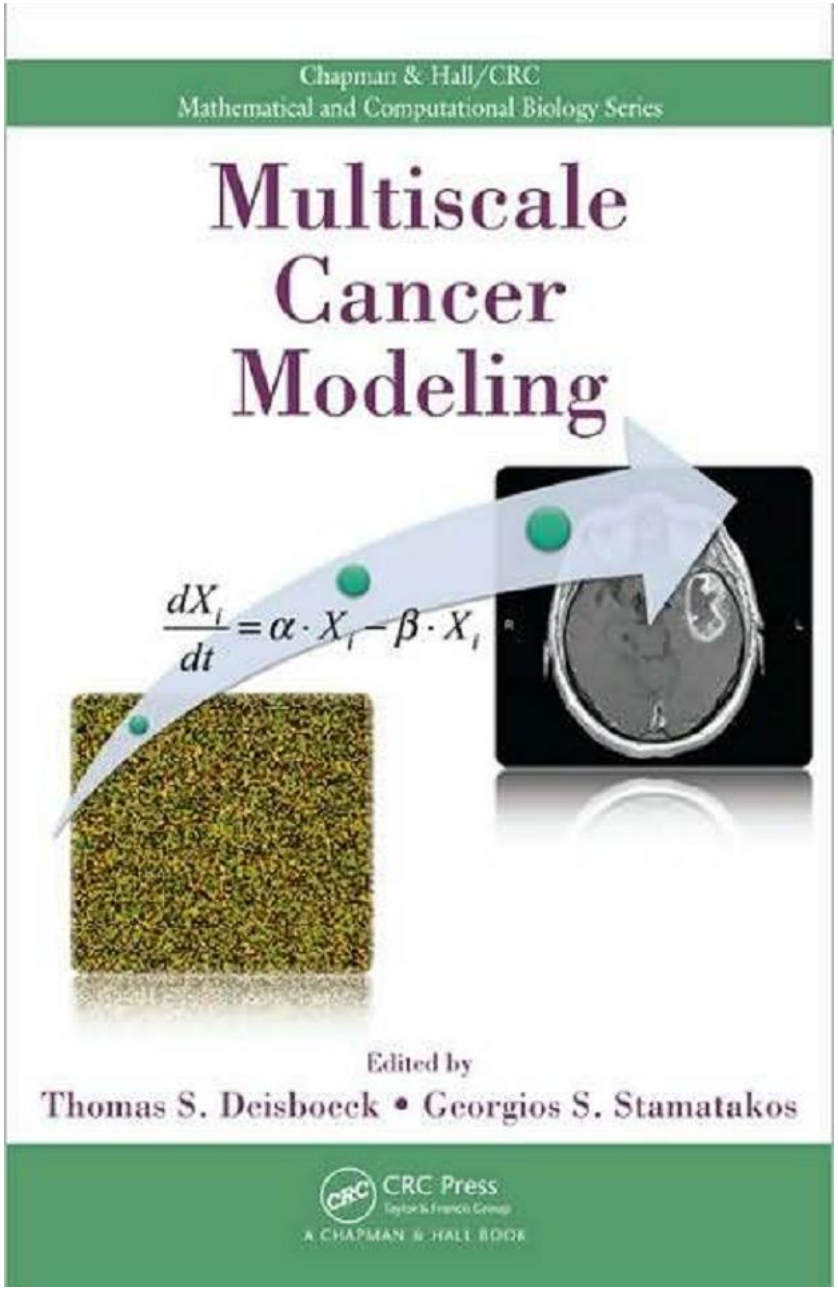

CRC Press
Taylor & Francis Group
6000 Broken Sound Parkway NW, Suite 300
Boca Raton, FL 33487-2742

© 2011 by Taylor and Francis Group, LLC
CRC Press is an imprint of Taylor & Francis Group, an Informa business

CHAPTER 16

Bridging from Multiscale Modeling to Practical Clinical Applications in the Study of Human Gliomas

Gargi Chakraborty, Rita Sodt,
Susan Massey, Stanley Gu, Russell Rockne,
Ellsworth C. Alvord, Jr., and Kristin R. Swanson

CONTENTS

Introduction 360
Quantifying In Vivo Glioma Kinetics Noninvasively 361
Anisotropic Tumor Cell Motility in Heterogeneous Brain Tissue 364
Assessing Glioma Ablation and Regrowth Posttherapy with Mathematical Parameters 365
- Does More Treatment Mean Better Survival? 366
- Resection 366
- Radiation Therapy 367
- Other Therapies 369

Capturing Influence of Tumor Microenvironment on Glioma Growth by Parallel Comparison of MRI and PET 370
- Hypoxia Assessed with FMISO-PET 371
- Hyperglycolysis Assessed with FDG-PET 373
- Tumor Proliferation Assessed with FLT-PET 374

Developing Multiscale Models of Gliomas from Animal Experimental Models 375

359

Discussion 377
Acknowledgments 377
References 377

INTRODUCTION

Gliomas are malignant lesions of the brain characterized by their propensity to proliferate and invade the normal-appearing tissue. These brain tumors show diverse anatomic and metabolic traits that manifest differently across patients, ranging in aggressiveness from low-grade gliomas (LGGs) to high-grade gliomas (HGGs). Approximately 50% of glioma patients are diagnosed with glioblastoma multiforme (GBM), a World Health Organization grade IV glioma, which is the most aggressive type of brain tumor in adults (Louis et al. 2007). Difficulty in treating gliomas arises primarily from the invasiveness of the cell populations comprising the tumor. Despite extensive treatments including surgical resection, radiotherapy, and chemotherapy, GBMs have a propensity to recur and prove to be fatal with a median survival of approximately 1 year (Burnet et al. 2007; Welsh et al. 2009).

Modern radiology offers imaging techniques such as magnetic resonance imaging (MRI) and positron emission tomography (PET) that allow noninvasive detection of brain tumor anatomy and aberrant molecular activity, respectively. Clinically, routine MRIs comprise a variety of modalities, including T1-weighted gadolinium-enhanced (T1Gd), which images the highly vascularized portion of the tumor and T2-weighted and fluid attenuation inversion recovery (FLAIR) MRI, which image the bulk mass as well as surrounding edema with isolated invading tumor cells. However, because of the diffuse invasion of gliomas cells into the normal appearing brain, even current advances in radiology do not allow detection of the glioma cells that lie beyond the imageable tumor periphery (Harpold et al. 2007).

Mathematical modeling utilizing experimental and/or human data provides a novel tool for understanding the spatial and temporal growth of brain tumors by allowing us to create patient-specific virtual tumors that show the distribution of glioma cells that exist beyond the imageable boundary (Harpold et al. 2007; Rockne et al. 2008a; Swanson et al. 2003; Hatzikirou et al. 2005). These virtual controls serve as novel tools for assessing and predicting response to therapy as well as for designing new therapy. In this chapter, we will consider recent contributions to the

mathematical modeling of gliomas, focusing on work bridging the gap between predictive multiscale mathematical modeling and current clinical care of gliomas.

QUANTIFYING IN VIVO GLIOMA KINETICS NONINVASIVELY

Recent models of tumor growth look at both the spatial motility and proliferation of tumor cells, and can be divided into two general modeling approaches: discrete and continuous. Cellular automata (CA) models are discrete in their approach (Hatzikirou and Deutsch 2008; Huang et al. 2008) and model individual tumor cells at discrete time-points along with cell–cell and cell–microenvironment interactions at the microscopic level. CA model predictions apply mostly to cell cultures because of the computational limitations of large numbers of cells typically seen in tumors of clinically detectable size. Continuum models assess the growth and spread of tumor cell density macroscopically, and have applications in predicting tumor growth on the scale of clinical imaging and gross tissue histology but with limited applicability at the cellular level. Both modeling approaches are necessary to understand glioma growth and connect cell or tissue culture experiments to clinical reality, which has led to proposals for multiscale models. A recent study by Tanaka et al. shows that hybridizing discrete continuum and compartment modeling allows assessment of tumor size as detected clinically, and individual cell behavior as detected in a cell culture (Tanaka et al. 2009). Deroulers et al. focus on multiscale migration study of gliomas and compare their results to in vitro data (Deroulers et al. 2009). These studies utilize mathematical tools to understand biological processes underlying glioma behavior; however, their current results cannot be paralleled to clinically available data such as medical imaging or gross tissue histology. For gliomas in particular, an ideal mathematical model would predict invasive tumor growth beyond the imageable abnormality and be easily amenable to input from the most commonly used (clinical) tools to assess glioma growth and response to therapy, namely clinical imaging and gross histology.

Professor J.D. Murray and colleagues, as reviewed in Murray (2003) and Harpold et al. (2007), proposed one of the first glioma models with prospects of clinical application. This is a reaction-diffusion model that captures both the diffuse dispersal and proliferation of glioma cells, hence denoted as the proliferation-invasion (PI) model. In other words, this equation says that the rate of change of glioma cell density is equal to the

net diffusion of the glioma cells plus the net proliferation of the glioma cells. Translated to math, we have

$$\frac{\partial c}{\partial t} = \nabla \bullet (D(x)\nabla c) + \rho c\left(1 - \frac{c}{K}\right)$$

$$D(x) = \begin{cases} D_g & x \in \text{Grey} \\ D_w & x \in \text{White} \end{cases} \qquad (16.1)$$

where c(x,t) defines the concentration of glioma cells over space (x) and time (t) and is spatially limited by the boundaries of the skull and ventricles, which are anatomical structures of the brain that serve as impenetrable walls for glioma cells. This model utilizes two main terms: *net dispersal/diffusion* (D) of tumor cells differentiated spatially in three dimensions, and *net proliferation* (ρ) of tumor cells with a logistic growth term, where K is the carrying capacity or maximum cell density allowed per cubic centimeter of tissue (about 10^8 cells/cc, assuming a typical cell with diameter of 10 μm). Simulations of this model are performed in the three-dimensional, anatomically-accurate brain domain, approximated by the BrainWeb atlas (Collins et al. 1998; Cocosco et al. 1997), to capture tumor growth in the complex architecture of the human brain (Swanson et al. 2002b; Swanson 1999).

In order to incorporate heterogeneous motility of tumor cells throughout the brain yet keep the model simple, the diffusion coefficient, D, is spatially defined according to the grey and white matter composition of the brain such that $D(x) = D_g$ in gray matter, which consists of densely packed neuronal cell bodies, and $D(x) = D_w$ in white matter, which comprises axon tracts originating from, and leading to, neuronal cell bodies in the gray matter (Swanson 1999). The density of glial cells is highest in white matter and organized as myelin surrounding axons. Gliomas preferentially migrate along white matter tracts with diffusion fastest parallel and slowest perpendicular to these fiber tracts (Stadlbauer et al. 2009). The variation in the net rate of diffusion in white matter (D_w) can be 5 to 100 times faster than in gray matter (D_g) (Swanson et al. 2000, 2002b; Harpold et al. 2007).

One result of the PI model is that of linear radial growth. That is, the radial growth pattern asymptotically approaches Fisher's approximation for a constant velocity of expansion $v = 2\sqrt{D\rho}$. An analysis of velocity for a set of patients with LGGs (one example shown in Figure 16.2) suggested that the rate of change of radial expansion is constant in untreated

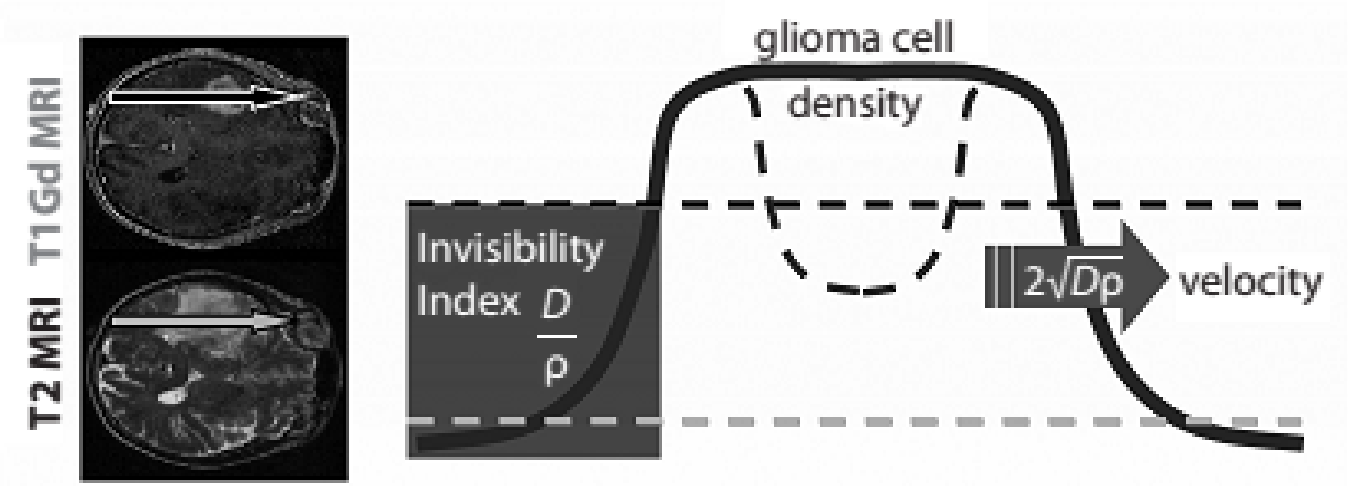

FIGURE 16.1 The left side shows a 2D slice through MRI scans (T1Gd on the top and T2 on the bottom). If we noted the diameter of the tumor abnormality through both images, we would obtain a theoretical 1D profile as shown on the right where glioma cell density is represented on the vertical axis and space is represented on the horizontal axis. The black dotted line is the threshold of detection for the T1Gd MRI (approximately 80% of total cell density), and the white dotted line is the threshold of detection for the T2 MRI (approximately 16% of total cell density). Velocity of the tumor growth asymptotically approaches Fisher's approximation and the invisibility index is given by the ratio of the diffusion and proliferation parameters.

gliomas (Swanson et al. 2004; Mandonnet et al. 2003, 2008) and that this constant velocity served as a prognostic factor for LGGs (Pallud et al. 2006). Swanson showed that the two parameters in Equation 16.1, D and ρ, could be derived from volumetric measurements of tumor abnormality as imaged with T1Gd and T2 MRI scans in humans (Harpold et al. 2007). Using this set of data collected at two time points prior to treatment or operation allows for the calculation of radial velocity of tumor growth (Figure 16.2). These results demonstrated that glioma growth prior to treatment could be predictively modeled in vivo in humans.

Many LGGs do not contrast-enhance, that is, these tumors are visible on T2 and FLAIR modalities, but not on T1Gd. This is because LGGs have little angiogenesis or new blood vessel formation, which allow leakage of the gadolinium-enhancement tracer. However, many LGGs progress to higher grades, although the time to progression (TTP) is quite variable (Chaichana et al. 2009; Michotte et al. 2004). In the study of LGGs, velocity of tumor growth predicted time to contrast enhancement on T1Gd MRI, thereby velocity could be utilized to predict TTP (Alvord and Swanson 2007). Prior to this result, malignant progression was considered an unpredictable event.

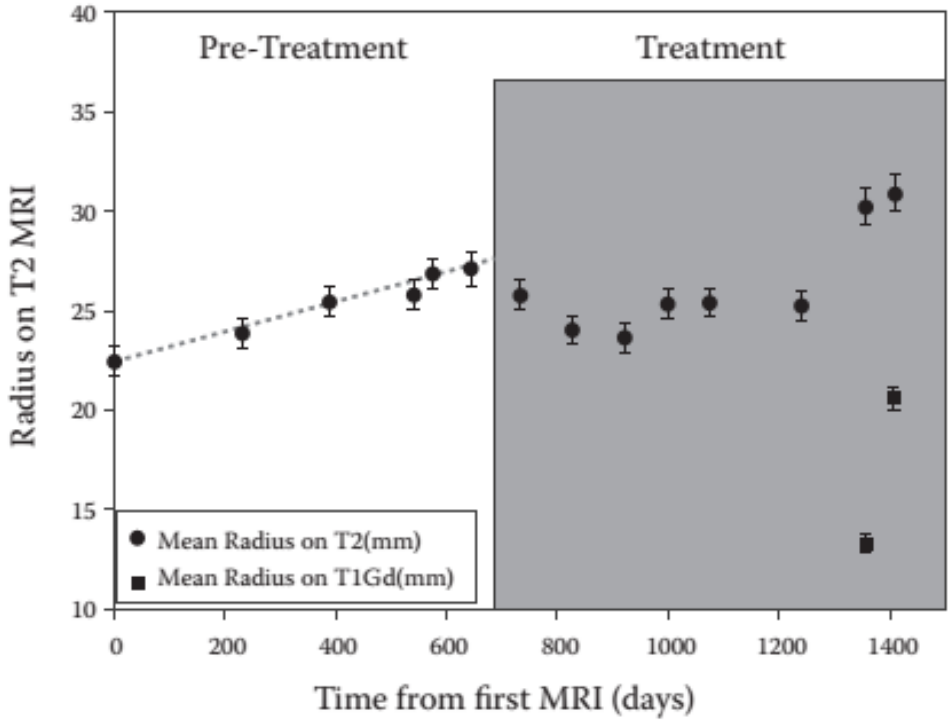

FIGURE 16.2 A patient with an LGG assessed serially on T1Gd and T2. The left part of the graph indicates measurements of mean tumor radius prior to treatment and shows that the velocity of radial expansion on T2 MRI is constant (change in radius is linear as displayed by the line of best fit—dotted gray line). The right part of the graph indicates tumor dynamics after treatment with radiation therapy and subtotal resection. The increase in T2 tumor radius along with contrast-enhancement on T1Gd seen after day 1200 is indicative of tumor progression. The drop in both T1Gd and T2 radius thereafter is due to the surgical removal of tumor.

ANISOTROPIC TUMOR CELL MOTILITY IN HETEROGENEOUS BRAIN TISSUE

Recently, the simulations of glioma invasion was improved by incorporating anisotropy using information from diffusion tensor imaging (DTI), a type of MRI that detects the directionality of water diffusion in the brain (Jbabdi et al. 2005). DTI scans provide a tensor at each spatial location (voxel) in the brain indicating the magnitude and direction that glioma cells would presumably prefer to migrate. It was shown that the shape and kinetic evolution of the tumors were better simulated with anisotropic rather than isotropic diffusion as expected because the tensors provided a patient-specific direction schema for the motility of glioma cells (Jbabdi et al. 2005). Implementation

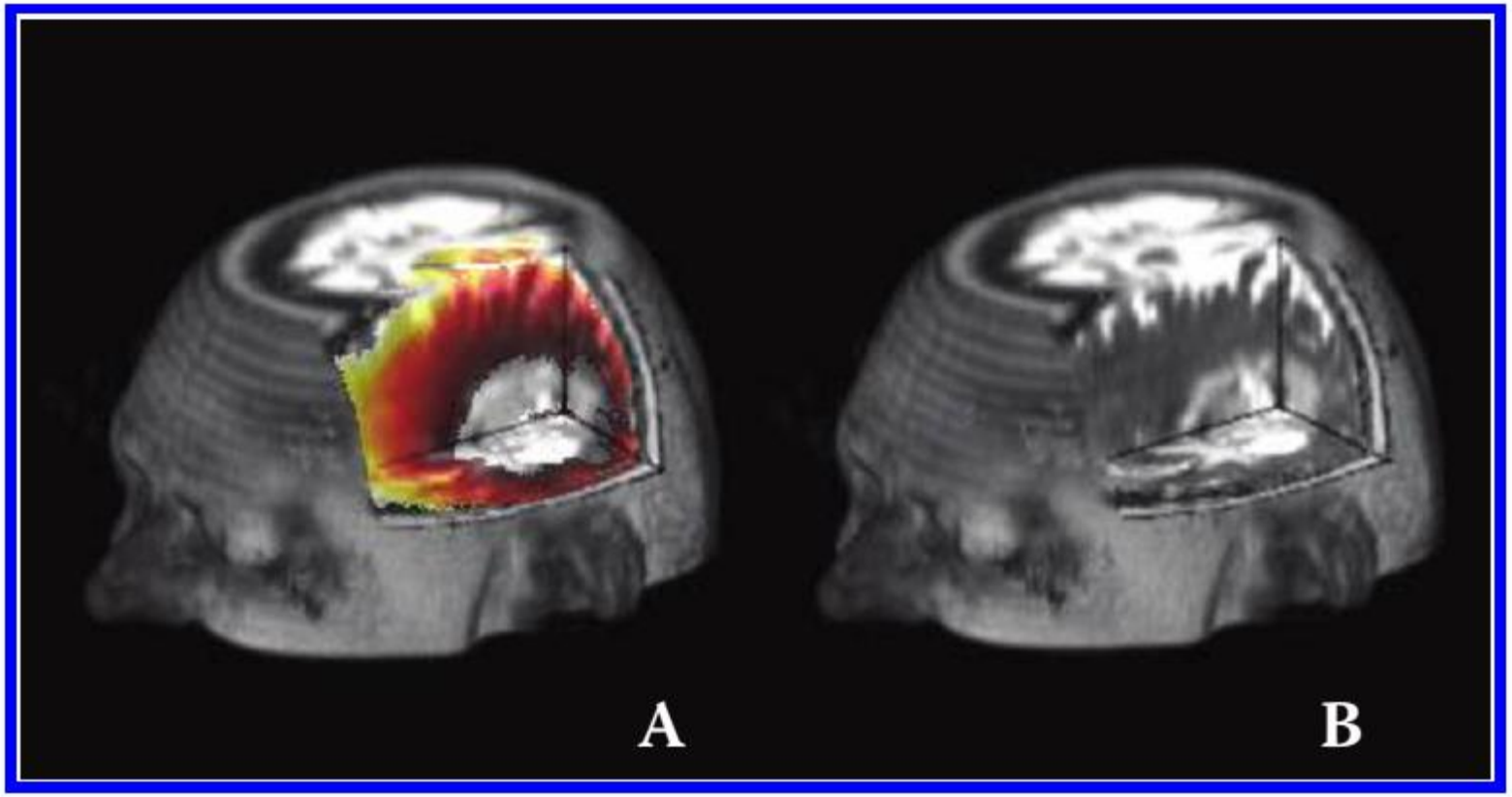

FIGURE 16.3 **(See color insert following page 40)** Panel A shows a patient-specific 3D simulation of the PI model including differential motility in the grey and white matter, while panel B shows the actual tumor detected by T2 MRI.

of the PI model in three dimensions by the Swanson group showed that the architecture of the brain segregated into gray and white matter dictating the tumor's spatial morphology as compared with T2-MRI, visualized in three dimensions (Figure 16.3). Including input from DTI scans to further dictate the motility of glioma cells, simulations of the PI model looking at radial growth of tumor over time indicates that there is indeed a difference in the predicted tumor radius in T1Gd and T2 MRIs with isotropy versus anisotropy (Sodt et al. 2009).

Other groups have considered extensions of the PI model incorporating DTI information as well as a biomechanical component of GBM growth that exerts a mass effect on surrounding brain structures such as skull and ventricles (Bondiau et al. 2008; Clatz et al. 2005). Mass effect is considered to be responsible for the mechanical impact of the tumor on surrounding brain tissue. However, for glioma models incorporating mass effect, the problem of parameter estimation from patient data such as imaging was unaddressed until a recent preliminary study by Hogea et al., which compares optimized parameter estimates for one patient case (Hogea et al. 2008).

ASSESSING GLIOMA ABLATION AND REGROWTH POSTTHERAPY WITH MATHEMATICAL PARAMETERS

Although glioma growth kinetics differ across patients, the standard of care is surprisingly homogeneous and consists of resection or biopsy, followed by radiation therapy along with adjuvant and concurrent chemotherapy. Mathematical modeling tools may be used to understand the extent to which certain therapies may improve survival for any individual patient and to develop a control method by which to assess whether certain patients will respond better to particular therapies.

Does More Treatment Mean Better Survival?

With the continual introduction and investigation of new and more aggressive therapies, assessing the benefits of treatment on decreasing tumor burden and improving a patient's quality of life can be a challenge for physicians. Recurrence of gliomas is common and likely arises from the fraction of cells that cannot be imaged and thus targeted for therapy. Although the diffuse extent of malignant glioma cell invasion cannot be imaged, it can be modeled in a virtual glioma with three-dimensional simulations of the PI model. As presented in Figure 16.1, 80% of the total tumor cell concentration is imageable by the T1Gd MRI and 16% (a five-fold increase) is imageable by the T2 MRI (Swanson et al. 2002b), from which a tumor cell gradient is inferred. The spatial distribution of invisible cells has been shown to lead to a better assessment of treatment planning and detect potential sites of tumor recurrence, which may aid physicians in designing an optimal time course for a glioma treatment-regimen that can be tailored to the patient (Swanson et al. 2004).

A survival analysis of 32 GBM patients indicated that regardless of therapy, the model-defined parameters correlated with patient prognosis (Wang et al. 2009). This result maintained statistical significance even while controlling for standard clinical parameters such as histology, age, and Karnofsky Performance Status (KPS) (Wang et al. 2009), showing the result to be robust. In particular, this pioneering work showed that in a univariate survival analysis, the net proliferation rate, and the ratio ρ/D, which is related to the shape of the gradient of invading glioma cells outside the T1Gd imageable region, strongly correlated with survival. This significant modeling result showed that patient-specific PI model parameters allow assessment of survival independent of standard clinical approaches.

Resection

It is not clear whether glioma patients in whom a larger mass of the tumor is removed tend to do better prognostically than those patients receiving a biopsy (McGirt et al. 2008, 2009; Laws et al. 2003; Devaux et al. 1993). Further, predicting survival based solely on the extent of resection (EOR)

is ambiguous since it is difficult to quantitatively determine the percent of tumor removed due to the diffuse nature of gliomas, as not all tumor cells can be visualized through current imaging or histology (Harpold et al. 2007). The tumor's location in the brain also plays a significant role in determining how much of the tumor is resected. Large resections are avoided in cases where removal of more tumor region in critical parts of the brain may lead to a worse quality of life. For example, for tumors straddling the precentral gyrus, which is the cortical area involved in controlling most body motor functions, large resection would result in impaired movement control and execution. Thus, to quantitatively assess whether the EOR is related to survival requires other tools such as mathematical models.

Woodward et al. (1996) considered resection in the context of the spatially homogeneous PI model showing that even with varying extents of surgical resection, gliomas could not be completely "cured" due to the diffuse infiltration of malignant tumor cells throughout the brain. Building upon this idea, Swanson et al. (2008) considered glioma patients who had undergone either partial or near-total resection of the tumor and applied the patient-specific growth kinetic parameters D and ρ from the PI model to model and predict survival based on patient-specific virtual controls. Interestingly, survival correlated better with D and ρ than with the extent of resection. Thus, tumors with a higher propensity to diffuse and proliferate led to shorter survival regardless of the extent of resection (Swanson et al. 2008). Further assessment of the net diffusion and net proliferation parameters combined with the spatial location of gliomas suggests that these parameters are independent of tumor location (Szeto et al. 2009). These studies lead to a dominating hypothesis in glioma that the kinetic parameters of growth dictate patterns of tumor growth irrespective of location and may allow better prediction of survival than location-dependent surgical removal of the tumor.

Radiation Therapy

After surgery, external beam radiation therapy (XRT) is typically the second-line of treatment in the clinical management of gliomas. XRT targets the tumor mass not removed by surgery and has been shown to improve survival over other postoperative therapies (Erpolat et al. 2009; Bloor et al. 1962). However, XRT does not affect all patients equally: some patients respond better to XRT than others, and this phenomenon cannot be predicted clinically prior to treatment. Rockne et al 2009, combined classic

linear-quadratic radiobiological mathematical models of the delivery of and response to XRT to equation (1). When applying this model to patient-specific tumor evolution seen on MR imaging, Rockne et al. (2008b) found that the model may help predict which patients will respond better to XRT and to what degree each will respond. Further, this sheds light on the patient-specific tailoring of XRT dose to actual disease distribution as opposed to the one-size-fits-all philosophy currently applied clinically in XRT dose design for each patient's tumor.

Dionysiou et al. (2004) introduced a four-dimensional model that considers the effects of XRT on the growth of GBMs. This model incorporated sensitivity to radiation, genetic profile of tumors, and dose fractionation. Updated work on the model explored the effect of XRT on tumor and normal tissue to simulate fractionation doses (Stamatakos et al. 2007). While the model utilizes tumor size from patient MRI to apply radiation fields, it does not yet have the predictive capacity to suggest patient-specific tailoring of therapy, although because of the large number of parameters to be estimated a method of optimizing treatment is provided (Dionysiou et al. 2008).

Swanson et al. (2008) provided a means of distinguishing glioma patients that are sensitive or resistant to XRT by using PI model-defined, patient-specific virtual controls. Studying eight patients with GBM, Swanson et al. (2008) developed virtual controls using the PI model that predicted untreated patient-specific glioma growth. Patients received XRT as per the standard of care, whereas virtually, patient-specific glioma growth was simulated without treatment. Determining time to reach fatal tumor burden as defined by the T1Gd radius of 35 mm allowed assessment of survival if the patient received no treatment (virtual control). Swanson et al. (2008) compared actual survival after treatment with XRT to the survival predicted by the PI model. Results indicated that approximately half the population survived as predicted by the PI model suggesting that even with XRT, survival was not improved. The other half of the population survived twice as long as predicted by the PI model suggesting that this population had radio-sensitive tumors.

Advancing the modeling methodology, Rockne et al. (2009; Rockne et al. 2008b) proposed an extension of the PI model to incorporate the delivery and effect of XRT as quantified by the classic linear-quadratic model (Hall 1994) for radiation efficacy. This study presents the effect of changing dose delivery from the current clinical standard on a virtual case study. Results suggest that a low-frequency and high-dose delivery scheme

would be optimal in reducing the targeted tumor volume (Rockne et al. 2009). Further, for the extended model Rockne et al. show that the parameter of radiation sensitivity, α, can be predicted from ρ (patient-specific parameter of net proliferation in the PI model) prior to treatment, and can be applied to study XRT in virtual glioma patients that can be paralleled to clinical cases (Rockne 2008b). Powathil et al. (2007) described a similar reaction-diffusion model, however, their model did not estimate patient-specific parameters.

Other Therapies

Beyond surgery and radiation therapy, chemotherapy targeting aberrant cell-cycle activity or factors controlling neoangiogenesis among others is utilized to minimize tumor recurrence. Chemotherapeutic agents such as Temozolomide and Bevacizumab have been shown to improve patient survival (Erpolat et al. 2009; Nishikawa 2009; Zhang et al. 2009). However, survival for glioma patients still remains dismal and the incidence of drug-induced toxicity in patients is increased (Calabrese and Schlegel 2009). Mathematical modeling may shed light on the design of optimal chemotherapy dosing such that drug toxicity can be minimized and the attack on tumor cells maximized. Challenges include modeling the spatial and temporal drug delivery, along with simulating how drugs cross the blood–brain barrier (BBB).

Similar work by Eikenberry et al. (2009) using a reaction-diffusion model provides an initial framework of how mathematical modeling can be utilized to monitor effects of multiple treatments in virtual GBM patients, but only qualitatively ties model simulations to clinical data. A model developed by Tian et al. (2009) on the other hand provides a purely theoretical perspective on assessing the effects of therapy on glioma growth. Powathil et al. (2007) come closer to describing effects of chemotherapy by modifying the base model studied by Murray's group, by appending death terms to a log-kill model. Modeling radiotherapy and chemotherapy simultaneously,

this investigation reports the clinical result that chemotherapy with Temozolomide following XRT results in less neurotoxicity, and considers improving the targeting of tumor cells with concurrent Temozolomide and XRT, which is the current clinical practice (Powathil et al. 2007). This result, though in an early phase, promises further study and validation in the clinic.

Swanson et al. (Swanson et al. 2002a) compare a clinical case study to homogenous and heterogeneous models of drug delivery, which suggests that drug delivery is necessarily a function of the varying vascular density in brain tissue and thus accounts for the clinical observation of tumor reduction in some locations and continued growth in other regions of the tumor surroundings. A recent model (Hinow et al. 2009) based on the spatial dynamics of tumor–host interaction, incorporates the tumor microenvironment along with angiogenesis and suggests that the time course and spatial delivery of drugs needs to be considered, and supports Swanson's result from 2002. In addition, model simulations by Hinow et al. (2009) propose that chemotherapy may either heavily reduce the tumor mass or increase tumor growth substantially depending on how the drug interacts with both tumor and nontumor cells (Hinow et al. 2009). These results provide support for clinicians to plan out both the spatial and temporal effects of chemotherapeutic agents, again with the use of virtual controls and careful consideration of the spatial element of glioma disease distribution and response to therapy.

CAPTURING INFLUENCE OF TUMOR MICROENVIRONMENT ON GLIOMA GROWTH BY PARALLEL COMPARISON OF MRI AND PET

While clinically routine MRIs conducted serially provide information about changes to gross tumor anatomy over the scale of months, PET imaging provides a dynamic picture of information about the tumor on the molecular level, conferred through radiolabeled tracer activity monitored over minutes to hours (Ullrich et al. 2008). Two common PET radio tracers used in assessing brain tumors are: 18F-Fluoromisonidazole (FMISO), which detects hypoxia or regions of low oxygenation (Rajendran et al., 2006), and 3′-Deoxy-3'-[18F]-Fluorothymidine (FLT), which detects cell proliferation (Hatakeyama et al. 2008). Another common PET tracer used in the clinical management of gliomas is [18F]-Fluorodeoxyglucose (FDG), which is a marker of hyperglycolytic activity (Spence et al. 2004). Studies focusing on the clinical use of PET and MRI show that functional

imaging tends to aid diagnosis and treatment planning of brain tumors (Krohn et al. 2007; Spence et al. 2008) because these scans capture regions of aberrant activity in the tumor microenvironment.

Hypoxia Assessed with FMISO-PET

Hypoxia not only decreases the radiation sensitivity of tumor cells, but also contributes to tumor progression and drives selection pressure for more aggressive cancer phenotypes (Lunt et al. 2009; Sullivan and Graham 2007). Hypoxic burden assessed in vivo by FMISO-PET (Figure 16.4c) correlates significantly with decreased survival and shorter time to tumor progression (Swanson et al. 2009; Spence et al. 2008). Comparison of hypoxic burden with tumor abnormality observed in spatially registered T1Gd MRI suggests a spatial link between bulk tumor mass and hypoxia (Swanson et al. 2009).

Due to the spatial link between MRI and FMISO-PET, the Swanson group hypothesized that metrics of glioma growth as quantified by the PI model along with MRI-based parameters might shed light upon the aggressiveness determined by the presence of hypoxic burden. This was in fact the case, and they confirmed the link between hypoxia and biological aggressiveness quantified by the ratio ρ/D, where higher ρ/D corresponded to a more aggressive tumor growth (Szeto et al. 2009). While hypoxia is a well-known hallmark of aggressive behavior, this work displayed the first quantitative connection between hypoxia imaged by PET and anatomical tumor data imaged by MRI as well as the profound implication that a mathematical model-based metric could link the two in a patient-specific manner.

While the PI model has been validated and shown to be accurate for assessing anatomical tumor growth and survival, it does not account for the role of the tumor microenvironment. Incorporating nutrient availability and deprivation into glioma kinetics necessitates an extension of the PI model that considers hypoxic burden and its connection to normoxic (tumor cells sufficiently supplied with oxygen) and necrotic (tumor cells that have died due to anoxia) cells. The link between the tumor cell populations relates the presence of vasculature, development of new vessels (angiogenesis) as needed to continue growth, and the communication between tumor cells and vessels through angiogenic growth factors. Incorporating a heterogeneous cell population and capturing the dynamics of tumor cells through the angiogenic cascade, an extended model, denoted the proliferation-invasion-hypoxia-necrosis-angiogenesis

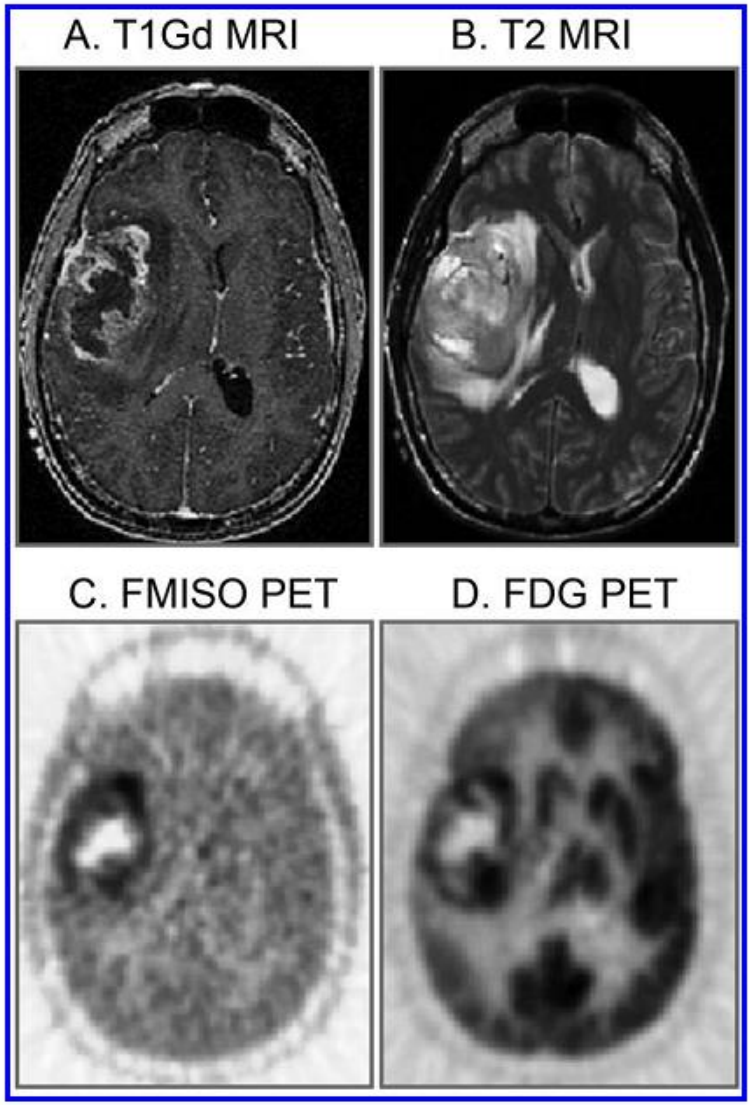

FIGURE 16.4 Panels A through D show a glioblastoma imaged in the axial plane on T1Gd-MRI, T2-MRI, FMISO-PET, and FDG-PET, respectively. The bright regions on the MRIs and the dark regions on the PETs represent tumor abnormality. In panel D, note that for an unprocessed FDG-PET, the gray matter contralateral to the glioma is isointense with the tumor abnormality making tumor identification challenging.

(PIHNA), is currently being investigated that builds upon the success of the PI model and is specifically designed to parallel MRI and PET imaging data (Swanson 2009; Harpold 2006b).

Hyperglycolysis Assessed with FDG-PET

FDG-PET, unlike FMISO-PET and FLT-PET is a clinically routine PET imaging modality, and indicates regions of hyperglycolysis (Figure 16.4d). Gray matter of the brain, however, demonstrates elevated levels of glycolysis relative to most normal body tissue, and even relative to other portions of the brain. This presents a challenge for differentiating regions of increased FDG signal intensity between the normal grey matter and that due to the tumor abnormality. Spence et al. (2004) investigated how to delineate tumor abnormality in FDG-PET using an ordinary differential equation based compartmental model for FDG metabolism kinetics. This study suggested that hyperactive tumor growth could be segmented visually and quantitatively from normal activity of gray matter by increasing the time interval between tracer delivery and PET acquisition (Spence et al. 2004). Additional studies considered patient-specific kinetic parameters derived from FDG-PET proved that different kinetics of glucose metabolism could aid in differentiating gliomas from other brain abnormalities such as lymphomas (Kimura et al. 2009). Further assessment of the abnormality seen on FDG-PET showed that this imaging modality served as a prognostic marker and could be utilized to evaluate response to therapy (Mankoff et al. 2007).

Since FDG-PET relays glucose metabolic activity in vivo, it can serve as a tool to assess the microenvironmental influence on tumor behavior. Harsh tumor microenvironment results from acidosis and hypoxia (Fang et al. 2008). In such conditions, better survival is conferred to those cancer cells that switch over to anaerobic respiration (glycolysis) from aerobic respiration (Gatenby et al. 2006). A recently proposed model of glioma growth applies game theory to capture the interaction between three distinct tumor phenotypes: autonomous growth, glycolysis, and invasion (Basanta et al. 2008). Results of this study implicate a switch to glycolysis in tumor cells to lead to more invasive tumor phenotypes, which agrees with biological hypothesis that cancerous cells display a switch from aerobic respiration to anaerobic respiration (Semenza et al. 2001; Gatenby et al. 2006). However, this model does not consider the spatial distribution of tumor cells and the interaction of the heterogeneous tumor cell population. Cellular automaton models exist for explaining tumor

growth spatially and agree with the game theory model results that harsh microenvironments select for more invasive phenotypes (Anderson et al. 2006). These models would suggest that reoxygenating tumor cells as a clinical therapeutic approach may prevent selection of highly invasive phenotypes. However, cellular automata or game theory models cannot be directly translated to monitor clinical tumor growth yet.

Tumor Proliferation Assessed with FLT-PET

The PI model currently utilizes volumetric measurements of tumor from two MRIs taken prior to any treatment to determine the parameters, D and ρ. Although, MRIs are clinically routine, in many instances two observations are not available pretreatment. FLT-PET (Figure 16.5C) conducted in a single day can capture dynamic hyperproliferative activity of brain tumors (Hatakeyama et al. 2008). This dynamic information in addition to one pretreat MRI showing anatomical tumor abnormality may overcome the need for another pretreat MRI in determining *D* and ρ for the PI model. A preliminary investigation by Harpold et al. looked at how the cellular proliferation rate in tumor versus nontumor cells could be separated. Voxel data from FLT-PET was utilized as input to generate parametric maps that translated to parameters for a compartmental kinetic model of FLT metabolism (Harpold et al. 2006a). This research is still in its early phase since the population of patients receiving FLT-PET, an image modality still in clinical trials, is a fraction of those receiving MRIs.

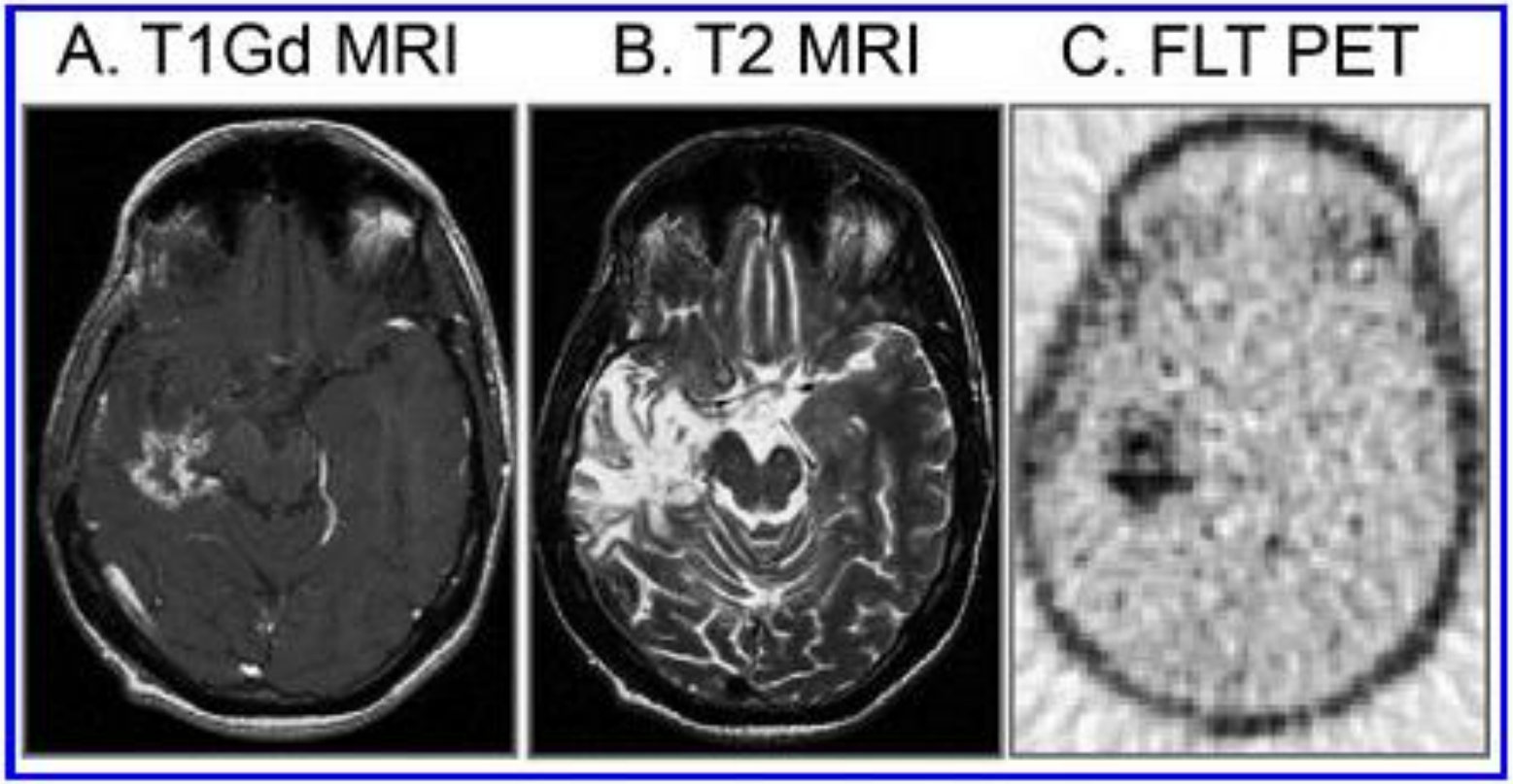

FIGURE 16.5 Panels A through C show a glioblastoma imaged in the axial plane on T1Gd-MRI, T2-MRI and FLT-PET, respectively. Note that the FLT-PET is a summed image of FLT activity recorded dynamically.

However, future studies are necessary to assess if D and ρ from combined FLT-PET and MRI at one time-point can be successfully applied to the PI model.

DEVELOPING MULTISCALE MODELS OF GLIOMAS FROM ANIMAL EXPERIMENTAL MODELS

New approaches aimed at resolving the challenges of conventional therapy to treat GBMs lie in understanding how these tumors originate. One hypothesis in tumorigenesis suggests that progenitor cells, which are precursors to glial cells, may be recruited to the heterogeneous population of brain tumor cells via platelet-derived growth factor (PDGF), a signaling protein with increasing evidence of involvement in brain tumors (Assanah et al. 2006; Shih et al. 2004). This pioneering work showed that injecting fluorescently-labeled retrovirus expressing human PDGF into the white matter of genetically normal adult rats resulted in the rats rapidly developing tumors, which appeared to be identical on histology and on MRI to human GBMs (Assanah et al. 2006, 2009). Assessing tumor cell populations through immunofluorescence analysis 14 days postinjection (DPI) of the retrovirus showed that less than 20% of the malignant mass consisted of the retrovirus-infected cells, and the tumor primarily comprised glial progenitors, which exhibited similar growth kinetics as retrovirus-infected tumor cells (Assanah et al. 2006). This experimental research suggested that simple overexpression of PDGF resulted in growth of a GBM-appearing abnormality in a previously disease-free brain. Moreover, the results pointed to a novel hypothesis for tumorigenesis: normal progenitor cells in the tumor periphery are recruited to the tumor mass through paracrine signaling of PDGF.

Results from in vivo experiments on rats highlighted a new avenue of glioma modeling. Capturing the microscopic interaction between tumor cells and normal progenitor cells via PDGF, while still modeling macroscopic diffusive and proliferative growth of the tumor, necessitated the development of a multiscale model. Like the PIHNA model, this model builds upon the success of the PI model and uses a reaction-diffusion continuum approach and incorporates two cell populations—the retrovirus infected tumor cells and uninfected glial progenitor cells—and looks at the molecular interaction between these populations via PDGF as illustrated in a biological schematic in Figure 16.6. Currently, this model is being studied to develop virtual controls that can provide simulations of both tissue histology and tumor appearance on MRIs (Massey et al. 2009).

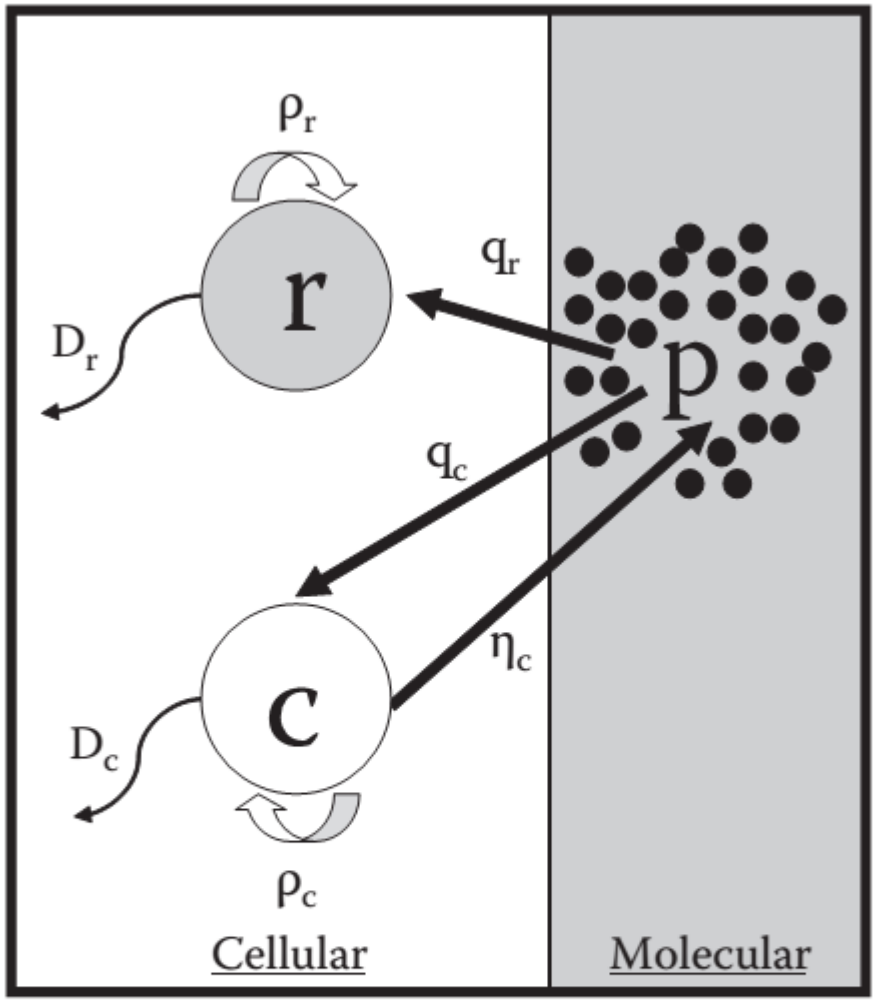

FIGURE 16.6 This schematic shows the hypothesized connection between recruited or uninfected glial progenitor cells (r) and infected tumor cells (c) that serves as a base for the multiscale model of tumorigenesis. Infected cells (c) secrete PDGF (p) at rate η_c in the extracellular space compartment. Via paracrine signaling, these ligands stimulate both the r and c cell populations to proliferate and migrate in a dose-dependent manner. The consumption of p by r and c in the process occurs at rates q_r and q_c, respectively, resulting in migration rates D_r and D_c, and proliferation rates ρ_r and ρ_c.

Such simulations can be compared to histological and MRI data on rats and can provide a channel to connect experimental animal models to in vivo human imaging data. Further, such multiscale models based in animal experimentation provide novel tools for bridging experimental results to human data by providing some assessment of the reasonability of the biological mechanism described.

DISCUSSION

The past few years have seen a surge of investigations in the mathematical modeling of gliomas. In this chapter, we have provided a glance at how mathematical modeling of gliomas relates to the clinical reality of brain tumor assessment. Multiple approaches exist to model glioma growth from the microscopic to the macroscopic scales. We specifically focus on the reaction-diffusion continuum models (PI, PIHNA, PDGF) as they come the closest to informing clinical reality because they can (a) be made specific to patients, thereby providing virtual controls of glioma growth, and (b) parallel clinical tools are utilized to assess gliomas such as MRI and PET imaging, and therefore show the highest promise of being clinically informative. However, quantitatively assessing the biological basis of glioma behavior necessitates both discrete and continuous modeling approaches, which can inform new areas of experimentation and modeling with the goal of generating tools for clinical use. Future directions of glioma modeling look towards the development of mathematical models that can be applied in optimizing glioma therapy, that can utilize PET imaging to extract biochemical parameters for reproducing the tumor microenvironment and parallel patient-specific PET scans, and that can connect analysis of animal-based experimentation to the clinical scale.

ACKNOWLEDGMENTS

We gratefully acknowledge the McDonnell Foundation, the Academic Pathology Fund, and the NIH (R01 NS060752, P01 CA42045) for their generous support.

REFERENCES

Alvord, E. C., Jr., and K. R. Swanson. 2007. Using mathematical modeling to predict survival of low-grade gliomas. *Ann Neurol* 61 (5):496; author reply 496–7.

Anderson, A. R., A. M. Weaver, P. T. Cummings, and V. Quaranta. 2006. Tumor morphology and phenotypic evolution driven by selective pressure from the microenvironment. *Cell* 127:905–15.

Assanah, M. C., J. N. Bruce, S. O. Suzuki, A. Chen, J. E. Goldman, and P. Canoll. 2009. PDGF stimulates the massive expansion of glial progenitors in the neonatal forebrain. *Glia* 57:1835–47.

Assanah, M., R. Lochhead, A. Ogden, J. Bruce, J. Goldman, and P. Canoll. 2006. Glial progenitors in adult white matter are driven to form malignant gliomas by platelet-derived growth factor-expressing retroviruses. *J Neurosci* 26 (25):6781–90.

Basanta, D., M. Simon, H. Hatzikirou, and A. Deutsch. 2008. Evolutionary game theory elucidates the role of glycolysis in glioma progression and invasion. *Cell Prolif* 41 (6):980–7.

Bloor, R. J., A. W. Templeton, and R. S. Quick. 1962. Radiation therapy in the treatment of intracranial tumors. *Am J Roentgenol Radium Ther Nucl Med* 87:463–72.

Bondiau, P., O. Clatz, M. Sermesant, P. Marcy, H. Delingette, M. Frenay, and N. Ayache. 2008. Biocomputing: numerical simulation of glioblastoma growth using diffusion tensor imaging. *Phys Med Biol* 53:879–93.

Burnet, N. G., A. G. Lynch, S. J. Jefferies, S. J. Price, P. H. Jones, N. M. Antoun, J. H. Xuereb, and U. Pohl. 2007. High grade glioma: imaging combined with pathological grade defines management and predicts prognosis. *Radiother Oncol* 85 (3):371–8.

Calabrese, P., and U. Schlegel. 2009. Neurotoxicity of treatment. *Recent Results Cancer Res* 171:165–74.

Chaichana, K. L., M. J. McGirt, A. Niranjan, A. Olivi, P. C. Burger, and A. Quinones-Hinojosa. 2009. Prognostic significance of contrast-enhancing low-grade gliomas in adults and a review of the literature. *Neurol Res* 31:931–9.

Clatz, O., M. Sermesant, P. Y. Bondiau, H. Delingette, S. K. Warfield, G. Malandain, and N. Ayache. 2005. Realistic simulation of the 3-D growth of brain tumors in MR images coupling diffusion with biomechanical deformation. *IEEE Trans Med Imaging* 24 (10):1334–46.

Collins, D. L., A. P. Zijdenbos, V. Kollokian, J. G. Sled, N. J. Kabani, C. J. Holmes, and A. C. Evans. 1998. Design and construction of a realistic digital brain phantom. *IEEE Trans Med Imaging* 17 (3):463–8.

Cocosco, C. A., V. Kollokian, Kwan R. K.-S., and A. C. Evans. 1997. Brainweb: online interface to a 3D simulated brain database. *Neuroimage* 5:S425.

Deroulers, C., M. Aubert, M. Badoual, and B. Grammaticos. 2009. Modeling tumor cell migration: From microscopic to macroscopic models. *Phys Rev E Stat Nonlin Soft Matter Phys* 79 (3 Pt 1):031917.

Devaux, B. C., J. R. O'Fallon, and P. J. Kelly. 1993. Resection, biopsy, and survival in malignant glial neoplasms: a retrospective study of clinical parameters, therapy, and outcome. *J Neurosurg* 78 (5):767–75.

Dionysiou, D. D., G. S. Stamatakos, D. Gintides, N. Uzunoglu, and K. Kyriaki. 2008. Critical parameters determining standard radiotherapy treatment outcome for glioblastoma multiforme: a computer simulation. *Open Biomed Eng J* 2:43–51.

Dionysiou, D. D., G. S. Stamatakos, N. K. Uzunoglu, K. S. Nikita, and A. Marioli. 2004. A four-dimensional simulation model of tumour response to radiotherapy in vivo: parametric validation considering radiosensitivity, genetic profile and fractionation. *J Theor Biol* 230 (1):1–20.

Eikenberry, S. E., T. Sankar, M. C. Preul, E. J. Kostelich, C. J. Thalhauser, and Y. Kuang. 2009. Virtual glioblastoma: growth, migration and treatment in a three-dimensional mathematical model. *Cell Prolif* 42 (4):511–28.

Erpolat, O. P., M. Akmansu, F. Goksel, H. Bora, E. Yaman, and S. Buyukberber. 2009. Outcome of newly diagnosed glioblastoma patients treated by radiotherapy plus concomitant and adjuvant temozolomide: a long-term analysis. *Tumori* 95 (2):191–7.

Fang, J. S., R. D. Gillies, and R. A. Gatenby. 2008. Adaptation to hypoxia and acidosis in carcinogenesis and tumor progression. *Semin Cancer Biol* 18 (5):330–7.

Gatenby, R. A., E. T. Gawlinski, A. F. Gmitro, B. Kaylor, and R. J. Gillies. 2006. Acid-mediated tumor invasion: a multidisciplinary study. *Cancer Res* 66 (10):5216–23.

Hall, E. 1994. *Radiobiology for the Radiologist*. 4th ed. Philadelphia: J.B. Lippincott Company.

Harpold, H. L., E. C. Alvord, Jr., and K. R. Swanson. 2007. The evolution of mathematical modeling of glioma proliferation and invasion. *J Neuropathol Exp Neurol* 66 (1):1–9.

Harpold, H. L. P., P. Vicini, and K. R. Swanson. 2006a. Kinetic modeling of FLT-PET to generate parametric maps of proliferation. *J Undergraduate Res Bioeng* 6 (1):49–68.

Harpold, H. L. P., Anderson, A. R. A., Alvord, E. C., Jr., and Swanson, K. R. 2006b. Simulating low and high-grade human gliomas: an in silico model integrating the angiogenic cascade. Paper read at Society for Neuro-Oncology.

Hatakeyama, T., N. Kawai, Y. Nishiyama, Y. Yamamoto, Y. Sasakawa, T. Ichikawa, and T. Tamiya. 2008. 11C-methionine (MET) and 18F-fluorothymidine (FLT) PET in patients with newly diagnosed glioma. *Eur J Nucl Med Mol Imaging* 35 (11):2009–17.

Hatzikirou, H., A. Deutsch, C. Schaller, M. Simon, and K. R. Swanson. 2005. Mathematical modelling of glioblastoma tumour development: a review. *Math Models Methods Appl Sci*, 11:1779–1794.

Hatzikirou, H., and A. Deutsch. 2008. Cellular automata as microscopic models of cell migration in heterogeneous environments. *Curr Top Dev Biol* 81:401–34.

Hinow, P., P. Gerlee, L. J. McCawley, V. Quaranta, M. Ciobanu, S. Wang, J. M. Graham, B. P. Ayati, J. Claridge, K. R. Swanson, M. Loveless, and A. R. Anderson. 2009. A spatial model of tumor-host interaction: application of chemotherapy. *Math Biosci Eng* 6 (3):521–46.

Hogea, C., C. Davatzikos, and G. Biros. 2008. An image-driven parameter estimation problem for a reaction-diffusion glioma growth model with mass effects. *J Math Biol* 56 (6):793–825.

Huang, S., D. Vader, Z. Wang, A. Stemmer-Rachamimov, D. A. Weitz, G. Dai, B. R. Rosen, and T. S. Deisboeck. 2008. Using magnetic resonance microscopy to study the growth dynamics of a glioma spheroid in collagen I: a case study. *BMC Med Imaging* 8:3.

Jbabdi, S., E. Mandonnet, H. Duffau, L. Capelle, K. R. Swanson, M. Pelegrini-Issac, R. Guillevin, and H. Benali. 2005. Simulation of anisotropic growth of low-grade gliomas using diffusion tensor imaging. *Magn Reson Med* 54 (3):616–24.

Kimura, N., Y. Yamamoto, R. Kameyama, T. Hatakeyama, N. Kawai, and Y. Nishiyama. 2009. Diagnostic value of kinetic analysis using dynamic 18F-FDG-PET in patients with malignant primary brain tumor. *Nucl Med Commun* 30 (8):602–9.

Krohn, K. A., F. O'Sullivan, J. Crowley, J. F. Eary, H. M. Linden, J. M. Link, D. A. Mankoff, M. Muzi, J. G. Rajendran, A. M. Spence, and K. R. Swanson. 2007. Challenges in clinical studies with multiple imaging probes. *Nucl Med Biol* 34 (7):879–85.

Laws, E. R., I. F. Parney, W. Huang, F. Anderson, A. M. Morris, A. Asher, K. O. Lillehei, M. Bernstein, H. Brem, A. Sloan, M. S. Berger, and S. Chang. 2003. Survival following surgery and prognostic factors for recently diagnosed malignant glioma: data from the Glioma Outcomes Project. *J Neurosurg* 99 (3):467–73.

Louis, D.N., H. Ohgaki, O. D. Wiestler, and W. K. Cavenee. 2007. *WHO Classification of Tumours of the Central Nervous System*. Edited by D. N. Louis, H. Ohgaki, O. D. Wiestler and W. K. Cavenee. 4th ed. Geneva, Switzerland: Renouf Publishing Co. Ltd.

Lunt, S. J., N. Chaudary, and R. P. Hill. 2009. The tumor microenvironment and metastatic disease. *Clin Exp Metastasis* 26 (1):19–34.

Mandonnet, E., J. Y. Delattre, M. L. Tanguy, K. R. Swanson, A. F. Carpentier, H. Duffau, P. Cornu, R. Van Effenterre, E. C. Alvord, Jr., and L. Capelle. 2003. Continuous growth of mean tumor diameter in a subset of grade II gliomas. *Ann Neurol* 53 (4):524–8.

Mandonnet, E., J. Pallud, O. Clatz, L. Taillandier, E. Konukoglu, H. Duffau, and L. Capelle. 2008. Computational modeling of the WHO grade II glioma dynamics: principles and applications to management paradigm. *Neurosurg Rev* 31 (3):263–9.

Mankoff, D. A., J. F. Eary, J. M. Link, M. Muzi, J. G. Rajendran, A. M. Spence, and K. A. Krohn. 2007. Tumor-specific positron emission tomography imaging in patients: [18F] fluorodeoxyglucose and beyond. *Clin Cancer Res* 13 (12):3460–9.

Massey, S., Canoll, P., and Swanson, K. R. 2009. Paracrine PDGF signaling and progression in experimental gliomas. Paper read at the International Conference on Mathematical Biology and Annual Meeting of the Society for Mathematical Biology., at the University of British Columbia.

McGirt, M. J., K. L. Chaichana, F. J. Attenello, J. D. Weingart, K. Than, P. C. Burger, A. Olivi, H. Brem, and A. Quinones-Hinojosa. 2008. Extent of surgical resection is independently associated with survival in patients with hemispheric infiltrating low-grade gliomas. *Neurosurgery* 63 (4):700–7; author reply 707–8.

McGirt, M. J., K. L. Chaichana, M. Gathinji, F. J. Attenello, K. Than, A. Olivi, J. D. Weingart, H. Brem, and A. R. Quinones-Hinojosa. 2009. Independent association of extent of resection with survival in patients with malignant brain astrocytoma. *J Neurosurg* 110 (1):156–62.

Michotte, A., B. Neyns, C. Chaskis, J. Sadones, and P. In 't Veld. 2004. Neuropathological and molecular aspects of low-grade and high-grade gliomas. *Acta Neurol Belg* 104 (4):148–53.

Murray, J. D. 2003. *Mathematical Biology II. Spatial Models and Biological Applications*. 3 ed. 2 vols. Vol. 2. New York: Springer-Verlag.

Nishikawa, R. 2009. Treatment of glioma with temozolomide. *Brain Nerve* 61 (7):849–54.

Pallud, J., E. Mandonnet, H. Duffau, M. Kujas, R. Guillevin, D. Galanaud, L. Taillandier, and L. Capelle. 2006. Prognostic value of initial magnetic resonance imaging growth rates for World Health Organization grade II gliomas. *Ann Neurol* 60 (3):380–3.

Powathil, G., M. Kohandel, S. Sivaloganathan, A. Oza, and M. Milosevic. 2007. Mathematical modeling of brain tumors: effects of radiotherapy and chemotherapy. *Phys Med Biol* 52 (11):3291–306.

Rajendran, J. G., Hendrickson, K. R., Spence, A. M., Muzi, M., Krohn, K. A., and Mankoff, D. A. 2006. Hypoxia imaging–directed radiation treatment planning, *Eur J Nucl Mol Imaging* 33 Suppl 13: 44–53.

Rockne, R., E. C. Alvord, Jr., J. K. Rockhill, and K. R. Swanson. 2009. A mathematical model for brain tumor response to radiation therapy. *J Math Biol* 58 (4–5):561–78.

Rockne, R., E. C. Alvord, P. Reed, and K. R. Swanson. 2008a. Modeling the growth and invasion of gliomas, from simple to complex: the Goldie Locks paradigm. Paper read at BIOMAT, at Rio de Janeiro.

Rockne, R., J. K. Rockhill, M. Mrugala, A. M. Spence, I. Kalet, K. Hendrickson, A. Lai, T. Cloughesy, E. C. Alvord, Jr., and K. R. Swanson. 2010. Predicting the efficacy of radiotheraphy in individual glioblastoma patients *in vivo*: a mathematical modeling approach *Phys Med Biol* 55: 3271–85.

Semenza, G. L., D. Artemov, A. Bedi, Z. Bhujwalla, K. Chiles, D. Feldser, E. Laughner, R. Ravi, J. Simons, P. Taghavi, and H. Zhong. 2001. "The metabolism of tumours": 70 years later. *Novartis Found Symp* 240:251–60; discussion 260–4.

Shih, A. H., C. Dai, X. Hu, M. K. Rosenblum, J. A. Koutcher, and E. C. Holland. 2004. Dose-dependent effects of platelet-derived growth factor-B on glial tumorigenesis. *Cancer Res* 64 (14):4783–9.

Sodt, R., R. Rockne, K. R. Swanson, I. Kalet. 2009. Simulation of anisotropic growth of gliomas using diffusion tensor imaging. International Conference on Mathematical Biology and Annual Meeting of the Society for Mathematical Biology, July 2009.

Spence, A. M., M. Muzi, D. A. Mankoff, S. F. O'Sullivan, J. M. Link, T. K. Lewellen, B. Lewellen, P. Pham, S. Minoshima, K. Swanson, and K. A. Krohn. 2004. 18F-FDG PET of gliomas at delayed intervals: improved distinction between tumor and normal gray matter. *J Nucl Med* 45 (10):1653–9.

Spence, A. M., M. Muzi, K. R. Swanson, F. O'Sullivan, J. K. Rockhill, J. G. Rajendran, T. C. H. Adamsen, J. M. Link, P. E. Swanson, K. J. Yagle, R. C. Rostomily,

D. L. Silbergeld, and K. Krohn. 2008. Regional hypoxia in glioblastoma multiforme quantified with [18F]fluoromisonidazole positron emission tomography before radiotherapy: correlation with time to progression and survival. *Clin Cancer Res* 14 (9):2623–30.

Stadlbauer, A., E. Polking, O. Prante, C. Nimsky, M. Buchfelder, T. Kuwert, R. Linke, M. Doelken, and O. Ganslandt. 2009. Detection of tumour invasion into the pyramidal tract in glioma patients with sensorimotor deficits by correlation of (18)F-fluoroethyl-L: -tyrosine PET and magnetic resonance diffusion tensor imaging. *Acta Neurochir (Wien)* 151 (9):1061–9.

Stamatakos, G., V. P. Antipas, and N. K. Ozunoglu. 2007. A patient-specific in vivo tumor and normal tissue model for prediction of the response to radiotherapy. *Methods Inf Med* 46 (3):367–75.

Sullivan, R., and C. H. Graham. 2007. Hypoxia-driven selection of the metastatic phenotype. *Cancer Metastasis Rev* 26 (2):319–31.

Swanson, K. R. 1999. Mathematical Modeling of the Growth and Control of Tumors. PhD Thesis, University of Washington, Seattle, WA.

_____. 2008. Quantifying glioma cell growth and invasion in vitro. *Math Computer Modeling* 47:638–48.

Swanson, K. R., E. C. Alvord, Jr., and J. D. Murray. 2000. A quantitative model for differential motility of gliomas in grey and white matter. *Cell Prolif* 33 (5):317–29.

_____. 2002a. Quantifying efficacy of chemotherapy of brain tumors with homogeneous and heterogeneous drug delivery. *Acta Biotheoretica* 50 (4):223–37.

_____. 2002b. Virtual brain tumours (gliomas) enhance the reality of medical imaging and highlight inadequacies of current therapy. *Br J Cancer* 86 (1):14–18.

Swanson, K. R., C. Bridge, J. D. Murray, and E. C. Alvord, Jr. 2003. Virtual and real brain tumors: using mathematical modeling to quantify glioma growth and invasion. *J Neurol Sci* 216 (1):1–10.

Swanson, K. R., G. Chakraborty, C. H. Wang, R. Rockne, H. L. Harpold, M. Muzi, T. C. Adamsen, K. A. Krohn, and A. M. Spence. 2009. Complementary but distinct roles for MRI and 18F-fluoromisonidazole PET in the assessment of human glioblastomas. *J Nucl Med* 50 (1):36–44.

Swanson, K. R., H. L. Harpold, D. L. Peacock, R. Rockne, C. Pennington, L. Kilbride, R. Grant, J. M. Wardlaw, and E. C. Alvord, Jr. 2008a. Velocity of radial expansion of contrast-enhancing gliomas and the effectiveness of radiotherapy in individual patients: a proof of principle. *Clin Oncol (R Coll Radiol)* 20 (4):301–8.

Swanson, K. R., R. C. Rostomily, and E. C. Alvord, Jr. 2008b. A mathematical modelling tool for predicting survival of individual patients following resection of glioblastoma: a proof of principle. *Br J Cancer* 98 (1):113–9.

Swanson, K. R. 2009. Bridging from Anatomic Imaging to Molecular Imaging through Multi-scale Models for Brain Tumor Growth and Invasion. Paper read at International Conference on Mathematical Biology and Annual Meeting of The Society for Mathematical Biology at University of British Columbia.

Swanson, K. R., E. C. Alvord, Jr., and J. D. Murray. 2004. Dynamics of a model for brain tumors reveals a small window for therapeutic intervention. *Discrete Cont Dyn—B* 4 (1):289–95.

Szeto, M. D., G. Chakraborty, J. Hadley, R. Rockne, M. Muzi, E. C. Alvord, Jr., K. A. Krohn, A. M. Spence, and K. R. Swanson. 2009a. Quantitative metrics of net proliferation and invasion link biological aggressiveness assessed by MRI with hypoxia assessed by FMISO-PET in newly diagnosed glioblastomas. *Cancer Res* 69 (10):4502–9.

Szeto, M., Rockne, R., and Swanson, K. R. 2009b. Anatomic Variation in Quantitative Measures of Glioma Aggressiveness. Paper read at International Conference on Mathematical Biology and Annual Meeting of the Society of Mathematical Biology., at University of British Columbia.

Tanaka, M. L., W. Debinski, and I. K. Puri. 2009. Hybrid mathematical model of glioma progression. *Cell Prolif* 42 (5):637–46.

Tian, J. P., A. Friedman, J. Wang, and E. A. Chiocca. 2009. Modeling the effects of resection, radiation and chemotherapy in glioblastoma. *J Neurooncol* 91 (3):287–93.

Tracqui, P., G. C. Cruywagen, D. E. Woodward, G. T. Bartoo, J. D. Murray, and E. C. Alvord, Jr. 1995. A mathematical model of glioma growth: the effect of chemotherapy on spatio-temporal growth. *Cell Prolif* 28 (1):17–31.

Ullrich, R. T., L. W. Kracht, and A. H. Jacobs. 2008. Neuroimaging in patients with gliomas. *Semin Neurol* 28 (4):484–94.

Wang, C. H., J. K. Rockhill, M. Mrugala, D. L. Peacock, A. Lai, K. Jusenius, J. M. Wardlaw, T. Cloughesy, A. M. Spence, R. Rockne, E. C. Jr. Alvord, and K. R. Swanson. 2009. Prognostic significance of growth kinetics in newly diagnosed glioblastomas revealed by combining serial imaging with a novel bio-mathematical model. *Cancer Res*. 69:9133–40.

Welsh, J. W., R. K. Ellsworth, R. Kumar, K. Fjerstad, J. Martinez, R. B. Nagel, J. Eschbacher, and B. Stea. 2009. Rad51 protein expression and survival in patients with glioblastoma multiforme. *Int J Radiat Oncol Biol Phys* 74 (4):1251–5.

Woodward, D. E., J. Cook, P. Tracqui, G. C. Cruywagen, J. D. Murray, and E. C. Alvord, Jr. 1996. A mathematical model of glioma growth: the effect of extent of surgical resection. *Cell Prolif* 29 (6):269–88.

Zhang, W., X. G. Qiu, B. S. Chen, S. W. Li, Y. Cui, H. Ren, and T. Jiang. 2009. Antiangiogenic therapy with Bevacizumab in recurrent malignant gliomas: analysis of the response and core pathway aberrations. *Chin Med J (Engl)* 122 (11):1250–4.

Further Suggested Reading

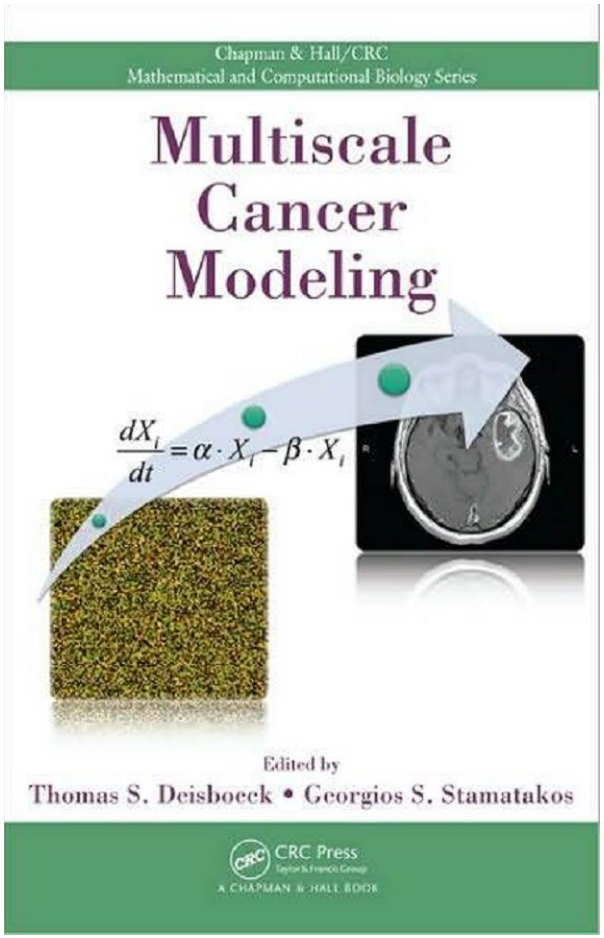

CRC Press
Taylor & Francis Group
6000 Broken Sound Parkway NW, Suite 300
Boca Raton, FL 33487-2742

© 2011 by Taylor and Francis Group, LLC
CRC Press is an imprint of Taylor & Francis Group, an Informa business

CHAPTER 17

Personalization of Reaction-Diffusion Tumor Growth Models in MR Images

Application to Brain Gliomas Characterization and Radiotherapy Planning

Ender Konukoglu, Olivier Clatz,
Hervé Delingette, and Nicholas Ayache

385

ΓΕΝΙΚΗ ΠΟΛΥΚΛΙΜΑΚΩΤΗ ΠΡΟΣΟΜΟΙΩΣΗ ΑΣΘΕΝΕΙΩΝ ΚΑΙ *IN SILICO* ΙΑΤΡΙΚΗ

Multi-scale integrative computational model the human atria and torso: a platform for the investigation of atrial fibrillation

Michael A Colman[1], Jonathan Stott[1], Oleg V Aslanidi[2], Phillip Langely[3], Henggui Zhang[1]

[1]*The University of Manchester,* [2]*King's College London, London,* [3]*University of Newcastle*

Correspondence: henggui.zhang@manchester.ac.uk, 0044161 306 3966, Oxford Road, M13 9PL, UK

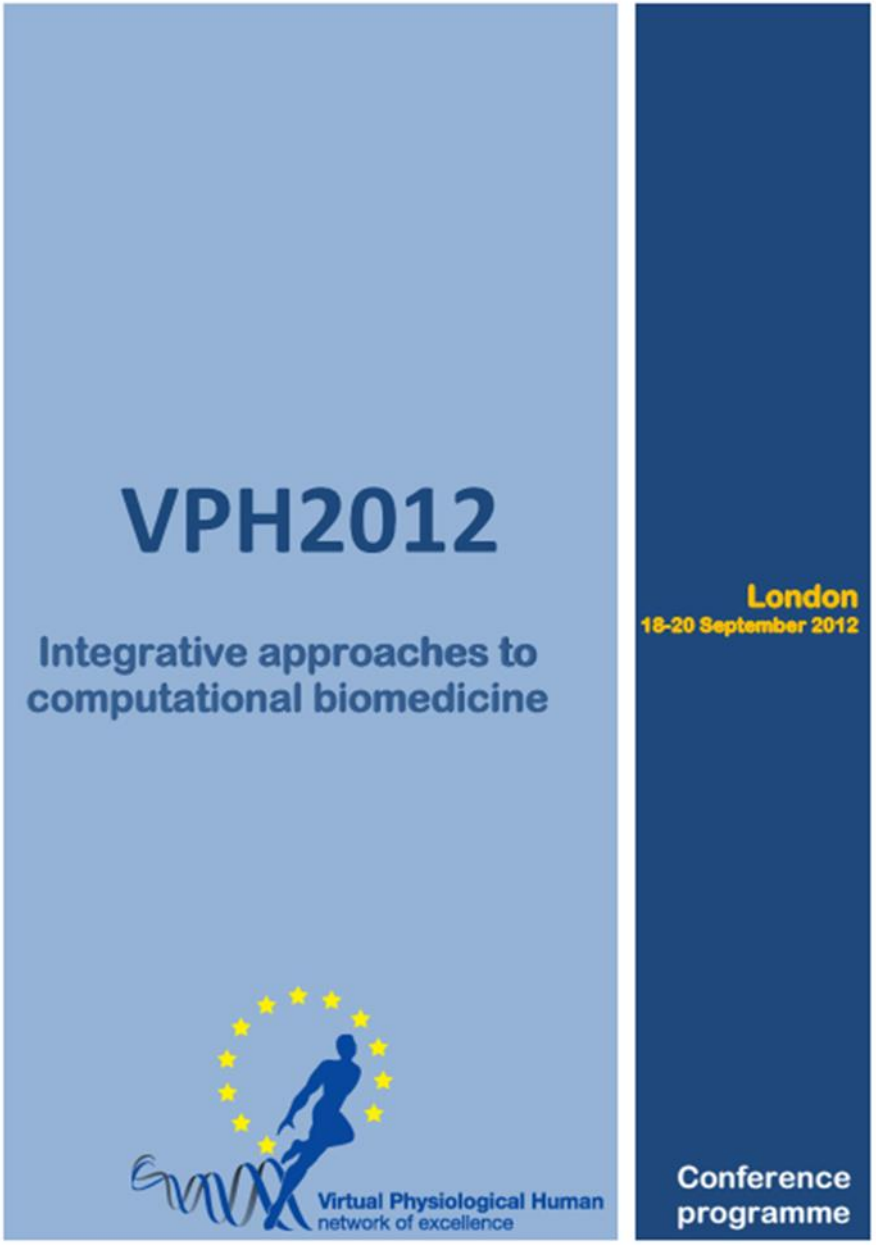
VPH2012
Integrative approaches to computational biomedicine
Virtual Physiological Human
network of excellence
London
18-20 September 2012
Conference programme

PROCEEDINGS-VPH2012_INTEGRATIVE_APPROACHES_TO_COMPUTATIONAL_BIOMEDICINE-LONDON_CONF_2012.pdf PAGE **289**/488 (PLEASE USE THE PDF PAGE COUNTER)

Multi-scale integrative computational model the human atria and torso: a platform for the investigation of atrial fibrillation

Michael A Colman[1], Jonathan Stott[1], Oleg V Aslanidi[2], Phillip Langely[3], Henggui Zhang[1]

[1]*The University of Manchester,* [2]*King's College London, London,* [3]*University of Newcastle*

Correspondence: henggui.zhang@manchester.ac.uk, 0044161 306 3966, Oxford Road, M13 9PL, UK

I. INTRODUCTION

Atrial arrhythmias, including atrial fibrillation (AF), are characterised by irregular and rapid electrical activation of the atria. AF are the most common cardiac diseases and can lead to heart failure, stroke and even death (1). The mechanisms underlying the initiation and sustenance of AF, however, are incompletely understood. The human atria are electrically heterogeneous and structurally anisotropic. Dramatic regional differences in atrial action potential (AP) morphology and duration have been observed in both human and animal models (2). The fibrous structure of the atria also shows far less organization than in the ventricles. In this study we have developed a 3D model of the human atria and body surface ECG to investigate the underlying mechanisms of AF.

II. METHODS

The multi scale model of the human atria involved mapping previously developed heterogeneous single cell models for the AP (3) onto their respective regions of the atria (Fig 1. A, B). A recently reconstructed model for the human SAN geometry, fibre orientation and AP (4) was incorporated into the 3D atrial model (Fig 1. A, B). This model was then placed inside a torso geometry mesh (5) and the forward problem was solved by the use of a boundary element method (BEM) in order to simulate realistic ECG P-waves (Fig 1. C). Excitation propagation was simulated by using a mono-domain reaction-diffusion partial differential equation with use of higher order numerical solvers and an anisotropy ratio for conduction longitudinal and transverse to fibres of 10:1, respectively.

Re-entrant excitation wave (mimicking AF) was initiated by an s1-s2 pacing protocol: two s1 stimuli were applied at a cycle length of 350ms, followed by an s2 stimulus applied after 250ms. The stimulation site was selected at a region of both high electrical heterogeneity and anisotropy, at the junction between the crista terminalis (CT) and the pectinate muscles (PMs) in the right atrium. The model is then left to run for 10s.

The atrial model was validated by comparing atrial activation patterns to experimental data in both normal (6) and abnormal (3,7) conditions. The BSP model was validated by directly comparing the simulated data with experimental BSP maps (8) and ECG P-waves under normal conditions.

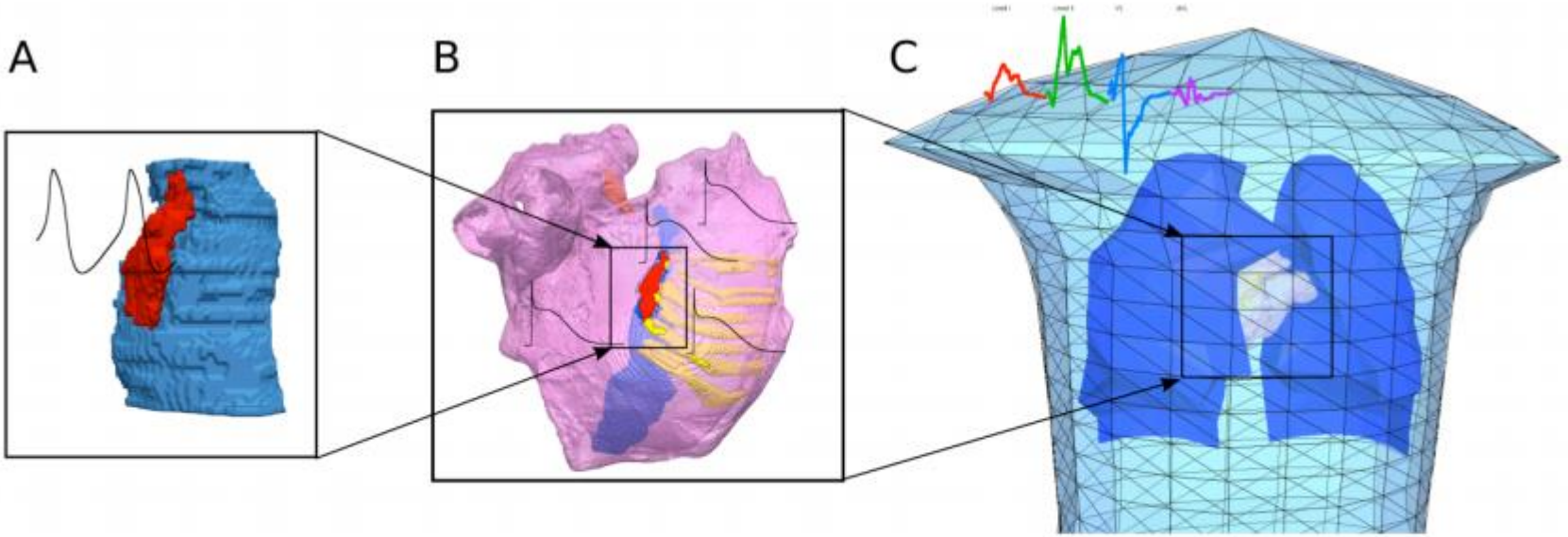

Figure 1. (A) Human sinoatrial node (SAN) geometry with representative AP displayed. (B) 3D heterogeneous anatomical model for the human atria with representative APs displayed over their respective regions. The SAN from A is incorporated into this model. (C) The 3D torso mesh model used to simulate the BSP, shown with the lungs and the orientation of the atria (shown in B). Representative ECG P-waves are displayed

Michael A Colman[1], Jonathan Stott[1], Oleg V Aslanidi[2], Phillip Langely[3], Henggui Zhang[1]

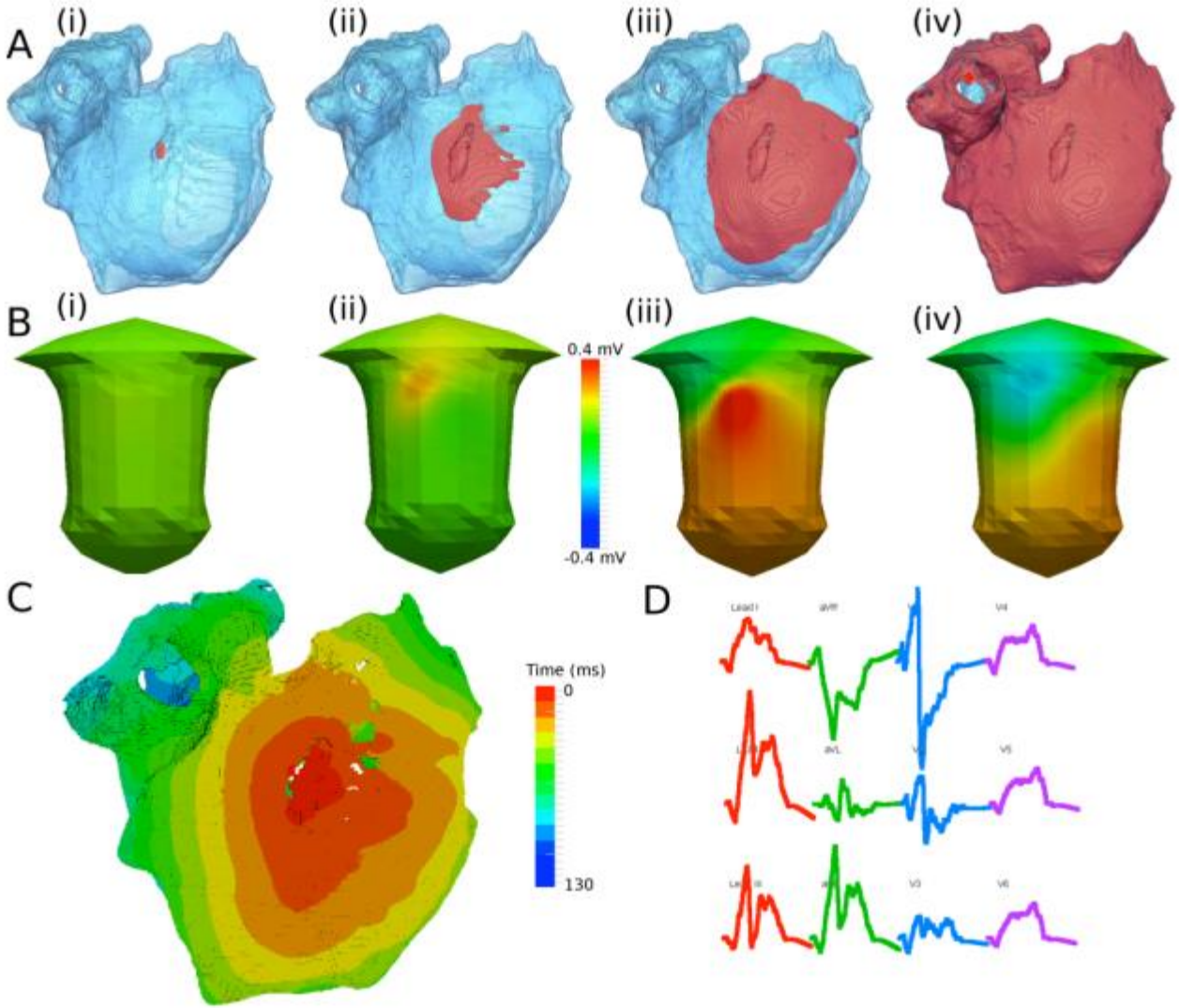

Figure 2. (A) Atrial excitation propagation. (B) BSP snapshots under normal conditions taken at i) 5 ms; ii) 25 ms; iii) 40 ms; and iv) 110 ms after the SAN initiates excitation. (C) Atrial activation pattern under normal conditions. (D) Corresponding P-wave profiles.

Michael A Colman[1], Jonathan Stott[1], Oleg V Aslanidi[2], Phillip Langely[3], Henggui Zhang[1]

III. RESULTS

Fig. 2 shows the simulated electrical excitation conduction under the normal condition. Excitation is initiated in the centre of the SAN (Fig 2Ai). At the corresponding time, the BSP is largely uniform due to the lack of a propagating wave-front (Fig 2Bi). At 20ms, excitation has exited the SAN and propagates preferentially along the fibres orientated along the CT and PMs (Fig 2Aii). The corresponding BSP map shows a clear positive peak forming over the lower right lung due to this atrial propagation (Fig2Bii). At 40ms, a larger portion of the right atrium has been excited (Fig 2Aiii) and the dipole direction in the BSP can be clearly seen to point downwards and to the left (Fig2Biii). By 110ms, the right atrium has completely depolarized and the left atrium has almost been fully depolarized (Fig 2 A iv). As such, the peak of the BSP has disappeared and it begins to return to a largely uniform state (Fig 1Biv). The atrial activation map and corresponding P-waves are shown in Fig 2 panels C and D, respectively.

Fig 3A shows the initiation and break down of re-entrant waves following the s2 stimulus (see Methods). In Fig 3Ai, the application of the shortly coupled s2 stimulus at a region of high electrical heterogeneity results in a conduction block towards the CT; the longer AP duration in the CT relative to the PMs implies that the CT cells have not fully recovered at this time, and therefore cannot be stimulated. The PMs, however, have fully repolarised and therefore the wave-front can propagate within them. The excitation then circulates back into the CT after it has propagated for some time (Fig 3Aii) and the CT has had time to recover. This forms a 'figure 8' style re-entrant pattern. After ~100ms, however, the wave begins to break up due to the slow and fast conduction pathways resulting from the high level of anisotropy (Fig 3Aiii). By ~150ms the multiple re-entrant wavelets which characterize AF have begun to form. Fig 3B shows the long term behaviour of the model after the initiation of AF. The different snapshots in time, taken from the sixth and seventh second of simulation, demonstrate chaotic, multiple re-entrant wavelets which would result in a significant reduction in cardiac output. Representative BSP snapshots during this time are shown in Fig 3C and can be seen to be highly irregular. This re-entry was sustained throughout the entire 10s simulation.

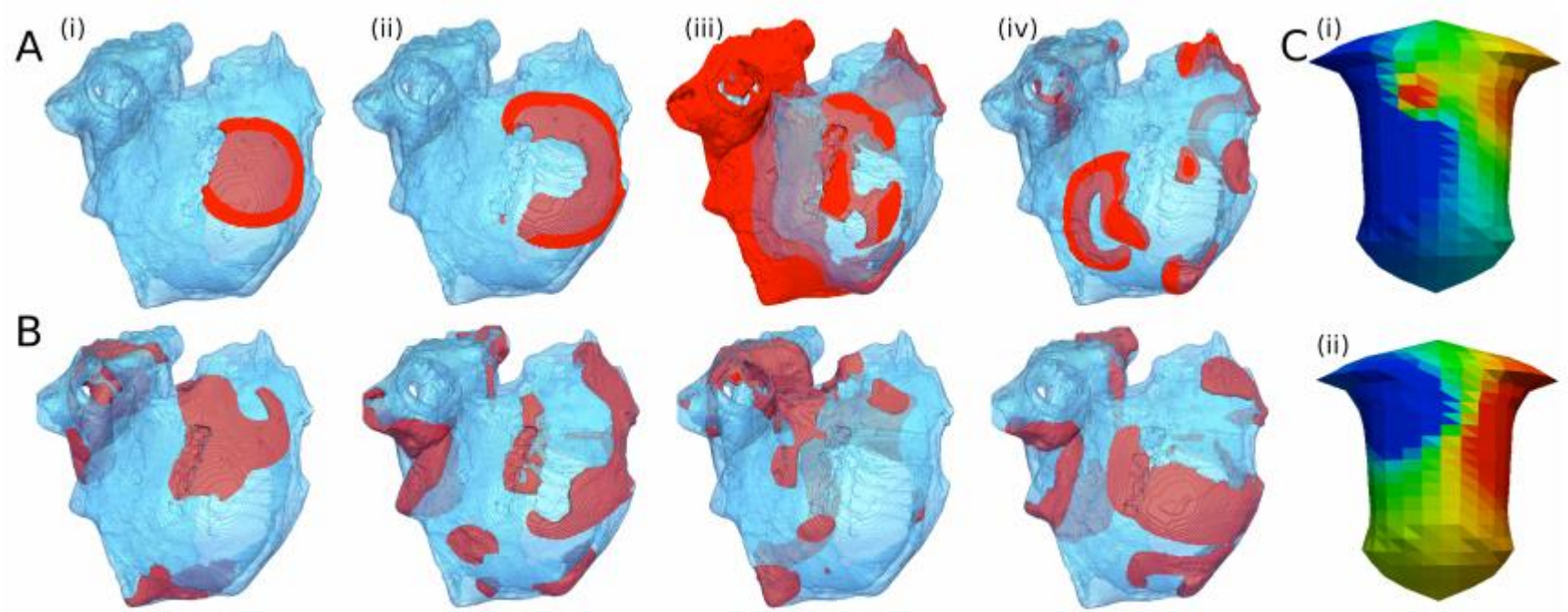

Figure 3. (A) Initiation and breakdown of a re-entrant wave following the s2 stimulus. Snapshots taken at i) 10ms; ii) 20 ms; iii) 100 ms; and iv) 150 ms after the stimulus. (B) Demonstration of multiple re-entrant wavelets characterizing AF. Snapshots taken at i) 605 ms; ii) 645 ms; iii) 690 ms; and iv) 735 ms after the s2 stimulus. (C) Snapshots of the BSP during AF.

Michael A Colman[1], Jonathan Stott[1], Oleg V Aslanidi[2], Phillip Langely[3], Henggui Zhang[1]

IV. SUMMARY

A multi-scale biophysically detailed model of the human atria and torso has been developed. The model is validated under normal and abnormal conditions and is used to investigate the underlying mechanisms of AF. It is shown that heterogeneity and anisotropy both play a role in the initiation and sustenance of AF.

V. REFERENCES

1. Dobrev D, Nattel S. New insights into the molecular basis of atrial fibrillation: mechanistic and therapeutic implications. Cardiovasc. Res. 2011 Mar 1;89(4):689–91.

2. Nattel S, Shiroshita-Takeshita A, Brundel BJJM, Rivard L. Mechanisms of atrial fibrillation: lessons from animal models. Prog Cardiovasc Dis. 2005 Aug;48(1):9–28.

3. Colman MA, Aslanidi OV, Stott J, Holden AV, Zhang H. Correlation between P-wave morphology and origin of atrial focal tachycardia--insights from realistic models of the human atria and torso. IEEE Trans Biomed Eng. 2011 Oct;58(10):2952–5.

4. Chandler N, Aslanidi O, Buckley D, Inada S, Birchall S, Atkinson A, et al. Computer three-dimensional anatomical reconstruction of the human sinus node and a novel paranodal area. Anat Rec (Hoboken). 2011 Jun;294(6):970–9.

5. Weixue L, Ling X. Computer simulation of epicardial potentials using a heart-torso model with realistic geometry. IEEE Trans Biomed Eng. 1996 Feb;43(2):211–7.

6. Lemery R, Birnie D, Tang ASL, Green M, Gollob M, Hendry M, et al. Normal atrial activation and voltage during sinus rhythm in the human heart: an endocardial and epicardial mapping study in patients with a history of atrial fibrillation. J. Cardiovasc. Electrophysiol. 2007 Apr;18(4):402–8.

7. Kistler PM, Roberts-Thomson KC, Haqqani HM, Fynn SP, Singarayar S, Vohra JK, et al. P-wave morphology in focal atrial tachycardia: development of an algorithm to predict the anatomic site of origin. J. Am. Coll. Cardiol. 2006 Sep 5;48(5):1010–7.

8. Mirvis DM. Body surface distribution of electrical potential during atrial depolarization and repolarization. Circulation. 1980 Jul;62(1):167–73.

Ευχαριστώ

Πρόγραμμα Διδακτορικών Σπουδών της Σχολής Ηλεκτρολόγων Μηχανικών και Μηχανικών Υπολογιστών ΕΜΠ

Πολυκλιμακωτή Προσομοίωση της Ασθένειας του Καρκίνου και *In Silico* Ιατρική (705)

Μάθημα 6ο

Αριθμητικές μέθοδοι για την επίλυση του χωρο-χρονικού προβλήματος της διήθησης καρκινικών όγκων σε υγιείς ιστούς με οριακές συνθήκες. Αντίστοιχα μαθηματικά και υπολογιστικά προβλήματα στη γενική *In Silico* Ιατρική

Γεώργιος Σ. Σταματάκος

Διευθυντής Ερευνών - Research Professor– Καθηγητής Ερευνας
Ερευνητικό Πανεπιστημιακό Ινστιτούτο Συστημάτων Επικοινωνιών και Υπολογιστών (ΕΠΙΣΕΥ)
Σχολή Ηλεκτρολόγων Μηχανικών και Μηχανικών Υπολογιστών (ΣΗΜΜΥ)
Εθνικό Μετσόβιο Πολυτεχνείο (ΕΜΠ)
Διευθυντής της Ερευνητικής Ομάδας για την In Silico Ογκολογία και την In Silico Ιατρική, ΕΠΙΣΕΥ-ΣΗΜΜΥ-ΕΜΠ
Επισκέπτης Καθηγητής της Ιατρικής Σχολής του Πανεπιστημίου του Saarland, Γερμανία (1/7/2019-15/9/2019)
Επισκέπτης Καθηγητής της ΣΗΜΜΥ, ΕΜΠ (2016-2019)
gestam@central.ntua.gr, http://in-silico-oncology.iccs.ntua.gr/

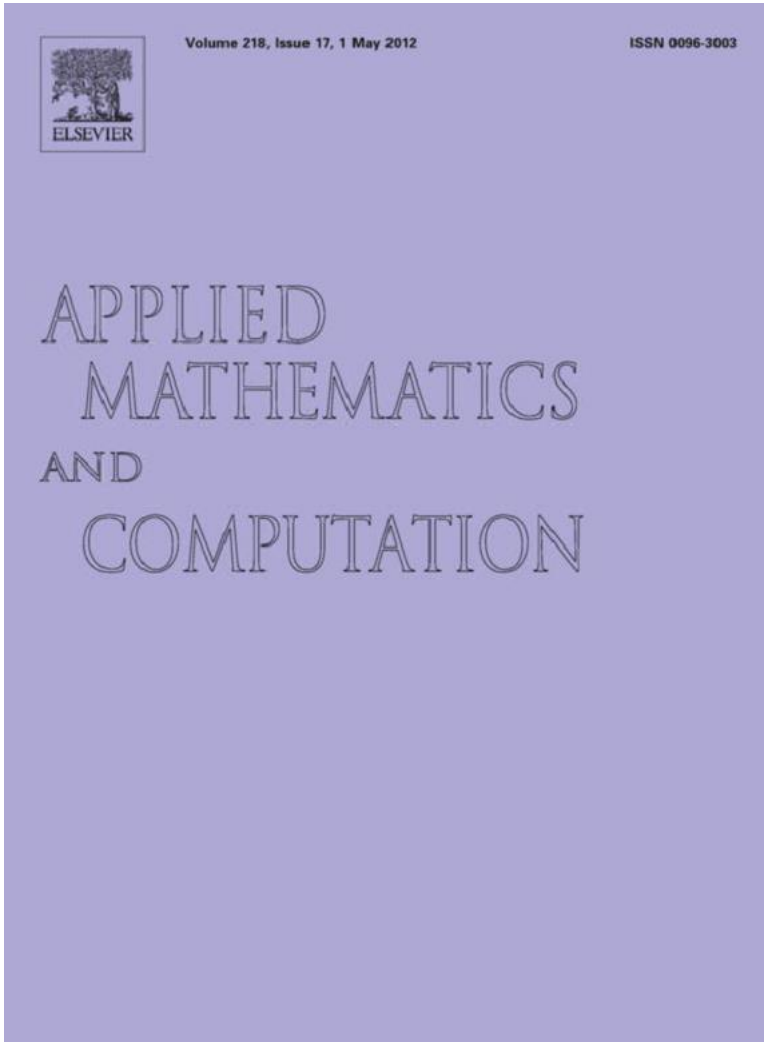
Volume 218, Issue 17, 1 May 2012
ISSN 0096-3003
ELSEVIER
APPLIED
MATHEMATICS
AND
COMPUTATION

Applied Mathematics and Computation 218 (2012) 8779–8799

Contents lists available at SciVerse ScienceDirect

Applied Mathematics and Computation

journal homepage: www.elsevier.com/locate/amc

A detailed numerical treatment of the boundary conditions imposed by the skull on a diffusion–reaction model of glioma tumor growth. Clinical validation aspects

Stavroula G. Giatili, Georgios S. Stamatakos *

In Silico Oncology Group, Laboratory of Microwave and Fiber Optics, Institute of Communication and Computer Systems, National Technical University of Athens 9, Iroon Polytechniou, Zografos GR-157 80, Greece

* Corresponding author.
E-mail addresses: giatili@mail.ntua.gr, stgiatili@gmail.com, giatili@otenet.gr (S.G. Giatili), gestam@central.ntua.gr (G.S. Stamatakos).

Keywords:
Glioma
Glioblastoma multiforme
Diffusion
Boundary conditions
Multiscale cancer modeling
In silico oncology

A B S T R A C T

The study of the diffusive behavior of glioma tumor growth is an active field of biomedical research with considerable therapeutic implications. An important aspect of the corresponding computational problem is the mathematical handling of boundary conditions. This paper aims at providing an explicit and thorough numerical formulation of the adiabatic Neumann boundary conditions imposed by the skull on the diffusive growth of gliomas and in particular on glioblastoma multiforme (GBM). Additionally, a detailed exposition of the numerical solution process for a homogeneous approximation of glioma invasion using the Crank–Nicolson technique in conjunction with the Conjugate Gradient system solver is provided. The entire mathematical and numerical treatment is also in principle applicable to mathematically similar physical, chemical and biological phenomena. A comparison of the numerical solution for the special case of pure diffusion in the absence of boundary conditions or equivalently in the presence of adiabatic boundaries placed in infinity with its analytical counterpart is presented. Numerical simulations for various adiabatic boundary geometries and non zero net tumor growth rate support the validity of the corresponding mathematical treatment. Through numerical experimentation on a set of real brain imaging data, a simulated tumor has shown to satisfy the expected macroscopic behavior of glioblastoma multiforme including the adiabatic behavior of the skull. The paper concludes with a number of remarks pertaining to both the biological problem addressed and the more generic diffusion–reaction context.

1. Introduction

The generic diffusion–reaction equation is applicable to a wide spectrum of physical, chemical and biomedical phenomena. In the context of cancer biology and oncology, diffusion has been regarded as one of the fundamental phenomena governing tumor invasion into neighboring normal tissues. Glioblastoma multiforme (GBM), a highly aggressive brain tumor, is a classical example of a highly invasive tumor. GBM cell diffusion in the brain is a reasonable first approximation of the migration of glioma cells along structures such as the basement membranes of blood vessels or the glial limitans externa that contain extracellular matrix (ECM) proteins. Frequently, invasive glioma cells are also found to migrate along myelinated fiber tracts of white matter. Due to its markedly diffusive character, a significant component of the tumor cannot be delineated based on standard tomographic imaging techniques (CT, MRI, PET etc). This constitutes an important limitation

to the optimal design of both surgical excision and therapeutic irradiation of the tumor. In order to partly alleviate the problem, mathematical modeling of diffusive tumor growth has been proposed. To this end a number of diffusion based models dealing primarily with the morphology of tumor growth have been developed [1–15].

An early study proposing a reaction–diffusion framework for the modeling of tumor growth in patients with glioma has been published by Cruywagen et al. [16] and Woodward et al. [17]. The effect of treatment has been included as a negative reaction term. Tumor cell invasion has been assumed isotropic, following homogeneous diffusion that is characterized by a global scalar diffusion coefficient. The prototypical modeling study of Burgess et al. [18] stipulates that glioma growth results from an interplay between cell diffusion and cell proliferation. The authors have introduced a simple model for glioma growth based on cell proliferation, cell loss, cell death and cell diffusion starting with an initial tumor lump. Their assumptions are spherical symmetry, homogeneous diffusion and exponential growth. It is noted that in order to facilitate focusing on the cell diffusion phenomena several models assume, either explicitly or implicitly, a mean angiogenesis potential characterizing the entire brain. Inadequate angiogenesis and poorly functioning neovascularization are taken into account indirectly through the consideration of a tumor cell loss rate which along with the tumor cell division rate produce the net tumor growth rate.

A number of publications deal with the macroscopic mechanical deformations of the brain imposed by various agents such as neurosurgery or the macroscopic volume effect of brain tumors [19]. Although such approaches usually ignore tumor cell diffusion within the brain, they may be combined with diffusion based modeling techniques dealing with glioma invasion in order to provide a more comprehensive quantitative perception of the related composite phenomena.

It should be noted, however, that a tumor growth modeling approach based exclusively on the continuous and/or finitized form of the diffusion–reaction equation has a limited potential to efficiently address the complexities of the treatment response phenomena in the multiscale context. The latter include *inter alia* the existence and dynamics of different proliferation potential cell categories (stem cells, limited mitotic potential cells, differentiated cells), different cell cycle phases (G1, S, G2, M), differing radiosensitivities and chemosensitivities, different times spent within each cell-cycle phase etc. Particularly efficient methods to mathematically describe and simulate tumor response to treatment have been based on the consideration of discrete entities and discrete events [20–24]. Therefore, in the future a more comprehensive model addressing both glioma invasion and response to complex treatment modalities could emerge by combining the continuous with the discrete mathematics approach mentioned so far.

For a biologically meaningful and computationally reliable diffusion based solution to the problem of diffusive clinical tumor growth and in particular glioma progression, a careful boundary condition handling is a *sine qua non* prerequisite. However, to the best of the authors' knowledge no explicit treatment of the numerical application of boundary conditions in this context has appeared in the literature as yet. The latter is also in contrast with the importance of a careful handling of the boundary conditions between bone and soft issue which has been demonstrated in a number of cases in the neurosurgery setting. Therefore, the aim of this paper is to outline a detailed numerical handling of the boundary conditions imposed by the presence of the skull in the case of gliomas and in particular of glioblastoma multiforme.

According to the diffusion–reaction based approach the tumor is considered a spatiotemporal distribution of continuous cell density which follows the general diffusion–reaction law [25]. The macroscopic formulation of diffusion, leads to a partial parabolic differential equation. A single tumor cell may constitute the initial tumor within a three-dimensional medium. Tumor growth can be expressed by the following statement [26,27]:

$$\text{Rate of change of tumor cell population} = \text{diffusion(motility)of tumor cells} + \text{net proliferation of tumor cells} - \text{loss of tumor cells due to treatment.}$$

In the case of glioma, the simulated region of interest may include part of the skull. The latter acts as an adiabatic boundary for the diffusion of the brain tumor, precluding migration beyond it. As a result, the mathematical treatment of the biophysical processes taking place in the vicinity of anatomic boundaries must satisfy specific constraints. Zero flux boundary conditions have to be applied on the anatomic boundaries of the skull surface. Thus if Ω is the brain domain on which the diffusion equation is to be solved the previous statement can be symbolically formulated through the following differential equation [1]:

$$\left\{ \begin{array}{c} \frac{\partial c(\vec{x},t)}{\partial t} = \nabla \cdot (D \nabla c(\vec{x},t)) + \rho c(\vec{x},t) - G(t) c(\vec{x},t) \ in \ \Omega \\ c(\vec{x},0) = f(\vec{x}), \quad \text{initial condition} \\ \hat{n} \cdot D \nabla c(\vec{x},t) = 0 \text{ on } \partial\Omega, \quad \text{boundary condition} \end{array} \right\}. \tag{1}$$

The variable c denotes the cell concentration at any spatial point defined by the position vector $\vec{x}$ and time t. The parameter D denotes the diffusion coefficient and represents the active motility of tumor cells. The term ρ represents the net rate of tumor growth including proliferation, loss and death, $\hat{n}$ is the unit vector normal to the boundary $\partial\Omega$ of the domain Ω and $f(\vec{x})$ is a known function that defines the initial spatial distribution of malignant cells. The term $G(t)$ accounts for the temporal profile of treatment and as a first facilitating approximation $G(t) = k$ may be assumed constant. The latter may crudely model a continuous administration of radiation e.g. through special radioisotope based implants. A more realistic assumption is to assign $G(t)$ different values for different time intervals reflecting various chemotherapeutic and/or radiotherapeutic schedules. The simulation domain R of which Ω is a subdomain is defined as:

$$R = \{(x, y, z) | a < x < b, s < y < d, e < z < f\}. \quad (2)$$

Little progress has been made towards developing analytical solutions to the three dimensional diffusion equation with constant diffusion coefficient D when initial and boundary conditions are complex [28]. Therefore, the study of the diffusion equation from both the analytical and even more from the numerical standpoint is still an active field of research. The objective is to approximate the exact solution to the boundary value problem at a discrete set of spatial points and convert the continuous partial differential equation into a system of discrete algebraic equations.

2. Gridding scheme

The initial steps of the numerical simulation of a diffusion–reaction process include the selection of a suitable and efficient gridding scheme in order to finitize (discretize) the partial differential equation and the introduction of a grid (computational mesh) to be applied on the simulation domain containing the anatomic region of interest. A Cartesian coordinate system and a cubic grid have been adopted and implemented in this paper (Fig. 1). The latter has become the standard (default) choice in most fields of science when it comes to the utilization of the finite difference technique. It has also been proved the simplest and most straightforward approach adopted by several brain invasion tumor modelers up to the present [2,16]. However, it should be noted that other lattices have been sporadically reported in literature too. Nevertheless, due to the complex geometry of the boundaries of the skull cavity, resorting to any coordinate system other than the Cartesian one and to any grid other than the cubic one does not seem to be an obvious optimal choice. A combination of a Cartesian coordinate system with a cubic mesh apparently provides the simplest geometrical substrate for the formulation and application of the finite difference equations. Adoption of a different gridding scheme might result to a much more complex numerical formulation of the overarching equation and boundary conditions and therefore it has been avoided in this paper. The derivatives of the variable c in Eq. (1) need to be approximated at each computational node.

Concerning spatial discretization, the intervals $[a,b]$, $[s,d]$, $[e,f]$ are divided into N, M, L equal sized sub-intervals respectively, where N, M, L are positive integers. For convenience, let:

$$\Delta x = \Delta y = \Delta z = \frac{b-a}{N} = \frac{d-s}{M} = \frac{f-e}{L} = h. \tag{3}$$

By inference, with the number of subintervals in each coordinate direction already selected, the computational grid consists of those points (x_i, y_j, z_k), where

$$x_i = a + ih, \tag{4}$$

$$y_j = s + jh, \tag{5}$$

$$z_k = e + kh \tag{6}$$

for $i = 0, 1, 2, \ldots, N$, $j = 0, 1, 2, \ldots, M$, $k = 0, 1, 2, \ldots, L$.

The discretization is completed by the division of the time axis into uniform steps of length Δt and $t_n = n\Delta t$, for $n = 0, 1, 2, \ldots$ and so on (n is a time step counter). The step size is based on the behavior of the solution and is determined through an attempt to obtain a solution with the minimum number of steps. Values for the approximate solution will be obtained at these discrete time levels. At each node of the discretizing mesh a value of cell density is assigned. Time is initialized and the continuous diffusion–reaction equation is formulated, discretized and applied on the mesh nodes.

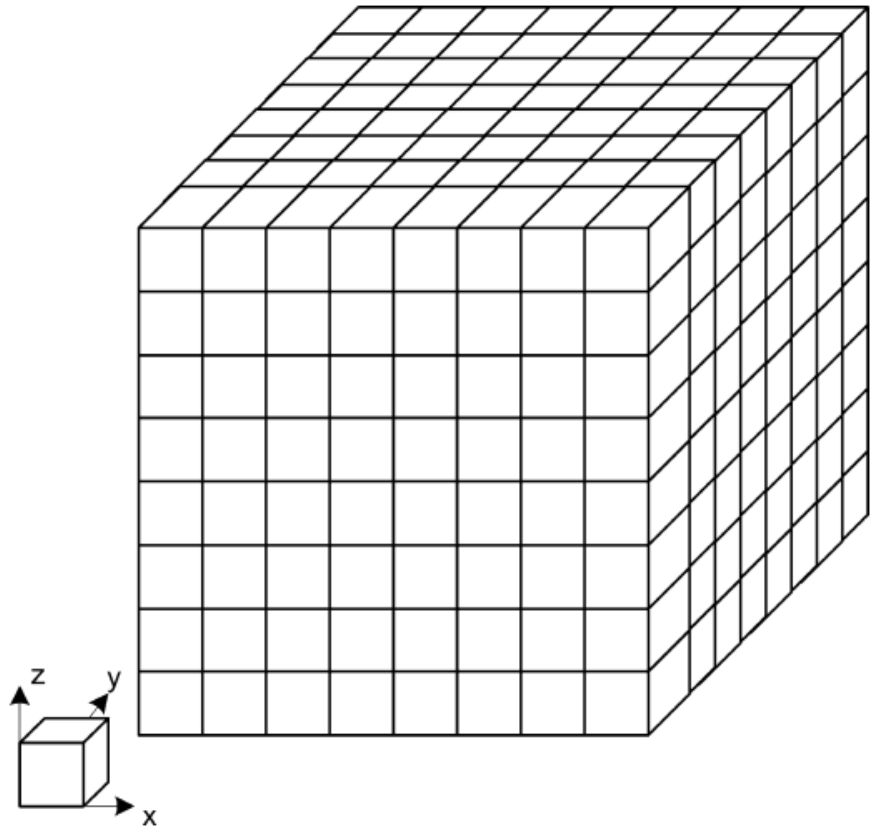

Fig. 1. The three dimensional (3D) Cartesian grid applied on the simulation domain. The latter includes the anatomic region of interest.

3. The differential-algebraic equation solver

Having defined the computational grid, finite-difference methods are applied. Many different numerical approaches, for solving multidimensional parabolic initial-boundary value problems have been proposed. Three indicative groups of methods that are widely adopted are the following:

i. The explicit method: it uses a forward difference at time t_n and is conditionally stable.
ii. The implicit method: it uses a backward difference at time t_{n+1}.
iii. The Crank–Nicolson method: it uses the central difference at time $t_{n+1/2}$.

The evaluation of numerical methods for initial value problems focuses on the discretization error and on the important properties of consistency, convergence and stability. The Crank–Nicolson method is considered the method of choice for many diffusion problems. It is the most accurate scheme for small time steps, in contrast with the explicit method which is the easiest one to implement but the least accurate and the most unstable. The implicit scheme works best for large time steps. The Crank–Nicolson method is second-order accurate in both time and space and unconditionally stable. It is recalled that an algorithm is called *numerically stable* if an error, whatever its cause, does not grow to be much larger during the calculation.

It is noted, however, that for large values of $D\Delta t/h^2$ and sharp initial transient conditions, the numerical solution based on Crank–Nicolson method may show oscillations related to the initial conditions. The oscillations may persist over a large number of steps. Several methods for damping the oscillations have been investigated [29].

The three dimensional problem described by Eq. (1) can be written equivalently as follows

$$\left\{\begin{array}{l} \frac{\partial c}{\partial t} = \frac{\partial}{\partial x}\left(D\frac{\partial c}{\partial x}\right) + \frac{\partial}{\partial y}\left(D\frac{\partial c}{\partial y}\right) + \frac{\partial}{\partial z}\left(D\frac{\partial c}{\partial z}\right) + \rho c - G(t)c \quad \text{in } \Omega \\ \qquad c(x,y,z,0) = f(x,y,z), \quad \text{initial condition} \\ \hat{n}\cdot D\left(\frac{\partial c}{\partial x}\hat{i} + \frac{\partial c}{\partial y}\hat{j} + \frac{\partial c}{\partial z}\hat{k}\right) = 0 \quad \text{on } \partial\Omega, \quad \text{boundary condition} \end{array}\right\}. \tag{7}$$

Replacing all spatial derivatives with the average of their values at the t and $t+1$ time levels and then substituting centered-difference forms for all derivatives, we obtain the Crank–Nicolson scheme:

$$\frac{\partial c}{\partial t} \to \frac{c_{i,j,k}^{t+1} - c_{i,j,k}^{t}}{\Delta t}, \tag{8}$$

$$\frac{\partial}{\partial x}\left(D\frac{\partial c}{\partial x}\right) \to \frac{1}{2}D\left(\frac{c_{i+1,j,k}^{t+1} - 2c_{i,j,k}^{t+1} + c_{i-1,j,k}^{t+1}}{\Delta x^2} + \frac{c_{i+1,j,k}^{t} - 2c_{i,j,k}^{t} + c_{i-1,j,k}^{t}}{\Delta x^2}\right), \tag{9}$$

$$\frac{\partial}{\partial y}\left(D\frac{\partial c}{\partial y}\right) \to \frac{1}{2}D\left(\frac{c_{i,j+1,k}^{t+1} - 2c_{i,j,k}^{t+1} + c_{i,j-1,k}^{t+1}}{\Delta y^2} + \frac{c_{i,j+1,k}^{t} - 2c_{i,j,k}^{t} + c_{i,j-1,k}^{t}}{\Delta y^2}\right), \tag{10}$$

$$\frac{\partial}{\partial z}\left(D\frac{\partial c}{\partial z}\right) \to \frac{1}{2}D\left(\frac{c_{i,j,k+1}^{t+1} - 2c_{i,j,k}^{t+1} + c_{i,j,k-1}^{t+1}}{\Delta z^2} + \frac{c_{i,j,k+1}^{t} - 2c_{i,j,k}^{t} + c_{i,j,k-1}^{t}}{\Delta z^2}\right), \tag{11}$$

$$\rho c - G(t)c \to \frac{1}{2}\left(\rho^{t+1}c_{i,j,k}^{t+1} - G^{t+1}c_{i,j,k}^{t+1} + \rho^{t}c_{i,j,k}^{t} - G^{t}c_{i,j,k}^{t}\right), \tag{12}$$

where $c_{i,j,k}^{t}$ is the finite difference approximation of c at the grid point (x_i, y_j, z_k) at time t. So, the following formula has been used for the solution:

$$\frac{c_{i,j,k}^{t+1}-c_{i,j,k}^{t}}{\Delta t}=\frac{1}{2}D\left(\frac{c_{i+1,j,k}^{t+1}-2c_{i,j,k}^{t+1}+c_{i-1,j,k}^{t+1}}{\Delta x^2}+\frac{c_{i+1,j,k}^{t}-2c_{i,j,k}^{t}+c_{i-1,j,k}^{t}}{\Delta x^2}\right)+\frac{1}{2}D\left(\frac{c_{i,j+1,k}^{t+1}-2c_{i,j,k}^{t+1}+c_{i,j-1,k}^{t+1}}{\Delta y^2}+\frac{c_{i,j+1,k}^{t}-2c_{i,j,k}^{t}+c_{i,j-1,k}^{t}}{\Delta y^2}\right)$$
$$+\frac{1}{2}D\left(\frac{c_{i,j,k+1}^{t+1}-2c_{i,j,k}^{t+1}+c_{i,j,k-1}^{t+1}}{\Delta z^2}+\frac{c_{i,j,k+1}^{t}-2c_{i,j,k}^{t}+c_{i,j,k-1}^{t}}{\Delta z^2}\right)+\frac{1}{2}\left(\rho^{t+1}c_{i,j,k}^{t+1}-G^{t+1}c_{i,j,k}^{t+1}+\rho^{t}c_{i,j,k}^{t}-G^{t}c_{i,j,k}^{t}\right). \quad (13)$$

In the case that ρ, G are time independent and $\Delta x = \Delta y = \Delta z = h$, it holds:

$$\left[1+6\lambda-\frac{\Delta t}{2}(\rho-G)\right]c_{i,j,k}^{t+1}-\lambda\left(c_{i+1,j,k}^{t+1}+c_{i-1,j,k}^{t+1}+c_{ij+1,k}^{t+1}+c_{ij-1,k}^{t+1}+c_{i,j,k+1}^{t+1}+c_{i,j,k-1}^{t+1}\right)$$
$$=\left[1-6\lambda+\frac{\Delta t}{2}(\rho-G)\right]c_{i,j,k}^{t}+\lambda\left(c_{i+1,j,k}^{t}+c_{i-1,j,k}^{t}+c_{i,j+1,k}^{t}+c_{i,j-1,k}^{t}+c_{i,j,k+1}^{t}+c_{i,j,k-1}^{t}\right), \quad (14)$$

where

$$\lambda = D\Delta t/[2(h)^2]. \quad (15)$$

4. Implementation of the iterative system solver adopted

The resulting system of Eq. (1) may be written equivalently in the form

$$\overleftrightarrow{A}\vec{x} = \vec{b}, \tag{16}$$

where $\vec{x}$ denotes a vector that contains an approximation of the solution c at the mesh nodes at time $t = t_n$.

To find the structure of the coefficient matrix A, a common numbering scheme has been used namely the lexicographic ordering. The number written next to the location of each unknown is the lexicographic number associated with the unknown (Fig. 2). Supposing m denotes the number of nodes in the computational mesh, the matrix $\overleftrightarrow{A} \in R^{m,m}$ is a sparse, symmetric matrix and $\vec{x} \in R^m$ denotes a vector that contains an approximation of the solution c at the mesh nodes at time $t = t_n$.

There are major ways of solving linear systems of equations: direct methods such as the Lower–Upper (LU) decomposition and Cholesky and iterative methods that are more efficient. In contrast to direct methods, iterative methods are not expected to terminate in a number of steps. Starting from an initial guess, iterative methods form successive approximations that converge to the exact solution only in the limit. A convergence criterion is specified in order to decide when a sufficiently accurate solution has been found. Additionally, with an iterative technique, there is no need to store the coefficient matrix. The only thing that must be known is the structure of the equations. In addition to that, an iterative solution requires fewer total operations. Due to the nature of the three dimensional problem, direct solution methods are not suitable for their prohibitive CPU and memory expenses.

The algorithm selected for the solution of this large sparse system (Eq. (16)) is the non-stationary iterative Conjugate Gradient method (CG) which generates a sequence of approximations that converges rapidly to the desired solution and is widely used for the solution of linear sparse systems. The stationary iterative methods like Jacobi (simultaneous relaxation), Gauss–Seidel (successive relaxation), SOR (successive overrelaxation) are not used due to their slow convergence which takes place after many iterations. Non-stationary iterative methods can basically be described by an iterative scheme which assumes that the next iteration point corresponds to the sum of the value of the initial point plus the correction terms of all iterations. The correctors are vectors, which means that they have both magnitude and direction.

5. Explicit formulation of the boundary conditions

For a numerical simulation a region of interest within which the actual simulation is to take place is defined. This region usually possesses a boundary separating it from the surrounding environment. Numerical simulations should address the physical processes taking place around the boundaries too. In most cases the boundary conditions are very important for the outcome of the simulation. Different boundary conditions may lead to different simulation results. Improper sets of boundary conditions may introduce non physical influences on the simulated system, while a proper set of boundary conditions can avoid that.

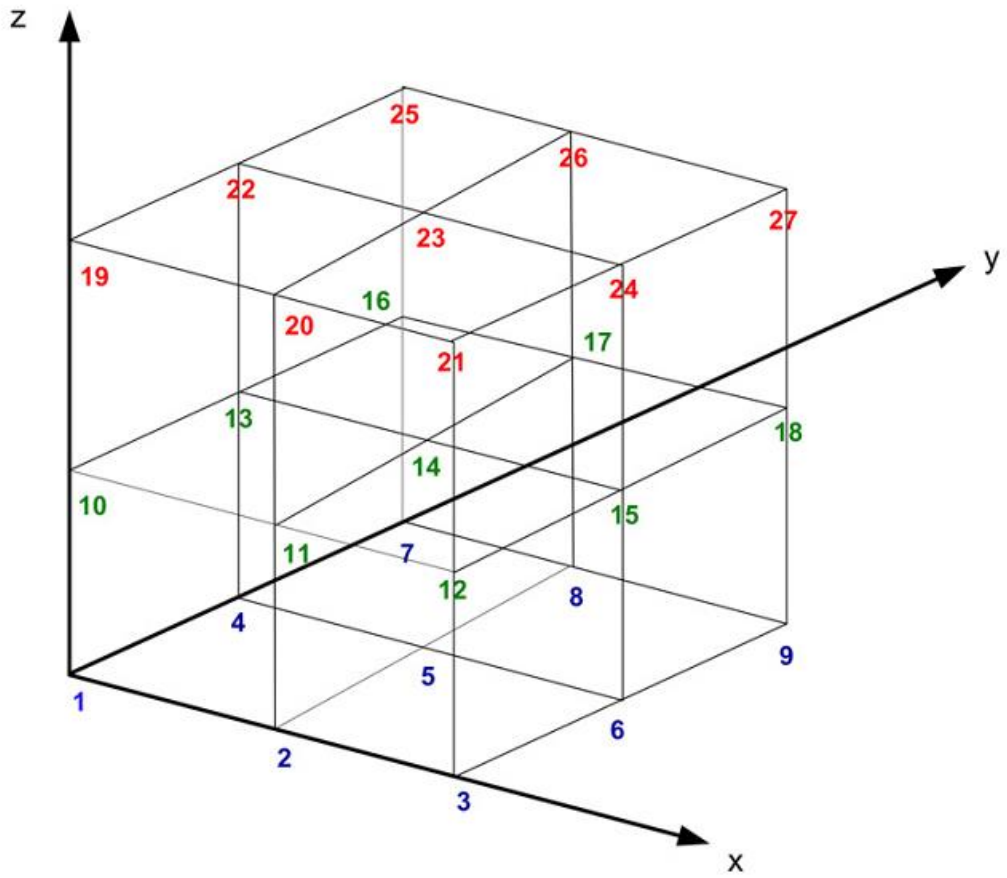

Fig. 2. Lexicographic order. To find the structure of the coefficient matrix $\overleftrightarrow{A}$, a common numbering scheme has been used namely the lexicographic ordering. Starting at the bottom left corner of the computational grid, the unknowns are numbered consecutively from left to right and from bottom to top. The number written next to the location of each unknown is the lexicographic number associated with the unknown.

In a spatiotemporal model of tumor growth, any anatomic boundaries of the space where tumor can grow must be taken into account. In order to complete the model formulation for clinical glioblastoma growth boundary conditions have to be added precluding migration beyond the skull boundary. The simulation of tumor growth and invasion can be viewed as a boundary value problem strongly dependent on the values assigned on the physical boundary of the definition domain. Thus the first step to be taken is to select the appropriate type of boundary conditions.

There are three types of boundary conditions commonly encountered in the solution of diffusion and in general in the solution of partial differential equations (PDEs) [30,31]:

i. Dirichlet boundary condition: The value of the unknown function c (solution of the PDE) on some domain Ω is specified on a boundary surface of Ω.

$$c(x,y,z) = f(x,y,z) \quad \forall (x,y,z) \in \partial\Omega, \tag{17}$$

where f is a known given function defined on the boundary $\partial\Omega$.

ii. Neumann boundary conditions: The normal derivative of the unknown function c (solution of the PDE) is specified over a boundary $\partial\Omega$ (that is, the derivative of the solution normal to $\partial\Omega$).

$$\frac{\partial c}{\partial n}(x,y,z) = \hat{n} \cdot \nabla c = f(x,y,z) \quad \forall (x,y,z) \in \partial\Omega. \tag{18}$$

iii. Robin boundary conditions (or mixed boundary conditions).

$$a(x,y,z)c(x,y,z) + \beta(x,y,z)\hat{n} \cdot grad\, c(x,y,z) = f(x,y,z) \quad \forall (x,y,z) \in \partial\Omega. \tag{19}$$

In the case of a diffusive glioma lying within the brain an eventual adoption of Dirichlet boundary conditions would lead to predefined values of tumor cell concentration on the brain–skull boundary. In the simplest case of pure diffusion, the latter could only be achieved through the emergence of (artifact) tumor cell sources and/or sinks that would keep the boundary tumor cell concentration values constant. Obviously such an approach would be unacceptable.

On the other hand an eventual adoption of Neumann boundary conditions would impose a predefined normal derivative of the tumor cell concentration on the brain-skull boundary. In the special case that $\partial c/\partial n = 0$, where c is the tumor cell concentration, adiabatic boundary conditions are implied. These are called homogeneous Neumann boundary conditions. The latter physically correspond to no net flow of tumor cells out of or into the brain region across the brain–skull boundary. In that case the diffusion region is insulated. Therefore, Neumann boundary conditions are the most appropriate for the problem addressed.

The mathematical problem was initially defined for a cubic domain. Since, however, the real glioma problem involves an irregularly shaped domain, a biologically meaningful solution had to allow for the investigation of a wide range of domain geometries. Several specific cases have been examined in order to address the geometry of the irregularly shaped skull boundary. For each boundary mesh node (lying at the center of the multi-colored structure of Fig. 3 and therefore not visible) all its 6 adjacent nodes (lying towards all the $x+$, $x-$, $y+$, $y-$, $z+$, $z-$ directions) are considered in order to numerically apply the boundary condition on it i.e. on (x_i, y_j, z_k).

The boundary condition according to Eq. (1) is:

$$\hat{n} \cdot D\nabla c = 0 \quad \text{on} \quad \partial\Omega. \tag{20}$$

In order to evaluate the boundary condition for each grid point (x_i, y_j, z_k) and maintain the block tridiagonal structure of the coefficient matrix $\underleftrightarrow{A}$ and the second-order accuracy of the approximation we introduce a "fictitious node" to the computational grid. The "fictitious node" produces an extra row of unknowns in the computational grid. Evaluating the boundary condition at each boundary grid point (x_i, y_j, z_k) yields the following.

At the boundary grid point (x_i, y_j, z_k) in the negative x direction $x-$:

$$-\left.\frac{\partial c}{\partial x}\right|_{(x_i, y_j, z_k)} = 0 \Rightarrow c_{i+1,j,k} = c_{F_{i-1,j,k}}. \tag{21}$$

At the boundary grid point (x_i, y_j, z_k) in the positive x direction $x+$:

$$\left.\frac{\partial c}{\partial x}\right|_{(x_i, y_j, z_k)} = 0 \Rightarrow c_{i-1,j,k} = c_{F_{i+1,j,k}}. \tag{22}$$

At the boundary grid point (x_i, y_j, z_k) in the negative y direction $y-$:

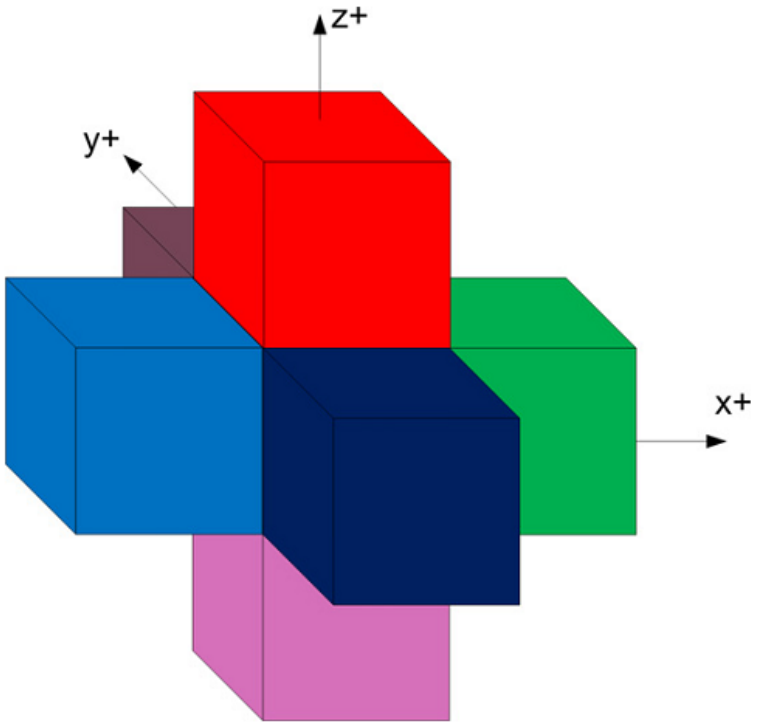

Fig. 3. A boundary mesh node with its 6 adjacent nodes. For each boundary mesh node (lying at the center of the multi-colored structure and therefore not visible) all its 6 adjacent nodes (lying towards the $x+$, $x-$, $y+$, $y-$, $z+$, $z-$ directions) are considered in order to numerically apply the boundary conditions on the node under consideration.

$$-\left.\frac{\partial c}{\partial y}\right|_{(x_i,y_j,z_k)} = 0 \Rightarrow c_{i,j+1,k} = c_{F_{i,j-1,k}}. \tag{23}$$

At the boundary grid point (x_i, y_j, z_k) in the positive y direction $y+$:

$$\left.\frac{\partial c}{\partial y}\right|_{(x_i,y_j,z_k)} = 0 \Rightarrow c_{i,j-1,k} = c_{F_{i,j+1,k}}. \tag{24}$$

At the boundary grid point (x_i, y_j, z_k) in the negative z direction $z-$:

$$-\left.\frac{\partial c}{\partial z}\right|_{(x_i,y_j,z_k)} = 0 \Rightarrow c_{i,j,k+1} = c_{F_{i,j,k-1}}. \tag{25}$$

At the boundary grid point (x_i, y_j, z_k) in the positive z direction $z+$:

$$\left.\frac{\partial c}{\partial z}\right|_{(x_i,y_j,z_k)} = 0 \Rightarrow c_{i,j,k-1} = c_{F_{i,j,k+1}}, \tag{26}$$

where $F_{i,j,k}$ denotes a fictitious node.

The total number of the different cases of nodes having boundary node(s) as their neighbor(s) that have been considered is 26. This has led to the formulation of 26 algebraic equations (denoted by Eqs. (27)–(52)). An appropriate equation out of the set of Eqs. (27)–(52) is used for any index triplet (i,j,k) belonging to the boundary. By fixing indices i, j, k to specific values, Eqs. (27)–(52) can produce all elementary boundary arrangements encountered in the case of an arbitrarily shaped boundary. The 26 different cases are the following:

At the boundary grid point (x_i,y_j,z_k) where the skull lies only in the positive x direction:

$$\left[1+6\lambda-\frac{\Delta t}{2}(\rho-G)\right]c_{i,j,k}^{t+1}-\lambda\left(2c_{i-1,j,k}^{t+1}+c_{i,j+1,k}^{t+1}+c_{i,j-1,k}^{t+1}+c_{i,j,k+1}^{t+1}+c_{i,j,k-1}^{t+1}\right)$$
$$=\left[1-6\lambda+\frac{\Delta t}{2}(\rho-G)\right]c_{i,j,k}^{t}+\lambda\left(2c_{i-1,j,k}^{t}+c_{i,j+1,k}^{t}+c_{i,j-1,k}^{t}+c_{i,j,k+1}^{t}+c_{i,j,k-1}^{t}\right). \quad (27)$$

At the boundary grid point (x_i,y_j,z_k) where the skull lies only in the negative x direction:

$$\left[1+6\lambda-\frac{\Delta t}{2}(\rho-G)\right]c_{i,j,k}^{t+1}-\lambda\left(2c_{i+1,j,k}^{t+1}+c_{i,j+1,k}^{t+1}+c_{i,j-1,k}^{t+1}+c_{i,j,k+1}^{t+1}+c_{i,j,k-1}^{t+1}\right)$$
$$=\left[1-6\lambda+\frac{\Delta t}{2}(\rho-G)\right]c_{i,j,k}^{t}+\lambda\left(2c_{i+1,j,k}^{t}+c_{i,j+1,k}^{t}+c_{i,j-1,k}^{t}+c_{i,j,k+1}^{t}+c_{i,j,k-1}^{t}\right). \quad (28)$$

At the boundary grid point (x_i,y_j,z_k) where the skull lies only in the positive y direction:

$$\left[1+6\lambda-\frac{\Delta t}{2}(\rho-G)\right]c_{i,j,k}^{t+1}-\lambda\left(c_{i+1,j,k}^{t+1}+c_{i-1,j,k}^{t+1}+2c_{i,j-1,k}^{t+1}+c_{i,j,k+1}^{t+1}+c_{i,j,k-1}^{t+1}\right)$$
$$=\left[1-6\lambda+\frac{\Delta t}{2}(\rho-G)\right]c_{i,j,k}^{t}+\lambda\left(c_{i+1,j,k}^{t}+c_{i-1,j,k}^{t}+2c_{i,j-1,k}^{t}+c_{i,j,k+1}^{t}+c_{i,j,k-1}^{t}\right). \quad (29)$$

At the boundary grid point (x_i, y_j, z_k) where the skull lies only in the negative y direction:

$$\left[1+6\lambda-\frac{\Delta t}{2}(\rho-G)\right]c_{i,j,k}^{t+1}-\lambda\left(c_{i+1,j,k}^{t+1}+c_{i-1,j,k}^{t+1}+2c_{i,j+1,k}^{t+1}+c_{i,j,k+1}^{t+1}+c_{i,j,k-1}^{t+1}\right)$$
$$=\left[1-6\lambda+\frac{\Delta t}{2}(\rho-G)\right]c_{i,j,k}^{t}+\lambda\left(c_{i+1,j,k}^{t}+c_{i-1,j,k}^{t}+2c_{i,j+1,k}^{t}+c_{i,j,k+1}^{t}+c_{i,j,k-1}^{t}\right). \quad (30)$$

At the boundary grid point (x_i, y_j, z_k) where the skull lies only in the positive z direction:

$$\left[1+6\lambda-\frac{\Delta t}{2}(\rho-G)\right]c_{i,j,k}^{t+1}-\lambda\left(c_{i+1,j,k}^{t+1}+c_{i-1,j,k}^{t+1}+c_{i,j+1,k}^{t+1}+c_{i,j-1,k}^{t+1}+2c_{i,j,k-1}^{t+1}\right)$$
$$=\left[1-6\lambda+\frac{\Delta t}{2}(\rho-G)\right]c_{i,j,k}^{t}+\lambda\left(c_{i+1,j,k}^{t}+c_{i-1,j,k}^{t}+c_{i,j+1,k}^{t}+c_{i,j-1,k}^{t}+2c_{i,j,k-1}^{t}\right). \quad (31)$$

At the boundary grid point (x_i, y_j, z_k) where the skull lies only in the negative z direction:

$$\left[1+6\lambda-\frac{\Delta t}{2}(\rho-G)\right]c_{i,j,k}^{t+1}-\lambda\left(c_{i+1,j,k}^{t+1}+c_{i-1,j,k}^{t+1}+c_{i,j+1,k}^{t+1}+c_{i,j-1,k}^{t+1}+2c_{i,j,k+1}^{t+1}\right)$$
$$=\left[1-6\lambda+\frac{\Delta t}{2}(\rho-G)\right]c_{i,j,k}^{t}+\lambda\left(c_{i+1,j,k}^{t}+c_{i-1,j,k}^{t}+c_{i,j+1,k}^{t}+c_{i,j-1,k}^{t}+2c_{i,j,k+1}^{t}\right). \quad (32)$$

At the boundary grid point (x_i, y_j, z_k) where the skull lies only in the negative x direction and the positive z direction:

$$\left[1+6\lambda-\frac{\Delta t}{2}(\rho-G)\right]c_{i,j,k}^{t+1}-\lambda\left(2c_{i+1,j,k}^{t+1}+c_{i,j+1,k}^{t+1}+c_{i,j-1,k}^{t+1}+2c_{i,j,k-1}^{t+1}\right)$$
$$=\left[1-6\lambda+\frac{\Delta t}{2}(\rho-G)\right]c_{i,j,k}^{t}+\lambda\left(2c_{i+1,j,k}^{t}+c_{i,j+1,k}^{t}+c_{i,j-1,k}^{t}+2c_{i,j,k-1}^{t}\right). \quad (33)$$

At the boundary grid point (x_i, y_j, z_k) where the skull lies only in the positive x direction and the positive z direction:

$$\left[1+6\lambda-\frac{\Delta t}{2}(\rho-G)\right]c_{i,j,k}^{t+1}-\lambda\left(2c_{i-1,j,k}^{t+1}+c_{i,j+1,k}^{t+1}+c_{i,j-1,k}^{t+1}+2c_{i,j,k-1}^{t+1}\right)$$
$$=\left[1-6\lambda+\frac{\Delta t}{2}(\rho-G)\right]c_{i,j,k}^{t}+\lambda\left(2c_{i-1,j,k}^{t}+c_{i,j+1,k}^{t}+c_{i,j-1,k}^{t}+2c_{i,j,k-1}^{t}\right). \quad (34)$$

At the boundary grid point (x_i, y_j, z_k) where the skull lies only in the positive y direction and the positive z direction:

$$\left[1+6\lambda-\frac{\Delta t}{2}(\rho-G)\right]c_{i,j,k}^{t+1}-\lambda\left(c_{i+1,j,k}^{t+1}+c_{i-1,j,k}^{t+1}+2c_{i,j-1,k}^{t+1}+2c_{i,j,k-1}^{t+1}\right)$$
$$=\left[1-6\lambda+\frac{\Delta t}{2}(\rho-G)\right]c_{i,j,k}^{t}+\lambda\left(c_{i+1,j,k}^{t}+c_{i-1,j,k}^{t}+2c_{i,j-1,k}^{t}+2c_{i,j,k-1}^{t}\right). \quad (35)$$

At the boundary grid point (x_i, y_j, z_k) where the skull lies only in the negative y direction and the positive z direction:

$$\left[1+6\lambda-\frac{\Delta t}{2}(\rho-G)\right]c_{i,j,k}^{t+1}-\lambda\left(c_{i+1,j,k}^{t+1}+c_{i-1,j,k}^{t+1}+2c_{i,j+1,k}^{t+1}+2c_{i,j,k-1}^{t+1}\right)$$
$$=\left[1-6\lambda+\frac{\Delta t}{2}(\rho-G)\right]c_{i,j,k}^{t}+\lambda\left(c_{i+1,j,k}^{t}+c_{i-1,j,k}^{t}+2c_{i,j+1,k}^{t}+2c_{i,j,k-1}^{t}\right). \quad (36)$$

At the boundary grid point (x_i, y_j, z_k) where the skull lies only in the negative x direction and the negative z direction:

$$\left[1+6\lambda-\frac{\Delta t}{2}(\rho-G)\right]c_{i,j,k}^{t+1}-\lambda\left(2c_{i+1,j,k}^{t+1}+c_{i,j+1,k}^{t+1}+c_{i,j-1,k}^{t+1}+2c_{i,j,k+1}^{t+1}\right)$$
$$=\left[1-6\lambda+\frac{\Delta t}{2}(\rho-G)\right]c_{i,j,k}^{t}+\lambda\left(2c_{i+1,j,k}^{t}+c_{i,j+1,k}^{t}+c_{i,j-1,k}^{t}+2c_{i,j,k+1}^{t}\right). \quad (37)$$

At the boundary grid point (x_i, y_j, z_k) where the skull lies only in the negative z direction and the positive x direction:

$$\left[1+6\lambda-\frac{\Delta t}{2}(\rho-G)\right]c_{i,j,k}^{t+1}-\lambda\left(2c_{i-1,j,k}^{t+1}+c_{i,j+1,k}^{t+1}+c_{i,j-1,k}^{t+1}+2c_{i,j,k+1}^{t+1}\right)$$
$$=\left[1-6\lambda+\frac{\Delta t}{2}(\rho-G)\right]c_{i,j,k}^{t}+\lambda\left(2c_{i-1,j,k}^{t}+c_{i,j+1,k}^{t}+c_{i,j-1,k}^{t}+2c_{i,j,k+1}^{t}\right). \quad (38)$$

At the boundary grid point (x_i, y_j, z_k) where the skull lies only in the negative z direction and the positive y direction:

$$\left[1+6\lambda-\frac{\Delta t}{2}(\rho-G)\right]c_{i,j,k}^{t+1}-\lambda\left(c_{i+1,j,k}^{t+1}+c_{i-1,j,k}^{t+1}+2c_{i,j-1,k}^{t+1}+2c_{i,j,k+1}^{t+1}\right)$$
$$=\left[1-6\lambda+\frac{\Delta t}{2}(\rho-G)\right]c_{i,j,k}^{t}+\lambda\left(c_{i+1,j,k}^{t}+c_{i-1,j,k}^{t}+2c_{i,j-1,k}^{t}+2c_{i,j,k+1}^{t}\right). \quad (39)$$

At the boundary grid point (x_i, y_j, z_k) where the skull lies only in the negative z direction and the negative y direction:

$$\left[1+6\lambda-\frac{\Delta t}{2}(\rho-G)\right]c_{i,j,k}^{t+1}-\lambda\left(c_{i+1,j,k}^{t+1}+c_{i-1,j,k}^{t+1}+2c_{i,j+1,k}^{t+1}+2c_{i,j,k+1}^{t+1}\right)$$
$$=\left[1-6\lambda+\frac{\Delta t}{2}(\rho-G)\right]c_{i,j,k}^{t}+\lambda\left(c_{i+1,j,k}^{t}+c_{i-1,j,k}^{t}+2c_{i,j+1,k}^{t}+2c_{i,j,k+1}^{t}\right). \quad (40)$$

At the boundary grid point (x_i, y_j, z_k) where the skull lies only in the positive y direction and the positive x direction:

$$\left[1+6\lambda-\frac{\Delta t}{2}(\rho-G)\right]c_{i,j,k}^{t+1}-\lambda\left(2c_{i-1,j,k}^{t+1}+2c_{i,j-1,k}^{t+1}+c_{i,j,k+1}^{t+1}+c_{i,j,k-1}^{t+1}\right)$$
$$=\left[1-6\lambda+\frac{\Delta t}{2}(\rho-G)\right]c_{i,j,k}^{t}+\lambda\left(2c_{i-1,j,k}^{t}+2c_{i,j-1,k}^{t}+c_{i,j,k+1}^{t}+c_{i,j,k-1}^{t}\right). \quad (41)$$

At the boundary grid point (x_i, y_j, z_k) where the skull lies only in the positive y direction and the negative x direction:

$$\left[1+6\lambda-\frac{\Delta t}{2}(\rho-G)\right]c_{i,j,k}^{t+1}-\lambda\left(2c_{i+1,j,k}^{t+1}+2c_{i,j-1,k}^{t+1}+c_{i,j,k+1}^{t+1}+c_{i,j,k-1}^{t+1}\right)$$
$$=\left[1-6\lambda+\frac{\Delta t}{2}(\rho-G)\right]c_{i,j,k}^{t}+\lambda\left(2c_{i+1,j,k}^{t}+2c_{i,j-1,k}^{t}+c_{i,j,k+1}^{t}+c_{i,j,k-1}^{t}\right). \quad (42)$$

At the boundary grid point (x_i, y_j, z_k) where the skull lies only in the negative y direction and the positive x direction:

$$\left[1+6\lambda-\frac{\Delta t}{2}(\rho-G)\right]c_{i,j,k}^{t+1}-\lambda\left(2c_{i-1,j,k}^{t+1}+2c_{i,j+1,k}^{t+1}+c_{i,j,k+1}^{t+1}+c_{i,j,k-1}^{t+1}\right)$$
$$=\left[1-6\lambda+\frac{\Delta t}{2}(\rho-G)\right]c_{i,j,k}^{t}+\lambda\left(2c_{i-1,j,k}^{t}+2c_{i,j+1,k}^{t}+c_{i,j,k+1}^{t}+c_{i,j,k-1}^{t}\right). \quad (43)$$

At the boundary grid point (x_i, y_j, z_k) where the skull lies only in the negative y direction and the negative x direction:

$$\left[1+6\lambda-\frac{\Delta t}{2}(\rho-G)\right]c_{i,j,k}^{t+1}-\lambda\left(2c_{i+1,j,k}^{t+1}+2c_{i,j+1,k}^{t+1}+c_{i,j,k+1}^{t+1}+c_{i,j,k-1}^{t+1}\right)$$
$$=\left[1-6\lambda+\frac{\Delta t}{2}(\rho-G)\right]c_{i,j,k}^{t}+\lambda\left(2c_{i+1,j,k}^{t}+2c_{i,j+1,k}^{t}+c_{i,j,k+1}^{t}+c_{i,j,k-1}^{t}\right). \quad (44)$$

At the boundary grid point (x_i, y_j, z_k) where the skull lies only in the negative x direction, the positive y direction and the positive z direction:

$$\left[1+6\lambda-\frac{\Delta t}{2}(\rho-G)\right]c_{i,j,k}^{t+1}-\lambda\left(2c_{i+1,j,k}^{t+1}+2c_{i,j-1,k}^{t+1}+2c_{i,j,k-1}^{t+1}\right)$$
$$=\left[1-6\lambda+\frac{\Delta t}{2}(\rho-G)\right]c_{i,j,k}^{t}+\lambda\left(2c_{i+1,j,k}^{t}+2c_{i,j-1,k}^{t}+2c_{i,j,k-1}^{t}\right). \quad (45)$$

At the boundary grid point (x_i, y_j, z_k) where the skull lies only in the negative x direction, the negative y direction and the positive z direction:

$$\left[1+6\lambda-\frac{\Delta t}{2}(\rho-G)\right]c_{i,j,k}^{t+1}-\lambda\left(2c_{i+1,j,k}^{t+1}+2c_{i,j+1,k}^{t+1}+2c_{i,j,k-1}^{t+1}\right)$$
$$=\left[1-6\lambda+\frac{\Delta t}{2}(\rho-G)\right]c_{i,j,k}^{t}+\lambda\left(2c_{i+1,j,k}^{t}+2c_{i,j+1,k}^{t}+2c_{i,j,k-1}^{t}\right). \quad (46)$$

At the boundary grid point (x_i, y_j, z_k) where the skull lies only in the negative x direction, the positive y direction and the negative z direction:

$$\left[1+6\lambda-\frac{\Delta t}{2}(\rho-G)\right]c_{i,j,k}^{t+1}-\lambda\left(2c_{i+1,j,k}^{t+1}+2c_{i,j-1,k}^{t+1}+2c_{i,j,k+1}^{t+1}\right)$$
$$=\left[1-6\lambda+\frac{\Delta t}{2}(\rho-G)\right]c_{i,j,k}^{t}+\lambda\left(2c_{i+1,j,k}^{t}+2c_{i,j-1,k}^{t}+2c_{i,j,k+1}^{t}\right). \quad (47)$$

At the boundary grid point (x_i,y_j,z_k) where the skull lies only in the negative x direction, the negative y direction and the negative z direction:

$$\left[1+6\lambda-\frac{\Delta t}{2}(\rho-G)\right]c_{i,j,k}^{t+1}-\lambda\left(2c_{i+1,j,k}^{t+1}+2c_{i,j+1,k}^{t+1}+2c_{i,j,k+1}^{t+1}\right)=\left[1-6\lambda+\frac{\Delta t}{2}(\rho-G)\right]c_{i,j,k}^{t}+\lambda\left(2c_{i+1,j,k}^{t}+2c_{i,j+1,k}^{t}+2c_{i,j,k+1}^{t}\right). \quad (48)$$

At the boundary grid point (x_i,y_j,z_k) where the skull lies only in the positive x direction, the positive y direction and the positive z direction:

$$\left[1+6\lambda-\frac{\Delta t}{2}(\rho-G)\right]c_{i,j,k}^{t+1}-\lambda\left(2c_{i-1,j,k}^{t+1}+2c_{i,j-1,k}^{t+1}+2c_{i,j,k-1}^{t+1}\right)=\left[1-6\lambda+\frac{\Delta t}{2}(\rho-G)\right]c_{i,j,k}^{t}+\lambda\left(2c_{i-1,j,k}^{t}+2c_{i,j-1,k}^{t}+2c_{i,j,k-1}^{t}\right). \quad (49)$$

At the boundary grid point (x_i,y_j,z_k) where the skull lies only in the positive x direction, the negative y direction and the positive z direction:

$$\left[1+6\lambda-\frac{\Delta t}{2}(\rho-G)\right]c_{i,j,k}^{t+1}-\lambda\left(2c_{i-1,j,k}^{t+1}+2c_{i,j+1,k}^{t+1}+2c_{i,j,k-1}^{t+1}\right)=\left[1-6\lambda+\frac{\Delta t}{2}(\rho-G)\right]c_{i,j,k}^{t}+\lambda\left(2c_{i-1,j,k}^{t}+2c_{i,j+1,k}^{t}+2c_{i,j,k-1}^{t}\right). \quad (50)$$

At the boundary grid point (x_i,y_j,z_k) where the skull lies only in the positive x direction, the positive y direction and the negative z direction:

$$\left[1+6\lambda-\frac{\Delta t}{2}(\rho-G)\right]c_{i,j,k}^{t+1}-\lambda\left(2c_{i-1,j,k}^{t+1}+2c_{i,j-1,k}^{t+1}+2c_{i,j,k+1}^{t+1}\right)=\left[1-6\lambda+\frac{\Delta t}{2}(\rho-G)\right]c_{i,j,k}^{t}+\lambda\left(2c_{i-1,j,k}^{t}+2c_{i,j-1,k}^{t}+2c_{i,j,k+1}^{t}\right). \quad (51)$$

At the boundary grid point (x_i,y_j,z_k) where the skull lies only in the positive x direction, the negative y direction and the negative z direction:

$$\left[1+6\lambda-\frac{\Delta t}{2}(\rho-G)\right]c_{i,j,k}^{t+1}-\lambda\left(2c_{i-1,j,k}^{t+1}+2c_{i,j+1,k}^{t+1}+2c_{i,j,k+1}^{t+1}\right)=\left[1-6\lambda+\frac{\Delta t}{2}(\rho-G)\right]c_{i,j,k}^{t}+\lambda\left(2c_{i-1,j,k}^{t}+2c_{i,j+1,k}^{t}+2c_{i,j,k+1}^{t}\right). \quad (52)$$

6. Numerical experiments

In order to test the numerical schemes implemented for solving Eq. (1) and support the correctness of the overall mathematical treatment presented, a number of pertinent computational scenarios have been executed. Initially, in order to provide quantitative checks exclusively of the linear component of the analysis presented in the most controllable way, pure diffusion has been considered in a number of numerical experiments performed. A special simplified problem for which an analytic solution is available [32] has been addressed in order to validate parts of the code and study the effects of several numerical factors on the simulation outcome.

In a cubic domain $R = \Omega$, with boundaries at $\partial R = \partial\Omega$ the following initial condition is assumed

$$c(x,y,z,0) = \exp\left(-\frac{(x-x_0)^2}{2\sigma_0^2} - \frac{(y-y_0)^2}{2\sigma_0^2} - \frac{(z-z_0)^2}{2\sigma_0^2}\right), \quad (x,y,z) \in \Omega, \tag{53}$$

where σ_0 is the initial standard deviation of the Gaussian hump. The net growth rate and the loss rate due to treatment are equal to zero. For an infinite domain, the analytical solution for pure diffusion [33] can be expressed as

$$c(x,y,z,t) = \frac{\sigma_0^3}{\sigma^3} \exp\left(-\frac{(x-x_0)^2}{2\sigma^2} - \frac{(y-y_0)^2}{2\sigma^2} - \frac{(z-z_0)^2}{2\sigma^2}\right), \tag{54}$$

$$\sigma^2 = \sigma_0^2 + 2Dt. \tag{55}$$

For $\sigma_0 = 3h$ and $t = n\Delta t$, where h is the nodal spacing, Δt is the time step, n is a time step counter, $\vec{x} = (x, y, z)$ are the spatial coordinates of the node, (x_0, y_0, z_0) is the center of the cube, D is the diffusion coefficient, $c(\vec{x}, t)$ is the concentration at time and spatial point $\vec{x}$ and $\lambda = D\Delta t/(2h^2)$. The domain is taken sufficiently large such that the application of the boundary conditions does not significantly affect the computations in the region of interest.

At the end of each simulation aiming at validating the numerical treatment by exploiting the analytical solution, the relative percentage error e is calculated. The latter is calculated by comparing the predicted values generated by the model with the ones obtained by the analytical solution. The relative percentage error is defined as

$$e = \left| \frac{c - c_{approx}}{c} \right| \times 100\%, \tag{56}$$

where c is the concentration calculated using the analytical solution and c_{approx} is the numerically calculated concentration.

6.1. Convergence and stability

In this section the pure diffusion aspects of the analysis presented are addressed. Checks of the non linear behavior of tumor cell proliferation are provided in Section 6.6. In order to study the convergence and stability characteristics of the Crank–Nicolson scheme that has been employed for the numerical solution of the partial diffusion–reaction differential equation, the spatiotemporal cell density distribution has been calculated for different values of the elementary time interval Δt and the elementary spatial (length) interval h for the initial value problem described in the previous part of Section 6. A numerical verification of the second order accuracy of the scheme in both time and space has been achieved. The diffusion coefficient D has been assumed equal to 0.0065 cm^2/d (d denotes the time unit day here). This is an estimated value of D in corpus callosum being the largest white matter structure in brain. The particular value expresses the advancing speed of the tumor margin across it [1]. It should be kept in mind that gliomas are expected to emerge within the white matter and therefore a large percentage of the spatial region with the highest concentration of tumor cells is expected to involve white matter. Since homogeneous diffusion has been assumed in this paper, for the needs of simulations presented the value of D has been assumed to hold true for the entire interior of the cranial cavity. The latter obviously constitutes a first gross approximation. Fig. 4 summarizes the relative percentage error in the approximate solution at $t = 200$ d for different values of h. For all calculations a time step of $\Delta t = 0.1$ d has been used. Fig. 5 presents the error of the approximate solution at $t = 200$ d for different values of Δt, with h fixed at 0.1 cm.

It is noted that the mean relative percentage error for the case of $h = 0.75$ cm approximately reaches the value 9% after 200 simulated days. This is pretty reasonable since the spatial discretization of the domain that includes the tumor is too sparse. The discretization of 0.1 cm is used in most of the simulations performed in the rest of the paper. The latter leads to an error of about 0.15% after 200 simulated days for typical model parameter values for the case of glioblastoma. According to Fig. 5, a temporal discretization with a temporal unit equal to 1 *d* would be acceptable since it leads to an error of less than 1% after 200 simulated days. In order to further improve accuracy a temporal discretization of $\Delta t = 0.5$ d is used in the rest of the paper.

6.2. Pure diffusion: mass conservation and linearity checks

Mass or matter conservation within a closed system is a fundamental law of classical physics. Based on this principle the mass of substances contained within a closed system, i.e. a completely isolated system, will remain constant over time no matter what processes are acting inside the system. In the following hypothetical problem where pure glioma cell diffusion takes place within an isolated domain in which tumor cells can neither be born nor die, mass conservation must hold true. It is stressed that this biologically unrealistic scenario has been considered exclusively for the sake of partial mathematical validation of the analysis presented. The total (non dimensional) tumor mass in this hypothetical problem is represented by the sum of tumor cells, assuming that each tumor cell possesses the same elementary cell mass. Mass conservation has been verified by the numerical experimentation described below.

An initial hypothetical spherical tumor of radius equal to 2 mm has been assumed. The computational domain has been taken sufficiently large such that the application of boundary conditions would not significantly affect the computations in the region of interest. The initial cell concentration is assumed 10^6 cells/mm^3 inside the sphere and 0 cells/mm^3 outside the sphere. The value of the 10^6 cells/mm^3 is a plausible estimate for at least an avascular glioma tumorlet of volume equal to 1 mm^3 according to literature [34]. Net tumor growth rate and loss rate due to treatment are considered zero. Homogeneous Neumann boundary conditions (no tumor cell flux through the boundary) have been applied on the boundaries of the domain.

Code executions have shown that the total number of tumor cells inside the mesh remains practically stable with only slight deviations due to the accumulation of minimal numerical errors for a considerable time interval. According to

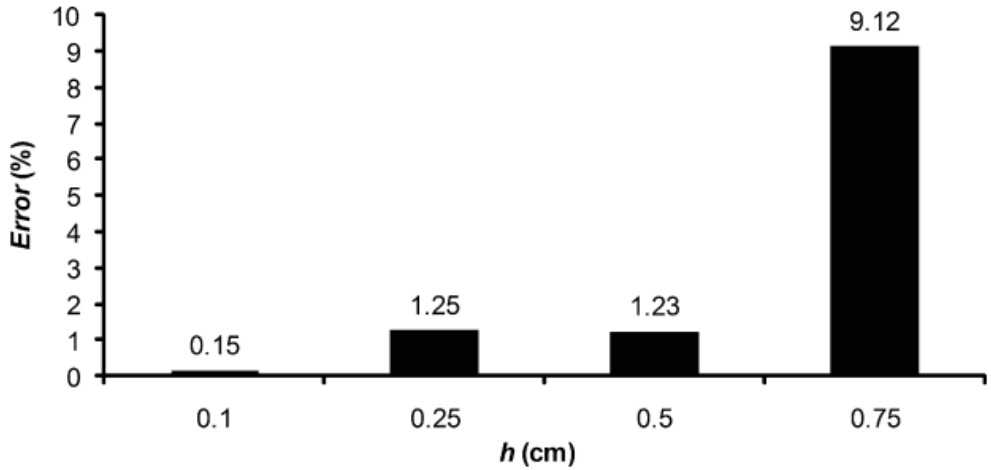

Fig. 4. Relative percentage error for different values of h. For all calculations a constant/ fixed time step of $\Delta t = 0.1$ d has been used and the approximate solution has been obtained at $t = 200$ d (see text for details).

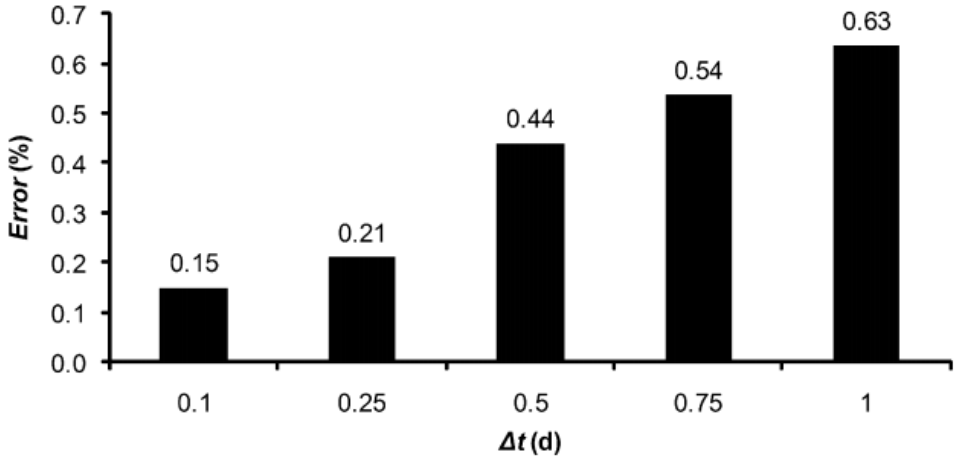

Fig. 5. Relative percentage error for different values of Δt. For all calculations a constant $h = 0.1$ cm has been used and the approximate solution has been obtained at $t = 200$ d (see text for details).

Fig. 6 for the above mentioned parameter values this is larger than 700 d. The latter is pretty reasonable since the initial total number of cells have been placed in a region very small in comparison with the dimensions of the discretization mesh.

The relative percentage error of the total number of tumor cells with regard to the initial number of tumor cells is depicted in Fig. 7. The error shown in Fig. 7 is mainly due to the replacement of the continuous expressions of the derivatives with their numerical (algebraic) counterpart. It is noted that after 700 simulated days the percentage relative error is kept less than 5%.

For the extreme case of pure diffusion (no sources, no sinks) described above, it has been verified that if the initial cell concentration is doubled at all points of the discretization mesh i.e.

$$c_2(x_i, y_j, z_k, 0) = 2c_1(x_i, y_j, z_k, 0), \tag{57}$$

the cell concentration at any given spatiotemporal point (x_i, y_j, z_k, t) is doubled in relation to its value corresponding to the reference initial cell concentration. Therefore, the new tumor cell concentration value at point (x_i, y_j, z_k, t) is:

$$c_2(x_i, y_j, z_k, t) = 2c_1(x_i, y_j, z_k, t). \tag{58}$$

The ratio $c_2(x_i, y_j, z_k, t)/c_1(x_i, y_j, z_k, t)$ is depicted in Fig. 8. It is clear that the ratio $c_2(x_i, y_j, z_k, t)/c_1(x_i, y_j, z_k, t)$ is equal to the ratio $c_2(x_i, y_j, z_k, 0)/c_1(x_i, y_j, z_k, 0)$. This is a validation of the purely diffusive linear component of the simulation code.

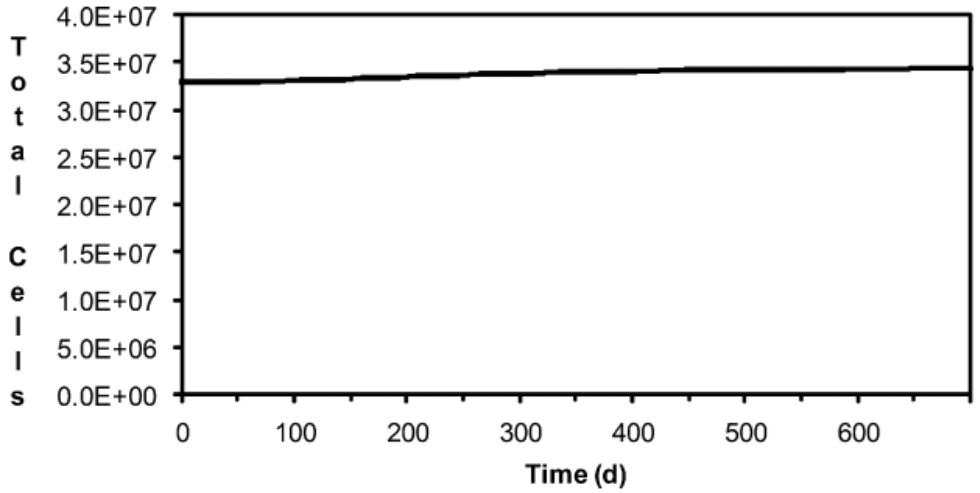

Fig. 6. Total number of cells for an exclusively mathematically relevant scenario of pure homogeneous diffusion of glioma cells within an isolated domain. A sphere of radius equal to 2 mm has been considered. The initial cell concentration inside the sphere is supposed to be 10^6 cells/mm^3 and 0 cells/ mm^3 elsewhere. The net tumor growth rate and loss rate due to treatment are considered zero. On the boundaries of the mesh homogeneous Neumann conditions (no tumor cell flux through the boundary) have been applied.

6.3. Comparison with the analytical solution for a special case

In order to study the accuracy of the diffusive component of the numerical algorithm, a comparison between the numerical and the analytical solution to the initial value problem described in the first part of Section 6 has been performed. The following parameter values have been considered: $\Delta t = 0.5$ d, $h = 0.1$ cm, $D = 0.0065$ cm^2/d ($\lambda = 0.1625$), zero net tumor growth rate and zero tumor loss rate due to treatment. The results are shown in Fig. 9. It is obvious that numerical results are in excellent agreement with the analytical solution. The mean percentage error at $t = 25$ d, $t = 50$ d and $t = 100$ d is depicted in Fig. 10. As simulated time increases a damping of numerical oscillations is observed leading to the minimization of the total error.

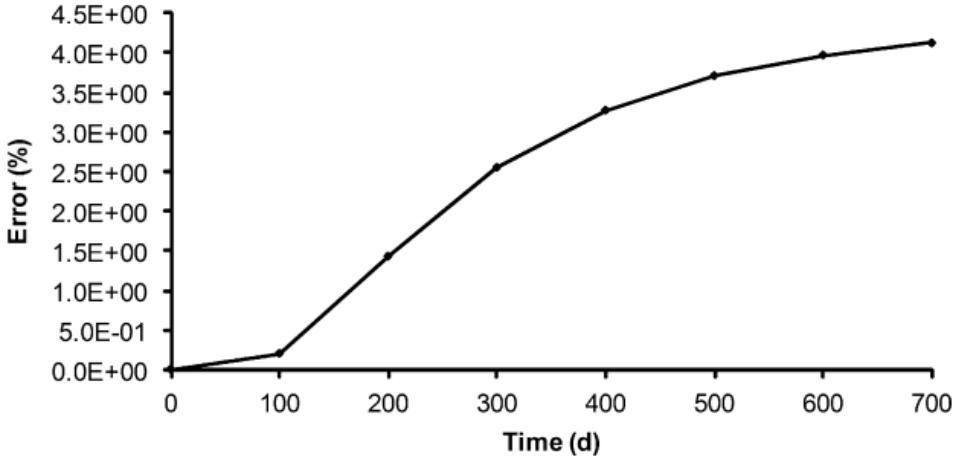

Fig. 7. Plot of the relative percentage error of the total number of tumor cells with regard to their initial number. Pure diffusion is considered for validation purposes only. The error is mainly due to the replacement of the continuous expressions of the derivatives with their numerical (algebraic) counterpart. It is noted that after 700 simulated days the percentage relative error is kept less than 5%.

6.4. Symmetry studies

Pure tumor cell diffusion is assumed here too. The following parameter and gridding values have been used: an initial hypothetical spherical tumor of *radius* = 2 cm centrally positioned inside a cubic mesh of 9 cm × 9 cm × 9 cm with adiabatic boundaries, zero net tumor growth rate and zero loss rate due to treatment, cell concentration within the initial spherical tumor equal to 10^6 cells/mm^3 diffusion coefficient $D = 0.0065$ cm^2/d. The cell concentration c at symmetric nodes has been calculated for $h = 0.1$ cm and $\Delta t = 0.5$ d at different simulated times. Code executions show that the shape of the tumor remains conformal to its initial geometrical form. The corresponding numerical predictions of the tumor cell concentration obtained after 100 and 200 simulated days assuming that (x_0, y_0, z_0) lies at the center of the gridding cube, are (Fig. 11):

$$c(x_0 + 0.5, y_0 + 0.5, z_0 + 0.5, 0) = c(x_0 - 0.5, y_0 - 0.5, z_0 - 0.5, 0) = 10^6 \text{ cells/mm}^3, \tag{59}$$

$$c(x_0 + 0.5, y_0 + 0.5, z_0 + 0.5, 100) = c(x_0 - 0.5, y_0 - 0.5, z_0 - 0.5, 100) = 535.358 \text{ cells/mm}^3, \tag{60}$$

$$c(x_0 + 0.5, y_0 + 0.5, z_0 + 0.5, 200) = c(x_0 - 0.5, y_0 - 0.5, z_0 - 0.5, 200) = 293.789 \text{ cells/mm}^3. \tag{61}$$

It is noted that the spatial coordinate values are in cm, whereas the temporal coordinate values are in d. Additionally, although biological cells are discrete entities, fractional values of the number of cells are accepted only as intermediate results of the mathematical treatment in order to minimize errors induced by numerical methods.

In conclusion, symmetry is conserved for the case of a symmetrical initial geometry of the purely diffusive system under consideration. Thus, for example, the symmetric points below have the same cell concentration at any time point.

$$c(x_0 + \xi, y_0 + \xi, z_0 + \xi, t) = c(x_0 - \xi, y_0 - \xi, z_0 - \xi, t), \tag{62}$$

$$c(x_0 + \xi, y_0 + \xi, z_0 + \xi, 2t) = c(x_0 - \xi, y_0 - \xi, z_0 - \xi, 2t). \tag{63}$$

This observation provides further support to the correctness of the diffusive component of the simulation code.

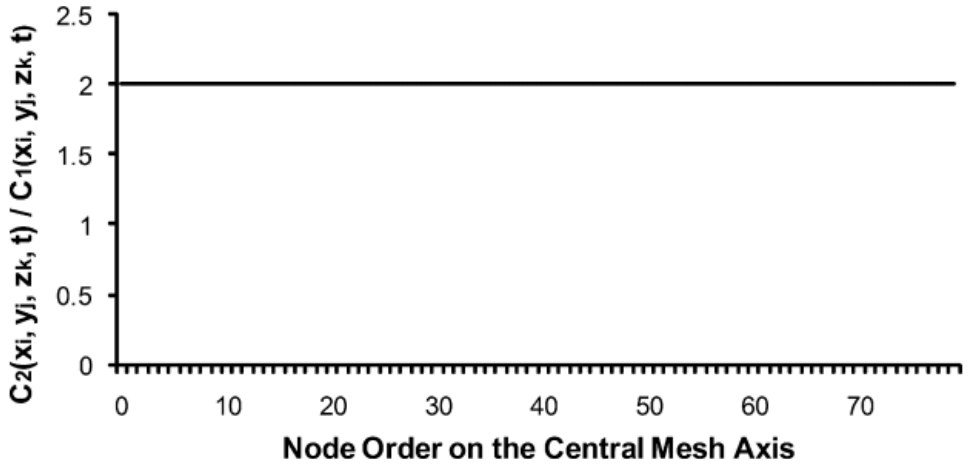

Fig. 8. Linearity check over a central axis of the discretization mesh. For the extreme hypothetical case of pure diffusion (no sources, no sinks), it is verified that if the initial cell concentration is doubled at all points of the discretization mesh, the cell concentration at any given spatiotemporal point (x_i, y_j, z_k, t) is doubled in relation to its value corresponding to the reference initial cell concentration.

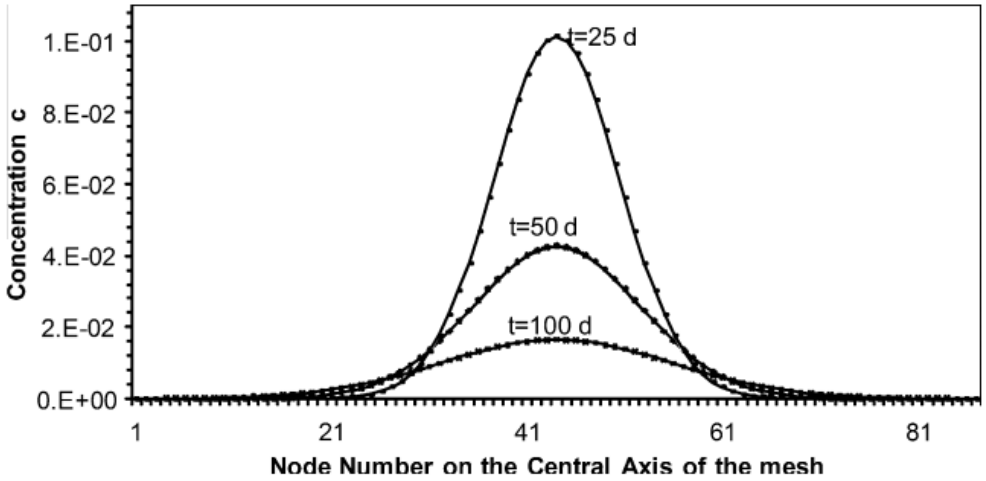

Fig. 9. Comparison between the numerical and the analytical solution for pure diffusion. The results have been obtained for points lying at the central axis of the mesh at t = 25 d, t = 50 d and t = 100 d. The following parameter values have been considered: Δt = 0.5 d, h = 0.1 cm, D = 0.0065 cm^2/d, zero net tumor growth rate and zero tumor loss rate due to treatment. The concentration c is in cells/mm^3 although concentration values in this figure do not necessarily correspond to biologically meaningful situations. They just correspond to a published particular general diffusion problem which is exploited for the mathematical checking of the code. It is obvious that numerical results are in excellent agreement with the analytical solution. Solid lines correspond to the analytical solutions whereas dots correspond to numerical solutions.

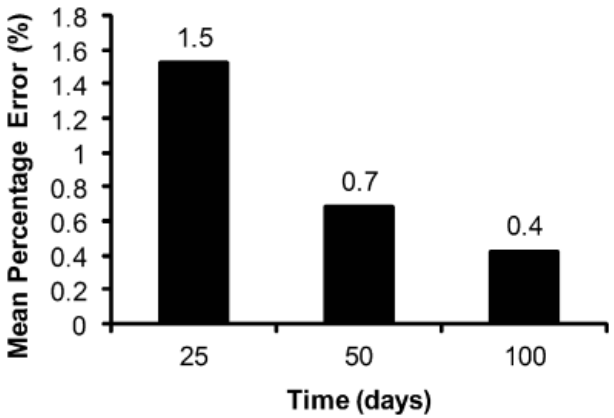

Fig. 10. The mean percentage error at $t = 25$ d, $t = 50$ d and $t = 100$ d. The following parameter values have been considered: $\Delta t = 0.5$ d, $h = 0.1$ cm, $D = 0.0065$ cm^2/d, zero net tumor growth rate and zero tumor loss rate due to treatment. As simulated time increases damping of numerical oscillations is observed leading to the minimization of the total error.

6.5. Numerical validation of the adiabatic behavior of the boundary implementation

Several pertinent boundary geometry scenarios have been addressed. In order to check the correctness of the boundary treatment component of the simulation code the following two criteria have been adopted:

i. prohibition of tumor cell transfer through the skull;
ii. conservation of the total number of tumor cells within the skull cavity *in the special fictitious* (and exclusively *mathematically* relevant) case of pure diffusion with neither cell generation nor cell death. Obviously, in the biologically relevant scenarios addressed where tumor cell proliferation and loss are present this criterion is irrelevant.

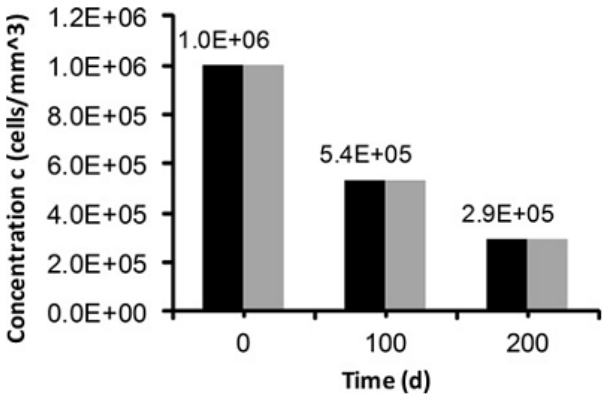

Fig. 11. Cell concentration c at symmetric nodes for an initial hypothetical spherical tumor of *radius* = 2 cm centrally positioned inside a cubic mesh of 9 cm × 9 cm × 9 cm. c has been calculated for a diffusion coefficient $D = 0.0065\ \text{cm}^2/\text{d}$, cell concentration within the initial spherical tumor equal to 10^6 cells/mm^3, $h = 0.1$ cm and $\Delta t = 0.5$ d at different simulated times. Pure diffusion is considered. The corresponding numerical predictions of the tumor cell concentration obtained after 100 and 200 simulated days at the point $(x_0 + 0.5, y_0 + 0.5, z_0 + 0.5)$ and at its symmetric point $(x_0 - 0.5, y_0 - 0.5, z_0 - 0.5)$ assuming that (x_0, y_0, z_0) lies at the center of the gridding cube are equal. All spatial values are in cm.

In order to check the validity of the macroscopic diffusive behavior of the mathematical treatment presented along with its boundary condition component various forms of a fictitious growing and diffusive entity starting with well defined initial cubic boundaries have been assumed.

Fig. 12, represents a two-dimensional slice of a fictitious growing and diffusive entity with the dynamic characteristics of glioblastoma with net growth rate equal to $\rho = 0.012\ d^{-1}$ [26] and loss rate due to treatment equal to $G = 0.0013\ d^{-1}$. Grey level intensity depends on cell concentration. Several snapshots of the simulation corresponding to various time points are depicted. As time increases the entity image is gradually becoming blurred due to diffusion as expected.

A three dimensional visualization of the simulation results for an arbitrary boundary geometry is shown in Fig. 13. An initial virtual spherical tumor is supposed to lie inside the boundary cavity. As time increases, the tumor grows and diffuses over the entire mesh. However, it does not migrate beyond the boundary. Thus criterion i is satisfied. Visualization details are provided in Fig. 14.

Fig. 15 demonstrate the adiabatic behavior of a perfect cubic boundary (different from the one considered in Figs. 13 and 14). The tumor located inside clearly shows a diffusive behavior. It is also noted that the final shape of the tumor is practically conformal to its initial counterpart for the first 150 simulated days.

For the case of pure diffusion described in the first part of Section 6 assuming adiabatic boundary conditions the concentration on the central axis of the mesh has been sampled at different time points (Fig. 16). As time increases all the nodes included within the domain tend to have the same cell concentration. Therefore, a state of equilibrium is approached as expected.

6.6. Towards a clinical validation of the model: initial steps

This section contains the initial steps of an envisaged systematic clinical validation of the composite model. A typical real human head has been considered (Fig. 17). The three dimensional image depicted in panel A of Fig. 17 has been constructed using a freely available T1 weighted MRI head dataset (J. Orchard, http://www.cs.uwaterloo.ca/~jorchard/mri/). To this end the ImageJ® software [35] has been utilized and the image has been exported in tif format. A slight size adaptation without loss of the original information has been performed by the authors for the needs of the numerical experiments described below.

The image characteristics are shown in Table 1. The embedded head atlas consists of 129 slices. In order to clinically check the tumor growth model presented, a segmentation of the internal surface of the skull cavity within which lies the brain is mandatory. This step has been implemented manually on the previously mentioned 3D MRI image using the Jasc Paint Shop Pro® software [36]. In order to identify the boundaries of the region of interest the anatomical data and annotations provided in [37, pp35-104] have been used. Additionally the Mango® software [38] has been used in order to obtain the virtual cuts of the head appearing in Fig. 17(B). Following the delineation of the skull/brain cavity boundary, a fictitious growing virtual spherical glioblastoma tumor of radius equal to 1.4 cm was virtually placed inside the cavity (Fig. 17(B)). The size of this virtual tumor is essentially consistent with the extensively made assumption that glioblastoma diagnosis is possible after the latter has reached a tomographically imageable size equivalent to a sphere with an average diameter of 3 cm [39].

For the sake of simplicity during the *in silico* model validation process the concentration of tumor cells within the initial tumor has been arbitrarily assumed uniform and equal to 10^6 cells/mm^3. Diffusion phenomena have been ignored before the time point corresponding to the start of the simulation. In other words, non diffusive compact tumor growth has been assumed *before* the start of the simulation (but not later). The following parameter values have been used: diffusion coefficient $D = 0.0065$ cm^2/d, $h = 0.2$ cm and $\Delta t = 0.5$ d, net tumor growth rate $\rho = 0.012$ d^{-1}. It is recalled that the net tumor growth rate ρ includes proliferation, loss and death of tumor cells.

The virtual tumor grows for 200 days after the initialization time point corresponding to Fig. 17. As time increases, the tumor diffuses over the free space of the entire gridding mesh. However, it does not migrate beyond the boundary as expected due to boundary conditions. The change of the total number of tumor cells inside the mesh is depicted in Fig. 18.

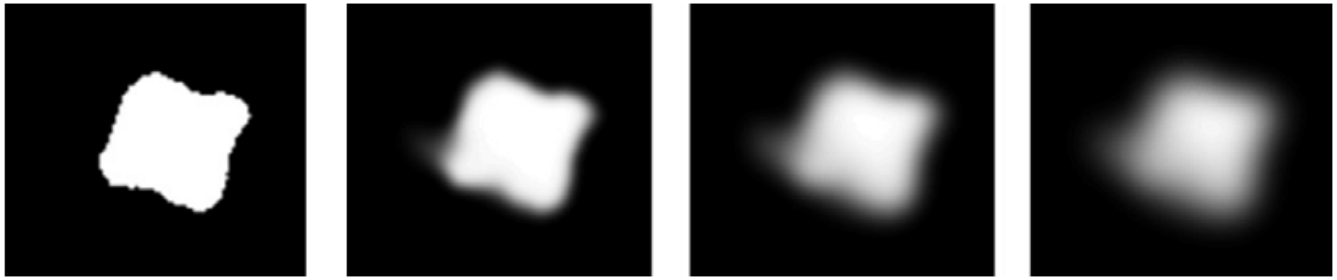

Fig. 12. Snapshots of a fictitious growing and diffusive entity with the dynamic characteristics of glioblastoma corresponding to various time points (far left hand side 1st panel: first simulated day (1 d), 2nd panel: 600 d, 3rd panel: 1000 d, 4th panel: 2000 d). The hypothetical entity starts with well defined initial cubic boundaries. A cubic mesh of 95 cm × 95 cm × 95 cm has been used. The following parameter values have been considered: diffusion coefficient $D = 0.0065$ cm^2/d, cell concentration within the initial entity equal to 10^6 cells/mm^3, $h = 1$ cm and $\Delta t = 1$ d, net growth rate $\rho = 0.012$ d^{-1} and loss rate due to treatment (arbitrary value) $G = 0.0013$ d^{-1}. Grey level intensity depends on cell concentration. As time increases the image of the entity is gradually becoming blurred due to diffusion as expected. It is noted that in this figure, the maximum and the minimum value of cell concentration *over each panel* has been assigned the value of pure white color (grey scale level = 255) and black color (grey scale level = 0), respectively.

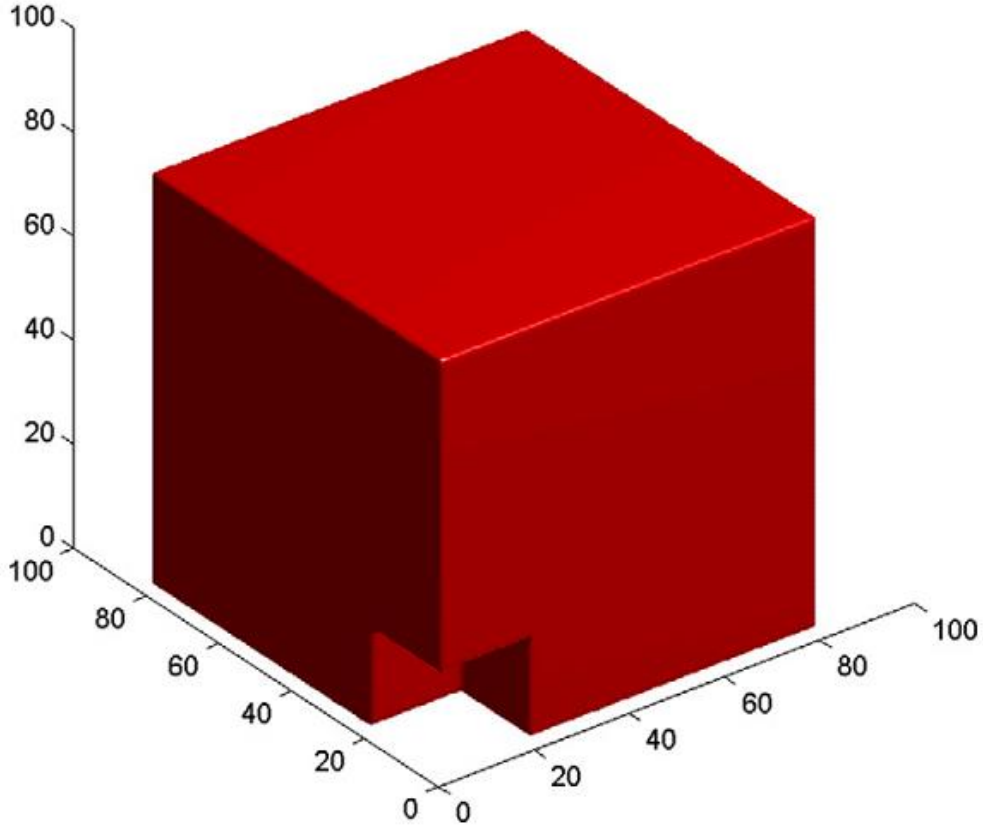

Fig. 13. An arbitrary boundary geometry. An initial virtual spherical tumor is supposed to lie inside the boundary cavity.

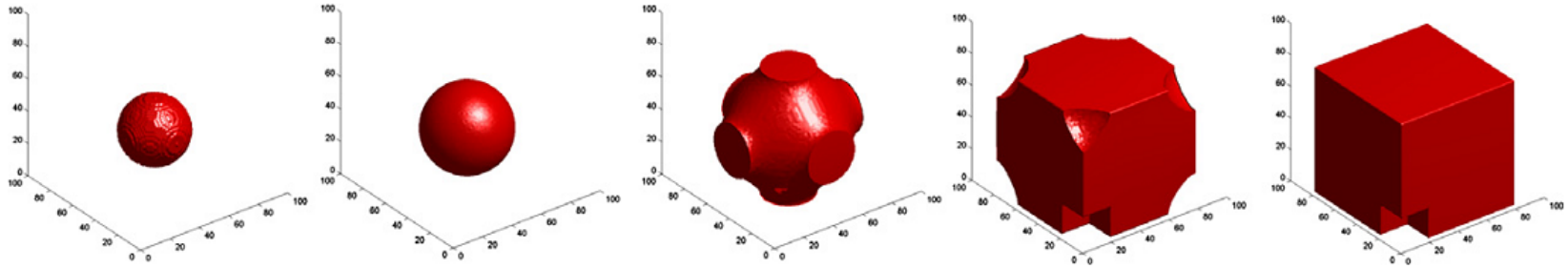

Fig. 14. An initial virtual spherical tumor of radius = 2 cm is supposed to lie inside the boundary cavity of Fig. 13. Panels from left to right correspond to days 1, 150, 299, 450, 899. For visualization purposes, for each time point considered, a concentration cutoff value has been assumed so that concentration values lower than the cutoff value are represented by white color. As time increases, the tumor diffuses over the free space of the entire mesh. However, it does not migrate beyond the boundary. A cubic mesh of 8 cm × 8 cm × 8 cm has been used. The following parameter values have been used: diffusion coefficient $D = 0.0065$ cm^2/d, cell concentration within the initial tumor equal to 10^6 cells/mm^3, $h = 0.1$ cm and $\Delta t = 1$ d, net tumor growth rate $\rho = 0.012$ d^{-1} and loss rate due to treatment (arbitrary value) $G = 0.0013$ d^{-1}.

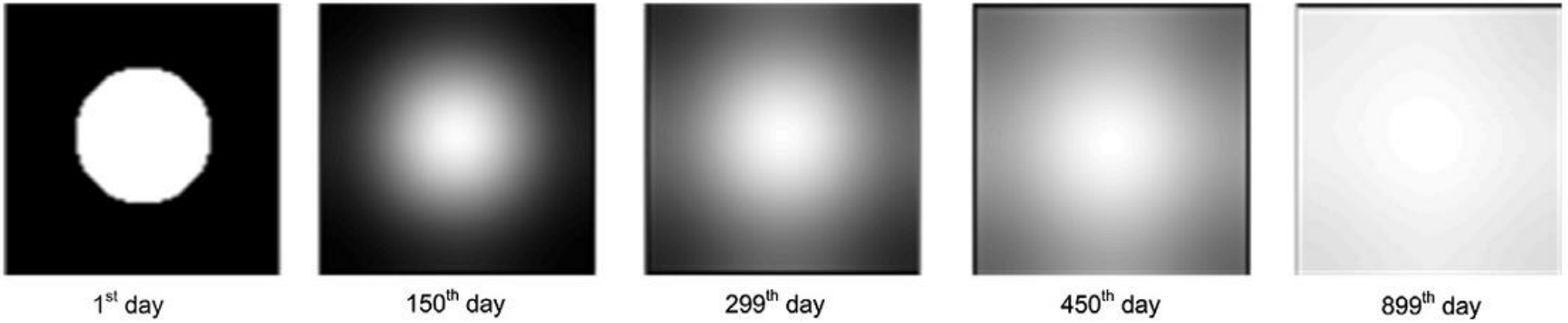

Fig. 15. Snapshots of a fictitious growing virtual spherical tumor of radius = 2 cm placed in a perfectly cubically bounded domain. Grey levels are proportional to cell concentration. In this figure, the maximum and the minimum value of tumor cell concentration over each panel is assigned the value of pure white (grey scale level = 255) and black (grey scale level = 0) respectively. A cubic mesh of 8 cm × 8 cm × 8 cm has been used. The following parameter values have been utilized: diffusion coefficient $D = 0.0065$ cm^2/d, cell concentration within the initial tumor equal to 10^6 cells/ mm^3, $h = 0.1$ cm and $\Delta t = 1$ d, net tumor growth rate $\rho = 0.012$ d^{-1} and loss rate due to treatment (arbitrary value) $G = 0.0013$ d^{-1}.

The first reported work on an exponentially growing population was performed by Reverend T.R. Malthus in 1798. The exponential growth is the simplest proliferation law. It describes the population density $P(t)$ at any time t as a function of the initial population density $P(0)$ and the constant growth rate k, which in the tumor growth context addressed depends on the intrinsic net tumor growth rate (aggressiveness of the tumor)

$$P(t) = P(0)e^{kt}. \tag{64}$$

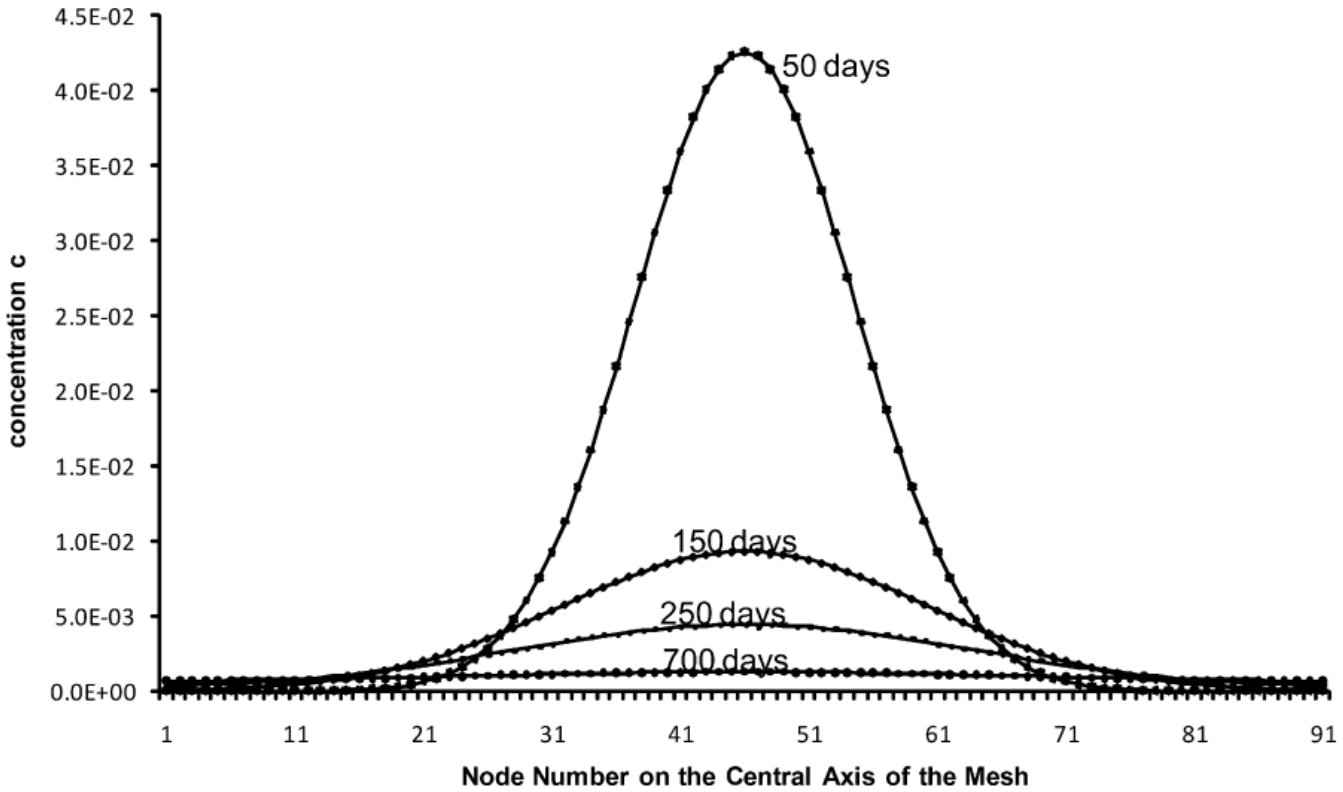

Fig. 16. Concentration on the central axis of the mesh has been sampled at different time points (50 d, 150 d, 250 d and 700 d). The results have been obtained for pure diffusion (zero net tumor growth rate and zero loss rate due to treatment) and the diffusion coefficient D has been set to 0.0065 cm^2/d. The concentration c is in cells/mm^3 although concentration values in this figure do not necessarily correspond to biologically meaningful situations. They just correspond to a published particular diffusion problem which is exploited for the mathematical checking of the code. As time increases all the nodes included within the domain tend to achieve the same cell concentration.

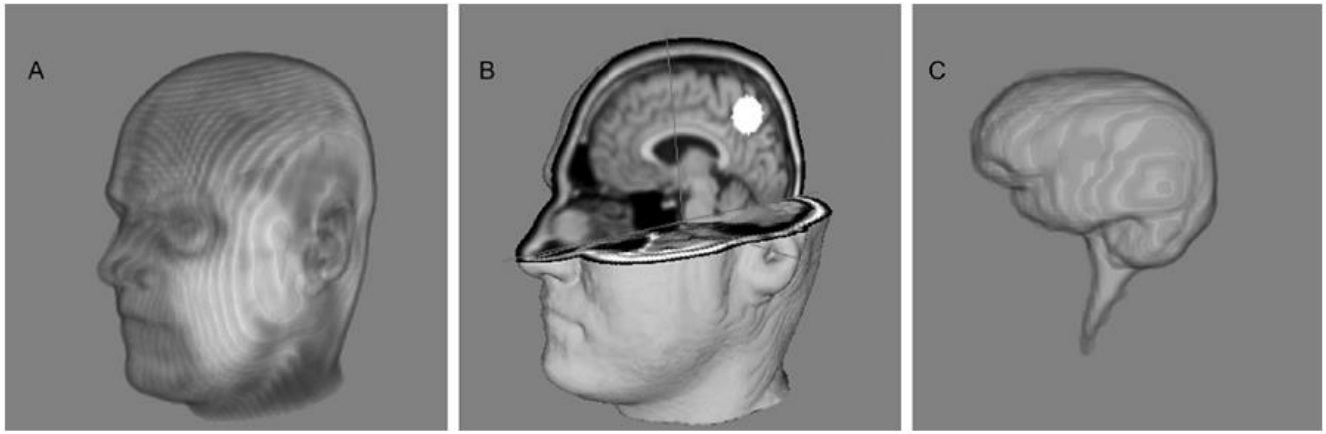

Fig. 17. (A) A three dimensional rendering of a set of T1 weighted MRI slices of a real human head. (B) An initial fictitious virtual spherical glioblastoma tumor of radius equal to 1.4 cm (denoted by white color) lying inside the skull cavity. (C) Reconstruction of the brain cavity of the skull following segmentation of each MRI slice. Further details are available in the text.

In our case $P(t)$ corresponds to the total number of tumor cells within the skull cavity. Fig. 19 depicts the relative percentage error of the total number of tumor cells calculated by comparing the predicted values generated by the model with the ones obtained by the application of the exponential growth (Eq. (64)). The increase in the error observed in the case of an "arbitrarily" shaped real human head as a function of time has been expected since a complex boundary is generally a source of numerical errors. A straightforward way to decrease the error is the exploitation of higher computational power so that a denser discretization mesh can be applied.

Table 1
Characteristics of the three dimensional head dataset.

Characteristics	Value
Width (mm)	384.00
Height (mm)	384.00
Depth (mm)	193.50
Resolution (pixels per mm)	0.667
Voxel size (mm)	$1.50 \times 1.50 \times 1.50$
Bits per pixel (unsigned)	16

Several snapshots of the fictitious growing virtual glioblastoma tumor corresponding to various time points are depicted in Fig. 20. It is noted that although the internal anatomy of brain is visible in the panels of this figure, homogeneous diffusion of tumor cells has been assumed within the skull cavity. Despite the fact that CT and MRI are two medical imaging techniques with high accuracy, there is a threshold of detection below which glioma cells are not detectable. Previous reports [18] have estimated the enhanced CT-delineated tumor boundary to correspond to a tumor cell concentration of about 8000 cells/mm^3. Therefore, as a first gross approximation the T1 gadolinium enhanced MRI delineated tumor boundary for the needs of the theoretical exploration presented in this paper is assumed to also correspond to a tumor cell concentration of 8000 cells/mm^3.

It should be noted that the gross spatial pattern of glioblastoma growth, especially in the vicinity of the skull boundary, is in good agreement with actual clinical observations [40,41]. The diameter of a sphere with volume equal to a glioblastoma tumor of fatal imageable dimensions is usually about 6 cm [39]. The latter corresponds to a volume V_{fatal} of 113.04 cm^3. In order for the tumor to increase in imageable volume from $V_{fatal}/2$ to V_{fatal}, 26 days are needed according to the simulations. This approximation to doubling time *VD* is in good agreement with the clinically reported glioblastoma doubling time in [42]. It is noted that in order to avoid a somewhat artificial diffusion behavior during the first simulated days which would be dictated by the deliberately assumed abrupt boundaries of the initial tumor, the first 14 simulated days have not been taken into account in the theoretical estimation of doubling time. A typical execution instance of the code for 6 simulated months, $\Delta t = 0.5$ d and for discretized mesh $130 \times 130 \times 130$, on a 32-bit Windows Vista Platform, 4 GB RAM and processor Intel® Core™2 Duo CPU P8600 @ 2.4 GHz, takes 214 s. Further acceleration of the code execution could be achieved by using high performance computers.

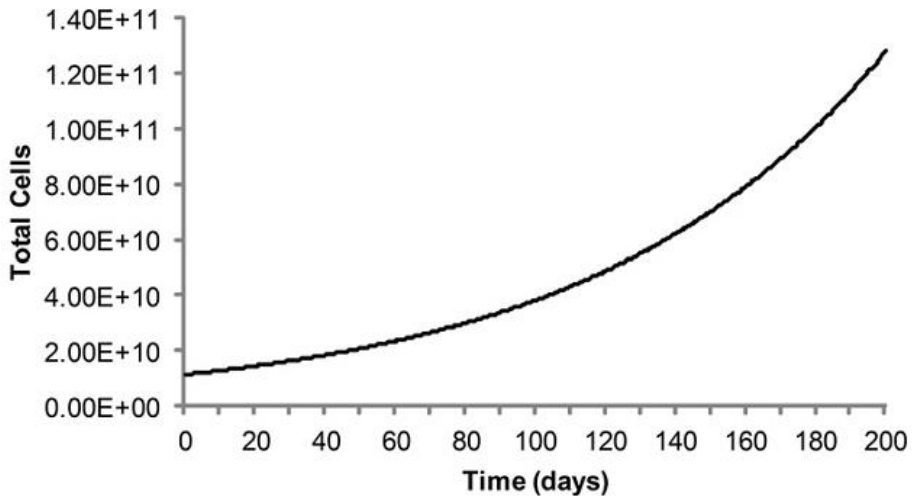

Fig. 18. Total number of tumor cells for the virtual spherical glioblastoma tumor of radius equal to 1.4 cm residing in the skull cavity of Fig. 17. The parameter values are available in Section 6.6.

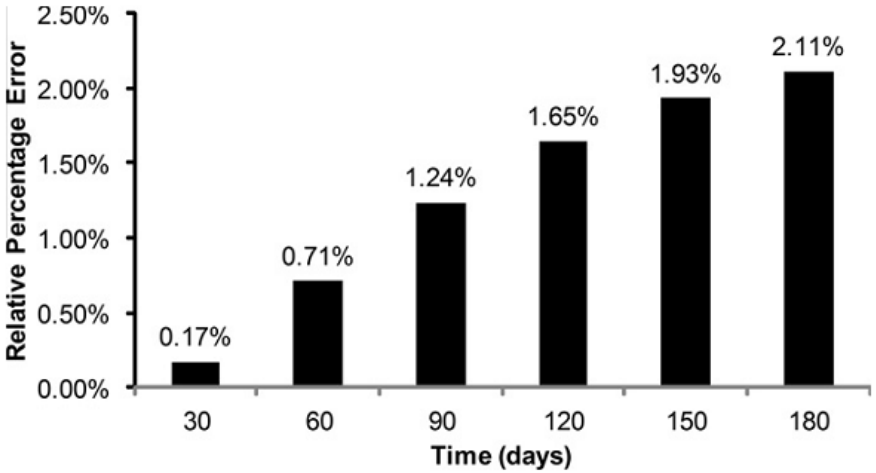

Fig. 19. Plot of the relative percentage error of the total number of tumor cells for the initial tumor of Fig. 17. The error has been calculated by comparing the predicted values generated by the model with the ones obtained by application of the exponential growth law. The parameter values are available in Section 6.6.

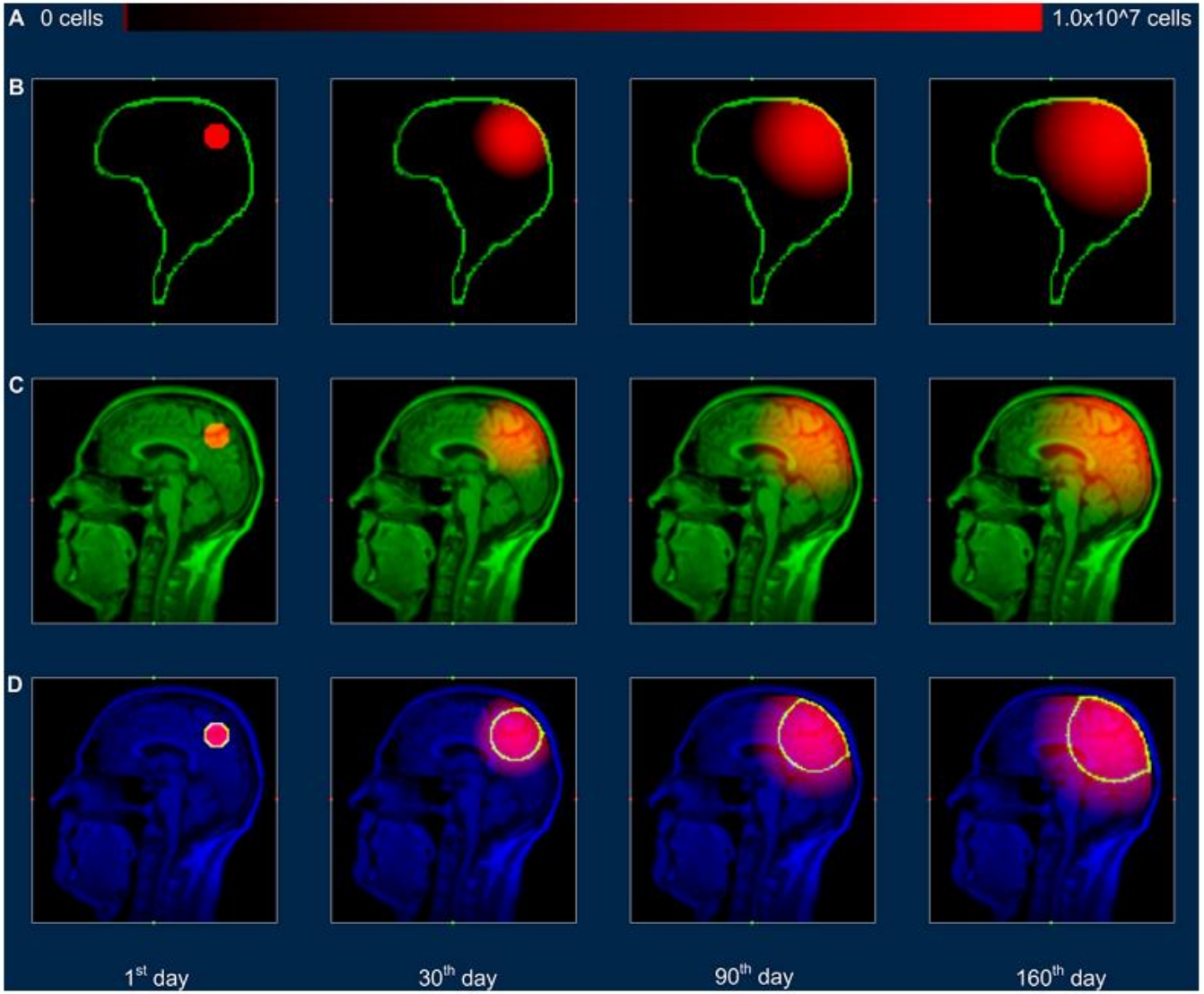

Fig. 20. Schematic representation of the growth of a virtual glioblastoma tumor *in vivo* in sagittal planes at various time points (panel columns from left to right correspond to days 1, 30, 90 and 160, respectively). (A) The red color intensity level I depends on cell concentration according to the function $I = k\log_{10}c$, where c denotes tumor cell concentration, the constant $k = 255/\log_{10}c_{max}$, c_{max} is the maximum value of tumor cell concentration *over the entire space and time range* considered during all simulations that have been included in this figure. It is noted that in order to ensure compatibility with the definition of $\log_{10}$ it is assumed that if $c < (1/8)$ cell/mm^3 then $I = 0$. Maximum and zero cell concentration corresponds to RGB (255,0,0) and RGB (0,0,0) respectively. The numerical values appearing on the intensity scale of panel A are per 8 mm^3. It is noted that the voxel in the present simulation has dimensions 2 mm × 2 mm × 2 mm. (B), (C) As time increases, the tumor diffuses theoretically over the interior space of the skull cavity of the human head. (D) The yellow/bright contour defines the boundary of the tumor component in 2D that is tomographically detectable and has a cell density higher than the assumed threshold of 8000 cells/mm^3. (For interpretation of the references to colour in this figure legend, the reader is referred to the web version of this article.)

7. Discussion

Two major *cancer* modeling schools of thought may be identified. The predominantly *continuous entity based formulation* school having the diffusion–reaction equation at its core (in practice in a *finitized* form) and the *discrete entity–discrete event formulation* school dealing with purely discrete notions such as proliferative potential cell categories, cell cycle phases, cycling or non cycling cell states etc. Both intuition and research experience suggest that none of the formulations can perform equally efficiently when dealing with (a) markedly diffusive tumor growth and (b) tumor response to treatment. The continuous entity based formulation seems to be better positioned in answering questions of the type "*what is the real spatial extent and the actual concentration profile of a glioblastoma tumor within the brain (including both imageable and non imageable components)?*" On the other hand the discrete entity – discrete event formulation seems to be better positioned in answering questions of the type "*what will spatiotemporally be the biological constitution of a tomographically, histopathologically and molecularly characterized tumor following administration of a chemotherapeutic cycle of a given drug?*". Therefore, care should be taken in formulating the questions to be addressed by mathematical and computer modeling before proceeding to the selection of the modeling approach. Obviously hybridization of major approaches is an option, especially when composite and wide scope biological and/or clinical problems are addressed. Since the subject of the present article is glioblastoma tumor growth morphology, a diffusion based continuous and subsequently finitized approach has been dealt with, focusing on the numerical handling of the boundary conditions imposed by the skull.

A detailed exposition of the mathematical treatment concerning the finitized diffusion equation with sources and sinks in conjunction with the corresponding Neumann boundary conditions has been presented. The algorithms and codes have been partly tested using an analytical solution to a simplified version of the problem. The intuitional, mathematical and logical validation of the numerical treatment presented as well as the corresponding computer codes support the validity of the latter. Pure diffusion has been considered in a number of numerical experiments performed in order to provide quantitative checks of the linear component of the analysis in the most controllable way. Qualitative and semi-quantitative checks based

on numerical simulations for various adiabatic boundary geometries and non zero net tumor growth rate as well as non zero loss rate due to treatment have supported the validity of the corresponding mathematical treatment. Through *in silico* experimentation on a set of real brain imaging data, a simulated tumor has shown to satisfy the clinically expected macroscopic behavior of glioblastoma multiforme including the adiabatic behavior of the skull.

It is worth citing that since the core biological problem addressed by the present paper is glioma cell diffusion within the brain, *in vitro* experimental studies might be only of limited relevance. Therefore, *in vivo* studies should be considered as the mainstream opportunity sources for real world validation. In this context, Section 6.6 has dealt with real brain data and has successfully attempted a comparison of the simulated GBM doubling time with a clinically reported value. Obviously, this observation cannot be considered as a statistically substantiated proof of the clinical validity of the model. It does however provide a preliminary indication of the correctness of the major aspects of the analysis presented as well as a way to proceed to a strict clinical validation of the model. Therefore, it appears that the composite model proposed has the potential – following a strict clinical adaptation and validation procedure – to predict clinically meaningful and measurable quantities of critical importance related to the course of the disease.

Possible extensions of the mathematical treatment presented might include tissue inhomogeneities and anisotropy combined with the boundary conditions numerical treatment module. Furthermore, the effect of treatment (e.g. chemotherapy, combined therapies) could be readily studied in a gross preliminary way *in silico* by assigning appropriate values to the term $G(t)$ in Eq. (1). The above mentioned extensions will be the subjects of future papers. Furthermore, translation or extension of the treatment presented to other mathematically similar natural phenomena (e.g. diffusion of chemicals in chemical engineering problems) could be reasonable scenarios.

8. Conclusions

An explicit numerical treatment of the boundary conditions to be used in conjunction with a homogeneous diffusion–reaction based glioma growth model has been presented. Systematic checking of the corresponding computer code based on numerical simulations for various adiabatic boundary geometries, zero and non zero net tumor growth rate and zero and non zero loss rate due to treatment have supported the validity of the corresponding mathematical treatment. Numerical experimentation on a set of real brain imaging data has demonstrated that a simulated glioblastoma tumor can satisfy the expected macroscopic behavior of its real counterpart, including the adiabatic behavior of the skull. The detailed treatment of the boundary conditions presented could considerably contribute to the accuracy of the solution to the diffusion–reaction equation in particular for glioblastoma tumors having their main bulk close to the skull. The composite model proposed appears to have the potential to correctly predict clinically meaningful and measurable quantities of critical importance related to the course of the disease, such as the imaging based doubling time. Obviously a strict clinical adaptation and validation procedure is a *sine qua non* requirement before clinical translation is envisaged. Additionally, translation or extension of the analysis presented to mathematically similar physical systems is a possibility.

Acknowledgements

This work has been supported in part by the European Commission under the projects ContraCancrum: Clinically Oriented Translational Cancer Multilevel Modeling" (FP7-ICT-2007-2- 223979), TUMOR: Transatlantic Tumor Model Repositories (FP7-ICT-2009.5.4-247754) and p-Medicine: Personalized Medicine (FP7-ICT-2009.5.3-270089). The authors are grateful to Eleni Georgiadi, ICCS, National Technical University of Athens (NTUA) for her suggestion concerning the exploitation of sets of MRI head images freely available on the web. Fruitful discussions with Norbert Graf, University Hospital of Saarland, Germany and Dimitra Dionysiou and Nikolaos Uzunoglu, ICCS, NTUA, Greece are duly acknowledged.

References

[1] J.D. Murray, Mathematical Biology II: Spatial Models and Biomedical Applications, third ed., Springer Verlag Inc., New York, 2003. pp. 536–613.
[2] K.R. Swanson, Quantifying glioma cell growth and invasion in vitro, Math. Comput. Model. 47 (2008) 638–648.
[3] O. Clatz, P.Y. Bondiau, H. Delingette, M. Sermesant, S.K. Warfield, G. Malandain, N. Ayache, Brain tumor growth simulation. Institute National de Recherché en Informatique et en Automatique, Rapp. Rech. 5187 (2004).
[4] O. Clatz, M. Sermesant, P.Y. Bondiau, H. Delingette, S.K. Warfield, G. Malandain, N. Ayache, Realistic simulation of the 3-D growth of brain tumors in MR images coupling diffusion with biomechanical deformation, IEEE Trans. Medical Imag. 24 (10) (2000) 1334–1346.
[5] P. Macklin, J.S. Lowengrub, A new ghost cell/level set method for moving boundary problems: application to tumor growth, J. Sci. Comput. 35 (2008) 266–299.
[6] O. Clatz, P. Bondiau, H. Delingette, G. Malandain, M. Sermesant, S. Warfield, N. Ayache, In silico tumor growth: application to glioblastomas, MICCAI 3217 (2004) 337–345.
[7] S. Becker, J.O. Jungmann, A. Mang, T.M. Buzug, An Adaptive Landmark Scheme for Modeling Brain Deformation in Diffusion-Based Tumor Growth, IFMBE Proc. 25 (4) (2010) 41–44.
[8] P. McCorquodale, P. Collela, H. Johansen, A cartesian grid embedded boundary method for the heat equation in irregular domains, J. Comput. Phys. 173 (2001) 620–635.
[9] A.R. Kansal, S. Torquato, G.R. Harsh, E.A. Chiocca, T.S. Deisboeck, Simulated brain tumor growth dynamics using a three-dimensional cellular automaton, J. Theor. Biol. 203 (2000) 367–382.
[10] S.M. Wise, J.S. Lowengrub, H.B. Frieboes, V. Cristini, Three-dimensional multispecies nonlinear tumor growth—I Model and numerical method, J. Theor. Biol. 253 (2008) 524–543.

[11] E. Konukoglou, O. Clatz, H. Delingette, N. Ayache, Personalization to Brain Gliomas Characterization and Radiotherapy Planning, in: T. Deisboeck, G. Stamatakos (Eds.), Multiscale Cancer Modelling, Chapman & Hall/ CRC Press, Boca Raton, FL, 2011, pp. 385–406.
[12] H.B. Frieboes, J.S. Lowengrub, S. Wise, X. Zheng, P. Macklin, E.L. Bearer, V. Cristini, Computer simulation of glioma growth and morphology, Neuroimage (2007).
[13] A. Roniotis, K. Marias, V. Sakkalis, G. Stamatakos, M. Zervakis, Comparing finite elements and finite differences for developing diffusive models of glioma growth, in: Conf. Proc. IEEE Eng. Med. Biol. Soc., vol. 1, 2010, pp. 6797–6800.
[14] S.G. Giatili, N.K. Uzunoglu, G.S. Stamatakos, An explicit boundary condition treatment of a diffusion-based glioblastoma tumor growth model, in: G. Stamatakos, D. Dionysiou (Eds.), in: Proc. 4th Int. Adv. Res. Workshop on *In Silico* Oncology and Cancer Investigation, Athens, Greece, 2010, pp. 86–88.
[15] E. Milotti, R. Chignola, Emergent properties of tumor microenvironment in a real-life model of multicell tumor spheroids, PLoS One 5 (11) (2010) e13942.
[16] G. Cruywagen, D. Woodward, P. Tracqui, G. Bartoo, J. Murray, E. Alvord, The modeling of diffusive tumours, J. Biol. Syst. 3 (1995) 937–945.
[17] D.E. Woodward, J. Cook, P. Tracqui, G.C. Cruywagen, J.D. Murray, E.C. Alvord, A mathematical model of glioma growth: the effect of extent of surgical resection, Cell. Prolif. 29 (1996) 269–288.
[18] P.K. Burgess, P.M. Kulesa, J.D. Murray, E.C. Alvord, The interaction of growth rates and diffusion coefficients in a three-dimensional mathematical model of gliomas, J. Neuropathol. Exp. Neurol. 56 (1997) 704.
[19] S. Ji, D.W. Roberts, A. Hartov, K.D. Paulsen, Brain–skull contact boundary conditions in an inverse computational deformation model, Med. Image Anal. 13 (2009) 659–672.
[20] G.S. Stamatakos, D.D. Dionysiou, E.I. Zacharaki, N.A. Mouravliansky, K.S. Nikita, N.K. Uzunoglu, *In silico* radiation oncology: combining novel simulation algorithms with current visualization techniques, Proc. IEEE, Special Issue on Bioinformatics: Advances and Challenges 90 (11) (2002) 1764–1777.
[21] D.D. Dionysiou, G.S. Stamatakos, N.K. Uzunoglu, K.S. Nikita, A. Marioli, A four dimensional in vivo model of tumor response to radiotherapy: parametric validation considering radiosensitivity, genetic profile and fractionation, J. Theor. Biol. 230 (2004) 1–20.
[22] G.S. Stamatakos, E.A. Kolokotroni, D.D. Dionysiou, E.Ch. Georgiadi, C. Desmedt, An advanced discrete state–discrete event multiscale simulation model of the response of a solid tumor to chemotherapy: mimicking a clinical study, J. Theor. Biol. 266 (2010) 124–139.
[23] G. Stamatakos, *In Silico* Oncology: PART I Clinically oriented cancer multilevel modeling based on discrete event simulation, in: T.S. Deisboeck, G.S. Stamatakos (Eds.), Multiscale Cancer Modeling, Chapman & Hall, CRC, Boca Raton, Florida, USA, 2011, ISBN 9781439814406.
[24] G.S. Stamatakos, E.Ch. Georgiadi, N. Graf, E.A. Kolokotroni, D.D. Dionysiou, Exploiting clinical trial data drastically narrows the window of possible solutions to the problem of clinical adaptation of a multiscale cancer model, PLoS One 6 (3) (2011) e17594.
[25] Incopera, Dewitt, Bergman, Lavine, Fundamentals of Heat and Mass Transfer, sixth ed., John Wiley & Sons, Unites States of America, 2007.
[26] K.R. Swanson, C. Bridge, J.D. Murray, E.C. Alvord Jr., Virtual and real brain tumors: using mathematical modeling to quantify glioma growth and invasion, J. Neurol. Sci. 216 (2003) 1–10.
[27] K.R. Swanson, E.C. Alvord Jr., J.D. Murray, Dynamics of a model for brain tumors reveals a small window for therapeutic intervention, Discrete Contin. Dynam. Syst. – Ser. B 4 (1) (2004) 289–295.
[28] M. Dehgan, Numerical solution of the three-dimensional advection–diffusion equation, Appl. Math. Comput. 150 (2004) 5–19.
[29] D. Britz, O. Osterby, J. Strutwolf, Damping of Crank–Nicolson error oscillations, Comput. Biol. Chem. 27 (2003) 253–263.
[30] B. Bradie, A friendly Introduction to Numerical Analysis, Pearson International ed., Unites States of America, 2006.
[31] A. Jeffrey, Applied Partial Differential Equations – An Introduction, Academic Press. An imprint of Elsevier Science, Unites States of America, 2003.
[32] L.A. Khan, P.L.-F. Liu, An operator-splitting algorithm for the three –dimensional diffusion equation, Numer. Methods Partial Differ. Equat. 11 (1995) 617–624.
[33] H.S. Carslaw, J.C. Jaeger, Conduction of Heat in Solids, second ed., Oxford University Press, London, 1959.
[34] G. Steel, Basic Clinical Radiobiology, third ed., Arnold, London, 2002, pp. 7–22.
[35] Image Processing and Analysis in Java, 2011. <http://rsbweb.nih.gov/ij/> (accessed 20.11.11).
[36] Corel, 2011. <http://www.corel.com/corel/>. (accessed 20.11.11).
[37] Andras Csillag, Anatomy of the Living Human – Atlas of Medical Imaging, Koenemann, Koeln, 1999.
[38] Multi-image Analysis GUI, 2011. <http://ric.uthscsa.edu/mango/> (accessed 20.11.11).
[39] K.R. Swanson, E.C. Alvord, J.D. Murray, Virtual brain tumors (gliomas) enhance the reality of medical imaging and highlight inadequacies of current therapy, British J. Cancer 86 (2002) 14–18.
[40] A.D. Waldman, A. Jackson, S.J. Price, C.A. Clark, T.C. Booth, D.P. Auer, P.S. Tofts, D.J. Collins, M.O. Leach, J.H. Rees, Quantitative imaging biomarkers in neuro-oncology, Nat. Rev. Clin. Oncol. 6 (2009) 445–454.
[41] Glioblastoma multiforme, 2011. http://en.wikipedia.org/wiki/Glioblastoma_multiforme (accessed 26.11.11).
[42] N.G. Burnet, R. Jena, S.J. Jefferies, S.P. Stenning, N.F. Kirkby, Mathematical modelling of survival of glioblastoma patients suggests a role for radiotherapy dose escalation and predicts poorer outcome after delay to start treatment, Clin. Oncol. 19 (2006) 93–103.

ΓΕΝΙΚΗ ΠΟΛΥΚΛΙΜΑΚΩΤΗ ΠΡΟΣΟΜΟΙΩΣΗ ΑΣΘΕΝΕΙΩΝ ΚΑΙ *IN SILICO* ΙΑΤΡΙΚΗ

The 'Virtual Population': Detailed, Whole-Body Anatomical Models Based On Medical Image Data

Esra Neufeld[1], Marie-C. Gosselin[1,2], Dominik Szczerba[1], Marcel Zefferer[1], Niels Kuster[1,2]
[1]*IT'IS Foundation for Research on Information Technologies in Society, Switzerland,* [2]*Swiss Federal Institute of Technology (ETHZ)*

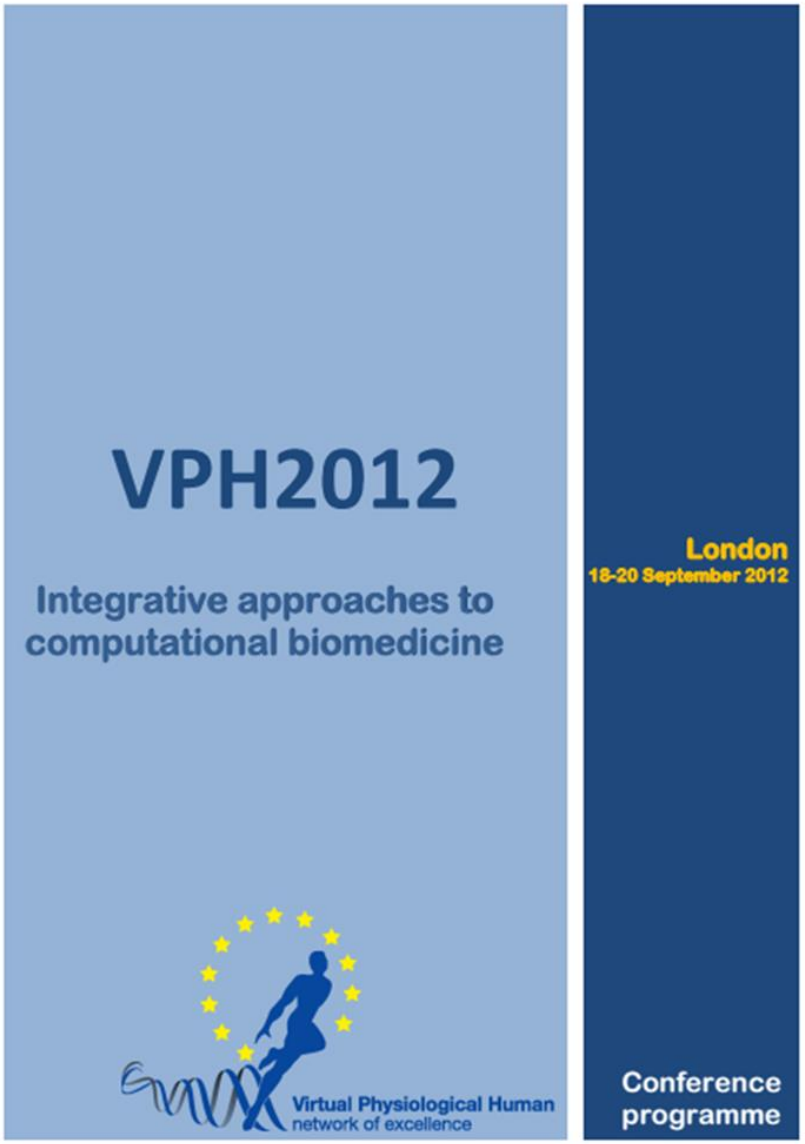
VPH2012
Integrative approaches to computational biomedicine
Virtual Physiological Human
network of excellence
London
18-20 September 2012
Conference programme

The 'Virtual Population': Detailed, Whole-Body Anatomical Models Based On Medical Image Data

Esra Neufeld[1], Marie-C. Gosselin[1,2], Dominik Szczerba[1], Marcel Zefferer[1], Niels Kuster[1,2]

[1]*IT'IS Foundation for Research on Information Technologies in Society, Switzerland,* [2]*Swiss Federal Institute of Technology (ETHZ)*

Correspondece: neufeld@itis.ethz.ch, 0041 44 2459698, Zeughausstrasse 43, 8004 Zurich, CH

Introduction

Numerical simulations involving anatomical models are increasingly employed to develop and optimize medical devices and treatments as well as to assess their safety and efficacy. To model the physical interactions and biological processes occurring in the human body, the model geometry, tissue properties and boundary conditions have to be known. Furthermore, it is often crucial to investigate the impact of anatomical differences between individuals in order to evaluate the resulting variations across a given population. For this, a wide range of representative, detailed and accurate models as well as the tools to manipulate these models (e.g., posing, morphing, voxeling/meshing) are required. A first set of anatomical models (the 'Virtual Family' [1]) has previously been developed jointly with the FDA, primarily for exposure assessment to EM waves. The development of a second generation of anatomical models is presented here in combination with a series of advanced tools that provide additional functionalities and are specifically designed to make use of the capabilities of those enhanced models. The improved set of anatomical models considerably extends the possibilities offered by the first generation and is generalized for a wider user community and a broader range of modeling tasks.

Methods

Image acquisition and segmentation: A series of healthy volunteers of average height and built were selected such that typical adults of both genders and children of different age classes (5-14 years old) are represented. Additionally, an obese and an elderly male were also included. MR images of the ten volunteers were acquired according to an optimized protocol to obtain an in-slice resolution better than 1mm, slice thicknesses smaller than 2mm, a good contrast (incl. special scans for vasculature) and acceptable noise. The image data were segmented, distinguishing between 80 and 200 different tissues and organs. For this a dedicated software was developed that allows coupling highly automated (e.g., improved k-means-based clustering, competitive fuzzy connectedness) with highly interactive (e.g., live wire, interactive watershed transformation, brush) segmentation methods, and that offers filters for noise reduction, hole and island removal, interpolation, etc. Dedicated routines for vasculature tree extraction from contrast-enhanced CT have been developed but the reconstruction of vessel walls still needs to be improved.

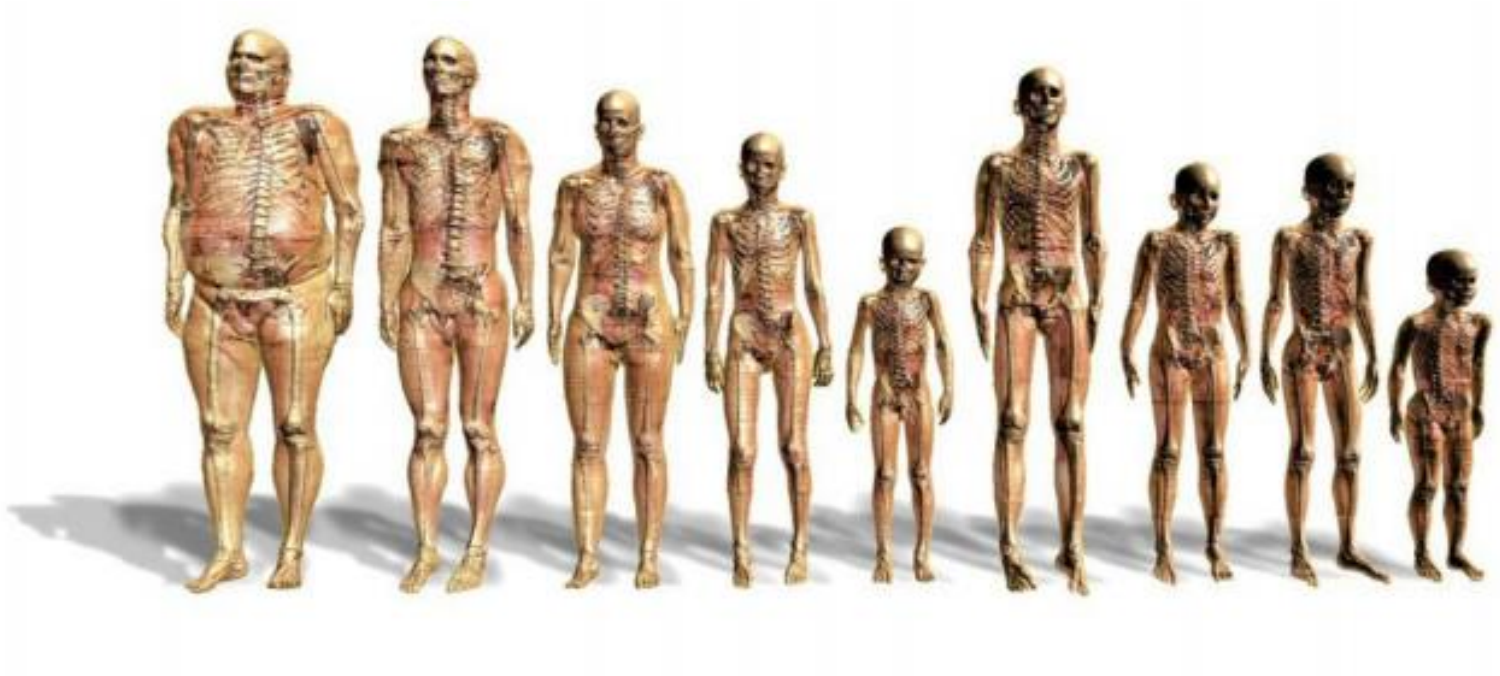

Figure 1: A selection of the Virtual Population models.

In addition to these models, pregnant women models at different gestational stages (3/7/9 months) were generated by incorporating available image data from fetuses into a modified version of the female adult model. Various non-human models were created as well (pig, dog, rats, mice).

Surface extraction: Routines were developed to extract triangle surfaces from the segmented image data, and to apply feature-preserving smoothing and surface simplification while maintaining topological compatibility (e.g., neighboring volumes share the same triangles on the interface) and avoiding self-intersecting surfaces. This resulted in 3D triangle-surface models of high fidelity.

Discretization: Routines allowing the discretization of the models for various numerical methods were developed. Those routines include homogeneous voxeling, voxeling on arbitrary rectilinear meshes (incl. conformal correction), and the generation of high-quality tetrahedral meshes. For the latter, two methods were implemented: an advancing front (with optimization) and a cut-cell octree (incl. smoothing) based method.

Morphing: To further parameterize the models with regard to BMI and thus extend the population coverage, a mechanical simulation-based approach was developed. FEM simulations were performed where the bones were treated as rigid, the fatty tissue was assigned a growing or shrinking force, and the remaining soft tissues were passively deforming. Meshes in the order of 100'000'000 elements were required to maintain the model quality, and high performance computing-enabled solvers capable of handling such problems had to be developed. In addition to this physics-based morphing approach, an interactive interpolation-based approach was implemented, where the user can move control points of various widgets to interactively define a deformation field.

Posing: To pose the models in different postures, two approaches were implemented: The first method uses a volume-preserving, skeleton- and influence-region-based approach from the field of computer graphics. This method allows articulating the models and real-time posing. The second approach uses mechanical simulations (similar to the previously described physics-based morphing) with actively prescribed bone movement and passively deforming soft tissue.

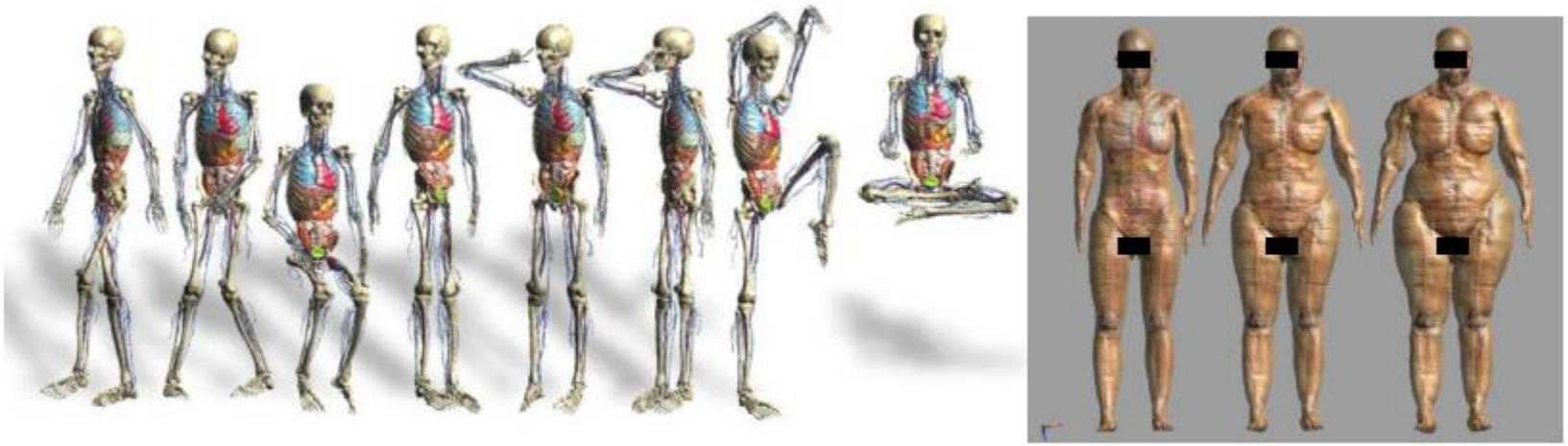

Figure 2: Interactive posture changing and physics-based morphing

Material properties: To provide the scientific community with the best possible tool, a literature-based public tissue parameters database was assembled. At the moment, only density, perfusion, dielectric and thermal properties are available (incl. information about spread of reported values in literature), but it is planned to compile data on mechanical and acoustic properties. An online user forum was established to discuss these properties and dynamically extend the database.

Results

The anatomical models have been used by a large number of groups for a wide range of applications. This includes for example the assessment of MRI safety in the presence and absence of active and passive implants, the development of novel therapies and applicators (e.g., for hyperthermia treatment of cancer, focused ultrasound, and RF ablation), the simulation of blood flow-induced surface potential changes in strong magnetic fields, the study of bone tumor resection and resulting mechanical stress, the improvement of imaging techniques (travelling wave and multi-transmit MRI), and the investigation of worker exposure. The models are one of the central components of the Sim4Life multiphysics simulation platform (see separate abstract) which allows simulating a wide range of physical and physiological phenomena involving the human anatomy. The Sim4Life platform permits multi-scale simulations, e.g., of blood flow (coupling of continuum models of perfusion with discrete pseudo-1D vessels, pipeline networks and full 3D CFD simulations).

Conclusions

A large number of high-resolution, detailed anatomical models are available, which have already been used for multiple relevant applications by over 250 groups worldwide. Methodologies have been developed that allow morphing, posing and BMI changes as well as discretization for various numerical methods. A continuously developing material database is publicly available. In addition, the project aims at collecting information on tissue inhomogeneity (e.g., perfusion and density maps) and boundary conditions (e.g., by coupling to lumped flow network models to obtain physiological inlet and outlet conditions for CFD). While new models are being segmented, the existing models are also subject to continuous improvement. Currently, the resolution and surface smoothness is being improved, the vasculature is being resegmented (to improve connectivity, resolution and shape), and refined models of specific sub-regions are being prepared. The goal is to extend the usefulness of the models beyond the current primary areas (EM, temperature, acoustics, ultrasound) to other physics applications (CFD, mechanics) and to enrich the models with a functional level (e.g., inclusion of neuron dynamics models, blood flow network). In the future, these models might be adapted to or enhanced with patient-specific data.

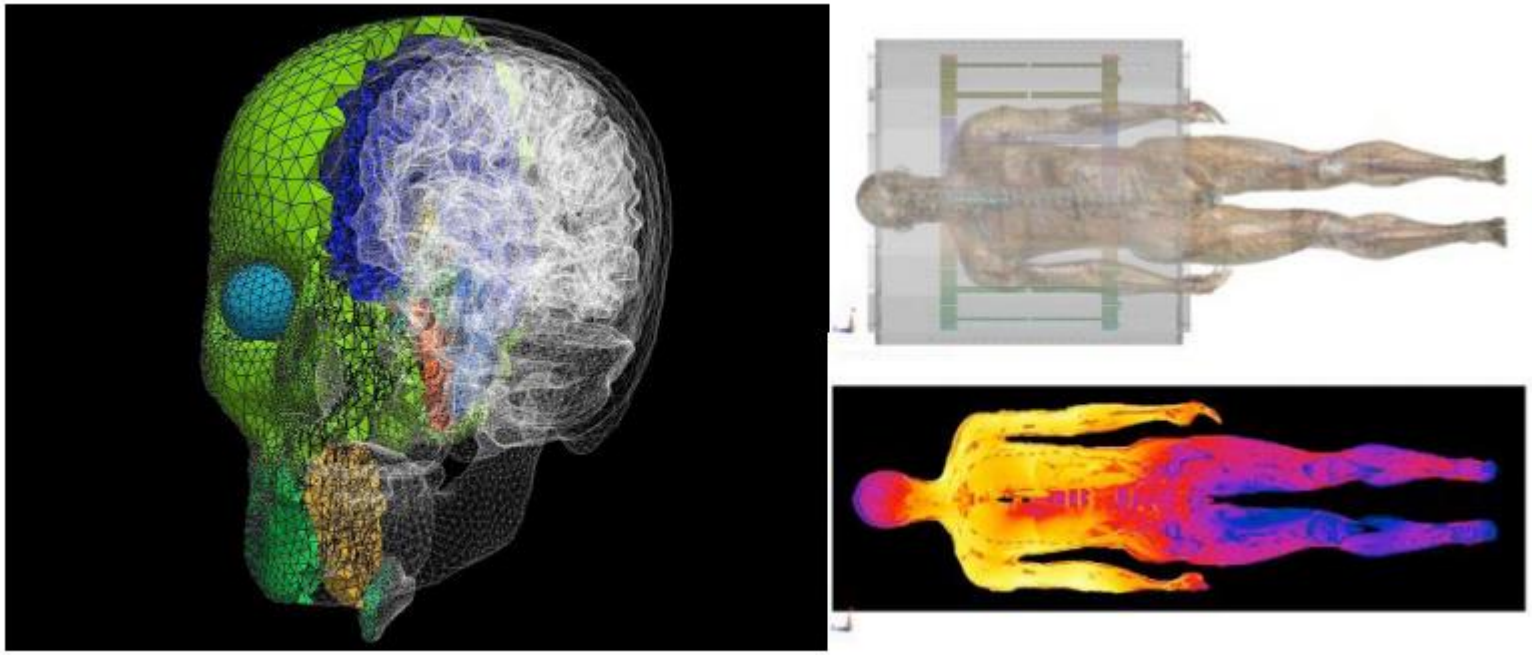

Figure 3: High-quality tetrahedral mesh for FEM simulations and voxel-based FDTD simulation (MRI exposure)

Esra Neufeld[1], Marie-C. Gosselin[1,2], Dominik Szczerba[1], Marcel Zefferer[1], Niels Kuster[1,2]
[1]*IT'IS Foundation for Research on Information Technologies in Society, Switzerland,* [2]*Swiss Federal Institute of Technology (ETHZ)*

Acknowledgement:
Various components of this work have been supported by different organizations: CTI/EUREKA, MMF/GSMA, BfS, SNRP57, ZonMw. Various groups have contributed to the development: FDA, University of Houston, FAU, Siemens Medical Solutions, Erasmus MC, University of Zurich, ETHZ, AIT, SPEAG, ZMT.

References

1. Andreas Christ et al, 2010. The Virtual Family—development of surface-based anatomical models of two adults and two children for dosimetric simulations. Phys. Med. Biol., 55:N23.

Ευχαριστώ

Πρόγραμμα Διδακτορικών Σπουδών της Σχολής Ηλεκτρολόγων Μηχανικών και Μηχανικών Υπολογιστών ΕΜΠ

Πολυκλιμακωτή Προσομοίωση της Ασθένειας του Καρκίνου και *In Silico* Ιατρική (705)

Μάθημα 7ο

Προσομοίωση της αγγειογένεσης κατά την αύξηση καρκινικών όγκων. Αντίστοιχα μαθηματικά και υπολογιστικά προβλήματα στη Γενική *In Silico* Ιατρική

Γεώργιος Σ. Σταματάκος

Διευθυντής Ερευνών - Research Professor– Καθηγητής Ερευνας
Ερευνητικό Πανεπιστημιακό Ινστιτούτο Συστημάτων Επικοινωνιών και Υπολογιστών (ΕΠΙΣΕΥ)
Σχολή Ηλεκτρολόγων Μηχανικών και Μηχανικών Υπολογιστών (ΣΗΜΜΥ)
Εθνικό Μετσόβιο Πολυτεχνείο (ΕΜΠ)
Διευθυντής της Ερευνητικής Ομάδας για την In Silico Ογκολογία και την In Silico Ιατρική, ΕΠΙΣΕΥ-ΣΗΜΜΥ-ΕΜΠ
Επισκέπτης Καθηγητής της Ιατρικής Σχολής του Πανεπιστημίου του Saarland, Γερμανία (1/7/2019-15/9/2019)
Επισκέπτης Καθηγητής της ΣΗΜΜΥ, ΕΜΠ (2016-2019)
gestam@central.ntua.gr, http://in-silico-oncology.iccs.ntua.gr/

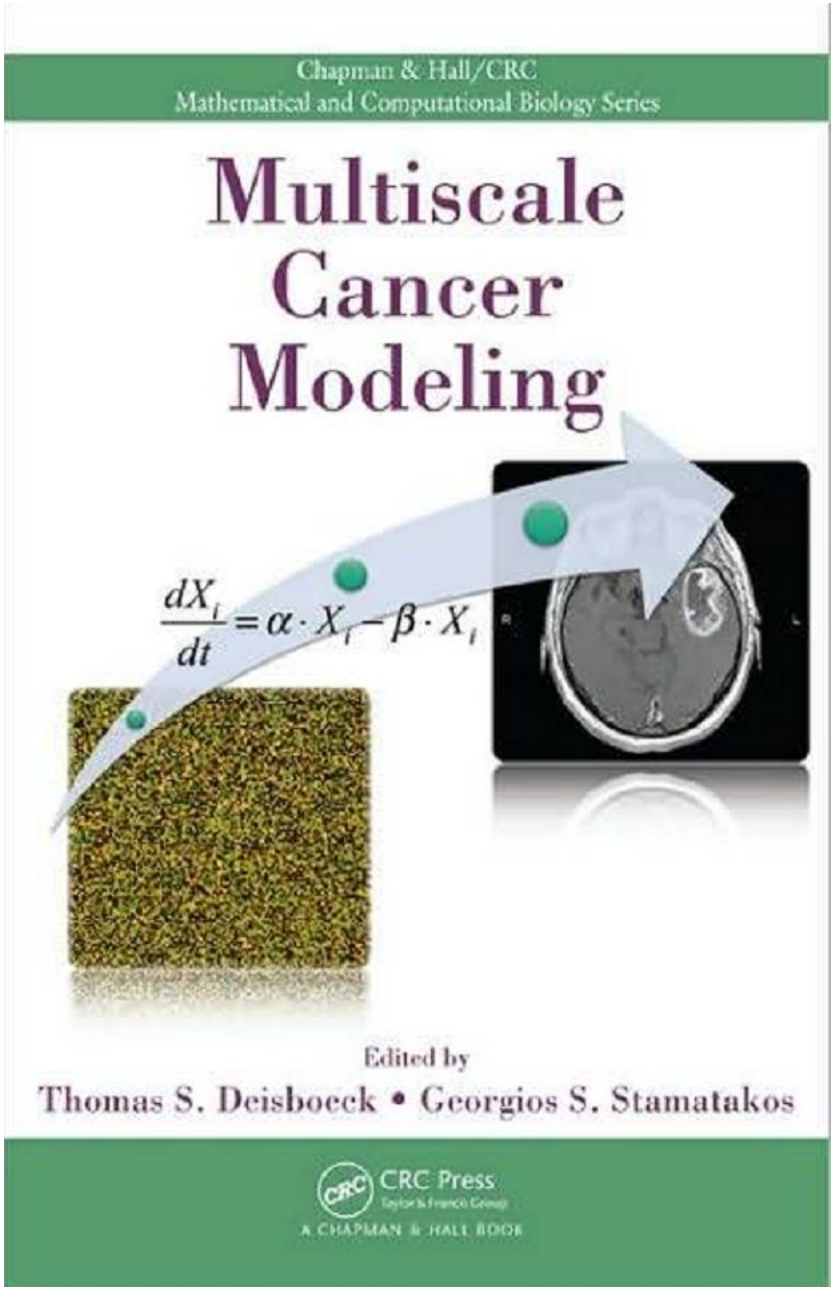

CRC Press
Taylor & Francis Group
6000 Broken Sound Parkway NW, Suite 300
Boca Raton, FL 33487-2742

© 2011 by Taylor and Francis Group, LLC
CRC Press is an imprint of Taylor & Francis Group, an Informa business

CHAPTER 13

Multiscale Mathematical Modeling of Vascular Tumor Growth

An Exercise in Transatlantic Cooperation

Mark A.J. Chaplain, Paul Macklin, Stephen McDougall, Alexander R.A. Anderson, Vittorio Cristini, and John Lowengrub

253

CHAPTER 13

Multiscale Mathematical Modeling of Vascular Tumor Growth

An Exercise in Transatlantic Cooperation

Mark A.J. Chaplain, Paul Macklin, Stephen McDougall, Alexander R.A. Anderson, Vittorio Cristini, and John Lowengrub

CONTENTS

Introduction 254
Model 259
The Tumor Invasion Model 259
Nutrient Transport 260
Tumor Mechanics and the Cell Velocity 263
Tumor–Microenvironment Interaction 265
Tumor Angiogenic Factors 268
Angiogenesis Model 268
Basic Network Model 268
Modeling Blood Flow in the Developing Capillary Network 270
Capillary Vessel Adaptation and Remodeling 273
Numerical Schemes 275
Tumor Invasion Model 275

The Dynamic Adaptive Tumor-Induced Angiogenesis Model 277
Overall Computational Solution Technique 277
Results 278
Avascular Growth to a Multicellular (2D) Spheroid 279
Tumor-Induced Angiogenesis and Vascular Growth: No Solid Pressure-Induced Neovascular Response 283
Tumor-Induced Angiogenesis and Vascular Growth: The Effect of Solid Pressure-Induced Neovascular Response 290
Avascular Growth to a Multicellular (2D) Spheroid with Enhanced ECM Degradation and Production 296
Tumor-Induced Angiogenesis and Vascular Growth: The Effect of Solid Pressure-Induced Neovascular Response and Enhanced ECM Degradation and Production 298
Discussion 302
Acknowledgments 303
References 303

INTRODUCTION

Cancer growth, and as a particular example in this paper, solid tumor growth, is a complicated phenomenon involving many interrelated processes across a wide range of spatial and temporal scales, and as such presents the mathematical modeler with a correspondingly complex set of problems to solve. The aim of this paper is to formulate a multiscale mathematical model of solid tumor growth, incorporating three key features: the avascular growth phase, the recruitment of new blood vessels by the tumor (angiogenesis), and the vascular growth and host tissue invasion phase.

Solid tumors are known to progress through two distinct phases of growth: the avascular phase and the vascular phase. The initial avascular growth phase can be studied in the laboratory by culturing cancer cells in the form of three-dimensional *multicell spheroids*. It is well known that these spheroids, whether grown from established tumor cell lines or actual in vivo tumor specimens, possess growth kinetics that are very similar to in vivo solid tumors. Typically, these avascular nodules grow to a few millimeters in diameter. Cells toward the center, being deprived of vital nutrients, die and give rise to a necrotic core. Proliferating cells can be found in the outer cell layers. Lying between these two regions is a layer of quiescent (or hypoxic) cells, a proportion of which can be recruited into the outer

layer of proliferating cells. Much experimental data have been gathered on the internal architecture of spheroids, and studies regarding the distribution of vital nutrients (e.g., oxygen) and metabolites within the spheroids have been carried out. See, for example, the recent reviews by Walles et al. (2007), Kim (2005), Kunz-Schugart et al. (2004), and Chomyak and Sidorenko (2001), and the references therein.

The transition from the relatively harmless and confined dormant avascular state to the vascular state, in which the tumor possesses the ability to invade surrounding tissue and metastasize to distant parts of the body, depends on the ability of the tumor to induce new blood vessels from the surrounding tissue to sprout toward and then gradually surround and penetrate the tumor, thus providing it with an adequate blood supply and microcirculation. Tumor-induced angiogenesis, the process by which new blood vessels develop from an existing vasculature, through endothelial cell sprouting, proliferation, and fusion, is therefore a crucial part of solid tumor growth. Sustained angiogenesis is a hallmark of cancer (Hanahan and Weinberg 2000). Mature endothelial cells are normally quiescent and, apart from certain developmental processes (e.g., embryogenesis and

wound healing), angiogenesis is generally a pathological process implicated in arthritis, some eye diseases, and solid tumor development, invasion, and metastasis. Tumor-induced angiogenesis is believed to start when a small avascular tumor exceeds a critical diameter (~2 mm), above which normal tissue vasculature is no longer able to support its growth. At this stage, the tumor cells lacking nutrients and oxygen become hypoxic. In response, the tumor cells secrete a number of diffusible chemical substances—tumor angiogenic factors (TAFs)—into the surrounding tissues and extracellular matrix (ECM). The TAF diffuses into the surrounding tissue and eventually reaches the endothelial cells (EC) that line nearby blood vessels. ECs subsequently respond to the TAF concentration gradient by degrading the basement membrane surrounding the parent vessel, forming sprouts, proliferating, and migrating towards the tumor. It takes approximately 10 to 21 days for the growing network to link the tumor to the parent vessel, and this vascular connection subsequently provides all the nutrients and oxygen required for continued tumor growth. An excellent summary of all the key cell-biological processes involved in angiogenesis can be found in the comprehensive review article of Paweletz and Knierim (1989). See also the recent review by Carmeliet (2005). Once vascularized, the solid tumors grow rapidly as exophytic masses. In certain types of cancer, for example, carcinoma arising within an organ, this process typically consists

of columns of cells projecting from the central mass of cells and extending into the surrounding tissue area. The local spread of these carcinoma often assume an irregular jagged shape. By the time a tumor has grown to a size whereby it can be detected by clinical means, there is a strong likelihood that it has already reached the vascular growth phase.

Cancers also possess the ability to actively invade the local tissue and then spread throughout the body. Invasion and metastasis are the most insidious and life-threatening aspects of cancer (Liotta and Stetler-Stevenson, 1991; Liotta and Clair, 2000). Indeed, the prognosis of a cancer is primarily dependent on its ability to invade and metastasize. Many steps that occur during tumor invasion and metastasis require the regulated turnover of ECM macromolecules. The breakdown of these barriers is catalyzed by proteolytic enzymes released from the invading tumor. Most of these proteases belong to one of two general classes: many are metalloproteases (Parsons et al., 1997), while others are serine proteases (Andreasen et al., 1997, 2000). Proteases give cancers their defining characteristic—the ability of malignant cells to break out of tissue compartments. Motility, coupled with regulated, intermittent adhesion to the ECM and degradation of matrix molecules, allows an invading cell to move through the ECM (Liotta and Stetler-Stevenson, 1991; Lauffenburger and Horwitz, 1996; Friedl and Wolf, 2003). However, proteolytic degradation of the ECM is essential for the key processes involved in tissue remodeling as well. These processes take place in a number of distinct physiological events in the healthy organism, such as trophoblast invasion, mammary gland involution, angiogenesis, and wound healing.

The most significant turning point in cancer, however, is the establishment of metastasis. The metastatic spread of tumor cells is the predominant cause of cancer deaths, and with few exceptions, all cancers can metastasize. Metastasis is defined as the formation of secondary tumor foci at a site discontinuous from the primary tumor (Liotta and Stetler-Stevenson, 1991; Liotta and Clair, 2000). Metastasis unequivocally signifies that a tumor is malignant, and this is, in fact, what makes cancer so lethal. In principle, metastases can form following invasion and penetration into adjacent tissues followed by dissemination of cells in the blood vascular system (hematogeneous metastasis) and lymphatics (lymphatic metastases).

Metastases can appear shortly after surgery, but can also remain undetected for more than a decade before manifesting themselves clinically (King, 2000; Chambers et al., 2002; Fidler, 2002). This indicates that disseminated cancer cells can persist in a dormant state (either individually

or as an avascular tumor spheroid), unable to form a progressively increasing tumor mass (Chambers et al., 2002). Such heterogeneity of outcome indicates that the fate of tumor cells that disseminate to distant organs before surgery must be regulated by either inherent cancer cell properties or the milieu of the target organs, or both. Identifying the mechanisms that keep metastases in their dormant, occult state is one of the most challenging and important avenues of cancer research (Chambers et al., 2002; Fidler, 2002).

Since the seminal work of Greenspan (1976), the mathematical modeling of avascular solid tumor growth, similar to its subject, has been rapidly expanding. Most models in this area consist of systems of nonlinear partial differential equations, and may be described as macroscopic. The review paper of Araujo and McElwain (2004) provides an excellent overview. See also the recent reviews by Quaranta et al. (2005), Byrne et al. (2006), Sanga et al. (2006), Graziano and Preziosi (2007), and Roose et al. (2007). Likewise, modeling tumor-induced angiogenesis has a well-established history, beginning with the work of Balding and McElwain (1983). The review paper of Mantzaris et al. (2004) provides an excellent overview of the work in this area. However, unlike avascular growth and angiogenesis, vascular tumor growth has received considerably less attention in the mathematical modeling literature.

Recently, Zheng et al. (2005) developed and coupled a level-set method for solid tumor growth with a hybrid continuous-discrete model of angiogenesis originally developed by Anderson and Chaplain (1998). This work served as a building block for studies of chemotherapy (Sinek et al. (2004)) and morphological instability and tumor invasion (Cristini et al. (2005); Frieboes et al. (2006)). Hogea et al. (2006) have also begun to investigate tumor-induced angiogenesis and vascular growth using a level-set method coupled with a continuous model of angiogenesis. Following the strategy pioneered by Zheng et al., Frieboes et al. (2007) coupled a mixture model with a lattice-free continuous-discrete model of angiogenesis (originally developed by Planck and Sleeman (2004)) and studied vascular tumor growth in three dimensions. In these works, however, the effects of blood flow through, and subsequent remodeling of, the vascular network were not included. Recently, the effects of blood flow through a vascular network on tumor growth were considered by Alarcon et al. (2005), Lee et al (2006), Bartha and Rieger (2007), and Welter et al. (2007) using cellular automaton (CA) tumor growth models coupled with network models for the vasculature. These authors

investigated vascular network inhomogeneities, the stress-induced collapse of blood vessels, and the implications for therapy. Because of the computational cost of simulating cell growth using CA, these studies are limited to small scales.

In this paper, we couple an improved continuum model of solid tumor invasion (following Macklin and Lowengrub 2007) that is capable of spanning the 10^2_m-cm scale and accounts for cell–cell, cell–ECM adhesion, ECM degradation, and tumor cell migration, proliferation, and necrosis with a model of tumor-induced angiogenesis (following McDougall et al. (2006)) that accounts for blood flow through the vascular network, non-Newtonian effects and vascular network remodeling, due to wall shear stress and mechanical stresses generated by the growing tumor, to produce a new multiscale model of vascular solid tumor growth. As in Zheng et al. (2005), the invasion and angiogenesis models are coupled through the tumor angiogenic factors (TAFs) that are released by the tumor cells and through the nutrient extravasated from the neovascular network. As the blood flows through the neovascular network, nutrients (e.g., oxygen) are extravasated and diffuse through the ECM, triggering further growth of the tumor, which in turn influences the TAF expression. In addition, the extravasation is mediated by the hydrostatic stress generated by the growing tumor and, as mentioned earlier, the hydrostatic stress also affects vascular remodeling by restricting the radii of the vessels. The vascular network and tumor progression are also coupled via the ECM as both the tumor cells and ECs upregulate matrix-degrading proteolytic enzymes, which cause localized degradation of the ECM, which in turn affects haptotactic migration.

We perform simulations of the multiscale model that demonstrate the importance, on tumor invasion of the host tissue, of the nonlinear coupling between the growth and remodeling of the vascular network, the blood flow through the network, and the tumor progression. Consistent with clinical observations, the hydrostatic stress generated by tumor cell proliferation shuts down large portions of the vascular network, dramatically affecting the flow, the subsequent network remodeling, the delivery of nutrients to the tumor, and the subsequent tumor progression. In addition, ECM degradation by tumor cells is seen to have a dramatic affect on both the development of the vascular network and the growth response of the tumor. In particular, when the ECM degradation is significant, the newly formed vessels tend to encapsulate, rather than penetrate, the tumor and are thus less effective in delivering nutrients.

The outline of the chapter is as follows. In the following section, the mathematical models are presented and the numerical methods are briefly described. In the section titled "Results," numerical results are presented, and conclusions and future work are discussed in the last section. Further details of the mathematical modelling and numerical methods can be found in Macklin et al. (2009).

MODEL

In this exposition, we present the nondimensional model, starting first with the model of tumor invasion in the section titled "The Tumor Invasion Model" and followed by the model of tumor-induced angiogenesis in the section titled "Angiogenesis Model." Here, time is nondimensionalized by the characteristic tumor cell proliferation time (i.e., $1/\lambda_m$, where $\lambda_m \approx 2/3\,\text{day}^{-1}$ is the mitosis rate), and space is nondimensionalized by the characteristic diffusion penetration length (i.e., $\left(D_\sigma^*/\lambda_\sigma^*\right)^{1/2} \approx 200\mu m$, where D_σ^* and λ_σ^* are characteristic values of the oxygen diffusion coefficient and uptake rate in the proliferating tumor region, respectively). In the following, quantities defined with an overbar correspond to nondimensional constants. The nondimensionalization of the parameters and the corresponding values used in the numerical simulations are presented in Tables 13.4–13.6. For the nondimensionalization and further biological discussion of the models, the reader is referred to Macklin and Lowengrub (2006, 2007) and McDougall et al. (2006).

The Tumor Invasion Model

To accurately model tumor growth in heterogeneous tissues, we develop a mathematical model that accounts for spatially dependent cell necrosis, cell apoptosis, cell–cell and cell–matrix adhesion, matrix degradation, cell proliferation and cell migration. The model is based on continuum reaction-diffusion equations that describe these processes and is a generalization and improvement of earlier models (see the reviews listed previously and recent work by Macklin and Lowengrub [2007b, 2007c]). We present the model in two dimensions, but it is equally valid for the three-dimensional case as well.

Let Ω denote a tumor mass, and let Σ denote its boundary. The tumor can be divided into three regions: a proliferating rim ΩP where the tumor cells have sufficient nutrient levels for proliferation; a hypoxic/quiescent region ΩH where the nutrient levels are too low for normal metabolic activity but not so low that the cells begin to die; and a necrotic region ΩN where the nutrient level has dropped so low that the tumor cells have died and are degraded. Because necrosis is irreversible, we track the necrotic core and its interface ΣN separately of the tumor interface (see Figure 13.1).

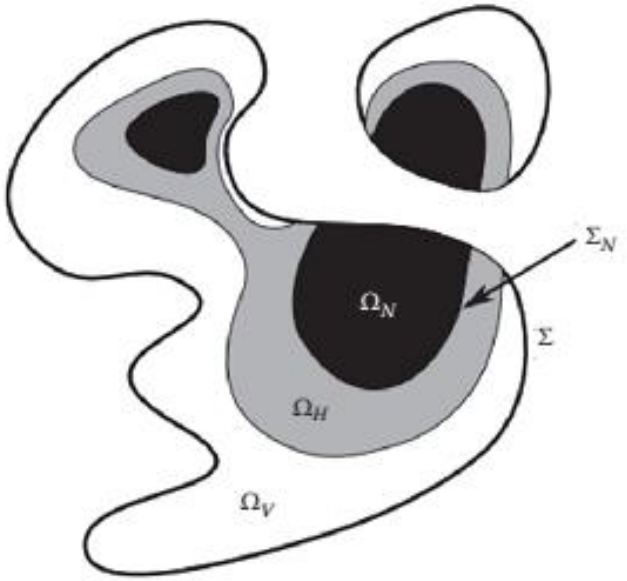

FIGURE 13.1 Schematic of the tumor regions. Ω_P, Ω_H, and Ω_N are the proliferating, quiescent/hypoxic, and necrotic regions, respectively.

Nutrient Transport

We model the net effect of nutrients (e.g., oxygen and glucose) and growth-promoting and growth–inhibiting factors with a single nutrient σ. Here, we focus our attention on the role of oxygen, which is supplied by the vascular network via the red blood cells. This can be modeled using the haematocrit, which represents the volume fraction of red blood cells contained in the blood. Oxygen, and other nutrients, are supplied by the preexisting bulk vasculature and the neovasculature at rates $\lambda\sigma_{\text{bulk}}$ and $\lambda\sigma_{\text{neo}}$, diffuses throughout the cancerous and noncancerous tissue, is uptaken in the non-necrotic portions of the tumor, and decays elsewhere (see the following text). Wherever the oxygen level inside the tumor drops below a threshold value σH, the tumor cells become hypoxic (quiescent), cease proliferating, and uptake nutrient at a lower rate. If the oxygen level falls further below a threshold value σN, then the tumor cells become necrotic. Inside the necrotic core, oxygen reacts with cellular debris to form reactive oxygen species (Kloner and Jennings 2001; Galaris et al. 2006), which we model by

a decay term. Since oxygen diffusion occurs more rapidly than cell mitosis (the time scale on which the equations are nondimensionalized), these processes are described by the quasi-steady reaction-diffusion equation

$$0 = \nabla \cdot (D \nabla \sigma) - \lambda^{\sigma}(\sigma)\sigma + \lambda^{\sigma}_{\text{pre}}(\mathbf{x}, t, B_{\text{pre}}, P, \sigma) + \lambda^{\sigma}_{\text{neo}}(\mathbf{x}, t, B_{\text{neo}}, P, \sigma, h), \quad (13.1)$$

where D is the diffusion coefficient, and the parameter λ^{σ} combines the effects of oxygen uptake and decay and takes the form

$$\lambda^{\sigma} = \begin{cases} \bar{\lambda}_{\text{tissue}} p_{\sigma}(E_0) & \text{outside } \Omega \\ \bar{\lambda}_{\sigma} & \text{in } \Omega_P \\ q_{\sigma}(\sigma) & \text{in } \Omega_H \\ \bar{\lambda}_{N} & \text{in } \Omega_N \end{cases}, \quad (13.2)$$

where p_σ and q_σ are smooth interpolating functions and E_0 the density of the original ECM, which is used to assess changes in uptake/decay in the host microenvironment (see the section titled "Tumor–Microenvironment Interaction"). The interpolating function $q_\sigma(\sigma_H + \sigma_N / 2) = \overline{\lambda}_H$, where σ_H and σ_N are the oxygen concentration thresholds for quiescence and necrosis, respectively, and $\overline{\lambda}_H$ is the rate of oxygen uptake by quiescent cells in the hypoxic tumor. Further, $\overline{\lambda}_{\text{tissue}}$ and $\overline{\lambda}_\sigma$ are the rates of oxygen uptake in the host microenvironment and in the proliferating tumor regions, respectively, and $\overline{\lambda}_N$ is the rate of oxygen decay in the necrotic portion of the tumor. We note that because the location of the viable, hypoxic, and necrotic tumor regions depends on the past and present values of the oxygen level σ, the uptake/decay term λ^σ introduces nonlinearity.

The two remaining sources $\lambda^{\sigma}_{\text{pre}}\left(\mathbf{x},t,B_{\text{pre}},P,\sigma\right)$ and $\lambda^{\sigma}_{\text{neo}}\left(\mathbf{x},t,B_{\text{neo}},P,\sigma,h\right)$ in Equation 13.1 reflect the oxygen-tissue transfer from the preexisting and neovascular blood vessels, respectively, and are given by:

$$\lambda^{\sigma}_{\text{pre}} = \bar{\lambda}^{\sigma}_{\text{pre}} B_{\text{pre}}(\mathbf{x},t)\left(1-\sigma\right)\left(1-\mathbf{1}_{\Omega}\right), \tag{13.3}$$

and

$$\lambda^{\sigma}_{\text{neo}} = \bar{\lambda}^{\sigma}_{\text{neo}} B_{\text{neo}}(\mathbf{x},t)\left(\frac{h}{\bar{H}_D}-\bar{h}_{\min}\right)_{+}\left(1-c(P_{\text{vessel}},P)\right)\left(1-\sigma\right), \tag{13.4}$$

where $\overline{\lambda}^{\sigma}_{pre}$ and $\overline{\lambda}^{\sigma}_{neo}$ are constant transfer rates from the preexisting and neovessels. Here, B_{pre} is the (nondimensional) blood vessel density of the preexisting vessels, whose locations are assumed to be unchanging in time. In fact, we take a uniform distribution of preexisting vessels in the host tissue, and B_{pre} satisfies Equation 13.19, where MDE is assumed to degrade the preexisting vasculature. The function $B_{neo}(\mathbf{x},t) = \mathbf{1}_{neo}$ is the characteristic or indicator function of the neovessels (i.e., equal to 1 at the locations of the neovessels), and 1_{Ω} is the characteristic function of the tumor region Ω (i.e., equal to 1 inside the tumor and is 0 in the tumor exterior). Further, P is the oncotic (solid/mechanical) pressure, P_{vessel} and h are the dimensional pressure and the haematocrit in the neovascular network, respectively. The constants $\overline{H}_D$ and $\overline{h}_{min}$ reflect the normal value of haematocrit in the blood (generally about 0.45) and the minimum haematocrit needed to extravasate oxygen, respectively. The haematocrit is modeled via the blood flow in the vascular network and is determined from the angiogenesis model. This provides one aspect of the *coupling* between the tumor growth and angiogenesis models. A second mode of coupling between the two models occurs through the cutoff function $c(P_{vessel},P)$, which is given by

$$c(P_{\text{vessel}}, P) = \begin{cases} 0 & \Delta P < 0 \\ p_{\text{cutoff}}(\Delta P) & 0 \le \Delta P \le 1, \\ 1 & \Delta P > 1 \end{cases} \tag{13.5}$$

where p_{cutoff} is a cubic, interpolating polynomial. That is, large oncotic pressures may prevent extravasation and transfer of oxygen from the vessels into the tissue. Later, we will discuss how the oncotic pressure may also constrict the neovessels. Further, in Equation 13.5,

$$\Delta P = \left(P - P_{\text{vessel}} / \overline{P}_{\text{vessel}}\right) / \overline{P}_{\text{scale}}, \tag{13.6}$$

where $\overline{P}_{\text{vessel}}$ is a characteristic pressure scale and $\overline{P}_{\text{scale}}$ is a scale factor. Note that we could have analogously taken the oxygen transfer rate from the preexisting vessels to also be coupled to the haematocrit and blood vessel pressure. This will be explored in a future work.

The oxygen source terms in Equations 13.3 and 13.4 are designed such that for sufficiently large transfer rates $\overline{\lambda}^{\sigma}_{\text{pre}}$ and $\overline{\lambda}^{\sigma}_{\text{neo}}$, the oxygen concentration $\sigma \approx 1$ at the spatial locations of the preexisting vessels and neovessels. In practice, we will take $\overline{\lambda}^{\sigma}_{\text{neo}}$ large but $\overline{\lambda}^{\sigma}_{\text{pre}}$ small, which models the supply

of only a small amount of oxygen in the host tissue from preexisting vessels. We will assume a parent vessel, located at the boundary of the computational microenvironment domain as discussed later, supplies the bulk of the oxygen in the host tissue. Note that oxygen flux conditions across the preexisting vessels and neovessels could be imposed (e.g., Alarcon et al. 2005).

The boundary conditions for Equation 13.1 are taken to be a combination of Dirichlet, Neumann conditions. In particular, in the simulations we present later, we assume that a parent vessel coincides with the upper boundary of the computational domain. Therefore, a Dirichlet condition, $\sigma = 1$, is posed along the upper boundary. Zero Neumann conditions, $\partial\sigma / \partial n = 0$, are imposed along the other boundaries of the computational domain.

Tumor Mechanics and the Cell Velocity

The tumor cells, the ECM, and host noncancerous cells are influenced by a combination of forces that contribute to the cellular velocity field. The proliferating cells generate an oncotic mechanical pressure (hydrostatic stress) that also exerts force on the ECM and host cells. The cells respond to pressure variations by overcoming cell–cell and cell–ECM adhesion and migrating through the microenvironment. The ECM may also deform, degrade, and remodel in response to pressure and to the chemical factors released by the cells. The cells may respond haptotactically to adhesion gradients in the ECM.

Following previous work, we assume that all solid phases move with a single cellular velocity field, and we model the cellular motion within the ECM as incompressible fluid flow in a porous medium. In the future, we plan to use mixture models (e.g., Ambrosi and Preziosi 2002; Byrne and Preziosi 2003; Araujo and McElwain 2005a, 2005b) to relax these assumptions. In this simplified description of tumor mechanics used here, Darcy's law is taken as the constitutive assumption and, thus, the velocity is proportional to the forces in the problem. See Ambrosi and Preziosi (2002) and Byrne and Preziosi (2003) for a motivation of this approach from a mixture modeling perspective. Accordingly, the nondimensional velocity is given by

$$\mathbf{u} = -\mu \nabla P + \chi_E \nabla E, \tag{13.7}$$

where μ is the cell mobility, which models the net effects of cell–cell and cell–matrix adhesion, E is the ECM density (e.g., a nondiffusible matrix

macromolecule such as fibronectin, collagen, or laminin), and χ_E is the haptotaxis coefficient. Models for μ and χ_E are given below in the next section. Further, assuming that the density of tumor cells is constant in the viable region, the growth of the tumor is then associated with the rate of volume change:

$$\nabla \bullet \mathbf{u} = \lambda_P, \tag{13.8}$$

where λ_P is the nondimensional net proliferation rate. This implies that the nondimensional pressure satisfies

$$-\nabla \cdot (\mu \nabla P) = \lambda_P - \nabla \bullet (\chi_E \nabla E) \tag{13.9}$$

We assume that in the proliferating region, cell mitosis is proportional to the amount of nutrient present and that apoptosis may occur. Volume loss may occur in the necrotic core, and there is no proliferation in either the host microenvironment or the hypoxic/quiescent regions. We therefore take

$$\lambda_P = \begin{cases} 0 & \text{if } \mathbf{x} \notin \Omega \\ \sigma - A\Omega & \text{if } \mathbf{x} \in \Omega_P \\ 0 & \text{if } \mathbf{x} \in \Omega_H \\ -G_N\Omega & \text{if } \mathbf{x} \in \Omega_N \end{cases}, \tag{13.10}$$

where A is the nondimensional apoptosis rate ("preprogrammed" cell death); and G_N is the nondimensional rate of volume loss in the necrotic core as water is removed and cellular debris is degraded. Assuming a uniform cell–cell adhesion throughout the tumor, cell–cell adhesion can be incorporated as a surface-tension-like jump boundary condition at the tumor–host interface Σ:

$$[P] = (P_{\text{inner}} - P_{\text{outer}}) = \frac{1}{G}\kappa, \tag{13.11}$$

where G is a nondimensional parameter that measures the aggressiveness of the tumor (the strength of cell proliferation relative to cell–cell adhesion), and κ is the mean curvature of the interface. At the necrotic

boundary Σ_N, we assume P is continuous. We assume that no voids form and, therefore, we take

$$[\mathbf{u}\cdot\mathbf{n}]=0 \text{ which implies that } \left[\mu\nabla P\cdot\mathbf{n}\right]=[\chi_E\nabla E\bullet\mathbf{n}], \qquad (13.12)$$

where $\mathbf{n}$ is the unit outward normal to Σ. For simplicity, we will also assume that $[\nabla E\bullet\mathbf{n}]=0$. At the necrotic boundary, we assume analogous conditions. The velocity of the tumor–host interface Σ is then given by

$$V=-\mu\nabla P\bullet\mathbf{n}+\chi_E\nabla E\bullet\mathbf{n}, \qquad (13.13)$$

and the velocity of the necrotic boundary Σ_N is

$$V_N=-\mu\nabla P\bullet\mathbf{n}_N+\chi_E\nabla E\bullet\mathbf{n}_N, \qquad (13.14)$$

where $\mathbf{n}_N$ is the outward unit normal vector along Σ_N. In the far field at the boundaries of the computational domain, the pressure is assumed to satisfy zero Neumann boundary conditions $\partial P/\partial n=0$.

Tumor–Microenvironment Interaction

We model the tumor microenvironment by introducing an ECM density E that represents the density of nondiffusible matrix macromolecules such as fibronectin, collagen, elastin, and laminin, etc. In addition, as mentioned earlier, we keep track of the density E_0 of the original ECM and the preexisting blood vessel density B_{pre} to assess the level of oxygen uptake and supply, respectively, in the microenvironment.

The tumor interacts with the microenvironment by responding to the nutrients supplied by the preexisting and the neovasculature (e.g., see Equation 13.1), remodeling the ECM locally by secreting both MDE and ECM macromolecules and by a heterogeneous response to pressure and ECM adhesion gradients through nonconstant cell mobility and haptotaxis coefficients. In order for tumors cells to migrate into the porous matrix, they must overcome cell–matrix adhesion. However, in experiments, a maximum migration speed is obtained that depends on the level of integrin expression (e.g., Palecek et al. (1997), DiMilla et al. (1991)) and, correspondingly, a nonmonotonic dependence of cell migration velocity on integrin expression and adhesion gradients in the ECM has been predicted (DiMilla et al. (1991); Dickinson and Tranquillo (1993)). This has been explained by the fact that while some integrins are required for focal

adhesion-based migration, too much focal contact strength can retard the detachment of the cell's trailing edge from the ECM. While we do not model integrin expression directly here, we take this effect into account by making the haptotaxis coefficient a nonmonotone function of E:

$$\chi_E = \begin{cases} \bar{\chi}_{E,\min} & E < \bar{E}^{\chi}_{\text{mincutoff}} \\ p_\chi(E) & \bar{E}^{\chi}_{\text{mincutoff}} \le E \le \bar{E}^{\chi}_{\text{maxcutoff}} \\ \bar{\chi}_{E,\min} & E > \bar{E}^{\chi}_{\text{maxcutoff}} \end{cases}, \tag{13.15}$$

where $\bar{\chi}_{E,\min}$ are the nondimensional haptotaxis in low-/high-density ECM, and p_χ is a nonmonotone interpolating function with a maximum $\bar{\chi}_{E,\min}$ located at $E = (\bar{E}^{\chi}_{\text{mincutoff}} + \bar{E}^{\chi}_{\text{maxcutoff}})/2$. Although the mobility μ may also be nonmonotone, for simplicity, we take a monotone decreasing function of E here:

$$\mu = \begin{cases} \bar{\mu}_{\max} & E < \bar{E}^{\mu}_{\text{mincutoff}} \\ p_\mu(E) & \bar{E}^{\mu}_{\text{mincutoff}} \le E \le \bar{E}^{\mu}_{\text{maxcutoff}} \\ \bar{\mu}_{\min} & E > \bar{E}^{\mu}_{\text{maxcutoff}} \end{cases}, \tag{13.16}$$

where p_μ is a smooth interpolating function. In a future work, we will investigate nonmonotonic cell mobilities μ. In addition, the mobility and chemotaxis parameters may also be functions of oxygen concentration σ as hypoxic conditions may result in upregulation of HIF-1 alpha target genes that may result in decreased cell–cell and cell–matrix adhesion, among other effects, and therefore enable cells to more easily migrate through and invade the tumor microenvironment (e.g., see Kaur et al. (2005); Erler et al. (2006); Pouyssegur et al. (2006)). These effects will also be explored in a forthcoming work.

In order to migrate through the ECM and invade the host tissue, tumor cells secrete matrix-degrading proteolytic enzymes (MDEs), for example, matrix metalloproteases and urokinase plasminogen activators, which cause the degradation of the ECM, provide space for the cells, and enhance the attachment of the cells to ECM macromolecules, enabling the cells to exert traction forces to propel themselves through the ECM. In addition, the tumor cells remodel the ECM by secreting insoluble matrix macromolecules and possibly reorienting them. We note that during the angiogenetic response of the host vasculature, an analogous molecular cascade occurs as tumor angiogenesis factors (TAFs) and ECM macromolecules

(e.g. fibronectin, collagen, and laminin) bind to specific membrane receptors on ECs and activate the cell's migratory machinery. This leads to a remodeling of ECM similar to that described earlier for tumor cells. Here, we will not consider the effect of orientational reordering. We model the remaining processes as follows. For the MDE, we take

$$\frac{\partial M}{\partial t} = \nabla \cdot \left(D_M \nabla M \right) + \bar{\lambda}^M_{\text{production}} \left(1 - M \right) \mathbf{1}_{\Omega_V} - \bar{\lambda}^M_{\text{decay}} M + \bar{\lambda}^M_{\text{sprout production}} \mathbf{1}_{\text{sprout tips}} \tag{13.17}$$

where M is the nondimensional MDE concentration, $D_M = \bar{D}_M$ is the diffusion coefficient (assumed to be constant), $\bar{\lambda}^M_{\text{production}}$ and $\bar{\lambda}^M_{\text{sprout production}}$ are the nondimensional rates of production of MDE by the viable tumor cells ($\Omega_V = \Omega_P \cup \Omega_H$) and the sprout tip ECs, respectively. Further, $\bar{\lambda}^M_{\text{decay}}$ is the rate of decay (it is assumed that MDE is not used up as a result of the interaction with the ECM (Quaranta, private communication)). Finally, $\mathbf{1}_{\text{sprout tips}}$ is the characteristic function of the sprout tips. Because the diffusion coefficient of MDE, D_M, is much smaller than that for oxygen diffusion, the full time-dependent diffusion equation is used (Stephanou et al., 2006). In the far field (boundary of the computational domain), we take the zero Neumann boundary conditions $\partial M / \partial \mathbf{n} = 0$.

The ECM density satisfies

$$\frac{\partial E}{\partial t} = -\bar{\lambda}^{E}_{\text{degradation}} EM + \bar{\lambda}^{E}_{\text{production}} (1-E)\mathbf{1}_{\Omega_V} + \bar{\lambda}^{E}_{\text{sprout production}} \mathbf{1}_{\text{sprout tips}}, \quad (13.18)$$

where $\bar{\lambda}^{E}_{\text{production}}$ and $\bar{\lambda}^{E}_{\text{sprout production}}$ are the nondimensional rates of production of ECM by the viable tumor cells and sprout tip ECs and the $\bar{\lambda}^{E}_{\text{degradation}}$ is the nondimensional rate of matrix degradation by the MDE.

Finally, the original ECM and the preexisting blood vessel density are assumed to be degraded by the MDE:

$$\frac{\partial B_{\text{pre}}}{\partial t} = -\bar{\lambda}^{B}_{\text{degradation}} MB_{\text{pre}} \quad \text{and} \quad \frac{\partial E_0}{\partial t} = -\bar{\lambda}^{E}_{\text{degradation}} ME_0, \quad (13.19)$$

where $\bar{\lambda}^{B}_{\text{degradation}}$ and $\bar{\lambda}^{E}_{\text{degradation}}$ are nondimensional degradation rates.

Tumor Angiogenic Factors

When tumor cells become hypoxic/quiescent, they are assumed to secrete TAFs, which diffuse into the surrounding tissue and attract ECs. ECs respond to the TAF by binding with it, proliferating and chemotaxing up the TAF gradient. The diffusion coefficient of TAF is similar to that of oxygen, and so we model the production, diffusion, decay, and binding of TAF by

$$0 = \nabla \cdot \left(D_T \nabla T \right) + \bar{\lambda}^T_{\text{production}} \left(1 - T \right) \mathbf{1}_{\Omega_H} - \bar{\lambda}^T_{\text{decay}} T - \bar{\lambda}^T_{\text{binding}} T \mathbf{1}_{\text{sprout tips}} \qquad (13.20)$$

where T is the nondimensional TAF concentration, $D_T = \bar{D}_T$ is the diffusion coefficient (assumed to be constant), and $\bar{\lambda}^T_{\text{production}}$, $\bar{\lambda}^T_{\text{decay}}$, and $\bar{\lambda}^T_{\text{binding}}$ denote the nondimensional production, natural decay, and binding rates of TAF. In the far field at the boundary of the computational domain, we also take zero Neumann boundary conditions $\partial T / \partial n = 0$.

Angiogenesis Model

We begin with a description, in the next section, of an initial mathematical model for the growth of a hollow capillary network in the absence of any blood flow; this follows Anderson and Chaplain (1998). Then, in the two succeeding sections, following McDougall et al. (2006), we will add the effects of blood flow and vascular network remodeling, respectively.

Basic Network Model

As described earlier, TAF and ECM macromolecules bind to specific membrane receptors on ECs and activate the cell's migratory machinery. The model of EC migration given in the following text describes how capillary sprouts emerging from a parent vessel migrate toward a tumor, leading to the formation of a vascular network that supplies nutrients for continued development (see Figure 13.2).

At this level, since there is no flow or vessel remodeling, this model may perhaps be considered more appropriate at describing in vitro endothelial cell migration and capillary sprout formation. The model, inspired by the tumor angiogenesis model developed by Anderson and Chaplain (1998), assumes that endothelial cells migrate through (1) random motility, (2) chemotaxis in response to TAF released by the tumor, and (3) haptotaxis in response to ECM gradients. If we denote by n the nondimensional endothelial cell density per unit area, then the nondimensional equation describing EC conservation is given by

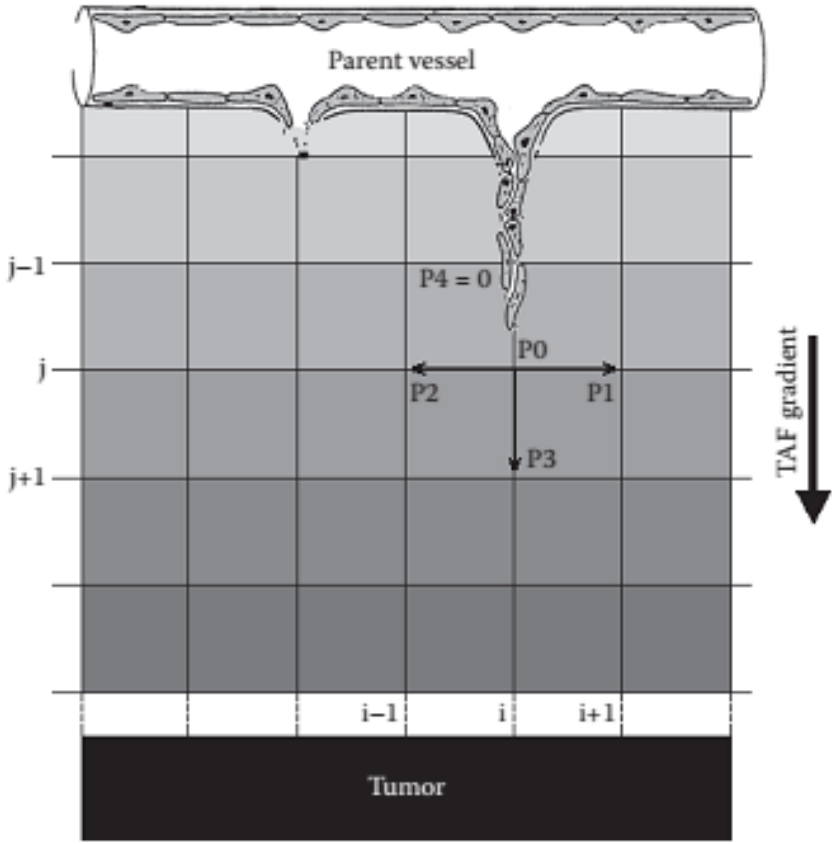

FIGURE 13.2 A schematic diagram of the basic network model of tumor-induced angiogenesis. P1, P2, P3, and P4 denote the probabilities of the sprout EC moving in the coordinate directions. P0 denotes the probability of its remaining stationary. (Reprinted with permission from McDougall et al. 2006. *Theor. Biol.* 241, 564–589.)

$$\frac{\partial n}{\partial t} = \nabla \bullet \left(D \nabla n \right) - \nabla \bullet \left(\chi^{T}_{\text{sprout}} (T) n \nabla T \right) - \nabla \bullet \left(\chi^{E}_{\text{sprout}} n \nabla E \right). \tag{13.21}$$

See McDougall et al. (2006) for the nondimensionalization. The diffusion (random migration) coefficient is $D = \bar{D}$ (assumed to be constant), and the chemotactic and haptotactic migration are characterized by the functions $\chi^{T}_{\text{sprout}} = \bar{\chi}^{T}_{\text{sprout}} / (1 + \delta \cdot T)$, which reflects the decrease in chemotactic sensitivity with increased TAF concentration and $\chi^{E}_{\text{sprout}} = \bar{\chi}^{E}_{\text{sprout}}$, where for simplicity we have taken the haptotactic migration parameter to be constant. In a future work, we will investigate the heterogeneous response of the ECs to the ECM and oxygen gradients as discussed earlier in the section titled "Tumor–Microenvironment Interaction." The coefficients $\bar{D}$, $\bar{\chi}^{T}_{\text{sprout}}$, and $\bar{\chi}^{E}_{\text{sprout}}$ characterize the nondimensional random, chemotactic, and haptotactic cell migration, respectively.

The displacement of each individual EC, located at the tips of each growing sprout, is given by the discretized form of the EC mass conservation equation (13.21) on a regular Cartesian mesh. The migration of each cell is consequently determined by a set of coefficients (P0–P4) emerging from this equation, which relate to the likelihood of the cell remaining stationary, moving left, right, up, or down. These coefficients incorporate the effects of random, chemotactic, and haptotactic movement and depend on the local chemical environment (ECM density and TAF concentration). Proliferation of the endothelial cells at the capillary tips and branching at capillary tips are implemented in the model at the discrete level. Tip branching depends on the TAF concentration at a given spatial location (see Table 13.1 and Anderson and Chaplain (1998) for details.). Using the foregoing model, it is possible to generate "hollow" capillary networks that are structurally similar to those observed experimentally.

Modeling Blood Flow in the Developing Capillary Network

Blood is a complex multiphase medium composed of many different constituents, including red blood cells (erythrocytes), white blood cells (leukocytes), and platelets involved in clotting cascades. These solid elements represent approximately 45% of the total blood composition—red cells are predominant—and are carried in the plasma, which constitutes the fluid phase. A measure of the solid phase is given by the blood *haematocrit*, which represents the volume fraction of red blood cells contained in the blood. The average human haematocrit has a value of around 0.45. Because of its multiphasic nature, blood does not behave as a continuum, and the viscosity measured while flowing at different rates in microvessels is not constant. The direct measurement of blood viscosity in living microvessels is very difficult to achieve with any degree of accuracy. However, by

TABLE 13.1 Vessel branching probabilities according to the local TAF (T) concentration and to the magnitude of the local wall shear stress (τw). TAF_{max} (T_{max}) is the maximum TAF concentration and τ_{max}= 5 Pa (50 dynes/cm²), the maximum shear stress derived from preliminary flow simulations

		WSS/τ_{max}				
		[0.0,0.2)	**[0.2,0.4)**	**[0.4,0.6)**	**[0.6,0.8)**	**[0.8,1.0)**
$[TAF]/TAF_{max}$	**[0,0,0.3)**	0.00	0.00	0.00	0.00	0.00
	[0.3,0.5)	0.00	0.02	0.04	0.06	0.08
	[0.5,0.7)	0.00	0.03	0.06	0.09	0.12
	[0.7,0.8)	0.00	0.04	0.08	0.12	0.16
	[0.8,1.0)	0.00	0.10	0.20	0.30	0.40

comparing the flow distribution in a numerical network (generated by a mathematical model) with a similar experimental system, Pries et al. (1996) determined a relationship between the apparent viscosity of blood, the blood haematocrit, and the radius of the vessel, through which the blood is flowing that provides a good fit with microvascular experimental data. The relationship is given as follows:

$$\mu_{\text{apparent}} = \mu_{\text{plasma}} \cdot \mu_{\text{rel}},$$

$$\mu_{\text{rel}}(R,h) = \left(1 + \left(\mu_{0.45} - 1\right) f(h, R/R^*) \left(\frac{2R/R^*}{2R/R^* - 1.1}\right)^2\right) \left(\frac{2R/R^*}{2R/R^* - 1.1}\right)^2 \quad (13.22)$$

where μ_{plasma} is the plasma viscosity, μ_{rel} is the relative viscosity, $\mu_{0.45}$ is the (nondimensional) viscosity corresponding to the normal value of the discharge haematocrit (i.e., $h = \bar{H}_D = 0.45$), R is the dimensional vessel radius (in μm), R^* is a radius scale factor (taken to be equal to 1 μm), and $f(h,R)$ is a modulating function of the haematocrit and vessel radius. These effects are modeled by:

$$\mu_{0.45} = 6e^{-0.17R/R^*} - 2.44e^{-0.06(2R/R^*)^{0.645}} + 3.2,$$

$$f(h,R/R^*) = \frac{(1-h)^{C(R/R^*)} - 1}{(1-\bar{H}_D)^{C(R/R^*)} - 1},$$

$$C(R/R^*) = \left(e^{-1.5\times10^{-7}R/R^*} + 0.8\right)\left(\frac{1}{1+10^{-23}(2R/R^*)^{12}} - 1\right) + \frac{1}{1+10^{-23}(2R/R^*)^{12}}. \quad (13.23)$$

The apparent blood viscosity (i.e., Equation 13.22) generally increases with decreasing capillary radius, although the precise relationship is nonlinear since it is actually haematocrit dependent.

In order to calculate flow within the entire interconnected network of capillaries, it is first necessary to decide upon a local relationship between the pressure gradient ΔP_{vessel} and flow rate $\dot{Q}$ at the scale of a single capillary element of length L and radius R. Such a relationship in the case of a non-Newtonian fluid can be approximated by the following Poiseuille-like expression:

$$\dot{Q} = \frac{\pi R^4 \Delta P_{vessel}}{8\mu_{app}(R,h)L}. \tag{13.24}$$

where $\mu_{app} = \mu_{apparent}$ from Equation 13.22. In order to determine the pressure (and flow rate) and in the vascular network of interconnected capillary elements having distributed radii, one simply conserves mass (or flow if the fluid is incompressible) at each junction where capillary elements meet (see Figure 13.3).

Hence, for each node the following expression can be written:

$$\sum_{k=1}^{N} \dot{Q}_{(i,j),k} = 0 \tag{13.25}$$

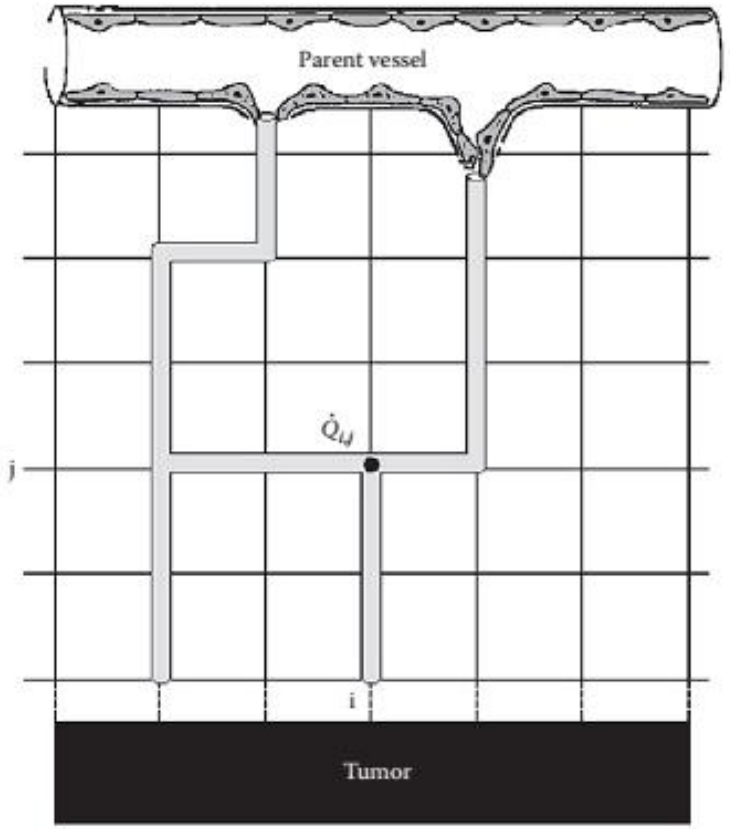

FIGURE 13.3 A schematic representation of the neovessels superimposed on the computational grid used for the flow calculation. (After McDougall et al. 2006. *Theor. Biol.* 241, 564–589.)

Mark A.J. Chaplain, et al.

where the index k refers to adjacent nodes and $N = 4$ in a fully connected regular $2D$ grid as considered in this paper (or $N = 6$ in $3D$). This procedure leads to a set of linear equations for the nodal pressures ($P_{vessel,i}$) that can be solved numerically using any of a number of different algorithms including successive over-relaxation (SOR). Once the nodal pressures are known, Equation 13.24 can be used to calculate the flow in each capillary element in turn. A more complete discussion of the procedure can be found in McDougall et al. (2002). The evolution of haematocrit h in the vessels is also calculated using mass conservation once the flow is determined.

Capillary Vessel Adaptation and Remodeling

Blood rheological properties and microvascular network remodeling are interrelated issues, as blood flow creates stresses on the vascular wall (shear stress, pressure, tensile stress) that lead to adaptation of the vascular diameters via either vasodilatation or constriction. In turn, blood rheology (viscosity, haematocrit, etc.) is affected by the new network architecture—consequently, we should expect adaptive angiogenesis to be a highly dynamic process. We follow the work of Pries et al. (1995, 1996, 1998, 2001a) in incorporating vessel adaptation into our model. In particular, we consider a number of stimuli that affect the vessel diameters. Specifically, we account for the influence of the wall shear stress (*Swss*), the intravascular pressure (*Sp*), a metabolic mechanism depending on the blood haematocrit (*Sm*), as well as the natural tendency for vessels to shrink (*Ss*). These stimuli form a basic set of requirements for obtaining stable network structures with realistic distributions of vessels diameters and flow velocities. The theoretical model for vessel adaptation assumes that the change in a flowing vessel radius _*R* over a time step __, where time is scaled by the rate of the response of the vessel to wall shear stress (k_w), is proportional to both the global stimulus acting on the vessel and to the initial vessel radius *R*. We refer the reader to McDougall et al. (2006) for the definitions of the stimuli and a brief discussion.

After the radius of the vessel is updated, the effect of the mechanical pressure *P*, generated by the proliferating and invading tumor on the vessel radius is then taken into account. The tendency of the pressure to shrink the vessel is modeled by the simple cutoff:

$$R \to R_{\min} + \left(R - R_{\min}\right) \cdot \left(1 - c(P, P_{\text{vessel}})\right), \tag{13.26}$$

where $c(P,P_{vessel})$ is the cutoff function introduced earlier in Equation 13.5 and R_{min} is a threshold minimum radius. This provides another means of coupling tumor invasion (and mechanics) with the angiogenic response and the developing neovascular network. In particular, the solid/mechanical pressure may constrict and cutoff vessels in the neovasculature. To prevent singularities in practice, the radius of the vessel is constrained to lie between 2.0 and 14 μm, which is the size of the parent capillary.

Inclusion of the foregoing mechanisms into our modeling framework now allows us to simulate dynamic remodeling of a flowing vasculature. This significant improvement in angiogenesis modeling, introduced by McDougall et al. (2006), allows us to describe vascular growth in a far more realistic manner, with areas of the capillary network dilating and constricting in response to variations in perfusion-related stresses, stimuli and pressure mechanical forces exerted on the host microenvironment by the invading tumor. The final step in the development of the complete *dynamic adaptive tumor-induced angiogenesis* (DATIA) model is to couple the network flow modeling approach outlined in this section to the "hollow capillary" model derived from the endothelial cell migration equations described earlier. This is achieved through the role of wall shear stress.

Wall shear stress is known to play a leading role in the growth and branching of capillary vessel networks (Pries et al. (2001a, 2001b)). In order to "bring the morphological and the physiological concepts together" (Thompson, 1917), the cell migration and flow models are coupled by incorporating the mechanism of *shear-dependent vessel branching* in addition to sprout-tip branching via local TAF concentrations. This enables the capillary network structures to adapt dynamically through adjuvant vessel branching in areas of the network experiencing increased shear stresses following anastomosis elsewhere in the system. We note that because the shear stress is due to the blood flowing through the capillaries, vessel branching can only occur after some degree of anastomosis has taken place. Therefore, the early stages of angiogenesis are primarily characterized by branching at the capillary tips, which depends only on the TAF concentration.

The combined effects of the local wall shear stress and TAF concentration on vessel branching probability have been implemented in the model as described in Table 13.1. In the absence of quantitative experimental data, the probabilities chosen for the vessel branching process have been defined on a qualitative basis and reflect the combined influence of the wall shear stress (WSS) and local TAF concentration. High values of WSS

TABLE 13.2 Sprout tip branching probabilities as a function of the local TAF concentration

TAF concentration	Sprout tip branching probability
≤0.3	0.0
[0.3–0.5]	0.2
[0.5–0.7]	0.3
[0.7–0.8]	0.4
>0.8	1.0

in tandem with high local TAF concentrations lead to a higher branching probability, while lower values of one or both of WSS and TAF concentration lead to lower branching probability. For each range of WSS (linearly distributed in the interval [0,1]), the corresponding TAF probability profile has been obtained via a linear scaling of the values reported in McDougall et al. (2002) and Stéphanou et al. (2005a, 2005b).

As mentioned earlier, in the absence of WSS, TAF-dependent sprout tip branching is the only means by which a migrating vessel can bifurcate. Sprout tip branching is performed using the algorithm developed by Anderson and Chaplain (1998) and the corresponding tip branching probabilities are shown in Table 13.2.

Numerical Schemes

Tumor Invasion Model

The tumor invasion model described in the section titled "The Tumor Invasion Model" consists of a coupled system of nonlinear, elliptic, and parabolic (reaction-diffusion) differential equations that must be solved on a complex, moving domain where the motion of the tumor/host boundary depends on gradients of the solutions to these equations. Further, one of these solutions—the pressure—is discontinuous across the tumor–host interface where the discontinuity depends on the geometry (i.e., the curvature) of the interface, which is an additional source of nonlinearity. Therefore, standard finite difference methods cannot be used to accurately solve the system. Instead, specialized methods that can accurately take into account discontinuities in solutions and complex domains must be used. Here, we use a ghost-cell/level-set method and adapt and extend the numerical techniques we recently developed (Macklin and Lowengrub 2005, 2006, 2007) to solve this system. In this approach, the equations are discretized on a regular Cartesian mesh and the difference stencils

TABLE 13.3 The variables in the tumor invasion model and their nondimensionalization

Biological quantity	Nondimensional variable	Scaled by
Oxygen concentration	σ	σ^*, the oxygen level in well-oxygenated tissue (assumed to be the same as the oxygen level in the blood vessels)
Proliferation-induced biomechanical pressure	P	$\lambda_M l^2 / \mu^*$, where μ^* is a characteristic mobility value, and λ_m is the mitosis rate
Tumor-secreted angiogenic growth factor (TAF)	T	T^*, the concentration of TAF secreted by tumor cells
Matrix-degrading enzyme (MDE)	M	M^*, the concentration of MDE secreted by the tumor cells
Extracellular matrix (ECM)	E	E^*, the concentration of ECM secreted by tumor cells
Original extracellular matrix	E_0	E^*, the concentration of ECM secreted by tumor cells
Endothelial cell (EC) density	n	n^*, a characteristic density of ECs
Preexisting blood vessel density	B_{pre}	B^*_{pre}, a characteristic density of preexisting vessels (e.g., value at the initial time)

near discontinuities are modified. We note that other alternatives exist (see the discussion in Macklin and Lowengrub 2007), but an advantage of our approach is that it can be implemented in a dimension-by-dimension manner, making the extension to 3D straightforward, and our algorithm is simpler to implement than the alternative approaches.

In this approach, the interface is captured as the zero set of an auxiliary function (the level-set function) φ satisfying $\varphi < 0$ inside Ω, $\varphi > 0$ outside Ω, and $\varphi = 0$ on the tumor–host interface Σ. Typically, φ is taken to be an approximation to the signed distance function; that is, $|\nabla\varphi| \approx 1$. The interface normal and curvature can easily be calculated from φ. The interface ΣN separating viable tumor cells from the necrotic cells is also captured using additional level-set function boundary φ_N that satisfies the same properties as φ, only with Ω_N and Σ_N in place of Ω and Σ.

Away from Σ, the elliptic/parabolic equations can be discretized using centered finite differences. However, near the interface, the difference stencils need to be modified to account for possible jumps in solutions and in their normal derivatives. To do this, ghost cells on either side of

the interface are introduced, and the variables are extrapolated across the interface to ensure that the difference stencil effectively does not include nodes on the other side of the interface. The resulting nonlinear system is solved using an iterative algorithm.

The Dynamic Adaptive Tumor-Induced Angiogenesis Model

For a fixed tumor geometry and TAF distribution, the tumor vasculature is first grown using the basic network model given in the section titled "Basic Network Model"; capillary tips may branch or anastomose during this stage. Further, the Cartesian mesh for the tumor growth system coincides with that used for the neovascular network. After a certain period of time, referred to as the capillary growth duration time, the fluid flow is solved in the fixed neovascular network and then the network is dynamically remodeled, following the algorithm described in sections titled "Modeling Blood Flow in the Developing Capillary Network" and "Capillary Vessel Adaptation and Remodeling," respectively. During the simulation of the flow, a CFL condition is imposed on the time step: $\Delta\tau \equiv \min(V_{cap} / \dot{Q}_{cap})$, where V_{cap} and $\dot{Q}_{cap}$ are the velocity and flow rate in a capillary element. The minimum is taken over the neovascular network. This ensures haematocrit remains conserved during the simulation (e.g., McDougall et al. 2002). Then, the process of blood flow, followed by remodeling, is repeated for an amount of time referred to as the *flow duration time*.

Overall Computational Solution Technique

Initially, the avascular tumor, the preexisting vascular network, the oxygen, and ECM and MDE concentrations are given. We will consider a single parent vessel placed at the top of the computational domain (see Figures 13.1 and 13.2). The algorithm then consists of iterating the following steps:

1. Solve Equation 13.1 for the oxygen concentration, where the oxygen source in Equation 13.4 is obtained from the haematocrit and the pressure in the existing vascular network and the tumor mechanical pressure from the previous time step. We then use the solution σ to update the position of the necrotic core:

$$\Omega_N^{\text{updated}} = \Omega_N^{\text{previous}} \cup \left(\left\{ \mathbf{x} : \sigma(\mathbf{x}, t) < \sigma_N \right\} \cap \Omega \right),$$

and to identify the hypoxic region ΩH. As described earlier, the necrotic core is expanded to include previously necrotic tissue as well as any tumor tissue where the oxygen level has dipped below the necrotic threshold σN. We then rebuild φN as a level-set function that represents the updated region ΩN. (See the Appendix 2, Macklin and Lowengrub (2007) and the level-set references earlier for information on initializing a new level-set function.)

2. Solve Equation 13.20 for the tumor angiogenic growth factor (TAF), and update the MDE and ECM according to Equations 13.17 and 13.18, respectively.

3. Determine the cellular mobility, and solve for the tumor biomechanical pressure from Equation 13.9.

4. Update the position of the tumor–host interface Σ and the necrotic/viable Σ_N by advecting the level-set functions φ and φ_N with the appropriate velocities. If necessary, the level-set functions are reinitialized to be local distance functions to Σ and Σ_N.

5. From the updated tumor position, TAF, MDE, and ECM fields, the neovascular network is grown using the basic network model.

6. Steps (1)–(5) are repeated until the growth duration time interval is reached. At this point, the fluid flow in the neovascular network is determined, and the network is adapted. The hydrostatic pressure P and the TAF are held fixed during this process. The flow and network adaption are repeated (for fixed tumor and capillary tip positions) until the flow duration time is reached.

7. Go to Step 1, and repeat the algorithm.

RESULTS

In this work, we shall focus on tumor growth coupled to angiogenesis in a square 4 × 4 mm region. Although we solve the nondimensional equations, we present dimensional results using the length scale $l \approx 200\,\mu m$ and the timescale $1/\lambda_m \approx 1.5$ day. A parent capillary vessel is located at the top of the computational domain. A preexisting vasculature is assumed to exist and provides a small level of nutrient uniformly throughout the host tissue domain. Initially, a small cluster of proliferating cells is placed approximately 3 mm from the parent vessel. The initial

ECM is taken to be nearly constant (=1) but with small random perturbations uniformly distributed throughout the computational domain (see the time $t = 0$ plot in Figure 13.7a. Accordingly, whenever we calculate gradients of E, we actually calculate the gradient of smoothed E, where a Gaussian smoothing with standard deviation 3.0 is used (see Macklin and Lowengrub 2005). We begin by demonstrating that in the absence of tumor-induced angiogenesis, the small tumor cluster grows to an avascular tumor (2D) spheroid. Actually, since there is a preexisting vasculature, this is a misuse of notation; however, we still refer to this case as avascular since there is no neovascular network. Then, tumor-induced angiogenesis is initiated and we present several simulations of angiogenesis and vascular growth. Finally, we examine the effect of increased ECM degradation by MDE and its affect on avascular and vascular growth. The parameters, and nondimensionalization, used in the simulations are given in Tables 13.3–13.6.

Avascular Growth to a Multicellular (2D) Spheroid

In Figure 13.4a, we present the growth of an avascular tumor. The spatial grid is 200×200 and the time step $\Delta t = 0.05$ and is adapted to satisfy the Courant–Friedrichs–Lewy (CFL) condition (see Macklin and Lowengrub 2006, 2007). The red, blue and brown colors denote Ω_P, Ω_H, and Ω_N the proliferating, hypoxic/quiescent, and necrotic regions, respectively. The nondimensional oxygen and ECM concentrations and the solid (oncotic) pressure are also shown. The oxygen diffuses only a short distance (about 0.2 mm from the diffusion length) from the parent vessel as can be observed from the figure. However, the preexisting vasculature (which yields a background oxygen concentration of approximately 0.4) provides enough oxygen for the tumor to grow. As the tumor grows, the pressure in the proliferating region increases, the oxygen is depleted in the tumor, and the ECM is degraded. A hypoxic/quiescent core forms at about 9 days, when the tumor radius is approximately 0.34 mm. While the tumor continues to grow and degrade the ECM, the pressure decreases and the tumor growth starts to slow, as can be seen in Figure 13.4b. A necrotic core forms around day 15, when the radius of the tumor is approximately 0.5 mm. The pressure drops significantly to reflect the volume loss in the necrotic core associated with the breakdown of the necrotic cells, and the growth of the tumor slows even further as the tumor approaches a steady state. As the growth of the tumor slows, the ECM degradation becomes more pronounced. This actually causes a competition between two effects: the

ATTENTION!
Since a number of typographical errors have been identified in this Table (Table 13.4 first page or first two slides of the same Table), please avoid using these two slides. Please refer to the main text for the definition of the relevant parameters instead.

TABLE 13.4 Values of the parameters for the tumor invasion model—Equations 13.1–13.20

Biological quantity	Nondimensional parameter	Scaled by	Value used in simulations
Uptake rate of oxygen in proliferating tumor region	$\bar{\lambda}_\sigma$	λ_σ^*, the characteristic rate of oxygen uptake in the proliferating tumor region	1
Uptake rate of oxygen in host microenvironment	$\bar{\lambda}_{tissue}$	λ_σ^*	0.25
Uptake rate oxygen in quiescent (hypoxic) tumor region	$\bar{\lambda}_H$	3.5×10^{-4}	0.5
Decay rate of oxygen in necrotic tumor region	$\bar{\chi}^T_{sprout}$	δ	0.25
Rate of blood-tissue oxygen transfer (extravasation) from preexisting vessels	$\bar{\chi}^E_{sprout}$	k_p	0.25
Rate of blood-tissue oxygen transfer (extravasation) from neovessels	k_w	$1\times10^{-6}m$	20

ATTENTION!
Since a number of typographical errors have been identified in this Table (Table 13.4 first page or first two slides of the same Table), please avoid using these two slides. Please refer to the main text for the definition of the relevant parameters instead.

Lower cutoff of original ECM, used in uptake in host microenvironment	τ_w^*	E^*, the concentration of ECM secreted by the tumor cells	1.0
Upper cutoff of original ECM, used in uptake in host microenvironment	τ_{ref}	E^*	0.625
Characteristic value of discharge haematocrit	τ_c^*	Already nondimensional	0.45
Minimum value of haematocrit needed for extravasation	τ_s^*	Already nondimensional	0.05
Characteristic dimensional value of pressure in the neovessels (Equation 13.6)	P_{vessel}^*	—	5000 Pa
Apoptosis rate	A	λ_m, the mitosis rate	0

TABLE 13.4 Values of the parameters for the tumor invasion model—Equations 13.1–13.20 (Continued)

Biological quantity	Nondimensional parameter	Scaled by	Value used in simulations
Scaling factor for hydrostatic (mechanical) pressure cutoff (Equation 13.6)	$\dot{Q}_{ref}$		0.33
Necrosis rate	GN	μ_m	*0.3*
Tumor aggressiveness (adhesion) rate	G	μ_m	*40*
Minimum haptotaxis rate	$1.909\times10^{-11}\,m^3/s$	$6\times10^{-6}m$, where l is the length scale	0
Maximum haptotaxis rate	$\overline{\chi}_{E,max}$	$\chi_E^* E^* / (l^2\lambda_m)$	0.25
Maximum value of ECM used in haptotaxis coefficient (Equation 13.15)	$\overline{E}^{\chi}_{maxcutoff}$	E^*	0.1
Minimum value of ECM used in haptotaxis coefficient (Equation 13.15)	$\overline{E}^{\chi}_{mincutoff}$	E^*	0.9
Minimum tumor mobility (response to hydrostatic/ mechanical pressure)	$\overline{\mu}_{min}$	μ^*, a characteristic value of mobility	1.0

Maximum tumor mobility (response to hydrostatic/ mechanical pressure)	$\bar{\mu}_{max}$	μ^*	4.0
Minimum value of ECM used in mobility coefficient (Equation 13.16)	$E^{\mu}_{mincutoff}$	E^*	0
Maximum value of ECM used in mobility coefficient (Equation 13.16)	$E^{\mu}_{maxcutoff}$	E^*	1.0
Oxygen diffusion coefficient	$\bar{D}_\sigma$	D^*_σ, a characteristic dimensional oxygen diffusion coefficient	1.0

(Continued)

TABLE 13.4 Values of the parameters for the tumor invasion model—Equations 13.1–13.20 (Continued)

Biological quantity	Nondimensional parameter	Scaled by	Value used in simulations
MDE diffusion coefficient	$\bar{D}_M$	$l^2 \lambda_m$	1.0
Production rate of MDE by tumor cells	$\bar{\lambda}^M_{\text{production}}$	λ_m	100
Natural decay of MDE	$\bar{\lambda}^M_{\text{decay}}$	λ_m	10
Production rate of MDE by EC sprout tips	$\bar{\lambda}^M_{\text{sprout production}}$	$\lambda_m M^*$	1.0
Rate of degradation of ECM by MDE	$\bar{\lambda}^E_{\text{degradation}}$	λ_m / M^*	(Figures 13.4–13.7) 1.0 (Figures 13.8–13.9)
Rate of production of ECM by tumor cells	$\bar{\lambda}^E_{\text{production}}$	λ_m	(Figures 13.4–13.7) 2.72 Figures 13.8–13.9)
Rate of production of ECM by EC sprout tips	$\bar{\lambda}^E_{\text{sprout production}}$	λ_m / E^*	0.1
Rate of degradation of preexisting blood vessels	$\bar{\lambda}^B_{\text{degradation}}$	λ_m / M^*	(Figures 13.4–13.7) 1.0 (Figures 13.8–13.9)
TAF diffusion coefficient	$\bar{D}_T$	D^*_σ	1.0
Rate of TAF production by hypoxic tumor cells	$\bar{\lambda}^T_{\text{production}}$	λ^*_σ	100
Rate of natural decay of TAF	$\bar{\lambda}^T_{\text{decay}}$	λ^*_σ	0.01
Rate of binding of TAF by EC sprout tips	$\bar{\lambda}^T_{\text{binding}}$	λ^*_σ	0.025

pressure-induced motion, which becomes more effective since the mobility increases when the ECM decreases; and haptotaxis, which tends to inhibit growth of the tumor into the less dense ECM outside the tumor (recall that haptotaxis induces motion up ECM gradients). Further, the MDE also degrades the preexisting vessels, which results in a reduction in the supply of oxygen. As a result of haptotaxis and the reduced oxygen supply, the tumor actually shrinks slightly after reaching a maximum radius of about 0.64 mm (see Figure 13.4b).

TABLE 13.5 Values of the nondimensional parameters for the angiogenesis model—Equations 13.21–13.26

Biological quantity	Nondimensional parameter	Scaled by	Value used in simulations
Random motion of EC	D	$l2\,\lambda_m$	3.5×10^{-4}
Chemotactic response of EC sprout tip	$\overline{\chi}^{T}_{sprout}$	$l^2\,\lambda_m/T^*$	0.38
Decrease in chemotactic sensitivity	δ	$1/T^*$	0.6
Haptotactic response of EC sprout tip	$\overline{\chi}^{E}_{sprout}$	$l^2\,\lambda_m/E^*$	0.16
Response rate of neovessel radius to intravascular pressure	k_p	k_w, the response rate of the neovessel radius to wall shear stress	0.1
Response rate of neovessel radius to metabolic stimulus	1×10^{-6} m	τ_w^*	0.07
Natural shrinking tendency of neovessel radius	τ_{ref}	Already nondimensional	0.35

Tumor-Induced Angiogenesis and Vascular Growth: No Solid Pressure-Induced Neovascular Response

We next consider tumor-induced angiogenesis where there is no effect of the solid pressure on either the radius of the neovessels or the extravasation of nutrient. In particular, we take $c(P_{vessel}, P) = 0$ in Equations 13.4 and 13.26. Angiogenesis is initiated from the avascular tumor configuration at $t = 45$ days from Figure 13.4. At this time, 10 sprout tips are released from the parent vessel. The initial vessel radii are $6\,\mu m$. The inlet pressure and outlet pressures in the parent vessel are $P_{vessel,in} = 3660\,Pa$ and $P_{vessel,out} = 2060\,Pa$, respectively. The growth duration is $t = 0.05$, which means that the intravascular flow and vessel adaption algorithms are called nearly every tumor growth time step. The flow duration is $\tau = 0.25$ with a time step approximately equal to $\Delta\tau = 0.005$ (again, $\Delta\tau$ is adaptive to satisfy an intravascular CFL condition). This means that 50

TABLE 13.6 Values of the dimensional parameters for the angiogenesis model—Equations 13.21–13.26

Biological quantity	Dimensional parameter	Value used in simulations
Dimensional Neovascular radius scale factor (Equation 13.22)	R^*	1×10^{-6} m
Dimensional Wall shear stress scale factor	τ_w^*	0.1 Pa
Dimensional Wall shear stress regularization factor	τ_{ref}	0.0103 Pa
Dimensional Intravascular pressure stress scale factor	τ_e^*	0.1 Pa
Dimensional Natural shrinking tendency scale factor	τ_s^*	1 Pa
Dimensional Intravascular pressure scale factor	P_{vessel}^*	103 Pa
Flow rate in the parent vessel	$\dot{Q}_{ref}$	1.909×10^{-11} m^3 / s
Threshold minimum neovessel radius for pressure cutoff (Equation 13.27)	R_{min}	6×10^{-6} m

iterations of the flow and vascular adaptation algorithms are performed every tumor growth time step. By flowing and adapting the vascular network so frequently, we hoped that a relatively short flow duration time could be used to get a reasonable approximation of the blood flow in the network. Indeed, preliminary simulations showed that increasing the flow duration did not change the results qualitatively or, in some cases depending on the vascular network configuration, quantitatively. In a future work, we will quantify the effect of the flow duration on the results.

The evolution of the tumor and the neovascular network is shown in Figures 13.5a and 13.5b. As can be seen from the figures, it takes some time for flow to develop after angiogenesis is initiated. Further, flow first occurs after about 7 days in a region near the parent vessel. This can be seen from the plots of haematocrit and oxygen, which are signatures of blood flow. Little additional oxygen diffuses to the tumor. Accordingly, the tumor maintains a steady size (or shrinks a little due to the reasons described earlier). This may be seen in Figure 13.5c. Some of the vessels continue to lengthen, branch, and migrate toward the tumor, heading in particular for the hypoxic region where TAF is released.

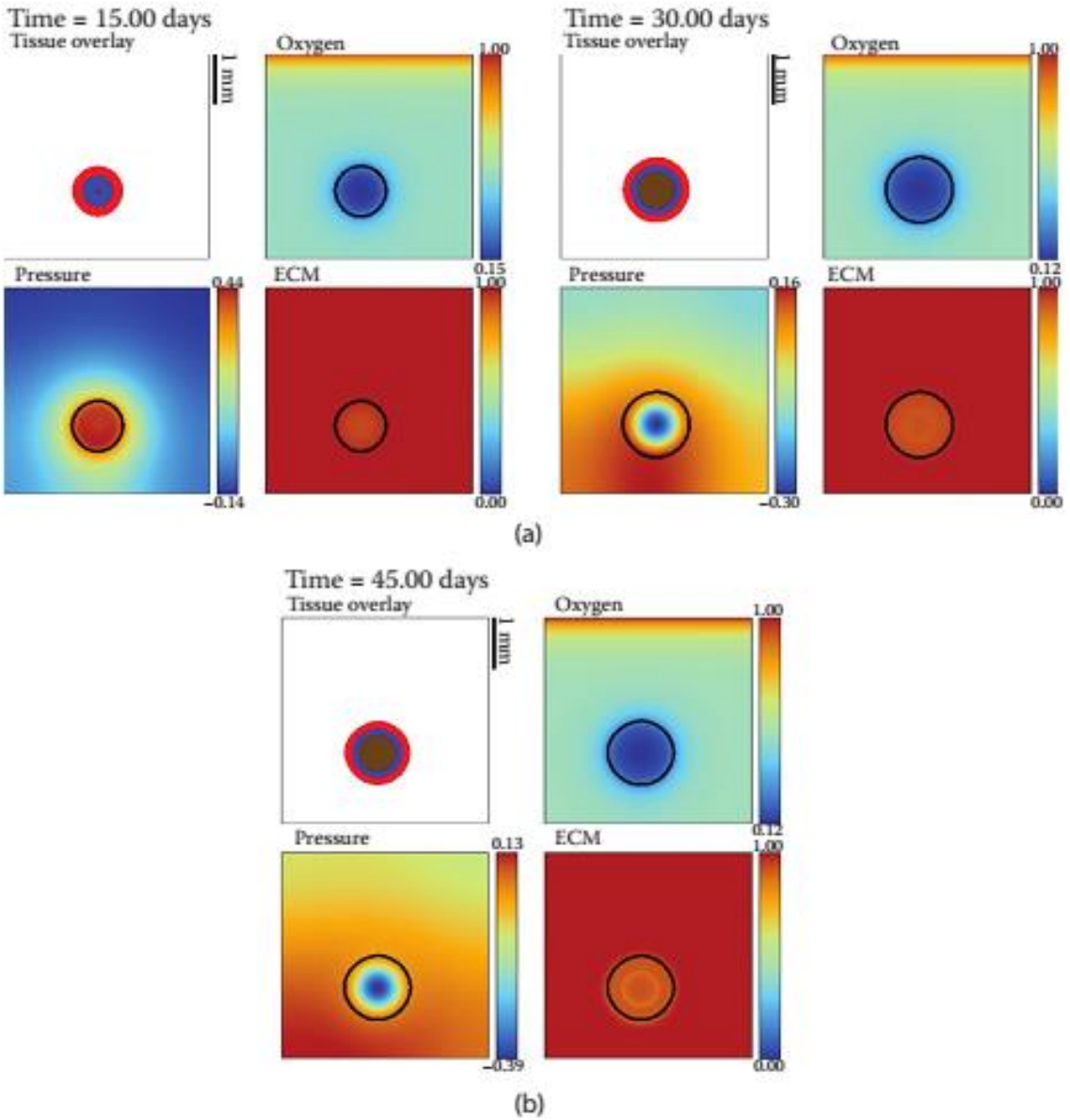

FIGURE 13.4 **(See color insert following page 40)** (a) The evolution toward a steady-state avascular multicell (2D) spheroid. The tumor regions (red—proliferating Ω_P, blue—hypoxic/quiescent Ω_H, brown—necrotic Ω_N), the oxygen, mechanical pressure, and ECM are shown at the times indicated.

After about 10 days, a large loop forms through which blood flows. The loop penetrates the tumor and provides the tumor cells with a direct source of oxygen. The tumor responds by rapidly growing along the oxygen source and co-opts the neovessels, and the hypoxic region shrinks and changes shape. As the tumor grows, the hypoxic and necrotic regions start to grow again as well and the neovessels near the tumor–host interface branch in response to wall shear stresses and increased TAF levels. This

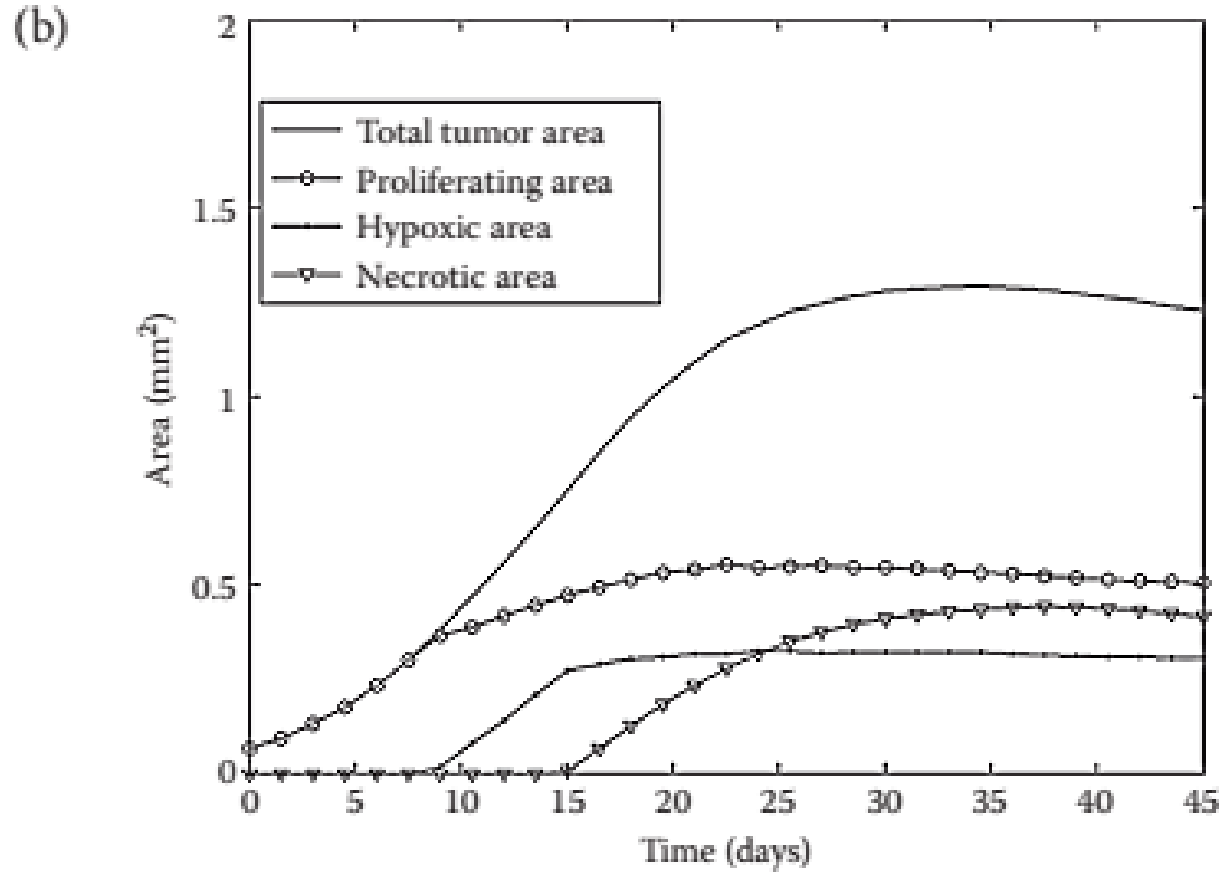

FIGURE 13.4 (Continued) (b) The areas (mm^2) of the total tumor (solid line), proliferating region ("o"), hypoxic region ("•"), and the necrotic region ("inverted triangle") as a function of time for the simulation in Figure 13.4a.

results in increased anastomosis and blood flow. The increased oxygen supply in turn causes large pressures to form in the proliferating region and the tumor to grow even more rapidly, enhancing this effect. Because there is no response of the neovessels to these large pressures, the tumor simply continues to co-opt the vessels, creating an effective tumor microvasculature. This microvasculature provides a nearly uniform source of nutrient in the upper two-thirds of the tumor; the lower third is primarily hypoxic and quiescent. As a consequence, the tumor shape remains compact as the tumor grows.

In Figure 13.5b, the dimensional neovessel radii (in m) and intravascular pressures (in *Pa*) are shown together with the nondimensional ECM and TAF concentrations. At early times, the radii are small and TAF diffuses from the quiescent zone. The ring of lowered ECM surrounding the tumor is clearly seen. The pressure is highest in the neovessels closest to the inlet of the parent capillary, where the highest pressures are. As blood flow starts, the radii increase and the overall pressure decreases, while the pressure in some vessels increases as blood spreads throughout the network. This process continues as the tumor grows and the vasculature continues to branch, anastomose, and carry more and more flow. As the

hypoxic and necrotic regions shrink, the TAF distribution changes, and the vessels respond accordingly. Observe that the degraded ECM just outside the tumor does not prevent the vessels from penetrating the tumor even though the sprout tips have to migrate up ECM gradients to accomplish this.

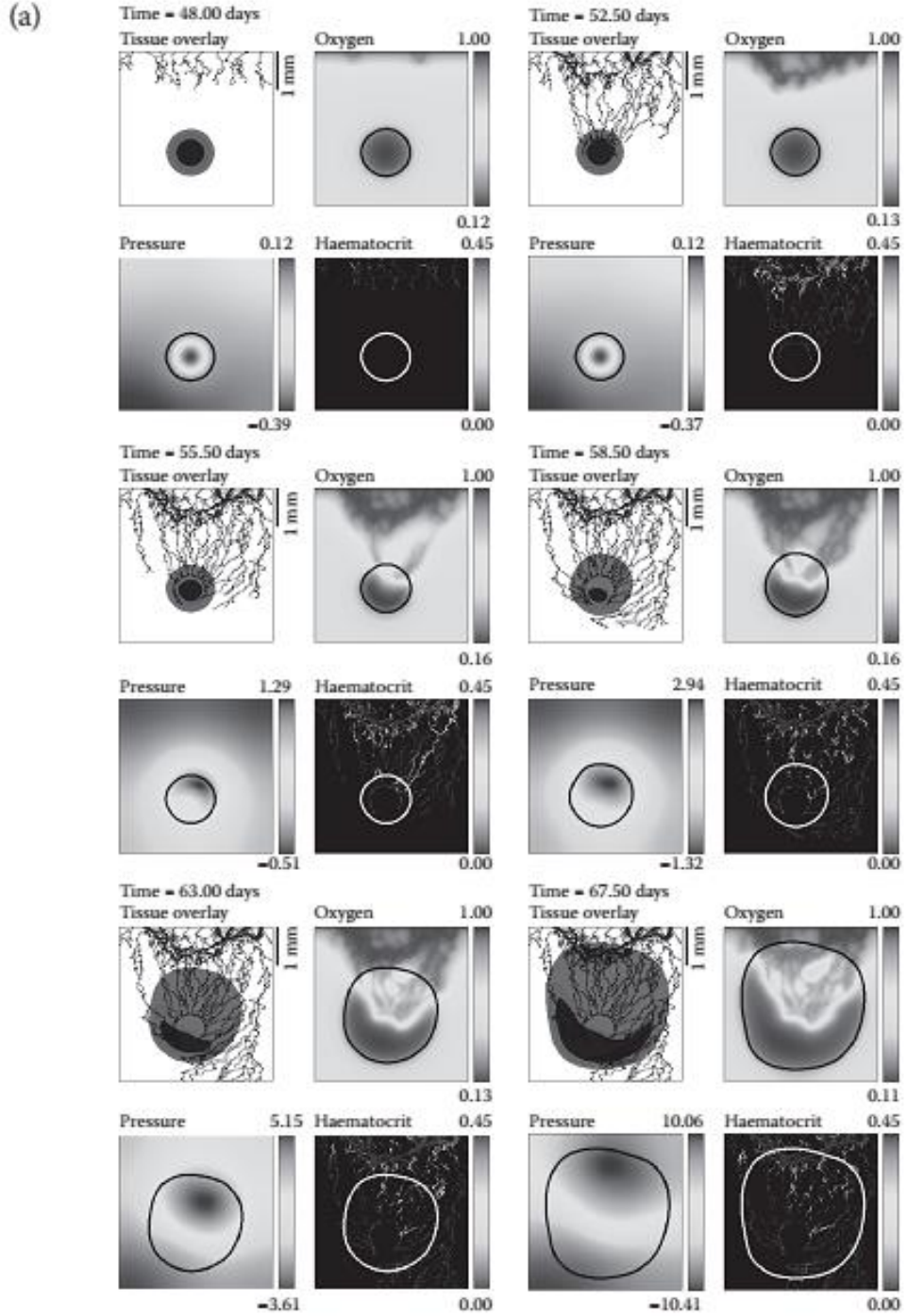
(a)
Time = 48.00 days
Tissue overlay
1 mm
Oxygen 1.00
0.12
Pressure 0.12
−0.39
Haematocrit 0.45
0.00
Time = 52.50 days
Tissue overlay
1 mm
Oxygen 1.00
0.13
Pressure 0.12
−0.37
Haematocrit 0.45
0.00
Time = 55.50 days
Tissue overlay
1 mm
Oxygen 1.00
0.16
Pressure 1.29
−0.51
Haematocrit 0.45
0.00
Time = 58.50 days
Tissue overlay
1 mm
Oxygen 1.00
0.16
Pressure 2.94
−1.32
Haematocrit 0.45
0.00
Time = 63.00 days
Tissue overlay
1 mm
Oxygen 1.00
0.13
Pressure 5.15
−3.61
Haematocrit 0.45
0.00
Time = 67.50 days
Tissue overlay
1 mm
Oxygen 1.00
0.11
Pressure 10.06
−10.41
Haematocrit 0.45
0.00

FIGURE 13.5 (a) Tumor-induced angiogenesis and vascular tumor growth. The vessels do not respond to the solid pressure generated by the growing tumor. The tumor develops a microvascular network that provides it with a direct source of oxygen and results in rapid growth with a compact (sphere-like) shape. The color scheme is the same as in Figure 13.4a.

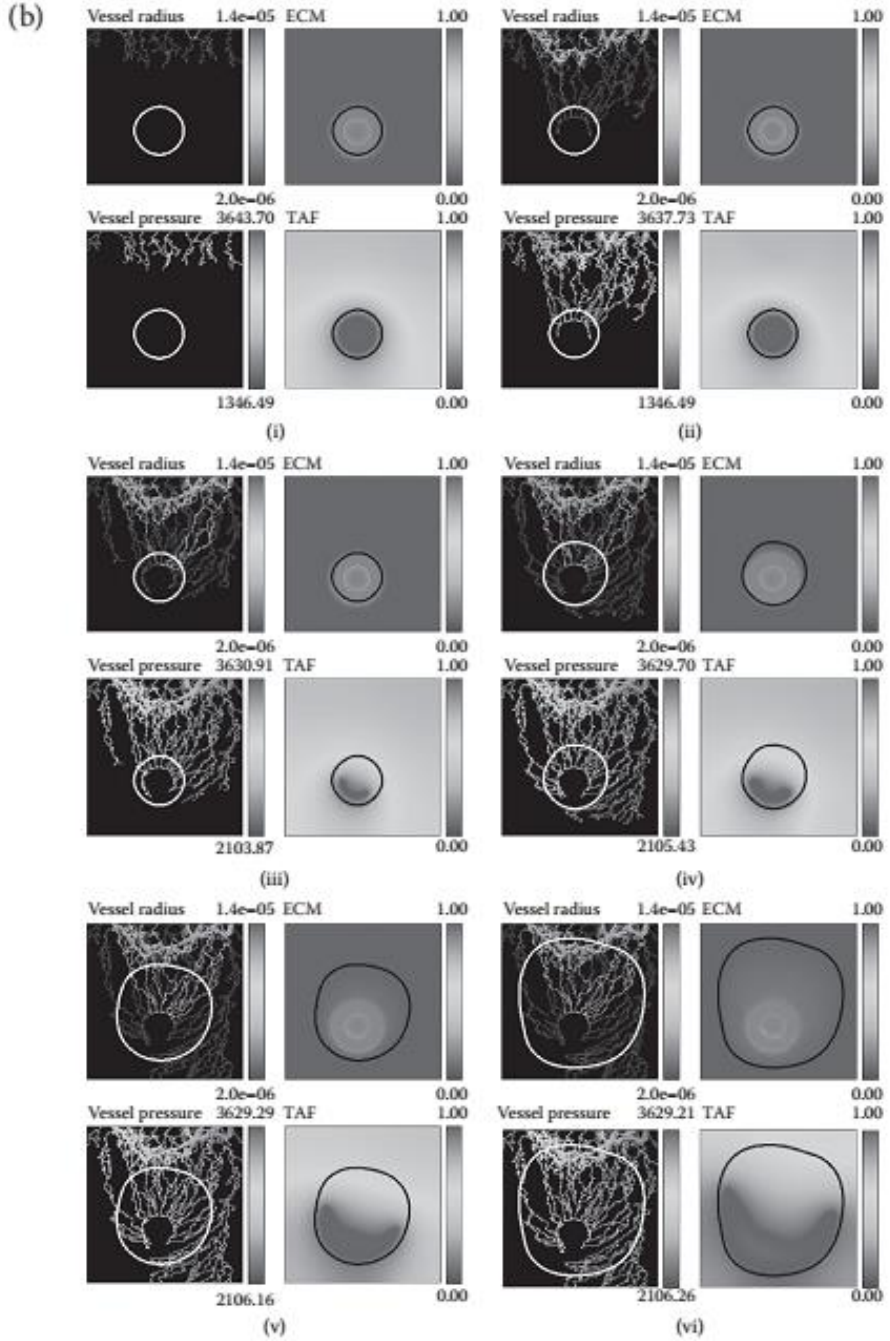
(b)
Vessel radius 1.4e-05
2.0e-06
ECM 1.00
0.00
Vessel pressure 3643.70
1346.49
TAF 1.00
0.00
(i)
Vessel radius 1.4e-05
2.0e-06
ECM 1.00
0.00
Vessel pressure 3637.73
1346.49
TAF 1.00
0.00
(ii)
Vessel radius 1.4e-05
2.0e-06
ECM 1.00
0.00
Vessel pressure 3630.91
2103.87
TAF 1.00
0.00
(iii)
Vessel radius 1.4e-05
2.0e-06
ECM 1.00
0.00
Vessel pressure 3629.70
2105.43
TAF 1.00
0.00
(iv)
Vessel radius 1.4e-05
2.0e-06
ECM 1.00
0.00
Vessel pressure 3629.29
2106.16
TAF 1.00
0.00
(v)
Vessel radius 1.4e-05
2.0e-06
ECM 1.00
0.00
Vessel pressure 3629.21
2106.26
TAF 1.00
0.00
(vi)

FIGURE 13.5 (Continued) (b) The dimensional intravascular radius (m) and pressure (Pa) together with the nondimensional ECM and TAF concentrations at different times from the simulation shown in Figure 13.5a. (1) Time (days) = 48, (2) 52.5, (3) 55.5, (4) 58.5, (5). 63.0, (6) 67.5.

(c)

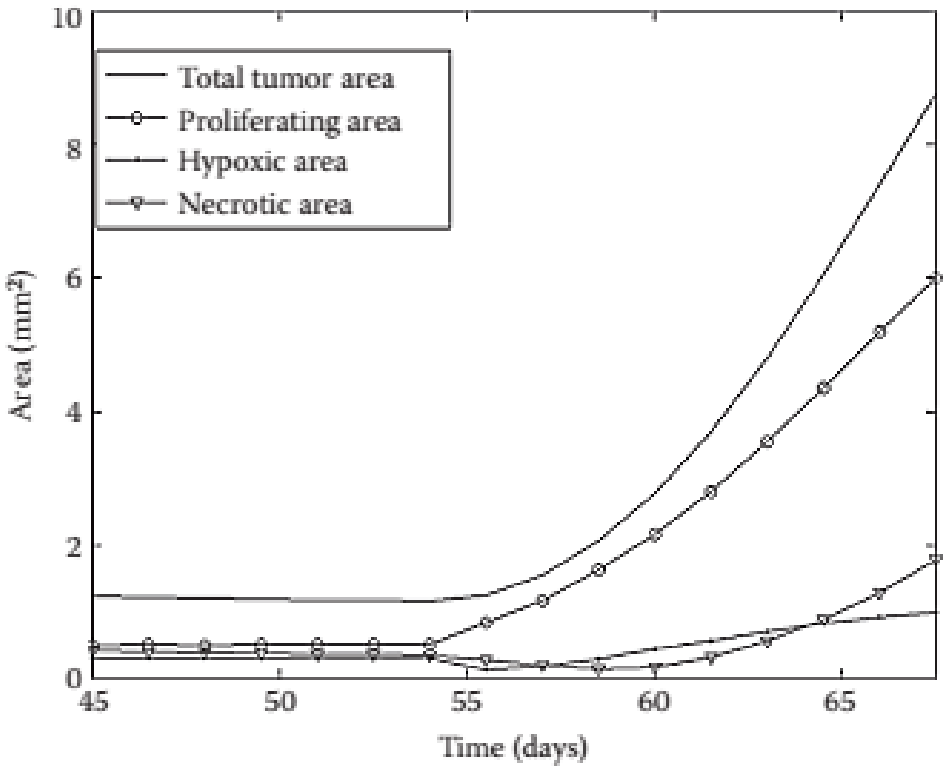

FIGURE 13.5 (Continued) (c) The areas (mm²) of the total tumor (solid line), proliferating region ("o"), hypoxic region ("•"), and the necrotic region ("inverted triangle") as a function of time for the simulation in Figure 13.5a.

The first vessels that penetrate the tumor do not carry blood and, thus, the tumor does not respond to their penetration. Instead, these vessels migrate toward the hypoxic region, where they tend to get stuck. This occurs because the TAF concentration is nearly uniform ($T = 1$) and so the sprout tips move randomly and tend to collide with their own trailing vessel, preventing further migration. At later times though, new vessels grow into the tumor center and anastomose. This leads to blood flow and oxygen extravasation deep in the tumor interior. Further, observe that the tumor grows so fast that it outruns the ring of degraded ECM around its boundary and is growing into only very slightly degraded ECM. The ECM in the tumor interior degrades rather slowly, and the ECM signature of the original avascular tumor spheroid can still be seen at late times.

This simulation shows that when the neovessels are not affected by the tumor solid pressure, dramatic growth occurs as the tumor co-opts the host vasculature to create its own microvasculature and receives a direct source of oxygen. In addition, the tumor growth and angiogenesis processes are nonlinearly coupled as the vasculature responds to the growth by migrating towards the ever-changing TAF distributions and by branching and anastomosing near the tumor–host interface. This leads to increased blood flow. At the same time, the increased blood flow in the vascular network affects how the tumor grows and, in particular, speeds growth up. This then affects the response of the vasculature.

Tumor-Induced Angiogenesis and Vascular Growth: The Effect of Solid Pressure-Induced Neovascular Response

Next, we consider, in Figures 13.6a–13.c, the effect of solid/mechanical pressure-induced vascular response on tumor-induced angiogenesis and vascular growth. We repeat the simulation in the section titled "Angiogenesis Model" except with $c(P_{\text{vessel}}, P)$ nonzero as given in Equation 13.5. This means that the transfer of oxygen from the neovessels to the tissue may be significantly reduced, and the vessel radii may be correspondingly constricted. With the values of the parameters used here (Tables 13.4–13.6), a solid pressure-induced vascular response begins to occur when the solid pressure $P \approx 0.8$.

At early times, the angiogenic response and the tumor growth are similar to the case presented earlier in Figures 13.5a–13.5c. The newly developing vessels migrate, proliferate, branch, and anastomose. It also takes some time for flow to begin with significant flow developing only after about 10 days. Blood flow in the neovasculature starts near the parent capillary and, eventually, the flow reaches the tumor. Because the initial ECM is slightly different from that in Figure 13.5 (due to the random component) and due to the random component of the sprout tip motion, the vascular network at early times is not identical to that obtained previously in Figure 13.5.

In contrast to the case considered in Figure 13.5, here the solid pressure prevents any delivery of oxygen internally to the tumor and, thus, the delivery of oxygen is heterogeneous, and significant oxygen gradients persist in the tumor interior. There is no functional microvasculature internal to the tumor. While the tumor responds by growing toward the oxygen-delivering neovessels, the solid pressure generated by tumor cell proliferation also constricts the neovessels in the direction of growth (where pressure is highest) and also correspondingly inhibits the transfer of oxygen from those vessels. As a consequence, the overall solid

pressure is significantly lower than that in Figure 13.5. This makes the tumor grow much more slowly than that in Figure 13.5, as can be seen in Figure 13.6c. Note that the vertical scale in Figure 13.6c is one half of that in Figure 13.5c.

(a1)

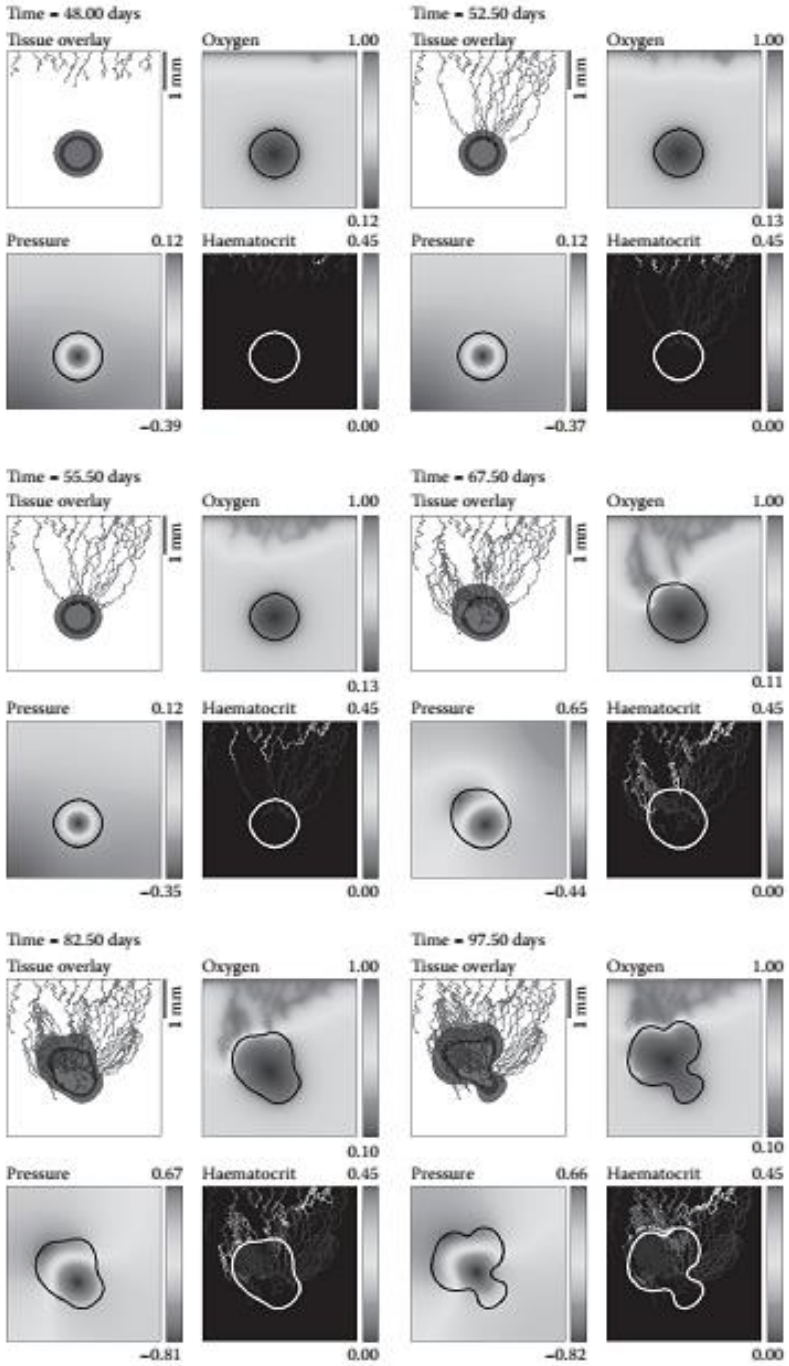
Time = 48.00 days
Tissue overlay
1 mm
Oxygen
1.00
0.12
Pressure
0.12
−0.39
Haematocrit
0.45
0.00
Time = 52.50 days
Tissue overlay
1 mm
Oxygen
1.00
0.13
Pressure
0.12
−0.37
Haematocrit
0.45
0.00
Time = 55.50 days
Tissue overlay
1 mm
Oxygen
1.00
0.13
Pressure
0.12
−0.35
Haematocrit
0.45
0.00
Time = 67.50 days
Tissue overlay
1 mm
Oxygen
1.00
0.11
Pressure
0.65
−0.44
Haematocrit
0.45
0.00
Time = 82.50 days
Tissue overlay
1 mm
Oxygen
1.00
0.10
Pressure
0.67
−0.81
Haematocrit
0.45
0.00
Time = 97.50 days
Tissue overlay
1 mm
Oxygen
1.00
0.10
Pressure
0.66
−0.82
Haematocrit
0.45
0.00

FIGURE 13.6 (a1) Tumor-induced angiogenesis and vascular tumor growth. The vessels respond to the solid pressure generated by the growing tumor. Accordingly, strong oxygen gradients are present that result in strongly heterogeneous tumor cell proliferation and shape instability. The color scheme is the same as in Figure 13.4a.

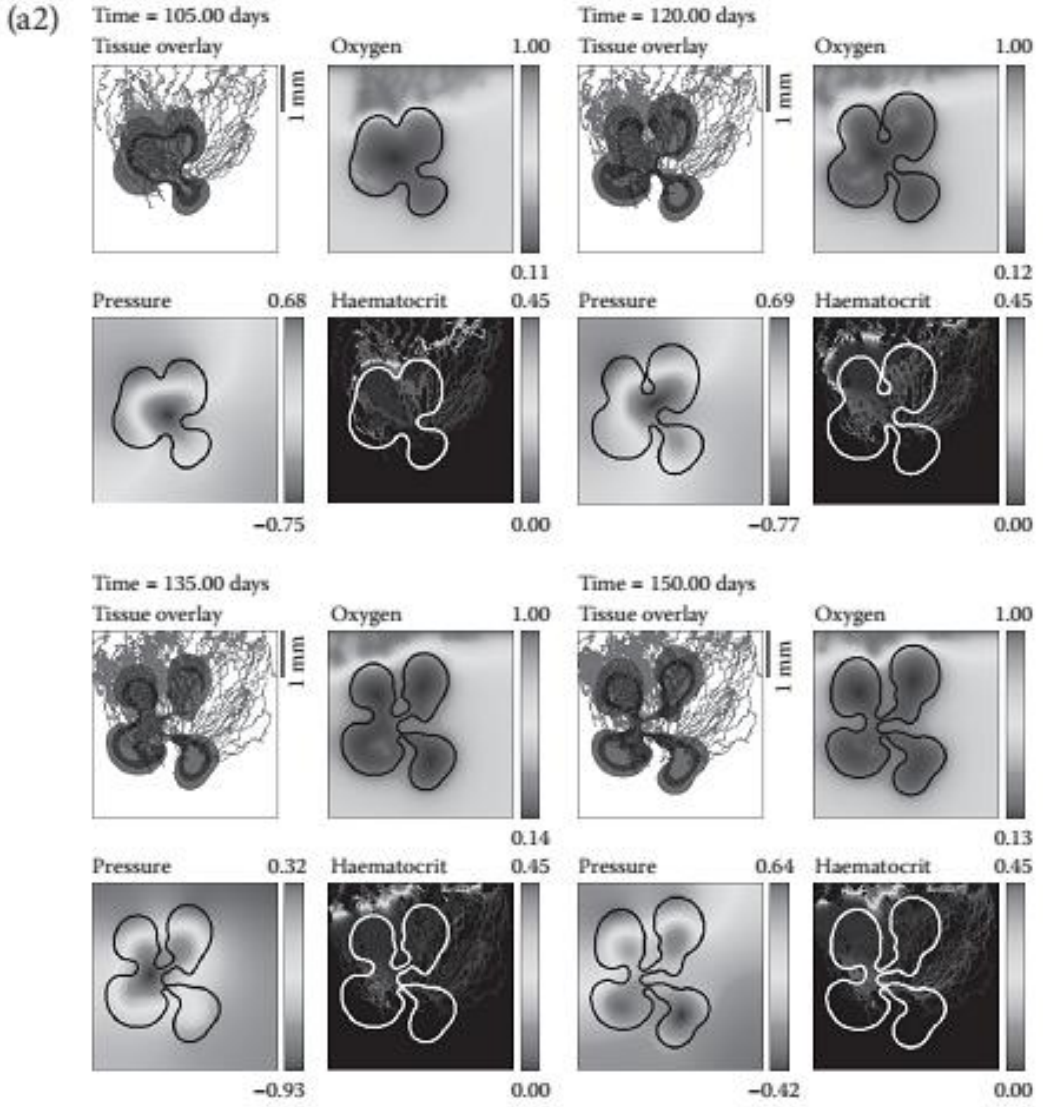

FIGURE 13.6 (Continued) (a2) Tumor-induced angiogenesis and vascular tumor growth. The vessels respond to the solid pressure generated by the growing tumor. Accordingly, strong oxygen gradients are present that result in strongly heterogeneous tumor cell proliferation and shape instability. The color scheme is the same as in Figure 13.4a.

The neovessels in other areas of the host microenvironment then provide a stronger source of oxygen. This triggers tumor–cell proliferation and growth in regions where proliferation had been decreased previously.

The heterogeneity of oxygen delivery and the associated oxygen gradients cause heterogeneous tumor cell proliferation. Unlike the case in Figure 13.5, proliferation is confined to regions close to the tumor–host interface. This results in morphological instability that leads to the formation of invasive tumor clusters (e.g., buds) and a complex tumor morphology. This result is consistent with the theory and predictions made earlier (see, for example, Cristini et al. (2003); Cristini et al. (2005); Anderson (2005); Macklin and Lowengrub (2005, 2006, 2007); Anderson et. al. (2006); and Gerlee and Anderson (2007)) that substrate inhomogeneities in the tumor microenvironment tend to cause morphological instabilities in growing tumors.

(c)

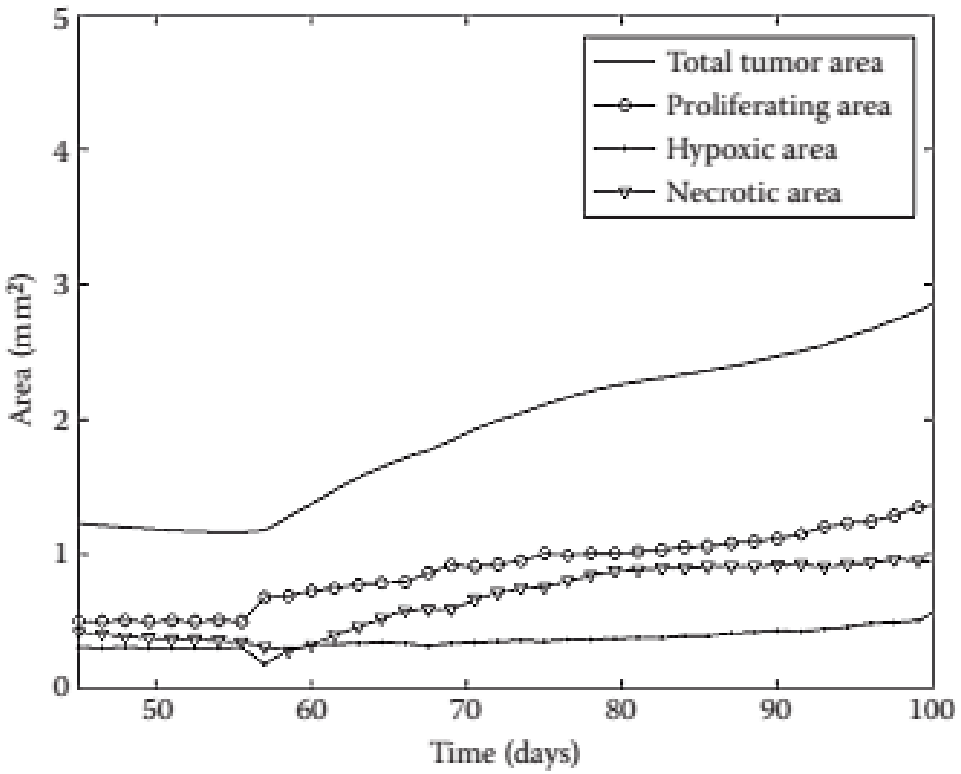

FIGURE 13.6 (Continued) (c) The areas (mm²) of the total tumor (solid line), proliferating region ("o"), hypoxic region ("•"), and the necrotic region ("inverted triangle") as a function of time for the simulation in Figure 13.6a.

Although nutrient-providing, functional vessels are not able to penetrate the tumor during growth, the growth of the tumor elicits a strong branching and anastomosis response from nearby neovessels in the host microenvironment. Although there is an analogous neovascular response seen in Figure 13.5, the effect here is much more pronounced as the levels of TAF are higher in these regions (because tumor hypoxia is increased) and, thus, the wall shear stresses initiate more significant branching.

In Figure 13.6b, the dimensional neovessel radii (in m) and intravascular pressures (in Pa) are shown together with the nondimensional ECM and TAF concentrations. As before, blood flow causes a dilation of the vessels and an overall decrease of pressure as branching, anastomosis, and increased blood flow occur throughout the neovascular network. The constriction of neovessels in response to the solid pressure is clearly seen.

The tumor-secreted MDE degrades the ECM in the host microenvironment near the tumor and in the tumor interior. As before (recall Figure 13.5b), the neovessels are still able to migrate through the region of lower ECM even though this acts against haptotaxis. Because the tumor grows more slowly than that in Figure 13.5b, only the tips of the invasive

clusters outrun the degraded ECM. As can be seen in Figure 13.6c, the host ECM is degraded in the region between the invading clusters. The ECM signature of the original avascular tumor spheroid can no longer be seen at later times.

This simulation shows even stronger nonlinear coupling between the tumor-induced angiogenesis and the progression of the tumor compared to the prior case shown in Figure 13.5. The pressure-induced vascular response of constricting neovessel radii and inhibiting blood-tissue oxygen transfer not only affects the tumor growth dramatically, but also significantly affects the growth of the neovascular network, and vice versa.

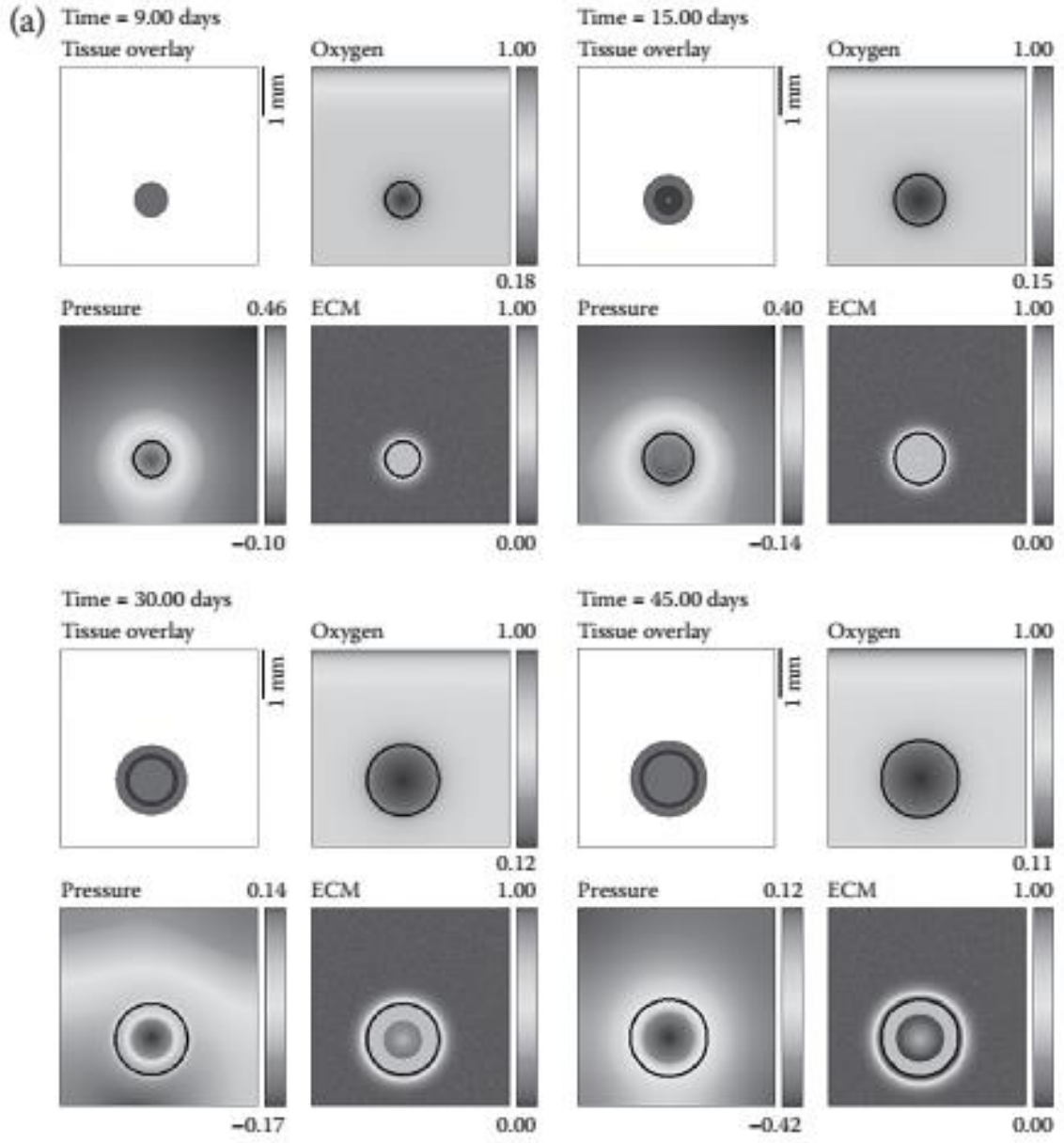

FIGURE 13.7 (a) The evolution toward a steady-state avascular multicell (2D) spheroid with enhanced ECM degradation. The MDE production and degradation parameters are larger than those used in Figure 13.4a; see Table 13.4.

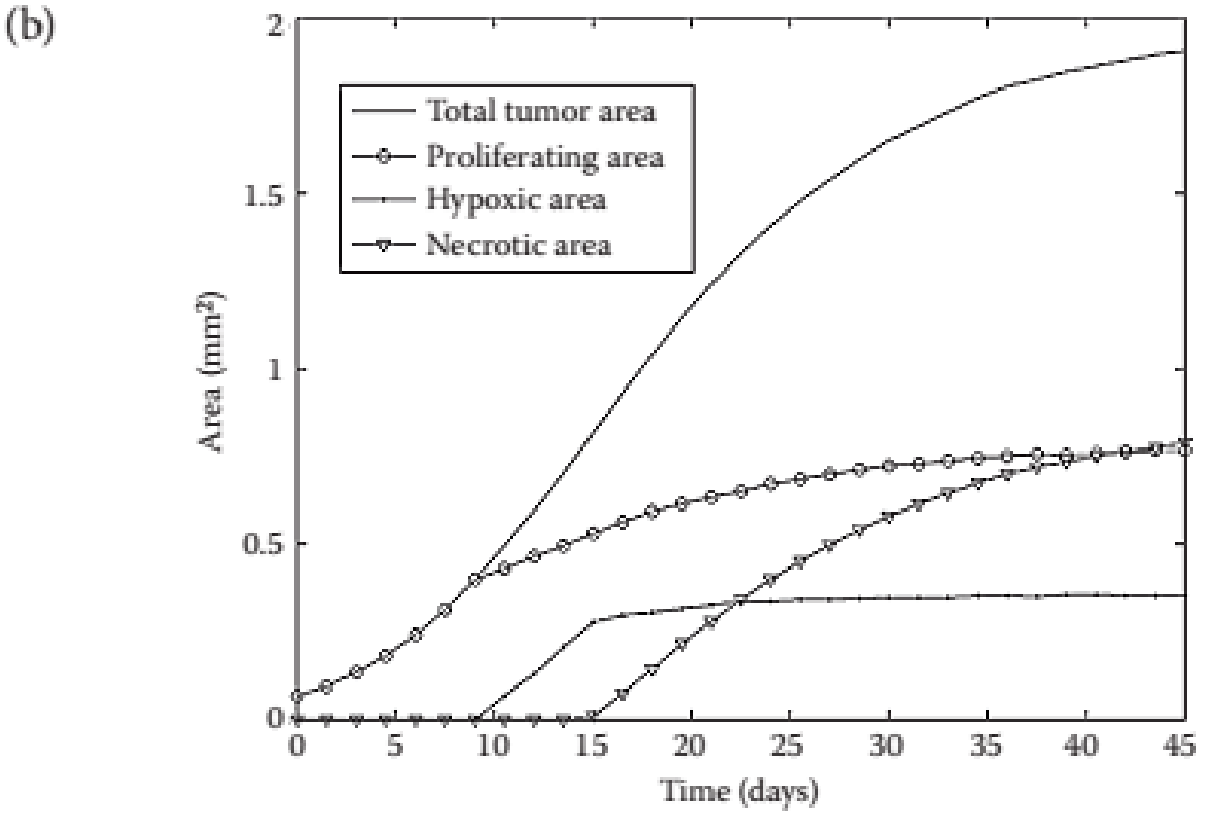

FIGURE 13.7 (Continued) (b) The areas (mm²) of the total tumor (solid line), proliferating region ("o"), hypoxic region ("•"), and the necrotic region ("inverted triangle") as a function of time for the simulation in Figure 13.7a.

Avascular Growth to a Multicellular (2D) Spheroid with Enhanced ECM Degradation and Production

We next examine the effect of ECM degradation on the results. In Figure 13.7a, we repeat the simulation in the section titled "The Tumor Invasion Model" except that both the MDE degradation and production parameters are increased (see Table 13.4). The tumor grows by uptaking oxygen delivered by the preexisting (uniform) vasculature and growth is more rapid than that for the avascular tumor shown in the aforementioned section (Figure 13.4a). This occurs because the mobility is greater here due to the enhanced degradation of ECM. This effect overcomes the tendency of haptotaxis to keep the tumor away from the degraded ECM.

The tumor reaches a nearly steady size, containing both a hypoxic and a necrotic core, that is significantly larger than that shown in Figures 13.4a and 13.4b; the radius at 45 days is approximately 0.78 mm (see Figure 13.7b). At the final time shown (45 days), the ECM is significantly degraded in the host microenvironment and in the tumor necrotic core to the point that there is even a thin annular "hole" in the ECM immediately surrounding the spheroid, and a circular hole in the necrotic region, where the density of ECM $E \approx 0$.

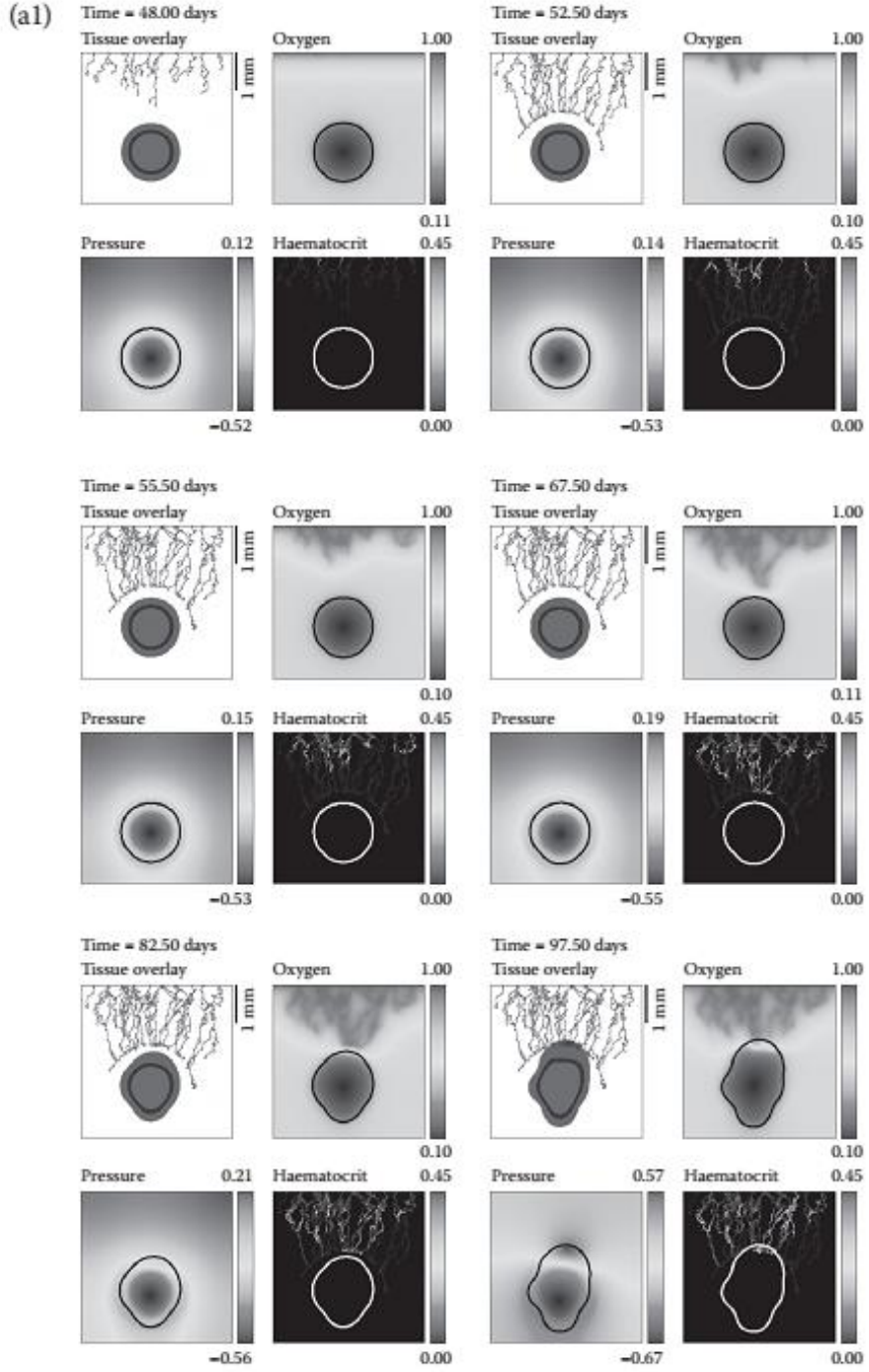
(a1)
Time = 48.00 days
Tissue overlay
Oxygen 1.00
1 mm
0.11
Pressure 0.12
Haematocrit 0.45
−0.52
0.00
Time = 52.50 days
Tissue overlay
Oxygen 1.00
1 mm
0.10
Pressure 0.14
Haematocrit 0.45
−0.53
0.00
Time = 55.50 days
Tissue overlay
Oxygen 1.00
1 mm
0.10
Pressure 0.15
Haematocrit 0.45
−0.53
0.00
Time = 67.50 days
Tissue overlay
Oxygen 1.00
1 mm
0.11
Pressure 0.19
Haematocrit 0.45
−0.55
0.00
Time = 82.50 days
Tissue overlay
Oxygen 1.00
1 mm
0.10
Pressure 0.21
Haematocrit 0.45
−0.56
0.00
Time = 97.50 days
Tissue overlay
Oxygen 1.00
1 mm
0.10
Pressure 0.57
Haematocrit 0.45
−0.67
0.00

FIGURE 13.8 (a1) Tumor-induced angiogenesis and vascular tumor growth with enhanced ECM degradation.

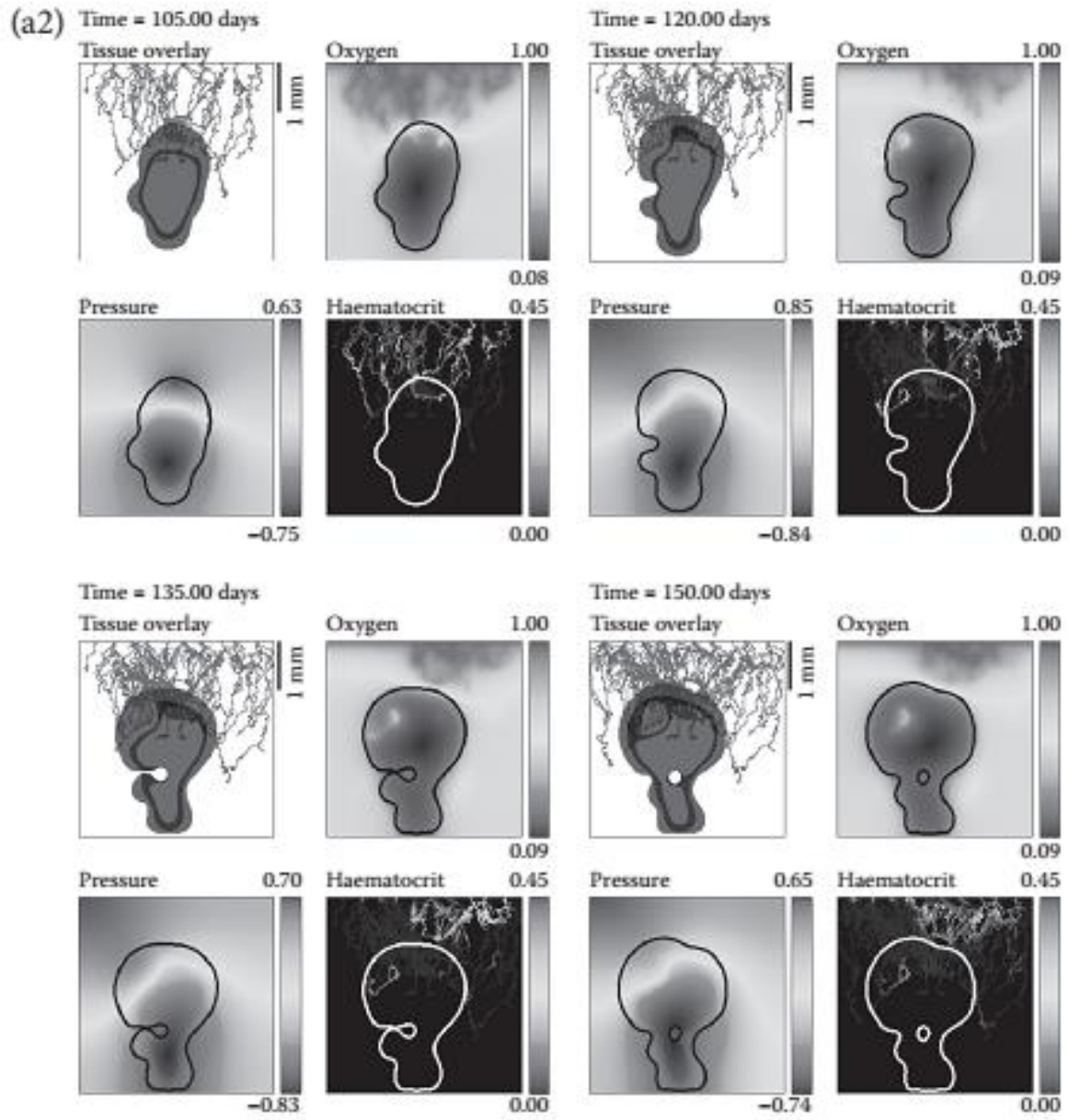

FIGURE 13.8 (Continued) (a2) Tumor-induced angiogenesis and vascular tumor growth with enhanced ECM degradation.

Tumor-Induced Angiogenesis and Vascular Growth: The Effect of Solid Pressure-Induced Neovascular Response and Enhanced ECM Degradation and Production

Next, we consider, in Figures 13.8a–13.8c, the effect of enhanced ECM degradation on tumor-induced angiogenesis and vascular growth. We repeat the simulation shown in the section titled "Numerical Schemes" except that the initial condition is the $t = 45$ day simulation from Figure 13.7a and the MDE parameters are the same as in the previous section (see Tables 13.4–13.6).

As in the simulation shown in the section titled "The Tumor Invasion Model," the neovessels grow and form loops near the parent capillary.

However, now because of the growing ECM annular hole surrounding the tumor, the neovessels are not able to reach the tumor and are instead trapped by the ECM hole due to haptotaxis. The vessels then encapsulate roughly the upper half of the tumor.

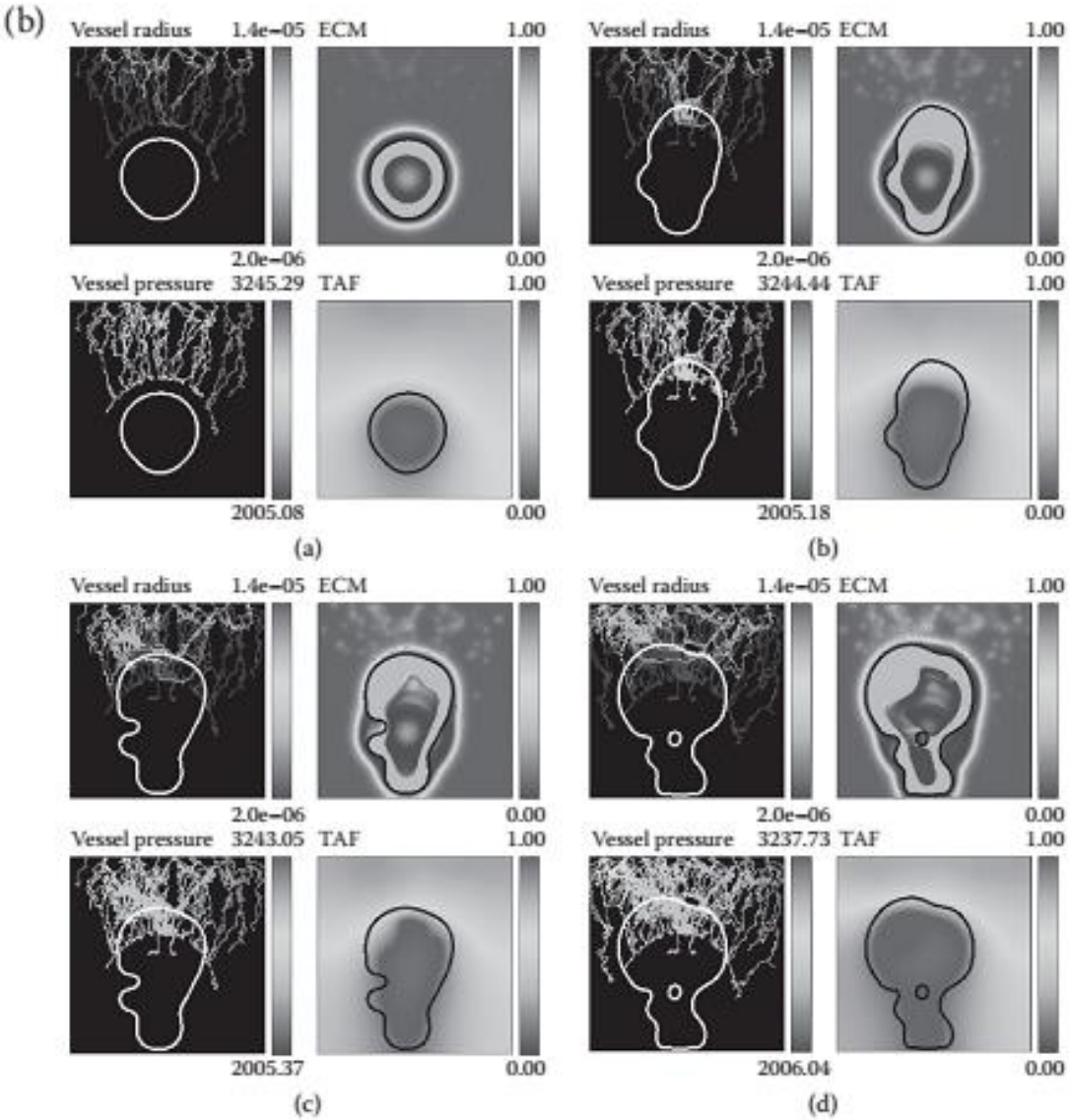

FIGURE 13.8 (Continued) (B) The dimensional intravascular radius (m) and pressure (Pa) together with the nondimensional ECM and TAF concentrations at different times from the simulation shown in Figure 13.8a. (1) Time (days) = 67.5, (2) 105, (3) 120, (4) 150.

As blood flows through the neovascular network and approaches the tumor, the tumor responds by growing toward the flowing neovessels that provide the oxygen source, as described in the section titled "Numerical Schemes." The tumor elongates, constricts the neovessels in its path, and prevents the transfer of oxygen from the neovessels to the host. This limits tumor cell proliferation and results in a roughly steady maximum solid pressure. Correspondingly, there are heterogeneous oxygen supply, heterogeneous tumor cell proliferation, and strong oxygen gradients. As in the aforementioned section, this results in a morphological instability of the growing solid tumor.

(b)

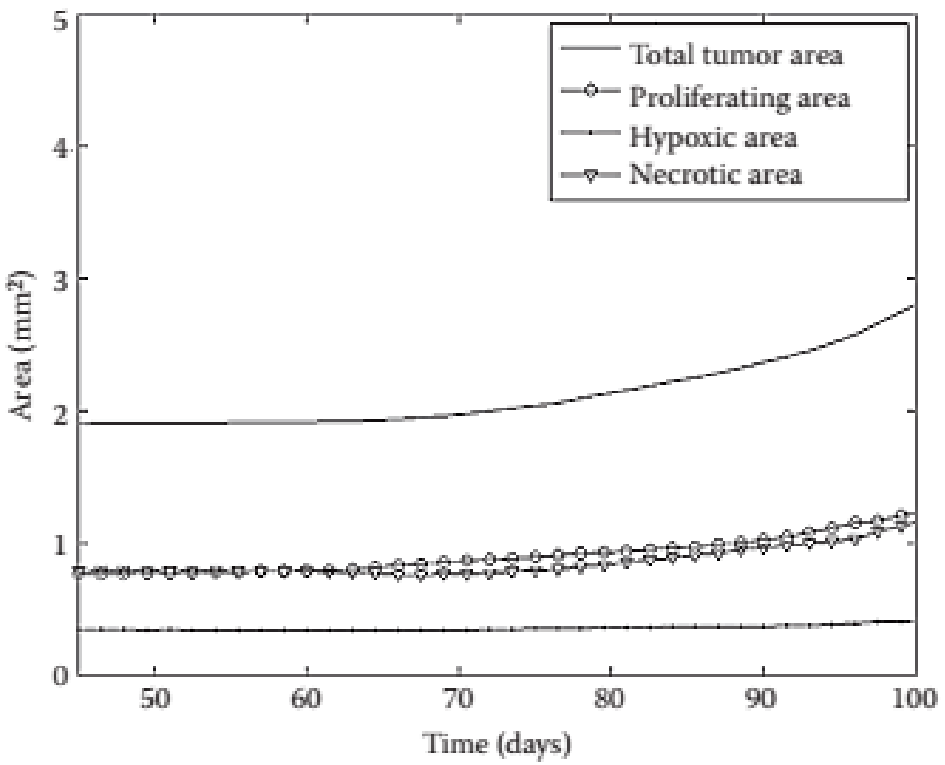

FIGURE 13.8 (Continued) (c) The areas (mm^2) of the total tumor (solid line), proliferating region ("o"), hypoxic region ("•"), and the necrotic region ("inverted triangle") as a function of time for the simulation in Figure 13.8a.

As the tumor continues to grow, the neovessels respond by increasing branching and anastomosing near the tumor–host interface. This results in a broader supply of oxygen in the part of the tumor closest to the parent capillary. Proliferation is increased, and the top of the tumor flattens. The increased proliferation leads to large solid pressures, which then constrict the nearby neovessels and inhibit oxygen supply. The tumor then begins to grow toward other vessels near the parent capillary, and the top of the tumor becomes unstable. Further, there is instability along the side of the tumor that leads to the encapsulation of host domain inside the tumor. Also, observe that a small amount of oxygen is able to be delivered to the tumor at very late times as haematocrit is trapped in a constricted vessel at a location where the pressure is sufficiently low to allow extravasation.

Figure 13.8b shows the dimensional neovessel radii (in m) and the intravascular pressures (in Pa) together with the nondimensional ECM and TAF concentrations. The results are similar to those obtained before except that the tumor does not outrun the ECM hole, although at the top of the tumor, the hole is quite shallow.

Interestingly, even though the initial tumor in Figure 13.8a is larger than that in Figure 13.6a, the final tumor size at $t = 150$ days is roughly the same for both cases (see Figures 13.8c and 13.6c). The ECM hole present in the simulation in Figure 13.8 prevents the neovessels from getting close to the tumor during the early stages of growth; this allows the tumor in Figure 13.6 to catch up and even grow slightly larger than that in Figure 13.8.

Finally, in Figure 13.9, we compare the average radii in the neovascular networks for the simulations in Figures 13.5, 13.6, and 13.8. At early times, the radii for the simulation in Figure 13.5, where the neovasculature does not respond to solid pressure, grows the fastest as blood flows uninhibited through the network. Later, however, the simulation with lower ECM degradation shows the most rapid radii increase. This occurs because the EC sprout tips are able to move more freely through the host domain and do not get caught by degraded ECM. This provides the vascular network with a more widely varying flow response.

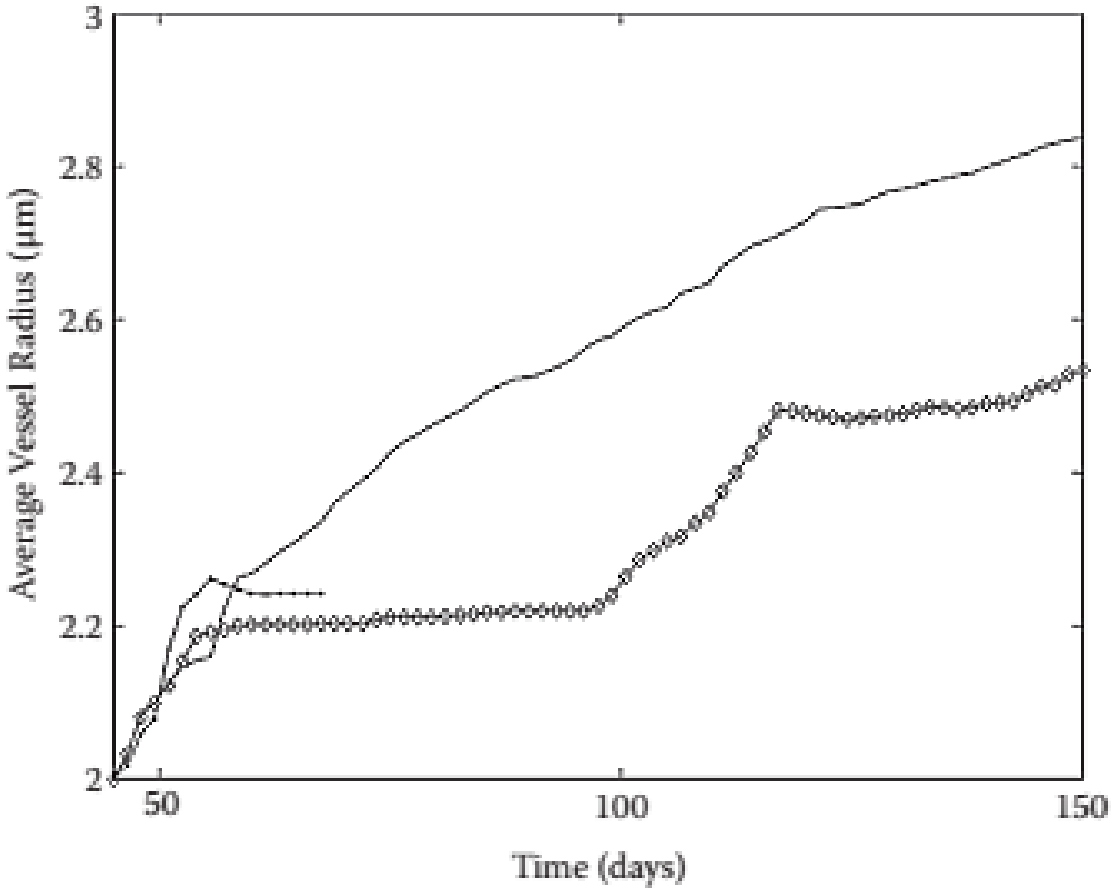

FIGURE 13.9 Average vessel radii. Simulation from Figure 13.6 (solid), simulation from Figure 13.5. ("•"), simulation from Figure 13.8 ("diamond").

DISCUSSION

In this paper, we have coupled an improved continuum model of solid tumor invasion (following Macklin and Lowengrub (2007)) with a model of tumor-induced angiogenesis (following McDougall et al. (2006)) to produce a new multiscale model of vascular solid tumor growth. The invasion and angiogenesis models were coupled through the tumor angiogenic factors (TAFs) released by the tumor cells and through the nutrient extravasated from the neovascular network. As the blood flows through the neovascular network, nutrients (e.g., oxygen) are extravasated and diffuse through the ECM, triggering further growth of the tumor, which in turn influences the TAF expression. In addition, the extravasation is mediated by the hydrostatic stress (solid pressure) generated by the growing tumor. The solid pressure also affects vascular remodeling by restricting the radii of the vessels and, thus, the flow pattern and wall shear stresses. The vascular network and tumor progression were also coupled via the ECM as both the tumor cells and ECs upregulate matrix-degrading proteolytic enzymes, which cause localized degradation of the ECM that in turn affects haptotactic migration.

We performed simulations of the multiscale model that demonstrated the importance of the nonlinear coupling between the growth and remodeling of the vascular network, the blood flow through the network and the tumor progression. The solid pressure generated by tumor cell proliferation effectively shuts down large portions of the vascular network, dramatically affecting the flow, the subsequent network remodeling, the delivery of nutrients to the tumor and the subsequent tumor progression. In addition, ECM degradation by tumor cells was seen to have a dramatic affect on both the development of the vascular network and the growth response of the tumor. In particular, when the ECM degradation is significant, the newly formed vessels tended to encapsulate, rather than penetrate, the tumor and were thus less effective in delivering nutrients.

There are many directions in which this work will be taken in the future both in terms of modeling additional biophysical effects as well as algorithmic improvements. Regarding the algorithm, we plan to upgrade the solid pressure/nutrient solver by solving for P and _ as a coupled system. This will prevent oscillations that may occur by lagging P in the source term for nutrient. We also plan to accelerate the solver for the intravascular pressure to improve performance of the coupled algorithm.

Regarding the model, we plan to develop a more detailed model of the effect of solid pressure on the constriction and collapse of vessels in the microvasculature and on the corresponding response of the microvascular network. We also plan to include, for the first time, the effects of the venous system. Other features, such as the recruitment of pericytes by the vascular ECs, will also be investigated. In addition, we will incorporate more realistic models for soft tissue mechanics.

The work presented here demonstrates that nonlinear simulations are a powerful tool for understanding phenomena fundamental to solid tumor growth. A biophysically justified computer model could provide an enormous benefit to the clinician, the patient, and society by efficiently searching parameter space to identify optimal, or nearly optimal, individualized treatment strategies involving, for example, chemotherapy and adjuvant treatments such as antiangiogenic or anti-invasive therapies. This is a direction we plan to explore in the future.

ACKNOWLEDGMENTS

MC was supported by a Leverhulme Trust Personal Research Fellowship and NIH Grant CA 113004. PM acknowledges partial support from a U.S. Department of Education GAANN (Graduate Assistance in Areas of National Need) fellowship. JSL acknowledges partial support from the National Science Foundation (NSF) through grants DMS-0352143 and DMS-0612878 and from the National Institutes of Health (NIH) grant P50GM76516 for a National Center of Excellence in Systems Biology at UCI. VC acknowledges partial support from the NSF and the (NIH) through grants NSF-DMS-0314463 and NIH-5R01CA093650-03. Further, PM, VC, and JL are grateful to Herman Frieboes for valuable discussions.

REFERENCES

Adalsteinsson, D., Sethian, J.A. 1999. The fast construction of extension velocities in level-set methods. *J. Comput. Phys.* 148:2–22.

Alarcon, T., Byrne, H.M., Maini, P.K. 2003. A cellular automaton model for tumour growth in a heterogeneous environment. *J. Theor. Biol.* 225:257–274.

Alarcon, T., Byrne, H.M., Maini, P.K., 2005. A multiple scale model for tumor growth, *Multiscale Mod. Simul.* 3:440–475.

Ambrosi, D., Preziosi, L. 2002. On the closure of mass balance models for tumor growth. *Math. Mod. Meth. Appl. Sci.* 12:737–754.

Anderson, A.R.A., Chaplain, M.A.J. 1998. Continuous and discrete mathematical models of tumor-induced angiogenesis. *Bull. Math. Biol.* 60: 857–899.

Anderson, A.R.A., Chaplain, M.A.J., Newman, E.L., Steele, R.J.C., and Thompson, A.M., 2000. Mathematical modelling of tumour invasion and metastasis. *J. Theor. Med.* 2:129–154.

Anderson, A.R.A., 2005. A hybrid mathematical model of solid tumour invasion: the importance of cell adhesion. *Math. Med. Biol.* 22: 163–186.

Araujo, R.P., McElwain, D.L.S. 2004. A history of the study of solid tumor growth: the contribution of mathematical modelling. *Bull. Math. Biol.* 66:1039–1091.

Araujo, R.P., McElwain, D.L.S. 2005a. A mixture theory for the genesis of residual stresses in growing tissues I: a general formulation. *SIAM J. Appl. Math.* 65:1261–1284.

Araujo, R.P., McElwain, D.L.S. 2005b. A mixture theory for the genesis of residual stresses in growing tissues II: solutions to the biphasic equations for a multicell spheroid. *SIAM J. Appl. Math.* 66:447–467.

Ausprunk, D.H., Folkman, J., 1977. Migration and proliferation of endothelial cells in preformed and newly formed blood vessels during tumour angiogenesis. *Microvasc. Res.* 14:53–65.

Balding, D., McElwain, D.L.S. 1985. A mathematical model of tumour-induced capillary growth. *J. Theor. Biol.* 114:53–73.

Byrne, H.M., Chaplain, M.A.J. 1995. Mathematical models for tumour angiogenesis: numerical simulations and nonlinear wave solutions. *Bull. Math. Biol.* 57:461–486.

Byrne, H.M., Chaplain, M.A.J., Pettet, G.J., and McElwain, D.L.S. 1999. A mathematical model of trophoblast invasion. *J. Theor. Med.* 1:275–286.

Byrne, H.M., Preziosi, L. 2003. Modeling of solid tumour growth using the theory of mixtures. *Math. Med. Biol.* 20:341–366.

Byrne, H.M., Alarcon, T., Owen, M.R., Webb, S.D., and Maini, P.K. 2006. Modeling aspects of cancer dynamics: a review. *Phil. Trans. R. Soc. A* 364:1563–1578.

Carmeliet, P. 2005. Angiogenesis in life, disease and medicine. *Nature* 438:932–936.

Chaplain, M.A.J., Stuart A.M. 1993. A model mechanism for the chemotactic response of endothelial cells to tumour angiogenesis factor. *IMA J. Math. Appl. Med. Biol.* 10:149–168.

Chaplain, M.A.J., 2000. Mathematical modelling of angiogenesis. *J. Neuro-Oncol.* 50:37–51.

Chaplain, M.A.J., Lolas, G. 2005. Mathematical modelling of cancer cell invasion of tissue: the role of the urokinase plasminogen activation system. *Math. Modell. Methods. Appl. Sci.* 15:1685–1734.

Chaplain, M.A.J., McDougall, S.R., Anderson, A.R.A. 2006. Mathematical modelling of tumour-induced angiogenesis. *Annu. Rev. Biomed. Eng.* 8:233–257.

Chaplain, M.A.J., Lolas, G. 2006. Mathematical modelling of cancer invasion of tissue: dynamic heterogeneity. *Net. Hetero. Med.* 1:399–439.

Chomyak, O.G., Sidorenko, M.V. 2001. Multicellular spheroids model in oncology. *Exp. Oncol.* 23:236–241.

Cristini, V., Lowengrub J., Nie, Q. 2003. Nonlinear simulation of tumour growth. *J. Math. Biol.* 46:191–224.

Deakin, A.S. 1976. Model for initial vascular patterns in melanoma transplants. *Growth* 40: 91–201.
Dickinson, R.B., Tranquillo, R.T. 1993. A stochastic model for adhesion-mediated cell random motility and haptotaxis, *J. Math. Biol.* 31:563–600.
DiMilla, P.A., Barbee, K., Lauffenburger, D.A. 1991. Mathematical model for the effects of adhesion and mechanics on cell migration speed, *Biophys. J.* 60:15–37.
Erler, J.T., Bennewith, K.L., Nicolau, M., Dornhoefer, N., Kong, C.L., Chi, Q-T., Jeffrey, S.S., and Siaccia, A.J. 2006. Lysyl oxidase is essential for hypoxia-induced metastasis. *Nature* 440:1222–1226.
Folkman, J., 1971. Tumor angiogenesis: therapeutic implications. *N. Eng. J. Med.* 285:1182–1186.
Folkman, J., 1995. Angiogenesis in cancer, vascular, rheumatoid and other disease. *Nature Med.* 1:21–31.
Folkman, J., Klagsbrun, M., 1987. Angiogenic factors. *Science* 235:442–447.
Friedl, P., Wolf, K. 2003. Tumor-cell invasion and migration: diversity and escape mechanisms. *Nature Rev.* 3:362–371.
Galaris, D., Barbouti, A., Korantzopoulos, P. 2006. Oxidative stress in hepatic ischemia—reperfusion injury: the role of antioxidants and iron chelating compounts. *Current Pharma. Design* 12:2875–2890.
Gerlee, P., Anderson, A.R.A. 2007. Stability analysis of a hybrid cellular automaton model of cell colony growth. *Phys. Rev. E* 75:0151911.
Gimbrone, M.A., Cotran, R.S., Leapman, S.B., and Folkman, J., 1974. Tumor growth and neovascularization: an experimental model using the rabbit cornea. *J. Natl. Cancer Inst.* 52:413–427.
Godde, R., Kurz, H., 2001. Structural and biophysical simulation of angiogenesis and vascular remodeling. *Dev. Dynam.* 220:387–401.
Graziano, L., Preziosi, L. 2007. Mechanics in tumor growth, in *Modelling of Biological Materials*, ed. F. Mollica, K.R. Rajagopal, and L. Preziosi, Birkhauser.
Greenspan, H.P. 1976. On the growth and stability of cell cultures and solid tumours. *J. Theor. Biol.* 56:229–242.
Hanahan, D., Weinberg, R.A. 2000. The hallmarks of cancer. *Cell* 100:57–70.
Jain, R.K., 1987. Transport of molecules in the tumor interstitium: a review. *Cancer Res.* 47:3039–3051.
Jain, R.K., 1988. Determinants of tumour blood flow: a review. *Cancer Res.* 48:2641–2658.
Jain, R.K., 2001. Normalizing tumor vasculature with anti-angiogenic therapy: a new paradigm for combination therapy. *Nature Med.* 7:987–989.
Jain, R.K., 2003. Molecular regulation of vessel maturation. *Nature Med.* 9:685–693.
Jain, R.K., 2004. Recognition of tumor blood vessel normalization as a new antiangiogenic concept. *Nature Med.* 10:329–330.
Kamiya, A., Bukhari, R., Togawa, T., 1984. Adaptive regulation of wall shear stress optimizing vascular tree function. *Bull. Math. Biol.* 46:127–137.

Kaur, B., Khwaja, F.W., Severson, E.A., Matheny, S.L., Brat, D.J., and VanMeir, E.G. 2005. Hypoxia and the hypoxia-inducible-factor pathway in glioma growth and angiogenesis. *Neuro-Oncol.* 7:134–153.

Kim, J.B. 2005. Three-dimensional tissue culture models in cancer biology. *Semin. Cancer Biol.* 15:365–377.

Kloner, R.A., Jennings, R.B. 2001. Consequences of brief ischemia: stunning, preconditioning and their clinical implications: Part 1. *Circulation* 104:2981–2989.

Krenz, G.S., Dawson, C.A., 2002. Vessel distensibility and flow distribution in vascular trees. *J. Math. Biol.* 44:360–374.

Kunz-Schughart, L.A., Freyer, J.P., Hofstaedter, F., and Ebner, R. 2004. The use of 3-D cultures for high-throughput screening: the multicellular spheroid model. *J. Biomol. Screening* 9:273–285.

Levine, H.A., Pamuk, S., Sleeman, B.D., Nielsen-Hamilton, M. 2001. Mathematical modeling of the capillary formation and development in tumor angiogenesis: penetration into the stroma. *Bull. Math. Biol.* 63: 801–863.

Liotta, L.A., Saidel, G.M., Kleinerman, J. 1977. Diffusion model of tumor vascularization and growth. *Bull. Math. Biol.* 39:117–129.

Macklin, P., McDougall, S.R., Anderson, A.R.A., Chaplain, M.A.J., Cristini, V., and Lowengrub, J., 2009. Multiscale modelling and nonlinear simulation of vascular tumour growth. *J. Math. Biol.* 58:765–798.

Mantzaris, N.V., Webb, S., Othmer, H.G., 2004. Mathematical modeling of tumor-induced angiogenesis. *J. Math. Biol.* 49:111–187.

McDougall, S.R., Sorbie, K., 1997. The application of network modelling techniques to multiphase flow in porous media. *Petrol. Geosci.* 3:161–169.

McDougall, S.R., Anderson, A.R.A., Chaplain, M.A.J., and Sherratt, J.A., 2002. Mathematical modelling of flow through vascular networks: implications for tumour-induced angiogenesis and chemotherapy strategies. *Bull. Math. Biol.* 64:673–702.

McDougall, S.R., Anderson, A.R.A., Chaplain, M.A.J. 2006. Mathematical modelling of dynamic adaptive tumour-induced angiogenesis: clinical implications and therapeutic targeting strategies. *J. Theor. Biol.* 241:564–589.

Morikawa, S., Baluk, P., Kaidoh, T., Haskell, A., Jain, R.K., and McDonald, D.M., 2002. Abnormalities in pericytes on blood vessels and endothelial sprouts in tumors. *Am. J. Pathol.* 160:985–1000.

Muthukkaruppan, V.R., Kubai, L., Auerbach, R., 1982. Tumor-induced neovascularization in the mouse eye. *J. Natl. Cancer Inst.* 69:699–705.

Olsen, L., Sherratt, J.A., Maini, P.K., and Arnold, F. 1997. A mathematical model for the capillary endothelial cell-extracellular matrix interactions in wound-healing angiogenesis. *IMA J. Math. Appl. Med. Biol.* 14:261–281.

Orme, M.E., Chaplain, M.A.J. 1996. A mathematical model of vascular tumour growth and invasion. *Math. Comp. Modelling* 23:43–60.

Orme, M.E., Chaplain, M.A.J., 1997. Two-dimensional models of tumour angiogenesis and anti-angiogenesis strategies. *IMA J. Math. Appl. Med. Biol.* 14:189–205.

Paweletz, N., Knierim, M., 1989. Tumor-related angiogenesis. *Crit. Rev. Oncol. Hematol.* 9:197–242.
Palecek, S.P., Loftus, J.C., Ginsberg, M.H., Lauffenburger, D.A., and Horwitz, A.F. 1997. Integrin-ligand binding properties govern cell migration speed through cell-substratum adhesiveness. *Nature* 385:537–540.
Plank, M.J., Sleeman, B.D., 2004. Lattice and non-lattice models of tumour angiogenesis. *Bull. Math. Biol.* 66:1785–1819.
Pouyssegur, J., Dayan, F., Mazure, N.M. 2006. Hypoxia signalling in cancer and approaches to enforce tumour regression. *Nature* 441:437–443.
Pries, A.R., Secomb, T.W., Gaehtgens, P., 1996. Biophysical aspects of blood flow in the microvasculature. *Cardiovasc. Res.* 32:654–667.
Pries, A.R., Secomb, T.W., Gaehtgens, P., 1998. Structural adaptation and stability of microvascular netwoks: theory and simulation. *Am. J. Physiol. Heart Circ. Physiol.* 275:H349–H360.
Pries, A.R., Reglin, B., Secomb, T.W., 2001a. Structural adaptation of microvascular networks: functional roles of adaptive responses. *Am. J. Physiol. Heart Circ. Physiol.* 281:H1015–H1025.
Pries, A.R., Reglin, B., Secomb, T.W., 2001b. Structural adaptation of vascular networks: role of the pressure response. *Hypertension* 38:1476–1479.
Quaranta, V., Weaver, A.M., Cummings, P.T., and Anderson, A.R.A. 2005. Mathematical modelling of cancer: the future of prognosis and treatment, *Clin. Chim. Acta* 357:173–179.
Risau, W., 1997. Mechanisms of angiogenesis. *Nature* 386:671–674.
Roose, T., Chapman, S.J., Maini, P.K. 2007. Mathematical models of avascular cancer. *SIAM Reviews* 49:179–208.
Secomb, T.W. 1995. Mechanics of blood flow in the microcirculation. In *Biological Fluid Dynamics*. ed. C.P. Ellington and T.J. Pedley. Company of Biologists, Cambridge.
Stéphanou, A., McDougall, S.R., Anderson, A.R.A., and Chaplain, M.A.J., 2005. Mathematical modelling of flow in 2D and 3D vascular networks: applications to anti-angiogenic and chemotherapeutic drug strategies. *Math. Comp. Model.* 41:1137–1156.
Stéphanou, A., McDougall, S.R., Anderson, A.R.A., and Chaplain, M.A.J., 2006. Mathematical modelling of the influence of blood rheological properties upon adaptive tumour-induced angiogenesis. *Math. Comp. Model.* 44:96–123.
Sternlicht, M.D., Werb, Z., 2001. How matrix metalloproteinases regulate cell behavior. *Annu. Rev. Cell Dev. Biol.* 17:463–516.
Stokes, C.L., Lauffenburger, D.A., 1991. Analysis of the roles of microvessel endothelial cell random motility and chemotaxis in angiogenesis. *J. Theor. Biol.* 152:377–403.
Thompson, D.W., 1917. *On Growth and Form*. Cambridge University Press, Cambridge.
Walles, T., Weimer, M., Linke, K., Michaelis, J., and Mertsching, H. 2007. The potential of bioartificial tissues in oncology research and treatment. *Onkologie* 30:388–394.

Yan, L., Moses, M.A., Huang, S., and Ingber, D., 2000. Adhesion-dependent control of matrix metalloproteinase-2 activation in human capillary endothelial cells. *J. Cell Sci.* 113:3979–3987.

Ylä-Herttuala, S., Alitalo, K., 2003. Gene transfer as a tool to induce therapeutic vascular growth. *Nature Med.* 9:694–701.

Zhao, H.K. 2005. A fast sweeping method for Eikonal equations. *Math. Comp.* 74:603–627.

Zheng, X., Wise, S.M., Cristini, V. 2005. Nonlinear simulation of tumor necrosis, neo-vascularization and tissue invasion via an adaptive finite-element/level-set method. *Bull. Math. Biol.* 67:211–259.

ΓΕΝΙΚΗ ΠΟΛΥΚΛΙΜΑΚΩΤΗ ΠΡΟΣΟΜΟΙΩΣΗ ΑΣΘΕΝΕΙΩΝ ΚΑΙ *IN SILICO* ΙΑΤΡΙΚΗ

Estimating changes to brain oxygenation delivery through multi-scale modelling of the cerebral microvasculature

Chang Sub Park, Piotr Orlowski, Michael Chappell, Vicente Grau, Stephen Payne
University of Oxford

Correspondence: chang.park@eng.ox.ac.uk, 00441865 617 660, Institute of Biomedical Engineering, Old Road Campus Research Building, Oxford OX3 7DQ, UK

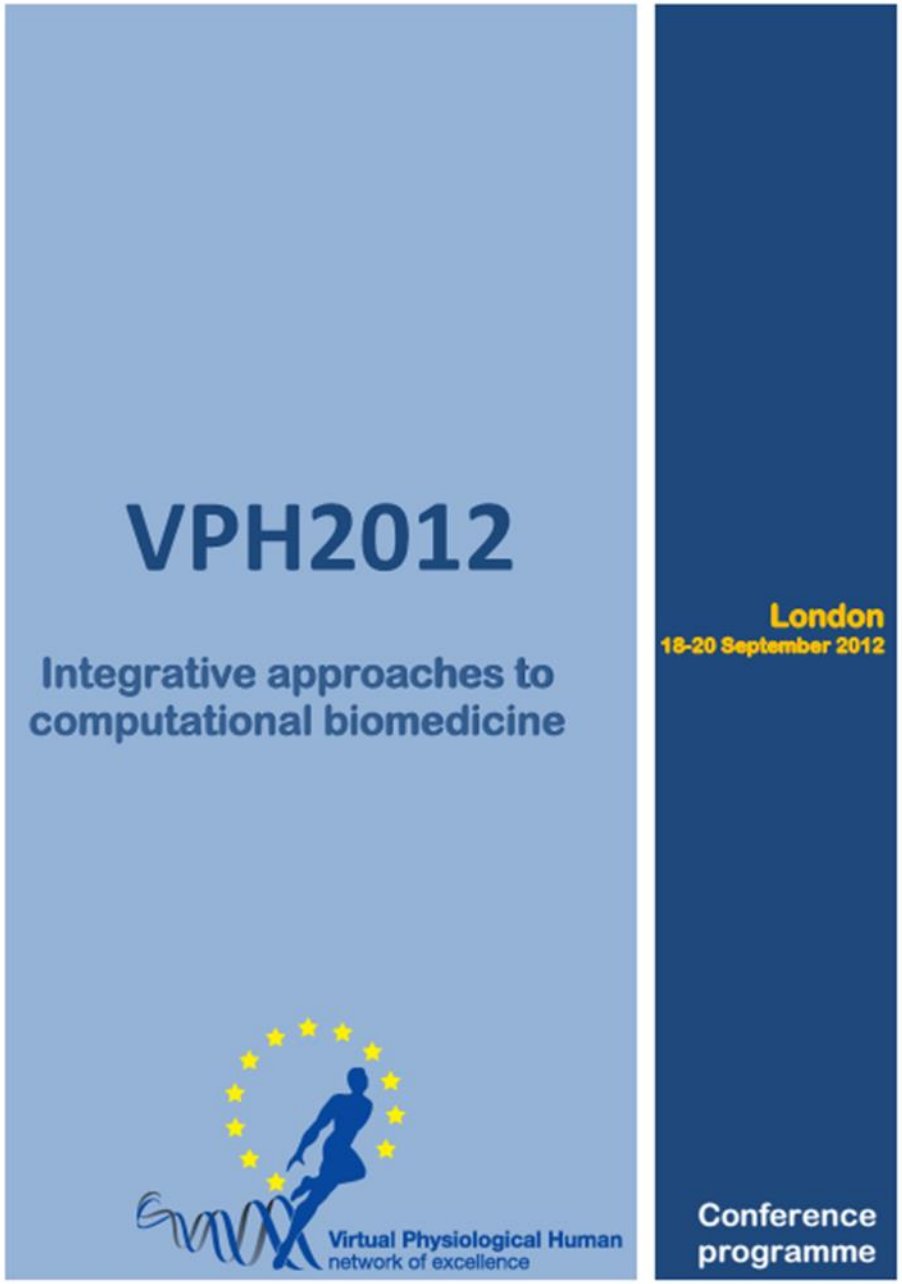
VPH2012
Integrative approaches to computational biomedicine
Virtual Physiological Human
network of excellence
London
18-20 September 2012
Conference programme

PROCEEDINGS-VPH2012_INTEGRATIVE_APPROACHES_TO_COMPUTATIONAL_BIOMEDICINE-LONDON_CONF_2012.pdf PAGE **300**/488 (PLEASE USE THE PDF PAGE COUNTER)

Estimating changes to brain oxygenation delivery through multi-scale modelling of the cerebral microvasculature

Chang Sub Park, Piotr Orlowski, Michael Chappell, Vicente Grau, Stephen Payne
University of Oxford

Correspondence: chang.park@eng.ox.ac.uk, 00441865 617 660, Institute of Biomedical Engineering, Old Road Campus Research Building, Oxford OX3 7DQ, UK

Introduction

The brain requires a constant supply of oxygenated blood to maintain its function. This is partly achieved by the well-developed collateral circulation, which allows for multiple pathways, and the high degree of interconnectedness of the capillary network. The dynamics of oxygen transport within the cerebral vasculature are thus complex. A detailed understanding of the oxygen transport dependence on local network properties would be valuable in helping to interpret how oxygen supply is affected under different pathological conditions. For example, recent studies have proposed a heterogeneous capillary transit time which becomes more homogeneous during ischemic conditions [4-5] in order to improve oxygen supply to surrounding tissue [3]. Using a novel model of the microvasculature, we investigate the

relationship between the residue function (the function measured experimentally in MRI that represents the amount of tracer remaining in the capillary bed at a given time) and the transit time for a physiologically realistic capillary network that matches experimentally obtained morphological data. The unsteady mass transport equation is solved to quantify local changes in concentration. This multi-scale modeling approach thus opens up the possibility of using residue function to gain quantitative information about the microvasculature in both healthy and pathological conditions, which could aid in clinical decision making for ischemic stroke patients.

Methods

A capillary network, within a cube with a length of $500\mu m$, matching both length and radial distribution obtained experimentally [1] is created based on Prim's algorithm [6]. The unsteady one-dimensional mass transport equation solely driven by convection is solved for the created capillary network assuming Poiseuille flow. We consider the pressure difference between the inlet and outlet to be 2000Pa, being a typical value. The concentration in the capillaries at a specific time is equal to the convolution of the inlet concentration with the residue function:

$$C(t) = C_a(t) * R(t). \quad (1)$$

The residue function can hence be obtained by deconvolving the inlet concentration with the capillary network concentration. A step impulse tracer concentration is considered at the inlet of our capillary network in order to observe the signal produced within the network. The concentration obtained for the capillary network is fitted to an exponential function of the form:

$$C(t) = A_0 + A_1 e^{-b_1 t} + A_2 e^{-b_2 t}. \quad (2)$$

Two exponential decay terms were considered as this was the minimum number of terms required to give a good fit. The transit time can then be obtained by taking the rate of change of the residue function:

$$h(t) = -dR/dt. \quad (3)$$

We consider first the case with a single inlet and outlet (1/1) and then the case when the numbers of inlets and outlets are matched to experimental data [2], 24 and 16 respectively for this volume of tissue (24/16). We also consider the cases for both a complete network and when 20% of the vessels are occluded.

Results and Discussion

Figure 1 shows the concentration, residue function and transit time for the different conditions. The first column considers the 1/1 case and the second column considers the 24/16 case; the solid and dashed lines representing the normal and 20% occluded cases respectively. The recovery in the concentration profile is faster as we increase the number of inlets and outlets as well as the number of vessels within the network. The residue function decays exponentially, the decay being faster for more inlets and outlets as well as for more vessels. There is a fast and a slow decay to replicate the variety between shorter and longer pathways. The difference between the normal case and the 20% occluded case is more significant for 1/1 than 24/16 as there are more available pathways in the latter case.

The residue function of a single vessel model can be expressed as a single exponentially decaying function. This single exponential decay approach has thus been considered in some studies. The capillary network, however, has many vessels connected in a complex manner, thus having numerous different pathways. It is thus not surprising that the residue function is not a single exponential decay. The decay is faster for increased numbers of inlets and outlets as there are more pathways available to the outlet. The transit time is heterogeneous for both conditions considered here, but further investigation will be required to observe whether the transit time becomes more homogeneous during ischemic conditions.

This model can thus provide information about the structure of the capillary network and its physiological conditions if the mass transport, residue function and/or transit time are known. An additional advantage of this model is that it could be used to analyse the effects of different perfusion levels, since we are able to quantify perfusion and how this will affect the residue function. This can be easily implemented by adding a perfusion term that depends on the concentration gradient as well as the diffusion coefficient along the vessel wall.

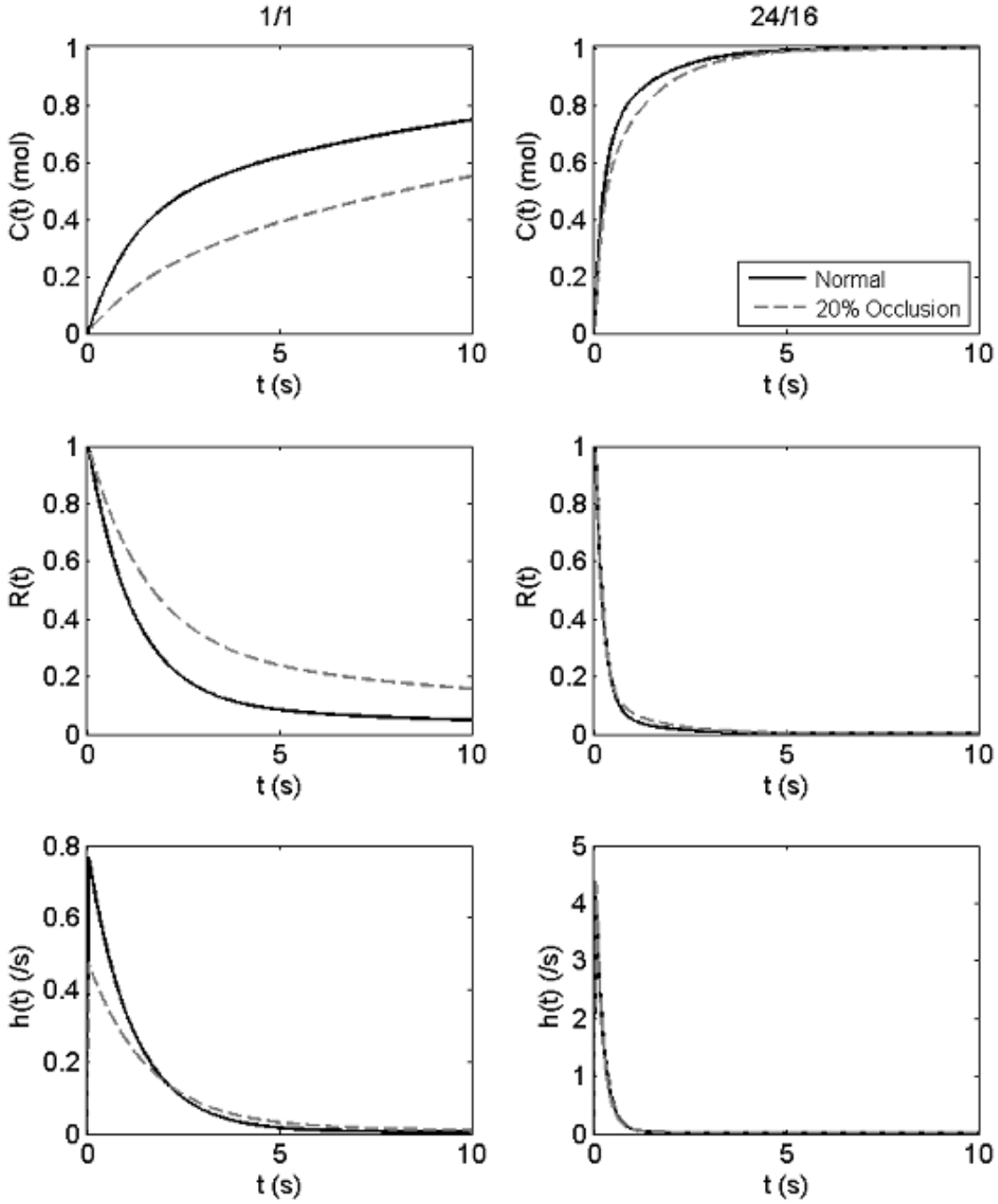

Figure 1. Plots of concentration, residue function and transit time for the different conditions.

Conclusion

We have considered here a multi-scale model to estimate mass transport with different network conditions and hence to calculate the residue function and the transit time. A simple double exponential function can be used to fit the concentration in a complexly connected capillary network. The different network structures are found to lead to different concentration profiles and thus residue functions and transit time distributions. This has significant potential to provide additional information about the localized properties of the microvasculature in both healthy tissue and tissue affected by stroke, via the information contained in experimentally estimated residue functions.

More detailed analysis will need to be performed to quantify the precise nature of the relationship between residue function parameters and the microvascular properties. This will also need to include the statistical variation inherent to such properties: one advantage of the model used here is that the network generation is statistical in nature and as such can be used to quantify this variability. Such estimates will give the robustness needed for these measurements to be of valuable in clinical studies: such multi-scale modeling opens up a real possibility of bridging the gap between modelling and clinical practice.

References

1. Cassot F, 2006 DOI: 10.1080/10739680500383407
2. Cassot F, 2010 DOI: 10.1016/j.brainres.2009.12.007
3. Jespersen SN, 2012 DOI: 10.1038/jcbfm.2011.153
4. Mouridsen K, 2006 DOI: 10.1016/j.neuroimage.2006.06.015
5. Ostergaard L, 1999 DOI: 10.1097/00004647-199906000-00013
6. Su S-W, 2012 DOI: 10.1111/j.1549-8719.2011.00148.x

Ευχαριστώ

Πρόγραμμα Διδακτορικών Σπουδών της Σχολής Ηλεκτρολόγων Μηχανικών και Μηχανικών Υπολογιστών ΕΜΠ

Πολυκλιμακωτή Προσομοίωση της Ασθένειας του Καρκίνου και *In Silico* Ιατρική (705)

Μάθημα 8ο

Προσομοίωση μοριακών μονοπατιών, μοριακών δικτύων, διαβίβασης μοριακών σημάτων και της προκύπτουσας συμπεριφοράς του καρκινικού κυττάρου. Αντίστοιχα μαθηματικά και υπολογιστικά προβλήματα στη Γενική *In Silico* Ιατρική

Γεώργιος Σ. Σταματάκος

Διευθυντής Ερευνών - Research Professor– Καθηγητής Ερευνας
Ερευνητικό Πανεπιστημιακό Ινστιτούτο Συστημάτων Επικοινωνιών και Υπολογιστών (ΕΠΙΣΕΥ)
Σχολή Ηλεκτρολόγων Μηχανικών και Μηχανικών Υπολογιστών (ΣΗΜΜΥ)
Εθνικό Μετσόβιο Πολυτεχνείο (ΕΜΠ)
Διευθυντής της Ερευνητικής Ομάδας για την In Silico Ογκολογία και την In Silico Ιατρική, ΕΠΙΣΕΥ-ΣΗΜΜΥ-ΕΜΠ
Επισκέπτης Καθηγητής της Ιατρικής Σχολής του Πανεπιστημίου του Saarland, Γερμανία (1/7/2019-15/9/2019)
Επισκέπτης Καθηγητής της ΣΗΜΜΥ, ΕΜΠ (2016-2019)
gestam@central.ntua.gr, http://in-silico-oncology.iccs.ntua.gr/

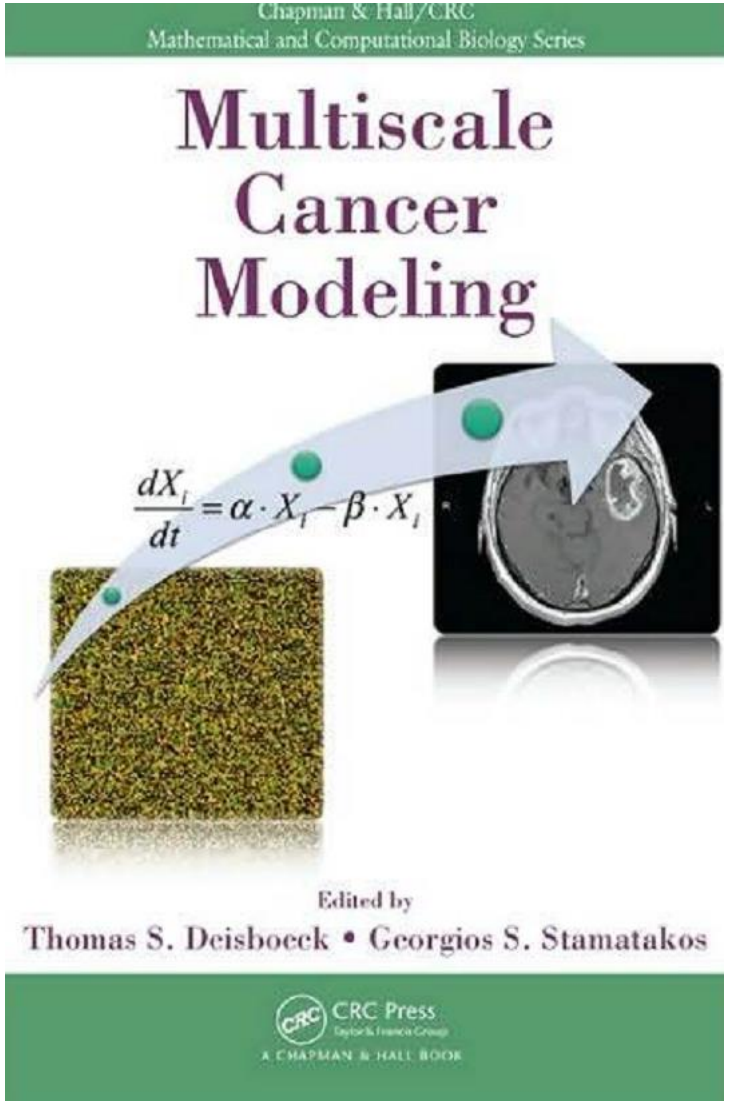

CRC Press
Taylor & Francis Group
6000 Broken Sound Parkway NW, Suite 300
Boca Raton, FL 33487-2742

© 2011 by Taylor and Francis Group, LLC
CRC Press is an imprint of Taylor & Francis Group, an Informa business

CHAPTER 2

Cancer Cell

Linking Oncogenic Signaling to Molecular Structure

Jeremy E. Purvis, Andrew J. Shih,
Yingting Liu, and Ravi Radhakrishnan

31

CHAPTER 2

Cancer Cell

Linking Oncogenic Signaling to Molecular Structure

Jeremy E. Purvis, Andrew J. Shih,
Yingting Liu, and Ravi Radhakrishnan

CONTENTS

Introduction 31
Model 33
Constructing Mechanistic Models of Oncogenic Signaling 35
Providing Alternate Parameterization through Docking Simulations 38
Resolving the Structure of Mutant Oncoproteins through Molecular Dynamics 38
Results 39
Activation of Wild-Type EGFRTK and L834R Mutant RTK 39
Ligand and Substrate Binding Affinities for EGFRTK 40
Differential Signaling through EGFRTK 41
Discussion 41
Acknowledgments 43
References 43

INTRODUCTION

The cancer phenotype may be viewed as a pathological dysregulation of cellular signals that control growth, survival, motility, cell–cell connectivity, and DNA synthesis and repair (Hanahan and Weinberg 2000). Generally speaking, the sources of dysregulation are an accumulated set of mutations that produce altered gene products. The interaction of these mutant oncoproteins with normal host signaling mechanisms perturbs proper signaling and confers the oncogenic behavior. For example, mutations affecting the catalytic activity, binding specificity, translation efficiency, or rate of degradation of an enzyme involved in DNA repair can predispose a cell to genomic instability by allowing replication of damaged genomic sequence (Zhivotovsky and Kroemer 2004). The specific identities and combinations of these cancer-causing mutations are known to vary considerably according to tissue and cell type and are strongly interdependent on the cellular/tumor microenvironment (Sjoblom, Jones, et al. 2006). In light of these complexities, mathematical models of cellular signaling networks have become indispensable tools for explaining oncogenic behaviors, predicting resistance mechanisms, and designing molecular therapies to attenuate defective signaling.

How can the altered activities of mutant oncoproteins be represented in a mathematical model? In many cases, wild-type and oncogenic signaling pathways share similar network structures but differ in the kinetic behavior and interaction topologies of only a few oncoproteins (Sharma and Settleman 2007). Unless these differences are resolved quantitatively, one cannot distinguish between normal and cancerous signaling networks in a mathematical model. Moreover, when attempting to resolve such crucial but subtle differences, it may be necessary to switch from a systems perspective of protein interaction networks to a molecular perspective of enzyme activation and protein–protein interaction. This chapter describes an approach for constructing models of intracellular signaling networks in which the oncogenic behavior of the network is encoded through calculations of altered kinetic and structural properties of mutant oncoproteins. Using molecular dynamics and docking simulations, atomistic models are exploited to quantify altered topologies of interactions as well as to provide the missing parameters for network models of both wild-type and oncogenic signaling. The global behavior of these networks may then be compared and functional roles may be assigned to the mutant oncoproteins. An application of this multiscale, multiresolution approach is presented in which structural alterations found in a mutant form of the epidermal growth factor receptor are represented as kinetic perturbations in a model of growth factor signaling. Based on network parameters estimated from molecular-level simulations, simulations at the network level show how small perturbations in molecular structure can lead to a profoundly altered cellular phenotype.

MODEL

A multiscale, multiresolution approach can be devised by encompassing four distinct length/time scales:

- Molecular modeling using Newton's equations: Based on a Hamiltonian $H(r_1,r_2,\ldots) = K + U$; r_i = atomic coordinates, K = kinetic energy, and U = Potential energy, we solve the system of equations (where F_i = Force, m_i = mass, t = time),

$$F_i = -\nabla U = m_i d^2 r_i / dt^2 \tag{2.1}$$

- Electronic structure using mixed quantum mechanics molecular mechanics simulations: We variationally minimize the energy function E,

$$E = \langle \varphi | H | \varphi \rangle \text{ and } \langle \varphi | \varphi \rangle = 1 \tag{2.2}$$

where, the bra-ket (Dirac) notation $\langle \varphi | \varphi \rangle$ represents vector dot product and $\langle \varphi | H | \varphi \rangle$ represents the expectation value (Szabo and Ostlund 1996). In Equation 2.2, φ is the electronic wave function satisfying the Pauli's exclusion principle and $H = H_{electronic}$, that is, the electronic Hamiltonian. We then solve Newton's equations given by Equation 2.1 for the nuclear degrees of freedom with some forces derived from $H_{electronic}$.

- Coarse-grained models: Using a coarse-grained Hamiltonian, $H[\lambda(r_1, r_2)] = F[\lambda(r_1, r_2)]$, where F = free energy, λ = generalized/collective coordinate, we solve the generalized Langevin equation (Agrawal, Weinstein, et al. 2008),

$$d\lambda/dt = -M\delta F/\delta\lambda + \xi \qquad (2.3)$$

In Equation 2.3, M represents the mobility term, ξ represents random thermal force satisfying $\langle\xi\rangle = 0$, and $\langle\xi(0)\xi(t)\rangle = 2k_BTM\delta(t)$, where $\langle\rangle$ represents an ensemble average in the equilibrium ensemble, k_B = Boltzmann's constant, and T = temperature.

- Deterministic network models: As an average solution to the Langevin dynamics using F(λ = reaction coordinate) for transitions between reactant and product states of chemical species, we solve deterministic network models for signal transduction using rate laws based on mass-action kinetics.

Based on the aforementioned formulations, the linking of oncogenic signaling to molecular structure in a mathematical model can be achieved in three separate but interconnected modeling steps:

- Deterministic ordinary differential equations (ODE) models are used to represent both wild-type and oncogenic signaling networks that differ in a defined set of molecular species. The pair of networks must both contain the mutant or overexpressed oncoproteins as well as one or more "output" components that can be monitored to evaluate the oncogenic behavior of the system (e.g., a master transcriptional regulator controlling cell survival).
- Molecular docking is used to predict ligand binding in the absence of a ligand-bound crystal structure and functional affinity data. These free energy-based simulations are used to calculate a new set of mutant kinetic parameters based on altered molecular structure.
- Molecular dynamics simulations are used to characterize the structural properties of mutant gene products from an altered polypeptide sequence. These calculations rely on the availability of solved crystal structures and may involve homology modeling.

By integrating these three modeling regimes, the phenotypic differences that define mutant systems at the network level are encoded through fine-scale calculations of the structural and kinetic properties of mutant oncoproteins (Figure 2.1).

The multiscale strategy portrayed in Figure 2.1 is illustrated through a model of dysregulated growth signaling caused by a single amino acid substitution in the epidermal growth factor receptor (EGFR). EGFR is a receptor tyrosine kinase (RTK) that is commonly mutated or overexpressed in human cancers (Mendelsohn and Baselga 2000). A mutant form of the receptor, L834R, exhibits an altered pattern of autophosphorylation caused by differences in its physical structure, binding affinities, and catalytic behavior. These perturbed phosphorylation patterns lead to constitutive activation of certain survival pathways that predispose L834R mutants to uncontrolled growth (Choi, Mendrola, et al. 2007). Thus, the goal of this multiscale model will be to track changes in the cellular growth pathways as a result of structural alterations in the mutant receptor. Accomplishing this goal will require a consideration of the receptor's biophysical properties on an atomic scale as well as its interaction with various binding partners and adaptor proteins.

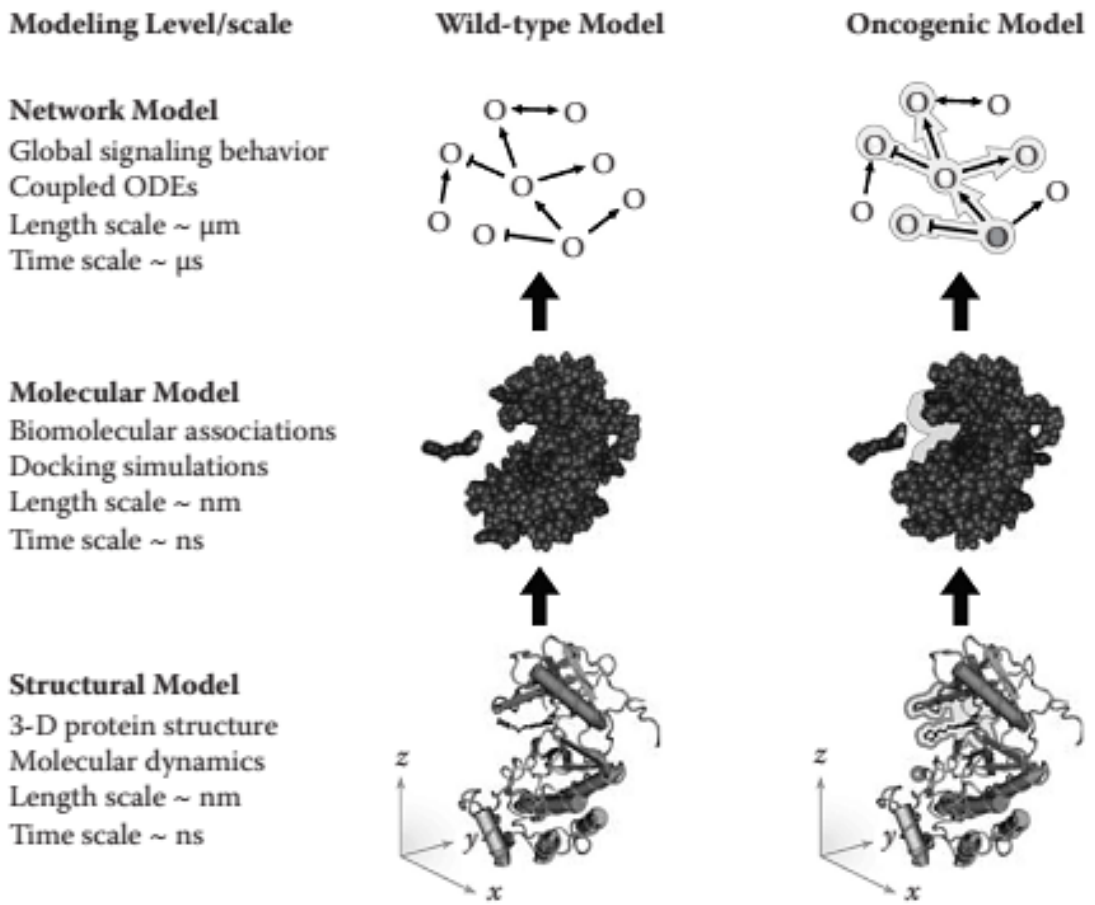

FIGURE 2.1 Overview of multiscale modeling method for linking molecular structure to oncogenic signaling. The aberrant signaling behavior of oncogenic networks is captured by monitoring the behavior of altered network models, typically ODE reaction networks. Alternate parameterization for the models is provided by docking simulations of mutant oncoproteins, which relies on structural models of the mutant proteins. Structural information is ultimately connected to mutations in genomic sequence. An example of oncogenic signaling behavior caused by altered structural and kinetic properties in a mutant of the epidermal growth factor receptor is presented in the text.

Constructing Mechanistic Models of Oncogenic Signaling

Kinetic models of cellular signaling pathways represent the highest level of modeling in this approach and are used to monitor the global behavior of both wild-type and mutant systems (Figure 2.1). Ordinary differential equations (ODEs) are used to represent coupled kinetic reactions that describe the rates of production and consumption of species in the model (Aldridge, Burke, et al. 2006). For large networks that contain species with posttranslational modifications or multiple binding partners, rules-based modeling (Hlavacek, Faeder, et al. 2006) provides the best method of generating ODEs that encode these kinetic differences.

In the signaling network presented here (Figure 2.2), EGF-induced activation of EGFR occurs through two parallel phosphorylation pathways corresponding to tyrosine 1068 (Y1068) and tyrosine 1173 (Y1173). Phosphorylated Y1068 (pY1068) binds only to the adaptor proteins Gab-1 and Grb2, while phosphorylated Y1173 (pY1173) binds only to the adaptor Shc. The major downstream pathways include EGF-ERK via the Ras-Raf MAP-kinase cascade (Citri and Yarden 2006), and the PI3K-AKT pathway, which results in the activation of the downstream protein—serine/threonine kinase AKT. In choosing the scope of a network, it is important to include one or more species that serve as indicators of the oncogenic potential of the system. Here, we include both AKT and ERK because they are well-studied indicators of EGFR-mediated growth and survival behaviors (Citri and Yarden 2006).

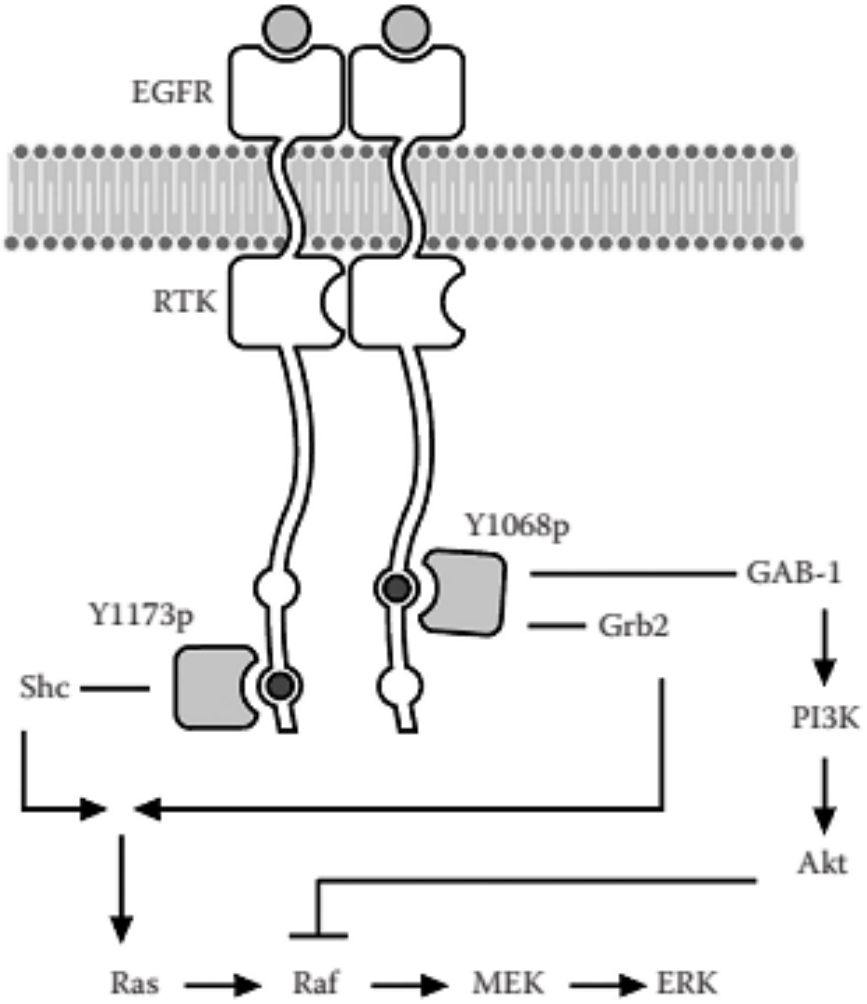

FIGURE 2.2 Network model of EGFR-mediated signaling used in this study. Phosphorylation of the EGFR dimer occurs at either Y1068, which can bind GAB-1 or Grb2, or at Y1173, which binds Shc. Activation of downstream proteins AKT and ERK was used as indicators of cell survival signaling. Multiscale modeling is achieved by calculating changes in dimerization, peptide binding affinity, and phosphorylation in structural mutants of the receptor.

The critical step in distinguishing wild-type and mutant signaling models is defining kinetic differences between the systems. Differences between the wild-type EGFR and L834R models are marked in Table 2.1 and include reactions affecting receptor dimerization, phosphorylation, and peptide binding. Rather than write each reaction equation separately, "reaction rules" (Hlavacek, Faeder, et al. 2006) are used to define general types of interactions between functional domains among the species in the model. For example, the rate constant k_7 in Table 2.1 that describes the catalytic turnover of Y1068 phosphorylation is applied to all forms of the receptor that participate in this phosphorylation reaction (e.g., monomer, dimer, ATP-bound). In this way, rules-based modeling ensures efficient and accurate construction of ODE-based signaling models.

TABLE 2.1 Reaction rules for two-site phosphorylation model of the EGF receptor

Event	Reaction rule	Forward	Reverse
Ligand/receptor binding	egfr(l) + egf(r) ↔ egfr(l!1).egf(r!1)	k_1	k_{-1}
Ligand-induced receptor dimerization	egfr(l!1,r) + egfr(l!2,r) ↔ egfr(l!1,r!3).egfr(l!2,r!3)	k_2*	k_{-2}
Spontaneous receptor dimerization	egfr(r) + egfr(r) ↔ egfr(r!1).egfr(r!1)	k_3*	k_{-3}†
Receptor/ATP binding	egfr(r!+,k) + ATP(r) ↔ egfr(r!+,k!1).ATP(r!1)	k_4	k_{-4}†
Y1068 entering active site	egfr(y1068~u) ↔ egfr(y1068~b)	k_5	k_{-5}†
Y1173 entering active site	egfr(y1173~u) ↔ egfr(y1173~b)	k_6	k_{-6}†
Autophosphorylation of Y1068	egfr(r!1,y1068~b).ADP → egfr(r!1,y1068~p) + ADP	k_7†	
Autophosphorylation of Y1173	egfr(r!1,y1173~b).ADP → egfr(r!1,y1173~p) + ADP	k_8†	
Dephosphorylation of Y1068	egfr(y1068~p) + phos → egfr(y1068~u)	V_9	K_9
Dephosphorylation of Y1173	egfr(y1173~p) + phos → egfr(y1173~u)	V_{10}	K_{10}

Note: The 10 rules generate 328 species and 3324 half-reactions representing all possible molecular intermediates and reaction steps. For simplicity, reaction rules for adaptor protein binding, MAP kinase cascade, and ERK/AKT activation are not shown.

* Denotes $k_2 = k_3$ because the on-rate of dimerization is diffusion limited.

† Denotes rate constants k_{-3}, k_{-4}, k_{-5}, k_{-6}, k_7, and k_8 are each affected by mutation L834R

! Denotes the site of association for two molecules. For example, egfr(l!1).egf(r!1) are bound through "l" and "r" sites on egfr and egf, respectively.

Providing Alternate Parameterization through Docking Simulations

Once the network has been defined and the mutant oncoproteins identified, molecular docking is used to predict ligand binding in the absence of a ligand-bound crystal structure and functional affinity data. Thus, docking simulations provide the missing parameters that characterize the mutant system. Automated docking tools such as AutoDock (Morris, Goodsell, et al. 1998) in combination with more accurate approaches such as free-energy perturbation may be used to predict how small molecules, such as substrates or drug candidates, bind to a receptor of known three-dimensional structure. The binding free energy is calculated based on the intermolecular energy between protein and ligands and changes to the solvation environment. For the EGFR/L834R model, binding modes were determined for ATP as well the C-terminal peptides Y1068 and Y1173 to the catalytic site. A global conformational search was performed using a multiple conformation docking strategy, in which the protein flexibility is taken into account implicitly. Note that rules-based modeling (Hlavacek, Faeder et al. 2006) facilitates the reuse of kinetic parameters calculating through docking simulations.

Resolving the Structure of Mutant Oncoproteins through Molecular Dynamics

In order to perform docking simulations, it is necessary to acquire accurate structural information about the molecules involved. In the EGFR/L834R model, we model the receptor activation characteristics (whether active as a monomer or requires dimerization) of the EGFR receptor tyrosine kinase using molecular dynamics simulations. 10–30 ns trajectories of atomistic and explicitly solvated systems of wild-type and mutant EGFR kinase monomers and dimers are obtained and analyzed for specific stabilizing interactions such as hydrogen bonds and salt bridges, hydrophobic interactions, and conformational changes.

RESULTS

Modeling the EGFR at the network, molecular, and structural levels allows one to determine how point mutations in the EGFR receptor can alter signaling characteristics leading to the onset of oncogenic transformations. The model was constructed in "top-down" fashion, beginning with identical signaling networks that were differentiated by a defined set of mutant oncoproteins. We now examine the effects of these differences in reverse order, beginning with structural alterations in the tyrosine kinase domain and proceeding to observe how these perturbations affect both receptor kinetics and network behavior.

Activation of Wild-Type EGFRTK and L834R Mutant RTK

Crystal structures of the EGFRTK suggest that the conformational switching from an inactive to an active conformation involves a rotation of the αC-helix and the shifting of the activation loop (A-loop) to make way for substrate peptide (harboring the tyrosine residue) and ATP binding. To assess the structural requirements for such a conformational shift, analyses of bond patterns and hydrophobic interactions were performed to identify specific interactions (H-bonds and salt bridges) between residues of the αC-helix, and those of the A-loop needed to reorganize the enzyme and allow conformational switching from inactive to active states. Most of the stabilizing interactions holding the kinase in the inactive conformation are influenced by the dimer-interface residues, supporting an allosteric activation mechanism proposed for the wild-type (Zhang, Gureasko, et al. 2006). Many of these interactions overlap with the residues associated with several clinically relevant mutations, including L834R. The R substitution of L at 834 destabilizes the specific (external H-bonds) interactions associated with A-loop and αC-helix in the inactive but not the active conformations. Thus, our analysis of stabilizing interactions presented in Figures 2.3a and 2.3b serves as a platform for unifying the effects of these mutations at a structural level. An important outcome of these simulations is the notion that the mutant receptor can be active (and thus mediate signaling) even as a monomer, that is, in the absence of any growth factor binding. This establishes a small but crucial variation in network topology between the wild-type and the mutant systems.

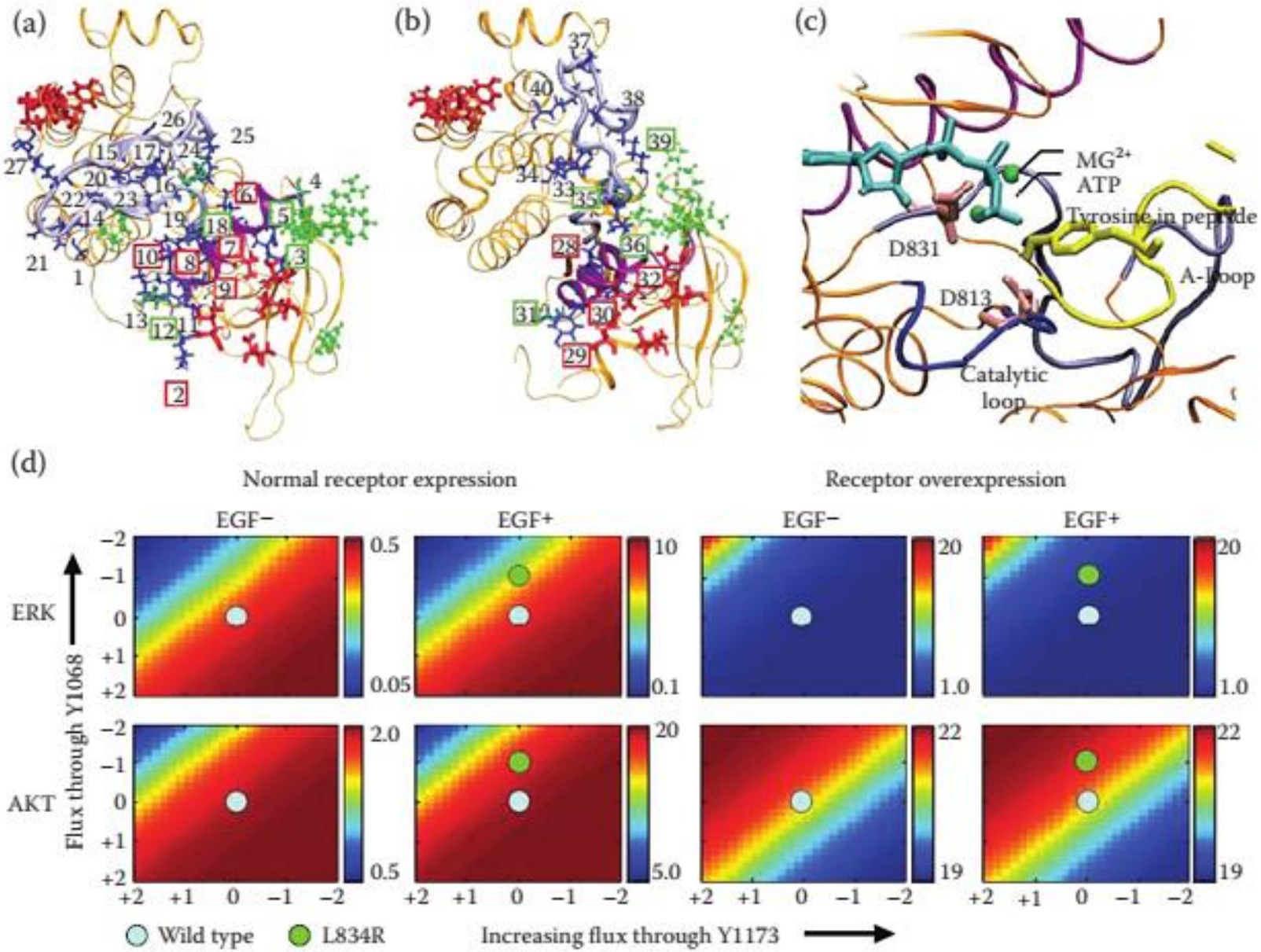

FIGURE 2.3 **(See Figure caption on page 40)**

FIGURE 2.3 **(See color insert following page 40)** Structural, kinetic, and network analysis of the effect of L834R mutation in the EGFRTK. Visualization of the stabilizing residues external to A-loop and αC-helix (*blue*), dimer interface residues (*red*), and clinical mutations (*green*) of both the active (*a*) and inactive (*b*) EGFR tyrosine kinases. (*c*) Binding modes for ATP (*cyan*) and the optimal peptide sequence (*yellow*) in the EGFRTK domain. (*d*) Calculated ERK and AKT phosphorylation levels in units of nM (peak-levels over an 1800 s time course) under serum-starved (EGF–) and serum-cultured (EGF+) conditions for cell types with normal EGFR expression and EGFR overexpression. The *x*- and *y*-axes represent log changes in the binding affinity (K_D) of the peptide relative to the wild type.

Ligand and Substrate Binding Affinities for EGFRTK

The structural basis for the context-specific kinetics of the C-terminal tyrosine substrates is provided by our computational docking calculations (Liu, Purvis, et al. 2007). Substrate peptides derived from tyrosine sites of the EGFR C-terminal tail—Y1068 (VPEYINQ) and Y1173 (NAEYLRV)—bound to the wild-type and the L834R mutant EGFR kinase revealed how the structure of the bound peptide–protein complex is altered at the catalytic site due to the arginine substitution of leucine in L834R (Figure 2.3c). By employing this method, we computed the binding affinities for wild-type and L834R mutant RTK binding to two peptide sequences consisting of Y1068 and Y1173. These calculations, reported in Table 2.1, are used to parameterize the reactions involving inhibitor binding and substrate phosphorylation in the systems model.

Differential Signaling through EGFRTK

To examine the effects of signaling through Y1068 and Y1173 on the downstream response, a series of 15 min simulations were performed for wild type and mutants under different initial conditions (varying [EGF] and [EGFR]) and monitoring the resulting total phosphorylated ERK and AKT responses (Figure 2.3d). A two-dimensional scan over K_D values associated with Y1068 and Y1173 phosphorylation in which the respective K_D values are allowed to deviate from their default (wild-type) value over a logarithmic range of 5 log units. This was achieved by adjusting k_{-5} and k_{-6} from Table 2.1. The result is a two-dimensional matrix in which each element represents the total ERK or AKT levels from a single simulation involving a unique pair of parameters. In Figures 2.3d and 2.3e each output state is quantified according to the peak level of phosphorylation over the simulated time of 1800 s.

As indicated by the color maps in these scans, the effect of altered affinities of the Y1068 and Y1173 sites to the catalytic domain of the EGFR is that the L834R under normal EGFR expression exhibits differential downstream response, that is, a pronounced decrease in ERK activation (5-fold) and relatively much smaller decrease AKT activation (15% decrease). Our calculated responses for ERK short-term signaling for normal EGFR expression (Figures 2.3d and 2.3e) agree with the experimental observations of Sordella et al. (Sordella, Bell, et al. 2004) and Tracy et al. (Tracy, Mukohara, et al. 2004), who have also reported a pronounced decrease in activated ERK to AKT ratio for the L834R mutant. These results suggest that preferential activation of AKT in L834R could be one of the factors leading to enhanced AKT activation observed in non-small-cell lung cancer cell lines.

DISCUSSION

While the genetic basis of cancer is well appreciated, the resulting complexity in intracellular signaling mechanisms relevant for the conquest of this disease resides at multiple levels of organization, ranging from the subatomic realm involving mutations in individual protein domains to the cellular level of macromolecular assemblies and membrane processes. Relating cancer genotypes to disease phenotypes will be aided by the development of specialized modeling tools to treat the hierarchy of interactions

ranging from molecular (nm, ns) to signaling (μm, ms) length and time scales. By introducing increased resolution in phosphorylation kinetics at the receptor level, the network model of EGFR-mediated signaling in wild-type and mutant cells showed how mutant forms of the receptor use an irregular pattern of tyrosine phosphorylation that preferentially activates the survival oncoprotein, AKT.

Recently, this type of multiscale analysis was used to explain why certain networks respond to antitumor tyrosine kinase inhibitors (TKIs) such as erlotinib and gefitinib (Purvis, Ilango, et al. 2008; Shih, Purvis, et al. 2008). Specifically, the branched signaling model was employed to analyze the inhibitory effects of the TKI erlotinib on EGFR phosphorylation and downstream ERK and AKT activation. The results provided a mechanistic basis for the enhanced inhibitor efficacy in mutant cell lines.

Thus, collectively, our results suggest that the clinically identified mutations of the EGFR kinase induce fragility in the stabilizing interactions of the inactive kinase conformation, providing a persistent stimulus for kinase activation even in the absence of any growth factor. At a cellular level, perturbations driving network hypersensitivity through the enhancement of phosphorylated ERK and AKT levels show a striking correlation with observed mutations of specific proteins in oncogenic cell lines as well as the observed mechanisms of drug resistance to EGFR inhibition. Therefore, we suggest that cascading mechanisms of network hypersensitivity/fragility at multiple scales enable molecular-level perturbations (clinical mutations) to induce oncogenic signaling. Moreover, our results describe a possible mechanism for preferential AKT activation in non-small-cell lung cancer lines harboring EGFR activating mutations. This preferential activation of a survival factor makes theses cell lines conducive to pathway addiction, that is, reliance on the L834R EGFR-mediated generation phosphorylated AKT for survival signals. The survival pathway addiction also results in a remarkable sensitivity to TKIs targeting the EGFR kinase.

The computational tools described here are ideal for assessing the likely effect of novel EGFR and HER2 mutations and determining whether the drug-sensitizing mutations implicated in non-small-cell lung cancer also occur in other cancers. Such approaches can also be employed effectively to address the issue of drug resistance to TKI therapy, which in the case of non-small-cell lung cancers is either mediated by point mutations in EGFR kinase (T790M) or the overexpression of HER3 and Met receptors and to investigate other molecular therapeutics targeting for (e.g., VEGF

and c-Met). Ultimately, these approaches could be used to optimize the development of small molecule inhibitor therapies.

The multiscale modeling approach illustrated in this chapter enables the incorporation of the molecular context and variability and their impact on intracellular signaling pathways of oncogenic relevance and subsequent cell-fate decisions. This approach also enables the rationalization and prediction of the role and nature of molecular variability in malignant transformed cells as well as drug-sensitive/drug-resistant cells by bridging the gap between molecular resolution/context and intracellular signaling. The approach employed here can be seamlessly integrated with subcellular resolution modeling in agent-based models emphasized in other chapters (see Chapter 9).

ACKNOWLEDGMENTS

We thank Mark Lemmon for valuable input. This work was funded in part by the National Science Foundation and the National Human Genome Research Institute. Computational resources were provided in part by the National Partnership for Advanced Computational Infrastructure.

REFERENCES

Agrawal, N., J. Weinstein, et al. (2008). Landscape of membrane-phase behavior under the influence of curvature-inducing proteins. *Mol. Phys.* 106: 1913–1923.

Aldridge, B. B., J. M. Burke, et al. (2006). Physicochemical modelling of cell signalling pathways. *Nat. Cell Biol.* 8(11): 1195–203.

Choi, S. H., J. M. Mendrola, et al. (2007). EGF-independent activation of cell-surface EGF receptors harboring mutations found in gefitinib-sensitive lung cancer. *Oncogene* 26(11): 1567–76.

Citri, A. and Y. Yarden (2006). EGF-ERBB signalling: towards the systems level. *Nat. Rev. Mol. Cell Biol.* 7(7): 505–16.

Hanahan, D. and R. A. Weinberg (2000). The hallmarks of cancer. *Cell* 100(1): 57–70.

Hlavacek, W. S., J. R. Faeder, et al. (2006). Rules for modeling signal-transduction systems. *Sci. STKE* 2006(344): re6.

Liu, Y., J. Purvis, et al. (2007). A multiscale computational approach to dissect early events in the Erb family receptor mediated activation, differential signaling, and relevance to oncogenic transformations. *Ann. Biomed. Eng.* 35(6): 1012–25.

Mendelsohn, J. and J. Baselga (2000). The EGF receptor family as targets for cancer therapy. [Review] [155 refs]. *Oncogene* 19(56): 6550–65.

Morris, G. M., D. S. Goodsell, et al. (1998). Automated docking using a Lamarckian genetic algorithm and an empirical binding free energy function. *J. Computational Chem.* 19(14): 1639–1662.

Purvis, J., V. Ilango, et al. (2008). Role of network branching in eliciting differential short-term signaling responses in the hypersensitive epidermal growth factor receptor mutants implicated in lung cancer. *Biotechnol. Prog.* 24(3): 540–53.

Sharma, S. V. and J. Settleman (2007). Oncogene addiction: setting the stage for molecularly targeted cancer therapy. *Genes Dev.* 21(24): 3214–31.

Shih, A. J., J. E. Purvis, et al. (2008). Molecular systems biology of ErbB1 signaling: bridging the gap through multiscale modeling and high-performance computing. *Mol. BioSyst.* 4(12): 1151–1159.

Sjoblom, T., S. Jones, et al. (2006). The consensus coding sequences of human breast and colorectal cancers. *Science* 314(5797): 268–274.

Sordella, R., D. W. Bell, et al. (2004). Gefitinib-sensitizing EGFR mutations in lung cancer activate anti-apoptotic pathways. *Science* 305(5687): 1163–7.

Szabo, A. and N. S. Ostlund (1996). *Modern Quantum Chem*. Mineola, New York, Dover Publications.

Tracy, S., T. Mukohara, et al. (2004). Gefitinib induces apoptosis in the EGFRL858R non-small-cell lung cancer cell line H3255. *Cancer Res.* 64(20): 7241–4.

Zhang, X., J. Gureasko, et al. (2006). An allosteric mechanism for activation of the kinase domain of epidermal growth factor receptor. *Cell* 125(6): 1137–49.

Zhivotovsky, B. and G. Kroemer (2004). Apoptosis and genomic instability. *Nat. Rev. Mol. Cell Biol.* 5(9): 752–62.

ΓΕΝΙΚΗ ΠΟΛΥΚΛΙΜΑΚΩΤΗ ΠΡΟΣΟΜΟΙΩΣΗ ΑΣΘΕΝΕΙΩΝ ΚΑΙ *IN SILICO* ΙΑΤΡΙΚΗ

A Quantitative Systems Pharmacology model of the nerve growth factor (NGF) pathway to aid drug discovery and development

Pinky Dua[a], Neil Benson[b,d] and Piet H. van der Graaf[c]
Pfizer/Neusentis, [a]Clinical Pharmacology, [b]PDM & [c]Pharmacometrics, Sandwich/Cambridge & [d]XenologiQ, Canterbury, UK

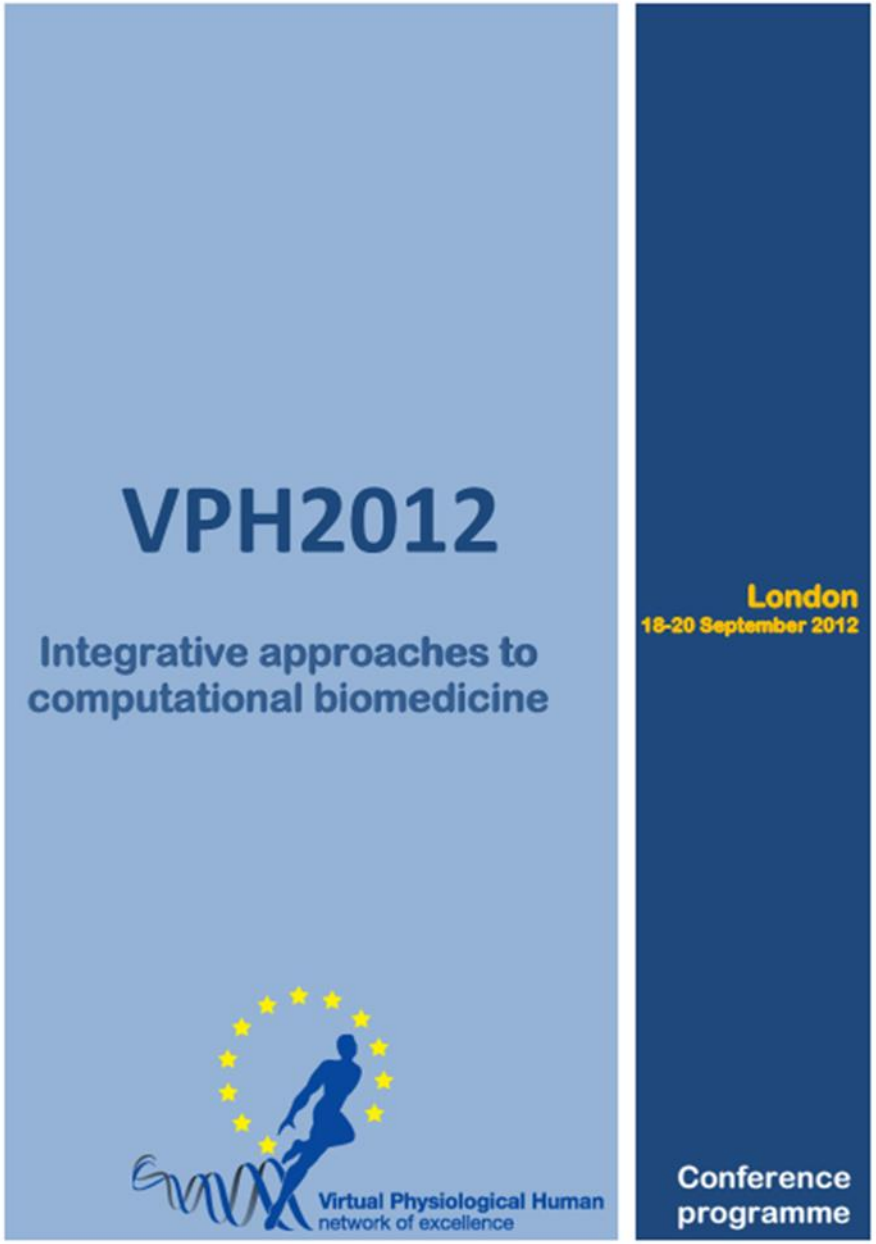
VPH2012
Integrative approaches to computational biomedicine
London
18-20 September 2012
Virtual Physiological Human
network of excellence
Conference programme

PROCEEDINGS-VPH2012_INTEGRATIVE_APPROACHES_TO_COMPUTATIONAL_BIOMEDICINE-LONDON_CONF_2012.pdf PAGE **281**/488 (PLEASE USE THE PDF PAGE COUNTER)

A Quantitative Systems Pharmacology model of the nerve growth factor (NGF) pathway to aid drug discovery and development

Pinky Dua[a], Neil Benson[b,d] and Piet H. van der Graaf[c]
Pfizer/Neusentis, [a]Clinical Pharmacology, [b]PDM & [c]Pharmacometrics, Sandwich/Cambridge & [d]XenologiQ, Canterbury, UK

The NGF pathway is of great interest as a potential source of drug targets, for example in the management of certain types of pain. The biology of the NGF response has been studied over a number of years in great detail and the aim of this work was to integrate this knowledge in a Quantitative Systems Pharmacology (QSP) framework to guide drug discovery and development programs, in particular with regards to novel drug target identification, target validation, biomarker and biomeasure [1] selection, dose prediction and ultimately patient selection ("precision medicine").

In sensory neurons, NGF engages with its receptor known as tropomyosin receptor kinase A (TrkA) and following auto-phosphorylation, the NGF:TrkA complex is internalised and trafficked to the neuronal cell bodies. Here it is then thought to cause an accumulation of diphosphorylated extracellular signal regulated kinase (dppERK) in the nucleus and subsequently the expression of numerous genes related to neuronal survival and pain sensation. Arguably the dppERK concentration could therefore be regarded as a biomarker of pain response. Two Systems Biology models for describing the events leading to dppERK migration [2] and nuclear-cytoplasmic shuttling of ERK [3] were coupled resulting in an ordinary differential equation model comprising 59 molecular species and 233 parameters. To facilitate the evaluation of drugs with diverse molecular properties from small molecules to monoclonal antibodies, this 'systems biology' model was converted into a more physiologically realistic integrated QSP model by expressing it in three inter-connected compartments representing the neuronal, interstitial fluid and plasma compartments (Scheme 1) with the signal transduction reactions expressed in the neuronal compartment. The model was calibrated using in-house and external preclinical and clinical data. All analyses were performed using Simbiology 2011b (Matlab, Natick, USA).

Using sensitivity analysis it was concluded that after NGF itself, TrkA was one of the most sensitive druggable targets (**target selection**). With the focus on TrkA, the model was then used to explore the characteristics required for a successful hypothetical TrkA inhibitor (**target validation**) relative to a monoclonal antibody. Thereafter, using in house pharmacokinetic (PK) and equilibrium binding constant data (K_i) data, the model was used to provide **dose predictions** for new entities, as a complement to data from animal models of 'disease'and *in vitro* assays.

We concluded that a hypothetical drug with typical PK and pharmacological characteristics could significantly inhibit the NGF pathway signalling at conceivable plasma concentrations and doses. However, the model also raised the caveat that the TrkA concentration strongly influenced the observed response and potentially the conclusions. Hence, TrkA concentrations were experimentally determined in a range of cell types including a mammalian neuronal cell line. We found that levels varied markedly between cell types, highlighting the need for a reliable estimate in a relevant human cell type. QSP models incorporating such biomeasure data could be of great utility at all stages in drug discovery and development.

Scheme 1.

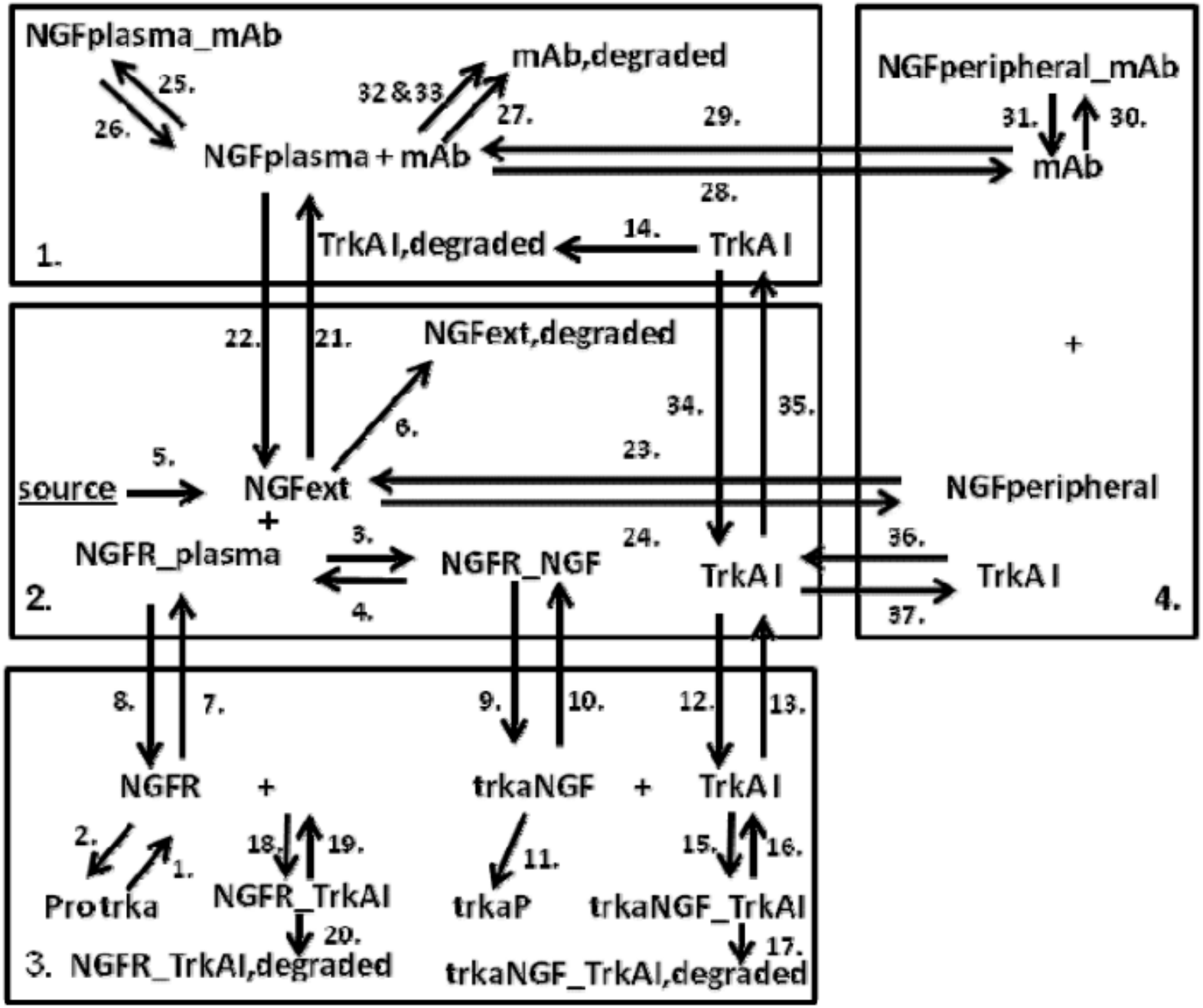
NGFplasma_mAb
mAb,degraded
NGFperipheral_mAb
25.
26.
32 &33
27.
29.
31.
30.
NGFplasma + mAb
mAb
28.
14.
TrkA I,degraded
TrkA I
1.
22.
21.
NGFext,degraded
+
34.
35.
6.
5.
23.
source
NGFext
NGFperipheral
+
3.
24.
36.
NGFR_plasma
NGFR_NGF
TrkA I
TrkA I
2.
4.
37.
4.
8.
7.
9.
10.
12.
13.
NGFR
+
trkaNGF
+
TrkA I
2.
1.
18.
19.
11.
15.
16.
Protrka
NGFR_TrkAI
trkaP
trkaNGF_TrkAI
20.
17.
3. NGFR_TrkAI,degraded
trkaNGF_TrkAI,degraded

Scheme 1. (1) refers to compartment 1 the plasma compartment of 3.35L. (2) is the interstitial fluid compartment (12L) (3) is the neuronal intracellular compartment (0.001L) and (4) is a peripheral compartment (2.85 L). I refers to a Mg.ATP non-competitive inhibitor of TrkA kinase and is assumed to be in rapid equilibrium between the compartments.

References:

[1] Van der Graaf P & Benson N (2011) Pharm. Res. 28, 1460-1464
[2] Sasagawa S *et al.* (2005) Nature Cell Biol. 7, 365-372
[3] Fujioka A *et al.* (2006) J. Biol. Chem. 281, 8917-8926

Ευχαριστώ